$$\frac{1}{|\mathbf{r}-\mathbf{r}'|} = \frac{\mathrm{erf}(\omega(\mathbf{r})|\mathbf{r}-\mathbf{r}'|)}{|\mathbf{r}-\mathbf{r}'|} + \frac{1-\mathrm{erf}(\omega(\mathbf{r})|\mathbf{r}-\mathbf{r}'|)}{|\mathbf{r}-\mathbf{r}'|}$$

$$E_{\mathrm{x}}^{\mathrm{lr,ex}} = -\sum_{i,j} \int \mathrm{d}\mathbf{r} \int \mathrm{d}\mathbf{r}' \phi_i(\mathbf{r})\phi_j(\mathbf{r}') \frac{\mathrm{erf}(\omega(\mathbf{r})|\mathbf{r}-\mathbf{r}'|)}{|\mathbf{r}-\mathbf{r}'|} \phi_i(\mathbf{r}')\phi_j(\mathbf{r})$$

$$\omega(\mathbf{r}) = \frac{\sqrt{5}}{18} \frac{|\nabla n(\mathbf{r})|}{n(\mathbf{r})} \frac{1}{1-\frac{1}{2}\left(z(\mathbf{r}) + z(\mathbf{r})\zeta^2(\mathbf{r})\right)}$$

Moritz Brütting

Electronic Properties of Light-Harvesting Systems: The Reaction Center of Heliobacteria and Hybrid Functionals with Local Range Separation

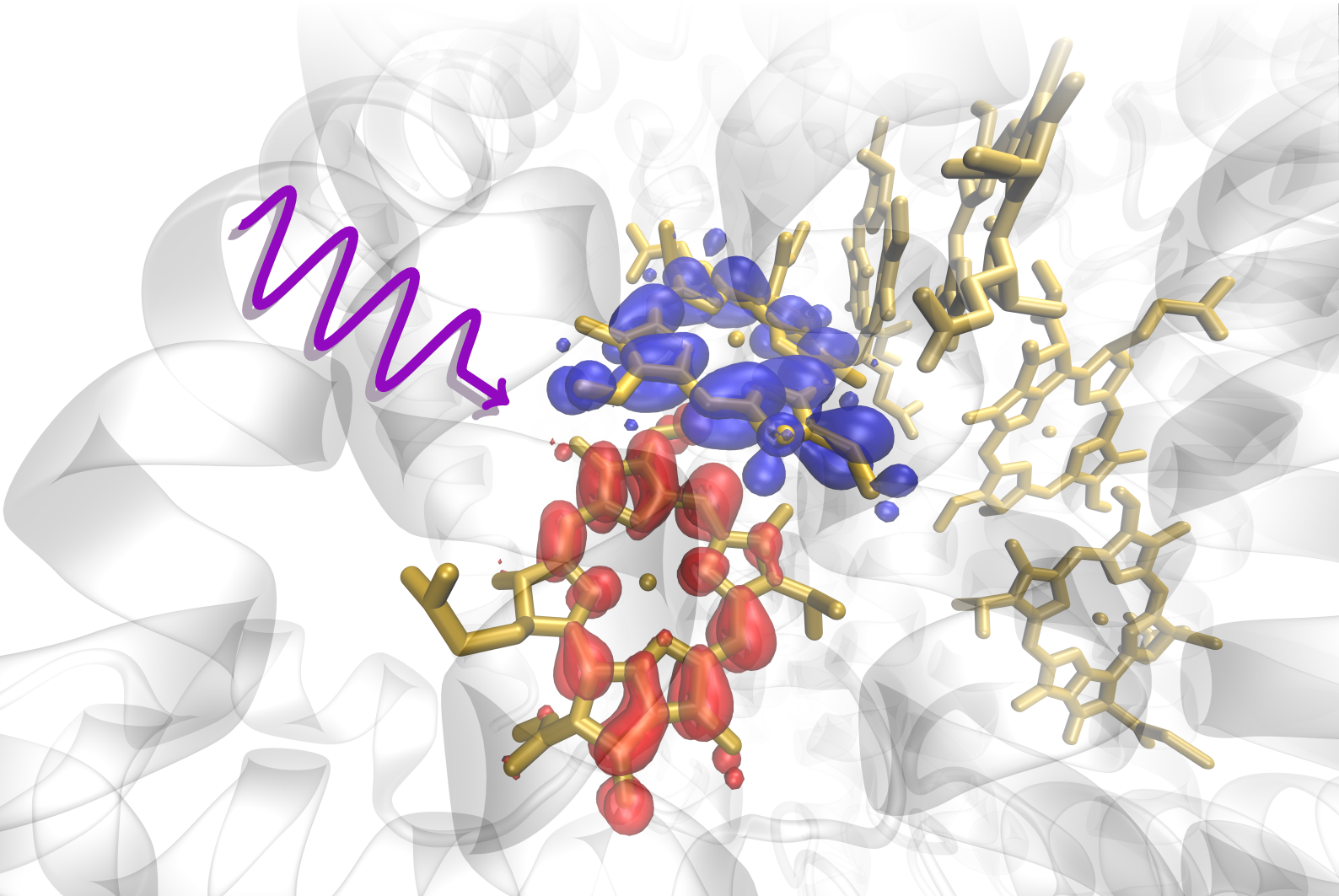

Electronic Properties of Light-Harvesting Systems: The Reaction Center of Heliobacteria and Hybrid Functionals with Local Range Separation

Von

Moritz Brütting

aus Bayreuth

Von der

Universität Bayreuth

zur Erlangung des Grades eines

Doktors der Naturwissenschaften (Dr. rer. nat.)

genehmigte Abhandlung

1. Gutachter: Prof. Dr. Stephan Kümmel
2. Gutachter: Prof. Dr. Stephan Gekle
3. Gutachter: Prof. Dr. Martin Kaupp

Tag der Einreichung: 24. Januar 2025
Tag des Kolloquiums: 15. Mai 2025

Contents

Abstract

Being able to predict the electronic properties of light-harvesting systems remains a major challenge for theoretical methods. A widely used method for the description of electronic structure and dynamics that comes at affordable computational effort is (time-dependent) density functional theory. Therein, electronic excitations can often be predicted reliably using range-separated hybrid functionals in the generalized Kohn-Sham framework. Especially, if the range-separation parameter is determined by optimal tuning, these functionals are equipped with true predictive power. Using this methodology, we perform first-principles calculations on the charge-separation process in the heliobacterial reaction center. This system has unique structural features and may provide insights into the evolution of photosynthesis. Primary charge separation is expected to proceed in a two-step mechanism along either of the two reaction center branches. Our results indicate that in the first charge-separation step, the electron is localized on the third cofactor and the hole on the second cofactor. To unravel the mechanisms that lead to efficient charge separation, we analyze the impact of the surrounding protein environment extensively. Furthermore, we include the effect of structural changes by diligently conducted Born-Oppenheimer molecular dynamics simulations. This reveals that a distinct structural mechanism is decisive for the relative energetic positioning of the electronic excitations: The energies of the charge-transfer excitations are specifically adjusted by the interaction with a small group of charged amino acids, lowering them with respect to the non-charge-transfer bright excitations. These results shed light on the microscopic origin of efficient charge separation in light-harvesting systems.

Challenging computational studies, such as ours on the heliobacterial reaction center, can reach the limits of optimal tuning due to the very different length scales and electronic properties of the constituents involved. Therefore, in this work, we consider the novel approach of hybrid density functionals with local range separation where the constant range-separation parameter is turned into a density functional. Formally, this can be motivated by the concept of coupling-constant integration. The construction of locally range-separated hybrid functionals can be guided by formal constraints such as the homogeneous and slowly varying density limits, the correct scaling to exact exchange in the high-density limit, and freedom from one-electron self-interaction errors. First, we explore the description of electronic binding properties. We show that a transparent functional form can lead to very accurate results for test sets of atomization energies and reaction barrier heights, and can compete with density functionals that contain multiple empirical parameters. Furthermore, we discuss the observable dilemma, i. e., the fact that hybrid functionals typically yield either a good description of binding energies or physically interpretable eigenvalues, in the

context of locally range-separated hybrid functionals. Especially, we explore the combination of the concepts of local range separation and local hybrids. Finally and most importantly, we construct a new hybrid functional with local range separation for spectroscopic purposes. The functional respects important constraints and closely approximates the piecewise linearity of the energy as a function of the particle number. As we demonstrate, this endows the eigenvalues with true physical meaning and the fundamental gap in generalized Kohn-Sham theory can be predicted with high accuracy for numerous systems, including organic semiconductors with a notoriously difficult electronic structure. This outcome is promising as well in view of future investigations of light-harvesting systems.

Zusammenfassung

Die Beschreibung der elektronischen Eigenschaften von lichtsammelnden Systemen ist und bleibt eine bedeutende Herausforderung für theoretische Methoden. Eine Methode zur Beschreibung der elektronischen Struktur und Dynamik, die mit vergleichsweise geringem numerischem Aufwand einhergeht, ist die (zeitabhängige) Dichtefunktionaltheorie. Unter Verwendung von reichweiten-separierten Hybridfunktionalen im Rahmen der generalisierten Kohn-Sham Theorie können elektronische Anregungen in vielen Fällen zuverlässig vorhergesagt werden. Insbesondere wenn der Parameter zur Reichweitenseparation mittels *optimal tuning* bestimmt wird, können diese Funktionale echte Vorhersagekraft entwickeln. Unter Verwendung dieser Methoden werden im Rahmen dieser Arbeit *first-principles* Rechnungen zur Ladungstrennung im Reaktionszentrum von Heliobakterien durchgeführt. Dieses System hat einzigartige Struktureigenschaften and kann Einsichten in den Evolutionsprozess der Photosynthese ermöglichen. Es wird erwartet, dass Ladungstrennung in einem zweistufigem Prozess entlang beider Zweige des Reaktionszentrums stattfindet. Die in dieser Arbeit erzielten Ergebnisse legen nahe, dass im ersten Schritt der Ladungstrennung das Elektron auf dem dritten Kofaktor und das Loch auf dem zweiten Kofaktor lokalisiert ist. Um die Mechanismen besser zu verstehen, die zu effizienter Ladungstrennung führen, wird der Einfluss der Proteinumgebung detailliert untersucht. Darüber hinaus wird der Effekt von Strukturveränderungen mittels besonders genauer und sorgfältig durchgeführter Born-Oppenheimer Molekulardynamik-Simulationen berücksichtigt. Dies zeigt, dass die relative energetische Positionierung der elektronischen Anregungen in entscheidender Weise durch einen ganz bestimmten Strukturmechanismus beeinflusst wird: Die Energien der Anregungen mit Ladungstransfercharakter werden spezifisch durch die Wechselwirkung mit einer kleinen Gruppe an geladenen Aminosäuren verändert, was dazu führt, dass deren Energien im Vergleich zu den hellen Anregungen ohne Ladungstransfercharakter abgesenkt werden. Diese Ergebnisse können Einsichten auf mikroskopischer Ebene in den Ursprung der effizienten Ladungstrennung in lichtsammelnden Systemen bieten.

Anspruchsvolle numerische Untersuchungen, wie eben jene, die in dieser Arbeit zum Reaktionszentrum von Heliobakterien durchgeführt werden, können aufgrund der sehr verschiedenen Größenskalen und elektronischen Eigenschaften der einzelnen Bestandteile die Grenzen dessen erreichen, was mit *optimal tuning* möglich ist. Darum wird im Rahmen dieser Arbeit der neuartige Ansatz der lokalen Reichweitenseparation in Hybridfunktionalen untersucht. Dabei wird der ursprünglich konstante Parameter zur Reichweitenseparation durch ein Dichtefunktional ersetzt. Mit dem Konzept der Kopplungskonstantenintegration kann dies auch formal motiviert werden. Bei der Konstruktion von Hybridfunktionalen mit lokaler Reichweitenseparation

können exakte Randbedingungen wie die Grenzfälle homogener und langsam veränderlicher Dichte, das korrekte Skalierungsverhalten im Hochdichtegrenzfall sowie die Freiheit von Einelektronen-Selbstwechselwirkungsfehlern wertvolle Anhaltspunkte bieten. Im ersten Schritt wird die Beschreibung von elektronischen Bindungseigenschaften untersucht. Dies zeigt, dass mit einer transparenten Funktionalform sehr genaue Ergebnisse für Bindungsenergien und Reaktionsbarrieren erreicht werden können. Die erreichte Genauigkeit ist vergleichbar mit der von Dichtefunktionalen, die auf zahlreichen empirischen Parametern beruhen. Darüber hinaus wird ein Observablendilemma, das sich darauf bezieht, dass Hybridfunktionale typischerweise entweder eine gute Beschreibung von Bindungsenergien oder physikalisch interpretierbaren Eigenwerten erreichen, im Kontext der Hybridfunktionale mit lokaler Reichweitenseparation diskutiert. Dabei wird insbesondere die Kombination von lokaler Reichweitenseparation mit lokalen Hybridfunktionalen untersucht. Schlussendlich und als besonders zentrales Ergebnis dieser Arbeit wird ein neues Hybridfunktional mit lokaler Reichweitenseparation für spektroskopische Anwendungen konstruiert. Dieses Funktional erfüllt wichtige exakte Randbedingungen und stellt eine gute Näherung an das abschnittsweise lineare Verhalten der Energie als Funktion der fraktionellen Teilchenzahl dar. Die erzielten Ergebnisse belegen, dass die Eigenwerte des Funktionals physikalisch interpretierbar sind und dass das neuentwickelte Funktional die *fundamental gap* in der generalisierten Kohn-Sham Theorie für eine große Zahl an Systemen, darunter organische Halbleiter mit einer besonders herausfordernden elektronischen Struktur, mit hoher Genauigkeit vorhersagen kann. Diese Ergebnisse sind insbesondere auch im Hinblick auf zukünftige Untersuchungen von lichtsammelnden Systemen vielversprechend.

Overview of publications

This cumulative dissertation is based on Publications [B1], [B2], [B3], [B4], and [B5], which are listed below in chronological order. Reprints are provided in the second part of this work from Page 119 onward. An overview of the results of each publication is given in the first part of this work in the sections specified below. In the following, we point out how the publications are related. All publications address the question of how the electronic properties of molecular systems – especially spectroscopy-related properties such as excitation energies – can be described by (time-dependent) density functional theory ((TD)DFT) using hybrid functionals with global or local range separation. Our work includes both methodological developments and application-oriented aspects of this question.

Publication [B1]

M. Brütting, J. M. Foerster, and S. Kümmel

Investigating primary charge separation in the reaction center of *Heliobacterium modesticaldum*

J. Phys. Chem. B **125**, 3468 (2021)

→ *Overview of results:* Section 4.3.1
→ *Reprint:* Page 119

Publication [B2]

M. Brütting, H. Bahmann, and S. Kümmel

Hybrid functionals with local range separation: Accurate atomization energies and reaction barrier heights

J. Chem. Phys. **156**, 104109 (2022)

→ *Overview of results:* Section 5.5.1
→ *Reprint:* Page 145

Publication [B3]

M. Brütting, J. M. Foerster, and S. Kümmel

Understanding primary charge separation in the heliobacterial reaction center

J. Phys. Chem. Lett. **14**, 3092 (2023)

→ *Overview of results:* Section 4.3.2
→ *Reprint:* Page 171

Publication [B4]

M. Brütting, H. Bahmann, and S. Kümmel

Predicting fundamental gaps accurately from density functional theory with non-empirical local range separation

J. Chem. Phys. **160**, 181101 (2024) *Rapid Communication*

→ *Overview of results:* Section 5.5.3
→ *Reprint:* Page 211

Publication [B5]

M. Brütting, H. Bahmann, and S. Kümmel

Combining local range separation and local hybrids: A step in the quest for obtaining good energies and eigenvalues from one functional

J. Phys. Chem. A **128**, 5212 (2024)

→ *Overview of results:* Section 5.5.2
→ *Reprint:* Page 229

Pubs. [B1] and [B3] contain our findings on the charge-separation process in the reaction center of heliobacteria. Using TDDFT calculations with an optimally tuned range-separated hybrid (RSH) functional and *ab initio* Born-Oppenheimer molecular dynamics simulations, we reveal the first charge-separation step and unravel distinct structural features that facilitate efficient charge separation. Pubs. [B2], [B4], and [B5] comprise the developments on hybrid functionals with local range separation. In Pub. [B2], we show that a transparent functional form can lead to an accurate description of electronic binding properties. Furthermore, we explore how well both electronic binding and properties related to spectroscopy can be described within a fixed functional form [B5]. Finally, based on these experiences, we construct a new hybrid functional with local range separation that leads to an accurate description of electronic excitations [B4].

Several important aspects connect both parts of this work: Some well-known failures of conventional RSH functionals with optimal tuning begin to appear in our calculations on the heliobacterial reaction center [B3]. In that respect, the progress made on local range separation is promising. Our newly developed spectroscopic functional [B4] may serve as a remedy in such applications, as it does not suffer from the shortcomings of optimal tuning. In particular, the calculations performed so far indicate that the level of accuracy achieved by our functional is comparable to (or even better than) optimal tuning and that our functional can cope with scenarios that are outside where optimal tuning is usually applied. Thereby, the increase in computational cost is expected to be moderate in the final, fully optimized implementation. However, due to limitations of the implementation at its current stage, it is beyond the scope of the present work to apply the new spectroscopic functional to systems with a size comparable to light-harvesting systems. Apart from that, the need for a functional

that is able to describe both electronic binding and spectroscopic properties at the same level of accuracy – an issue that we take up in our work on local range separation – manifests itself in the context of light harvesting when the coupling of nuclear and electronic dynamics is relevant. Overall, taking advantage of the potential of local range separation in applications on light-harvesting systems appears as a promising perspective of future work, and the present work constitutes an important step into this direction.

Background and Overview of results

1 Introduction

The importance of photosynthesis for life on earth can hardly be overestimated [1, 2]. It is the sole source of energy for most living organisms and – either directly or indirectly – provides most of the energy consumed by modern societies [3]. The formation of molecular dioxygen as a side product of oxygenic photosynthesis has led to the aerobic atmosphere we are living in today and allows for the aerobic respiration of heterotrophic organisms. Natural light harvesting is initiated by the absorption of incident solar radiation and the formation of an excited state [4]. Then, as one key step in the light-harvesting process, a charge-separated state is formed in the reaction center [5–8], leading to the electron and hole being localized on opposite sides of the photosynthetic membrane. These processes are accomplished by the fine-tuned interplay of one or several pigment-protein complexes integrated into the photosynthetic membrane. The efficiency with which light-harvesting complexes convert light into a charge-separated state even under adverse conditions is impressive [9]. Another striking feature of this process is that nature achieves this using an arrangement of identical or very similar chromophores. On the other hand, human-made devices for charge separation rely on donor and acceptor compartments with distinct electronic properties [10]. Thus, understanding the functional principles of natural light harvesting is a fascinating and worthwhile intellectual challenge, which can provide inspiration for the construction of human-made supramolecular structures for energy conversion [6, 11–14].

In principle, theoretical methods provide the tools to examine the underlying energy- and charge-transfer processes, and this can lead to valuable complementary insights due to (full) access to the nuclear and electronic dynamics. However, computational investigations can be a complicated task in practice. Typically, the relevant physical processes extend over an appreciable number of chromophores. These chromophores are integrated into a large protein complex, which itself is embedded into a membrane and surrounded by a solvent. Further effects, e. g., due to temperature, can influence the physics of the chromophores as well. These elements contribute to a different degree but, in principle, all of them need to be taken into consideration when building theoretical models [15–17]. Even if we neglect all the surroundings and just focus on the chromophores only, describing the electronic properties can be challenging due to the intricate nature of the excitations involved, e. g., when charge-transfer processes are relevant [18–20]. Therefore, practical calculations with true predictive power demand for a method that combines high accuracy with numerical efficiency.

A method for the description of electronic structure and dynamics that comes at moderate computational effort [21] is density functional theory (DFT) [22, 23] and its time-dependent variant (TDDFT) [24]. While this approach holds the promise of

being formally exact in principle, practical calculations require an approximation for the exchange-correlation energy. Thereby, the correct description of spectroscopically relevant features can be particularly challenging because several of the notorious failures of DFT have to be addressed to reach this goal [25]. This is to a certain extent a consequence of a fundamental aspect of DFT: In its (original) Kohn-Sham (KS) formulation, the many-electron problem is mapped onto a system of non-interacting particles that is inappropriate to mimic the many-body nature of electronic excitations [26]. These shortcomings can be alleviated by range-separated hybrid (RSH) functionals within the generalized KS formalism. The concept of non-empirical optimal tuning [27], which is specifically designed for spectroscopic purposes, equips these functionals with predictive power and often leads to reliable results for electronic excitations. In Chaps. 2 and 3 we introduce the central concepts of DFT, outline the challenges associated with the description of electronic excitations, and discuss how RSH functionals address these challenges.

Based on these methods, we examine the charge-transfer process in the reaction center of heliobacteria [28–31]. This system has unique structural properties and may provide insights into the evolution of photosynthesis [32–34]. Until recently, structural information has not been available and only little was known on the detailed mechanism of charge separation in this organism [35–37]. Using TDDFT calculations with an optimally tuned RSH functional and *ab initio* Born-Oppenheimer molecular dynamics [38, 39] simulations, we reveal the first charge-separation step. Importantly, we identify distinct structural features that are decisive for the energetic positioning of the charge-transfer excitations. The background and main results of our work on the heliobacterial reaction center are summarized in Chap. 4 and have been published in Pubs. [B1, B3].

Despite their achievements, common RSH functionals are far from being a panacea. Challenging computational studies, such as ours on the heliobacterial reaction center, can reach the limits of optimal tuning due to the very different length scales and electronic properties of the constituents involved [40, 41]. One way to overcome the limitations of optimal tuning is by going from global to local range separation, where the constant range-separation parameter is turned into an explicit functional of the density [42–45]. Formally, this can be motivated by the concept of coupling-constant integration that is central in understanding the physical motivation of hybrid functionals, which mix exact and semi-local exchange [46–49]. In particular, if the amount of exact exchange is no longer determined by a constant parameter but by a density functional, this changes qualitatively how the coupling-constant dependence is modelled. This might be a way to tackle a longstanding dilemma for hybrid functionals: Usually observables related to electronic binding, on the one hand, and electronic excitations, on the other hand, cannot be described at the same level of accuracy within a fixed functional form [41, 50–53]. This can be a serious limitation in practical calculations.

We pursue the novel concept of local range separation [45, 54–56] as part of this work. We show that local range separation can be a promising approach for the description

of electronic binding or spectroscopic properties, and we explore how well both types of properties can be described within a fixed functional form. In our approach, we are guided by a few, relevant constraints that we incorporate into transparent functional constructions. As a central result, we construct a new functional for spectroscopic purposes that yields very promising results for excitation gaps of a broad range of systems. Our work on local range separation is presented in Chap. 5 and has been published in Pubs. [B2, B4, B5]. Future computational studies of light-harvesting systems and other technologically relevant materials like organic semiconductors for efficient solar energy conversion [10], may benefit from advanced hybrid functional constructions with a flexible admixture of exact exchange as achieved via local range separation.

2 Fundamentals of density functional theory

Density functional theory (DFT) is a well-established framework to describe quantum-mechanical many-electron systems, and has become the workhorse of quantum chemistry and material science [22, 23, 57–61]. It is a reformulation of wavefunction quantum mechanics and builds upon the electron density instead of the wavefunction as the central variable. One major strength of DFT is that this reformulation is in principle exact. Second, it significantly reduces the computational cost, since it overcomes the infamous "exponential wall" that one is faced with when trying to solve the Schrödinger equation directly [21]. Third, its central object – the electron density – is a descriptive and intelligible variable with a clear physical interpretation. In the following, we summarize the most salient aspects of DFT.

The central pillar of DFT is the seminal work by Hohenberg and Kohn [62]. In one line, this theorem guarantees that the many-electron wavefunction $\Psi(\mathbf{r}_1, \ldots, \mathbf{r}_N)$ of an N-electron system (and, hence, any observable that can be calculated from it) is a unique functional of the ground-state electron density $n(\mathbf{r})$. Relevant within this work are systems that are specified by a Hamiltonian of the form,[1]

$$\hat{H} = \underbrace{-\frac{1}{2}\sum_{i=1}^{N}\nabla_i^2}_{=\hat{T}} + \underbrace{\frac{1}{2}\sum_{\substack{i,j=1\\ i\neq j}}^{N}\frac{1}{|\mathbf{r}_i-\mathbf{r}_j|}}_{=\hat{V}_{\mathrm{ee}}} + \underbrace{\sum_{i=1}^{N} v_{\mathrm{ext}}(\mathbf{r}_i)}_{=\hat{V}_{\mathrm{ext}}}, \tag{2.1}$$

where $\hat{T}$ corresponds to the kinetic energy, $\hat{V}_{\mathrm{ee}}$ to the Coulomb interaction between the electrons, and $\hat{V}_{\mathrm{ext}}$ to the external potential, e. g., due to the interaction of the electrons with the nuclei. Following the constrained search approach by Levy [63] the ground-state energy can be expressed as a two-step minimization procedure,

$$E = \min_{\tilde{n}}\left(\underbrace{\min_{\tilde{\Psi}\to\tilde{n}}\langle\tilde{\Psi}|\hat{T}+\hat{V}_{\mathrm{ee}}|\tilde{\Psi}\rangle}_{=F[\tilde{n}]} + \int \mathrm{d}\mathbf{r}\; v_{\mathrm{ext}}(\mathbf{r})\,\tilde{n}(\mathbf{r})\right), \tag{2.2}$$

where in the first step the minimization is performed in the space of those trial wavefunctions $\tilde{\Psi}$ that yield a prescribed trial density $\tilde{n}$.[2] In the second step, the

[1] All equations in this work are given in Hartree atomic units (i. e., the reduced Planck constant $\hbar$, the elementary charge e, the electron rest mass m_{e}, and the permittivity $4\pi\epsilon_0$ are set to unity) if not specified otherwise.

[2] Here we denote the trial densities and wavefunctions by $\tilde{n}$ and $\tilde{\Psi}$ to indicate the difference to the respective ground-state quantities, n and Ψ. In the following, we omit this distinction to simplify the notation when the meaning becomes clear from the context.

ground-state energy is determined by minimization in the space of trial densities. The corresponding density is the ground-state density n. Note that the space of trial densities is restricted to those densities that integrate to the given electron number N.

Most commonly, DFT is expressed in the Kohn-Sham (KS) formalism [64], where the *real* interacting system is mapped to a *fictitious* non-interacting KS system whose external potential $v_\mathrm{s}(\mathbf{r})$ is chosen such that both the interacting and non-interacting systems have the same density $n(\mathbf{r})$. Since the KS system is non-interacting, its wavefunction is a single Slater determinant $\Phi(\mathbf{r}_1, \ldots, \mathbf{r}_N)$ that is composed of N single-particle orbitals $\phi_i(\mathbf{r})$. This is an important conceptual advantage since it allows obtaining the ground-state energy and density viably. The density is expressed straightforwardly in terms of the single-particle orbitals as

$$n(\mathbf{r}) = \sum_{i=1}^{N} |\phi_i(\mathbf{r})|^2. \tag{2.3}$$

The KS system can be described by a non-interacting Schrödinger equation,

$$\left(-\frac{1}{2}\nabla^2 + v_\mathrm{s}([n], \mathbf{r})\right) \phi_i(\mathbf{r}) = \varepsilon_i \phi_i(\mathbf{r}), \tag{2.4}$$

where the KS potential $v_\mathrm{s}([n], \mathbf{r})$ is itself a functional of the density. In terms of the exchange-correlation (xc) energy $E_\mathrm{xc}[n]$ (to be defined below) it can be expressed as

$$v_\mathrm{s}([n], \mathbf{r}) = v_\mathrm{ext}(\mathbf{r}) + \int \mathrm{d}\mathbf{r}' \, \frac{n(\mathbf{r}')}{|\mathbf{r} - \mathbf{r}'|} + \frac{\delta E_\mathrm{xc}[n]}{\delta n(\mathbf{r})} \tag{2.5}$$

where the functional derivative of the xc energy, the xc potential $v_\mathrm{xc}([n], \mathbf{r})$, is evaluated at the ground-state density. In summary, Eqs. (2.3) to (2.5) constitute a closed set of equations that can be solved self-consistently to determine the ground-state wavefunction of the KS system and the ground-state density,[3] provided that an explicit expression for $E_\mathrm{xc}[n]$ is given.

Before we further dwell on the xc energy, we make some brief comments on how the electron spin is taken into account. All relations above can be generalized to their spin-polarized form [65, 66]. For later reference, we quote some important results. The density is split into two contributions from different spin channels, $n = n_\uparrow + n_\downarrow$,

$$n_\sigma(\mathbf{r}) = \sum_{i=1}^{N_\sigma} |\phi_{i\sigma}(\mathbf{r})|^2. \tag{2.6}$$

[3] For clarity we point out that the KS Slater determinant and the ground-state density are composed of the N single-particle orbitals with the lowest eigenvalues. Throughout this work, see, e. g., Eqs. (2.3) and (2.9), we assume that the orbitals are numbered such that $\varepsilon_1 \leq \varepsilon_2 \leq \ldots \varepsilon_N \leq \ldots$, i. e., $i = N$ corresponds to the highest occupied molecular orbital (HOMO) and $i = N + 1$ to the lowest unoccupied molecular orbital (LUMO).

The total electron number is $N = N_\uparrow + N_\downarrow$. The KS equation reads

$$\left(-\frac{1}{2}\nabla^2 + v_{\text{ext}}(\mathbf{r}) + \int \mathrm{d}\mathbf{r}' \, \frac{n(\mathbf{r}')}{|\mathbf{r}-\mathbf{r}'|} + \frac{\delta E_{\text{xc}}[n_\uparrow, n_\downarrow]}{\delta n_\sigma(\mathbf{r})}\right)\phi_{i\sigma}(\mathbf{r}) = \varepsilon_{i\sigma}\phi_{i\sigma}(\mathbf{r}). \tag{2.7}$$

Closed-shell systems, where each orbital is occupied twice, can be described using the spin-unpolarized form of the equations, cf. Eqs. (2.3) to (2.5); for open-shell systems the spin-polarized form is used.

The xc energy is implicitly defined by a splitting of the functional $F[n]$, cf. Eq. (2.2), into three distinct parts,

$$F[n] = T_{\text{s}}[n] + E_{\text{H}}[n] + E_{\text{xc}}[n]. \tag{2.8}$$

$T_{\text{s}}[n]$ is the non-interacting kinetic energy and an explicit expression in terms of the KS single-particle orbitals is available,

$$T_{\text{s}}[\{\phi_i[n]\}] = \sum_{i=1}^{N} \left\langle \phi_i \left| -\frac{1}{2}\nabla^2 \right| \phi_i \right\rangle. \tag{2.9}$$

$E_{\text{H}}[n]$ is the Hartree energy that represents the classical Coulomb interaction of the electron distribution $n(\mathbf{r})$ and is given by

$$E_{\text{H}}[n] = \frac{1}{2}\int \mathrm{d}\mathbf{r} \int \mathrm{d}\mathbf{r}' \, n(\mathbf{r}) \, \frac{1}{|\mathbf{r}-\mathbf{r}'|} \, n(\mathbf{r}'). \tag{2.10}$$

The xc energy can be split into exchange and correlation, $E_{\text{xc}} = E_{\text{x}} + E_{\text{c}}$. The exchange energy is defined as

$$E_{\text{x}}[n, \{\phi_i[n]\}] = \langle \Phi | \hat{V}_{\text{ee}} | \Phi \rangle - E_{\text{H}}[n] \tag{2.11}$$

and, thus, the correlation energy follows as

$$E_{\text{c}}[\{\phi_i[n]\}, \Psi[n]] = \langle \Psi | \hat{T} + \hat{V}_{\text{ee}} | \Psi \rangle - \langle \Phi | \hat{T} + \hat{V}_{\text{ee}} | \Phi \rangle. \tag{2.12}$$

The density dependence in Eq. (2.12) is an implicit one, via the generally unknown many-electron wavefunction $\Psi[n]$.

Practical applications of DFT crucially rely on useful approximations to the xc energy. Finding such approximations is a long-standing task and, despite many successful developments in the recent decades, a matter of ongoing efforts [67–76]. Typical approximations to the xc energy consist of one approximation for the exchange part and another (compatible) approximation for the correlation part. Very often, these are defined in terms of the respective energy densities,

$$e_{\text{xc}}([n_\uparrow, n_\downarrow], \mathbf{r}) = \sum_{\sigma=\uparrow,\downarrow} e_{\text{x}}([n_\sigma], \mathbf{r}) + e_{\text{c}}([n_\uparrow, n_\downarrow], \mathbf{r}), \tag{2.13}$$

which integrate to the xc energy as

$$E_{\mathrm{xc}}[n_\uparrow, n_\downarrow] = \int \mathrm{d}\mathbf{r}\; e_{\mathrm{xc}}([n_\uparrow, n_\downarrow], \mathbf{r}). \tag{2.14}$$

Thereby, the exchange energy density $e_{\mathrm{x}}([n_\sigma], \mathbf{r})$ is given in its spin-polarized form. The relation between the spin-unpolarized and spin-polarized forms of the exchange energy is explained in Sec. 5.2.2 below. One of the simplest xc approximations is the local density approximation (LDA). It is based on the model system of the homogeneous electron gas where an analytical and explicitly density-dependent expression for the exchange energy can be derived from first-order perturbation theory [22]. For the correlation energy no exact analytical expression is known but reliable parametrizations [77–79] based on accurate quantum Monte Carlo data [80] have been devised. In LDA, these expressions for *homogeneous* densities are used to approximate the exchange and correlation energy of systems with (in general) *inhomogeneous* densities. For example, the approximation to the exchange energy density is

$$e_{\mathrm{x}}^{\mathrm{LDA}}[n_\sigma] = -\frac{3}{2}\left(\frac{3}{4\pi}\right)^{1/3} n_\sigma^{4/3}(\mathbf{r}). \tag{2.15}$$

The LDA functional has certain desirable features [23, 81, 82] but further improvements are usually required. As a step forward, further semi-local ingredients [23] such as the density gradient $|\nabla n_\sigma(\mathbf{r})|$ or the kinetic energy density

$$\tau_\sigma(\mathbf{r}) = \frac{1}{2}\sum_{i=1}^{N_\sigma} |\nabla \phi_{i\sigma}(\mathbf{r})|^2, \tag{2.16}$$

can be used, giving rise to functionals that are referred to as generalized gradient approximations (GGAs) [83–87] or meta-GGAs [88–92], respectively. Among popular functionals are the GGA PBE [71] and the meta-GGA SCAN [72]. However, as we show in Chap. 3, many semi-local functionals still suffer from non-negligible shortcomings which can have serious consequences especially in the context of theoretical spectroscopy.[4]

One additional ingredient to model the xc energy that can help to overcome these limitations is the exact exchange energy $E_{\mathrm{x}}^{\mathrm{ex}}$,[5]

$$E_{\mathrm{x}}^{\mathrm{ex}}[n_\uparrow, n_\downarrow] = -\frac{1}{2}\sum_{\sigma=\uparrow,\downarrow}\sum_{i,j=1}^{N_\sigma}\int \mathrm{d}\mathbf{r}\int \mathrm{d}\mathbf{r}'\; \phi_{i\sigma}^*(\mathbf{r})\phi_{j\sigma}^*(\mathbf{r}')\frac{1}{|\mathbf{r}-\mathbf{r}'|}\phi_{i\sigma}(\mathbf{r}')\phi_{j\sigma}(\mathbf{r}). \tag{2.17}$$

[4] Recently developed meta-GGAs that follow certain construction principles show promising progress for some of these issues [93–96].

[5] $E_{\mathrm{x}}^{\mathrm{ex}}$ has the same mathematical form as the Fock exchange term in the well-known Hartree-Fock method [97, 98]. However, the (KS) orbitals entering Eq. (2.17) are not the same as the Hartree-Fock orbitals. We mention in passing that Hartree-Fock is intrinsically an approximate method, while DFT is formally exact.

This exact and explicit expression for the exchange energy follows from evaluating the expectation value in Eq. (2.11). However, using $E_{\mathrm{x}}^{\mathrm{ex}}$ as a part of E_{xc} in Eq. (2.7) immediately raises several questions: First, it is unclear how the functional derivative with respect to the spin-density of $E_{\mathrm{x}}^{\mathrm{ex}}[n_\uparrow, n_\downarrow]$ can be evaluated based on Eq. (2.17) where only the single-particle orbitals appear. One answer to this question is the optimized effective potential method [49]. Another answer is given in Sec. 3.2 below. Second, since $E_{\mathrm{x}}^{\mathrm{ex}}$ provides the exact value of the exchange energy by definition, one may ask why approximations for the exchange energy such as those in LDA, GGAs, or meta-GGAs are required at all. The answer to this question is too complicated to fit into a single line and needs to be postponed to Sec. 5.2. In fact, it emerges as a powerful strategy to mix both exact and semi-local exchange. This gives rise to a class of xc approximations referred to as "hybrid functionals" [46] which play a central role in this work. Their theoretical footing and practical usefulness are elaborated in the following chapters.

3 Electronic excitations in density functional theory

One of the central tasks in theoretical spectroscopy is the computation of electronic excitations. A typical example are optical excitations, i. e., light is absorbed by a molecule and, in response, the state of the molecule changes, which is represented by a change in the time-dependent many-electron wavefunction $\Psi(\mathbf{r}_1, \ldots, \mathbf{r}_N, t)$ in standard quantum mechanics. This basic thought already alludes to the many-electron character of electronic excitations. Incorporating this decisive feature meaningfully into a theory such as density functional theory (DFT) that does not offer access to the full many-electron wavefunction can lead to serious challenges [26, 27]. The same is true for the description of dynamical processes within time-dependent density functional theory (TDDFT), see Sec. 3.4 below. To understand these challenges, it is instructive to consider one of the most basic (non-dynamical) spectroscopic observables – the fundamental gap. It is defined as the difference between the first ionization potential IP, the energy required to remove an electron from a system with N_0 electrons, and the first electron affinity EA, the energy gain upon insertion of an electron,

$$\Delta_\mathrm{g} = \mathrm{IP}(N_0) - \mathrm{EA}(N_0). \tag{3.1}$$

The definition of Δ_g is visualized in Fig. 3.1. The physical processes underneath the fundamental gap reveal important characteristics of the many-electron nature of electronic excitations: As an electron is inserted into a system, all other electrons in the system respond to the presence of that extra electron. Similarly, if an electron is removed from a system, i. e., a "hole" is created, the remaining electrons respond to that hole. An intuitive way to describe these processes is via the concept of quasi-particles. Thereby, a quasi-electron or -hole contains the response effects of the correlated many-electron system to the presence of an extra electron or hole. Thus, this leads to an effective single-particle description where the ionization potential and electron affinity correspond to the lowest quasi-particle excitation energies. This concept can be formalized by many-body perturbation theory and, therein, the GW approach [26, 99] provides a way to calculate these excitation energies. However, this usually comes at the price of significantly increased computational cost.

Therefore, in this chapter, we discuss whether electronic excitations can be described at more moderate numerical effort using DFT. Thereby, our focus is on finite-sized molecular systems (in vacuum). First, in Sec. 3.1 we show why it is challenging to obtain correct excitation energies within Kohn-Sham (KS) DFT. Subsequently, in Secs. 3.2 and 3.3 we present an alternative approach based on the concept of hybrid functionals that can often describe electronic excitations reliably. Finally, we cover TDDFT and optical excitations in Sec. 3.4. Some of the central aspects of this chapter are summarized in Fig. 3.1 and will be explained in detail in the following.

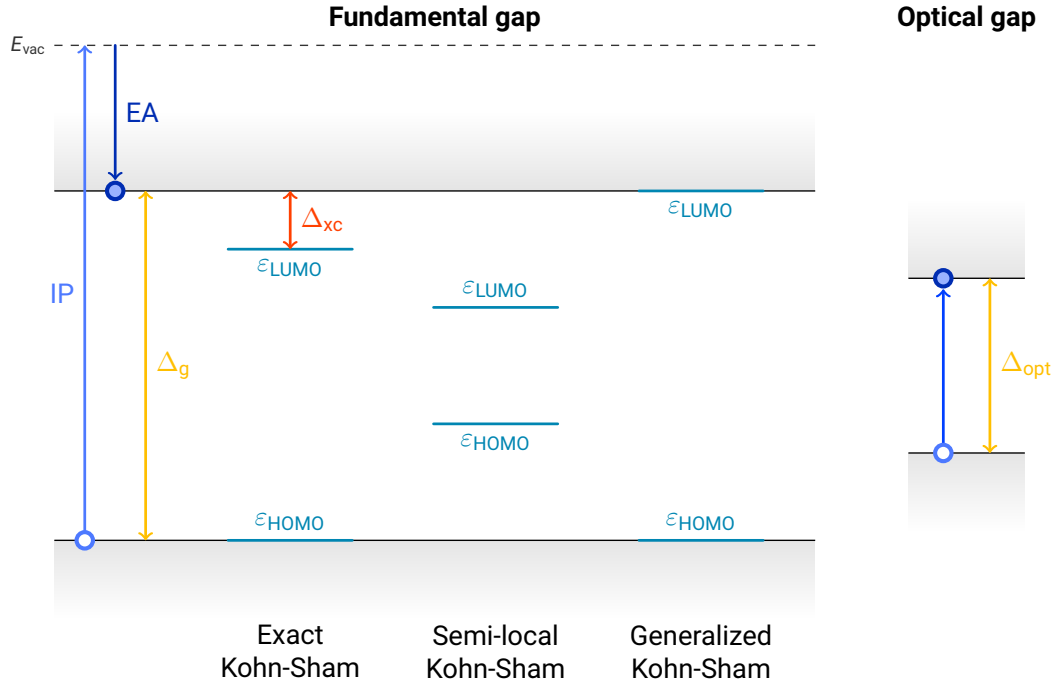

Fig. 3.1: Left: Schematic visualization of the fundamental gap $\Delta_g = \mathrm{IP} - \mathrm{EA}$ and the energetic positions of the HOMO and LUMO eigenvalues from an exact KS calculation, cf. Sec. 3.1.1, a KS calculation with a typical semi-local functional, and a calculation within a judiciously constructed generalized KS scheme, cf. Sec. 3.2. For the exact KS calculation, the derivative discontinuity Δ_{xc} is indicated. Right: Schematic visualization of the corresponding optical gap Δ_{opt}, cf. Sec. 3.4. The optical gap is drawn such that its relation to the size of Δ_g and the various HOMO–LUMO gaps is indicated.

3.1 Electronic excitations within the Kohn-Sham formalism

An object in the KS formalism that is similar to the quasi-particle excitation energies in many-body perturbation theory are the energy eigenvalues in the KS equation Eq. (2.4). However, this equation is a single-particle equation where the many-electron effects are incorporated only via the multiplicative KS potential, i. e., its mathematical structure is different to the form of the equations of motion in many-body perturbation theory [22, 99, 100]. Furthermore, the KS orbitals are introduced just as auxiliary quantities to obtain the ground-state density. Therefore, it is completely unclear *a priori* whether true physical meaning can be assigned to the KS orbitals and energies. In particular, it remains to be explored whether the frontier eigenvalue difference (for an N_0-electron system)

$$\Delta_\varepsilon = \varepsilon_{\mathrm{LUMO}}(N_0) - \varepsilon_{\mathrm{HOMO}}(N_0) \tag{3.2}$$

can be identified with the fundamental gap Δ_g. We point out that KS DFT is an exact theory by virtue of the Hohenberg-Kohn theorem. This guarantees that the

exact result for the fundamental gap can be obtained in principle. For finite-sized molecular systems, ionization potential and electron affinity can be defined as

$$\mathrm{IP}(N_0) = E(N_0 - 1) - E(N_0) \tag{3.3}$$

and

$$\mathrm{EA}(N_0) = E(N_0) - E(N_0 + 1). \tag{3.4}$$

Thus, the fundamental gap can be calculated in a straightforward way from ground-state energy differences of the neutral N_0-electron system and its associated cation and anion. Nevertheless, equality of Δ_g and Δ_ε is desirable. First, Eqs. (3.3) and (3.4) have the practical disadvantage that computation of the cation and anion is required, which can be numerically challenging. Calculating the gap (3.2) is less demanding. Second, for periodic systems such as semiconductors, ionization potential and electron affinity cannot be calculated via Eqs. (3.3) and (3.4). Third, meaningful (KS) eigenvalues are usually required for a reliable outcome from TDDFT calculations. The eigenvalues from a preceding DFT calculation enter the linear-response TDDFT equations, cf. Sec. 3.4 and, thus, the quality of the eigenvalues influences the accuracy of the results from TDDFT. Fourth and finally, it is also desirable from a fundamental point of view to restore the quasi-particle picture of electronic excitations in DFT. This can lead to (frontier) eigenvalues with an intuitive physical meaning.

3.1.1 Piecewise linearity and derivative discontinuity

We now explore whether the (frontier) KS eigenvalues have true physical meaning. For this purpose, we generalize DFT to fractional electron numbers $N = N_0 + \nu$ with an integer N_0 and $0 \leq \nu \leq 1$. Following the seminal work by Perdew *et al.* [101], a fractional number of electrons can be viewed as the time average of the number of electrons in a zero-temperature open system that is coupled to an electron bath.[1] The state of the open system with $N_0 + \nu$ electrons can be described as an ensemble state Γ, i. e., a statistical mixture of the integer-electron states containing N_0 and $N_0 + 1$ electrons.[2] The expectation value of an operator $\hat{O}$ then follows as

$$\langle \hat{O} \rangle_\Gamma = (1 - \nu) \langle \Psi_{N_0} | \hat{O} | \Psi_{N_0} \rangle + \nu \langle \Psi_{N_0+1} | \hat{O} | \Psi_{N_0+1} \rangle \tag{3.5}$$

where the values of the coefficients are such that the expectation value of the particle number operator, $\langle \hat{N} \rangle_\Gamma \equiv N$, correctly is $N_0 + \nu$. From Eq. (3.5) it follows that the ground-state energy $E(N)$ as a function of the fractional electron number N is

[1] Later an alternative interpretation of fractional electron numbers was given by Yang *et al.* [102] which only involves pure states.

[2] As detailed in Ref. [101] this follows from applying Levy's constrained search [63] to statistical mixtures of pure states that satisfy a certain concavity condition. This condition can be formulated as $2E(N_0) < E(N_0 - 1) + E(N_0 + 1)$ which is satisfied in all ordinary electronic systems.

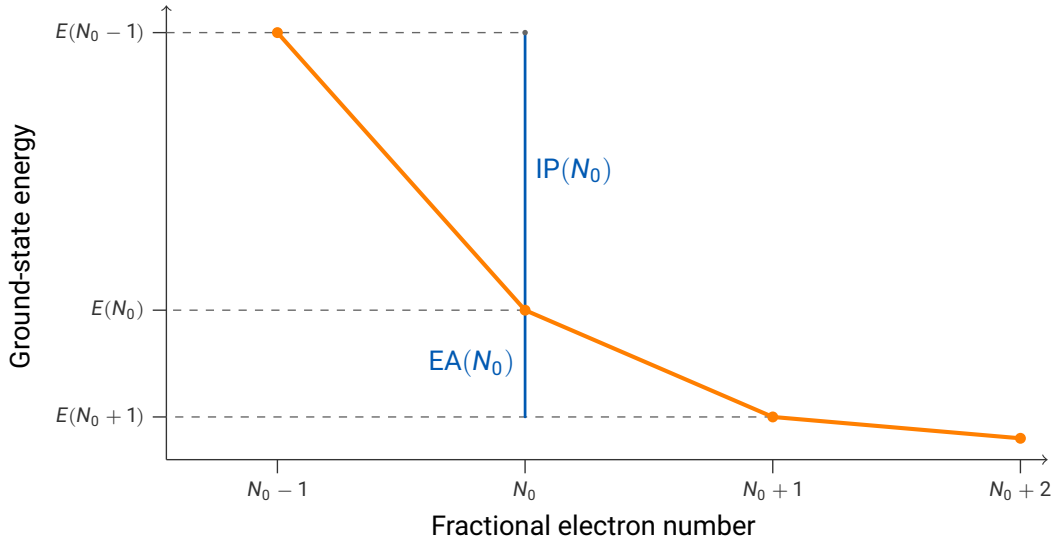

Fig. 3.2: Sketch of the ground-state energy $E(N)$ as a function of the fractional electron number N. $E(N)$ is a series of linear segments connecting the values at integer electron numbers. The slope on the left (right) of an integer electron number N_0 is equal to the negative of the respective ionization potential $\mathrm{IP}(N_0)$ (or electron affinity $\mathrm{EA}(N_0)$, respectively), as indicated.

given by a linear combination of the ground-state energies $E(N_0)$ and $E(N_0 + 1)$ at neighboring integer electron numbers,

$$E(N) = (1 - \nu)\, E(N_0) + \nu\, E(N_0 + 1). \tag{3.6}$$

This implies that the curve of $E(N)$ is a series of straight-line segments connecting the values at integer electron numbers. This feature of the ground-state energy is referred to as piecewise linearity. It is illustrated in Fig. 3.2. As a consequence, the derivative of $E(N)$ – the chemical potential $\mu(N) = \partial E/\partial N$ – is constant between points of integer electron numbers and discontinuously jumps at an integer electron number N_0 from the negative of the respective ionization potential $\mathrm{IP}(N_0)$ to the negative of the electron affinity $\mathrm{EA}(N_0)$,

$$\mu(N) = \begin{cases} -\mathrm{IP}(N_0), & \text{for } N_0 - 1 < N < N_0, \\ -\mathrm{EA}(N_0), & \text{for } N_0 < N < N_0 + 1. \end{cases} \tag{3.7}$$

Furthermore, using Janak's theorem [103] the eigenvalue of the highest occupied molecular orbital (HOMO) of the KS equation is identical to the chemical potential [104],

$$\varepsilon_{\mathrm{HOMO}}(N) = \mu(N), \tag{3.8}$$

since variations of the total electron number translate to changing the occupation of the HOMO orbital in the KS system. Therefore, the curve of $\varepsilon_{\mathrm{HOMO}}(N)$ is a

series of constant segments with steps at integer electron numbers. Real calculations, where the KS potential is chosen such that it vanishes asymptotically, correspond to approaching the integer particle number N_0 from below. Thus, it follows that the HOMO eigenvalue of a system with N_0 electrons is identical to the negative of its ionization potential [104–106],

$$\varepsilon_{\mathrm{HOMO}}(N_0) = -\mathrm{IP}(N_0). \tag{3.9}$$

This important relation is known as IP theorem. It means that the HOMO eigenvalue from KS calculations has precisely the same physical meaning as in the quasi-particle picture invoked above.[3]

On the other hand, the eigenvalue of the lowest unoccupied molecular orbital (LUMO) cannot be identified with the negative of the electron affinity. This can be understood by returning to Eq. (3.7). The size of the discontinuity that $\mu(N)$ exhibits at integer electron numbers is precisely the fundamental gap Δ_{g} [108–110]. It must arise from discontinuities in the derivative of contributions to the total energy $E[n] = T_{\mathrm{s}}[n] + E_{\mathrm{H}}[n] + E_{\mathrm{xc}}[n] + V_{\mathrm{ext}}[n]$. Thereby, the Hartree energy $E_{\mathrm{H}}[n]$ and the term due to the external potential $V_{\mathrm{ext}}[n]$ are continuous with respect to the density. Thus, only the non-interacting kinetic energy and the exchange-correlation (xc) energy contribute to the discontinuity,

$$\Delta_{\mathrm{g}} = \underbrace{\left(\left.\frac{\delta T_{\mathrm{s}}[n]}{\delta n(\mathbf{r})}\right|_{N_0+\eta} - \left.\frac{\delta T_{\mathrm{s}}[n]}{\delta n(\mathbf{r})}\right|_{N_0-\eta} \right)}_{=\Delta_\varepsilon} + \underbrace{\left(\left.\frac{\delta E_{\mathrm{xc}}[n]}{\delta n(\mathbf{r})}\right|_{N_0+\eta} - \left.\frac{\delta E_{\mathrm{xc}}[n]}{\delta n(\mathbf{r})}\right|_{N_0-\eta} \right)}_{=\Delta_{\mathrm{xc}}}, \tag{3.10}$$

where $\eta > 0$ means an infinitesimal variation of the fractional electron number. The first term on the right hand side of Eq. (3.10) is precisely the fundamental gap of the KS system, which is given by the HOMO–LUMO eigenvalue gap (3.2). The second term is referred to as derivative discontinuity Δ_{xc} and cannot be calculated in a straightforward way. It corresponds to a discontinuous "jump" that the xc potential exhibits at integer particle numbers. From Eqs. (3.1), (3.9), and (3.10) it follows that

$$\varepsilon_{\mathrm{LUMO}}(N_0) = -\mathrm{EA}(N_0) - \Delta_{\mathrm{xc}}(N_0), \tag{3.11}$$

i. e., the derivative discontinuity separates $-\varepsilon_{\mathrm{LUMO}}$ from the electron affinity. The relation of the HOMO and LUMO eigenvalues to ionization potential and electron affinity is visualized in Fig. 3.1. This shows that it is precisely Δ_{xc} that separates Δ_ε from Δ_{g}.

These relations have important practical implications: The derivative discontinuity is usually a sizable and relevant contribution to the fundamental gap such that Δ_ε is

[3] We point out that the other occupied eigenvalues can often be interpreted physically as well. For example, it has been demonstrated that the occupied KS eigenvalues *approximate* relaxed ionization potentials [107]. However, *rigorous* physical meaning can only be assigned to the HOMO eigenvalue via Eq. (3.9).

a poor approximation to Δ_g even in exact KS theory [108–111]. Usual semi-local xc approximations such as the local density approximation (LDA) or generalized gradient approximations (GGAs) that depend only on the density and its gradient average over the derivative discontinuity.[4] As a consequence, even their HOMO eigenvalue is upshifted by $\sim \Delta_\mathrm{xc}/2$ with respect to the ionization potential [111, 116, 117]. Thus, the HOMO–LUMO gap is even smaller than that of exact KS theory. This is depicted schematically in Fig. 3.1. The missing derivative discontinuity of semi-local functionals manifests in an approximate parabolic behavior of $E(N)$ [118]. Since Janak's theorem holds for approximate functionals as well, the corresponding HOMO eigenvalue varies approximately linearly between integer electron number. The deviation from piecewise linearity for approximate functionals, which often leads to a convex $E(N)$ curve, is also referred to as "many-electron self-interaction error" or "delocalization error" [119–125]. This term alludes to the observation that functionals with a convex $E(N)$ curve tend to overestimate the delocalization of the electrons. This erroneous behavior bears resemblance to the one-electron self-interaction error introduced in the following section, but is not equivalent [25, 126].

3.1.2 One-electron self-interaction and asymptotic exchange-correlation potential

Apart from the piecewise linearity condition, two further exact constraints are of particular relevance for theoretical spectroscopy; often the three properties are mentioned together [25]. First, this is the asymptotic behavior of the xc potential [127–129]. It can be proven rigorously that the xc potential of a finite neutral system decays asymptotically as [105, 106]

$$\lim_{r\to\infty} v_\mathrm{xc}(\mathbf{r}) = -\frac{1}{r}, \tag{3.12}$$

with $r = |\mathbf{r}|$. The whole KS potential exhibits the same asymptotic behavior. Intuitively, this can be understood as follows: In the asymptotic region far away from the nuclei, a single orbital – the highest occupied one – dominates. Hence, at asymptotically large distances r the KS potential, which is the effective external potential that this orbital "feels", takes a particularly simple form. It is the sum of the Coulomb attraction $-Q/r$ by the nuclei of total charge Q which is screened by the Coulomb repulsion $(Q-1)/r$ from all other $Q-1$ KS "electrons". Thus, the KS potential decays as $-1/r$. The decay of the xc potential is the same since the Hartree potential exactly cancels the external potential which contains the Coulomb attraction by the nuclei.

Typical semi-local functionals such as LDA or GGAs fail to exhibit the correct asymptotic Coulomb decay of Eq. (3.12). This can be seen easily for the LDA exchange functional (2.15) whose potential, $v_\mathrm{x}^\mathrm{LDA}(\mathbf{r}) \sim n^{1/3}(\mathbf{r})$, simply follows the

[4] For completeness we mention that parts of the missing derivative discontinuity of semi-local functionals can be restored by using alternative forms of ensemble generalization [112–115].

exponential decay of the density distribution [130]. Hence, their xc potential is not binding enough, which can make the description of loosely bound electrons problematic [131, 132]. For example, this leads to unoccupied eigenvalues of limited interpretability or anions that are spuriously predicted to be unstable. A functional which leads to the correct $-1/r$ decay is exact exchange (2.17). This is one motivation for a certain form of hybrid functionals, on which this work focuses, cf. Sec. 3.3.

Another constraint that is important for theoretical spectroscopy is freedom from one-electron self-interaction [133, 134]. To understand this constraint, consider Eqs. (2.2) and (2.8) for a one-electron system. As there is no electron-electron interaction in one-electron systems, it immediately follows that the total energy is entirely given by the contributions due to the (non-interacting) kinetic energy and the external potential. In other words, the Hartree and xc energy contributions to $F[n]$ have to cancel out. That is, for any one-electron ground-state density $n_{1\mathrm{e}}(\mathbf{r})$ we have the exact condition

$$E_{\mathrm{H}}[n_{1\mathrm{e}}] + E_{\mathrm{xc}}[n_{1\mathrm{e}}, 0] = 0, \tag{3.13}$$

or, more precisely, it is the exchange energy that must cancel the Hartree energy,

$$E_{\mathrm{H}}[n_{1\mathrm{e}}] + E_{\mathrm{x}}[n_{1\mathrm{e}}, 0] = 0, \tag{3.14}$$

since the correlation energy has to vanish in one-electron systems (cf. Eqs. (2.11) and (2.12)),

$$E_{\mathrm{c}}[n_{1\mathrm{e}}, 0] = 0. \tag{3.15}$$

These conditions are well-grounded theoretically. However, it is not straightforward how this formulation can be applied to systems beyond the one-electron case and how approximate xc functionals can be assessed or constructed to fulfill Eq. (3.13) for any n_{1e}. Therefore, following the seminal work by Perdew and Zunger [78], freedom from one-electron self-interaction is typically formulated in a more general way that goes beyond Eq. (3.13). That is, one demands

$$E_{\mathrm{H}}[|\phi_{i\sigma}|^2] + E_{\mathrm{xc}}[|\phi_{i\sigma}|^2, 0] = 0 \tag{3.16}$$

for all one-spin-orbital densities $|\phi_{i\sigma}(\mathbf{r})|^2$.[5] It can be motivated as follows: If we express the Hartree energy (2.10) explicitly in terms of spin-orbitals,

$$E_{\mathrm{H}}[n] = \frac{1}{2} \int \mathrm{d}\mathbf{r} \int \mathrm{d}\mathbf{r}' \sum_{\sigma,\sigma'} \sum_{i,j} |\phi_{i\sigma}(\mathbf{r})|^2 \frac{1}{|\mathbf{r} - \mathbf{r}'|} |\phi_{j\sigma'}(\mathbf{r}')|^2, \tag{3.17}$$

it becomes apparent that it contains terms (with $i = j$ and $\sigma = \sigma'$) that involve the interaction of a spin-orbital with itself. This appears nonphysical and an xc functional that obeys Eq. (3.16) ensures that this "self-interaction" is canceled on

[5] Eqs. (3.14) and (3.15) can be generalized to one-spin-orbital densities in an analogous way.

a per-orbital basis. However, one should be aware that the generalization from Eq. (3.13) to (3.16) is by no means straightforward. In particular, it involves the identification of KS orbital densities with electrons, which is outside the usual KS framework, and raises further questions which are discussed, e. g., in Ref. [135].

Semi-local functionals typically exhibit significant one-electron self-interaction errors. These errors have been associated with, e. g., an erroneous description of energy eigenvalues [78, 136]. There are two common ways to correct for one-electron self-interaction errors. First, the Perdew-Zunger self-interaction correction [78] subtracts the self-interaction error of Eq. (3.16) on a per-orbital basis from the approximate xc functional $E_{\mathrm{xc}}^{\mathrm{ap}}$ of interest,

$$E_{\mathrm{xc}}^{\text{PZ-SIC}}[n_\uparrow, n_\downarrow] = E_{\mathrm{xc}}^{\mathrm{ap}}[n_\uparrow, n_\downarrow] - \sum_{\sigma=\uparrow,\downarrow} \sum_{i=1}^{N_\sigma} \left(E_{\mathrm{H}}[|\phi_{i\sigma}|^2] + E_{\mathrm{xc}}^{\mathrm{ap}}[|\phi_{i\sigma}|^2, 0] \right). \tag{3.18}$$

However, this method is not invariant under unitary transformations of the orbitals which requires special care, see, e. g., Refs. [134, 135] and references therein. Second, one can use exact exchange. The exact exchange expression (2.17) cancels the self-interaction contained in the Hartree energy (3.17) on a per-orbital basis and, thus, fulfills both Eqs. (3.14) and (3.16). We further elaborate on how this can be exploited in actual functional constructions in Sec. 5.2.6 below.

3.2 Generalized Kohn-Sham framework

The KS formalism has several limitations. First, one has to calculate the functional derivative $\delta E_{\mathrm{xc}}[n]/\delta n(\mathbf{r})$, i. e., with respect to the *density*, to obtain the xc potential. This can be non-trivial for functionals such as exact exchange, for which an explicit expression is known only in terms of the *single-particle orbitals* [49]. Moreover, the mapping of the many-electron problem onto a system of non-interacting particles, which the KS formalism provides, appears inherently inappropriate to mimic the many-electron nature of electronic excitations (cf. Sec. 3.1.1). Thus, the applicability of the KS framework to theoretical spectroscopy is intrinsically limited. In this section we show how a generalization of KS can alleviate these issues. Thereby, one desirable feature of the KS construction is that the real system is mapped onto an auxiliary system that can be represented by a *single* Slater determinant. This ensures that tractable single-particle equations are obtained [137]. The crucial difference to standard KS is that the particles of the generalized auxiliary system that we introduce below may be (partially) interacting. By that, the resulting single-particle orbitals and energies can incorporate xc effects to some extent, and this may result in a better representation of the interacting nature of the true many-electron system.

These thoughts motivate the generalized KS framework by Seidl *et al.* [137]. In their seminal work, they present the rigorous theoretical foundations of the approach. In this work, we limit ourselves to pointing at some relevant aspects. As in KS, the

mapping from the real to the auxiliary generalized KS system is achieved by a suitable external potential $v^S(\mathbf{r})$ that acts in the auxiliary system and that is constructed such that both the real system and the generalized KS system have the same density $n(\mathbf{r})$. At the heart of generalized KS is the energy functional $S[\{\phi_i\}]$ that depends on the set of single-particle orbitals $\{\phi_i\}$ generating the Slater determinant Φ of the generalized KS system. Thereby, the form of $S[\{\phi_i\}]$ can be chosen provided that certain constraints, especially invariance under unitary transformations of the orbitals, are obeyed. The generalized KS single-particle equation is

$$\left(\hat{O}^S[\{\phi_j\}] + v^S([n],\mathbf{r})\right)\phi_i(\mathbf{r}) = \varepsilon_i\phi_i(\mathbf{r}). \tag{3.19}$$

Thereby, the operator $\hat{O}^S[\{\phi_i\}]$ is nonlocal in general. Its form depends on the choice of $S[\{\phi_i\}]$ and is invariant with respect to unitary transformations of the orbitals as well. The local multiplicative potential $v^S([n],\mathbf{r})$ is a functional of the density and given by

$$v^S([n],\mathbf{r}) = v_{\text{ext}}(\mathbf{r}) + \frac{\delta R^S[n]}{\delta n(\mathbf{r})}. \tag{3.20}$$

Therein, $R^S[n]$ is the remainder functional which emerges from splitting the functional $F[n]$ in Eq. (2.2) as

$$F[n] = F^S[n] + R^S[n], \tag{3.21}$$

where the functional $F^S[n]$ arises from minimizing S in the space of those trial unitary orbitals $\{\tilde{\phi}_i\}$ which yield the prescribed density $n(\mathbf{r})$,

$$F^S[n] = \min_{\{\tilde{\phi}_i\}\to n} S[\{\tilde{\phi}_i\}]. \tag{3.22}$$

$R^S[n]$ is an explicit density functional whose form depends upon the functional $S[\{\phi_i\}]$ as well. Therefore, once a specific form of $S[\{\phi_i\}]$ is chosen, Eqs. (3.19) and (3.20) together with the relation (2.3) between the single-particle orbitals and the density form a closed set of equations that can be solved self-consistently to determine the ground-state density, just as in standard KS theory. A conceptual difference is that there are infinitely many choices of $S[\{\phi_i\}]$ and, thus, different generalized KS schemes. As in the KS approach, practical calculations require to approximate the functional $R^S[n]$. However, the advantage of generalized KS is that a suitable choice of $S[\{\phi_i\}]$ can lead to a functional $R^S[n]$ that is easier to approximate than the xc functional of KS.

To elucidate the meaning of the generalized KS framework, it is instructive to look at a concrete choice of $S[\{\phi_i\}]$. An important and widely used choice is

$$S^{\text{hyb}}[\{\phi_i\}] = \langle\Phi|\hat{T} + a\hat{V}_{\text{ee}}|\Phi\rangle = T_{\text{s}}[\{\phi_i\}] + a\,E_{\text{H}}[\{\phi_i\}] + a\,E_{\text{x}}^{\text{ex}}[\{\phi_i\}] \tag{3.23}$$

with a constant parameter $0 \le a \le 1$. Therein, the form of $S[\{\phi_i\}]$ and, accordingly, also $F^S[n]$ can be related to the non-interacting kinetic energy (2.9), the Hartree

energy (2.10), and the exact exchange energy (2.17) familiar from KS theory.[6] Importantly, the limiting value $a = 0$ in Eq. (3.23) leads back to conventional KS, which is thus incorporated in generalized KS as a special case [137]. The other limit $a = 1$ is called Hartree-Fock-Kohn-Sham scheme. If the correlation energy is neglected, it becomes identical to the well-known Hartree-Fock method. The general case is commonly referred to as (global) "hybrid functional" [138].[7] Thereby, the remainder functional is typically approximated as

$$R^{S,\mathrm{hyb}}[n] = (1-a)\,E_{\mathrm{H}}[n] + (1-a)\,E_{\mathrm{x}}^{\mathrm{sl}}[n] + E_{\mathrm{c}}^{\mathrm{sl}}[n], \tag{3.24}$$

where some approximate semi-local functionals – $E_{\mathrm{x}}^{\mathrm{sl}}[n]$ and $E_{\mathrm{c}}^{\mathrm{sl}}[n]$ – for exchange and correlation from KS theory are taken. Although the xc energy is defined as an object of KS theory [138], hybrid functionals are typically viewed as a density functional approximation to the xc energy that augments semi-local functionals for exchange and correlation with some fraction of exact exchange,

$$E_{\mathrm{xc}}^{\mathrm{hyb}}[n] = a\,E_{\mathrm{x}}^{\mathrm{ex}}[\{\phi_i[n]\}] + (1-a)\,E_{\mathrm{x}}^{\mathrm{sl}}[n] + E_{\mathrm{c}}^{\mathrm{sl}}[n]. \tag{3.25}$$

As an example, the PBE0 functional [139, 140] uses the exchange and correlation functionals of PBE and $a = 0.25$. This fraction of exact exchange admixture can be motivated by formal considerations [141]. Most of the other common hybrid functionals have a form that is more complicated than the one-parameter form (3.25) and rely on parameters that are determined empirically by fitting to reference data [49, 69, 73, 142]. A popular representative is the B3LYP functional [143].

The single-particle equation of hybrid functionals,

$$\begin{aligned}\left(-\frac{1}{2}\nabla^2 + v_{\mathrm{ext}}(\mathbf{r}) + \int \mathrm{d}\mathbf{r}'\,\frac{n(\mathbf{r}')}{|\mathbf{r}-\mathbf{r}'|} + (1-a)\,v_{\mathrm{x}}^{\mathrm{sl}}(\mathbf{r}) + v_{\mathrm{c}}^{\mathrm{sl}}(\mathbf{r})\right)\phi_i(\mathbf{r}) \\ + a\,\hat{v}_{\mathrm{x}}^{\mathrm{ex}}(\mathbf{r})\,\phi_i(\mathbf{r}) = \varepsilon_i\,\phi_i(\mathbf{r}),\end{aligned} \tag{3.26}$$

contains the non-local exact exchange operator,

$$\hat{v}_{\mathrm{x}}^{\mathrm{ex}}(\mathbf{r})\,\phi_i(\mathbf{r}) = -\sum_{j=1}^{N}\int \mathrm{d}\mathbf{r}'\;\phi_j^*(\mathbf{r}')\frac{1}{|\mathbf{r}-\mathbf{r}'|}\phi_j(\mathbf{r})\phi_i(\mathbf{r}'). \tag{3.27}$$

Hence, its mathematical structure is qualitatively different to that of the KS equation. This has important implications for the resulting energy eigenvalues and electronic excitations. Seidl *et al.* [137] argue on the basis of Hartree-Fock-Kohn-Sham that the frontier eigenvalue gap in generalized KS, $\Delta_\varepsilon^{\mathrm{GKS}}$, already contains a fraction of the exchange derivative discontinuity in KS, Δ_{x}. Thus, $\Delta_\varepsilon^{\mathrm{GKS}}$ is increased with

[6] At this point we emphasize that KS and generalized KS are formally different and relations between the two frameworks should be made with care. In particular, the generalized KS orbitals entering Eq. (3.23) differ from the KS orbitals [49].

[7] Originally, hybrid functionals have been introduced by Becke [46] based on coupling-constant integration. We present this approach in Sec. 5.1 below.

respect to the KS gap $\Delta_\varepsilon^{\mathrm{KS}}$. Generalizing these considerations to hybrid functionals with only a fraction a of exact exchange leads to the approximate relation

$$\Delta_\varepsilon^{\mathrm{GKS}} \approx \Delta_\varepsilon^{\mathrm{KS}} + a\,\Delta_{\mathrm{x}}. \tag{3.28}$$

Thus, the frontier eigenvalue gap can come closer to the fundamental gap Δ_{g}. Furthermore, the identity of ionization potential and $-\varepsilon_{\mathrm{HOMO}}$ is also valid for hybrid functionals in generalized KS. Therefore, $-\varepsilon_{\mathrm{LUMO}}$ can come close to the electron affinity. At this point, we stress that typical hybrid functionals do not achieve this goal. While their HOMO–LUMO gap is indeed increased compared to LDA or GGAs, it is still much smaller than the fundamental gap. In particular, this is because they contain a fraction of exact exchange of $a \sim 0.25$ which is well-suited for thermochemistry but too small to reduce the derivative discontinuity of the remainder $R^{S,\mathrm{hyb}}[n]$ effectively. This alludes to a parameter dilemma, which is further discussed in Chap. 5.

Nevertheless, the simple considerations for the case of hybrid functionals leading to Eq. (3.28) illustrate transparently the more general observation that a generalized KS scheme can be constructed judiciously such that the derivative discontinuity of the remainder becomes small, and the frontier eigenvalues are endowed with true physical meaning [27]. This is illustrated in Fig. 3.1. It can be achieved in practice by introducing a more sophisticated hybrid scheme, as we show in the following section. Overall, the generalized KS approach appears physically sound, since the non-local character that the single-particle equation (3.19) can have (cf. Eq. (3.26)) seems to be more appropriate to mimic the quasi-particle nature of electronic excitations.

3.3 Range-separated hybrid functionals

A class of hybrid functionals that is particularly successful for spectroscopic purposes are range-separated hybrids (RSHs) [144, 145]. The basic idea is to split the electron-electron interaction into a long-range and a short-range part. In the past, different forms of this splitting have been proposed [42, 43, 146–150]. Relevant within this work is the form[8]

$$\frac{1}{|\mathbf{r}-\mathbf{r}'|} = \underbrace{\frac{\operatorname{erf}(\omega|\mathbf{r}-\mathbf{r}'|)}{|\mathbf{r}-\mathbf{r}'|}}_{\text{long range}} + \underbrace{\frac{1-\operatorname{erf}(\omega|\mathbf{r}-\mathbf{r}'|)}{|\mathbf{r}-\mathbf{r}'|}}_{\text{short range}} \tag{3.29}$$

which contains a single range-separation parameter ω. Further complexity can be added by generalizing the splitting of the Coulomb interaction which leads to more parameters [152–154]. A popular example of this approach is the CAM-B3LYP functional [149]. In solid-state calculations, typically, the short-range part of the

[8] Using the error function in Eq. (3.29) is advantageous for reasons of computational performance in quantum chemistry programs that use Gaussian basis sets since it allows for an analytical evaluation of certain integrals involving exact exchange [98, 151].

interaction is modeled by exact exchange with the HSE functional being a prominent example of this type [155–157]. On the other hand, as we show, RSH functionals where the long-range part of the Coulomb interaction is described by exact exchange (sometimes referred to as "long-range correction") are well-suited for spectroscopic applications in finite (molecular) systems. This is the form of hybrid functionals we focus on in this work.

Formally, RSH functionals can be regarded as a realization of the generalized KS framework. Their long-range corrected form can be obtained by the choice [137, 158]

$$S^{\mathrm{RSH}}[\{\phi_i\}] = \langle\Phi|\hat{T} + \hat{V}_{\mathrm{ee}}^{\mathrm{lr}}|\Phi\rangle = T_{\mathrm{s}}[\{\phi_i\}] + E_{\mathrm{H}}^{\mathrm{lr}}[\{\phi_i\}] + E_{\mathrm{x}}^{\mathrm{lr,ex}}[\{\phi_i\}], \tag{3.30}$$

for the constituting energy functional of generalized KS. Therein, $\hat{V}_{\mathrm{ee}}^{\mathrm{lr}}$ is the long-range Coulomb operator,

$$\hat{V}_{\mathrm{ee}}^{\mathrm{lr}} = \frac{1}{2}\sum_{\substack{i,j=1\\ i\neq j}}^{N} \frac{\operatorname{erf}(\omega|\mathbf{r}_i - \mathbf{r}_j|)}{|\mathbf{r}_i - \mathbf{r}_j|}. \tag{3.31}$$

Correspondingly, $E_{\mathrm{x}}^{\mathrm{lr,ex}}[\{\phi_i\}]$ is the long-range part of the exact exchange energy,

$$E_{\mathrm{x}}^{\mathrm{lr,ex}}[\{\phi_i\}] = -\frac{1}{2}\sum_{\sigma=\uparrow,\downarrow}\sum_{i,j=1}^{N_\sigma}\int \mathrm{d}\mathbf{r}\int \mathrm{d}\mathbf{r}'\ \phi_{i\sigma}^*(\mathbf{r})\phi_{j\sigma}^*(\mathbf{r}')\frac{\operatorname{erf}(\omega|\mathbf{r}-\mathbf{r}'|)}{|\mathbf{r}-\mathbf{r}'|}\phi_{i\sigma}(\mathbf{r}')\phi_{j\sigma}(\mathbf{r}), \tag{3.32}$$

and $E_{\mathrm{H}}^{\mathrm{lr}}[\{\phi_i\}]$ the long-range part of the Hartree energy defined in analogy to Eq. (3.32). The remainder functional $R^{\mathrm{S}}[n]$ is typically approximated as

$$R^{S,\mathrm{RSH}}[n] = E_{\mathrm{H}}^{\mathrm{sr}}[n] + E_{\mathrm{x}}^{\mathrm{sr,sl}}[n] + E_{\mathrm{c}}^{\mathrm{sl}}[n]. \tag{3.33}$$

Thereby, $E_{\mathrm{x}}^{\mathrm{sr,sl}}[n]$ is a semi-local approximation for the short-range part of the exchange energy, see Refs. [145, 147, 148, 155–157, 159–162] for various examples and Sec. 5.4 for further explanation, and $E_{\mathrm{c}}^{\mathrm{sl}}[n]$ a (usual) semi-local correlation functional. RSH functionals of the form of Eqs. (3.30) and (3.33) are typically viewed as approximating the xc energy as

$$E_{\mathrm{xc}}[n] = E_{\mathrm{x}}^{\mathrm{lr,ex}}[\{\phi_i[n]\}] + E_{\mathrm{x}}^{\mathrm{sr,sl}}[n] + E_{\mathrm{c}}^{\mathrm{sl}}[n]. \tag{3.34}$$

This way of mixing exact and semi-local exchange is well suited to capture the interplay of long- and short-range interactions and appears well motivated by the physics of electron-electron interaction: wavefunction-based approaches can describe the long-range part of the interaction efficiently while they struggle to correctly account for the cusp that the wavefunction exhibits for vanishing interelectronic distances due to the singularity of the Coulomb interaction [144]. On the other hand, at short range the compatibility of semi-local exchange and correlation is maintained and semi-local xc functionals are known to be most accurate for the

short-range part of the interaction [82]. Finally, using exact exchange at long range has specific advantages for describing electronic excitations: It ensures that the correct asymptotic form of the xc potential is obtained and eliminates the long-range part of the one-electron self-interaction error, cf. Sec. 3.1.2.

The value of the range-separation parameter influences the behavior of RSH functionals decisively. Empirically determined parameter values, i. e., by optimization with respect to reference test sets, have led to some widely and successfully used functionals [73, 142, 149, 153]. However, empirical fitting strategies can have drawbacks [163–166]. In particular, in the case of RSH functionals one may question whether such a fixed range-separation parameter can be appropriate for diverse systems and different electronic properties [42, 44, 50]. This is one motivation for a different and very successful approach to determine a value for ω: The optimal-tuning procedure [27, 44, 167]. This is a non-empirical strategy to adjust the value of ω in a system-specific fashion, which is designed with spectroscopic applications in mind. It is inspired by one of the central insights explained in Sec. 3.1.1: A reliable and robust prediction of excitation gaps requires the HOMO and LUMO eigenvalues to resemble ionization potential and electron affinity. This can be achieved by enforcing the IP theorem,

$$-\varepsilon^{\omega}_{\mathrm{HOMO}}(N_0) \stackrel{!}{=} E^{\omega}_0(N_0-1) - E^{\omega}_0(N_0), \tag{3.35}$$

where the ionization potential is calculated as a ground-state energy difference. An analogous relation for the LUMO eigenvalue is not available. But this issue can be circumvented by using the IP theorem (3.35) for the corresponding anion with N_0+1 electrons as an additional constraint,

$$-\varepsilon^{\omega}_{\mathrm{HOMO}}(N_0+1) \stackrel{!}{=} E^{\omega}_0(N_0) - E^{\omega}_0(N_0+1). \tag{3.36}$$

Therein, the right hand side is the same as the electron affinity of the neutral N_0 electron system. Eqs. (3.35) and (3.36) can be combined in a cost function. A common choice is [168]

$$\begin{aligned} J^2(\omega) = {} & \left(\varepsilon^{\omega}_{\mathrm{HOMO}}(N_0) + E^{\omega}_0(N_0-1) - E^{\omega}_0(N_0)\right)^2 \\ & + \left(\varepsilon^{\omega}_{\mathrm{HOMO}}(N_0+1) + E^{\omega}_0(N_0) - E^{\omega}_0(N_0+1)\right)^2 . \end{aligned} \tag{3.37}$$

In the optimal-tuning procedure that particular value of ω is taken that minimizes $J^2(\omega)$. The calculations done in this work involving optimally tuned RSH functionals are based upon this tuning strategy, if not stated otherwise. RSHs that have been applied within the optimal tuning strategy in past work include the BNL [44, 169] and ωPBE [159] functionals. Practical experience suggests that ωPBE may be more robust under certain circumstances, see, e. g., Ref. [41], and is therefore taken for the calculations done in this work.

There is ample numerical evidence that RSH fundamentals with optimal tuning are a powerful tool for the prediction of excitation gaps, see, e. g., Ref. [27] for a review.

Importantly, it has been demonstrated repeatedly, e. g., in Refs. [170–172], that the optimal tuning approach leads to frontier eigenvalues that describe ionization potentials, electron affinities, and fundamental gaps very accurately. These studies also reveal that the optimal value for ω varies significantly among different systems. This has been investigated thoroughly for conjugated molecules of different lengths, where ω is found to exhibit clear trends depending on conjugation length [40]. These results underline that employing a fixed value for ω, independent of the systems under study, appears inappropriate, which again highlights the need for a system-specific treatment as achieved via optimal tuning. Finally, it has been demonstrated that optimally tuned RSH functionals do not only endow the frontier eigenvalues with true physical meaning but also approximate the piecewise-linear behavior of the total energy as a function of fractional electron number well [118]. All of these results show that optimal tuning is a physically sound strategy to obtain spectroscopic observables.

In Fig. 3.3, we show the fundamental gap of tetraphenylporphyrin. This example illustrates typical trends of the HOMO–LUMO gaps calculated with different density functional approximations [27, 170]. We compare these numbers with experimental results for ionization potential, electron affinity, and the fundamental gap as well as results from many-body perturbation theory using GW-BSE [26]. First, for PBE, as typical for GGAs, the HOMO and LUMO eigenvalues are a very poor approximation to ionization potential and electron affinity, yielding a gap that underestimates the fundamental gap by more than a factor of 2. These numbers are somewhat improved by the global hybrid B3LYP. However, the gap is still underestimated significantly. This discrepancy has been attributed to the fact that not enough of the derivative discontinuity has been incorporated into the non-local potential on the one hand, and one-electron self-interaction errors and an incorrect asymptotic potential on the other hand [27]. All of these shortcomings are mostly eliminated by the optimally tuned BNL functional. In that case, both the frontier eigenvalues and their gap nicely agree with the GW-BSE and the experimental results. This demonstrates once more that RSH functionals with optimal tuning can alleviate the limitations of simpler semi-local and global hybrid functionals for theoretical spectroscopy.

3.4 Time-dependent density functional theory

So far in this chapter, we have limited ourselves to ground-state DFT. However, in practical calculations, one is often interested in optical excitations that result from the response of the quantum system of interest to incident light. Such dynamic processes are beyond ground-state DFT but require an extension of the theoretical framework to the time domain, which is provided by TDDFT [24, 173, 174]. This is the subject of this section. The term TDDFT summarizes different approaches that comprise a variety of conceptual and computational aspects, see, e. g., Ref. [24] for a review. In the following, we focus on those aspects that are most relevant within the scope of this work.

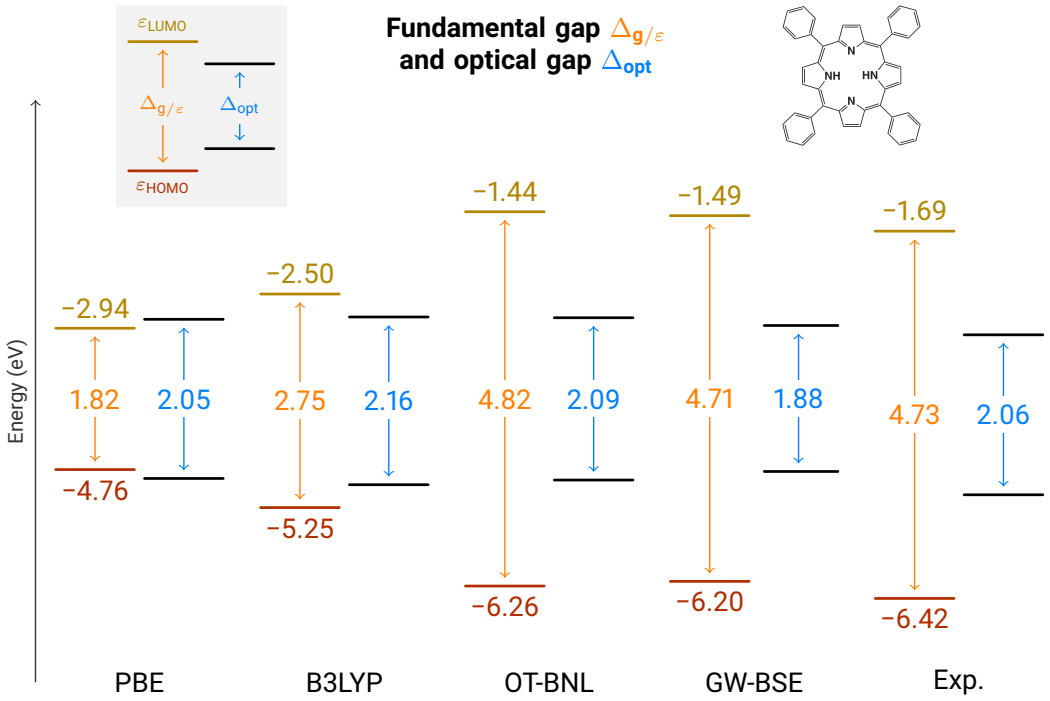

Fig. 3.3: Frontier eigenvalues $\varepsilon_{\mathrm{HOMO}}$ and $\varepsilon_{\mathrm{LUMO}}$, their gap Δ_ε, and the optical gap Δ_{opt}, cf. Sec. 3.4, computed with different density functionals (PBE, B3LYP, and OT-BNL) for a single tetraphenylporphyrin molecule [170]. For comparison, experimental results (Exp.) for ionization potential, electron affinity, and the fundamental gap Δ_{g} as well as results from many-body perturbation theory using GW-BSE are shown. Figure adapted from Ref. [27], see also references therein for the origin of the data.

3.4.1 Theoretical framework

The formal foundation of TDDFT is the theorem by Runge and Gross [175] which can be considered – despite conceptual differences, see, e. g., Ref. [24] – as the analogue of the Hohenberg-Kohn theorem for the time-dependent case. As in the ground-state case, there is also a time-dependent KS equation,

$$\left(-\frac{1}{2}\nabla^2 + v_{\mathrm{s}}(\mathbf{r},t)\right)\phi_i(\mathbf{r},t) = \mathrm{i}\frac{\partial\phi_i(\mathbf{r},t)}{\partial t}, \tag{3.38}$$

where

$$v_{\mathrm{s}}(\mathbf{r},t) = v_{\mathrm{ext}}(\mathbf{r},t) + \int \mathrm{d}\mathbf{r}'\,\frac{n(\mathbf{r}',t)}{|\mathbf{r}-\mathbf{r}'|} + v_{\mathrm{xc}}(\mathbf{r},t) \tag{3.39}$$

is the time-dependent KS potential. This equation *defines* the time-dependent xc potential $v_{\mathrm{xc}}(\mathbf{r},t)$. It is a functional of the full time evolution of the density $n(\mathbf{r},t)$ and the initial state. Many practical implementations of TDDFT, including the one used in this work, rely on linear-response TDDFT in the frequency domain [176, 177].

Following Ref. [24], this addresses essentially the following physical process: Assume the system of interest is initially, at $t = 0$, in its ground-state. Then, a weak perturbation $\delta v_{\text{ext}}(\mathbf{r}, t)$ of the external potential is switched on ($\delta v_{\text{ext}}(\mathbf{r}, t) = 0$, for $t \leq 0$),

$$v_{\text{ext}}(\mathbf{r}, t) = v_{\text{ext}}^{(0)}(\mathbf{r}) + \delta v_{\text{ext}}(\mathbf{r}, t). \tag{3.40}$$

Here and in the following the superscript (0) indicates the respective time-independent, ground-state properties. The perturbation can be thought of as being due to an external laser field, and it is "weak" in comparison to the interactions within the system. Since it is weak, only the first-order term $\delta n(\mathbf{r}, t)$ of the density response is relevant,

$$n(\mathbf{r}, t) = n^{(0)}(\mathbf{r}) + \delta n(\mathbf{r}, t). \tag{3.41}$$

The response function $\chi(\mathbf{r}, t, \mathbf{r}', t')$ connects δn and δv_{ext},

$$\delta n(\mathbf{r}, t) = \int \mathrm{d}t' \int \mathrm{d}\mathbf{r}' \; \chi(\mathbf{r}, t, \mathbf{r}', t') \, \delta v_{\text{ext}}(\mathbf{r}', t'), \tag{3.42}$$

and is formally given by the functional derivative

$$\chi(\mathbf{r}, t, \mathbf{r}', t') = \left. \frac{\delta n(\mathbf{r}, t)}{\delta v_{\text{ext}}(\mathbf{r}', t')} \right|_{v_{\text{ext}}^{(0)}}. \tag{3.43}$$

The strength of TDDFT is that it offers for a computationally feasible way to obtain this response function via the noninteracting KS system, as explained in the following [24]. First, the relation (3.42) between the external perturbation and the density response can also be expressed within the KS system, as

$$\delta n(\mathbf{r}, t) = \int \mathrm{d}t' \int \mathrm{d}\mathbf{r}' \; \chi_{\text{s}}(\mathbf{r}, t, \mathbf{r}', t') \, \delta v_{\text{s}}(\mathbf{r}', t'). \tag{3.44}$$

Thereby, the response function of the KS system can be calculated directly from the orbitals and eigenvalues of the ground-state KS equation (see, e. g., Eq. (4.55) in Ref. [24]). Importantly, $\delta v_{\text{s}}(\mathbf{r}, t)$ depends again on the density response due to the self-consistent nature of Eqs. (3.38) and (3.39),

$$\delta v_{\text{s}}(\mathbf{r}, t) = \delta v_{\text{ext}}(\mathbf{r}, t) + \int \mathrm{d}t' \int \mathrm{d}\mathbf{r}' \; f_{\text{Hxc}}(\mathbf{r}, t, \mathbf{r}', t') \, \delta n(\mathbf{r}', t') \tag{3.45}$$

where we have introduced the Hartree-xc kernel,

$$f_{\text{Hxc}}(\mathbf{r}, t, \mathbf{r}', t') = \frac{\delta(t - t')}{|\mathbf{r} - \mathbf{r}'|} + \left. \frac{\delta v_{\text{xc}}(\mathbf{r}, t)}{\delta n(\mathbf{r}', t')} \right|_{n^{(0)}}. \tag{3.46}$$

Connecting Eqs. (3.42), (3.44), and (3.45) and taking the Fourier transform from the time to the frequency domain yields an exact equation for the response function [24, 178],

$$\chi(\mathbf{r}, \mathbf{r}', \omega) = \chi_{\text{s}}(\mathbf{r}, \mathbf{r}', \omega) + \int \mathrm{d}\mathbf{r}_1 \int \mathrm{d}\mathbf{r}_2 \; \chi_{\text{s}}(\mathbf{r}, \mathbf{r}_1, \omega) f_{\text{Hxc}}(\mathbf{r}_1, \mathbf{r}_2, \omega) \chi(\mathbf{r}_2, \mathbf{r}', \omega), \tag{3.47}$$

from which the excitation energies and oscillator strengths of optical transitions can be obtained [179].

Under certain constraints, this problem can be formulated as an eigenvalue equation that can be written in a transparent way as a matrix equation. In this work, we are interested in closed-shell singlet systems and spin-singlet excitations. Like virtually all practical realizations of TDDFT we employ the adiabatic approximation for the semi-local components of the xc energy, i. e., the dependence of the Hartree-xc kernel on the time evolution of the density is neglected. Then, the kernel simplifies to

$$f_{\mathrm{Hxc}}^{\mathrm{ad}}(\mathbf{r},\mathbf{r}') = \frac{1}{|\mathbf{r}-\mathbf{r}'|} + \left.\frac{\delta^2 E_{\mathrm{xc}}[n]}{\delta n(\mathbf{r})\delta n(\mathbf{r}')}\right|_{n^{(0)}}. \tag{3.48}$$

Following Ref. [173], under these constraints the matrix formulation of linear-response TDDFT can be expressed as

$$\begin{pmatrix} A & B \\ -B^* & -A^* \end{pmatrix} \begin{pmatrix} X \\ Y \end{pmatrix} = \omega \begin{pmatrix} X \\ Y \end{pmatrix}. \tag{3.49}$$

Therein, the elements of the matrix,

$$A_{ia,jb} = \delta_{ij}\delta_{ab}(\varepsilon_a - \varepsilon_i) + M_{ia,jb}^{\mathrm{Hxc}}, \tag{3.50}$$

$$B_{ia,jb} = M_{ia,bj}^{\mathrm{Hxc}}, \tag{3.51}$$

with

$$M_{ia,jb}^{\mathrm{Hxc}} = \int \mathrm{d}\mathbf{r} \int \mathrm{d}\mathbf{r}'\ \phi_i^*(\mathbf{r})\phi_a(\mathbf{r}) f_{\mathrm{Hxc}}^{\mathrm{ad}}(\mathbf{r},\mathbf{r}')\phi_b^*(\mathbf{r}')\phi_j(\mathbf{r}'), \tag{3.52}$$

are calculated from the occupied (indices i, j) and unoccupied (a, b) eigenvalues and orbitals of the underlying ground-state KS equation. In Eq. (3.49), the eigenvalues ω correspond to the excitation energies. The related eigenvector components indicate the contributions of occupied–unoccupied (elements X_{ia}) and unoccupied–occupied (Y_{ai}) KS orbital pairs to the respective excitation. The quality of the xc density functional approximation employed in the underlying KS calculation influences the outcome of a subsequent linear-response TDDFT calculation in two ways: First, the KS orbitals and eigenvalues enter the matrices A and B. Second, the adiabatic Hartree-xc kernel is related to the xc energy. The formulation of linear-response TDDFT given so far, i. e., Eqs. (3.48) to (3.52), applies only to functionals within time-dependent KS. To handle global hybrid or RSH functionals within time-dependent generalized KS [168, 180] an additional term is required to account for the non-local part of the xc functional [173],

$$M_{ia,jb}^{u} = -\int \mathrm{d}\mathbf{r} \int \mathrm{d}\mathbf{r}'\ \phi_i^*(\mathbf{r})\phi_j(\mathbf{r}) u(|\mathbf{r}-\mathbf{r}'|)\phi_b^*(\mathbf{r}')\phi_a(\mathbf{r}'). \tag{3.53}$$

It is added to the matrices A and B,

$$A_{ia,jb} = \delta_{ij}\delta_{ab}(\varepsilon_a - \varepsilon_i) + M_{ia,jb}^{\mathrm{Hxc}} + M_{ia,jb}^{u}, \tag{3.54}$$

$$B_{ia,jb} = M^{\mathrm{Hxc}}_{ia,bj} + M^{u}_{ia,bj}, \tag{3.55}$$

which then enter Eq. (3.49) instead of Eqs. (3.50) and (3.51). As before, the local part of the xc functional enters via M^{Hxc}, cf. Eq. (3.52). In Eq. (3.53), the interaction $u(|\mathbf{r} - \mathbf{r}'|)$ can either be a fraction of the full Coulomb interaction,

$$u(|\mathbf{r} - \mathbf{r}'|) = \frac{a}{|\mathbf{r} - \mathbf{r}'|}, \tag{3.56}$$

in the case of global hybrids or the long-range part of the Coulomb interaction,

$$u(|\mathbf{r} - \mathbf{r}'|) = \frac{\operatorname{erf}(\omega|\mathbf{r} - \mathbf{r}'|)}{|\mathbf{r} - \mathbf{r}'|}, \tag{3.57}$$

in the case of RSH functionals.

3.4.2 Prediction of optical excitations

In the following, we discuss how well optical excitations are predicted by TDDFT calculations. To keep the description transparent, we focus on the optical gap Δ_{opt} first [27]. It can be defined as the energy gap between the first excited state and the ground state. Experimentally, it corresponds to the onset of the absorption spectrum. Conceptually, it can be related to the fundamental gap by invoking the picture of quasi-particles again, cf. Sec. 3.1. As explained above, the response effects of the correlated many-electron system upon inserting (or removing) an electron into (or from) the system are accounted for by a quasi-electron (or quasi-hole, respectively). The fundamental gap is the difference between the lowest quasi-hole and quasi-electron energies. On the other hand, optical excitations, where the electrons respond to the absorption of light by the formation of an excited state, can be considered as the simultaneous formation of a quasi-electron and a quasi-hole. Unlike in the case of the fundamental gap, the interaction between the quasi-electron and quasi-hole needs to be taken into account. Therefore, the optical gap is reduced compared to the fundamental gap by the attractive interaction within this quasi-particle pair – also known as exciton binding energy [27]. This reduction of the gap is illustrated in Fig. 3.1.

At this point, we recall that TDDFT, in either its KS or generalized KS form, is an exact theory. Consequently, accurate optical excitations can be obtained from KS TDDFT in principle.[9] Indeed, the form of the linear-response equations of TDDFT (3.49) may appear suitable to account for the many-electron nature of optical excitations: Without the matrices M the excitation energies were just given by the KS eigenvalue differences $\varepsilon_a - \varepsilon_i$ between the respective unoccupied and

[9] This is a conceptual difference to ground-state DFT: There, the orbitals and eigenvalues are introduced just as auxiliary objects. Therefore, there is no guarantee that the eigenvalue differences are physically interpretable and, indeed, this is not the case of the KS HOMO–LUMO gap, cf. Sec. 3.1.1.

occupied orbitals, i. e., were described as a single-particle excitation from orbital i to a. On the other hand, the matrices M interlink different pairs of occupied and unoccupied orbitals, (i, a) and (j, b). Hence, this can introduce many-electron effects that lead to reasonable optical gaps. This is illustrated by returning to the example of tetraphenylporphyrin, see Fig. 3.3. For the semi-local functional PBE, the global hybrid B3LYP, and the optimally tuned BNL functional the optical gap computed from linear-response TDDFT is very similar and agrees rather well with the reference data. However, PBE and B3LYP obtain a correctly predicted optical gap by the many-electron effects acting in an unphysical way. For PBE, the poor quality of the KS eigenvalues leads to a HOMO–LUMO eigenvalue gap that is smaller than even the optical gap. Consequently, the many-body interactions introduced via linear-response TDDFT actually *increase* the gap, which is contrary to the physical picture of gap *reduction* by electron-hole attraction. Thus, PBE predicts the exciton binding energy with a wrong, negative sign. The results from B3LYP are somewhat better, but the binding energy is still too small. Only BNL is able to provide the correct picture of gap reduction and an exciton binding energy that agrees with the GW-BSE calculation and the experimental value. In other words, only the optimally tuned RSH functional describes both fundamental and optical gap consistent with the quasi-particle nature of electronic excitations.

The unsatisfactory description of energy eigenvalues by semi-local and global hybrid functionals can have even more severe consequences for optical excitations with charge-transfer character [18, 19, 181–185]. To see this, it is instructive to focus on a special case known as Mulliken limit [27] – a donor-acceptor complex in the limit of large separation between donor and acceptor where the lowest optical excitation corresponds to a charge-transfer excitation from donor to acceptor. In this case, the optical gap is given by[10]

$$\Delta_{\mathrm{opt}} = \mathrm{IP} - \mathrm{EA} - \frac{1}{R} = \Delta_{\mathrm{g}} - \frac{1}{R}, \tag{3.58}$$

where R is the donor-acceptor distance. If we assume that the excitation is dominated by a transition from the HOMO orbital, located on the donor, to the LUMO orbital, located on the acceptor, the linear-response equations simplify considerably and can be analyzed analytically. First, in the case of *exact* KS TDDFT the (exact) optical gap emerges as the eigenvalue difference $\Delta_\varepsilon = \varepsilon_{\mathrm{LUMO}} - \varepsilon_{\mathrm{HOMO}}$ modified by contributions from an overlap integral similar to Eq. (3.52) but with the *exact* Hartree-xc kernel. This overlap integral must account for both the exciton binding energy and the derivative discontinuity that separates Δ_ε from Δ_{g}. Since the overlap of the occupied and unoccupied orbitals involved in the excitation almost vanishes, the xc kernel must be divergent to obtain the correct optical gap [184, 186]. Indeed, it has been demonstrated numerically that the exact xc kernel can exhibit pronounced spatial and temporal non-localities [187]. However, if we turn to *approximate* KS

[10] In Hartree atomic units, the term $-1/R$ corresponds to the Coulomb interaction (energy) of the electron and hole located on acceptor and donor, respectively, at distance R.

TDDFT, cf. Eqs. (3.48) to (3.52), and use a semi-local xc functional, the xc kernel, which is now limited to the adiabatic approximation, lacks such non-localities. This can be seen easily for the LDA exchange functional where the corresponding exchange kernel, $f_{\mathrm{x}}^{\mathrm{ad,LDA}}(\mathbf{r},\mathbf{r}') \sim n^{-2/3}(\mathbf{r})\delta(\mathbf{r}-\mathbf{r}')$, is purely local. Hence, the optical gap is just given by the eigenvalue gap Δ_ε. However, developing xc kernels that go beyond the adiabatic approximation is highly non-trivial and such kernels are not common in actual calculations [24, 188, 189]. As a practical remedy, one can opt for time-dependent generalized KS with orbital-dependent exact exchange and, thus, incorporate non-locality in this way. In this case, the optical gap emerges from Eqs. (3.49), (3.54), and (3.55) as [27]

$$\Delta_{\mathrm{opt}}^{u} = \varepsilon_{\mathrm{LUMO}} - \varepsilon_{\mathrm{HOMO}} - \int \mathrm{d}\mathbf{r} \int \mathrm{d}\mathbf{r}' \; |\phi_{\mathrm{HOMO}}(\mathbf{r})|^2 u(|\mathbf{r}-\mathbf{r}'|) |\phi_{\mathrm{LUMO}}(\mathbf{r}')|^2. \quad (3.59)$$

Thereby, the overlap integral yields a/R for a global hybrid, and $1/R$ in the case of RSH functionals, cf. Eqs. (3.56) and (3.57), respectively. Thus, RSH functionals can provide the correct $1/R$ exciton binding energy and the optimal-tuning procedure ensures that the HOMO–LUMO gap correctly yields the fundamental gap.

The trends demonstrated for the two examples above are confirmed by numerous computational studies, see, e. g., Refs. [25, 27] for reviews. Very often, valence excitations, where the involved orbitals extend over similar regions of space, are reasonably well described by semi-local functionals [190]. However, this agreement does not conform with the physical quasi-particle interpretation of optical excitations, as explained above, and, indeed, the agreement has been attributed to cancellation of self-interaction errors [18]. RSH functionals with optimal tuning retain this favorable performance for valence excitations and, moreover, can provide a realistic description of excitations with charge-transfer character, which has been demonstrated in scenarios of practical relevance [167, 169, 191–193]. Furthermore, optimally tuned RSH functionals can also cover further challenging excitations without explicit charge-transfer character [168, 194]. In conclusion, RSH functionals with optimal tuning emerge as a promising route to obtain optical excitation with (and without) charge-transfer character reliably from TDDFT.

4 Reaction center of heliobacteria

Photosynthesis is a biological process by which plants, certain bacteria, and algae are able to capture solar radiation and convert it to a useful form of chemical energy [1, 2]. Specialized pigment-protein complexes that have chlorophyll (Chl), bacteriochlorophyll (BChl), and other pigments integrated into their polypeptide chains play a vital role for the functioning of photosynthetic organisms. The first step of photosynthesis is the absorption of incident photons by the light-harvesting antenna and the subsequent transfer of excitation energy toward the reaction center. These pigment-protein complexes are integrated into the photosynthetic membrane. As an example, the well-known and frequently studied purple bacteria [4] have two main types of light-harvesting antenna: The LH2 complex contains two rings of BChl molecules with absorption maxima at $\sim 800\,\mathrm{nm}$ and $\sim 850\,\mathrm{nm}$, respectively. The LH1 complex absorbs light around $\sim 875\,\mathrm{nm}$. Antenna systems usually rely on an energetic funneling mechanism: Pigments at the periphery of the complex absorb at higher energies than those close to the reaction center. Therefore, the excitation energy can be transferred "downhill" toward the reaction center. In purple bacteria this is realized by a transfer cascade through the different rings, beginning at the 800 nm ring and ending at the 875 nm ring, before the excitation energy is finally transferred to the reaction center.

The reaction center is a further pigment-protein complex that is bound to the photosynthetic membrane. There, the primary charge-separation steps take place, which are explained in more detail in Sec. 4.1. Eventually, this leads to an electron-hole pair where electron and hole are located at different ends of the photosynthetic membrane. Usually, quite a number of antenna complexes are grouped around a single reaction center. This increases their effective absorption cross section and ensures efficient operation even under low-light conditions [9]. The electron-hole pair generated in the reaction center is being processed in secondary electron-transfer reactions. Eventually, this leads to the formation of chemical energy, which can power various cellular processes. In the case of purple bacteria charge separation in the reaction center leads to the reduction of quinones. These quinones leave the reaction center and contribute to a cyclic electron pathway which establishes a proton gradient across the photosynthetic membrane. Subsequently, this electrochemical gradient can be used to fuel the formation of adenosine triphosphate as an energy source of the bacterial metabolism.

In this chapter, we first give an overview of the principles of primary charge separation in photosynthetic reaction centers in Sec. 4.1. Subsequently, in Sec. 4.2, we introduce the reaction center of heliobacteria and summarize insights on the charge separation process gained from previous experimental studies. Finally, in Sec. 4.3, we present

our results on primary charge separation in the heliobacterial reaction center from first-principles computations. This is a summary of Pubs. [B1, B3].

4.1 Primary charge separation in photosynthetic reaction centers

All photosynthetic reaction centers share common structural features [2, 7]. The main pigments of the charge-separation process are arranged in a two-branched structure, where one end of the branches is formed by a pair of closely packed Chl or BChl chromophores, referred to as special pair (SPP). These are followed by two further chromophores on each branch (Chl, BChl, or similar molecules), which are called electron transfer cofactor 2 (EC2) and 3 (EC3) in this work.[1] Finally, the branches end with the terminal electron acceptors. Two different types of terminal electron acceptors have been found in different reaction centers – quinones and iron-sulfur clusters. Depending on the type of terminal electron acceptor present, reaction centers are being classified as type I (with iron-sulfur clusters) or type II (with quinones). In oxygenic photosynthesis systems, both types of reaction centers – referred to as photosystem I and II – are combined. In anoxygenic photosynthesis, only one type is present. As an example, purple bacteria employ a type-II reaction center, whereas heliobacteria and green sulfur bacteria rely on a type-I reaction center. An overview of the different types of reaction centers is shown in Fig. 4.1.

Although the types of chromophores incorporated in the two different branches and their spatial arrangement are rather similar, their function is usually highly asymmetric and the relevant steps of the charge-separation process take place only on one of the branches, as indicated in Fig. 4.1. It is well established that the first major step of charge separation upon excitation of the reaction center – by direct absorption of sunlight or by excitation energy transfer from the antenna domain – is the formation of an $\mathrm{SPP}^{+}\mathrm{EC3}^{-}$ charge-separated state, where the hole is localized on the SPP and the electron on EC3 [5, 8]. However, the details of primary charge separation, i. e., the intermediate steps that lead to the formation of the $\mathrm{SPP}^{+}\mathrm{EC3}^{-}$ state, turn out to be much more difficult to resolve. This question has been addressed repeatedly in previous years but continues to be a matter of ongoing research efforts [6, 198–202]. This literature is far too vast to be covered comprehensively in this work. Generally speaking, two different mechanisms seem plausible,[2]

$$\mathrm{RC}^{*} \rightarrow \mathrm{SPP}^{+}\mathrm{EC2}^{-} \rightarrow \mathrm{SPP}^{+}\mathrm{EC3}^{-}, \tag{CT2}$$

$$\mathrm{RC}^{*} \rightarrow \mathrm{EC2}^{+}\mathrm{EC3}^{-} \rightarrow \mathrm{SPP}^{+}\mathrm{EC3}^{-}, \tag{CT3}$$

[1] Different names are common in the literature for EC2 and EC3, in particular for type-II reaction centers usually a different nomenclature is used. Within this work we use a consistent notation for all reaction centers to keep the presentation transparent.

[2] The charge-transfer ("CT") mechanisms are numbered according to the initial electron acceptor (EC2 or EC3).

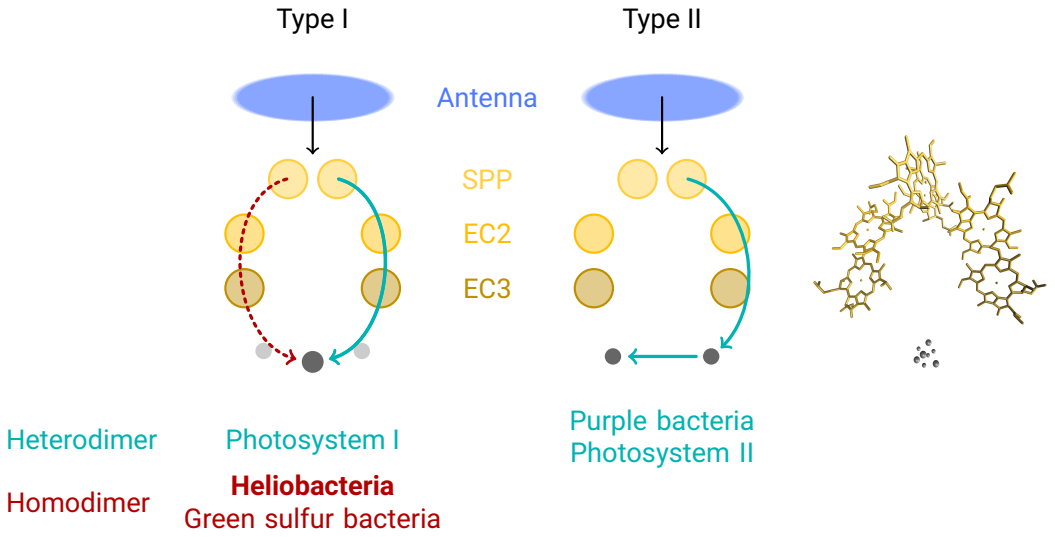

Fig. 4.1: Schematic overview of the charge-separation process and the different types of reaction centers present in photosynthetic organisms. Both type-I and type-II reaction centers contain SPP, EC2, and EC3 pigments (colored yellow) but differ in the terminal electron acceptors (quinones and iron-sulfur clusters; colored gray). Charge separation is mainly initiated by excitation-energy transfer from the antenna (colored blue; sketched at the top). In heterodimeric reaction centers electron transfer proceeds exclusively or primarily along one branch (indicated by the cyan arrows), in homodimers both branches contribute equally (indicated red). For comparison, the structure of the pigments in the type I reaction center of heliobacteria [35], cf. Fig. 4.3 below, is depicted on the right. The role of quinones in this reaction center is being debated [29–31, 195–197]; the crystal structure of the heliobacterial reaction center lacks quinones while they are present in photosystem I [35].

where RC* denotes the initial excited state of the reaction center. In other words, the central question is whether EC2 or EC3 serves as the initial electron acceptor. Details neglected by this slightly simplified picture include the extension of the initial excited state RC*, the degree of delocalization of the electron or hole of the intermediate charge-transfer state, and the potential formation of an additional partial charge-transfer state following RC*.

Purple bacteria employ the mechanism (CT2) *in vivo* [203–205]; evidence for the presence of the alternative charge-separation pathway (CT3) has been found, but only in mutant reaction centers [206–208]. The picture has been less clear in photosystem II where evidence for both mechanisms has been found [6, 209–211]. However, the more recent studies consistently indicate that variant (CT3) is the central charge-transfer pathway in photosystem II [212–216], although there might be a minor, slower pathway as well [217]. The mechanism (CT3) is also present in photosystem I [218–221]. It is interesting to note that, in contrast to purple bacteria and photosystem II, both branches contribute to the charge-separation process in photosystem I, albeit one branch is the dominant one. A remarkable exception to the rule that charge separation occurs exclusively or primarily along one of the two

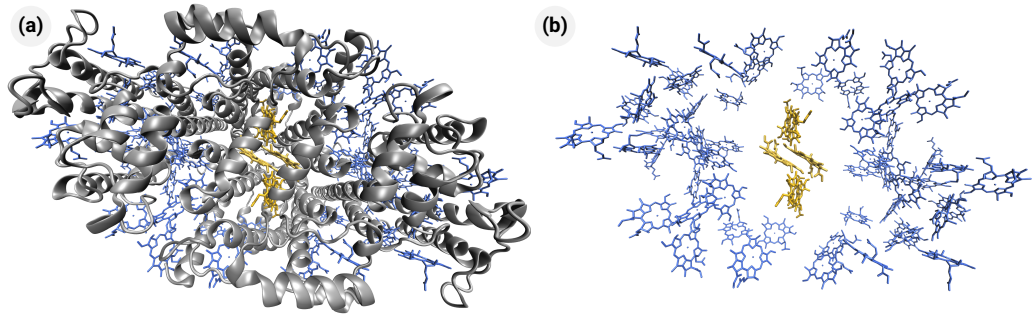

Fig. 4.2: Overview of the Chl and BChl chromophores in the reaction center of *Heliobacterium modesticaldum* [35] **(a)** with and **(b)** without the polypeptide chains (colored gray), as viewed from one side of the photosynthetic membrane. The antenna domain is colored blue, the reaction center domain yellow. The other pigments, the phythyl tails of Chl and BChl, and the hydrogen atoms are omitted for clarity. The C_2 symmetry axis of the reaction center complex is perpendicular to the plane of projection. Structural data from the Protein Data Bank under file ID 5V8K [35].

branches constitute the reaction centers of heliobacteria and green sulfur bacteria [7]. These reaction centers are made up of homodimeric core polypeptides and, thus, the two cofactor branches are equivalent. The structures of both reaction centers have been resolved just recently by Gisriel *et al.* [35] (heliobacteria) and Chen *et al.* [222] (green sulfur bacteria) and, hence, their charge-separation process is not understood to the same extent as in purple bacteria or photosystem I and II. The heliobacterial reaction center is the main focus of this work and is further described in the following section.

4.2 Overview of the reaction center of heliobacteria

Heliobacteria are anoxygenic phototrophic bacteria with a homodimeric type-I reaction center [30, 31, 223]. The structure of *Heliobacterium modesticaldum* [224] has been resolved recently by Gisriel *et al.* [35]. The light-harvesting apparatus is relatively simple and consists only of a single pigment-protein complex that comprises both the antenna domain that is responsible for light absorption and excitation-energy transfer and the actual reaction center domain where charge separation takes place. Often the whole complex is collectively referred to as "reaction center". In contrast to, e. g., purple bacteria, no peripheral antenna complexes have been identified so far [35]. The pigment-protein complex is homodimeric, i. e., it is composed of two identical copies of the same subunit; each subunit consists of two polypeptide chains. The chromophores are integrated into the polypeptide chains. In total, the heliobacterial reaction center binds 54 BChl *g*, four BChl *g'*, and two 8^1-hydroxychlorophyll *a* (OH-Chl *a*) pigments as well as two carotenoids and one [4Fe-4S] cluster [28, 29, 35, 225–228]. Fig. 4.2 shows the structure of the Chl and BChl chromophores, which are arranged in two distinct groups [35]: The antenna

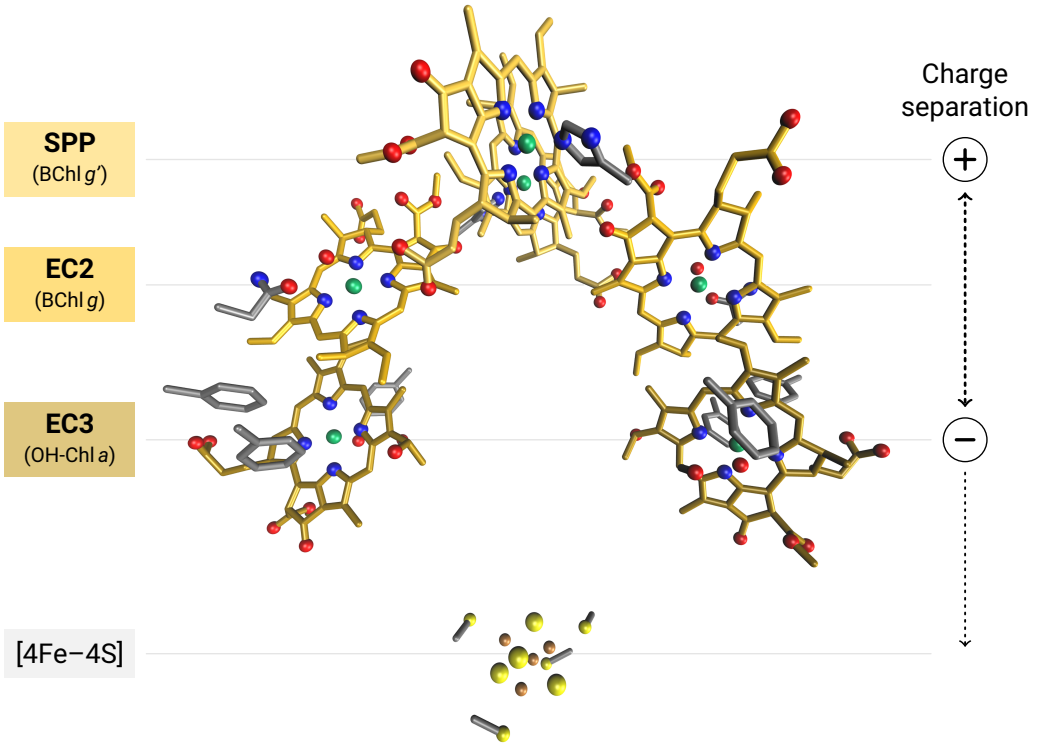

Fig. 4.3: Arrangement of the charge-separation cofactors in the reaction center of *Heliobacterium modesticaldum* [35], as viewed from within the membrane (i. e., the plane of projection is perpendicular to that in Fig. 4.2). Displayed along with the cofactors are the coordinating amino acids and water molecules (as described in the text). The carbon atoms of SPP, EC2, and EC3 are colored yellow, the carbon atoms of the coordinating amino acids gray. Otherwise, the atoms are colored according to the atom type (blue: nitrogen; red: oxygen; green: magnesium; yellow: sulfur; ocher: iron). The phythyl tails of Chl and BChl and the hydrogen atoms are omitted for clarity. On the right, the two major steps of charge separation are indicated schematically [227]. Structural data from the Protein Data Bank under file ID 5V8K [35].

domain, which has a roughly toroidal shape, surrounds the chromophores involved in the charge-separation process. The antenna domain consists of 52 BChl *g* and two BChl *g'*. The majority of them are more than 14 Å away from the reaction center domain; only three pigments in each monomer are within 13 Å to the reaction center domain.

The reaction center domain contains two BChl *g*, two BChl *g'*, and two OH-Chl *a* [35]. Their detailed arrangement is depicted in Fig. 4.3. The BChl *g'* pigments form the SPP with a center-to-center distance of only 5.7 Å. On each branch, it is followed by a BChl *g* (EC2) and a OH-Chl *a* (EC3) before both branches terminate in a single [4Fe-4S] cluster. The center-to-center distance between one BChl *g'* from the SPP and the neighboring EC2 is 12.1 Å and it is 9.1 Å between EC2 and EC3, respectively. All chromophores are coordinated by amino acid residues or interstitial

water molecules that are linked to neighboring amino acid residues by hydrogen bonds. Specifically, the SPP is coordinated by His 537; EC2 is coordinated by "a small molecule approximately the size of water" [35] which we treat as water in this work and which itself is hydrogen-bonded by Gln 548; EC3 is coordinated by a water molecule hydrogen-bonded by Ser 545; the [4Fe-4S] cluster is coordinated by Cys 432 and Cys 441. All of these molecules are less than 3 Å away from the magnesium atoms in the center of the respective chromophores. Along with these molecules, which are specified in Ref. [35] as "coordinating molecules", we include Phe 399, Phe 450, and Phe 542 in our calculations (cf. Sec. 4.3), due to their positions close to the chlorin ring of OH-Chl *a*. The spatial arrangement of these coordinating amino acid residues and water molecules can be seen in Fig. 4.3.

The absorption spectrum of Chl and BChl has well-known characteristics [4, 229–231]. It exhibits two distinct peaks that are referred to as Q_y and Q_x transitions and have characteristic transition dipole moments, which are oriented along approximately orthogonal directions in the plane of the chlorin ring. In the case of BChl *g*, the Q_y transition has been measured at $\sim 760 \ldots 780$ nm and the Q_x transition at $\sim 560 \ldots 570$ nm, respectively, depending on the solvent [226]. The absorption spectrum of the reaction center of heliobacteria is dominated by a peak around 800 nm which originates from the Q_y excitations of the BChl *g* and BChl *g'* chromophores, see Refs. [28, 29, 227, 228] for absorption spectra of heliobacterial reaction centers. Several distinct bands between $\sim 780 \ldots 810$ nm have been identified, which have been interpreted as indication of clusters of chromophores with slightly different excitation energies. The excitations of OH-Chl *a* are higher in energy than those of BChl *g* [225]. Thus, the Q_y transitions of the OH-Chl *a* pigments lead to an additional, smaller absorption peak around 670 nm in the absorption spectrum of the reaction center.

The excitation-energy transfer and the charge-separation process in the heliobacterial reaction center have been the subject of multiple previous experimental studies [232–239]. In particular, there is well-grounded evidence that the SPP^+EC3^- charge-separated state is formed within ~ 25 ps upon light absorption [227]. However, despite these research efforts it has remained completely unclear until up to a few years ago whether primary charge separation proceeds along path (CT2) or (CT3). More recently, some light has been shed onto this question. Here we especially want to point at two works. In the study by Song *et al.* [36], the charge-separation process has been investigated by multispectral two-dimensional electronic spectroscopy. Orf and Redding [37] have conducted site-directed mutagenesis experiments to perturb the vicinity of EC3. Both groups interpret their results as indicating that EC3 serves as the primary electron donor. Apart from that, the electronic dynamics upon light absorption have also been investigated in several theoretical works based on model Hamiltonians by Kimura and coworkers [240–242]. Thereby, in particular, the excitation energy transfer within the Chl and BChl network has been examined. However, these studies do not provide direct insights into the details of the charge-separation process. In our work, we take a step forward and investigate the process

of primary charge separation in the heliobacterial reaction center by first-principles theoretical methods. Thereby, our focus is twofold: We identify the first intermediate step in the charge-transfer chain and, moreover, unravel how the structure of the pigment-protein complex, especially the interaction of the chromophores with the protein environment, influences the charge-separation process. Our methods and main results are described in the following section.

4.3 Primary charge separation in the reaction center of heliobacteria

Computational studies on an atomistic level can provide valuable insights into the photophysical dynamics of light-harvesting systems, since they offer direct access to the (full) electronic and nuclear dynamics. This can make the interactions between different chromophores and further parts of the biochemical systems, e. g., the amino acid residues of the surrounding protein, transparent and shed light on the interplay of the different constituents. Due to the complexity of the biochemical systems and their sheer size, computations can be challenging and a variety of different methods is being used [15–17]. Approaches based on model Hamiltonians [243] and multiscale techniques that combine quantum mechanical and semiclassical methods [244, 245] can be an efficient way to cover an appreciable number of chromophores and to mimic the biochemical environment of light-harvesting pigments. These methods can lead to valuable insights [212–214, 246–252]. However, one should be aware of that they are by no means a panacea. Approaches that are based on model assumptions can only cover those effects that have been considered in the design of the underlying models. Furthermore, the semiclassical methods need to be appropriate for the specific electronic properties of light-harvesting systems and special care is required at the interface between the semiclassical and quantum mechanical regions. Finally, if model parameters are explicitly fit to resemble experimental results, the insights gained from this theoretical description are not independent of the corresponding experiments.

In our work, we choose an approach that avoids relying on empirical input. We calculate the electronic excitations using linear-response time-dependent density functional theory (TDDFT). To reduce the computational burden, we analyze the structure carefully to disclose those chromophores and parts of the environment that are relevant to capture the characteristics of primary charge separation. The resulting systems can be included entirely in the TDDFT calculations. In choosing our TDDFT methods, we are guided by the insights described in Chap. 3. Especially, it is mandatory to use an approach that can describe charge-transfer states correctly [18–20, 167, 253]. Therefore, in previous works, range-separated hybrid (RSH) functionals have been applied successfully to light-harvesting systems [254–258]. In particular, it has been demonstrated that non-empirical optimal tuning can approach the accuracy of higher-level methods [259–261]. In our work, we rely on a RSH functional with optimal tuning.

The dynamics of the nuclei, e. g., driven by temperature effects, can have a relevant impact on excitation energy transfer and charge separation [6, 262, 263]. This is an important piece of physics that needs to be considered in theoretical descriptions. Apart from that, the strong influence that details in the structure of the nuclei have on the electronic excitations of light-harvesting systems leads to an important technical issue. For very reliable quantum-chemical results, the resolution of the experimentally determined crystal structure is usually not high enough to represent structural details such as the bond length alternation in conjugated systems with the required accuracy [17, 264, 265]. This limitation can be addressed by combining quantum-chemical calculations with ground-state Born-Oppenheimer molecular dynamics (MD) simulations [16, 17, 266, 267]. Thereby, classical force fields may be problematic, e. g., due to the so-called "geometry mismatch problem" [15, 267–270]. Hence, we combine the TDDFT calculations with *ab initio* Born-Oppenheimer MD simulations [38, 39] on the basis of DFT [271–273] to avoid such issues and to take into account temperature effects.

In our work, we focus on the initial steps of charge separation in the reaction center of heliobacteria. This means, we are interested in the processes leading to the formation of the $SPP^{+}EC3^{-}$ charge-separated state upon excitation of the reaction center domain. Therefore, the SPP, EC2, and EC3 pigments are relevant (cf. Fig. 4.3). Our study is divided into two parts. The first part corresponds to Pub. [B1] and is summarized in Sec. 4.3.1. Therein, we focus on SPP and EC2, i. e., we initially omit EC3.[3] This leads to a structure of moderate size where the computational effort is tractable. Thus, this setup is well-suited to test the numerical methods and to establish a robust computational protocol. Apart from that, excluding EC3 can be motivated physically as well. In purple bacteria SPP and EC2 are the pigments that are relevant for the first charge-separated state and, thus, this setup can be used as a first step to examine whether a similar charge-transfer mechanism is also present in heliobacteria.[4] In the second part of our study, we rely on these experiences and include EC3 to cover the full charge-separation chain. This part is published in Pub. [B3] and summarized in Sec. 4.3.2. It contains our central results on the heliobacterial reaction center.

4.3.1 Special pair and adjacent cofactors

As a basic input for our calculations we rely on the crystal structure of *Heliobacterium modesticaldum* by Gisriel *et al.* [35] which can be obtained from the Protein Data Bank under file ID 5V8K. From that, we obtain the structures of the chromophores and the amino acid residues, whereby we remove the phythyl tails from the BChls

[3] As a guidance for the reader, we mention that some of the cofactors are abbreviated differently in Pub. [B1]. In particular, EC2 is labelled "Acc" there.

[4] We conducted the first part of our study before Refs. [36, 37] provided more detailed experimental insights into the site of the initial charge-separation event.

and neglect the polypeptide backbone [B1]. As a first step, we perform linear-response TDDFT calculations using the crystal structure geometry. This provides a first impression of the coupling of the chromophores and allows assessing the impact of the surrounding amino acids. We employ the ωPBE RSH functional with $\omega = 0.171\,\mathrm{a_0^{-1}}$ determined from optimal tuning for a single BChl. The calculations are performed using the quantum chemistry program Q-Chem [274]. Details can be found in Pub. [B1]; our choice of the range-separation parameter is discussed in more detail in the Supporting Information of Pubs. [B1, B3]. We analyze the charge-transfer character of the TDDFT excitations using natural transition orbitals [275] and difference densities, defined as the difference of the electron densities of the excited state and the ground state [B1]. These methods allow identifying $\mathrm{SPP^+EC2^-}$ charge-transfer excitations in the spectrum of the reduced subsystem containing only the SPP and EC2 pigments [B1]. The lowest $\mathrm{SPP^+EC2^-}$ charge-transfer excitation is separated by an energy gap of $\sim 0.3\,\mathrm{eV}$ from the dominant BChl Q_y excitations. This energy gap is strongly influenced by the amino acids and water molecules that coordinate the SPP and EC2 chromophores (cf. Fig. 4.3), which are therefore included in all calculations. Further amino acids within 3 Å to the chromophores lead to a small overall redshift of $\lesssim 0.05\,\mathrm{eV}$ but hardly affect the relative energetic ordering of the excitations and, thus, are not considered for further analysis.

As a second step, we perform *ab initio* Born-Oppenheimer MD simulations at room temperature. The forces on the nuclei are calculated from ground-state DFT calculations using the PBE functional with D3 dispersion correction [276, 277]. The MD simulations are performed using the quantum chemistry program Turbomole [278]; details can be found in Pub. [B1]. We evaluate the MD data by taking equally distant snapshots of the atomic structure along the trajectories. Then, we calculate the corresponding TDDFT excitation spectra based on these structures and determine the charge-transfer excitations by an analysis of the natural transition orbitals. To make the evaluation of numerous excitation spectra feasible in practice, we developed an automated computational protocol for these steps [B1]. Since we start our MD trajectories at the crystal structure geometry, the structure is equilibrated at the beginning of the trajectories and, hence, we exclude the first part of the trajectories from further evaluation. The analysis of the MD data confirms the observation that the $\mathrm{SPP^+EC2^-}$ charge-transfer excitations occur at higher energies than the dominant BChl Q_y excitations; the observed energy gap is even increased to $\sim 0.4\,\mathrm{eV}$.

The observed energy gap between the Q_y band and the onset of the charge-transfer excitations has important implications on the interpretation in view of possible charge-separation mechanisms in the heliobacterial reaction center. A typical mechanism for efficient charge separation is the following: Light is absorbed by the dominant Q_y excitations of the antenna BChls and transferred to the reaction center, where a Q_y excited state is formed on the cofactors. Then, a charge-separated state at an energy lower than that of the BChl Q_y band is formed. Our calculations strongly suggest that coupling to a $\mathrm{SPP^+EC2^-}$ state is not possible in that way. Although alternative charge-transfer mechanisms that may involve the Q_x excitations or relaxation effects

in the Q_y excitation cannot be ruled out completely, the most likely interpretation of our results is that the charge-separation mechanism (CT2) is not the dominant one in the heliobacterial reaction center [B1]. In other words, the first intermediate state of primary charge separation may involve the EC3 cofactor, which has not been considered so far.

4.3.2 Full cofactor chain

In the second part of our study, we build upon the work described in the previous section. The basic idea of our computational approach remains unchanged, but we considerably extend it in several aspects [B3]. First, we enhance our MD approach: We generate more and longer trajectories to obtain a better sampling of the space of nuclear configurations, exclude a longer time interval at the beginning of the trajectories from the evaluation to ensure better equilibrated structures, and increase the time interval between subsequent snapshots used for evaluation to avoid correlations between the snapshots. Furthermore, we adapt the way of how the MD snapshots are evaluated. Overall, these measures increase the reliability of our findings. Second, we consider the full charge-separation branches of the heliobacterial reaction center (from SPP to EC3, cf. Fig. 4.3) which is important to reveal the first intermediate state of primary charge separation. Moreover, we extend our analysis of the protein environment: We consider the amino acid residues within ~ 6 to 10 Å of the chromophores. In the following, we summarize our main results; further details on the methods can be found in Ref. [B3].

Our first finding is related to the symmetry of the structure. The crystal structure exhibits perfect C_2 symmetry due to the way the X-ray data is obtained. However, in a realistic setup one would expect small asymmetries between the two charge-separation branches, which we observe, e. g., in our MD simulations [B1, B3]. The electronic excitations are very sensitive to this symmetry breaking. Specifically, this means that the charge-transfer excitations are always localized on one of the two branches. Therefore, despite the homodimeric nature of the heliobacterial reaction center, it turns out that one cofactor branch is sufficient in practice to capture the charge-separation characteristics correctly [B3]. Our minimal model of the reaction center thus consists of both SPP chromophores (due to the small separation between them), one EC2, and one EC3 chromophore. Since we know from Pub. [B1] that the amino acids and water molecules that coordinate the chromophores (cf. Fig. 4.3) have a relevant influence on the excited states, we include them as well. This minimal model is termed the tetramer model. Its excitation spectrum is shown in Fig. 4.4. We find all charge-transfer excitations that we expect – SPP^+EC2^-, $EC2^+EC3^-$, and SPP^+EC3^-– albeit at energies above the band of BChl Q_y excitations [B3].

Our second and most important finding is related to the (protein) environment of the cofactors. Apart from the coordinating amino acids and water molecules, we consider further parts of the environment. Thereby, we find that most of the amino acids within ~ 6 Å of the pigments, the phythyl tails of the pigments (which are neglected

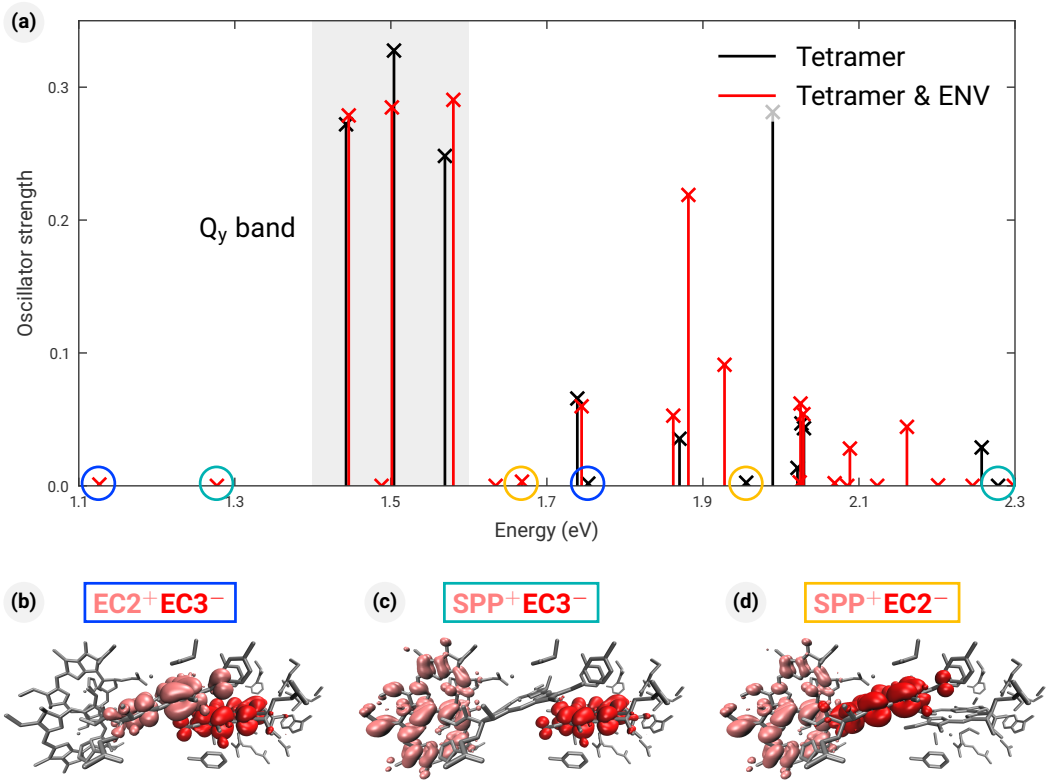

Fig. 4.4: (a) TDDFT excitation spectrum of the tetramer model (SPP, one EC2, and one EC3; see text) without and with a cluster of surrounding amino acids (named ENV). As detailed in Pub. [B3], this cluster (named ENV^{R+} therein) contains, in particular, charged amino acids. The gray box indicates the band of the brightest BChl Q_y excitations. The circles indicate the lowest charge-transfer excitations of each type (blue: EC2$^+$EC3$^-$; teal: SPP$^+$EC3$^-$; yellow: SPP$^+$EC2$^-$). In panels **(b)**, **(c)**, and **(d)** the corresponding difference densities of the lowest charge-transfer excitations (spectrum: Tetramer & ENV) are shown; displayed are the isosurfaces with an isovalue of $\pm 0.0002\,a_0^{-3}$. Note that the structure is tilted with respect to Fig. 4.3, i. e., the SPP appears here at the left and EC3 at the right hand side. Figure adapted from Pub. [B3].

in all calculations shown), and some interstitial water molecules only have very little influence on the excitation spectrum: These elements shift the charge-transfer excitations only by less than 0.1 eV [B3]. On the other hand, there are charged amino acids in the vicinity of the chromophores that can have a very pronounced effect. In that respect, it is a remarkable structural feature that several charged amino acids can be found in proximity ($\sim$ 3 to 4 Å distance) to EC3. This can be seen in detail in Fig. 3 in Pub. [B3]. This cluster of charged amino acids (together with some uncharged polar and aromatic amino acids) has a very significant impact on the charge-transfer excitations, which is considerably stronger than all other components of the environment that we consider [B3]: As shown in Fig. 4.4, the lowest EC2$^+$EC3$^-$ excitation is shifted from 1.75 to 1.13 eV, the lowest SPP$^+$EC3$^-$

excitation from 2.28 to 1.28 eV, and the lowest SPP^+EC2^- excitation from 1.96 to 1.67 eV.

The MD analysis confirms our main findings [B3]. Since the energetic position of the charge-transfer excitations with respect to the band of dominant Q_y excitations changes slightly, most of the SPP^+EC3^- excitations appear somewhat above the Q_y band. On the other hand, the $EC2^+EC3^-$ excitations are (mostly) found at energies below the Q_y band. In conclusion, our results consistently suggest that (CT3) is the most likely charge-separation mechanism, i. e., EC3 is the primary electron acceptor. Importantly, very specific charged amino acids substantially stabilize the $EC2^+EC3^-$ (and SPP^+EC3^-) excitations. This can enable downhill energy transfer from the BChl Q_y band to an $EC2^+EC3^-$ state and, thus, may be a key element in establishing an efficient charge-separation mechanism.

5 Hybrid functionals with local range separation

Range-separated hybrid (RSH) functionals, introduced in Chap. 3, are one of the most popular options available to obtain spectroscopic properties from (time-dependent) density functional theory ((TD)DFT) calculations. In particular, if the range-separation parameter ω is determined by optimal tuning, these functionals are equipped with true predictive power. However, despite their achievements, common RSH functionals are far from being a panacea. We discuss the limitations of optimally tuned RSH functionals for spectroscopic applications later in this chapter in Sec. 5.4. At this point, we highlight an issue that is shared by many functionals that combine exact and semi-local exchange – the "observable dilemma", see, e. g., Pub. [B5], Ref. [51], and references therein. It refers to the quite broad observation that hybrid functionals usually fail to describe both electronic binding, e. g., probed by atomization energies, and electronic excitations, e. g., probed by fulfillment of the IP theorem, at the same level of accuracy within a fixed functional form. For global hybrid functionals such as PBE0 this becomes manifest in a parameter dilemma: A fraction of exact exchange of about 0.25 leads to atomization energies with high accuracy whereas much larger values, around 0.75, are required to obtain physically interpretable eigenvalues. This raises fundamental conceptual questions of how to properly construct hybrid functionals.

In this chapter, we approach these shortcomings by reconsidering the concept of hybrid functionals. In Sec. 5.1 we re-introduce the concept of hybrid functionals via the coupling-constant integration and show how this motivates a more flexible way of mixing exact and semi-local exchange. Subsequently, in Sec. 5.2 we discuss several exact constraints that can guide on how this additional freedom can be utilized in actual functional constructions. One approach based on these insights are local hybrid functionals, which are introduced in Sec. 5.3. The approach that we mostly focus on in our work is local range separation. The fundamental concepts of local range separation are explained in Sec. 5.4. Finally, in Sec. 5.5, we present our progress made on local range separation; this is a summary of Pubs. [B2, B4, B5].

5.1 From coupling-constant integration to hybrid functionals

Historically, the first hybrid functional has been proposed by Becke [46] before the generalized Kohn-Sham (KS) framework, cf. Sec. 3.2 above, has been established. This was motivated by a different theoretical concept – the coupling-constant integration [23, 131, 279, 280]. It is based on a series of fictitious auxiliary systems where the electron-electron interaction is scaled by a continuous parameter λ between 0

and 1, i. e., their Hamiltonian reads

$$\hat{H}^\lambda = \hat{T} + \lambda\,\hat{V}_{\mathrm{ee}} + V_{\mathrm{ext}}^\lambda. \tag{5.1}$$

The ground-state wavefunction of $\hat{H}^\lambda$ is denoted by Ψ^λ and determined via a minimization procedure analogous to the one in Eq. (2.2). The minimization is performed under the constraint that Ψ^λ yields the true density $n(\mathbf{r})$, which is achieved by adjusting the external potential $v_{\mathrm{ext}}^\lambda(\mathbf{r})$ in the auxiliary systems accordingly. The limiting case $\lambda = 1$ corresponds to the true, fully interacting system, and the opposite limit $\lambda = 0$ to the non-interacting KS system. Under the assumption that there is a smooth, "adiabatic connection" as λ is varied between the interacting and non-interacting limits, the exchange-correlation (xc) energy can be expressed as

$$E_{\mathrm{xc}}[n] = \int_0^1 \mathrm{d}\lambda\, \underbrace{\left(\left\langle \Psi^\lambda \middle| \hat{V}_{\mathrm{ee}} \middle| \Psi^\lambda \right\rangle - E_{\mathrm{H}}[n]\right)}_{=E_{\mathrm{xc}}^\lambda[n]}. \tag{5.2}$$

The integrand is referred to as the λ-resolved xc energy $E_{\mathrm{xc}}^\lambda[n]$. At $\lambda = 0$ it is precisely the exchange energy, which can be represented by the exact exchange expression $E_{\mathrm{x}}^{\mathrm{ex}}$ (2.17) (compare Eq. (5.2) to Eq. (2.11) above and recall that $\Psi^{\lambda=0} \equiv \Phi$). The value at $\lambda = 1$ is referred to as the "potential contribution" to the xc energy,

$$U_{\mathrm{xc}}[n] = \langle \Psi^{\lambda=1} | \hat{V}_{\mathrm{ee}} | \Psi^{\lambda=1} \rangle - E_{\mathrm{H}}[n], \tag{5.3}$$

with $\Psi^{\lambda=1} \equiv \Psi$. The dependence of E_{xc}^λ on λ is sketched in Fig. 5.1.

For later reference, we introduce the xc hole $n_{\mathrm{xc}}^\lambda(\mathbf{r}, \mathbf{r}')$. As detailed, e. g., in Ref. [23], Eq. (5.2) can then be reformulated as

$$E_{\mathrm{xc}}[n] = \frac{1}{2} \int \mathrm{d}\mathbf{r} \int \mathrm{d}\mathbf{r}'\, n(\mathbf{r})\, \frac{1}{|\mathbf{r} - \mathbf{r}'|} \int_0^1 \mathrm{d}\lambda\, n_{\mathrm{xc}}^\lambda(\mathbf{r}, \mathbf{r}'). \tag{5.4}$$

Hence, the xc energy can be viewed as the Coulomb interaction of the electron density distribution $n(\mathbf{r})$ with the corresponding xc hole. The xc hole can be split into the exchange hole $n_{\mathrm{x}}(\mathbf{r}, \mathbf{r}')$, which is the $\lambda = 0$ value of $n_{\mathrm{xc}}^\lambda(\mathbf{r}, \mathbf{r}')$, and the λ-dependent correlation hole $n_{\mathrm{c}}^\lambda(\mathbf{r}, \mathbf{r}')$, with $n_{\mathrm{xc}}^\lambda(\mathbf{r}, \mathbf{r}') = n_{\mathrm{x}}(\mathbf{r}, \mathbf{r}') + n_{\mathrm{c}}^\lambda(\mathbf{r}, \mathbf{r}')$. Sometimes, the λ-averaged xc hole $n_{\mathrm{xc}}(\mathbf{r}, \mathbf{r}') = \int_0^1 \mathrm{d}\lambda\, n_{\mathrm{xc}}^\lambda(\mathbf{r}, \mathbf{r}')$ is used. As for the exchange energy, an explicit expression for the exchange hole can be given in terms of the single-particle orbitals,

$$n_{\mathrm{x}}^{\mathrm{ex}}(\mathbf{r}, \mathbf{r}') = -\frac{1}{n(\mathbf{r})} \sum_{\sigma=\uparrow,\downarrow} \sum_{i,j=1}^{N_\sigma} \phi_{i\sigma}^*(\mathbf{r}) \phi_{j\sigma}^*(\mathbf{r}') \phi_{i\sigma}(\mathbf{r}') \phi_{j\sigma}(\mathbf{r}), \tag{5.5}$$

which is referred to as "exact exchange hole".

Hybrid functionals are directly connected to the concept of coupling-constant integration. As first described in Ref. [46] and further explored in Refs. [47, 81, 281–283],

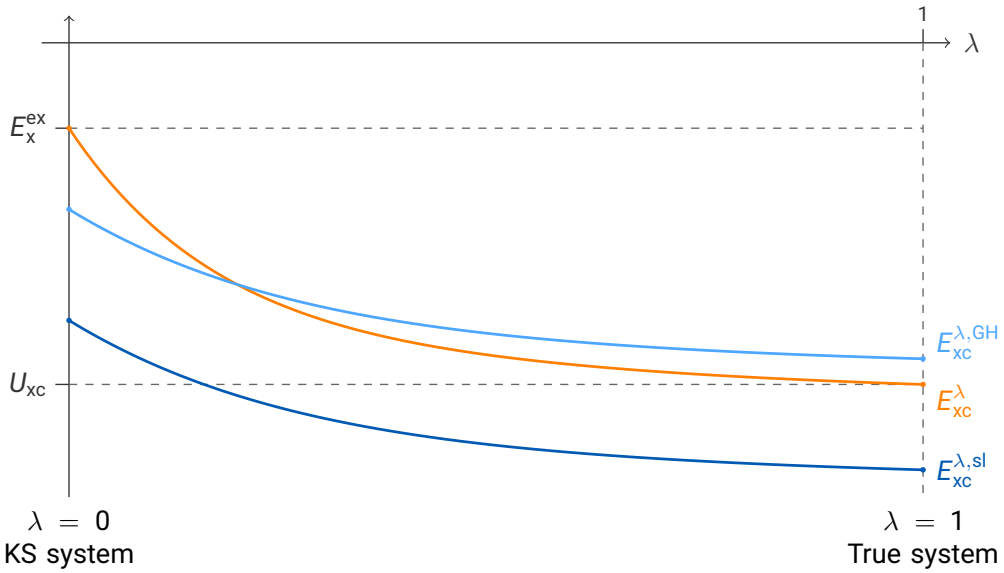

Fig. 5.1: Sketch of the (exact) λ-resolved xc energy E_{xc}^{λ} as the coupling-constant parameter λ is varied from $\lambda = 0$ (corresponding to the non-interacting KS system) to $\lambda = 1$ (corresponding to the true, fully interacting system). Indicated are the end-point values $E_{xc}^{\lambda=0} = E_x^{ex}$ and $E_{xc}^{\lambda=1} = U_{xc}$. The size of the area under the curve of E_{xc}^{λ} is precisely the value of the xc energy E_{xc}. Additionally, the λ-resolved xc energy is shown for approximate semi-local and global hybrid functionals, $E_{xc}^{\lambda,sl}$ and $E_{xc}^{\lambda,GH}$, respectively. Note that the shape of the curves of $E_{xc}^{\lambda,sl}$ and $E_{xc}^{\lambda,GH}$ is the same, but differs from the exact curve E_{xc}^{λ}. $E_{xc}^{\lambda,GH}$ is upshifted with respect to $E_{xc}^{\lambda,sl}$ such that the area under the curve of $E_{xc}^{\lambda,GH}$ approximates E_{xc}.

the coupling-constant integral (5.2) can be represented exactly by a weighted sum of the integrand at the end points of the integration by virtue of the mean value theorem. This leads to [47]

$$E_{xc}[n] = a[n]\, E_x^{ex}[n] + (1 - a[n])\, U_{xc}[n]. \tag{5.6}$$

The mixing coefficient $a[n]$ is bound between 0 and 1, and is, in general, a functional of the density. Since $a[n]$ can be related to different pieces of the correlation energy, the term $(1 - a[n])\, U_{xc}[n]$ in Eq. (5.6) can formally be expressed as $(1 - a[n])\, E_x[n] + E_c[n]$ [47]. The usual global hybrid functionals approximate $E_x[n]$ and $E_c[n]$ in this expression by semi-local functionals and neglect the density-dependence of $a[n]$, leading to the xc approximation

$$E_{xc}^{GH} = a\, E_x^{ex} + (1 - a)\, E_x^{sl} + E_c^{sl} \tag{5.7}$$

familiar from Sec. 3.2. Scaling the electron-electron interaction in Eq. (5.1) is related to uniform scaling of the density, defined in Sec. 5.2.4. In particular, this manifests in the expression [141, 284, 285]

$$E_{xc}^{\lambda}[n] = \frac{\mathrm{d}}{\mathrm{d}\lambda}\left(\lambda^2 E_{xc}[n_{1/\lambda}]\right) \tag{5.8}$$

which connects the λ-resolved xc energy to the full xc energy via density scaling. The scaled density $n_{1/\lambda}$ is defined in Eq. (5.17) below. Therefore, the density dependence of $a[n]$ implicitly contains a λ-dependence and neglecting it, as in global hybrids, can change considerably how $E_{\mathrm{xc}}^{\lambda}$ is modeled. This is visualized in Fig. 5.1: The λ-dependence of the global hybrid, $E_{\mathrm{xc}}^{\lambda,\mathrm{GH}}$, is determined entirely by that of the semi-local functional, $E_{\mathrm{xc}}^{\lambda,\mathrm{sl}}$. The fraction of exact exchange just leads to a global shift of $E_{\mathrm{xc}}^{\lambda,\mathrm{GH}}$ with respect to $E_{\mathrm{xc}}^{\lambda,\mathrm{sl}}$, where the magnitude of the shift is controlled by the fraction a of exact exchange. That is, by a suitable value for a, $E_{\mathrm{xc}}^{\lambda,\mathrm{GH}}$ can be shifted such that its integral matches the exact xc energy but its λ-dependent shape cannot be adjusted. By that, global hybrids can lead to a significant improvement for properties that are computed directly from total energy differences such as atomization energies.[1] On the other hand, the benefit is much smaller for other observables. These shortcomings of global hybrids have been associated with the observable dilemma, see Pub. [B5] and references therein.

Baer and coworkers [42, 43] showed that one can obtain an expression similar to Eq. (5.6) with an approach based on range separation of the Coulomb interaction. Based on interpolating between the non-interacting ($\omega = 0$) and the fully interacting ($\omega \to \infty$) limits by a descreened interaction $\operatorname{erf}(\omega|\mathbf{r}-\mathbf{r}'|)/|\mathbf{r}-\mathbf{r}'|$ and using a generalization of the coupling-constant integration [286], this leads to

$$E_{\mathrm{xc}}[n] = \langle\Phi|\hat{V}_{\mathrm{ee}}^{\mathrm{lr}}|\Phi\rangle + \langle\Psi|\hat{V}_{\mathrm{ee}}^{\mathrm{sr}}|\Psi\rangle - E_{\mathrm{H}}[n]. \tag{5.9}$$

Therein, Φ is again the non-interacting and Ψ the fully interacting wavefunction; $\hat{V}_{\mathrm{ee}}^{\mathrm{lr}}$ is the long-range Coulomb operator, see Eq. (3.31) above, and $\hat{V}_{\mathrm{ee}}^{\mathrm{sr}}$ the complementary short-range version ($\operatorname{erf}(\cdot)$ is replaced by $1-\operatorname{erf}(\cdot)$); $\hat{V}_{\mathrm{ee}}^{\mathrm{lr}}$ and $\hat{V}_{\mathrm{ee}}^{\mathrm{sr}}$ both contain the range-separation parameter ω. Baer and coworkers argue that Eq. (5.9) is exact for a particular, system-dependent value of ω. In other words, the value of the range-separation "parameter" is governed by the density distribution of the system of interest, i. e., it is a density functional $\omega[n]$. Using the xc hole, Eq. (5.9) can be rewritten as

$$\begin{aligned} E_{\mathrm{xc}}[n] = {} & \frac{1}{2}\int \mathrm{d}\mathbf{r} \int \mathrm{d}\mathbf{r}'\; n(\mathbf{r})\, \frac{\operatorname{erf}(\omega[n]|\mathbf{r}-\mathbf{r}'|)}{|\mathbf{r}-\mathbf{r}'|}\, n_{\mathrm{x}}^{\mathrm{ex}}(\mathbf{r},\mathbf{r}') \\ & + \frac{1}{2}\int \mathrm{d}\mathbf{r} \int \mathrm{d}\mathbf{r}'\; n(\mathbf{r})\, \frac{1-\operatorname{erf}(\omega[n]|\mathbf{r}-\mathbf{r}'|)}{|\mathbf{r}-\mathbf{r}'|}\, n_{\mathrm{xc}}^{\lambda=1}(\mathbf{r},\mathbf{r}'). \end{aligned} \tag{5.10}$$

The form of this range-separation scheme is different to the one introduced in Sec. 3.3 since it employs the short-range version of the correlation hole at full coupling strength instead of the usual coupling-constant averaged correlation hole. However, in this work we stick to the most commonly used form of RSH functionals where the range separation is only performed in the exchange part and the correlation energy remains unaffected.

[1] As an example, the atomization energy AE of a diatomic molecule AB is computed from the difference between the ground-state energies of the molecule and the separate atoms A and B: $\mathrm{AE} = |E(AB) - (E(A) + E(B))|$.

In conclusion, the concept of coupling-constant integration suggests that the mixing of exact and semi-local exchange in both global hybrid and RSH functionals should not be determined by a constant parameter, a or ω, but by a density functional, $a[n]$ or $\omega[n]$, respectively. Realizing this density dependence might be a way to tackle the observable dilemma by changing the shape of $E_{\mathrm{xc}}^{\lambda}$ instead of just shifting it. In particular, these insights have lead [48, 51, 283] to the two concepts of local hybrid functionals and hybrid functionals with local range separation (also referred to as locally RSH functionals). For reasons to be explained below, these approaches go beyond a space-independent parameter, $a[n]$ or $\omega[n]$, and build upon local functions of the density, $a([n], \mathbf{r})$ or $\omega([n], \mathbf{r})$, respectively, to control the mixing of exact and semi-local exchange. Their functional form is explained in detail in Secs. 5.3 and 5.4.

5.2 Construction principles of hybrid exchange-correlation approximations

One reason for the success of semi-local functionals is that they rely on subtle error cancellation effects between their exchange and correlation contributions [82, 287, 288]. This statement can be elucidated by taking a closer look at the physical meaning of exchange and correlation. Exchange reflects the Pauli exclusion principle due to the antisymmetry requirement of the electronic wavefunction. Correlation is a more intricate interaction effect. Loosely, two types of correlation can be distinguished: Dynamical and static correlation [49, 289]. Dynamical correlation refers to the effect that two electrons mutually try to avoid each other, thereby lowering the repulsion between them. Due to screening effects, this is inherently a short-range phenomenon. On the other hand, static correlation can be a long-range effect. This can be understood by returning to the concept of the xc hole. Consider $n_{\mathrm{xc}}(\mathbf{r}, \mathbf{r}')$ for a dimeric molecule with the reference point $\mathbf{r}$ close to one of the nuclei. Even at almost infinite distance, the exchange contribution to the hole is delocalized over the regions of both nuclei. This delocalization needs to be cancelled by a complementary delocalization of the correlation contribution. Overall, this yields an xc hole that is properly localized near the reference point. From a wavefunction perspective, this effect is significant if the many-electron wavefunction is well-represented by a few nearly degenerate Slater determinants. In practice, it is relevant not only for the dissociation of molecules but also at equilibrium bond lengths, e. g., in systems with triple bonds such as N_2. In the case of semi-local functionals, both the exchange and correlation holes are intrinsically localized. While their sum can still provide a reasonable approximation to the full xc hole, exchange and correlation alone often do not match their exact counterparts accurately. Instead, it turns out that semi-local correlation captures dynamical correlation effects, while exchange and static correlation are buried into semi-local exchange approximations [69, 81, 290, 291].

These insights have important implications for hybrid functionals: If one puts together full exact exchange and semi-local correlation, the static correlation, an important piece of the physics underneath the xc energy, is missing. Instead, the mixing of exact and semi-local exchange models both exchange and static correlation. This can

be emphasized by rewriting the xc energy of hybrid functionals in the "correlation picture". In the simplest case of global hybrids this reads

$$E_{\mathrm{xc}}^{\mathrm{GH}} = \underbrace{E_{\mathrm{x}}^{\mathrm{ex}}}_{\text{“exchange”}} + \underbrace{(1-a)\left(E_{\mathrm{x}}^{\mathrm{sl}} - E_{\mathrm{x}}^{\mathrm{ex}}\right) + E_{\mathrm{c}}^{\mathrm{sl}}}_{\text{“correlation”}}. \tag{5.11}$$

This underlines that the fraction of exact-exchange admixture enters that part of the xc energy that is supposed to describe correlation effects. Therefore, when constructing approximate hybrid functionals, it is a crucial question how to properly incorporate the delicate balance between exchange and correlation by a suitable ratio of exact and semi-local exchange [288]. In the construction of semi-local xc approximations, known exact constraints to the xc energy provide important guidance and this can lead to robust functionals that work well even for systems and properties that have not been considered in their design [71, 72, 134, 165, 166]. However, the information that exact constraints provide on the interplay of the different exchange and correlation contributions that is desired in hybrid functionals is limited. This might be one of the reasons why virtually all hybrid functional constructions available so far rely on empiricism to a certain degree [288]. Nevertheless, exact constraints can serve as guide rails in the construction of hybrid functionals [51, 288] and, in our work, we make use of them with the objective of avoiding empiricism as much as possible. In particular, this can aid in distinguishing between regions where semi-local exchange is desirable, e. g., if the density is slowly varying, cf. Sec. 5.2.3, and regions where exact exchange should dominate, e. g., in high-density, asymptotic, and one-electron regions, cf. Secs. 5.2.4 to 5.2.6. In the following, we give an overview of these and other xc constraints that are relevant within this work. An overview of further constraints can be found, e. g., in Refs. [23, 134].

5.2.1 Size consistency

Size consistency [23, 134, 292] is defined as follows: Consider a system $A \cdots B$ that is composed of two well-separated subsystems A and B. Then, the density in the combined system should be the sum of the densities in the separate parts,

$$n_{A\cdots B}(\mathbf{r}) = n_A(\mathbf{r}) + n_B(\mathbf{r}). \tag{5.12}$$

Similarly, the total energy should be additive,

$$E[n_{A\cdots B}] = E[n_A] + E[n_B]. \tag{5.13}$$

In typical semi-local functionals size consistency of the xc energy is ensured since their xc energy density $e_{\mathrm{xc}}(\mathbf{r})$ depends on the density and related semi-local ingredients only locally, i. e., at point $\mathbf{r}$. Global hybrid or RSH functionals, with constant parameter a or ω, respectively, have a similar mathematical structure and are size-consistent as well. However, if the exact-exchange admixture is governed by a global functional of the density, $a[n]$ or $\omega[n]$, this can lead to a different form that is not size-consistent.

Size consistency can be restored by using a local, space-dependent function of the density instead, $a([n], \mathbf{r})$ or $\omega([n], \mathbf{r})$, as it is done in local hybrid or local range separation approaches.

5.2.2 Spin scaling of exchange

The exchange energy emerges from two independent contributions for the different spin channels, cf. Eq. (2.17). This implies the following relation between the spin-unpolarized and spin-polarized forms, $E_\mathrm{x}[n]$ and $E_\mathrm{x}[n_\uparrow, n_\downarrow]$, respectively, of the exchange energy [293],

$$E_\mathrm{x}[n_\uparrow, n_\downarrow] = \frac{1}{2}\left(E_\mathrm{x}[2n_\uparrow] + E_\mathrm{x}[2n_\downarrow]\right). \tag{5.14}$$

This expression can be used to generate the spin-polarized version of an approximate exchange functional from its corresponding spin-unpolarized form.

5.2.3 Homogeneous-electron-gas limit and gradient expansion

One important limiting case for the xc energy is its behavior for a spatially uniform density [22]. This case is known as homogeneous electron gas and an analytical expression for the exchange energy and accurate parametrizations for the correlation energy exist, cf. Chap. 2. The local density approximation (LDA) xc functional directly builds upon these expressions. More generally, a density functional approximation is said to respect the homogeneous-electron-gas limit if it reduces to LDA in the limit of uniform densities. This limit can be characterized by vanishing density variations, e. g., $\nabla n(\mathbf{r}) \to 0$, and when the kinetic energy density $\tau(\mathbf{r})$ reduces to its homogeneous-electron-gas limit $\tau^\mathrm{HEG}(\mathbf{r}) = (3/10)\left(3\pi^2\right)^{2/3} n^{5/3}(\mathbf{r})$, given here for the spin-unpolarized case. For small density variations the exact xc energy can be expanded systematically around the homogeneous-electron-gas limit. Expressions are known up to second order in the (full) xc energy and up to fourth order in the exchange energy [23, 58, 92, 294]. Within this work, only the second-order gradient expansion of the exchange energy is relevant. In terms of the exchange energy density, this can be expressed as

$$e_{\mathrm{x}\sigma}^\mathrm{GE}([n_\sigma], \mathbf{r}) = e_{\mathrm{x}\sigma}^\mathrm{LDA}([n_\sigma], \mathbf{r})\left(1 + \frac{10}{81}\, s_\sigma^2(\mathbf{r}) + \ldots\right) \tag{5.15}$$

for the spin-polarized case. It depends on the reduced density gradient

$$s_\sigma(\mathbf{r}) = \frac{|\nabla n_\sigma(\mathbf{r})|}{2k_{\mathrm{F}\sigma}(\mathbf{r}) n_\sigma(\mathbf{r})}, \tag{5.16}$$

where $k_{\mathrm{F}\sigma}(\mathbf{r}) = \left(6\pi^2 n_\sigma(\mathbf{r})\right)^{1/3}$ is the spin-polarized version of the Fermi wave vector.

Local hybrid and locally RSH functionals are usually constructed such that the homogeneous-electron-gas limit is fulfilled or closely approximated by their semi-local components and the exact-exchange contribution vanishes [B2, 51, 295]. Formally, the homogeneous-electron-gas limit could also be fulfilled by the combination of full exact exchange and some appropriate LDA-based semi-local correlation functional. However, there are at least two reasons why the second approach does not appear promising: First, exact exchange can be tedious to evaluate numerically for large systems which do not have a sizable frontier eigenvalue gap. Second, the limit of slowly varying densities is well-described by typical semi-local functionals. Therefore, by a vanishing exact-exchange contribution the compatibility of semi-local exchange and correlation is maintained.

5.2.4 Uniform density scaling

The work by Levy and Perdew [284, 296] offers another complementary viewpoint on exchange and correlation based on their behavior under scaling of the density. In this work, we consider uniform scaling of the density defined as

$$n_\gamma(\mathbf{r}) = \gamma^3 n(\gamma\mathbf{r}), \tag{5.17}$$

with a positive scaling parameter $\gamma > 0$. The scaling of the density is defined such that the particle number is conserved. For $\gamma > 1$ it leads to a more compressed density distribution with higher maximum value; for $\gamma < 1$ the density distribution is lower and more expanded. In other words, the high-density limit is obtained for $\gamma \to \infty$ whereas $\gamma \to 0$ is the low-density limit. The exchange energy scales linearly under uniform density scaling,

$$E_\mathrm{x}[n_\gamma] = \gamma\, E_\mathrm{x}[n], \tag{5.18}$$

while the correlation energy has a more complex scaling behavior. It can be characterized by the inequalities $E_\mathrm{c}[n_\gamma] > \gamma\, E_\mathrm{c}[n]$, for $\gamma > 1$, and $E_\mathrm{c}[n_\gamma] < \gamma\, E_\mathrm{c}[n]$, for $\gamma < 1$, as well as the high-density limit $\lim_{\gamma\to\infty} E_\mathrm{c}[n_\gamma] = \text{const}$. In other words, correlation can be important in low-density regions, while the high-density limit is dominated by exact exchange.

The scaling behavior can be used to separate a given (approximate) xc expression into its exchange and correlation parts,

$$E_\mathrm{x}[n] = \lim_{\gamma\to\infty} \frac{E_\mathrm{xc}[n_\gamma]}{\gamma} \tag{5.19}$$

and

$$E_\mathrm{c}[n] = E_\mathrm{xc}[n] - \lim_{\gamma\to\infty} \frac{E_\mathrm{xc}[n_\gamma]}{\gamma}. \tag{5.20}$$

One can demand that both the "wavefunction definition", cf. Eqs. (2.11) and (2.12) above, and the "scaling definition", cf. Eqs. (5.19) and (5.20), should be consistent for hybrid functionals. This condition can be formalized as [288]

$$\lim_{\gamma\to\infty} \frac{E_{\mathrm{xc}}[n_\gamma]}{E_{\mathrm{x}}^{\mathrm{ex}}[n_\gamma]} = 1, \tag{5.21}$$

i. e., the functional scales to exact exchange in the high-density limit. A functional that obeys this condition satisfies all constraints on exchange automatically. Eq. (5.21) cannot be satisfied by global hybrid functionals (with $a \neq 1$). However, it can be satisfied by local hybrids and locally RSHs. In this case, it translates to constraints for the admixture of exact exchange via $a([n], \mathbf{r})$ or $\omega([n], \mathbf{r})$, respectively [B2, B5, 51, 54, 288].

5.2.5 Asymptotic exchange-correlation potential

The KS and xc potential of a finite neutral system decay asymptotically as $-1/r$, cf. Sec. 3.1.2. Semi-local functionals violate this constraint since their potential follows the asymptotic decay of the density distribution. One way to introduce the correct asymptotic behavior is the Perdew-Zunger self-interaction correction [78], introduced in Eq. (3.18). Another way is the usage of exact exchange. However, simple global hybrid functionals, which use a fixed fraction a of exact exchange, decay asymptotically as $-a/r$, i. e., for typical values of $a \sim 0.25$ miss a large fraction of the correct behavior. On the other hand, RSH functionals can achieve the correct asymptotic decay of the xc potential by using full exact exchange at long range. The correct asymptotics is ensured as well for hybrid functionals with local range separation with a form for $\omega([n], \mathbf{r})$ that does not vanish asymptotically. The asymptotic potential of local hybrid functionals is discussed in Sec. 5.3.

5.2.6 Freedom from self-interaction errors

Two types of shortcomings of approximate xc functionals are referred to as self-interaction errors – one-electron and many-electron self-interaction [78, 119–126]. The two types of self-interaction errors are different but not unrelated since both refer to some form of spurious interaction of electrons with themselves. On the one hand, one-electron self-interaction, introduced in Sec. 3.1.2, refers to the spurious interaction encountered in one-electron systems. On the other hand, many-electron self-interaction errors, cf. Sec. 3.1.1, manifest in many-electron systems as a convex (or concave) behavior of the total energy $E(N)$ as a function of fractional particle numbers and can be interpreted as underestimating (or overestimating, respectively) the localization of the electrons. This can even be the case for those approximate functionals that are free from one-electron self-interaction, e. g., exact exchange or the functional from Ref. [51]. We aim to reduce or, as far as possible, eliminate both types of self-interaction errors in our functional constructions.

The issue of one-electron self-interaction is easier to tackle. In our approach, we follow the logic common in self-interaction corrections and aim to fulfill the more general condition (3.16). This is ensured if in regions of space with only one non-vanishing occupied spin-orbital, first, the exchange energy reduces to exact exchange and, second, the correlation energy vanishes. One-spin-orbital regions can be detected with a combination of iso-orbital indicator functions and spin functions [51, 89–91, 297–302]. In our work, we use, first, the ratio

$$z_\sigma(\mathbf{r}) = \frac{\tau_\sigma^{\mathrm{W}}(\mathbf{r})}{\tau_\sigma(\mathbf{r})} \tag{5.22}$$

of the non-interacting kinetic energy density $\tau_\sigma(\mathbf{r})$ (2.16) and its single-orbital limit (the *von Weizsäcker* kinetic energy density),

$$\tau_\sigma^{\mathrm{W}}(\mathbf{r}) = \frac{|\nabla n_\sigma(\mathbf{r})|^2}{8 n_\sigma(\mathbf{r})}, \tag{5.23}$$

or its spin-channel independent analog $z(\mathbf{r})$ and, second, the spin polarization,

$$\zeta(\mathbf{r}) = \frac{n_\uparrow(\mathbf{r}) - n_\downarrow(\mathbf{r})}{n(\mathbf{r})}. \tag{5.24}$$

z_σ (or z) is bound between its limit for uniform densities, 0, and its single-orbital limit, 1; ζ^2 obtains its maximum, 1, for $n_\uparrow = 0$ or $n_\downarrow = 0$ and vanishes for spin-unpolarized systems, where $n_\uparrow \equiv n_\downarrow$. The product of the two, $z_\sigma\zeta^2$ (or $z\zeta^2$), takes its maximum value, 1, only in one-spin-orbital regions.

Many-electron self-interaction errors are much more difficult to formulate [78, 104, 122]. As a consequence, it is by no means straightforward how to correct for them [303, 304]. Therefore, the strategy we pursue in our work is the following: We explore different functional forms and assess how their total energy $E(N)$ behaves as a function of the fractional particle number as an indication of how effective many-electron self-interaction errors are reduced. Some guidance on the form of promising functional candidates is provided by the following observations: First, semi-local functionals typically lead to a pronounced convex shape of $E(N)$, while the curve for exact exchange is too concave. This suggests that piecewise linearity can be achieved by a delicate balance between semi-local and exact exchange. In practical functional constructions, this balance can be attained, e. g., by optimally tuned RSH functionals, where the tuning often leads to approximate piecewise linearity [118]. Second, it is interesting to note that the Perdew-Zunger self-interaction correction (3.18) [78], although being designed to eliminate *one*-electron self-interaction errors, can lead to a significant reduction of *many*-electron self-interaction errors as well, at least in special cases [120, 122]. Furthermore, our own experience from numerous exploratory calculations shows that the way of how exact and semi-local exchange are mixed to correct for one-electron self-interaction errors has a relevant impact on the shape of $E(N)$ as well. Therefore, it appears as a reasonable and pragmatic approach to

construct one-electron self-interaction corrections such that this effectively also leads to a reduction of many-electron self-interaction errors. We take advantage of this strategy in constructing a locally RSH functional [B4] as detailed in Sec. 5.5.3.

5.3 Local hybrid functionals

The xc energy of local hybrid functionals [305] can be written in the form

$$E_{\mathrm{xc}}^{\mathrm{LH}}[n_\uparrow, n_\downarrow] = \sum_{\sigma=\uparrow,\downarrow} \int \mathrm{d}\mathbf{r}\ \Big(a_\sigma(\mathbf{r})\, e_{\mathrm{x}\sigma}^{\mathrm{ex}}(\mathbf{r}) + (1 - a_\sigma(\mathbf{r})) \Big(e_{\mathrm{x}\sigma}^{\mathrm{sl}}(\mathbf{r}) + G_\sigma(\mathbf{r}) \Big) \Big) + E_{\mathrm{c}}^{\mathrm{sl}}. \tag{5.25}$$

Therein, $a_\sigma([n_\uparrow, n_\downarrow], \mathbf{r})$ is a local, space-dependent function of the density that is bound between 0 and 1. In its most general form, it can be different for both spin channels, denoted by the subscript σ, and depend on both spin-densities $n_\uparrow(\mathbf{r})$ and $n_\downarrow(\mathbf{r})$. $a_\sigma(\mathbf{r})$ is often called local mixing function. $e_{\mathrm{x}\sigma}^{\mathrm{ex}}(\mathbf{r})$ is the exact energy density (in the "conventional gauge" [306], cf. Eq. (2.17)); $e_{\mathrm{x}}^{\mathrm{sl}}([n_\sigma], \mathbf{r})$ and $E_{\mathrm{c}}^{\mathrm{sl}}[n_\uparrow, n_\downarrow]$ are typical semi-local exchange and correlation functionals. $G_\sigma(\mathbf{r})$ is called calibration function. It has been introduced to account for the gauge ambiguity of exchange energy densities [306–308]: In semi-local or global hybrid functionals the exchange energy *densities*, $e_{\mathrm{x}\sigma}^{\mathrm{ex}}$ and $e_{\mathrm{x}\sigma}^{\mathrm{sl}}$, can be modified by an additive term $G_\sigma(\mathbf{r})$ without changing the resulting (integrated) exchange energy if $\int \mathrm{d}\mathbf{r}\ G_\sigma(\mathbf{r}) = 0$. On the other hand, in local hybrids terms adding the function $G_\sigma(\mathbf{r})$, e. g., as in Eq. (5.25), leads to terms of the form $\int \mathrm{d}\mathbf{r}\ a_\sigma(\mathbf{r})\, G_\sigma(\mathbf{r})$ that even change the (integrated) exchange energy. This so-called "gauge problem" has been associated with spurious positive static correlation contributions and unphysically repulsive binding energy curves of noble gas dimers. Adding a suitable function $G_\sigma(\mathbf{r})$ to the semi-local exchange functional, cf. Eq. (5.25), can alleviate these issues [309].[2]

A further issue related to local hybrid functionals is a technical one [311]: In codes using Gaussian basis sets, the exact exchange energy and the corresponding potential in the form they appear, e. g., in global hybrids, can be evaluated analytically. However, in local hybrids, this is no longer possible since, i. a., terms of the form $\int \mathrm{d}\mathbf{r}\ a_\sigma(\mathbf{r})\, e_{\mathrm{x}\sigma}^{\mathrm{ex}}(\mathbf{r})$ appear, where the exact exchange energy density is modified by the local mixing function before the "outer" integration ("over $\mathbf{r}$") is performed. This challenge has been solved with a semi-numerical scheme where one integration of the exact exchange term ("over $\mathbf{r}'$"), which is independent of the local mixing function, is computed analytically on each point of a numerical grid, while the second integral ("over $\mathbf{r}$") is performed numerically on this grid [312–314]. The implementation becomes efficient by employing several prescreening techniques [315, 316]. The idea of this semi-numerical scheme is explained in more detail in App. A.

[2] As an alternative, it has been shown very recently in Ref. [310] that a judiciously constructed local mixing function can strongly reduce the spurious positive static correlation contributions associated with the gauge problem.

The first explicit form of a local hybrid functional was proposed by Jaramillo *et al.* [317] and, since then, local hybrid functionals have been constructed by different groups [51, 75, 288, 295, 305, 318]. On the one hand, there have been approaches to construct the local mixing function in a non-empirical fashion, see, e. g., Refs. [48, 51, 288], which may lead to quite complicated mathematical forms. On the other hand, in practical calculations it turns out that a transparent form is one of the most promising candidates [295],[3]

$$a([n], \mathbf{r}) = c \cdot z(\mathbf{r}). \tag{5.26}$$

It depends on the ratio $z(\mathbf{r})$, cf. Eq. (5.22), scaled by an empirical prefactor c (with typical values of $c \approx 0.5$). This choice for the local mixing function exhibits many desirable features [305]: It takes small values in regions that are relevant for the formation of molecular bonds, whereas it takes much larger values in regions close to atomic nuclei and in the asymptotic regions far away from the atoms of a finite system. Furthermore, the form of this local mixing function can be motivated by the aim to reduce one-electron self-interaction errors. However, it leads to local hybrid functionals that satisfy only some exact constraints identified in Sec. 5.2: Full freedom from one-electron self-interaction errors is only achieved by setting the prefactor to a value of $c = 1$ (provided that a correlation functional is used that vanishes in one-spin-orbital regions). Moreover, Eq. (5.26) does not lead to a local hybrid that satisfies the scaling condition (5.21). Nevertheless, the impressive results that have been achieved by functionals based on Eq. (5.26) demonstrate that this form of $a(\mathbf{r})$ can allow incorporating a lot of the desirable physics into local hybrid functionals [309].

One might believe that local hybrid functionals can lead to the correct asymptotic xc potential: Their local mixing function can be constructed such that it approaches 1 in asymptotic regions, e. g., by setting $c = 1$ in Eq. (5.26) or by the function proposed in Ref. [319]. Indeed, this leads to the correct $-1/(2r)$ asymptotics of the xc *energy density* [305]. However, it has been shown in Ref. [128] that the local hybrid form in general does not lead to the correct xc *potential* (except if $a(\mathbf{r}) = 1$ everywhere in space). Thus, local hybrids suffer from a conceptual shortcoming as compared to RSH functionals and this is reflected, e. g., in the observation that typical local hybrids offer only limited accuracy in problems of long-range charge-transfer character [309, 320]. One approach to overcome this limitation is the one of range-separated local hybrids, where local hybrids are augmented by a fixed fraction of long-range exact exchange, see Refs. [52, 53] and Sec. 5.5.2. Another approach is the one of local range separation, which is introduced in the following section.

5.4 Fundamentals of hybrid functionals with local range separation

Replacing the constant range-separation parameter ω of (globally) RSH functionals by a space-resolved and explicitly density-dependent function $\omega([n], \mathbf{r})$ leads to the

[3] In Eq. (5.26), $a([n], \mathbf{r})$ is the same for both spin channels.

concept of local range separation. On the one hand, this can be motivated by formal considerations based on coupling-constant integration, cf. Sec. 5.1. On the other hand, calculations using globally RSH functionals, both with and without optimal tuning, point out several concrete limitations of a constant range-separation parameter. First, the optimal-tuning approach is computationally involved, as it requires many calculations to determine the optimal value for ω. Second, adjustment of the highest occupied molecular orbital (HOMO) and lowest unoccupied molecular orbital (LUMO) eigenvalues via optimal tuning does not necessarily lead to similar improvements of the other orbitals [152, 321]. Third, special care has to be taken if optimal tuning is used in periodic systems or in combination with a dielectric medium [322, 323]. Fourth, optimal tuning suffers from size-consistency issues that can prohibit the reliable prediction of atomization energies [41]. Fifth and most importantly, optimal tuning raises intrinsic questions of consistency. Tuning is inappropriate for systems that are composed of constituents of largely different chemical nature, where the optimal values of ω differ significantly for the different compartments. Moreover, for systems with delocalized electrons, the tuning procedure spuriously yields ever smaller values of ω with increasing system size [40, 324]. In this case, a RSH functional becomes dominated by its semi-local components and the well-known problems of semi-local functionals, e. g., seriously underestimated fundamental gaps or spuriously low charge-transfer states reappear. Finally, irrespective of how the value of ω is determined, experience suggests that a universal value for the range-separation parameter is usually not appropriate for the description of both ground-state properties, e. g., atomization energies, and electronic excitations [50]. Once more, this is a manifestation of the notorious observable dilemma of hybrid functionals.

In the context of range separation, reconsidering the concept of optimal tuning reveals a way to tackle these issues: As realized early on [42–44] the range-separation "parameter" should not have a fixed value but rather depend on the density. In fact, this insight has been one motivation for the optimal tuning strategy. However, the fact that the density dependence is not known explicitly prevents one to develop this idea further. Likewise, taking this idea seriously would require to consider the additional contributions to the functional derivative that arise from the density dependence of the range-separation "parameter" [41]. This cannot be done, though, as the explicit form of this density-dependence remains unknown within the optimal-tuning approach. As a step forward, the density-dependence of ω is modelled explicitly in the approach of local range separation. The structure of the xc energy is familiar from conventional, globally RSH functionals,

$$E_{\mathrm{xc}}^{\mathrm{LRS}}[n_\uparrow, n_\downarrow] = E_{\mathrm{x}}^{\mathrm{lr,ex}}[n_\uparrow, n_\downarrow] + E_{\mathrm{x}}^{\mathrm{sr,sl}}[n_\uparrow, n_\downarrow] + E_{\mathrm{c}}^{\mathrm{sl}}[n_\uparrow, n_\downarrow], \tag{5.27}$$

with the long-range part of the exact exchange energy,

$$E_{\mathrm{x}}^{\mathrm{lr,ex}} = -\frac{1}{2} \sum_{\sigma=\uparrow,\downarrow} \sum_{i,j=1}^{N_\sigma} \int \mathrm{d}\mathbf{r} \int \mathrm{d}\mathbf{r}' \; \phi_{i\sigma}^*(\mathbf{r}) \phi_{j\sigma}^*(\mathbf{r}') \frac{\operatorname{erf}\left(\omega_\sigma(\mathbf{r}) |\mathbf{r} - \mathbf{r}'|\right)}{|\mathbf{r} - \mathbf{r}'|} \phi_{i\sigma}(\mathbf{r}') \phi_{j\sigma}(\mathbf{r}), \tag{5.28}$$

and semi-local approximations to the short-range part of the exchange energy and the correlation energy, $E_{\mathrm{x}}^{\mathrm{sr,sl}}$ and $E_{\mathrm{c}}^{\mathrm{sl}}$. Importantly, instead of the constant range-separation parameter ω the function $\omega_\sigma([n_\uparrow, n_\downarrow], \mathbf{r})$, referred to as range separation function, enters. In the form that we consider [B2] it can be different for both spin channels, denoted by the subscript σ, and depend on both spin-densities $n_\uparrow$ and $n_\downarrow$ locally, i. e., at each point $\mathbf{r}$. We model this dependence by using the spin-density $n_\sigma(\mathbf{r})$ itself, its gradient $|\nabla n_\sigma(\mathbf{r})|$, and the non-interacting kinetic energy density $\tau_\sigma(\mathbf{r})$ of both spin channels ($\sigma = \uparrow, \downarrow$).

The spin-scaling behavior of locally RSH functionals is influenced by the form of the range-separation function [B2, 54]. If the spin-unpolarized form $\omega([n], \mathbf{r})$ and the spin-polarized form $\omega_\sigma([n_\sigma], \mathbf{r})$ are connected via the relation

$$\omega_\sigma([n_\sigma], \mathbf{r}) = \omega([2n_\sigma], \mathbf{r}), \tag{5.29}$$

the "exchange" terms in Eq. (5.27), $E_{\mathrm{x}}^{\mathrm{lr,ex}}$ and $E_{\mathrm{x}}^{\mathrm{sr,sl}}$, follow the spin-scaling relation of exchange (5.14) (provided that the semi-local exchange functional does). However, the latter is not mandatory. This becomes apparent by rewriting the xc energy in the correlation picture,

$$E_{\mathrm{xc}}^{\mathrm{LRS}} = \underbrace{E_{\mathrm{x}}^{\mathrm{ex}}}_{\text{“exchange”}} + \underbrace{E_{\mathrm{x}}^{\mathrm{sr,sl}} - E_{\mathrm{x}}^{\mathrm{sr,ex}} + E_{\mathrm{c}}^{\mathrm{sl}}}_{\text{“correlation”}}. \tag{5.30}$$

The first term is (full) exact exchange and the remaining terms essentially describe correlation effects. Therein, the $\omega_\sigma(\mathbf{r})$ enters via $E_{\mathrm{x}}^{\mathrm{sr,sl}}[n_\uparrow, n_\downarrow]$ and $E_{\mathrm{x}}^{\mathrm{sr,ex}}[n_\uparrow, n_\downarrow]$. This indicates that the range-separation function captures correlation physics and, thus, it does not seem natural to enforce Eq. (5.29). This idea is particularly appealing because it allows to use the spin polarization $\zeta(\mathbf{r})$ as part of the range-separation function [B2, 54]. $\zeta(\mathbf{r})$ offers a straightforward way to distinguish between one-spin-orbital and one-orbital regions, which can be beneficial with respect to the behavior of locally RSH functionals [B2].[4]

While the correlation energy is independent of the range separation and, thus, typical semi-local approximations can be used directly, the semi-local short-range exchange energy $E_{\mathrm{x}}^{\mathrm{sr,sl}}$ entering Eq. (5.27) deserves further explanation. Its spin-unpolarized form can be expressed in terms of the exchange hole of the chosen semi-local approximation $n_{\mathrm{x}}^{\mathrm{sl}}(\mathbf{r}, \mathbf{r}')$ as

$$E_{\mathrm{x}}^{\mathrm{sr,sl}}[n] = \frac{1}{2} \int \mathrm{d}\mathbf{r} \int \mathrm{d}\mathbf{r}'\, n(\mathbf{r}) \, \frac{1 - \mathrm{erf}\left(\omega(\mathbf{r})|\mathbf{r} - \mathbf{r}'|\right)}{|\mathbf{r} - \mathbf{r}'|} \, n_{\mathrm{x}}^{\mathrm{sl}}(\mathbf{r}, \mathbf{r}'). \tag{5.31}$$

Implementations usually require an explicit closed form of the exchange energy density, i. e., one has to evaluate the integral over $\mathbf{r}'$ in Eq. (5.31) analytically. The mathematical form of the LDA exchange hole permits analytical integration, and

[4] We point out that our view on the spin-scaling behavior of locally RSH functionals stands in contrast to the work by Maier *et al.* [56] in several aspects as detailed in Pub. [B2].

the spin-polarized form can be deduced via the spin-scaling relation (5.14) [B2, 325]. For semi-local functionals beyond LDA, such as generalized gradient approximations (GGAs), the situation is more complex: First, such functionals are typically constructed directly on the level of exchange energy densities. Hence, an expression for the exchange hole may not be available at all. Second, even if such an expression is known, its more complex mathematical form may prohibit direct analytical evaluation of the required integral in Eq. (5.31). An example is the PBE functional where an exchange hole is known [326] but cannot be integrated analytically [155]. As a remedy, the integral can be represented numerically (as done in the construction of the ωPBE functional) [156, 157, 159] or a short-range version of the exchange functional is re-engineered [147, 148, 160–162]. A general alternative is to rely on the scheme by Iikura *et al.* [145], where approximate short-range exchange expressions are obtained based on generalizing the short-range LDA expression. In exploratory calculations, we have tested some existing GGA-based short-range exchange functionals with limited success. Therefore, we keep the LDA-based short-range exchange functional in our work.

The idea of local range separation has been pioneered more than 15 years ago [45]. However, since then, only very few further works that take up this concept have been published [54, 56, 327, 328]. To a certain extent this is related to a technical issue that we have discussed in Sec. 5.3 in the context of local hybrids: In RSH functionals with a constant parameter for range separation, the long-range exact exchange energy can be evaluated analytically in codes which use Gaussian basis sets. This is no longer possible if ω is space-dependent. Fortunately, this issue has been solved recently by the work of Klawohn and Bahmann [55] who have adapted the semi-numerical scheme of local hybrids for local range separation. It is implemented in the quantum chemistry program Turbomole [278]. The idea of this semi-numerical scheme is explained in App. A. Thus, fully self-consistent DFT calculations for finite systems are now possible with locally RSH functionals. This implementation may be extended, e. g., to TDDFT in future work. In this work we focus on the question of how to model the range-separation function and the semi-local exchange and correlation contributions.

5.5 Construction of hybrid functionals with local range separation

In this section, we summarize our progress made on the construction of locally RSH functionals. We cover Pub. [B2] in Sec. 5.5.1, Pub. [B5] in Sec. 5.5.2, and, finally, Pub. [B4] in Sec. 5.5.3. This final section contains the central results of our work on local range separation.

5.5.1 Electronic binding: The ωBT21 functional

In the first step, we explore the self-consistent implementation of local range separation by Klawohn and Bahmann [55]. To this end, we implement several previously

proposed [45, 54] and new locally RSH functionals. We assess these functionals with a focus on their description of electronic binding properties, in particular atomization energies [B2]. From these calculations the following functional emerges as the most promising candidate [B2]. First, as a range-separation function we use

$$\omega_\sigma^{\omega\mathrm{BT21}}(\mathbf{r}) = c_1 \frac{|\nabla n_\sigma(\mathbf{r})|}{n_\sigma(\mathbf{r})} \left(1 + \ln\left(c_2\, \mathrm{a}_0 \cdot c_1 \frac{|\nabla n_\sigma(\mathbf{r})|}{n_\sigma(\mathbf{r})}\right)\right) \frac{1}{1 - z_\sigma(\mathbf{r})\zeta^2(\mathbf{r})}. \tag{5.32}$$

It contains the iso-orbital indicators $z_\sigma(\mathbf{r})$ and $\zeta(\mathbf{r})$ defined in Eqs. (5.22) and (5.24) and two parameters $c_1 = 0.115$ and $c_2 = 0.202$, which are fixed as described below. Second, we employ the LDA expression of the short-range exchange energy [325] and, third, the correlation functional [51]

$$E_\mathrm{c}^{\omega\mathrm{BT21}}[n_\uparrow, n_\downarrow] = \int \mathrm{d}\mathbf{r}\ \Big(1 - z(\mathbf{r})\zeta^2(\mathbf{r})\Big)\, e_\mathrm{c}^{\mathrm{LDA}}[n_\uparrow(\mathbf{r}), n_\downarrow(\mathbf{r})], \tag{5.33}$$

which contains the LDA correlation energy density $e_\mathrm{c}^{\mathrm{LDA}}[n_\uparrow(\mathbf{r}), n_\downarrow(\mathbf{r})]$ (in the parametrization by Perdew and Wang [79]) and the term $1 - z\zeta^2$ for self-interaction correction. This defines all terms in the xc energy of locally RSH functionals, cf. Eq. (5.27). We refer to this functional as ωBT21 in the following.[5]

The form of the ωBT21 functional is constructed to satisfy or approximate many of the conditions identified in Sec. 5.2 [B2]. First, the range-separation function and the self-interaction correction of the correlation functional vanish in the limit of a uniform density. Thus, the functional reduces to LDA which describes the homogeneous-electron-gas limit correctly. Second, the leading term of the gradient expansion of $\omega_\sigma(\mathbf{r})$ is

$$\omega_\sigma^{\mathrm{GE}}(\mathbf{r}) = c_1 \frac{|\nabla n_\sigma(\mathbf{r})|}{n_\sigma(\mathbf{r})}. \tag{5.34}$$

This form can be motivated by imposing the gradient expansion of the exchange energy in the limit of a slowly varying density (5.15) for $E_\mathrm{x}^{\mathrm{lr,ex}} + E_\mathrm{x}^{\mathrm{sr,LDA}}$. The exact coefficient of the gradient expansion is obtained if the parameter is set to $c_1 = \sqrt{5}/18 \simeq 0.124$ [B2, 56]; with $c_1 = 0.115$ the coefficient is approximated closely. Third, the logarithmic term in the range-separation function ensures that the functional correctly scales to exact exchange in the high-density limit, i. e., it fulfills condition (5.21) [B2, 54]. Fourth and finally, ωBT21 is free from one-electron self-interaction errors. This is achieved, first, by the term $1 - z\zeta^2$ in Eq. (5.33) which ensures that the correlation energy correctly vanishes in one-electron systems. Second, the third term in Eq. (5.32), $1/(1 - z_\sigma\zeta^2)$, leads to a divergence of $\omega_\sigma(\mathbf{r})$ in one-spin-orbital regions. Thus, the functional reduces to exact exchange which is one-electron self-interaction free [B2, 54].

[5] In ωBT21, "ω" indicates that the functional is based on a range-separation approach, the acronym "BT" refers to "Bayreuth", the university city of the author, and "21" is the year when the functional was constructed. Note that the functional is originally referred to as SIC-ωLDA in Pub. [B2]; the new functional name is consistent with our later nomenclature [B4, B5].

Functional		AE6		BH6		Total
Name	Type	MSD	MAD	MSD	MAD	MAD
LDA		74.93	74.93	−17.49	17.49	46.21
PBE	GGA	10.40	14.27	−9.22	9.22	11.75
PBE0	Hybrid	−1.70	5.22	−4.49	4.49	4.86
ωPBE	RSH	−2.20	5.34	−1.22	1.42	3.38
B3LYP	Hybrid	−4.21	4.21	−4.68	4.68	4.45
CAM-B3LYP	RSH	−1.83	1.95	−3.75	3.75	2.85
MN15	Hybrid	−0.04	1.62	−0.47	0.99	1.31
ωBT21	Locally RSH	0.24	1.53	−1.66	1.66	1.60

Tab. 5.1: Comparison of the ωBT21 locally RSH functional to several common functionals (including global hybrids and globally RSHs) for the AE6 and BH6 test sets. MN15 is included as an example of an empirically constructed functional with many parameters. For each functional, the mean signed deviation (MSD) and the mean absolute deviation (MAD) of calculated and reference values is given for AE6 and BH6, as well as the MAD across both test sets. All numbers are in kcal/mol. Table adapted from Pub. [B2].

The range-separation function of ωBT21, cf. Eq. (5.32), contains two parameters c_1 and c_2. Although one of them could be fixed by non-empirical considerations (see above), we determine both of them empirically to explore the level of accuracy that can be achieved with this functional form. As described in Pub. [B2], we optimize the parameters for the AE6 and BH6 test sets [329–331] of atomization energies and reaction barrier heights, which leads to the values above. In Tab. 5.1, we show results for these sets [B2]. Overall, the mean absolute deviation (MAD) achieved with ωBT21 across both AE6 and BH6 is 1.60 kcal/mol. This number is very close to the "chemical accuracy" of ~ 1 kcal/mol that is often considered as the accuracy one aims to achieve ultimately with density functionals. In Tab. 5.1, we show results with common xc functionals as well. As an example, the well-known ωPBE and CAM-B3LYP globally RSH functionals have a total MAD of ~ 3 kcal/mol. These functionals contain a few empirical parameters. One approach that can bring modern functionals closer to chemical accuracy is to rely on many empirical parameters (> 10) that are determined by fitting to large databases of chemical properties. As an example of this approach, we consider the MN15 functional [332], with a total MAD of 1.31 kcal/mol. ωBT21 achieves a comparable accuracy but with much fewer parameter – only two. One many interpret this as indicating that, in the latter case, the functional form itself has already built in a lot of the proper physics. The trends shown here for AE6 and BH6 are confirmed by calculations using a larger test set [B5]. The recently developed range-separated local hybrid functional ωLH22t functional achieves a very favorable performance for different electronic binding properties as well [B5, 52]. This underlines that mixing exact and semi-local exchange locally can be a fruitful strategy to describe electronic binding with high accuracy.

5.5.2 Short-range exact exchange and the observable dilemma

The ωBT21 functional constitutes a step forward in the description of electronic binding properties by locally RSH functionals, see Sec. 5.5.1 and Pub. [B2]. In Pub. [B5], we examine whether ωBT21 yields physically interpretable eigenvalues. As described in Sec. 3.1.1, an important exact condition in the context of the KS (and generalized KS) eigenvalues is the IP theorem, i. e., the identity of the negative of the HOMO eigenvalue and the ionization potential calculated as a ground-state energy difference. Therefore, checking how well the IP theorem is fulfilled constitutes a hallmark test by which one can assess the quality of the eigenvalues of a given xc approximation in a non-empirical way. In Pub. [B5], we do this for the molecules in the AE6 test set, i. e., for a set of systems that is similar to the ones considered in the analysis of electronic binding. ωBT21 leads to an MAD of 1.11 eV [B5]. This value is considerably better than for typical semi-local and global hybrid functionals, where one obtains an MAD between about 2 and 4 eV [B5]. However, it is not the level of accuracy that can be obtained from functionals such as optimally tuned RSHs and that is required for reliable spectroscopic applications where an MAD close to 0.1 eV is desirable. On the other hand, this level of accuracy can be obtained from local range separation. For example, one can keep the functional form of ωBT21 and reoptimize the parameters of the range-separation function for the IP theorem of the AE6 molecules [B5]. This leads to a very small MAD of 0.16 eV for the IP theorem of AE6 and a similar level of accuracy is obtained for a larger set of molecules [B5]. However, the corresponding parameter values ($c_1 = 0.220$ and $c_2 = 0.225$) are very different to those of ωBT21. Thus, the notorious observable dilemma of hybrid functionals appears in the context of local range separation as well.

One option to make further progress is the combination of different hybrid functional concepts. This has been proposed very early [333–335] and recently functionals have been developed that combine the concepts of local hybrids and range separation [52, 336, 337]. On general grounds, this appears promising, since the additional complexity of the new functional form offers further flexibility to adjust the amount of exact exchange in a way that targets certain regions of space more specifically. In particular, adding a local hybrid term to RSH functionals may alleviate the observable dilemma: This extra term allows for exact exchange in the short range which may lead to an overall more attractive potential and, thus, more strongly bound eigenvalues without changing the range-separation part. For the ωLH22t range-separated local hybrid functional [52] high accuracy has been demonstrated for many observables, including fundamental gaps of organic semiconductor molecules [53]. However, the accuracy that this functional achieves with respect to fulfillment of the IP theorem is not yet generally *on par* with optimally tuned RSH functionals, in particular for smaller molecules. Therefore, while ωLH22t is among those functionals that presently do best in reducing the observable dilemma, it does not solve it conclusively.

In Pub. [B5], we explore whether the combination of the concepts of local range separation and local hybrids can reduce the observable dilemma as compared to

ωBT21. This new form of hybrid functionals can be referred to as locally range-separated local hybrid functionals. Their xc energy can be written as[6]

$$E_{\mathrm{xc}}^{\mathrm{LRSLH}} = E_{\mathrm{x}}^{\mathrm{lr,ex}} + \sum_{\sigma=\uparrow,\downarrow} \int \mathrm{d}\mathbf{r} \, \left(a_\sigma(\mathbf{r}) \, e_{\mathrm{x}\sigma}^{\mathrm{sr,ex}}(\mathbf{r}) + (1 - a_\sigma(\mathbf{r})) \, e_{\mathrm{x}\sigma}^{\mathrm{sr,sl}}(\mathbf{r}) \right) + E_{\mathrm{c}}^{\mathrm{sl}}. \quad (5.35)$$

Therein, $E_{\mathrm{x}}^{\mathrm{lr,ex}}$ is the long-range part of the exact exchange energy, cf. Eq. (5.28), $e_{\mathrm{x}\sigma}^{\mathrm{sr,ex}}$ the energy density of the complementary short-range part ($\mathrm{erf}\,(\cdot)$ replaced by $1 - \mathrm{erf}\,(\cdot)$), $e_{\mathrm{x}\sigma}^{\mathrm{sr,sl}}$ the energy density of a semi-local approximation to the short-range part of exchange, and $E_{\mathrm{c}}^{\mathrm{sl}}$ a (typical) semi-local approximation to the correlation energy. $a_\sigma(\mathbf{r})$ is the local mixing function familiar from local hybrids, cf. Sec. 5.3. In Eq. (5.35), it controls the admixture of exact exchange at short range. The range-separation function $\omega_\sigma(\mathbf{r})$ enters via the long- and short-range parts of the exchange energy. For $a_\sigma(\mathbf{r}) = 0$, Eq. (5.35) reduces to the xc energy of local range separation; for $\omega_\sigma(\mathbf{r}) = 0$, it reduces to the xc energy of local hybrids. As part of this work, locally range-separated local hybrid functionals have been implemented in Turbomole [B5]. The concepts of the implementation are explained in App. A.

Based on the mathematical structure of Eq. (5.35), we construct a new xc functional [B5]. We model the semi-local functional components in the same way as in ωBT21, cf. Sec. 5.5.1. On the other hand, we change the range-separation function to

$$\omega_\sigma^{\omega\mathrm{BT21a}}(\mathbf{r}) = c_3 \frac{|\nabla n_\sigma(\mathbf{r})|}{n_\sigma(\mathbf{r})} \frac{1}{1 - z_\sigma(\mathbf{r})\zeta^2(\mathbf{r})}. \quad (5.36)$$

In addition, we use the local mixing function [51]

$$a^{\omega\mathrm{BT21a}}(\mathbf{r}) = 1 - \frac{1}{1 + c_4 \, t^2(\mathbf{r})}, \quad (5.37)$$

with[7]

$$t^2(\mathbf{r}) = \left(\frac{\pi}{3}\right)^{1/3} \frac{\mathrm{a}_0}{4\left((1+\zeta(\mathbf{r}))^{2/3} + (1-\zeta(\mathbf{r}))^{2/3}\right)^2} \frac{|\nabla n(\mathbf{r})|^2}{n^{7/3}(\mathbf{r})}. \quad (5.38)$$

We refer to this functional as ωBT21a. It satisfies the same constraints as the ωBT21 functional. Notably, correct scaling to exact exchange in the high-density limit is obtained differently: In ωBT21 it is obtained via an appropriate form of $\omega_\sigma^{\omega\mathrm{BT21}}(\mathbf{r})$; in ωBT21a, this constraint is fulfilled via an appropriate scaling behavior of the local mixing function, $\lim_{\gamma\to\infty} a([n_\gamma], \mathbf{r}) = 1$ [51]. The new ωBT21a functional contains two not yet determined parameters c_3 and c_4. As in the case of ωBT21, we fix them

[6] In the most general form, Eq. (5.35) may contain an additional calibration function [52], similar to Eq. (5.25). This is deliberately not considered in this work.

[7] On finalizing this manuscript, we realized that the definition of $t^2(\mathbf{r})$ in Pub. [B5], between Eqs. (12) and (13) therein, is misprinted. Eq. (5.38) is the correct form, in agreement with the definition of $t^2(\mathbf{r})$ common in the literature, see, e. g., Ref. [51].

empirically, either by fitting to the AE6 and BH6 test sets or the IP theorem of the AE6 molecules [B5]. This yields two functional variants with different parameters. As detailed in Pub. [B5], the two variants of ωBT21a have very different parameter values, i. e., the observable dilemma remains. Moreover, the results for electronic binding or eigenvalues are not improved on a relevant scale as compared to ωBT21. This finding can be rationalized by a real-space analysis of the exact-exchange admixture, which reveals that the qualitative behavior of the functionals with and without short-range exact-exchange admixture is rather similar [B5]. Therefore, short-range exact exchange – at least in the form that we have explored so far – does not alleviate the observable dilemma.

5.5.3 Electronic excitations: The ωBT23 functional

In Pub. [B4], we present a locally RSH functional that is specifically designed for spectroscopic purposes. Describing electronic excitations reliably is a great challenge for DFT, cf. Chap. 3. One method that addresses some of these challenges are RSH functionals with optimal tuning. However, optimal tuning suffers from a number of shortcomings, which is one of the motivations to introduce local range separation. On the one hand, it is thus an interesting intellectual challenge to examine whether the same level of accuracy as with optimal tuning can be attained in an actual functional construction based on local range separation. On the other hand, this is a worthwhile task also from a practical perspective since such a functional, where the range separation is governed by an explicit density functional, can serve as a remedy in scenarios where optimal tuning fails.

In our functional construction, we build on the experiences from our previous work [B2, B5]. Our strategy is to incorporate those constraints that we identify as being relevant for theoretical spectroscopy in a transparent and non-empirical functional form [B4]. The mathematical structure of our xc functional is that of Eq. (5.27), i. e., we do not include short-range exact exchange. We employ a newly developed range-separation function,

$$\omega_\sigma^{\omega\mathrm{BT23}}(\mathbf{r}) = \frac{\sqrt{5}}{18}\frac{|\nabla n_\sigma(\mathbf{r})|}{n_\sigma(\mathbf{r})}\frac{1}{1-\frac{1}{2}\left(z_\sigma(\mathbf{r})+z_\sigma(\mathbf{r})\zeta^2(\mathbf{r})\right)}. \tag{5.39}$$

The short-range exchange energy is described by the LDA expression [B2, 325]. The correlation functional [301]

$$E_\mathrm{c}^{\omega\mathrm{BT23}}[n_\uparrow, n_\downarrow] = \int \mathrm{d}\mathbf{r}\, \left(e_\mathrm{c}^\mathrm{LDA}[n_\uparrow(\mathbf{r}), n_\downarrow(\mathbf{r})] - \sum_\sigma z_\sigma(\mathbf{r}) e_\mathrm{c}^\mathrm{LDA}[n_\sigma(\mathbf{r}), 0] \right) \tag{5.40}$$

is based on LDA with a correction to eliminate one-electron self-interaction. The objects in Eqs. (5.39) and (5.40) are explained in Eqs. (5.22), (5.24), and (5.33) above. We refer to this functional as ωBT23. The key idea of our functional construction is the way self-interaction errors are corrected [B4]. Thereby, we follow the logic

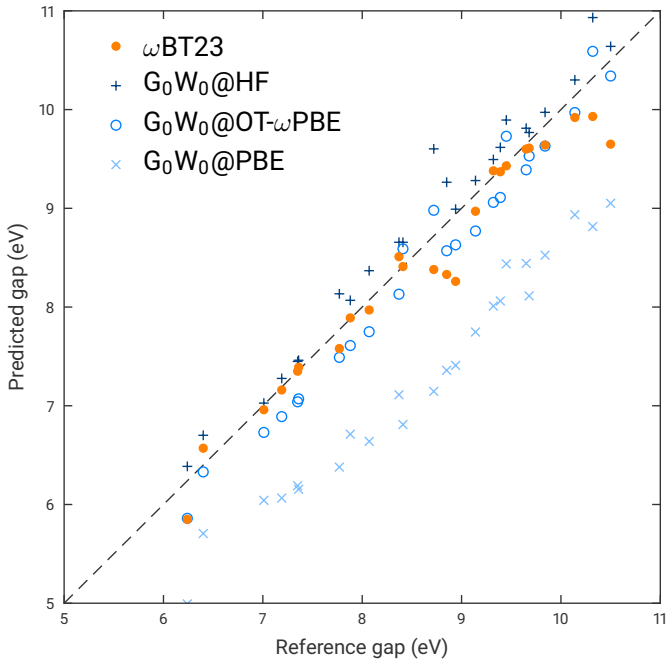

Fig. 5.2: Fundamental gaps of a diverse set of organic molecules calculated as the HOMO–LUMO eigenvalue difference with the ωBT23 functional, and plotted against the reference gaps calculated from CCSD(T) [338]. Three variants of G_0W_0 using PBE, Hartree-Fock (HF), and optimally tuned (OT) ωPBE as a starting point are also shown [339]. Figure adapted from Pub. [B4].

explained in Sec. 5.2.6. First, we ensure that our functional construction removes one-electron self-interaction errors. Moreover, we do this in a way that leads to the reduction of many-electron self-interaction as well. This requires to attain a delicate balance between, on the one hand, the overcorrection characteristic for full exact exchange or the Perdew-Zunger form of self-interaction correction and, on the other hand, a functional with a too modest correction that retains too much of its semi-local character. The form of self-interaction correction chosen in Eqs. (5.39) and (5.40) ensures that one-electron systems are fully self-interaction corrected, while other systems – in particular closed-shell systems – are subject to a more moderate correction. As we show in Pub. [B4], this leads to a functional that approximates piecewise linearity well. This is a relevant feature in the context of theoretical spectroscopy and is an important verification of the guiding principles of our functional construction.

In Pub. [B4], we report results with the new ωBT23 functional for different test cases. Therein, we also compare to the recently published ωLH22t functional [52, 53]. In the following, we focus on the results from ωBT23 for the fundamental gaps of practically relevant organic molecules. The fundamental gap is one of the most

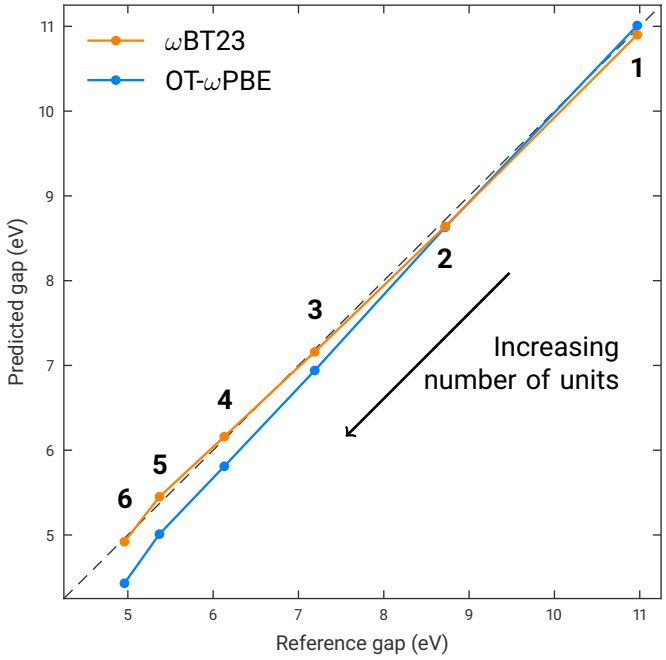

Fig. 5.3: Size dependence of the fundamental gap for the series of oligoacenes (from benzene to hexacene, i. e., one to six molecular units) calculated as the HOMO–LUMO eigenvalue difference with the ωBT23 functional and optimally tuned (OT) ωPBE [40], and plotted against the reference gaps calculated from CCSD(T) [340, 341]. Figure adapted from Pub. [B4].

important spectroscopic observables, cf. Sec. 3.1.1. It is instructive to compare the HOMO–LUMO gap calculated with the new ωBT23 functional to accurate and reliable reference data [B4]. From a fundamental point of view, this is relevant as an indication of whether the eigenvalues of ωBT23 are endowed with proper physical meaning. Moreover, being able to calculate the fundamental gap from the frontier eigenvalue difference is of interest in view of practical applications as well.

We first focus on a diverse set of organic molecules, which is typical for the type of systems that are used in organic electronics [172, 338, 339]. For this set, highly accurate reference results have been obtained in wavefunction-based calculations [338]. In Fig. 5.2, the results from ωBT23 are plotted against the wavefunction reference [B4]. Except for a few systems, for which the difference is as large as a few 0.1 eV, the results are close to the diagonal dashed line that indicates perfect agreement. The MAD across the set is 0.20 eV for ωBT23. For the same set of molecules, results from other popular methods to predict spectroscopic properties based on DFT and many-body perturbation theory have been reported. On the one hand, the ωPBE RSH functional with optimal tuning leads to a MAD of 0.38 eV [172]. On the other hand, Fig. 5.2 shows the gaps that are obtained with G_0W_0 based on different starting points [339]. Using PBE as a starting points leads to a serious underestimation of the fundamental

gap, whereas Hartree-Fock as a starting point leads to a slight overestimation. Using optimally tuned ωPBE as a starting point, which has been reported as one of the best possible GW approaches for this benchmark set [339], leads to an MAD of 0.26 eV. Thus, gap prediction based on the non-empirical locally RSH functional ωBT23 can clearly compete with both a RSH based on optimal tuning and G_0W_0 with a diligently chosen starting point. While the GW approach requires performing a DFT calculation first and then, in addition, the computationally expensive G_0W_0 calculation, a single DFT calculation is sufficient to reach the same accuracy with our locally RSH functional.

One of the paradigm test cases for which optimal tuning fails are conjugated systems of increasing size. Fig. 5.3 shows the fundamental gaps calculated with ωBT23 and optimally tuned ωPBE [40] for a series of oligoacenes of increasing size [B4]. Comparing to accurate wavefunction-based reference gaps [340, 341], we find that the accuracy reached with optimal tuning is good for the smaller systems. However, as visible in the deviation from the diagonal dashed line, the errors increase noticeably with the size of the conjugated systems – a well-known trend for optimal tuning. On the other hand, with our locally RSH functional ωBT23 the accuracy is consistently high (deviations below 0.1 eV) for all system sizes, with an MAD of 0.06 eV. In conclusion, the successful concept of RSH functionals can become even more powerful for the prediction of spectroscopic observables when going from global to local range separation.

6 Conclusions

In conclusion, we have shown that (time-dependent) density functional theory ((TD)DFT) based on optimally tuned range-separated hybrid (RSH) functionals in the generalized Kohn-Sham (KS) framework can become a powerful tool to predict electronic excitations. Using this methodology, we have performed first-principles TDDFT calculations on the charge-separation branches of the heliobacterial reaction center [B1, B3]. We have extensively analyzed the impact of the surrounding protein environment. Furthermore, we have included the effect of structural changes by diligently conducted Born-Oppenheimer molecular dynamics simulations. All results consistently indicate that the first step of charge separation takes place on the second and third cofactor (i. e., it is a $EC2^{+}EC3^{-}$ state) [B3]. This finding of our study is consistent with the recent experimental works by Song *et al.* [36] and Orf and Redding [37]. Moreover, we have revealed that the interaction with a small group of charged amino acids specifically adjusts the energies of the charge-transfer excitations, lowering them with respect to the non-charge-transfer bright excitations [B3]. This can enable downhill energy transfer from the dominant Q_y excitations to an $EC2^{+}EC3^{-}$ state and, thus, may facilitate efficient charge separation. For other light-harvesting systems, the influence that the protein environment in general and specific amino acids in particular can have on electronic excitations and charge separation has been investigated in previous works [213, 220, 342–346]. To the best of our knowledge, our results are the first such findings for the heliobacterial reaction center. This may be an important step toward a better understanding of the microscopic origin of efficient charge separation and shed light on the relation of the heliobacterial reaction center to other light-harvesting systems [7, 242].

However, the commonly used form of RSH functionals is far from being a panacea. The implicit way by which the optimal-tuning approach leads to a system-specific value for ω, comes at the expense of non-negligible drawbacks. In our own work on the heliobacterial reaction center, we have encountered spuriously low charge-transfer excitations involving charged amino acids. This observation indicates that our study reaches the limits of optimal tuning due to the very different length scales and electronic properties of chromophores and amino acids. Overcoming the limitations of optimal tuning is one motivation for the approach of local range separation, where the constant range-separation parameter is turned into a local function of the density $\omega([n], \mathbf{r})$. We pursue this novel form of hybrid functionals in the second part of our work [B2, B4, B5]. We have shown that a transparent functional, which is constructed to fulfill important exact constraints and which contains only two empirical parameters, can describe binding energies and reaction barrier heights very

accurately [B2]. Thereby, it reaches a similar accuracy as density functionals that contain multiple empirical parameters.

Subsequently, we have explored describing both electronic binding and electronic excitations reliably within a fixed functional form [B5]. This observable dilemma is a longstanding challenge for hybrid functionals. Very generally speaking, the challenge is that, on average, a larger fraction of exact exchange is required to obtain physically interpretable eigenvalues than for a reliable description of electronic binding. One option to address this dilemma might be admixing exact exchange more specifically in those regions of space that have the strongest influence on the eigenvalues. As one way to achieve this, we have explored using a fraction of exact exchange at short range but find that this cannot alleviate the observable dilemma, at least not in the form that we have been using in our work [B5]. Another option to tackle the observable dilemma might be developing semi-local functional components that are specifically designed to be used within hybrid functionals. In that respect, constructing a semi-local correlation functional that is "compatible" with a larger fraction of exact exchange, i. e., it leads to a reasonable prediction of electronic binding at an amount of exact exchange that is suitable for meaningful eigenvalues, appears as one promising [52, 89, 309] but very challenging [49, 96] option. Apart from that, exciting avenues of further development include extending the implementation to TDDFT [313] or improving the description of strongly correlated systems [123, 347, 348], inspired by progress made recently for local hybrid functionals [349–352]. All of these perspectives are clearly beyond the scope of the present work.

This outlook should not obstruct the view on the very promising results that have been obtained with local range separation already at the present stage. Most importantly, we have constructed a functional for spectroscopic purposes [B4]. The functional is constructed non-empirically and respects relevant constraints, such as the homogeneous and slowly varying density limits, and eliminates one-electron self-interaction errors. As a verification of the guiding principles of the construction, we have shown that our functional approximates piecewise linearity well. We have demonstrated that our functional predicts the fundamental gap in generalized KS theory very reliably for a large and diverse set of organic molecules, including organic semiconductor materials with a notoriously difficult electronic structure, thereby reaching the accuracy of higher-level wavefunction-based methods [B4]. Due to the explicit density dependence of $\omega([n], \mathbf{r})$, the new functional does not suffer from the well-known issues of optimal tuning and, moreover, offers the flexibility to adjust locally to the electronic properties of the system of interest. Thus, our new locally RSH functional is a very promising perspective as well for future applications to light-harvesting systems.

A Implementation of local range separation in Gaussian basis sets

In this appendix, we explain the implementation of locally range-separated local hybrid functionals, cf. Sec. 5.5.2, in quantum-chemistry programs using Gaussian basis sets. Within this work, this implementation has been realized in Turbomole [B5]. It is based on previous implementations of local hybrids [312], locally range-separated hybrids (RSHs) [55], and range-separated local hybrids [52]. The generalized Kohn-Sham (KS) single-particle orbitals $\phi_{i\sigma}(\mathbf{r})$ are expressed as linear combinations of Gaussian basis functions $\chi_\mu(\mathbf{r})$ [98, 151],

$$\phi_{i\sigma}(\mathbf{r}) = \sum_\mu C_{\mu,i\sigma}\chi_\mu(\mathbf{r}). \tag{A.1}$$

We treat the basis functions as being real and independent of the spin. The generalized KS equation $\hat{h}_{i\sigma}(\mathbf{r})\phi_{i\sigma}(\mathbf{r}) = \varepsilon_{i\sigma}\phi_{i\sigma}(\mathbf{r})$ can be rewritten as a matrix equation for the coefficients $C_{\mu,i\sigma}$,

$$\sum_\nu C_{\nu,i\sigma}\left(\langle\chi_\mu(\mathbf{r})|\hat{h}_{i\sigma}|\chi_\nu(\mathbf{r})\rangle - \varepsilon_{i\sigma}\langle\chi_\mu(\mathbf{r})|\chi_\nu(\mathbf{r})\rangle\right) = 0. \tag{A.2}$$

Therein, $\hat{h}_{i\sigma}(\mathbf{r})$ is an effective single-particle Hamiltonian where the kinetic energy, the external potential, the Hartree potential, and the exchange-correlation (xc) potential $\hat{v}_{\mathrm{xc}}(\mathbf{r})$ enter (compare, e. g., Eq. (3.26)). The xc potential follows from

$$\hat{v}_{\mathrm{xc}}(\mathbf{r})\phi_{i\sigma}(\mathbf{r}) = \frac{\delta E_{\mathrm{xc}}}{\delta\phi^*_{i\sigma}(\mathbf{r})}. \tag{A.3}$$

We show below how the xc potential of locally range-separated local hybrid functionals can be evaluated using Gaussian basis functions. In the following, we recapitulate the relevant ideas for the case of (full) exact exchange, since the fundamental concepts are the same as for hybrid functionals with a locally space-dependent admixture of exact exchange but the equations have a more transparent form.

Evaluation of the exact exchange potential

$$\hat{v}^{\mathrm{ex}}_{\mathrm{x}}(\mathbf{r})\phi_{i\sigma}(\mathbf{r}) = -\sum_j \int \mathrm{d}\mathbf{r}'\ \phi^*_{j\sigma}(\mathbf{r}')\frac{1}{|\mathbf{r}-\mathbf{r}'|}\phi_{i\sigma}(\mathbf{r}')\phi_{j\sigma}(\mathbf{r}) \tag{A.4}$$

corresponds to evaluating the exact exchange matrix elements

$$\begin{aligned} K_{\mu\nu,\sigma} &= \langle\chi_\mu(\mathbf{r})|\hat{v}^{\mathrm{ex}}_x(\mathbf{r})|\chi_\nu(\mathbf{r})\rangle \\ &= -\sum_{\kappa,\lambda} D_{\kappa\lambda,\sigma}\int \mathrm{d}\mathbf{r}\int \mathrm{d}\mathbf{r}'\ \chi_\mu(\mathbf{r})\chi_\kappa(\mathbf{r}')\frac{1}{|\mathbf{r}-\mathbf{r}'|}\chi_\nu(\mathbf{r}')\chi_\lambda(\mathbf{r}), \end{aligned} \tag{A.5}$$

with the density matrix elements

$$D_{\mu\nu,\sigma} = \sum_i C^*_{\mu,i\sigma} C_{\nu,i\sigma}. \tag{A.6}$$

In a similar way, the exact exchange energy density

$$e^{\mathrm{ex}}_{\mathrm{x}\sigma}(\mathbf{r}) = -\frac{1}{2} \sum_{i,j} \int \mathrm{d}\mathbf{r}' \; \phi^*_{i\sigma}(\mathbf{r}) \phi^*_{j\sigma}(\mathbf{r}') \frac{1}{|\mathbf{r} - \mathbf{r}'|} \phi_{i\sigma}(\mathbf{r}') \phi_{j\sigma}(\mathbf{r}) \tag{A.7}$$

can be expressed as

$$e^{\mathrm{ex}}_{\mathrm{x}\sigma}(\mathbf{r}) = -\frac{1}{2} \sum_{\mu,\nu,\kappa,\lambda} D_{\mu\nu,\sigma} D_{\kappa\lambda,\sigma} \int \mathrm{d}\mathbf{r}' \; \chi_\mu(\mathbf{r}) \chi_\kappa(\mathbf{r}') \frac{1}{|\mathbf{r} - \mathbf{r}'|} \chi_\nu(\mathbf{r}') \chi_\lambda(\mathbf{r}). \tag{A.8}$$

Eqs. (A.5) and (A.8) can be evaluated analytically. Hybrid functionals with a locally space-dependent admixture of exact exchange lead to expressions where this is no longer possible.

Instead, a semi-numerical scheme has been developed [312, 315, 316]. Thereby, the integral $\int \mathrm{d}\mathbf{r}$ is replaced by numerical integration on a grid. The latter is performed as a sum $\sum_g w_g$ over all grid points g; w_g is the numerical weight of grid point g. The evaluation of Eqs. (A.5) and (A.8) is divided into different steps. This facilitates an efficient implementation using prescreening techniques. First, the integral

$$A^{(g)}_{\mu\nu} = \int \mathrm{d}\mathbf{r}' \; \chi_\mu(\mathbf{r}') \frac{1}{|\mathbf{r}_g - \mathbf{r}'|} \chi_\nu(\mathbf{r}') \tag{A.9}$$

is evaluated analytically on each grid point. Then, the exact exchange matrix elements,

$$K_{\mu\nu,\sigma} = -\sum_g X^{(g)}_\mu G^{(g)}_{\nu,\sigma}, \tag{A.10}$$

and the exact exchange energy density,

$$w_g \, e^{\mathrm{ex}}_{\mathrm{x}\sigma}(\mathbf{r}_g) = -\frac{1}{2} \sum_\mu F^{(g)}_{\mu,\sigma} G^{(g)}_{\mu,\sigma}, \tag{A.11}$$

are calculated numerically using the auxiliary quantities

$$F^{(g)}_{\mu,\sigma} = \sum_\nu D_{\mu\nu,\sigma} X^{(g)}_\nu, \tag{A.12}$$

$$G^{(g)}_{\mu,\sigma} = \sum_\nu F^{(g)}_{\nu,\sigma} A^{(g)}_{\mu\nu}, \tag{A.13}$$

where we have introduced the abbreviation $X^{(g)}_\mu = \sqrt{w_g} \chi_\mu(\mathbf{r}_g)$.

The xc energy of locally range-separated local hybrid functionals, cf. Eq. (5.35), can be rewritten as

$$\begin{aligned} E_{\mathrm{xc}}^{\mathrm{LRSLH}} = & \underbrace{\sum_{\sigma} \int \mathrm{d}\mathbf{r}\; a_\sigma(\mathbf{r}) e_{\mathrm{x}\sigma}^{\mathrm{ex}}(\mathbf{r})}_{= E_{\mathrm{x}}^{\mathrm{ex},a}} + \underbrace{\sum_{\sigma} \int \mathrm{d}\mathbf{r}\; (1 - a_\sigma(\mathbf{r})) e_{\mathrm{x}\sigma}^{\mathrm{lr,ex}}(\mathbf{r})}_{= E_{\mathrm{x}}^{\mathrm{lr,ex},a}} \\ & + \sum_{\sigma} \int \mathrm{d}\mathbf{r}\; (1 - a_\sigma(\mathbf{r})) e_{\mathrm{x}\sigma}^{\mathrm{sr,sl}}(\mathbf{r}) + E_{\mathrm{c}}^{\mathrm{sl}}. \end{aligned} \tag{A.14}$$

This form resembles the way the functionals have been implemented in Turbomole [B5]. Eq. (A.14) contains the long-range exact exchange energy density

$$e_{\mathrm{x}\sigma}^{\mathrm{lr,ex}}(\mathbf{r}) = -\frac{1}{2} \sum_{i,j} \int \mathrm{d}\mathbf{r}'\; \phi_{i\sigma}^*(\mathbf{r}) \phi_{j\sigma}^*(\mathbf{r}') \frac{\mathrm{erf}\left(\omega_\sigma(\mathbf{r}) |\mathbf{r} - \mathbf{r}'|\right)}{|\mathbf{r} - \mathbf{r}'|} \phi_{i\sigma}(\mathbf{r}') \phi_{j\sigma}(\mathbf{r}). \tag{A.15}$$

In Eq. (A.14), the two terms $E_{\mathrm{x}}^{\mathrm{ex},a}$ and $E_{\mathrm{x}}^{\mathrm{lr,ex},a}$ are exact-exchange contributions; the remaining terms have the form of (normal) semi-local functionals. The term $E_{\mathrm{x}}^{\mathrm{ex},a}$ is the same as the exact-exchange term appearing in local hybrid functionals, cf. Eq. (5.25); the term $E_{\mathrm{x}}^{\mathrm{lr,ex},a}$ is new in locally range-separated local hybrids but similar to the exact-exchange term appearing in locally RSH functionals, cf. Eq. (5.27). In the following, we explain how the exact-exchange contributions are handled numerically. The corresponding exchange potential consists of the terms

$$\begin{aligned} \frac{\delta E_{\mathrm{x}}^{\mathrm{ex},a}}{\delta \phi_{i\sigma}^*(\mathbf{r})} = & -\frac{1}{2} \sum_{j} \int \mathrm{d}\mathbf{r}'\; \phi_{j\sigma}^*(\mathbf{r}') \frac{a_\sigma(\mathbf{r}) + a_\sigma(\mathbf{r}')}{|\mathbf{r} - \mathbf{r}'|} \phi_{i\sigma}(\mathbf{r}') \phi_{j\sigma}(\mathbf{r}) \\ & + \sum_{\sigma'} \int \mathrm{d}\mathbf{r}''\; \frac{\delta a_{\sigma'}(\mathbf{r}'')}{\delta \phi_{i\sigma}^*(\mathbf{r})} e_{\mathrm{x}\sigma'}^{\mathrm{ex}}(\mathbf{r}''), \end{aligned} \tag{A.16}$$

$$\begin{aligned} \frac{\delta E_{\mathrm{x}}^{\mathrm{lr,ex},a}}{\delta \phi_{i\sigma}^*(\mathbf{r})} = & -\frac{1}{2} \sum_{j} \int \mathrm{d}\mathbf{r}'\; (1 - a_\sigma(\mathbf{r})) \phi_{j\sigma}^*(\mathbf{r}') \frac{\mathrm{erf}\left(\omega_\sigma(\mathbf{r}) |\mathbf{r} - \mathbf{r}'|\right)}{|\mathbf{r} - \mathbf{r}'|} \phi_{i\sigma}(\mathbf{r}') \phi_{j\sigma}(\mathbf{r}) \\ & - \frac{1}{2} \sum_{j} \int \mathrm{d}\mathbf{r}'\; (1 - a_\sigma(\mathbf{r}')) \phi_{j\sigma}^*(\mathbf{r}') \frac{\mathrm{erf}\left(\omega_\sigma(\mathbf{r}') |\mathbf{r} - \mathbf{r}'|\right)}{|\mathbf{r} - \mathbf{r}'|} \phi_{i\sigma}(\mathbf{r}') \phi_{j\sigma}(\mathbf{r}) \\ & - \sum_{\sigma'} \int \mathrm{d}\mathbf{r}''\; \frac{\delta a_{\sigma'}(\mathbf{r}'')}{\delta \phi_{i\sigma}^*(\mathbf{r})} e_{\mathrm{x}\sigma'}^{\mathrm{lr,ex}}(\mathbf{r}'') \\ & + \sum_{\sigma'} \int \mathrm{d}\mathbf{r}''\; (1 - a_{\sigma'}(\mathbf{r}'')) \frac{\delta \omega_{\sigma'}(\mathbf{r}'')}{\delta \phi_{i\sigma}^*(\mathbf{r})} \mathcal{E}_{\sigma'}^{\mathrm{exp}}(\mathbf{r}''), \end{aligned} \tag{A.17}$$

with

$$\mathcal{E}_{\sigma}^{\mathrm{exp}}(\mathbf{r}) = -\frac{1}{\sqrt{\pi}} \sum_{i,j} \int \mathrm{d}\mathbf{r}'\; \phi_{i\sigma}^*(\mathbf{r}) \phi_{j\sigma}^*(\mathbf{r}') \exp\left(-\omega_\sigma^2(\mathbf{r}) |\mathbf{r} - \mathbf{r}'|^2\right) \phi_{i\sigma}(\mathbf{r}') \phi_{j\sigma}(\mathbf{r}). \tag{A.18}$$

The corresponding exchange matrix elements are

$$K_{\mu\nu,\sigma} = \frac{K_{\mu\nu,\sigma}^{a} + K_{\nu\mu,\sigma}^{a}}{2} + K_{\mu\nu,\sigma}^{\delta a} + \frac{K_{\mu\nu,\sigma}^{\mathrm{lr}} + K_{\nu\mu,\sigma}^{\mathrm{lr}}}{2} + K_{\mu\nu,\sigma}^{\mathrm{lr},\delta a} + K_{\mu\nu,\sigma}^{\mathrm{lr},\delta\omega}, \tag{A.19}$$

where the terms with the superscript "lr" arise from Eq. (A.17), the terms without from Eq. (A.16). Two contributions to Eq. (A.19) are non-local,

$$K^{a}_{\mu\nu,\sigma} = -\sum_{\kappa,\lambda} D_{\kappa\lambda,\sigma} \int \mathrm{d}\mathbf{r} \int \mathrm{d}\mathbf{r}'\; a_\sigma(\mathbf{r})\chi_\mu(\mathbf{r})\chi_\kappa(\mathbf{r}')\frac{1}{|\mathbf{r}-\mathbf{r}'|}\chi_\nu(\mathbf{r}')\chi_\lambda(\mathbf{r}), \tag{A.20}$$

$$\begin{aligned} K^{\mathrm{lr}}_{\mu\nu,\sigma} = -\sum_{\kappa,\lambda} D_{\kappa\lambda,\sigma} \int \mathrm{d}\mathbf{r} \int \mathrm{d}\mathbf{r}'\; (1-a_\sigma(\mathbf{r}))\cdot \\ \cdot\, \chi_\mu(\mathbf{r})\chi_\kappa(\mathbf{r}')\frac{\mathrm{erf}\left(\omega_\sigma(\mathbf{r})|\mathbf{r}-\mathbf{r}'|\right)}{|\mathbf{r}-\mathbf{r}'|}\chi_\nu(\mathbf{r}')\chi_\lambda(\mathbf{r}). \end{aligned} \tag{A.21}$$

$K^{\delta a}_{\mu\nu,\sigma}$, $K^{\mathrm{lr},\delta a}_{\mu\nu,\sigma}$, and $K^{\mathrm{lr},\delta\omega}_{\mu\nu,\sigma}$ are local. The local contributions share the same mathematical form,

$$\begin{aligned} K^{\mathrm{loc}}_{\mu\nu,\sigma}(f_\sigma(\mathbf{r}),\epsilon_\sigma(\mathbf{r})) = &\sum_{\sigma'} \int \mathrm{d}\mathbf{r}\; \chi_\mu(\mathbf{r})\chi_\nu(\mathbf{r})\; \frac{\partial f_{\sigma'}(\mathbf{r})}{\partial n_\sigma(\mathbf{r})}\epsilon_{\sigma'}(\mathbf{r}) \\ &+ 2\sum_{\sigma'} \int \mathrm{d}\mathbf{r}\; (\nabla(\chi_\mu(\mathbf{r})\chi_\nu(\mathbf{r}))) \cdot (\nabla n_\sigma(\mathbf{r}))\; \frac{\partial f_{\sigma'}(\mathbf{r})}{\partial \gamma_{\sigma\sigma}(\mathbf{r})}\epsilon_{\sigma'}(\mathbf{r}) \\ &+ \sum_{\sigma'} \int \mathrm{d}\mathbf{r}\; (\nabla(\chi_\mu(\mathbf{r})\chi_\nu(\mathbf{r}))) \cdot (\nabla n_{\bar\sigma}(\mathbf{r}))\; \frac{\partial f_{\sigma'}(\mathbf{r})}{\partial \gamma_{\sigma\bar\sigma}(\mathbf{r})}\epsilon_{\sigma'}(\mathbf{r}) \\ &+ \frac{1}{2}\sum_{\sigma'} \int \mathrm{d}\mathbf{r}\; (\nabla\chi_\mu(\mathbf{r})) \cdot (\nabla\chi_\nu(\mathbf{r}))\; \frac{\partial f_{\sigma'}(\mathbf{r})}{\partial \tau_\sigma(\mathbf{r})}\epsilon_{\sigma'}(\mathbf{r}), \end{aligned} \tag{A.22}$$

where $f_\sigma(\mathbf{r})$ and $\epsilon_\sigma(\mathbf{r})$ are "dummy variables" that are replaced according to

$$K^{\delta a}_{\mu\nu,\sigma} = K^{\mathrm{loc}}_{\mu\nu,\sigma}(a_\sigma(\mathbf{r}), e^{\mathrm{ex}}_{\mathrm{x}\sigma}(\mathbf{r})), \tag{A.23}$$

$$K^{\mathrm{lr},\delta a}_{\mu\nu,\sigma} = K^{\mathrm{loc}}_{\mu\nu,\sigma}(a_\sigma(\mathbf{r}), -e^{\mathrm{lr,ex}}_{\mathrm{x}\sigma}(\mathbf{r})), \tag{A.24}$$

$$K^{\mathrm{lr},\delta\omega}_{\mu\nu,\sigma} = K^{\mathrm{loc}}_{\mu\nu,\sigma}(\omega_\sigma(\mathbf{r}), (1-a_\sigma(\mathbf{r}))\mathcal{E}^{\mathrm{exp}}_{\sigma}(\mathbf{r})). \tag{A.25}$$

In Eq. (A.22), $\bar\sigma \neq \sigma$ means the respective "other" spin channel, i. e., if $\sigma = \uparrow$ then $\bar\sigma = \downarrow$ and vice versa, and $\gamma_{\sigma\sigma'}(\mathbf{r}) = |\nabla(n_\sigma(\mathbf{r})) \cdot \nabla(n_{\sigma'}(\mathbf{r}))|$. $e^{\mathrm{lr,ex}}_{\mathrm{x}\sigma}(\mathbf{r})$ and $\mathcal{E}^{\mathrm{exp}}_{\sigma}(\mathbf{r})$ can be expressed in terms of Gaussian basis functions similar to $e^{\mathrm{ex}}_{\mathrm{x}\sigma}(\mathbf{r})$, see Eq. (A.8) and compare Eqs. (A.7), (A.15), and (A.18).

Eq. (A.19) can be evaluated in a semi-numerical scheme, which is similar to Eqs. (A.9) to (A.13). A key step is to introduce two further analytical integrals [55],

$$A^{(g),\mathrm{erf}}_{\mu\nu} = \int \mathrm{d}\mathbf{r}'\; \chi_\mu(\mathbf{r}')\frac{\mathrm{erf}\left(\omega_\sigma(\mathbf{r}_g)|\mathbf{r}_g-\mathbf{r}'|\right)}{|\mathbf{r}_g-\mathbf{r}'|}\chi_\nu(\mathbf{r}'), \tag{A.26}$$

$$A^{(g),\mathrm{exp}}_{\mu\nu} = \int \mathrm{d}\mathbf{r}'\; \chi_\mu(\mathbf{r}')\exp\left(-\omega^2_\sigma(\mathbf{r}_g)|\mathbf{r}_g-\mathbf{r}'|^2\right)\chi_\nu(\mathbf{r}'), \tag{A.27}$$

in addition to Eq. (A.9). Eq. (A.26) resembles an integral appearing in (common) global range separation; Eq. (A.27) can be viewed as a simple overlap integral of

three Gaussian basis functions. In analogy to Eq. (A.13), the auxiliary quantities

$$G^{(g),\mathrm{erf}}_{\mu,\sigma} = \sum_{\nu} F^{(g)}_{\nu,\sigma} A^{(g),\mathrm{erf}}_{\mu\nu}, \tag{A.28}$$

$$G^{(g),\mathrm{exp}}_{\mu,\sigma} = \sum_{\nu} F^{(g)}_{\nu,\sigma} A^{(g),\mathrm{exp}}_{\mu\nu}, \tag{A.29}$$

are introduced. By that, the non-local contributions to Eq. (A.19) can be calculated as

$$K^{a}_{\mu\nu,\sigma} = -\sum_{g} a_\sigma(\mathbf{r}_g) X^{(g)}_{\mu} G^{(g)}_{\nu,\sigma}, \tag{A.30}$$

$$K^{\mathrm{lr}}_{\mu\nu,\sigma} = -\sum_{g} (1 - a_\sigma(\mathbf{r}_g)) X^{(g)}_{\mu} G^{(g),\mathrm{erf}}_{\nu,\sigma}. \tag{A.31}$$

The local contributions can be calculated in a similar way as (normal) semi-local functionals that depend on the spin density $n_\sigma(\mathbf{r})$, its gradient, and the non-interacting kinetic energy density $\tau_\sigma(\mathbf{r})$ of both spin channels ($\sigma = \uparrow, \downarrow$), using the expressions

$$w_g \, e^{\mathrm{lr,ex}}_{\mathrm{x}\sigma}(\mathbf{r}_g) = -\frac{1}{2} \sum_{\mu} F^{(g)}_{\mu,\sigma} G^{(g),\mathrm{erf}}_{\mu,\sigma}, \tag{A.32}$$

$$w_g \, \mathcal{E}^{\mathrm{exp}}_{\sigma}(\mathbf{r}_g) = -\frac{1}{\sqrt{\pi}} \sum_{\mu} F^{(g)}_{\mu,\sigma} G^{(g),\mathrm{exp}}_{\mu,\sigma}, \tag{A.33}$$

and the exact energy density calculated according to Eq. (A.11). Then, it is straightforward to evaluate the integrals in Eq. (A.22) numerically on the grid. From this scheme for locally range-separated local hybrid functionals [B5], the corresponding scheme for local hybrids [312] can be obtained by setting $\omega_\sigma(\mathbf{r}) \equiv 0$. Similarly, setting $a_\sigma(\mathbf{r}) \equiv 0$ leads to the scheme for locally RSHs [55].

Bibliography

[B1] M. Brütting, J. M. Foerster, and S. Kümmel, Investigating primary charge separation in the reaction center of *Heliobacterium modesticaldum*, J. Phys. Chem. B **125**, 3468 (2021).

[B2] M. Brütting, H. Bahmann, and S. Kümmel, Hybrid functionals with local range separation: Accurate atomization energies and reaction barrier heights, J. Chem. Phys. **156**, 104109 (2022).

[B3] M. Brütting, J. M. Foerster, and S. Kümmel, Understanding primary charge separation in the heliobacterial reaction center, J. Phys. Chem. Lett. **14**, 3092 (2023).

[B4] M. Brütting, H. Bahmann, and S. Kümmel, Predicting fundamental gaps accurately from density functional theory with non-empirical local range separation, J. Chem. Phys. **160**, 181101 (2024).

[B5] M. Brütting, H. Bahmann, and S. Kümmel, Combining local range separation and local hybrids: A step in the quest for obtaining good energies and eigenvalues from one functional, J. Phys. Chem. A **128**, 5212 (2024).

[1] G. Renger, "Overview of primary processes of photosynthesis", in *Primary processes of photosynthesis, Part 1: Principles and apparatus* (Royal Society of Chemistry, 2007), pp. 5–35.

[2] R. E. Blankenship, *Molecular mechanisms of photosynthesis*, 2nd ed. (Wiley Blackwell, Chichester, 2014).

[3] J. R. Schramski, D. K. Gattie, and J. H. Brown, Human domination of the biosphere: Rapid discharge of the earth-space battery foretells the future of humankind, Proc. Natl. Acad. Sci. **112**, 9511 (2015).

[4] R. J. Cogdell, A. Gall, and J. Köhler, The architecture and function of the light-harvesting apparatus of purple bacteria: From single molecules to *in vivo* membranes, Q. Rev. Biophys. **39**, 227 (2006).

[5] A. J. Hoff and J. Deisenhofer, Photophysics of photosynthesis. Structure and spectroscopy of reaction centers of purple bacteria, Phys. Rep. **287**, 1 (1997).

[6] E. Romero, V. I. Novoderezhkin, and R. van Grondelle, Quantum design of photosynthesis for bio-inspired solar-energy conversion, Nature **543**, 355 (2017).

[7] C. J. Gisriel, C. Azai, and T. Cardona, Recent advances in the structural diversity of reaction centers, Photosynth. Res. **149**, 329 (2021).

[8] M. Gorka, A. Baldansuren, A. Malnati, E. Gruszecki, J. H. Golbeck, and K. V. Lakshmi, Shedding light on primary donors in photosynthetic reaction centers, Front. Microbiol. **12**, 735666 (2021).

[9] T. Mirkovic, E. E. Ostroumov, J. M. Anna, R. van Grondelle, Govindjee, and G. D. Scholes, Light absorption and energy transfer in the antenna complexes of photosynthetic organisms, Chem. Rev. **117**, 249 (2017).

[10] J.-L. Brédas, J. E. Norton, J. Cornil, and V. Coropceanu, Molecular understanding of organic solar cells: The challenges, Acc. Chem. Res. **42**, 1691 (2009).

[11] B. P. Fingerhut, W. Zinth, and R. de Vivie-Riedle, Design criteria for optimal photosynthetic energy conversion, Chem. Phys. Lett. **466**, 209 (2008).

[12] W. A. Johnson and K. E. Redding, Reconstitution of the heliobacterial photochemical reaction center and cytochrome c_{553} into a proteoliposome system, Photosynth. Res. **143**, 241 (2020).

[13] N. M. Ennist, Z. Zhao, S. E. Stayrook, B. M. Discher, P. L. Dutton, and C. C. Moser, De novo protein design of photochemical reaction centers, Nat. Commun. **13**, 4937 (2022).

[14] N. M. Ennist *et al.*, De novo design of proteins housing excitonically coupled chlorophyll special pairs, Nat. Chem. Biol. **20**, 906 (2024).

[15] S. Jurinovich, L. Viani, C. Curutchet, and B. Mennucci, Limits and potentials of quantum chemical methods in modelling photosynthetic antennae, Phys. Chem. Chem. Phys. **17**, 30783 (2015).

[16] C. Curutchet and B. Mennucci, Quantum chemical studies of light harvesting, Chem. Rev. **117**, 294 (2017).

[17] E. Cignoni, V. Slama, L. Cupellini, and B. Mennucci, The atomistic modeling of light-harvesting complexes from the physical models to the computational protocol, J. Chem. Phys. **156**, 120901 (2022).

[18] A. Dreuw and M. Head-Gordon, Failure of time-dependent density functional theory for long-range charge-transfer excited states: The zincbacteriochlorin-bacteriochlorin and bacteriochlorophyll-spheroidene complexes, J. Am. Chem. Soc. **126**, 4007 (2004).

[19] N. T. Maitra, Charge transfer in time-dependent density functional theory, J. Phys.: Condens. Matter **29**, 423001 (2017).

[20] I. Schelter *et al.*, Assessing density functional theory in real-time and real-space as a tool for studying bacteriochlorophylls and the light-harvesting complex 2, J. Chem. Phys. **151**, 134114 (2019).

[21] W. Kohn, Nobel lecture: Electronic structure of matter – Wave functions and density functionals, Rev. Mod. Phys. **71**, 1253 (1999).

[22] R. M. Dreizler and E. K. U. Gross, *Density functional theory* (Springer, Berlin, 1990).

[23] J. P. Perdew and S. Kurth, "Density functionals for non-relativistic Coulomb systems in the new century", in *A primer in density functional theory*, edited by C. Fiolhais, F. Nogueira, and M. Marques (Springer, Berlin, 2003), pp. 1–55.

[24] M. Marques, C. Ullrich, F. Nogueira, A. Rubio, K. Burke, and E. Gross, *Time-dependent density functional theory* (Springer, Berlin, 2006).

[25] L. Kronik and S. Kümmel, Piecewise linearity, freedom from self-interaction, and a Coulomb asymptotic potential: Three related yet inequivalent properties of the exact density functional, Phys. Chem. Chem. Phys. **22**, 16467 (2020).

[26] G. Onida, L. Reining, and A. Rubio, Electronic excitations: Density-functional versus many-body Green's-function approaches, Rev. Mod. Phys. **74**, 601 (2002).

[27] L. Kronik, T. Stein, S. Refaely-Abramson, and R. Baer, Excitation gaps of finite-sized systems from optimally tuned range-separated hybrid functionals, J. Chem. Theory Comput. **8**, 1515 (2012).

[28] J. Amesz, The heliobacteria, a new group of photosynthetic bacteria, J. Photochem. Photobiol., B **30**, 89 (1995).

[29] S. Neerken and J. Amesz, The antenna reaction center complex of heliobacteria: Composition, energy conversion and electron transfer, Biochim. Biophys. Acta **1507**, 278 (2001).

[30] H. Oh-oka, Type 1 reaction center of photosynthetic heliobacteria, Photochem. Photobiol. **83**, 177 (2007).

[31] M. Heinnickel and J. H. Golbeck, Heliobacterial photosynthesis, Photosynth. Res. **92**, 35 (2007).

[32] G. S. Orf, C. Gisriel, and K. E. Redding, Evolution of photosynthetic reaction centers: Insights from the structure of the heliobacterial reaction center, Photosynth. Res. **138**, 11 (2018).

[33] N. Taylor and I. Kassal, Why are photosynthetic reaction centres dimeric?, Chem. Sci. **10**, 9576 (2019).

[34] G. Tcherkez and N. Papon, Origin and evolution of photosystems: Lessons from green sulfur bacteria, ChemPhotoChem **5**, 418 (2021).

[35] C. Gisriel, I. Sarrou, B. Ferlez, J. H. Golbeck, K. E. Redding, and R. Fromme, Structure of a symmetric photosynthetic reaction center-photosystem, Science **357**, 1021 (2017).

[36] Y. Song *et al.*, Excitonic structure and charge separation in the heliobacterial reaction center probed by multispectral multidimensional spectroscopy, Nat. Commun. **12**, 2801 (2021).

[37] G. S. Orf and K. E. Redding, Perturbation of the primary acceptor chlorophyll site in the heliobacterial reaction center by coordinating amino acid substitution, Biochim. Biophys. Acta **1862**, 148324 (2021).

[38] D. Marx and J. Hutter, *Ab initio molecular dynamics: Basic theory and advances methods* (Cambridge University Press, 2009).

[39] N. Liguori, R. Croce, S. J. Marrink, and S. Thallmair, Molecular dynamics simulations in photosynthesis, Photosynth. Res. **144**, 273 (2020).

[40] T. Körzdörfer, J. S. Sears, C. Sutton, and J.-L. Brédas, Long-range corrected hybrid functionals for π-conjugated systems: Dependence of the range-separation parameter on conjugation length, J. Chem. Phys. **135**, 204107 (2011).

[41] A. Karolewski, L. Kronik, and S. Kümmel, Using optimally tuned range separated hybrid functionals in ground-state calculations: Consequences and caveats, J. Chem. Phys. **138**, 204115 (2013).

[42] R. Baer and D. Neuhauser, Density functional theory with correct long-range asymptotic behaviour, Phys. Rev. Lett. **94**, 043002 (2005).

[43] R. Baer, E. Livshits, and D. Neuhauser, Avoiding self-repulsion in density functional description of biased molecular junctions, Chem. Phys. **329**, 266 (2006).

[44] E. Livshits and R. Baer, A well-tempered density functional theory of electrons in molecules, Phys. Chem. Chem. Phys. **9**, 2932 (2007).

[45] A. V. Krukau, G. E. Scuseria, J. P. Perdew, and A. Savin, Hybrid functionals with local range separation, J. Chem. Phys. **129**, 124103 (2008).

[46] A. D. Becke, A new mixing of Hartree-Fock and local density-functional theories, J. Chem. Phys. **98**, 1372 (1993).

[47] M. Ernzerhof, J. P. Perdew, and K. Burke, Coupling-constant dependence of atomization energies, Int. J. Quantum Chem. **64**, 285 (1997).

[48] A. V. Arbuznikov and M. Kaupp, What can we learn from the adiabatic connection formalism about local hybrid functionals?, J. Chem. Phys. **128**, 214107 (2008).

[49] S. Kümmel and L. Kronik, Orbital-dependent density functionals: Theory and applications, Rev. Mod. Phys. **80**, 3 (2008).

[50] M. A. Rohrdanz and J. M. Herbert, Simultaneous benchmarking of ground- and excited-state properties with long-range-corrected density functional theory, J. Chem. Phys. **129**, 034107 (2008).

[51] T. Schmidt, E. Kraisler, A. Makmal, L. Kronik, and S. Kümmel, A self-interaction-free local hybrid functional: Accurate binding energies vis-à-vis accurate ionization potentials from kohn-sham eigenvalues, J. Chem. Phys. **140**, 18A510 (2014).

[52] S. Fürst, M. Haasler, R. Grotjahn, and M. Kaupp, Full mmplementation, optimization, and evaluation of a range-separated local hybrid functional with wide accuracy for ground and excited states, J. Chem. Theory Comput. **19**, 488 (2023).

[53] S. Fürst and M. Kaupp, Accurate ionization potentials, electron affinities, and band gaps from the ωLH22t range-separated local hybrid functional: No tuning required, J. Chem. Theory Comput. **19**, 3146 (2023).

[54] T. Aschebrock and S. Kümmel, Exploring local range separation: The role of spin scaling and one-electron self-interaction, J. Chem. Phys. **151**, 154108 (2019).

[55] S. Klawohn and H. Bahmann, Self-consistent implementation of hybrid functionals with local range separation, J. Chem. Theory Comput. **16**, 953 (2020).

[56] T. M. Maier, Y. Ikabata, and H. Nakai, Assessing locally range-separated hybrid functionals from a gradient expansion of the exchange energy density, J. Chem. Phys. **154**, 214101 (2021).

[57] K. Capelle, A bird's-eye view of density-functional theory, Braz. J. Phys. **36**, 1318 (2006).

[58] E. Engel and R. M. Dreizler, *Density functional theory* (Springer, Berlin, 2011).

[59] K. Burke, Perspective on density functional theory, J. Chem. Phys. **136**, 150901 (2012).

[60] A. M. Teale *et al.*, DFT exchange: Sharing perspectives on the workhorse of quantum chemistry and materials science, Phys. Chem. Chem. Phys. **24**, 28700 (2022).

[61] M. Bursch, J.-M. Mewes, A. Hansen, and S. Grimme, Best-practice DFT protocols for basic molecular computational chemistry, Angew. Chem. Int. Ed. **61**, e202205735 (2022).

[62] P. Hohenberg and W. Kohn, Inhomogeneous electron gas, Phys. Rev. **136**, B864 (1964).

[63] M. Levy, Universal variational functionals of electron densities, first-order density matrices, and natural spin-orbitals and solution of the v-representability problem, Proc. Natl. Acad. Sci. **76**, 6062 (1979).

[64] W. Kohn and L. J. Sham, Self-consistent equations including exchange and correlation effects, Phys. Rev. **140**, A1133 (1965).

[65] U. v. Barth and L. Hedin, A local exchange-correlation potential for the spin polarized case. I, J. Phys. C **5**, 1629 (1972).

[66] A. K. Rajagopal and J. Callaway, Inhomogeneous electron gas, Phys. Rev. B **7**, 1912 (1973).

[67] A. D. Becke, Density-functional exchange-energy approximation with correct asymptotic behavior, Phys. Rev. A **38**, 3098 (1988).

[68] C. Lee, W. Yang, and R. G. Parr, Development of the Colle-Salvetti correlation-energy formula into a functional of the electron density, Phys. Rev. B **37**, 785 (1988).

[69] A. D. Becke, Density-functional thermochemistry. III. The role of exact exchange, J. Chem. Phys. **98**, 5648 (1993).

[70] J. P. Perdew, K. Burke, and Y. Wang, Generalized gradient approximation for the exchange-correlation hole of a many-electron system, Phys. Rev. B **54**, 16533 (1996).

[71] J. P. Perdew, K. Burke, and M. Ernzerhof, Generalized gradient approximation made simple, Phys. Rev. Lett. **77**, 3865 (1996).

[72] J. Sun, A. Ruzsinszky, and J. P. Perdew, Strongly constrained and appropriately normed semilocal density functional, Phys. Rev. Lett. **115**, 036402 (2015).

[73] N. Mardirossian and M. Head-Gordon, Thirty years of density functional theory in computational chemistry: An overview and extensive assessment of 200 density functionals, Mol. Phys. **115**, 2315 (2017).

[74] K. R. Bryenton, A. A. Adeleke, S. G. Dale, and E. R. Johnson, Delocalization error: The greatest outstanding challenge in density-functional theory, WIREs Comput. Mol. Sci. **13**, e1631 (2022).

[75] C. Holzer and Y. J. Franzke, A local hybrid exchange functional approximation from first principles, J. Chem. Phys. **157**, 034108 (2022).

[76] M. Kaupp, A. Wodyński, A. V. Arbuznikov, S. Fürst, and C. J. Schattenberg, Toward the next generation of density functionals: Escaping the zero-sum game by using the exact-exchange energy density, Acc. Chem. Res. **57**, 1815 (2024).

[77] S. H. Vosko, L. Wilk, and M. Nusair, Accurate spin-dependent electron liquid correlation energies for local spin density calculations: A critical analysis, Can. J. Phys. **58**, 1200 (1980).

[78] J. P. Perdew and A. Zunger, Self-interaction correction to density-functional approximations for many-electron systems, Phys. Rev. B **23**, 5048 (1981).

[79] J. P. Perdew and Y. Wang, Accurate and simple analytic representation of the electron-gas correlation energy, Phys. Rev. B **45**, 13244 (1992).

[80] D. M. Ceperley and B. J. Alder, Ground state of the electron gas by a stochastic method, Phys. Rev. Lett. **45**, 566 (1980).

[81] K. Burke, J. P. Perdew, and M. Ernzerhof, Why the generalized gradient approximation works and how to go beyond it, Int. J. Quantum Chem. **61**, 287 (1997).

[82] K. Burke, J. P. Perdew, and M. Ernzerhof, Why semilocal functionals work: Accuracy of the on-top pair density and importance of system averaging, J. Chem. Phys. **109**, 3760 (1998).

[83] S.-K. Ma and K. A. Brueckner, Correlation energy of an electron gas with a slowly varying high density, Phys. Rev. **165**, 18 (1968).

[84] D. C. Langreth and J. P. Perdew, Theory of nonuniform electronic systems. I. Analysis of the gradient approximation and a generalization that works, Phys. Rev. B **21**, 5469 (1980).

[85] D. C. Langreth and M. J. Mehl, Beyond the local-density approximation in calculations of ground-state electronic properties, Phys. Rev. B **28**, 1809 (1983).

[86] J. P. Perdew, Accurate density functional for the energy: Real-space cutoff of the gradient expansion for the exchange hole, Phys. Rev. Lett. **55**, 1665 (1985).

[87] J. P. Perdew and W. Yue, Accurate and simple density functional for the electronic exchange energy: Generalized gradient approximation, Phys. Rev. B **33**, 8800 (1986).

[88] A. D. Becke, Hartree-Fock exchange energy of an inhomogeneous electron gas, Int. J. Quantum Chem. **23**, 1915 (1983).

[89] A. D. Becke, Density-functional thermochemistry. IV. A new dynamical correlation functional and implications for exact-exchange mixing, J. Chem. Phys. **104**, 1040 (1996).

[90] A. D. Becke, A new inhomogeneity parameter in density-functional theory, J. Chem. Phys. **109**, 2092 (1998).

[91] J. P. Perdew, S. Kurth, A. Zupan, and P. Blaha, Accurate density functional with correct formal properties: A step beyond the generalized gradient approximation, Phys. Rev. Lett. **82**, 2544 (1999).

[92] J. Tao, J. P. Perdew, V. N. Staroverov, and G. E. Scuseria, Climbing the density functional ladder: Nonempirical meta-generalized gradient approximation designed for molecules and solids, Phys. Rev. Lett. **91**, 146401 (2003).

[93] T. Aschebrock and S. Kümmel, Ultranonlocality and accurate band gaps from a meta-generalized gradient approximation, Phys. Rev. Res. **1**, 033082 (2019).

[94] T. Lebeda, T. Aschebrock, J. Sun, L. Leppert, and S. Kümmel, Right band gaps for the right reason at low computational cost with a meta-GGA, Phys. Rev. Materials **7**, 093803 (2023).

[95] T. Aschebrock, T. Lebeda, M. Brütting, R. Richter, I. Schelter, and S. Kümmel, Exact exchange-like electric response from a meta-generalized gradient approximation: A semilocal realization of ultranonlocality, J. Chem. Phys. **159**, 234107 (2023).

[96] T. Lebeda, T. Aschebrock, and S. Kümmel, Balancing the contributions to the gradient expansion: Accurate binding and band gaps with a nonempirical meta-GGA, Phys. Rev. Lett. **133**, 136402 (2024).

[97] I. N. Levine, *Quantum chemistry*, 5th ed. (Pearson, 2000).

[98] F. Jensen, *Introduction to computational chemistry*, 2nd ed. (Wiley, 2007).

[99] D. Golze, M. Dvorak, and P. Rinke, The GW compendium: A practical guide to theoretical photoemission spectroscopy, Front. Chem. **7**, 377 (2019).

[100] L. Hedin, New method for calculating the one-particle Green's function with application to the electron-gas problem, Phys. Rev. **139**, A796 (1965).

[101] J. P. Perdew, R. G. Parr, M. Levy, and J. L. Balduz, Density-functional theory for fractional particle number: Derivative discontinuities of the energy, Phys. Rev. Lett. **49**, 1691 (1982).

[102] W. Yang, Y. Zhang, and P. W. Ayers, Degenerate ground states and a fractional number of electrons in density and reduced density matrix functional theory, Phys. Rev. Lett. **84**, 5172 (2000).

[103] J. F. Janak, Proof that $\partial E/\partial n_i = \epsilon_i$ in density-functional theory, Phys. Rev. B **18**, 7165 (1978).

[104] J. P. Perdew and M. Levy, Comment on "Significance of the highest occupied Kohn-Sham eigenvalue", Phys. Rev. B **56**, 16021 (1997).

[105] M. Levy, J. P. Perdew, and V. Sahni, Exact differential equation for the density and ionization energy of a many-particle system, Phys. Rev. A **30**, 2745 (1984).

[106] C.-O. Almbladh and U. von Barth, Exact results for the charge and spin densities, exchange-correlation potentials, and density-functional eigenvalues, Phys. Rev. B **31**, 3231 (1985).

[107] D. P. Chong, O. V. Gritsenko, and E. J. Baerends, Interpretation of the Kohn-Sham orbital energies as approximate vertical ionization potentials, J. Chem. Phys. **116**, 1760 (2002).

[108] J. P. Perdew and M. Levy, Physical content of the exact Kohn-Sham orbital energies: Band gaps and derivative discontinuities, Phys. Rev. Lett. **51**, 1884 (1983).

[109] L. J. Sham and M. Schlüter, Density-functional theory of the energy gap, Phys. Rev. Lett. **51**, 1888 (1983).

[110] R. W. Godby, M. Schlüter, and L. J. Sham, Accurate exchange-correlation potential for silicon and its discontinuity on addition of an electron, Phys. Rev. Lett. **56**, 2415 (1986).

[111] M. J. Allen and D. J. Tozer, Eigenvalues, integer discontinuities and NMR shielding constants in Kohn-Sham theory, Mol. Phys. **100**, 433 (2002).

[112] E. Kraisler and L. Kronik, Piecewise linearity of approximate density functionals revisited: Implications for frontier orbital energies, Phys. Rev. Lett. **110**, 126403 (2013).

[113] E. Kraisler and L. Kronik, Fundamental gaps with approximate density functionals: The derivative discontinuity revealed from ensemble considerations, J. Chem. Phys. **140**, 18A540 (2014).

[114] E. Kraisler, T. Schmidt, S. Kümmel, and L. Kronik, Effect of ensemble generalization on the highest-occupied Kohn-Sham eigenvalue, J. Chem. Phys. **143**, 104105 (2015).

[115] A. Görling, Exchange-correlation potentials with proper discontinuities for physically meaningful Kohn-Sham eigenvalues and band structures, Phys. Rev. B **91**, 245120 (2015).

[116] A. M. Teale, F. D. Proft, and D. J. Tozer, Orbital energies and negative electron affinities from density functional theory: Insight from the integer discontinuity, J. Chem. Phys. **129**, 044110 (2008).

[117] D. J. Tozer, Effective homogeneity of the exchange-correlation energy functional, Phys. Rev. A **58**, 3524 (1998).

[118] T. Stein, J. Autschbach, N. Govind, L. Kronik, and R. Baer, Curvature and frontier orbital energies in density functional theory, J. Phys. Chem. Lett. **3**, 3740 (2012).

[119] Y. Zhang and W. Yang, A challenge for density functionals: Self-interaction error increases for systems with a noninteger number of electrons, J. Chem. Phys. **109**, 2604 (1998).

[120] P. Mori-Sánchez, A. J. Cohen, and W. Yang, Many-electron self-interaction error in approximate density functionals, J. Chem. Phys. **125**, 201102 (2006).

[121] A. Ruzsinszky, J. P. Perdew, G. I. Csonka, O. A. Vydrov, and G. E. Scuseria, Spurious fractional charge on dissociated atoms: Pervasive and resilient self-interaction error of common density functionals, J. Chem. Phys. **125**, 194112 (2006).

[122] A. Ruzsinszky, J. P. Perdew, G. I. Csonka, O. A. Vydrov, and G. E. Scuseria, Density functionals that are one- and two- are not always many-electron self-interaction-free, as shown for H_2^+, He_2^+, LiH^+, and Ne_2^+, J. Chem. Phys. **126**, 104102 (2007).

[123] A. J. Cohen, P. Mori-Sánchez, and W. Yang, Challenges for density functional theory, Chemical Reviews **112**, 289 (2012).

[124] A. J. Cohen, P. Mori-Sánchez, and W. Yang, Fractional charge perspective on the band gap in density-functional theory, Phys. Rev. B **77**, 115123 (2008).

[125] A. J. Cohen, P. Mori-Sánchez, and W. Yang, Insights into current limitations of density functional theory, Science **321**, 792 (2008).

[126] T. Schmidt and S. Kümmel, One- and many-electron self-interaction error in local and global hybrid functionals, Phys. Rev. B **93**, 165120 (2016).

[127] D. J. Tozer, The asymptotic exchange potential in Kohn-Sham theory, J. Chem. Phys. **112**, 3507 (2000).

[128] T. Schmidt, E. Kraisler, L. Kronik, and S. Kümmel, One-electron self-interaction and the asymptotics of the Kohn-Sham potential: An impaired relation, Phys. Chem. Chem. Phys. **16**, 14357 (2014).

[129] E. Kraisler, Asymptotic behavior of the exchange-correlation energy density and the Kohn-Sham potential in density functional theory: Exact results and strategy for approximations, Isr. J. Chem. **60**, 805 (2020).

[130] B. Y. Tong and L. J. Sham, Application of a self-consistent scheme including exchange and correlation effects to atoms, Phys. Rev. **144**, 1 (1966).

[131] O. Gunnarsson and B. I. Lundqvist, Exchange and correlation in atoms, molecules, and solids by the spin-density-functional formalism, Phys. Rev. B **13**, 4274 (1976).

[132] R. van Leeuwen and E. J. Baerends, Exchange-correlation potential with correct asymptotic behavior, Phys. Rev. A **49**, 2421 (1994).

[133] J. P. Perdew, Orbital functional for exchange and correlation: Self-interaction correction to the local density approximation, Chem. Phys. Lett. **64**, 127 (1979).

[134] A. D. Kaplan, M. Levy, and J. P. Perdew, The predictive power of exact constraints and appropriate norms in density functional theory, Annu. Rev. Phys. Chem. **74**, 193 (2023).

[135] D. Hofmann and S. Kümmel, Self-interaction correction in a real-time Kohn-Sham scheme: Access to difficult excitations in time-dependent density functional theory, J. Chem. Phys. **137**, 064117 (2012).

[136] A. Svane and O. Gunnarsson, Transition-metal oxides in the self-interaction-corrected density-functional formalism, Phys. Rev. Lett. **65**, 1148 (1990).

[137] A. Seidl, A. Görling, P. Vogl, J. A. Majewski, and M. Levy, Generalized Kohn-Sham schemes and the band-gap problem, Phys. Rev. B **53**, 3764 (1996).

[138] R. Garrick, A. Natan, T. Gould, and L. Kronik, Exact generalized Kohn-Sham theory for hybrid functionals, Phys. Rev. X **10**, 021040 (2020).

[139] C. Adamo and V. Barone, Toward reliable density functional methods without adjustable parameters: The PBE0 model, J. Chem. Phys. **110**, 6158 (1999).

[140] M. Ernzerhof and G. E. Scuseria, Assessment of the Perdew-Burke-Ernzerhof exchange-correlation functional, J. Chem. Phys. **110**, 5029 (1999).

[141] J. P. Perdew, M. Ernzerhof, and K. Burke, Rationale for mixing exact exchange with density functional approximations, J. Chem. Phys. **105**, 9982 (1996).

[142] R. Peverati and D. G. Truhlar, Quest for a universal density functional: The accuracy of density functionals across a broad spectrum of databases in chemistry and physics, Philos. Trans. R. Soc. A: Math. Phys. Eng. Sci. **372**, 20120476 (2014).

[143] P. J. Stephens, F. J. Devlin, C. F. Chabalowski, and M. J. Frisch, Ab initio calculation of vibrational absorption and circular dichroism spectra using density functional force fields, J. Phys. Chem. **98**, 11623 (1994).

[144] T. Leininger, H. Stoll, H.-J. Werner, and A. Savin, Combining long-range configuration interaction with short-range density functionals, Chem. Phys. Lett. **275**, 151 (1997).

[145] H. Iikura, T. Tsuneda, T. Yanai, and K. Hirao, A long-range correction scheme for generalized-gradient-approximation exchange functionals, J. Chem. Phys. **115**, 3540 (2001).

[146] A. Savin and H.-J. Flad, Density functionals for the Yukawa electron-electron interaction, Int. J. Quantum Chem. **56**, 327 (1995).

[147] J. Toulouse, F. Colonna, and A. Savin, Long-range – short-range separation of the electron-electron interaction in density-functional theory, Phys. Rev. A **70**, 062505 (2004).

[148] J. Toulouse, A. Savin, and H.-J. Flad, Short-range exchange-correlation energy of a uniform electron gas with modified electron–electron interaction, Int. J. Quantum Chem. **100**, 1047 (2004).

[149] T. Yanai, D. P. Tew, and N. C. Handy, A new hybrid exchange-correlation functional using the Coulomb-attenuating method (CAM-B3LYP), Chem. Phys. Lett. **393**, 51 (2004).

[150] A. Savin, Models and corrections: Range separation for electronic interaction – Lessons from density functional theory, J. Chem. Phys. **153**, 160901 (2020).

[151] F. Jensen, Atomic orbital basis sets, WIREs Comput. Mol. Sci. **3**, 273 (2012).

[152] S. Refaely-Abramson *et al.*, Quasiparticle spectra from a nonempirical optimally tuned range-separated hybrid density functional, Phys. Rev. Lett. **109**, 226405 (2012).

[153] J.-D. Chai and M. Head-Gordon, Systematic optimization of long-range corrected hybrid density functionals, J. Chem. Phys. **128**, 084106 (2008).

[154] M. A. Rohrdanz, K. M. Martins, and J. M. Herbert, A long-range-corrected density functional that performs well for both ground-state properties and time-dependent density functional theory excitation energies, including charge-transfer excited states, J. Chem. Phys. **130**, 054112 (2009).

[155] J. Heyd, G. E. Scuseria, and M. Ernzerhof, Hybrid functionals based on a screened Coulomb potential, J. Chem. Phys. **118**, 8207 (2003), Erratum: J. Chem. Phys. **124**, 219906 (2006).

[156] J. Heyd and G. E. Scuseria, Assessment and validation of a screened Coulomb hybrid density functional, J. Chem. Phys. **120**, 7274 (2004).

[157] O. A. Vydrov, J. Heyd, A. V. Krukau, and G. E. Scuseria, Importance of short-range versus long-range Hartree-Fock exchange for the performance of hybrid density functionals, J. Chem. Phys. **125**, 074106 (2006).

[158] R. Garrick, L. Kronik, and T. Gould, Adiabatic connection for range-separated hybrid functionals, Advanced Theory and Simulations **5**, 2100550 (2022).

[159] O. A. Vydrov and G. E. Scuseria, Assessment of a long-range corrected hybrid functional, J. Chem. Phys. **125**, 234109 (2006).

[160] J. Toulouse, F. Colonna, and A. Savin, Short-range exchange and correlation energy density functionals: Beyond the local-density approximation, J. Chem. Phys. **122**, 014110 (2005).

[161] T. M. Henderson, B. G. Janesko, and G. E. Scuseria, Generalized gradient approximation model exchange holes for range-separated hybrids, J. Chem. Phys. **128**, 194105 (2008).

[162] E. Weintraub, T. M. Henderson, and G. E. Scuseria, Long-range-corrected hybrids based on a new model exchange hole, J. Chem. Theory Comput. **5**, 754 (2009).

[163] A. D. Becke, Density-functional theory vs density-functional fits, J. Chem. Phys. **156**, 214101 (2022).

[164] S. Schwalbe, K. Trepte, and S. Lehtola, How good are recent density functionals for ground and excited states of one-electron systems?, J. Chem. Phys. **157**, 174113 (2022).

[165] R. Pederson and K. Burke, The difference between molecules and materials: Reassessing the role of exact conditions in density functional theory, J. Chem. Phys. **159**, 214113 (2023).

[166] T. Gould, B. Chan, S. G. Dale, and S. Vuckovic, Identifying and embedding transferability in data-driven representations of chemical space, Chem. Sci. **15**, 11122 (2024).

[167] T. Stein, L. Kronik, and R. Baer, Reliable prediction of charge-transfer excitations in molecular complexes using time-dependent density functional theory, J. Am. Chem. Soc. **131**, 2818 (2009).

[168] N. Kuritz, T. Stein, R. Baer, and L. Kronik, Charge-transfer-like $\pi \to \pi^*$ excitations in time-dependent density functional theory: A conundrum and its solution, J. Chem. Theory Comput. **7**, 2408 (2011).

[169] T. Stein, L. Kronik, and R. Baer, Prediction of charge-transfer excitations in coumarin-based dyes using a range-separated functional tuned from first principles, J. Chem. Phys. **131**, 244119 (2009).

[170] S. Refaely-Abramson, R. Baer, and L. Kronik, Fundamental and excitation gaps in molecules of relevance for organic photovoltaics from an optimally tuned range-separated hybrid functional, Phys. Rev. B **84**, 075144 (2011).

[171] T. Stein, H. Eisenberg, L. Kronik, and R. Baer, Fundamental gaps in finite systems from eigenvalues of a generalized Kohn-Sham method, Phys. Rev. Lett. **105**, 266802 (2010).

[172] L. Gallandi, N. Marom, P. Rinke, and T. Körzdörfer, Accurate ionization potentials and electron affinities of acceptor molecules II: Non-empirically tuned long-range corrected hybrid functionals, J. Chem. Theory Comput. **12**, 605 (2016).

[173] A. Dreuw and M. Head-Gordon, Single-reference ab initio methods for the calculation of excited states of large molecules, Chem. Rev. **105**, 4009 (2005).

[174] C. Adamo and D. Jacquemin, The calculations of excited-state properties with time-dependent density functional theory, Chem. Soc. Rev. **42**, 845 (2013).

[175] E. Runge and E. K. U. Gross, Density-functional theory for time-dependent systems, Phys. Rev. Lett. **52**, 997 (1984).

[176] M. E. Casida, "Time-dependent density functional response theory for molecules", in *Recent advances in density functional methods*, Vol. 1, edited by D. P. Chong, Recent advances in computational chemistry (World Scientific, Singapore, 1995), pp. 155–192.

[177] M. E. Casida, Time-dependent density functional response theory of molecular systems: Theory, computational methods, and functionals, Theoretical and Computational Chemistry **4**, 391 (1996).

[178] M. Petersilka, U. J. Gossmann, and E. K. U. Gross, Excitation energies from time-dependent density-functional theory, Phys. Rev. Lett. **76**, 1212 (1996).

[179] T. Grabo, M. Petersilka, and E. Gross, Molecular excitation energies from time-dependent density functional theory, J. Mol. Struct. THEOCHEM **501–502**, 353 (2000).

[180] R. Baer and L. Kronik, Time-dependent generalized Kohn-Sham theory, Eur. Phys. J. B **91**, 170 (2018).

[181] N. T. Maitra, Undoing static correlation: Long-range charge transfer in time-dependent density-functional theory, J. Chem. Phys. **122**, 234104 (2005).

[182] A. Dreuw, J. L. Weisman, and M. Head-Gordon, Long-range charge-transfer excited states in time-dependent density functional theory require non-local exchange, J. Chem. Phys. **119**, 2943 (2003).

[183] D. J. Tozer, Relationship between long-range charge-transfer excitation energy error and integer discontinuity in Kohn-Sham theory, J. Chem. Phys. **119**, 12697 (2003).

[184] S. Kümmel, Charge-transfer excitations: A challenge for time-dependent density functional theory that has been met, Adv. Energy Mater. **7**, 1700440 (2017).

[185] J. Autschbach, Charge-transfer excitations and time-dependent density functional theory: Problems and some proposed solutions, ChemPhysChem **10**, 1757 (2009).

[186] O. Gritsenko and E. J. Baerends, Asymptotic correction of the exchange-correlation kernel of time-dependent density functional theory for long-range charge-transfer excitations, J. Chem. Phys. **121**, 655 (2004).

[187] M. Thiele and S. Kümmel, Frequency dependence of the exact exchange-correlation kernel of time-dependent density-functional theory, Phys. Rev. Lett. **112**, 083001 (2014).

[188] G. Vignale and W. Kohn, Current-dependent exchange-correlation potential for dynamical linear response theory, Phys. Rev. Lett. **77**, 2037 (1996).

[189] L. Lacombe and N. T. Maitra, Non-adiabatic approximations in time-dependent density functional theory: Progress and prospects, npj Comput. Mater. **9**, 124 (2023).

[190] F. Furche and R. Ahlrichs, Adiabatic time-dependent density functional methods for excited state properties, J. Chem. Phys. **117**, 7433 (2002).

[191] A. Karolewski, T. Stein, R. Baer, and S. Kümmel, Communication: Tailoring the optical gap in light-harvesting molecules, J. Chem. Phys. **134**, 151101 (2011).

[192] T. Körzdörfer and J.-L. Brédas, Organic electronic materials: Recent advances in the DFT description of the ground and excited states using tuned range-separated hybrid functionals, Acc. Chem. Res. **47**, 3284 (2014).

[193] A. Karolewski, A. Neubig, M. Thelakkat, and S. Kümmel, Optical absorption in donor-acceptor polymers – Alternating vs. random, Phys. Chem. Chem. Phys. **15**, 20016 (2013).

[194] W. Hieringer and A. Görling, Failure of time-dependent density functional methods for excitations in spatially separated systems, Chem. Phys. Lett. **419**, 557 (2006).

[195] T. Kondo, S. Itoh, M. Matsuoka, C. Azai, and H. Oh-oka, Menaquinone as the secondary electron acceptor in the type I homodimeric photosynthetic reaction center of *Heliobacterium modesticaldum*, J. Phys. Chem. B **119**, 8480 (2015).

[196] T. S. Kashey, D. D. Luu, J. C. Cowgill, P. L. Baker, and K. E. Redding, Light-driven quinone reduction in heliobacterial membranes, Photosynth. Res. **138**, 1 (2018).

[197] T. Kondo, M. Matsuoka, C. Azai, M. Kobayashi, S. Itoh, and H. Ohoka, Light-induced electron spin-polarized (ESP) EPR signal of the $P800^{+}$ menaquinone^{-} radical pair state in oriented membranes of *Heliobacterium modesticaldum*: Role/location of menaquinone in the homodimeric type I reaction center, J. Phys. Chem. B **122**, 2536 (2018).

[198] J. Amesz and S. Neerken, Excitation energy trapping in anoxygenic photosynthetic bacteria, Photosynth. Res. **73**, 73 (2002).

[199] T. C. Stuart and R. van Grondelle, Multipulse spectroscopy on the wild-type and YM210W bacterial reaction centre uncovers a new intermediate state in the special pair excited state, Chem. Phys. Lett. **474**, 352 (2009).

[200] M. Gorka, P. Charles, V. Kalendra, A. Baldansuren, K. V. Lakshmi, and J. H. Golbeck, A dimeric chlorophyll electron acceptor differentiates type I from type II photosynthetic reaction centers, iScience **24**, 102719 (2021).

[201] H. Tamura, K. Saito, and H. Ishikita, Long-range electron tunneling from the primary to secondary quinones in photosystem II enhanced by hydrogen bonds with a nonheme Fe complex, J. Phys. Chem. B **125**, 13460 (2021), Erratum: J. Phys. Chem. B **126**, 996 (2022).

[202] S.-J. Yang, E. A. Arsenault, K. Orcutt, M. Iwai, Y. Yoneda, and G. R. Fleming, From antenna to reaction center: Pathways of ultrafast energy and charge transfer in photosystem II, Proc. Natl. Acad. Sci. **119**, e2208033119 (2022).

[203] W. Zinth and J. Wachtveitl, The first picoseconds in bacterial photosynthesis? – Ultrafast electron transfer for the efficient conversion of light energy, ChemPhysChem **6**, 871 (2005).

[204] A. Niedringhaus *et al.*, Primary processes in the bacterial reaction center probed by two-dimensional electronic spectroscopy, Proc. Natl. Acad. Sci. **115**, 3563 (2018).

[205] P. N. Dominguez *et al.*, Primary reactions in photosynthetic reaction centers of *Rhodobacter sphaeroides* – Time constants of the initial electron transfer, Chem. Phys. Lett. **601**, 103 (2014).

[206] M. E. V. Brederode, M. R. Jones, F. V. Mourik, I. H. M. V. Stokkum, and R. V. Grondelle, A new pathway for transmembrane electron transfer in photosynthetic reaction centers of *Rhodobacter sphaeroides* not involving the excited special pair, Biochemistry **36**, 6855 (1997).

[207] M. E. van Brederode and R. van Grondelle, New and unexpected routes for ultrafast electron transfer in photosynthetic reaction centers, FEBS Letters **455**, 1 (1999).

[208] M. E. van Brederode, F. van Mourik, I. H. M. van Stokkum, M. R. Jones, and R. van Grondelle, Multiple pathways for ultrafast transduction of light energy in the photosynthetic reaction center of *Rhodobacter sphaeroides*, Proc. Natl. Acad. Sci. **96**, 2054 (1999).

[209] E. Romero, I. H. M. van Stokkum, V. I. Novoderezhkin, J. P. Dekker, and R. van Grondelle, Two different charge separation pathways in photosystem II, Biochemistry **49**, 4300 (2010).

[210] V. I. Prokhorenko and A. R. Holzwarth, Primary processes and structure of the photosystem II reaction center: A photon echo study, J. Phys. Chem. B **104**, 11563 (2000).

[211] J. P. Dekker and R. V. Grondelle, Primary charge separation in Photosystem II, Photosynth. Res. **63**, 195 (2000).

[212] F. Müh, M. Plöckinger, and T. Renger, Electrostatic asymmetry in the reaction center of photosystem II, J. Phys. Chem. Lett. **8**, 850 (2017).

[213] A. Sirohiwal, F. Neese, and D. A. Pantazis, Protein matrix control of reaction center excitation in photosystem II, J. Am. Chem. Soc. **142**, 18174 (2020).

[214] A. Sirohiwal and D. A. Pantazis, The electronic origin of far-red-light-driven oxygenic photosynthesis, Angew. Chem. Int. Ed. **61**, e202200356 (2022).

[215] Y. Yoneda, E. A. Arsenault, S.-J. Yang, K. Orcutt, M. Iwai, and G. R. Fleming, The initial charge separation step in oxygenic photosynthesis, Nat. Commun. **13**, 2275 (2022).

[216] H. H. Nguyen *et al.*, Charge separation in the photosystem II reaction center resolved by multispectral two-dimensional electronic spectroscopy, Sci. Adv. **9**, eade7190 (2023).

[217] M. Capone, A. Sirohiwal, M. Aschi, D. A. Pantazis, and I. Daidone, Alternative fast and slow primary charge-separation pathways in photosystem II, Angew. Chem. Int. Ed. **62**, e202216276 (2023).

[218] M. G. Müller, J. Niklas, W. Lubitz, and A. R. Holzwarth, Ultrafast transient absorption studies on photosystem I reaction centers from *Chlamydomonas reinhardtii*. 1. A new interpretation of the energy trapping and early electron transfer steps in photosystem I, Biophys. J. **85**, 3899 (2003).

[219] M. G. Müller, C. Slavov, R. Luthra, K. E. Redding, and A. R. Holzwarth, Independent initiation of primary electron transfer in the two branches of the photosystem I reaction center, Proc. Natl. Acad. Sci. **107**, 4123 (2010).

[220] K. Mitsuhashi, H. Tamura, K. Saito, and H. Ishikita, Nature of asymmetric electron transfer in the symmetric pathways of photosystem I, J. Phys. Chem. B **125**, 2879 (2021).

[221] T. Kanda and H. Ishikita, Energetic diversity in the electron-transfer pathways of type I photosynthetic reaction centers, Biochemistry **62**, 934 (2023).

[222] J.-H. Chen *et al.*, Architecture of the photosynthetic complex from a green sulfur bacterium, Science **370**, eabb6350 (2020).

[223] H. Gest and J. L. Favinger, *Heliobacterium chlorum*, an anoxygenic brownish-green photosynthetic bacterium containing a new form of bacteriochlorophyll, Arch. Microbiol. **136**, 11 (1983).

[224] L. K. Kimble, L. Mandelco, C. R. Woese, and M. T. Madigan, *Heliobacterium modesticaldum*, sp. nov., a thermophilic heliobacterium of hot springs and volcanic soils, Arch. Microbiol. **163**, 259 (1995).

[225] E. J. van de Meent, M. Kobayashi, C. Erkelens, P. A. van Veelen, J. Amesz, and T. Watanabe, Identification of 8^1-hydroxychlorophyll *a* as a functional reaction center pigment in heliobacteria, Biochim. Biophys. Acta **1058**, 356 (1991).

[226] M. Kobayashi, E. J. van de Meent, C. Erkelens, J. Amesz, I. Ikegami, and T. Watanabe, Bacteriochlorophyll *g* epimer as a possible reaction center component of heliobacteria, Biochim. Biophys. Acta **1057**, 89 (1991).

[227] A. Chauvet *et al.*, Temporal and spectral characterization of the photosynthetic reaction center from *Heliobacterium modesticaldum*, Photosynth. Res. **116**, 1 (2013).

[228] T. Kondo *et al.*, Cryogenic single-molecule spectroscopy of the primary electron accceptor in the photosynthetic reaction center, J. Phys. Chem. Lett. **11**, 3980 (2020).

[229] M. Gouterman, Spectra of porphyrins, J. Mol. Spectrosc. **6**, 138 (1961).

[230] M. Gouterman, G. H. Wagnière, and L. C. Snyder, Spectra of porphyrins, J. Mol. Spectrosc. **11**, 108 (1963).

[231] D. Sundholm, Comparison of the electronic excitation spectra of chlorophyll *a* and pheophytin *a* calculated at density functional theory level, Chem. Phys. Lett. **317**, 545 (2000).

[232] F. A. M. Kleinherenbrink, I. Ikegami, A. Hiraishi, S. C. M. Otte, and J. Amesz, Electron transfer in menaquinone-depleted membranes of *heliobacterium chlorum*, Biochim. Biophys. Acta **1142**, 69 (1993).

[233] S. Lin, H. C. Chiou, F. A. Kleinherenbrink, and R. E. Blankenship, Time-resolved spectroscopy of energy and electron transfer processes in the photosynthetic bacterium *heliobacillus mobilis*, Biophys. J. **66**, 437 (1994).

[234] S. Neerken, T. J. Aartsma, and J. Amesz, Pathways of energy transformation in antenna reaction center complexes of *Heliobacillus mobilis*, Biochemistry **39**, 3297 (2000).

[235] I. Sarrou *et al.*, Purification of the photosynthetic reaction center from *Heliobacterium modesticaldum*, Photosynth. Res. **111**, 291 (2012).

[236] B. Ferlez *et al.*, Thermodynamics of the electron acceptors in *Heliobacterium modesticaldum*: An example of an early homodimeric type I photosynthetic reaction center, Biochemistry **55**, 2358 (2016).

[237] R. Kojima *et al.*, Energy transfer and primary charge separation upon selective femtosecond excitation at 810 nm in the reaction center complex from *heliobacterium modesticaldum*, J. Photochem. Photobiol., A **401**, 112758 (2020).

[238] G. S. Orf, C. J. Gisriel, J. Granstrom, P. L. Baker, and K. E. Redding, The PshX subunit of the photochemical reaction center from *heliobacterium modesticaldum* acts as a low-energy antenna, Photosynth. Res. **151**, 11 (2021).

[239] T. Kondo *et al.*, Energy transfer fluctuation observed by single-molecule spectroscopy of red-shifted bacteriochlorophyll in the homodimeric photosynthetic reaction center, J. Chem. Phys. **156**, 105102 (2022).

[240] A. Kimura and S. Itoh, Theoretical model of exciton states and ultrafast energy transfer in heliobacterial type I homodimeric reaction center, J. Phys. Chem. B **122**, 11852 (2018).

[241] H. Kitoh-Nishioka, Y. Shigeta, S. Itoh, and A. Kimura, Excitonic coupling on a heliobacterial symmetrical type-I reaction center: Comparison with photosystem I, J. Phys. Chem. B **124**, 389 (2020).

[242] A. Kimura, H. Kitoh-Nishioka, Y. Shigeta, and S. Itoh, Comparison between the light-harvesting mechanisms of type-I photosynthetic reaction centers of heliobacteria and photosystem I: Pigment site energy distribution and exciton state, J. Phys. Chem. B **125**, 3727 (2021).

[243] S. J. Jang and B. Mennucci, Delocalized excitons in natural light-harvesting complexes, Rev. Mod. Phys. **90**, 035003 (2018).

[244] B. Mennucci, Polarizable continuum model, WIREs Comput. Mol. Sci. **2**, 386 (2012).

[245] B. Mennucci and S. Corni, Multiscale modelling of photoinduced processes in composite systems, Nat. Rev. Chem. **3**, 315 (2019).

[246] M. E.-A. Madjet, F. Müh, and T. Renger, Deciphering the influence of short-range electronic couplings on optical properties of molecular dimers: Application to "Special Pairs" in photosynthesis, J. Phys. Chem. B **113**, 12603 (2009).

[247] C. König and J. Neugebauer, First-principles calculation of electronic spectra of light-harvesting complex II, Phys. Chem. Chem. Phys. **13**, 10475 (2011).

[248] H. Aksu, A. Schubert, E. Geva, and B. D. Dunietz, Explaining spectral asymmetries and excitonic characters of the core pigment pairs in the bacterial reaction center using a screened range-separated hybrid functional, J. Phys. Chem. B **123**, 8970 (2019).

[249] H. Aksu, A. Schubert, S. Bhandari, A. Yamada, E. Geva, and B. D. Dunietz, On the role of the special pair in photosystems as a charge transfer rectifier, J. Phys. Chem. B **124**, 1987 (2020).

[250] A. Kimura *et al.*, Theoretical model of the far-red-light-adapted photosystem I reaction center of cyanobacterium *Acaryochloris marina* using chlorophyll *d* and the effect of chlorophyll exchange, J. Phys. Chem. B **126**, 4009 (2022).

[251] A. Sirohiwal and D. A. Pantazis, Reaction center excitation in photosystem II: From multiscale modeling to functional principles, Acc. Chem. Res. **56**, 2921 (2023).

[252] A. Kimura, H. Kitoh-Nishioka, T. Kondo, H. Oh-oka, S. Itoh, and C. Azai, Experimental and theoretical mutation of exciton states on the smallest type-I photosynthetic reaction center complex of a green sulfur bacterium *chlorobaclum tepidum*, J. Phys. Chem. B **128**, 731 (2024).

[253] J. Kehrer, R. Richter, J. M. Foerster, I. Schelter, and S. Kümmel, Self-interaction correction, electrostatic, and structural influences on time-dependent density functional theory excitations of bacteriochlorophylls from the light-harvesting complex 2, J. Chem. Phys. **153**, 144114 (2020).

[254] M. Higashi, T. Kosugi, S. Hayashi, and S. Saito, Theoretical study on excited states of bacteriochlorophyll *a* in solutions with density functional assessment, J. Phys. Chem. B **118**, 10906 (2014).

[255] T. J. Frankcombe, Explicit calculation of the excited electronic states of the photosystem II reaction centre, Phys. Chem. Chem. Phys. **17**, 3295 (2015).

[256] B. M. Bold *et al.*, Benchmark and performance of long-range corrected time-dependent density functional tight binding (LC-TD-DFTB) on rhodopsins and light-harvesting complexes, Phys. Chem. Chem. Phys. **22**, 10500 (2020).

[257] M. A. Kavanagh, J. K. G. Karlsson, J. D. Colburn, L. M. C. Barter, and I. R. Gould, A TDDFT investigation of the photosystem II reaction center: Insights into the precursors to charge separation, Proc. Natl. Acad. Sci. **117**, 19705 (2020).

[258] S. Volpert *et al.*, Delocalized electronic excitations and their role in directional charge transfer in the reaction center of *Rhodobacter sphaeroides*, J. Chem. Phys. **158**, 195102 (2023).

[259] Z. Hashemi and L. Leppert, Assessment of the *ab initio* Bethe-Salpeter equation approach for the low-lying excitation energies of bacteriochlorophylls and chlorophylls, J. Phys. Chem. A **125**, 2163 (2021).

[260] A. Förster and L. Visscher, Quasiparticle self-consistent GW-Bethe-Salpeter equation calculations for large chromophoric systems, J. Chem. Theory Comput. **18**, 6779 (2022).

[261] Z. Hashemi, M. Knodt, M. R. G. Marques, and L. Leppert, Mapping charge-transfer excitations in bacteriochlorophyll dimers from first principles, Electron. Struct. **5**, 024006 (2023).

[262] C. A. Rozzi *et al.*, Quantum coherence controls the charge separation in a prototypical artificial light-harvesting system, Nat. Commun. **4**, 1602 (2013).

[263] F. Ma, E. Romero, M. R. Jones, V. I. Novoderezhkin, and R. van Grondelle, Both electronic and vibrational coherences are involved in primary electron transfer in bacterial reaction center, Nat. Commun. **10**, 933 (2019).

[264] A. Dreuw, P. H. P. Harbach, J. M. Mewes, and M. Wormit, Quantum chemical excited state calculations on pigment-protein complexes require thorough geometry re-optimization of experimental crystal structures, Theor. Chem. Acc. **125**, 419 (2010).

[265] A. Sirohiwal, F. Neese, and D. A. Pantazis, How can we predict accurate electrochromic shifts for biochromophores? A case study on the photosynthetic reaction center, J. Chem. Theory Comput. **17**, 1858 (2021).

[266] L. Cupellini *et al.*, An ab initio description of the excitonic properties of LH2 and their temperature dependence, J. Phys. Chem. B **120**, 11348 (2016).

[267] S. Maity *et al.*, DFTB/MM molecular dynamics simulations of the FMO light-harvesting complex, J. Phys. Chem. Lett. **11**, 8660 (2020).

[268] T. Renger and F. Müh, Understanding photosynthetic light-harvesting: A bottom up theoretical approach, Phys. Chem. Chem. Phys. **15**, 3348 (2013).

[269] A. M. Rosnik and C. Curutchet, Theoretical characterization of the spectral density of the water-soluble chlorophyll-binding protein from combined quantum mechanics/molecular mechanics molecular dynamics simulations, J. Chem. Theory Comput. **11**, 5826 (2015).

[270] S. Maity and U. Kleinekathöfer, Recent progress in atomistic modeling of light-harvesting complexes: A mini review, Photosynth. Res. **156**, 147 (2022).

[271] S. M. Blau, D. I. G. Bennett, C. Kreisbeck, G. D. Scholes, and A. Aspuru-Guzik, Local protein solvation drives direct down-conversion in phycobiliprotein PC645 via incoherent vibronic transport, Proc. Natl. Acad. Sci. **115**, E3342 (2018).

[272] T. J. Eisenmayer, H. J. de Groot, E. van de Wetering, J. Neugebauer, and F. Buda, Mechanism and reaction coordinate of directional charge separation in bacterial reaction centers, J. Phys. Chem. Lett. **3**, 694 (2012).

[273] T. J. Eisenmayer, J. A. Lasave, A. Monti, H. J. M. de Groot, and F. Buda, Proton displacements coupled to primary electron transfer in the *rhodobacter sphaeroides* reaction center, J. Phys. Chem. B **117**, 11162 (2013).

[274] Y. Shao *et al.*, Advances in molecular quantum chemistry contained in the Q-Chem 4 program package, Mol. Phys. **113**, 184 (2015), `https://www.q-chem.com`.

[275] R. L. Martin, Natural transition orbitals, J. Chem. Phys. **118**, 4775 (2003).

[276] S. Grimme, J. Antony, S. Ehrlich, and H. Krieg, A consistent and accurate ab initio parametrization of density functional dispersion correction (DFT-D) for the 94 elements H-Pu, J. Chem. Phys. **132**, 154104 (2010).

[277] S. Grimme, Density functional theory with London dispersion corrections, WIREs Comput. Mol. Sci. **1**, 211 (2011).

[278] Y. J. Franzke *et al.*, TURBOMOLE: Today and tomorrow, J. Chem. Theory Comput. **19**, 6859 (2023).

[279] D. C. Langreth and J. P. Perdew, The exchange-correlation energy of a metallic surface, Solid State Commun. **17**, 1425 (1975).

[280] M. Levy, N. H. March, and N. C. Handy, On the adiabatic connection method, and scaling of electron-electron interactions in the Thomas-Fermi limit, J. Chem. Phys. **104**, 1989 (1996).

[281] M. Ernzerhof, Construction of the adiabatic connection, Chem. Phys. Lett. **263**, 499 (1996).

[282] K. Burke, M. Ernzerhof, and J. P. Perdew, The adiabatic connection method: A non-empirical hybrid, Chem. Phys. Lett. **265**, 115 (1997).

[283] F. G. Cruz, K.-C. Lam, and K. Burke, Exchange-correlation energy density from virial theorem, J. Phys. Chem. A **102**, 4911 (1998).

[284] M. Levy and J. P. Perdew, Hellman-Feynman, virial, and scaling requisites for the exact universal density functionals. Shape of the correlation potential and diamagnetic susceptibility for atoms, Phys. Rev. A **32**, 2010 (1985).

[285] A. Görling and M. Levy, Correlation-energy functional and its high-density limit obtained from a coupling-constant perturbation expansion, Phys. Rev. B **47**, 13105 (1993).

[286] W. Yang, Generalized adiabatic connection in density functional theory, J. Chem. Phys. **109**, 10107 (1998).

[287] J. P. Perdew *et al.*, Exchange and correlation in open systems of fluctuating electron number, Phys. Rev. A **76**, 040501 (2007).

[288] J. P. Perdew, V. N. Staroverov, J. Tao, and G. E. Scuseria, Density functional with full exact exchange, balanced nonlocality of correlation, and constraint satisfaction, Phys. Rev. A **78**, 052513 (2008).

[289] K. Molawi, A. J. Cohen, and N. C. Handy, Left-right and dynamic correlation, Int. J. Quantum Chem. **89**, 86 (2002).

[290] R. Neumann, R. H. Nobes, and N. C. Handy, Exchange functionals and potentials, Mol. Phys. **87**, 1 (1996).

[291] D. Cremer, Density functional theory: Coverage of dynamic and non-dynamic electron correlation effects, Mol. Phys. **99**, 1899 (2001).

[292] A. Savin, Is size-consistency possible with density functional approximations?, Chem. Phys. **356**, 91 (2009).

[293] G. L. Oliver and J. P. Perdew, Spin-density gradient expansion for the kinetic energy, Phys. Rev. A **20**, 397 (1979).

[294] P. S. Svendsen and U. von Barth, Gradient expansion of the exchange energy from second-order density response theory, Phys. Rev. B **54**, 17402 (1996).

[295] H. Bahmann, A. Rodenberg, A. V. Arbuznikov, and M. Kaupp, A thermochemically competitive local hybrid functional without gradient corrections, J. Chem. Phys. **126**, 011103 (2007).

[296] M. Levy, Density-functional exchange correlation through coordinate scaling in adiabatic connection and correlation hole, Phys. Rev. A **43**, 4637 (1991).

[297] A. D. Becke, Local exchange-correlation approximations and first-row molecular dissociation energies, Int. J. Quantum Chem. **27**, 585 (1985).

[298] J. Toulouse, A. Savin, and C. Adamo, Validation and assessment of an accurate approach to the correlation problem in density functional theory: the kriger-chen-iafrate-savin model, J. Chem. Phys. **117**, 10465 (2002).

[299] J. P. Perdew, J. Tao, V. N. Staroverov, and G. E. Scuseria, Meta-generalized gradient approximation: Explanation of a realistic nonempirical density functional, J. Chem. Phys. **120**, 6898 (2004).

[300] A. V. Arbuznikov, H. Bahmann, and M. Kaupp, Local hybrid functionals with an explicit dependence on spin polarization, J. Phys. Chem. A **113**, 11898 (2009).

[301] A. V. Arbuznikov and M. Kaupp, Importance of the correlation contribution for local hybrid functionals: Range separation and self-interaction corrections, J. Chem. Phys. **136**, 014111 (2012).

[302] J. Sun *et al.*, Density functionals that recognize covalent, metallic, and weak bonds, Phys. Rev. Lett. **111**, 106401 (2013).

[303] P. Mori-Sánchez, A. J. Cohen, and W. Yang, Self-interaction-free exchange-correlation functional for thermochemistry and kinetics, J. Chem. Phys. **124**, 091102 (2006).

[304] A. J. Cohen, P. Mori-Sánchez, and W. Yang, Development of exchange-correlation functionals with minimal many-electron self-interaction error, J. Chem. Phys. **126**, 191109 (2007).

[305] T. M. Maier, A. V. Arbuznikov, and M. Kaupp, Local hybrid functionals: Theory, implementation, and performance of an emerging new tool in quantum chemistry and beyond, WIREs Comput. Mol. Sci. **9**, e1378 (2019).

[306] J. Tao, V. N. Staroverov, G. E. Scuseria, and J. P. Perdew, Exact-exchange energy density in the gauge of a semilocal density-functional approximation, Phys. Rev. A **77**, 012509 (2008).

[307] A. V. Arbuznikov and M. Kaupp, Towards improved local hybrid functionals by calibration of exchange-energy densities, J. Chem. Phys. **141**, 204101 (2014).

[308] T. M. Maier, M. Haasler, A. V. Arbuznikov, and M. Kaupp, New approaches for the calibration of exchange-energy densities in local hybrid functionals, Phys. Chem. Chem. Phys. **18**, 21133 (2016).

[309] M. Haasler, T. M. Maier, R. Grotjahn, S. Gückel, A. V. Arbuznikov, and M. Kaupp, A local hybrid functional with wide applicability and good balance between (de)localization and left-right correlation, J. Chem. Theory Comput. **16**, 5645 (2020).

[310] A. V. Arbuznikov, A. Wodyński, and M. Kaupp, Suppressing the gauge problem in local hybrid functionals without a calibration function: The choice of local mixing function, J. Chem. Phys. **161**, 164104 (2024).

[311] A. V. Arbuznikov, M. Kaupp, and H. Bahmann, From local hybrid functionals to "localized local hybrid" potentials: Formalism and thermochemical tests, J. Chem. Phys. **124**, 204102 (2006).

[312] H. Bahmann and M. Kaupp, Efficient self-consistent implementation of local hybrid functionals, J. Chem. Theory Comput. **11**, 1540 (2015).

[313] T. M. Maier, H. Bahmann, and M. Kaupp, Efficient semi-numerical implementation of global and local hybrid functionals for time-dependent density functional theory, J. Chem. Theory Comput. **11**, 4226 (2015).

[314] S. Klawohn, H. Bahmann, and M. Kaupp, Implementation of molecular gradients for local hybrid density functionals using seminumerical integration techniques, J. Chem. Theory Comput. **12**, 4254 (2016).

[315] F. Neese, F. Wennmohs, A. Hansen, and U. Becker, Efficient, approximate and parallel Hartree-Fock and hybrid DFT calculations. A 'chain-of-spheres' algorithm for the Hartree-Fock exchange, Chem. Phys. **356**, 98 (2009).

[316] P. Plessow and F. Weigend, Seminumerical calculation of the Hartree-Fock exchange matrix: Application to two-component procedures and efficient evaluation of local hybrid density functionals, J. Comput. Chem. **33**, 810 (2012).

[317] J. Jaramillo, G. E. Scuseria, and M. Ernzerhof, Local hybrid functionals, J. Chem. Phys. **118**, 1068 (2003).

[318] E. R. Johnson, Local-hybrid functional based on the correlation length, J. Chem. Phys. **141**, 124120 (2014).

[319] A. V. Arbuznikov and M. Kaupp, Local hybrid exchange-correlation functionals based on the dimensionless density gradient, Chem. Phys. Lett. **440**, 160 (2007).

[320] T. M. Maier, H. Bahmann, A. V. Arbuznikov, and M. Kaupp, Validation of local hybrid functionals for TDDFT calculations of electronic excitation energies, J. Chem. Phys. **144**, 074106 (2016).

[321] T. Körzdörfer, R. M. Parrish, N. Marom, J. S. Sears, C. D. Sherrill, and J.-L. Brédas, Assessment of the performance of tuned range-separated hybrid density functionals in predicting accurate quasiparticle spectra, Phys. Rev. B **86**, 205110 (2012).

[322] L. Kronik and S. Kümmel, Dielectric screening meets optimally tuned density functionals, Adv. Mater. **30**, 1706560 (2018).

[323] D. Wing *et al.*, Band gaps of crystalline solids from Wannier-localization-based optimal tuning of a screened range-separated hybrid functional, Proc. Natl. Acad. Sci. **118**, e2104556118 (2021).

[324] T. B. de Queiroz and S. Kümmel, Charge-transfer excitations in low-gap systems under the influence of solvation and conformational disorder: Exploring range-separation tuning, J. Chem. Phys. **141**, 084303 (2014).

[325] P. M. W. Gill, R. D. Adamson, and J. A. Pople, Coulomb-attenuated exchange energy density functionals, Mol. Phys. **88**, 1005 (1996).

[326] M. Ernzerhof and J. P. Perdew, Generalized gradient approximation to the angle- and system-averaged exchange hole, J. Chem. Phys. **109**, 3313 (1998).

[327] K. Schwinn, F. Zapata, A. Levitt, É. Cancès, E. Luppi, and J. Toulouse, Photoionization and core resonances from range-separated density-functional theory: General formalism and example of the beryllium atom, J. Chem. Phys. **156**, 224106 (2022).

[328] J. Toulouse, K. Schwinn, F. Zapata, A. Levitt, É. Cancès, and E. Luppi, Photoionization and core resonances from range-separated time-dependent density-functional theory for open-shell states: Example of the lithium atom, J. Chem. Phys. **157**, 244104 (2022).

[329] B. J. Lynch and D. G. Truhlar, Small representative benchmarks for thermochemical calculations, J. Phys. Chem. A **107**, 8996 (2003), Erratum: J. Phys. Chem. A **108**, 1460 (2004).

[330] Y. Zhao and D. G. Truhlar, The M06 suite of density functionals for main group thermochemistry, thermochemical kinetics, noncovalent interactions, excited states, and transition elements: Two new functionals and systematic testing of four M06-class functionals and 12 other functionals, Theor. Chem. Acc. **120**, 215 (2008).

[331] J. Zheng, Y. Zhao, and D. G. Truhlar, The DBH24/08 database and its use to assess electronic structure model chemistries for chemical reaction barrier heights, J. Chem. Theory Comput. **5**, 808 (2009).

[332] H. S. Yu, X. He, S. L. Li, and D. G. Truhlar, MN15: a Kohn-Sham global-hybrid exchange-correlation density functional with broad accuracy for multi-reference and single-reference systems and noncovalent interactions, Chem. Sci. **7**, 5032 (2016), Erratum: Chem. Sci. **7**, 6278 (2016).

[333] T. M. Henderson, B. G. Janesko, and G. E. Scuseria, Range separation and local hybridization in density functional theory, J. Phys. Chem. A **112**, 12530 (2008).

[334] B. G. Janesko, A. V. Krukau, and G. E. Scuseria, Self-consistent generalized Kohn-Sham local hybrid functionals of screened exchange: Combining local and range-separated hybridization, J. Chem. Phys. **129**, 124110 (2008).

[335] R. Haunschild and G. E. Scuseria, Range-separated local hybrids, J. Chem. Phys. **132**, 224106 (2010).

[336] J. Kirkpatrick *et al.*, Pushing the frontiers of density functionals by solving the fractional electron problem, Science **374**, 1385 (2021).

[337] T. M. Maier, Combining real-space and local range separation – The MH24 locally range-separated local hybrid functional, J. Chem. Phys. **161**, 074106 (2024).

[338] R. M. Richard *et al.*, Accurate ionization potentials and electron affinities of acceptor molecules I. Reference data at the CCSD(T) complete basis set limit, J. Chem. Theory Comput. **12**, 595 (2016).

[339] J. W. Knight *et al.*, Accurate ionization potentials and electron affinities of acceptor molecules III. A benchmark of GW methods, J. Chem. Theory Comput. **12**, 615 (2016).

[340] M. S. Deleuze, L. Claes, E. S. Kryachko, and J.-P. François, Benchmark theoretical study of the ionization threshold of benzene and oligoacenes, J. Chem. Phys. **119**, 3106 (2003).

[341] B. Hajgató, M. S. Deleuze, D. J. Tozer, and F. De Proft, A benchmark theoretical study of the electron affinities of benzene and linear acenes, J. Chem. Phys. **129**, 084308 (2008).

[342] E. Fresch, E. Meneghin, A. Agostini, H. Paulsen, D. Carbonera, and E. Collini, How the protein environment can tune the energy, the coupling, and the ultrafast dynamics of interacting chlorophylls: The example of the water-soluble chlorophyll protein, J. Phys. Chem. Lett. **11**, 1059 (2020).

[343] H. Tamura, K. Saito, and H. Ishikita, Acquirement of water-splitting ability and alteration of the charge-separation mechanism in photosynthetic reaction centers, Proc. Natl. Acad. Sci. **117**, 16373 (2020).

[344] K. Dubas, S. Szewczyk, R. Białek, G. Burdziński, M. R. Jones, and K. Gibasiewicz, Antagonistic effects of point mutations on charge recombination and a new view of primary charge separation in photosynthetic proteins, J. Phys. Chem. B **125**, 8742 (2021).

[345] H. Tamura, K. Saito, and H. Ishikita, The origin of unidirectional charge separation in photosynthetic reaction centers: Nonadiabatic quantum dynamics of exciton and charge in pigment-protein complexes, Chem. Sci. **12**, 8131 (2021).

[346] T. Kanda and H. Ishikita, Energetics of the electron transfer pathways in the homodimeric photosynthetic reaction center, Biochemistry **61**, 2621 (2022).

[347] A. D. Becke, Real-space post-hartree-fock correlation models, J. Chem. Phys. **122**, 064101 (2005).

[348] S. Vuckovic, A. Gerolin, T. J. Daas, H. Bahmann, G. Friesecke, and P. Gori-Giorgi, Density functionals based on the mathematical structure of the strong-interaction limit of DFT, WIREs Comput. Mol. Sci. **13**, e1634 (2023).

[349] A. Wodyński, A. V. Arbuznikov, and M. Kaupp, Local hybrid functionals augmented by a strong-correlation model, J. Chem. Phys. **155**, 144101 (2021).

[350] A. Wodyński and M. Kaupp, Local hybrid functional applicable to weakly and strongly correlated systems, J. Chem. Theory Comput. **18**, 6111 (2022).

[351] S. Fürst, M. Kaupp, and A. Wodyński, Range-separated local hybrid functionals with small fractional-charge and fractional-spin errors: Escaping the zero-sum game of DFT functionals, J. Chem. Theory Comput. **19**, 8639 (2023).

[352] A. Wodyński, A. V. Arbuznikov, and M. Kaupp, Strong-correlation density functionals made simple, J. Chem. Phys. **158**, 244117 (2023).

Reprints of publications

Reprint of publication [B1]

Publication [B1]

M. Brütting, J. M. Foerster, and S. Kümmel

Investigating primary charge separation in the reaction center of *Heliobacterium modesticaldum*

J. Phys. Chem. B **125**, 3468 (2021)

DOI: 10.1021/acs.jpcb.0c10283

Author contribution statement: M.B. and S.K. conceptualized the work with support from J.F. J.F. prepared and re-optimized the crystal structure. M.B. prepared the structure models with help from J.F. M.B. did all the TDDFT and BOMD calculations, and prepared all figures and tables in discussion with S.K. All authors discussed the results. M.B. and S.K. wrote the manuscript, and J.F. proofread it and gave comments.

Note: Pub. [B1] relies on computations performed during the Master thesis of the author [Investigating primary charge separation in the reaction centre of *Heliobacterium modesticaldum*, University of Bayreuth (2020)]. However, the interpretation of the data was done partly within the doctoral project. Furthermore, the manuscript of Pub. [B1] was written fully as part of the doctoral project.

THE JOURNAL OF PHYSICAL CHEMISTRY B
A JOURNAL OF THE AMERICAN CHEMICAL SOCIETY

pubs.acs.org/JPCB

Article

Investigating Primary Charge Separation in the Reaction Center of *Heliobacterium modesticaldum*

Moritz Brütting, Johannes M. Foerster, and Stephan Kümmel*

Cite This: *J. Phys. Chem. B* 2021, 125, 3468−3475

Read Online

ACCESS | Metrics & More | Article Recommendations | Supporting Information

ABSTRACT: We compute the primary charge separation step in the homodimeric reaction center (RC) of *Heliobacterium modesticaldum* from first principles. Using time-dependent density functional theory with the optimally tuned range-separated hybrid functional ωPBE, we calculate the excitations of a system comprising the special pair, the adjacent accessory bacteriochlorophylls, and the most relevant parts of the surrounding protein environment. The structure of the excitation spectrum can be rationalized from coupling of the individual bacteriochlorophyll pigments similar to molecular J- and H-aggregates. We find excited states corresponding to forward-charge transfer along the individual branches of the RC of *H. modesticaldum*. In the spectrum, these are located at an energy between the coupled Q_y and Q_x transitions. With ab initio Born−Oppenheimer molecular dynamics simulations, we reveal the influence of thermal vibrations on the excited states. The results show that the energy gap between the coupled Q_y and the forward-charge transfer excitations is ∼0.4 eV, which we consider to conflict with the concept of a direct transfer mechanism. Our calculations, however, reveal a certain spectral overlap of the forward-charge transfer and the coupled Q_x excitations. The reliability and robustness of the results are demonstrated by several numerical tests.

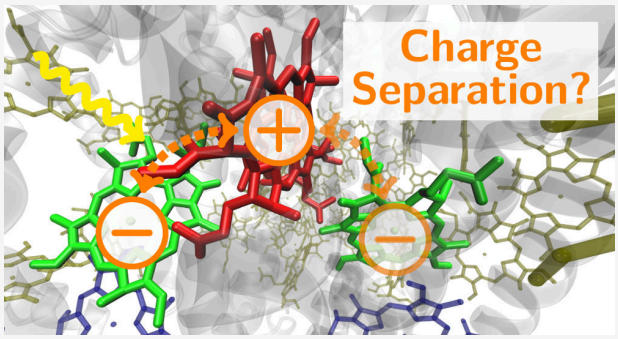

1. INTRODUCTION

Revealing the basic functional principles of natural light harvesting constitutes a great intellectual challenge.[1−4] The involved biomolecules are large pigment−protein complexes, which are optimized to perform specialized tasks. Radiation energy is captured by the pigments of the light-harvesting complex and, subsequently, transferred to a photochemical reaction center (RC), where it is transformed into a charge-separated state (*cf.* Figure 1). These primary reactions of photosynthesis exhibit an internal quantum efficiency close to one.[4] The cofactors along which charge separation in the RC proceeds are arranged in a dimer of two branches. If the C_2 symmetry is broken, for example, by the interaction with the surrounding protein matrix, the complex is referred to as a heterodimer and only one branch is involved in the charge separation process. The well-studied purple bacteria belong to this group.[5−7] By contrast, in homodimeric RCs, which can be found, e.g., in heliobacteria,[8−11] both branches contribute to charge separation.

Structural information for a homodimeric type-I RC has become available only recently, when Gisriel et al.[12] have resolved the crystal structure of the RC of *Heliobacterium modesticaldum* (HbRC) by X-ray analysis. The HbRC possesses two homodimeric core polypeptides (PshA), which enclose the cofactors of charge separation (*cf.* Figure 1). The first cofactor is a pair of close lying bacteriochlorophyll g′ (Bcl g′) pigments commonly known as the special pair (SPP). It is followed, one in each branch, by a Bcl g, referred to as accessory bacteriochlorophyll (Acc), and a 8^1-hydroxy chlorophyll a (OH-Chl a). Both branches terminate in a single [4Fe−4S] cluster, which serves as the terminal electron acceptor. All cofactors are coordinated by amino acid residues from the polypeptide chains of PshA, as described in detail in ref 12. Furthermore, multiple antenna pigments (52 Bcl g and 2 Bcl g′), which are responsible for the light-harvesting process, are integrated into the protein matrix of the HbRC.

Model Hamiltonians[3] can make a numerical treatment of all these pigments computationally feasible. In fact, the excitonic coupling among the pigments of the HbRC has been investigated in a few recent studies.[13,14] Computationally efficient multiscale models can account for the influence of environmental effects in an approximate way via empirical force fields or by treating them as a dielectric medium.[3,15,16] Recent numerical studies on the RC of *Rhodobacter sphaeroides*

Received: November 14, 2020
Revised: March 20, 2021
Published: March 31, 2021

https://doi.org/10.1021/acs.jpcb.0c10283
J. Phys. Chem. B 2021, 125, 3468−3475

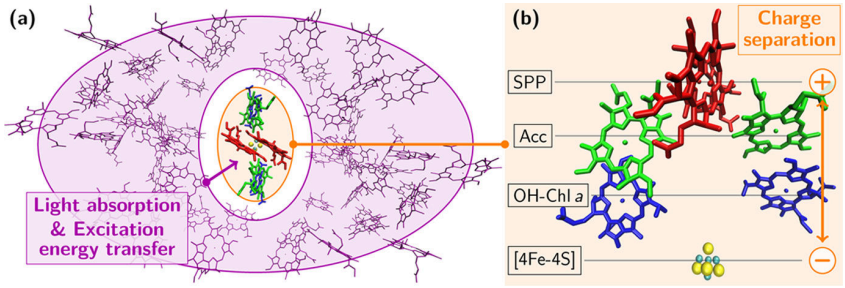

Figure 1. Schematic overview of the light-harvesting steps in the HbRC.[12] (a) Light absorption by the antenna Bcl and subsequent excitation energy transfer toward the cofactors of charge separation. (b) Charge separation along the cofactors SPP, Acc, OH-Chl a, and a [4Fe−4S] cluster; eventually leading to the SPP^{+} $[4Fe{-}4S]^{-}$ charge-separated state.[10,11]

suggest that the charge transfer (CT) properties of the SPP might be influenced by dielectric screening.[17,18] Our aim in this study, however, is to gain insights into the primary charge separation step in a fully first-principles approach.

Density functional theory (DFT)[19,20] and its time-dependent version (TDDFT)[21] allow us to treat both ground and excited state properties of quantum mechanical systems ab initio and, hence, there is no need to rely on the empirical input. However, the applicability of the corresponding numerical methods is limited to smaller systems, i.e., a few Bcl pigments, due to their computational expense. On the other hand, the underlying conceptual framework is formally exact. Hence, if a suitable approximation for the exchange−correlation functional is chosen, the numerical outcome can be of high accuracy.[22−24]

The key challenge for TDDFT calculations of light-harvesting systems in general and RCs in particular is a qualitatively correct description of the excited states,[25] and especially those with CT character.[26] Range-separated hybrid functionals[27−30] are able to fulfill this task by splitting the Coulomb interaction into a long-range and a short-range contribution.[31−34] Then, the long-range contribution to the exchange energy is treated exactly via the Fock integral, whereas the short-range piece is approximated by a semilocal exchange functional. Hence, the correct asymptotic exchange−correlation potential is obtained and, at the same time, the compatibility between semilocal exchange and correlation is maintained at short range. The length scale of the transition from short-range to long-range is controlled by the so-called range separation parameter ω, which can be determined without the empirical input for a particular system by the optimal tuning procedure.[31,34,35]

To our knowledge, no ab initio study of the homodimeric HbRC has been published yet. In this work, we take a first step to retrace possible charge-separation mechanisms in the HbRC by full TDDFT calculations, which employ the optimally tuned range-separated hybrid functional ωPBE.[38] Thereby, we start from the SPP−Acc system, which is depicted in Figure 2 and which was prepared according to the protocol described in Section 2.1. It consists of the SPP, the adjacent Accs, and the amino acid residues His 537 and Gln 458 as well as two water molecules.[36,37] Each water molecule is H bonded by one Gln and coordinates an Acc; the His residues coordinate the SPP.[12] To simplify the notation, we abbreviate the combination of SPP and both His as SPP−His, the combination of water and Gln as H_2O−Gln, and the combination of Accs and both H_2O−Gln as Acc−Gln in the following.

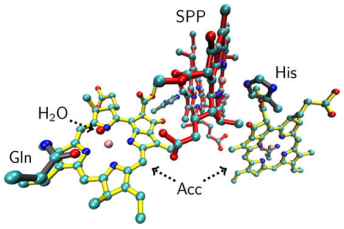

Figure 2. Arrangement of the SPP−Acc system.[12] The SPP (2 Bcl g′, colored red) is coordinated by His 537 from PshA; the Accs (2 Bcl g, colored yellow) by water, which is H-bonded by Gln 458.[36,37] The coordinating residues are colored gray. The atoms are colored according to their atom type. Phythyl tails are cropped (*cf.* Section 2.1). H atoms are omitted for clarity.

The main findings of our study are the following. The excitation spectrum of the SPP−Acc system in the crystal structure geometry exhibits a transparent structure, which results from coupling of the individual pigments similar to molecular J- and H-aggregates.[39,40] Additionally, we find forward-CT excitations, which correspond to electron transfer from the SPP to one of the Acc. The energy of these excitations is noticeably larger, 0.3 eV or more, than the energy of the bright coupled Q_y excitations. Taking larger parts of the protein environment into account hardly changes this picture. Nuclear vibrations, which we obtain in an ab initio Born−Oppenheimer molecular dynamics (BOMD) simulation,[41] change the character of the coupled bright excitations. This is visible in the excitation spectra that we calculate for multiple molecular geometry snapshots along the BOMD trajectory. However, in these spectra, the forward-CT excitations are yet higher in energy, $\gtrsim$0.4 eV, than the coupled Q_y excitations. Some of the coupled Q_x excitations on the other hand occur at similar energies as the forward-CT states. Our findings may help to elucidate possible energy transfer pathways from (bright) localized to CT excitations. Throughout the study, we carefully check and report the numerical reliability of our results. In the following sections, we describe our findings in detail.

2. COMPUTATIONAL METHODS

2.1. Structure Preparation. The crystal structure of the HbRC, which can be obtained from the Protein Data Bank under file ID 5V8K,[12] constitutes the basic input for the quantum chemical calculations. Beforehand, several common[23] modifications of the original experimental data are required, which we describe in the Supporting Information.

https://doi.org/10.1021/acs.jpcb.0c10283
J. Phys. Chem. B 2021, 125, 3468−3475

To account for the impact of the protein environment, further amino acid residues are added to the SPP–Acc system. The positions of the H atoms, which replace the linkage to the polypeptide chain, are optimized using the universal force field[42] and the steepest descent method as implemented in Avogadro, version 1.2.[43] The other atoms remain at their crystal structure positions. Deciding on an appropriate amino acid selection is a delicate task as the Fock integral causes the numerical cost to scale roughly quadratic with the number of atoms. On the other hand, it is desired to capture the effect of the protein environment on the excitations of the SPP–Acc system as exhaustive as possible. On general grounds, we may expect that the influence of the amino acid residues decreases with their distance to the pigments. A distance of ∼3 Å to the pigments is a reasonable guideline (S. Kroll, S. Kümmel, and L. Leppert; unpublished). As a further guidance, we focus on polar amino acids and those molecules that are located at the interface of SPP and Accs, which is in the front line of CT (*cf.* Section 3.1). The amino acid residues resulting from this trade-off are listed in Table 1, their arrangement around the SPP–Acc system is illustrated in Figure 3.

Table 1. Overview of the Amino Acid Residues that are Added to the SPP–Acc System to Account for the Impact of the Protein Environment[a]

name	sequence number[36]
Ala	541
Cys	601
Ile	514 515
Leu	533 534 605
Phe	454 465 475 511 538 542 594
Thr	345 348 518 598
Trp	540
Tyr	341 510

[a]Their spatial layout is illustrated in Figure 3.

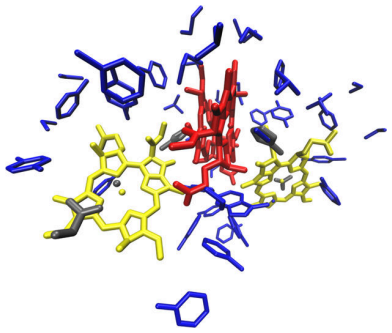

Figure 3. Spatial distribution of the amino acid residues from Table 1 (colored blue) around the SPP–Acc system (*cf.* Figure 2 for labels and an explanation of the color scheme). The polypeptide backbone and the phythyl tails are cropped. H atoms are omitted for clarity.

2.2. TDDFT Calculations. The TDDFT calculations of the electronic excitations rely on the Casida approach[44] and are performed using the quantum chemistry program Q-Chem, version 5.2.2.[45] For the exchange–correlation functional, we use the range-separated hybrid functional ωPBE.[38] The range separation parameter ω is determined by optimal tuning.[30,31,35] Hereby, ω is varied to minimize the difference between the eigenvalue of the highest occupied molecular orbital and the ionization potential for both the neutral and the anionic system (J2-tuning procedure).[46] For a single Bcl g′ taken from the SPP, this procedure yields $\omega_g = 0.160 a_0^{-1}$. However, for the results presented here, we use the value $\omega_a = 0.171 a_0^{-1}$, which stems from previous work by Schelter et al.[23] where optimal tuning has been performed for a single Bcl a. This choice eases comparison with other work, and the small difference in the range separation parameter does not influence the outcome of our calculations on a relevant scale. We verify this explicitly and discuss our choice of the parameter ω and earlier literature on this topic[47,48] in the Supporting Information.

Finally, we mention one technical aspect that is important: the excitation energies and oscillator strengths of optical excitations that we report in this article are calculated without the Tamm-Dancoff approximation. The latter leads to large, implausible deviations from the full solution for our system.

2.3. Born–Oppenheimer Molecular Dynamics. We perform an ab initio BOMD simulation[41] of the SPP–Acc system at room temperature (300 K). For incorporating the mechanical constraints induced by the protein environment, we fix the terminal C_β of His and Gln, which are bound to the polypeptide chains in the full protein complex. Furthermore, we also fix the terminal O of the phythyl tails of the Bcls, as the phythyl side chains are sterically hindered within the protein due to their length. This procedure has already been employed in previous BOMD studies of a bacterial RC.[49,50] It inhibits an overall drift of the system and ensures that the relative positions of its individual parts are sustained.

For the BOMD simulation, we use the PBE functional[51] with the Grimme DFT–D3 dispersion correction and rely on the program TURBOMOLE, version 7.4.0.[52] The technical setup is reported in the Supporting Information.

To investigate the impact of the BOMD dynamics on the excited states, we take snapshots of the molecular structure every 9.7 fs along the BOMD trajectory—after an initial equilibration phase—and calculate the corresponding excitation spectra according to the protocol described in Section 2.2. Here, we use the 6-31G basis set for all calculations. From these excitation spectra, we calculate an "ensemble-averaged" histogram to represent the influence of thermal vibrations on the excitation spectrum. In fact, this is a histogram of the excitations (with energy ε), which are weighted by their oscillator strengths $f(\varepsilon)$ and accumulated in bins $B(\varepsilon, \Delta\varepsilon) \equiv [\varepsilon - \Delta\varepsilon/2, \varepsilon + \Delta\varepsilon/2]$

$$\bar{f}(\epsilon) = \frac{1}{N} \sum_{\varepsilon \in B(\epsilon, \Delta\epsilon)} f(\varepsilon) \tag{1}$$

where N denotes the number of underlying excitation spectra. This yields the mean oscillator strength $\bar{f}(\varepsilon)$. The whole procedure is insensitive to the character of the excitations, i.e., localized as well as CT excitations enter. However, as obvious from eq 1, the ensemble-averaged spectrum will be dominated by the bright excitations.

Within the scope of this work, we are particularly interested in comparing the ensemble-averaged spectrum to the spectral positions of the forward-CT excitations. These are best represented by a common histogram of only this type of excitation. Here, the oscillator strength is not taken into account as, being close to zero, it is not a helpful characteristic of this type of excitation. As we illustrate in Section 3.1, the CT character of an excitation can be determined by a natural transition orbital (NTO) analysis.[53] For our purposes here, this tool is particularly well suited as forward-CT excitations

https://doi.org/10.1021/acs.jpcb.0c10283
J. Phys. Chem. B 2021, 125, 3468–3475

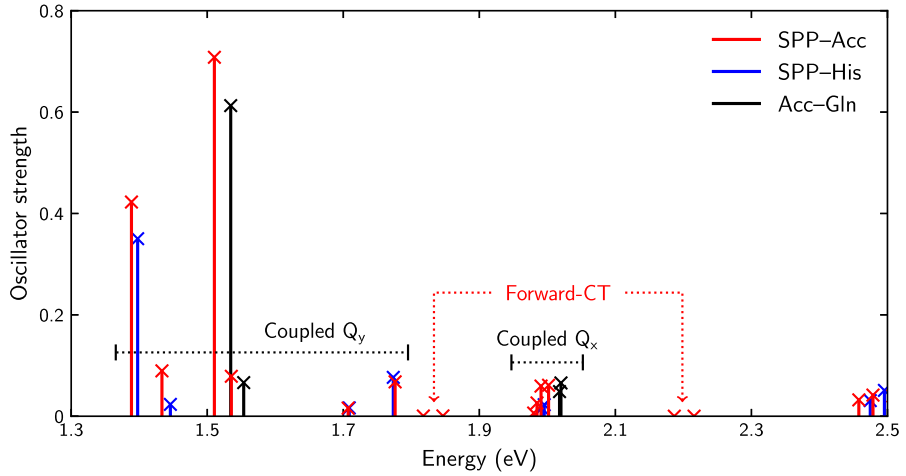

Figure 4. Excitation spectrum of the SPP–Acc system and its two constituent subsystems SPP–His (SPP and coordinating His) and Acc–Gln (Accs and coordinating H_2O–Gln), calculated with the 6-31G(d,p) basis set. The character of the states is indicated (see the text).

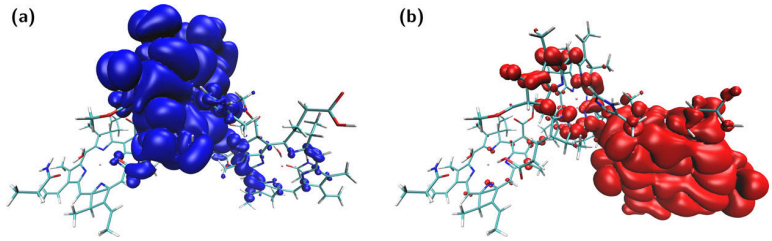

Figure 5. First NTO pair of the forward-CT state at 1.88 eV of the SPP–Acc system: (a) hole density and (b) electron density. Displayed is the isosurface with an isovalue of 4×10^{-6} a_0^{-3}. A comparison of the first NTO pairs of all forward-CT states is provided in the Supporting Information.

are the only type of excitation that are clearly dominated by a single electron–hole pair. Empirically, it turns out that for our system, a threshold of 0.984 for the normalized amplitude of the respective first NTO pair is well suited to discriminate forward-CT (above) from other (localized or CT) excitations (below).[54] This criterion enables the automated evaluation of the excitation spectra.

3. RESULTS AND DISCUSSION

3.1. Excited States of the SPP–Acc System. We begin the discussion with the excited states of the SPP–Acc system based on the crystal structure geometry. The spectrum is depicted in Figure 4. As a preview, its excitations can be divided into four groups: six bright excitations between ∼1.4 and 1.8 eV ("coupled Q_y"), two pairs of dark excitations at 1.88...1.90 eV and 2.24...2.26 eV, four bright excitations at ∼2.0 eV ("coupled Q_x"), and a broader band of bright and dark transitions beginning at ∼2.45 eV, which is the Soret band of the coupled Bcls.

As foretold by the labels, the smaller groups of bright excitations arise from the coupling of the Q_y and Q_x transition dipole moments of the Bcls, respectively. The mechanism behind the coupling is best retraced by comparing the spectrum of the SPP–Acc system to the spectra of the two subsystems SPP–His and Acc–Gln, which are also shown in Figure 4. Apparently, in the case of the coupled Q_y[55] excitations, each excitation of the SPP–Acc system almost coincides with an excitation of either the SPP–His or Acc–Gln subsystem. Analyzing the underlying transition densities indeed reveals that the character of the excitations remains widely unchanged upon combining SPP–His and Acc–Gln to SPP–Acc. The same conclusion can be drawn for the coupled Q_x[55] excitations, although this is less obvious to see when just comparing the spectra.

We discuss the excitation spectra of the individual subsystems SPP–His and Acc–Gln in detail in the Supporting Information. The analysis there reveals that each of the coupled Q_x excitations is localized mostly on one of the Bcl pigments. In the case of the Q_y excitations, we find that the coupling of the Acc dimer is of J-type,[39,40] which leads to the two coupled excitations visible in Figure 4. In the case of the SPP dimer, four coupled Q_y excitations emerge in two pairs, which exhibit the characteristics of either a J-aggregate or a H-aggregate. The fact that both types of coupling exist can be attributed to the strong coupling in the SPP dimer.

By contrast, the two pairs of dark excitations are novel in the spectrum of SPP–Acc, i.e., do not have an equivalent in the spectra of SPP–His or Acc–Gln. As common for dark excitations, the transition density is less instructive. Instead, an NTO analysis[53] can unravel their character. The outcome is that all four excitations are dominated by one electron–hole pair with a normalized amplitude of more than 0.99. The spatial distribution of the corresponding NTO densities is depicted in Figure 5 for one of the excitations. They reveal that the NTO hole and electron are astonishingly well localized on the SPP and on one of the Acc pigments, respectively. This very clearly indicates a forward-CT state, i.e., an electron is being transferred from the SPP toward the Acc.

https://doi.org/10.1021/acs.jpcb.0c10283
J. Phys. Chem. B 2021, 125, 3468–3475

The first NTO pairs of all forward-CT excitations are shown in the Supporting Information. Comparing them reveals that each pair consists of two excitations, which correspond to CT along the two different branches of the HbRC. They are separated by only a small energy gap of ∼0.02 eV. Our experience tells us that a systematic relative energy difference of this size and reproducibility is not a numerical error. Therefore, we seek for a structural cause of this apparent asymmetry in the spectrum.[56] As the structure of the SPP−Acc system is prepared according to the protocol described in Section 2.1 from the crystal structure of the HbRC, the backbone of the structure with its C, O, N, and Mg atoms inherits the perfect C_2 symmetry that the X-ray data suggest. Only the force field optimized positions of the H atoms are asymmetric. We were able to verify the assumption that this asymmetry leads to the ∼0.02 eV energy splitting by explicitly symmetrizing the structure of SPP−Acc. As discussed in greater detail in the Supporting Information, the pairs of forward-CT states emerge at equal energies when the complete structure including the H-atom positions is symmetrized. In this case, the NTOs also do no longer display a preference for a particular branch. Instead, the electron orbital is delocalized over both Accs. By contrast, the localized excitations basically remain unchanged upon symmetrization. We, therefore, conclude that the forward-CT states are sensitive to small deviations from the perfect C_2 symmetry.

In the Supporting Information, we compare our results to the experimental data from ref 57, and argue that also in view of previous work,[58−60] reasonable accuracy can be expected from TDDFT for Bcls. We further present several tests to validate our numerical setup and demonstrate the reliability of our results. The main conclusions from these tests are that, first, the size of the basis sets—we used 6-31G, 6-31G(d,p), and 6-311G(d,p)− is not a limiting factor for our conclusions. Second, our choice of $\omega = 0.171 a_0^{-1}$ for the range-separation parameter is reasonable. Third and finally, the coordinating His and H_2O−Gln have a noticeable influence on the excitation spectrum and thus need to be taken into account in all cases.

3.2. Protein Environment. In the following, we study the influence of the protein environment on the excited states of the SPP−Acc system. As discussed in Section 2.1, only a small fraction of the surrounding amino acid residues can be included in the full TDDFT calculation. However, one may expect on general grounds that the influence of the amino acids in the direct vicinity is the largest. We confirmed this expectation explicitly in our calculations by including several residues of the same type at different distances to the pigments.

The amino acid residues whose influence we further discuss now are listed in Table 1. The spectrum of the SPP−Acc system within this environment is compared to the bare SPP−Acc system in Figure 6. We observed a small, overall redshift $\lesssim$ 0.05 eV of the excitation spectrum, but its familiar pattern, i.e., coupled Q_y and Q_x excitations as well as forward-CT states, is retained. The splitting of the forward-CT pairs is somewhat increased. We again attribute this to the asymmetric distribution of the H atoms.

Additionally, we investigated the influence of individual amino acid residues, as also detailed in the Supporting Information. This reveals that particular polar or aromatic amino acids, Thr, Trp, and Tyr, when taken into account separately, can have a significant influence on the forward-CT states and shift them up to 0.14 eV. However, when these residues are taken into account together, the effects cancel out mutually. The other amino acids in the vicinity shift the forward-CT states by only $\lesssim$0.02 eV.

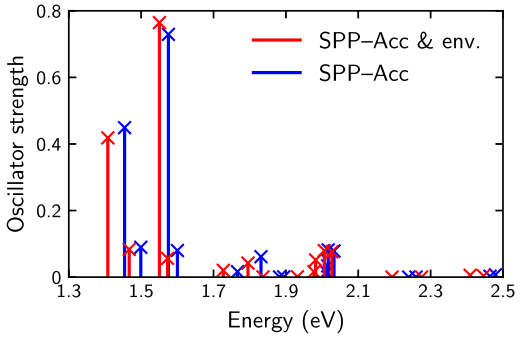

Figure 6. Excitation spectrum of the SPP−Acc system with and without the environment amino acids (*cf.* Table 1, abbreviated as "env."), calculated with the 6-31G basis set.

3.3. Born−Oppenheimer Molecular Dynamics. The previous results based on the (static) crystal structure of the HbRC do not suggest that a coupling of the bright Q_y and the forward-CT excitations is possible. However, it is well known that molecular vibrations can have an influence on CT pathways. To include the effects of the nuclear motion into our calculations, we have performed a BOMD simulation of the SPP−Acc system.

At the heart of the following discussion is a BOMD trajectory, which consists of 8790 steps corresponding to 1063.1 fs. As a coarse-grained measure of the dynamics, we monitor the root mean square deviation (RMSD) of the atoms from their original positions as a function of time. After an initial equilibration phase, in which the RMSD increases within 105.2 fs to 0.49 Å, it increases slowly during the following 957.9 fs to 1.26 Å at the end of the BOMD run. If alternatively the temporal dynamics of the RMSD of the Mg−Mg distances (as a measure of the interpigment separation) is monitored, we find that its average oscillates around 0.3 Å shortly after the beginning of the BOMD run. Unlike the Bcls and the amino acid tails, the interstitial H_2O molecules are not subject to any (external) constraint. However, during the simulation, intermolecular interactions prevent the H_2O molecules from exiting their binding pockets between Acc and Gln, consistent with the observations described in other BOMD studies of a bacterial RC.[49,50]

As described in Section 2.3, we calculated the excitation spectra of $N = 100$ snapshots of the BOMD trajectory after the above-mentioned initial equilibration phase. They reveal that the transparent structuring of the spectrum obtained for the case of the crystal structure, *cf.* Section 3.1, is not retained. It is still possible to identify coupled Q_y and Q_x excitations. However, an analysis of the underlying transition densities reveals that the picture of J- and H-type coupling within the SPP−His or Acc−Gln compartments is no longer applicable. Instead, the transition density may extend over a single, several, or all pigments, i.e., the nature of the coupling changes with time. These changes are rapid, i.e., no trends can be deduced from comparing the subsequent snapshots. Apart from these (bright) localized excitations, the spectra still contain well-emphasized forward-CT states.

To put the comparison of localized and CT excitations on a firm footing, we accumulated all excitation spectra in a weighted histogram ("ensemble-averaged" spectrum), *cf.*

https://doi.org/10.1021/acs.jpcb.0c10283
J. Phys. Chem. B 2021, 125, 3468−3475

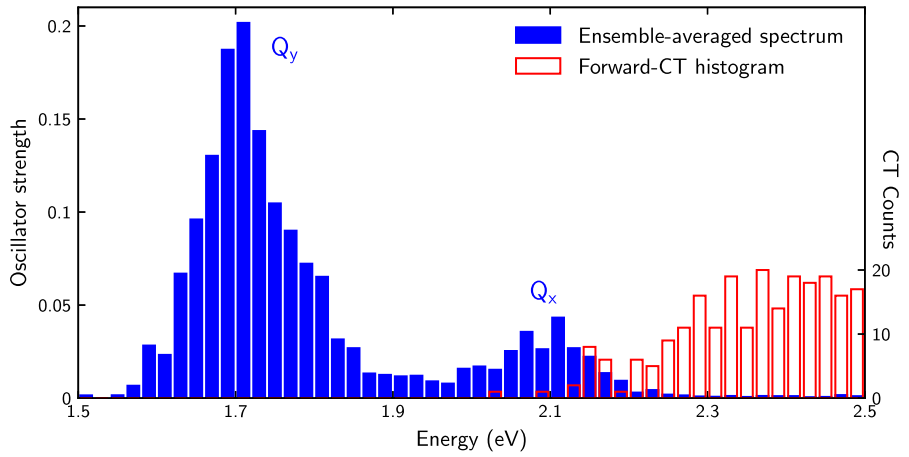

Figure 7. Weighted histogram of the BOMD-based excitation spectra (solid blue bars, left axis). It is calculated according to eq 1 from the excitation spectra of 100 equally separated snapshots of the BOMD between 105.2 and 1063.1 fs. The labels of the peaks in the spectrum are explained in the text. Additionally, a common histogram of the number of forward-CT excitations occurring in these spectra is shown (light red bars, right axis). The bin width of both histograms is 0.02 eV.

Section 2.3, which we compare to a common histogram of the forward-CT excitations. An overlay of both histograms is depicted in Figure 7. The ensemble-averaged spectrum exhibits two distinct peaks at ∼1.7 and 2.1 eV, which correspond to the Q_y and Q_x lines, respectively, of the Bcl pigments (labeled in Figure 7). As compared to the spectrum originating from the crystal structure of SPP−Acc, these bright excitations are blue-shifted by 0.1...0.2 eV. By contrast, the blueshift is considerably larger for the forward-CT excitations; the onset of the corresponding histogram is at ∼2.1 eV. Clearly, there is no overlap of the forward-CT states with the coupled Q_y excitations in the spectrum. Instead, we find a (small) overlap of the forward-CT states with the Q_x transitions.

As an alternative to the histogram-based approach of evaluating the BOMD data, we show and discuss in the Supporting Information the time evolution of several energy levels, which represent the main features of the BOMD-based excitation spectra. This analysis confirms the conclusions drawn from Figure 7, i.e., a spectral gap of $\gtrsim$0.4 eV between the Q_y peak and the onset of the forward-CT excitations on one hand, and a small spectral overlap of the forward-CT states with the Q_x excitations on the other hand.

4. CONCLUSIONS

We investigated the charge separation properties of the SPP and its adjacent cofactors (Accs) from the homodimeric HbRC using TDDFT with the range-separated hybrid functional ωPBE. Analysis of the excited states of the (symmetric) crystal structure revealed that its Q_y and Q_x excitations emerge from coupling of the individual pigments similar to molecular J- and H-aggregates. In the case of the SPP, we encountered a considerable redshift of the J-aggregated Q_y lines (by 0.15 eV), which is absent for the Accs. We attribute this observation to the small interpigment separation in the SPP. This conforms with the conclusion from exciton models where the coupling of the SPP is found to be dominated by short-range mechanisms.[14,61] Notably, several distinct forward-CT states emerged that can be interpreted as an electron moving from the SPP to one of the Acc pigments. We demonstrated that this (small) preference for CT along a particular branch arises from small deviations from perfect C_2 symmetry, which are induced by the H atoms. We investigated the influence of the protein environment and performed several numerical tests to verify that our setup is appropriate to capture the relevant physical effects. We consistently obtained an energy gap of ∼0.3 eV between the major Q_y and the lowest forward-CT excitations.

To further investigate the influence of structural changes, we performed an ab initio BOMD simulation of the SPP−Acc system and calculated the excitation spectra of multiple snapshots along the resulting trajectory. This mimics the influence of molecular vibrations on the excited states. It turned out that a clear designation of J- and H-type-coupled excitations is no longer feasible for the distorted geometries. An important finding regarding potential charge separation pathways is that the energy gap between the Q_y peak and the onset of the forward-CT excitations increased to $\gtrsim$0.4 eV during this simulation. On the other hand, however, we find a (small) spectral overlap with the coupled Q_x excitations.

Several conclusions regarding potential charge separation mechanisms in the HbRC can be drawn from our study. Due to the redshift of its J-type-coupled Q_y excitations,[14] the SPP is typically considered to serve as a sink for the excitation energy transferred from the antenna pigments to the cofactors. Our results based on the crystal structure of SPP−Acc seem to confirm this concept. However, this conclusion is put into question by the spectra based on the BOMD simulation, which takes into account (thermally driven) structural distortions. Then, the lowest Q_y excitations may as well be localized on the Accs. Most strikingly, the BOMD results suggest that direct energy transfer from the lowest and brightest excitations of the SPP and Accs (coupled Q_y) to the lowest SPP−Acc CT state is not possible. Instead, higher excited states with smaller oscillator strengths (coupled Q_x) might be involved.[62]

This work paves the way for continuative TDDFT studies of the HbRC. By including further cofactors, the full CT chain can be taken into account, as done in ref 22 for the PS II of plants. This may help to clarify whether the charge separation chain is initiated at the SPP or the Accs.[12] A full understanding of the light-harvesting complex requires also considering the antenna pigments. On the level of full TDDFT calculations, this can become computationally feasible by limiting oneself to

https://doi.org/10.1021/acs.jpcb.0c10283
J. Phys. Chem. B 2021, 125, 3468−3475

a reduced system of the antenna pigments in the vicinity of the CT cofactors. The analysis of BOMD may be extended to investigate the interplay of nuclear dynamics and CT. Work along this line on the RC of *R. sphaeroides* can be found in refs 49 and 50. A nonadiabatic MD simulation technique such as Ehrenfest MD[3,41] can account for the coupled dynamics of the nuclear and electronic degrees of freedom and may be the ultimate goal for future work.

■ ASSOCIATED CONTENT

Supporting Information

The Supporting Information is available free of charge at https://pubs.acs.org/doi/10.1021/acs.jpcb.0c10283.

Structure preparation and the numerical setup of the BOMD simulation; coupling of the individual Bcl pigments, the forward-CT excitations in the SPP−Acc system, the numerical tests (influence of the basis set, the range separation parameter, and the coordinating His and H_2O−Gln on the excitation energies of the SPP−Acc system), and the influence of the protein environment; and an alternative approach to the evaluation of the BOMD data and excitation energies and corresponding oscillator strengths of all excitation spectra (PDF)

■ AUTHOR INFORMATION

Corresponding Author

Stephan Kümmel − *University of Bayreuth, Bayreuth 95440, Germany;* orcid.org/0000-0001-5914-6635; Email: stephan.kuemmel@uni-bayreuth.de

Authors

Moritz Brütting − *University of Bayreuth, Bayreuth 95440, Germany;* orcid.org/0000-0002-1021-0007

Johannes M. Foerster − *University of Bayreuth, Bayreuth 95440, Germany;* orcid.org/0000-0003-0442-9413

Complete contact information is available at: https://pubs.acs.org/10.1021/acs.jpcb.0c10283

Notes

The authors declare no competing financial interest.

■ ACKNOWLEDGMENTS

We gratefully acknowledge discussions with S. Kroll, I. Schelter, and L. Leppert about the reaction center of purple bacteria. S.K. thanks R. J. Cogdell for inspiring comments about light harvesting and heliobacteria. This work was supported by the Elite Study Program "Biological Physics" of the Elite Network of Bavaria. We are also grateful for support from the Bavarian State Ministry of Science, Research, and the Arts for the Collaborative Research Network "Solar Technologies go Hybrid", and from the Bavarian Polymer Institute in terms of computing resources.

■ REFERENCES

(1) Blankenship, R. E. *Molecular Mechanisms of Photosynthesis*, 2nd ed.; Wiley Blackwell: Chichester, 2014.

(2) Renger, G. *Primary Processes of Photosynthesis, Part 1: Principles and Apparatus*; Royal Society of Chemistry, 2007; pp 5−35.

(3) Curutchet, C.; Mennucci, B. Quantum Chemical Studies of Light Harvesting. *Chem. Rev.* **2017**, *117*, 294−343.

(4) Mirkovic, T.; Ostroumov, E. E.; Anna, J. M.; van Grondelle, R.; Govindjee; Scholes, G. D. Light Absorption and Energy Transfer in the Antenna Complexes of Photosynthetic Organisms. *Chem. Rev.* **2017**, *117*, 249−293.

(5) Cogdell, R. J.; Gall, A.; Köhler, J. The architecture and function of the light-harvesting apparatus of purple bacteria: from single molecules to *in vivo* membranes. *Q. Rev. Biophys.* **2006**, *39*, 227−324.

(6) Hoff, A. J.; Deisenhofer, J. Photophysics of photosynthesis. Structure and spectroscopy of reaction centers of purple bacteria. *Phys. Rep.* **1997**, *287*, 1−247.

(7) Zinth, W.; Wachtveitl, J. The First Picoseconds in Bacterial Photosynthesis? Ultrafast Electron Transfer for the Efficient Conversion of Light Energy. *ChemPhysChem* **2005**, *6*, 871−880.

(8) Amesz, J. The heliobacteria, a new group of photosynthetic bacteria. *J. Photochem. Photobiol., B* **1995**, *30*, 89−96.

(9) Neerken, S.; Amesz, J. The antenna reaction center complex of heliobacteria: compostion, energy conversion and electron transfer. *Biochim. Biophys. Acta* **2001**, *1507*, 278.

(10) Heinnickel, M.; Golbeck, J. H. Heliobacterial photosynthesis. *Photosynth. Res.* **2007**, *92*, 35−53.

(11) Oh-oka, H. Type 1 Reaction Center of Photosynthetic Heliobacteria†. *Photochem. Photobiol.* **2007**, *83*, 177−186.

(12) Gisriel, C.; Sarrou, I.; Ferlez, B.; Golbeck, J. H.; Redding, K. E.; Fromme, R. Structure of a symmetric photosynthetic reaction center-photosystem. *Science* **2017**, *357*, 1021−1025.

(13) Kimura, A.; Itoh, S. Theoretical Model of Exciton States and Ultrafast Energy Transfer in Heliobacterial Type I Homodimeric Reaction Center. *J. Phys. Chem. B* **2018**, *122*, 11852−11859.

(14) Kitoh-Nishioka, H.; Shigeta, Y.; Itoh, S.; Kimura, A. Excitonic Coupling on a Heliobacterial Symmetrical Type-I Reaction Center: Comparison with Photosystem I. *J. Phys. Chem. B* **2020**, *124*, 389−403.

(15) Tomasi, J.; Mennucci, B.; Cammi, R. Quantum Mechanical Continuum Solvation Models. *Chem. Rev.* **2005**, *105*, 2999−3094.

(16) Mennucci, B.; Corni, S. Multiscale modelling of photoinduced processes in composite systems. *Nat. Rev. Chem.* **2019**, *3*, 315−330.

(17) Aksu, H.; Schubert, A.; Geva, E.; Dunietz, B. D. Explaining Spectral Asymmetries and Excitonic Characters of the Core Pigment Pairs in the Bacterial Reaction Center Using a Screened Range-Separated Hybrid Functional. *J. Phys. Chem. B* **2019**, *123*, 8970−8975.

(18) Aksu, H.; Schubert, A.; Bhandari, S.; Yamada, A.; Geva, E.; Dunietz, B. D. On the Role of the Special Pair in Photosystems as a Charge Transfer Rectifier. *J. Phys. Chem. B* **2020**, *124*, 1987−1994.

(19) Dreizler, R. M.; Gross, E. K. U. *Density Functional Theory*; Springer: Berlin, Heidelberg, 1990.

(20) Perdew, J. P.; Kurth, S. *A Primer in Density Functional Theory*; Fiolhais, C., Nogueira, F., Marques, M., Eds.; Springer: Berlin, Heidelberg, 2003; pp 1−55.

(21) *Time-dependent Density Functional Theory*; Marques, M., Ullrich, C., Nogueira, F., Rubio, A., Burke, K., Gross, E., Eds.; Springer: Berlin, 2006.

(22) Frankcombe, T. J. Explicit calculation of the excited electronic states of the photosystem II reaction centre. *Phys. Chem. Chem. Phys.* **2015**, *17*, 3295−3302.

(23) Schelter, I.; Foerster, J. M.; Gardiner, A. T.; Roszak, A. W.; Cogdell, R. J.; Ullmann, G. M.; de Queiroz, T. B.; Kümmel, S. Assessing density functional theory in real-time and real-space as a tool for studying bacteriochlorophylls and the light-harvesting complex 2. *J. Chem. Phys.* **2019**, *151*, 134114.

(24) Kehrer, J.; Richter, R.; Foerster, J. M.; Schelter, I.; Kümmel, S. Self-interaction correction, electrostatic, and structural influences on time-dependent density functional theory excitations of bacteriochlorophylls from the light-harvesting complex 2. *J. Chem. Phys.* **2020**, *153*, 144114.

(25) Bold, B. M.; Sokolov, M.; Maity, S.; Wanko, M.; Dohmen, P. M.; Kranz, J. J.; Kleinekathöfer, U.; Höfener, S.; Elstner, M. Benchmark and performance of long-range corrected time-dependent density functional tight binding (LC-TD-DFTB) on rhodopsins and light-harvesting complexes. *Phys. Chem. Chem. Phys.* **2020**, *22*, 10500−10518.

(26) Dreuw, A.; Head-Gordon, M. Failure of Time-Dependent Density Functional Theory for Long-Range Charge-Transfer Excited States: The Zincbacteriochlorin−Bacteriochlorin and Bacteriochlorophyll−Spheroidene Complexes. *J. Am. Chem. Soc.* **2004**, *126*, 4007−4016.
(27) Iikura, H.; Tsuneda, T.; Yanai, T.; Hirao, K. A long-range correction scheme for generalized-gradient-approximation exchange functionals. *J. Chem. Phys.* **2001**, *115*, 3540−3544.
(28) Tawada, Y.; Tsuneda, T.; Yanagisawa, S.; Yanai, T.; Hirao, K. A long-range-corrected time-dependent density functional theory. *J. Chem. Phys.* **2004**, *120*, 8425.
(29) Yanai, T.; Tew, D. P.; Handy, N. C. A new hybrid exchange-correlation functional using the Coulomb-attenuating method (CAM-B3LYP). *Chem. Phys. Lett.* **2004**, *393*, 51−57.
(30) Kronik, L.; Stein, T.; Refaely-Abramson, S.; Baer, R. Excitation Gaps of Finite-Sized Systems from Optimally Tuned Range-Separated Hybrid Functionals. *J. Chem. Theory Comput.* **2012**, *8*, 1515−1531.
(31) Stein, T.; Kronik, L.; Baer, R. Reliable Prediction of Charge Transfer Excitations in Molecular Complexes Using Time-Dependent Density Functional Theory. *J. Am. Chem. Soc.* **2009**, *131*, 2818−2820.
(32) Stein, T.; Kronik, L.; Baer, R. Prediction of charge-transfer excitations in coumarin-based dyes using a range-separated functional tuned from first principles. *J. Chem. Phys.* **2009**, *131*, 244119.
(33) Karolewski, A.; Stein, T.; Baer, R.; Kümmel, S. Communication: Tailoring the optical gap in light-harvesting molecules. *J. Chem. Phys.* **2011**, *134*, 151101.
(34) Karolewski, A.; Kronik, L.; Kümmel, S. Using optimally tuned range separated hybrid functionals in ground-state calculations: Consequences and caveats. *J. Chem. Phys.* **2013**, *138*, 204115.
(35) Livshits, E.; Baer, R. A well-tempered density functional theory of electrons in molecules. *Phys. Chem. Chem. Phys.* **2007**, *9*, 2932.
(36) The numbering of the amino acid residues follows that in the Protein Data Bank file 5V8K. Only the contribution from chain A of PshA is noted explicitly.
(37) In the original work by Gisriel *et al.*[12] the interstitial molecule between Acc and Gln 458 could not be resolved properly and was only recognized as "a small molecule approximately the size of water".
(38) Vydrov, O. A.; Scuseria, G. E. Assessment of a long-range corrected hybrid functional. *J. Chem. Phys.* **2006**, *125*, 234109.
(39) Kasha, M.; Rawls, H. R.; Ashraf El-Bayoumi, M. The exciton model in molecular spectroscopy. *Pure Appl. Chem.* **1965**, *11*, 371−392.
(40) Köhler, A.; Bässler, H. *Electronic Processes in Organic Semiconductors*; Wiley-VCH Verlag GmbH & Co. KGaA, 2015.
(41) Marx, D.; Hutter, J. *Ab Initio Molecular Dynamics: Basic Theory and Advances Methods*; Cambridge University Press, 2009.
(42) Rappe, A. K.; Casewit, C. J.; Colwell, K. S.; Goddard, W. A.; Skiff, W. M. UFF, a full periodic table force field for molecular mechanics and molecular dynamics simulations. *J. Am. Chem. Soc.* **1992**, *114*, 10024−10035.
(43) Hanwell, M. D.; Curtis, D. E.; Lonie, D. C.; Vandermeersch, T.; Zurek, E.; Hutchison, G. R. Avogadro: An advanded semantic chemical editor, visualization, and analysis platform. *J. Cheminf.* **2012**, *4*, 17.
(44) Casida, M. E. *Recent Advances in Density Functional Methods*; Chong, D. P., Ed.; Recent Advances in Computational Chemistry; World Scientific: Singapore, 1995; Vol. *1*; pp 155−192.
(45) Shao, Y.; Gan, Z.; Epifanovsky, E.; Gilbert, A. T.; Wormit, M.; Kussmann, J.; Lange, A. W.; Behn, A.; Deng, J.; Feng, X.; et al. Advances in molecular quantum chemistry contained in the Q-Chem 4 program package. *Mol. Phys.* **2015**, *113*, 184.
(46) Kuritz, N.; Stein, T.; Baer, R.; Kronik, L. Charge-Transfer-Like $\pi\rightarrow\pi^*$ Excitations in Time-Dependent Density Functional Theory: A Conundrum and Its Solution. *J. Chem. Theory Comput.* **2011**, *7*, 2408−2415.
(47) Körzdörfer, T.; Sears, J. S.; Sutton, C.; Brédas, J.-L. Long-range corrected hybrid functionals for π-conjugated systems: Dependence of the range-separation parameter on conjugation length. *J. Chem. Phys.* **2011**, *135*, 204107.
(48) de Queiroz, T. B.; Kümmel, S. Charge-transfer excitations in low-gap systems under the influence of solvation and conformational disorder: Exploring range-separation tuning. *J. Chem. Phys.* **2014**, *141*, 084303.
(49) Eisenmayer, T. J.; de Groot, H. J. M.; van de Wetering, E.; Neugebauer, J.; Buda, F. Mechanism and Reaction Coordinate of Directional Charge Separation in Bacterial Reaction Centers. *J. Phys. Chem. Lett.* **2012**, *3*, 694−697.
(50) Eisenmayer, T. J.; Lasave, J. A.; Monti, A.; de Groot, H. J. M.; Buda, F. Proton Displacements Coupled to Primary Electron Transfer in the *Rhodobacter sphaeroides* Reaction Center. *J. Phys. Chem. B* **2013**, *117*, 11162−11168.
(51) Perdew, J. P.; Burke, K.; Ernzerhof, M. Generalized Gradient Approximation Made Simple. *Phys. Rev. Lett.* **1996**, *77*, 3865−3868.
(52) Ahlrichs, R.; Bär, M.; Häser, M.; Horn, H.; Kölmel, C. Electronic Structure Calculations on Workstation Computers: The Program System TURBOMOLE. *Chem. Phys. Lett.* **1989**, *162*, 165−169.
(53) Martin, R. L. Natural transition orbitals. *J. Chem. Phys.* **2003**, *118*, 4775.
(54) By manually evaluating the spatial distribution of the corresponding NTOs, we have explicitly checked for a test set of ∼ 20 excitations that the character of less than 2 % of all CT excitations has been detected erroneously. Moreover, all forward-CT excitations below 2.2 eV have been verified as such explicitly.
(55) We use the term "coupled" Q_y or Q_x, respectively, excitation to point out that the excitation appears in an oligomer of several coupled Bcl pigments. If this coupling is weak, the excitation may be localized on one or a few pigments.
(56) Ref 18 discusses the relation between symmetry breaking and the role of the special pair as a charge rectifier.
(57) Chauvet, A.; Sarrou, J.; Lin, S.; Romberger, S. P.; Golbeck, J. H.; Savikhin, S.; Redding, K. E. Temporal and spectral characterization of the photosynthetic reaction center from *Heliobacterium modesticaldum*. *Photosynth. Res.* **2013**, *116*, 1−9.
(58) Sundholm, D. A density-functional-theory study of bacteriochlorophyll b. *Phys. Chem. Chem. Phys.* **2003**, *5*, 4265.
(59) Linnanto, J.; Korppi-Tommola, J. Quantum chemical simulation of excited states of chlorophylls, bacteriochlorophylls and their complexes. *Phys. Chem. Chem. Phys.* **2006**, *8*, 663−687.
(60) Cai, Z.-L.; Crossley, M. J.; Reimers, J. R.; Kobayashi, R.; Amos, R. D. Density Functional Theory for Charge Transfer: The Nature of the N-Bands of Porphyrins and Chlorophylls Revealed through CAM-B3LYP, CASPT2, and SAC-CI Calculations. *J. Phys. Chem. B* **2006**, *110*, 15624−15632.
(61) Madjet, M. E.-A.; Müh, F.; Renger, T. Deciphering the Influence of Short-Range Electronic Couplings on Optical Properties of Molecular Dimers: Application to "Special Pairs" in Photosynthesis. *J. Phys. Chem. B* **2009**, *113*, 12603−12614.
(62) We note that our results allow for the alternative interpretation that the next cofactor OH-Chl a is involved in the first CT step.[12] Checking this is beyond our present work as OH-Chl a is not included in our model.

https://doi.org/10.1021/acs.jpcb.0c10283
J. Phys. Chem. B 2021, 125, 3468−3475

Supporting Information for

Investigating Primary Charge Separation in the Reaction Center of *Heliobacterium modesticaldum*

Journal of Physical Chemistry B

Moritz Brütting, Johannes M. Foerster, and Stephan Kümmel

Theoretical Physics IV • University of Bayreuth

Contents

Computational Methods

Structure Preparation

As a complement to the main text, we describe the preparation of the structure of the SPP–Acc system in the following. To reduce the computational effort the phythyl tails of the Bcl pigments, which just serve to keep the pigments in position, are not included in our calculations. Therefore, these hydrocarbon chains are cropped from their ester linkages to the side chains of the bacteriochlorin rings and replaced by an H atom. Furthermore, the bonds of the amino acid residues to the polypeptide chains are cut between C_α and C_β and replaced by further H atoms. This procedure keeps the terminal C_β saturated. The positions of the H atoms, which cannot be resolved by the X-ray analysis, are energetically optimized using the CHARMM force field as described in [1]. Thereby, the positions of the other atoms (C, N, O, Mg) are kept fixed.

Born-Oppenheimer Molecular Dynamics

For the BOMD simulations we use the Ahlrichs def2–SV(P) Gaussian basis set, the `m3` grid, and the resolution-of-the-identity approximation. The size of the BOMD time steps is 0.12 fs, which is small enough to resolve the fast vibrations of the H atoms. A Nosé-Hoover thermostat is used to keep the pseudo-temperature around 300 K. The thermostat relaxation time is 0.73 fs.

As fixing atomic coordinates is not supported by the standard BOMD implementation of `TURBOMOLE`, we use a modified version of a `TURBOMOLE` in-house tool originally developed by Arnim Hellweg (`TURBOMOLE` GmbH, Karlsruhe) to perform the MD cycles. In order to make our calculations transparent, we describe its functionality in the following. In each BOMD time step three separate computational tasks are performed by different (standard) `TURBOMOLE` routines: determining the electronic ground state corresponding to the current positions of the nuclei from a DFT self consistent iteration (`ridft`), calculating the (classical) forces on the nuclei resulting from this particular electronic configuration (`rdgrad`), and, finally, updating the positions and velocities of the nuclei (`frog`). The routines exchange the information on positions and velocities of the nuclei via specific files. Hence, by zeroing the velocities and forces corresponding to the fixed atoms in these files between the second and third computational step, the mechanical constraints can be ensured in a straightforward way. This particular functionality is not integrated into the standard BOMD implementation of `TURBOMOLE`.

Results and Discussion

Coupling of the Bacteriochlorophyll-Pigments

As a complement to the discussion of the excitation spectrum of the SPP–Acc system in the main text we analyze the spectra of its constituent subsystems, SPP–His and Acc–Gln, in this section. SPP–His consists of two Bcl *g'* pigments which are each coordinated by His 537 ("Bcl *g'*–His"). Similarly, Acc–Gln is composed of two Bcl *g* pigments which are each coordinated by a water molecule H-bonded by Gln 458 ("Bcl *g*–Gln"). In Figure S1 (a) the spectra of SPP–His and Bcl *g'*–His, and in (b) the spectra of Acc–Gln and Bcl *g*–Gln are compared.

We begin the discussion with case (b) as it is somewhat more transparent. Strikingly, the Q_y and Q_x transitions in the spectrum of the individual Bcl *g*–Gln correspond to two excitations with virtually the same energies in the spectrum of the Acc–Gln aggregate. To rationalize this result it is instructive to think of the coupled excitations of Acc–Gln as resulting from combined excitations of the individual Bcl *g*–Gln subsystems. This approximation is appropriate if the subsystems can be treated as well separated entities. For estimating whether this is the case one can compare the intermolecular distance of the Accs pigments (19.5 Å center-to-center) to the "diameter" of one bacteriochlorin ring (~ 7 Å). The character of the coupling among the subunits is revealed by analyzing the transition densities for the excitations of Acc–Gln. They are depicted in Figure S2. For the

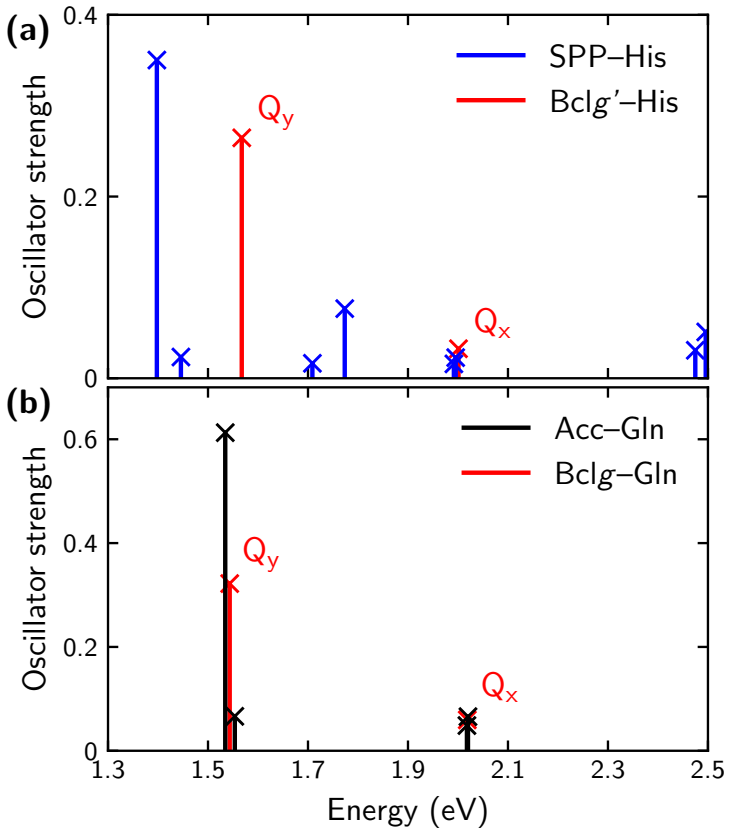

Figure S1: (a) Excitation spectra of SPP–His and a single Bcl g'–His, calculated with the 6–31G(d,p) basis set. **(b)** Excitation spectra for Acc–Gln and a single Bcl g–Gln. The Q_y and Q_x transitions of Bcl g'–His and Bcl g–Gln, respectively, are indicated.

Q_x excitations ((c) and (d)) the transition density in each case is predominantly localized on one of the Bcl g–Gln and the other chromophore carries much less transition density. In these cases, exciting Acc–Gln in fact corresponds to exciting predominantly just one of its Bcl g–Gln subunits. By contrast, the Q_y transition densities (cf. Figure S2 (a) and (b)) are fully delocalized over both rings. It turns out that the transition dipoles that one can associate with the individual Bcl g–Gln subunits are ordered roughly parallel for the transition with lower energy and higher oscillator strength, and antiparallel for the transition with higher energy and lower oscillator strength. This corresponds to the well-known concept of a J-aggregate [2, 3]: The delocalized excited state with lower (higher) energy results from the symmetric (antisymmetric) coupling of the excitations of the individual subunits.

Similar coupling mechanisms are also observed for the spectrum of SPP–His, cf. Figure S1 (a). However, here the situation is more complex due to the significantly lower inter-pigment distance – the SPP pigments have a center-to-center distance of only 5.9 Å

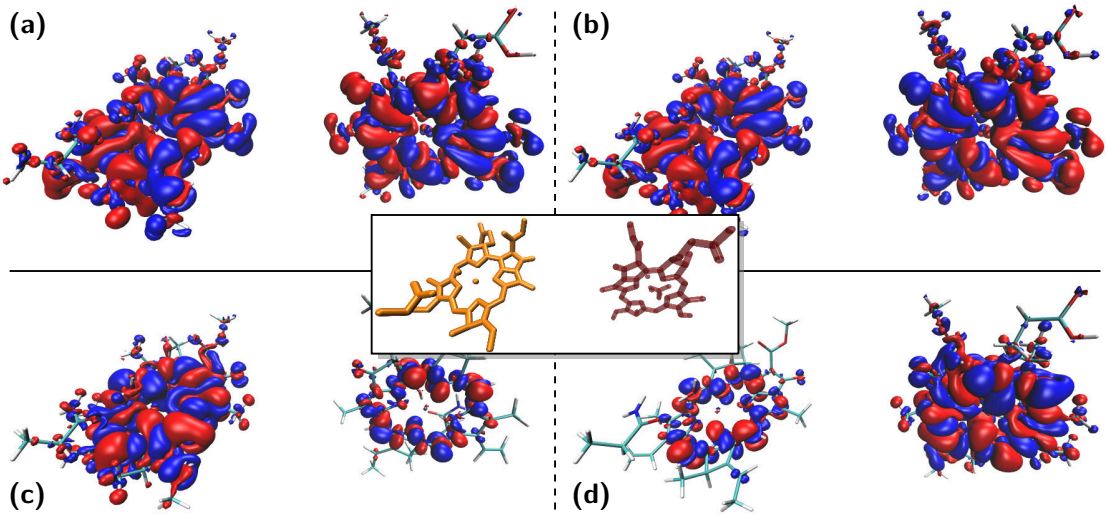

Figure S2: Transition densities of the coupled Q_y (**(a)** and **(b)**) and Q_x (**(c)** and **(d)**) transitions of Acc–Gln (in order of increasing excitation energy). Isosurfaces with isovalues of $\pm 0.0002\,a_0^{-3}$ are displayed. The isosurface corresponding to the positive (negative) isovalue is colored red (blue). The inset schematically shows the molecules without transition densities to clarify the chosen point of view.

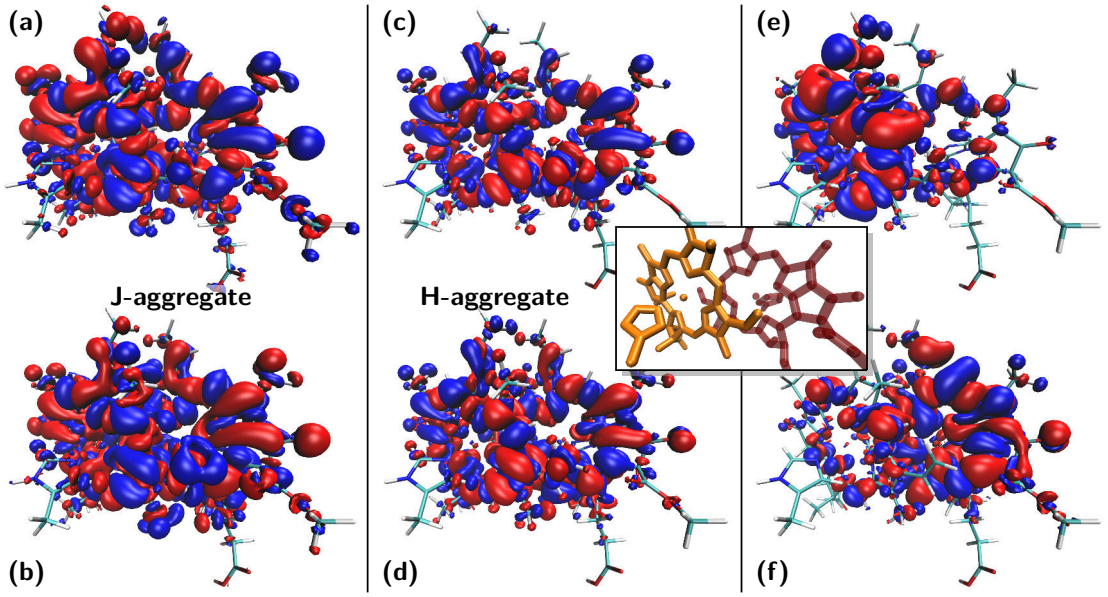

Figure S3: Transition densities of the coupled Q_y (**(a)** – **(d)**) and Q_x (**(e)** and **(f)**) transitions of SPP–His (in order of increasing excitation energy). The isosurface representation is the same as in Figure S2. The inset schematically shows the molecules without transition densities to clarify the chosen point of view.

– and, hence, stronger coupling of the individual Bcl *g'*–His subunits. Upon coupling, the Q_y excitation splits into four coupled excitations, which group into two pairs consisting of one excitation with higher and one with lower oscillator strength each. The excitation energies of these pairs are red-shifted (blue-shifted) by 0.15 eV (0.17 eV) compared to the Q_y transition of the isolated Bcl *g'*–His subunit. The Q_x transition splits, as before, into two coupled excitations of similar energy. The corresponding transition densities are depicted in Figure S3. Once again, the Q_x transition densities of the aggregate are predominantly localized on single Bcl *g'*–His entities, i. e., are rather uncoupled. The coupling of the Q_y excitations can be rationalized by the theory of molecular aggregates again. Here, the coupling of the Q_y pair with lower energy is approximately of J-type, whereas that of the pair with higher energy is of H-type. In the latter case the delocalized excited state with lower (higher) energy results from antisymmetric (symmetric) coupling. We attribute the fact that both J-type and H-type couplings emerge to the strong coupling of the SPP.

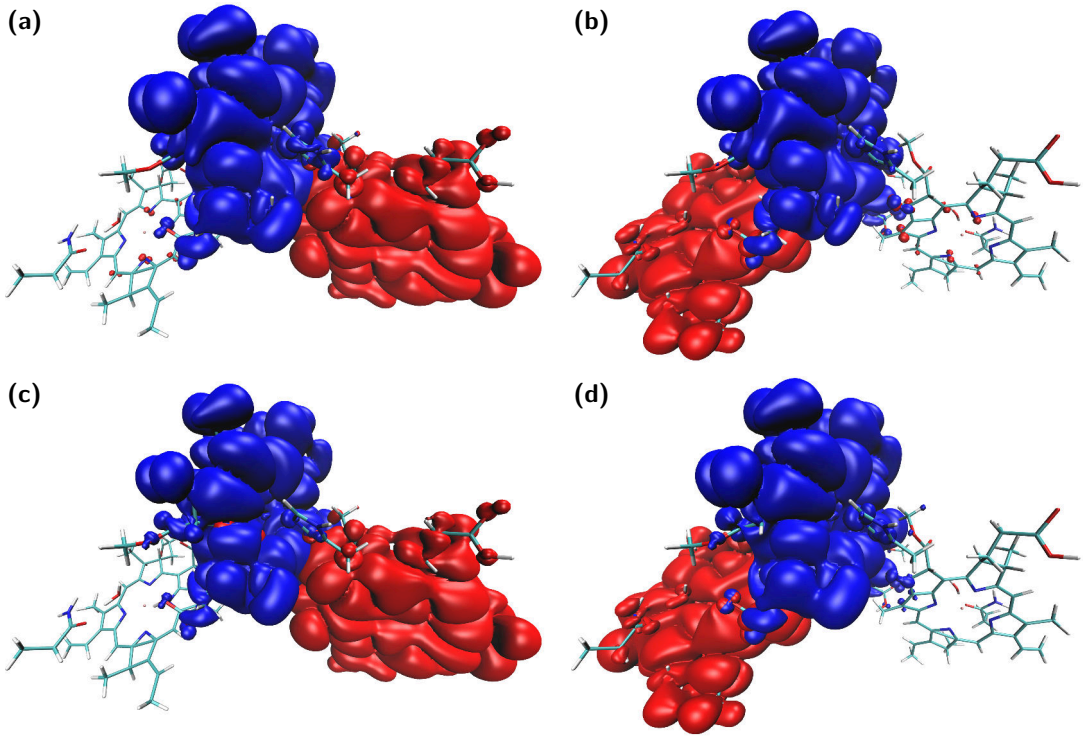

Figure S4: Hole (blue) and electron (red) densities of the first NTO pairs of the four forward-CT states identified in the spectrum of SPP–Acc. The arrangement of the subfigures is in the order of increasing excitation energy: **(a)** 1.882 eV, **(b)** 1.894 eV, **(c)** 2.240 eV, and **(d)** 2.260 eV. In all cases the isosurfaces represent an isovalue of $4 \cdot 10^{-6}\ a_0^{-3}$.

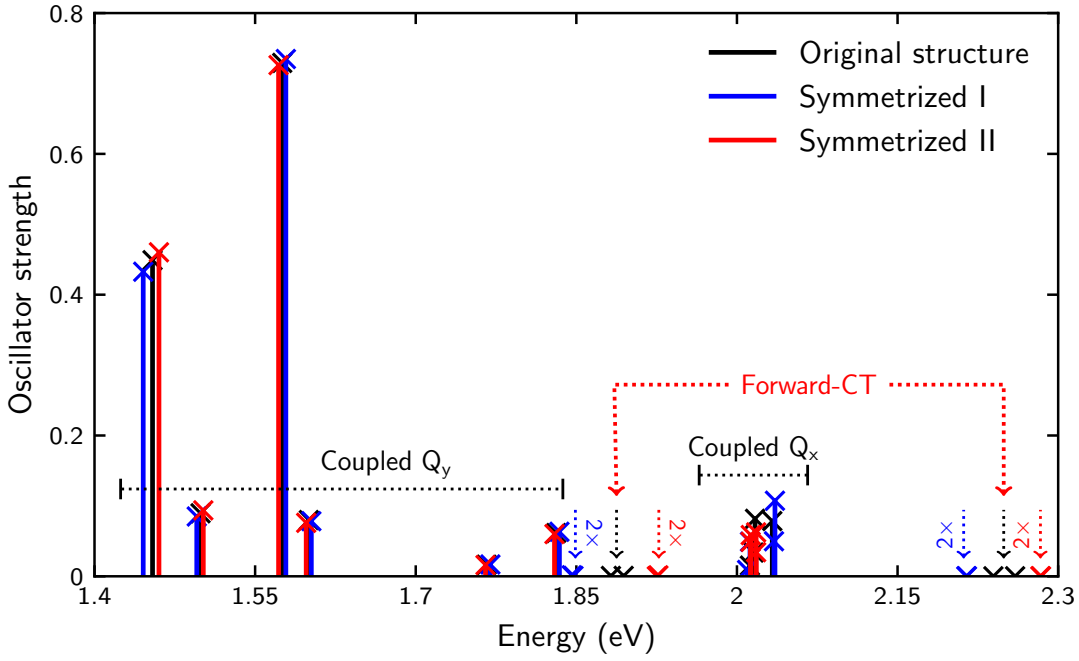

Figure S5: Comparison of the excitation spectra emerging from the original structure of SPP–Acc and its two symmetrized variants ("Symmetrized I" and "Symmetrized II"), calculated with the 6–31G basis set. The character of the states is indicated as described in the main text. Note that for the symmetrized structures the forward-CT states emerge in pairs of virtually identical excitation energies (as indicated).

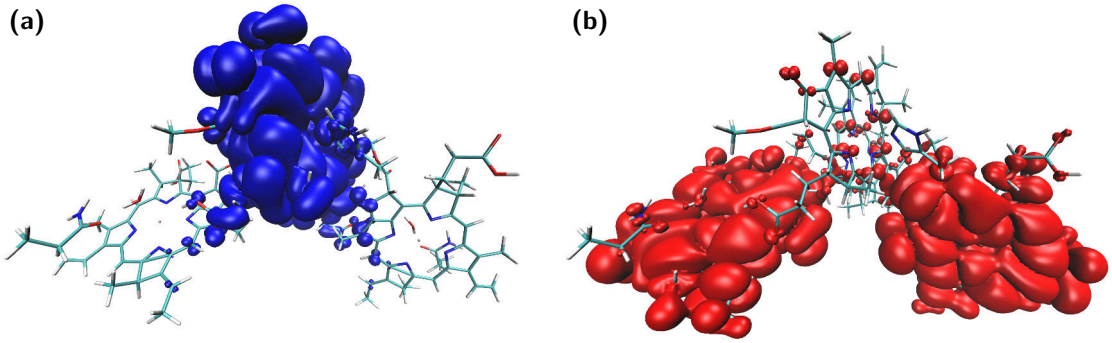

Figure S6: **(a)** Hole and **(b)** electron density of the first NTO pair of the lowest forward-CT state (at 1.846 eV) in the spectrum of one symmetrized structure of SPP–Acc ("Symmetrized I"). The corresponding NTOs of the other forward-CT states (of both symmetrized structures) look virtually identical. The isosurface representation is the same as in Figure S4.

Excited States of the SPP–Acc System

The forward-CT excitations in the SPP–Acc system emerge in pairs of two states, cf. Figure 4 (main text). Figure S4 provides additional information on the NTOs of these forward-CT states. This illustrates that CT is directed along different branches of the HbRC for the two states of such a pair. Otherwise the shape of the NTOs barely changes.

We argue in the main text, that the small energy gap of $\sim 0.02\,\mathrm{eV}$ between the individual excitations of each forward-CT state pair arises from small structural asymmetries between the different branches of the HbRC. We are able to verify this assumption by explicitly symmetrizing the structure of SPP–Acc. We generate the symmetrized structures by splitting the original unsymmetric structure into two halves, each consisting of one half of the SPP–His and Acc–Gln. We then rotate each of these two parts by 180° around the C2 symmetry axis to generate two symmetric versions of the SPP–Acc system ("symmetrized I" and "symmetrized II"). These symmetrized versions differ from the crystal structure and among each other merely in the position of the H atoms. The corresponding excitation spectra ("Symmetrized I" and "Symmetrized II") are compared in Figure S5 to the one emerging from the original structure that exhibits the slight asymmetry. The coupled Q_y and Q_x excitations are barely influenced by the symmetrization process. In contrast, the forward-CT states exhibit qualitative differences. The small energetic difference within each pair of excitations disappears, and the forward-CT excitation energies for the symmetrized structures are red-shifted (Symmetrized I) or blue-shifted (Symmetrized II), respectively, by $\sim 0.04\,\mathrm{eV}$ on average, compared to the original spectrum. An NTO analysis reveals that also the character of the forward-CT excitations changes. An example is depicted in Figure S6; the corresponding NTOs of all other forward-CT states look virtually identical. The electron density is delocalized equally over both Acc pigments for the symmetrized structures.

Numerical Tests

Q-Chem represents functions by Gaussian basis sets and we used the 6–31G, 6–31G(d,p), and 6–311G(d,p) Pople basis sets in our work. In Figure S7 we demonstrate the influence that the basis set has on the excitations of the SPP–Acc system. It turns out that the variation of the basis set leaves the order of the excitations and their relative spectral separation unchanged and merely induces a global red-shift of the excitation energies. Its magnitude decreases with increasing basis set size, from 0.05 eV between 6–31G and 6–31G(d,p) to 0.02 eV between 6–31G(d,p) and 6–311G(d,p). Therefore, we conclude that already the 6–31G basis set is sufficient to identify and observe the relative spectral positions of the forward-CT states within the spectrum.

We note that in order to ensure proper convergence of the self-consistent iterations that provide the orbitals and eigenvalues that are used in the Casida equations, the corresponding convergence threshold needs to be set to `cis_convergence 7`.

As another numerical test, we explored the influence of adding or removing the coordinating His or H_2O–Gln, respectively, in the calculations, cf. Figure S8. We find

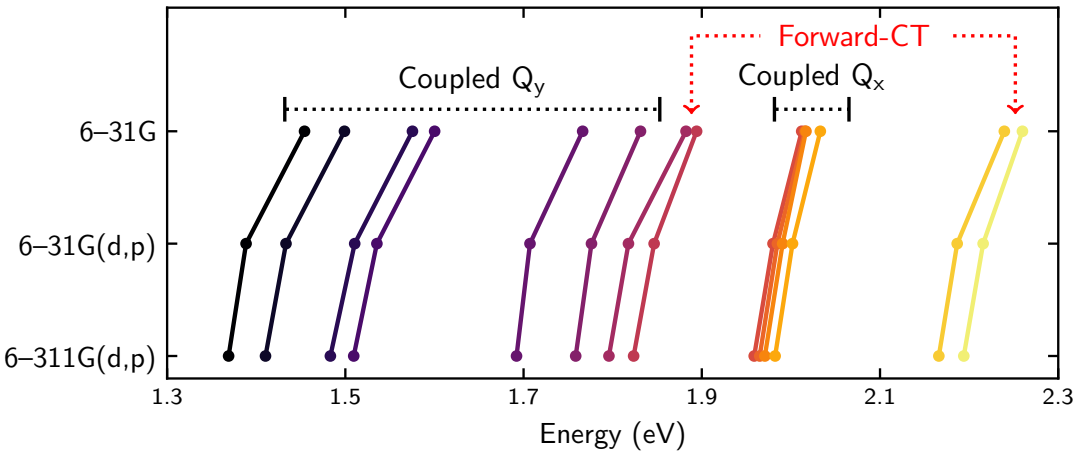

Figure S7: Excitation energies of the SPP–Acc system calculated with different basis sets: 6–31G, 6–31G(d,p), and 6–311G(d,p). The character of the excitations is indicated as in the main text. The lines connect corresponding excitations. Upon change of the basis set, the average shift of the excitation energies is −0.05 (top) and −0.02 eV (bottom).

that the coupled Q_y and Q_x excitations are barely influenced by these amino acid residues, as they are shifted by only $\lesssim 0.02$ and 0.06 eV, respectively. The forward-CT states exhibit more significant energy variations. Upon addition of His they are red-shifted by 0.50 eV. The effect of H_2O–Gln is smaller, yet still significant with a blue-shift by 0.16 eV. Hence, the influence of His and H_2O–Gln is important regarding the position of the CT states in the spectrum.

For all calculations presented in this work the range separation parameter ω of ωPBE has been set to $\omega_a = 0.171\,a_0^{-1}$. This value stems from applying the optimal tuning procedure to a single Bcl *a* [1]. The central building block of our particular system is Bcl *g'*, though. Given the similarity between these molecules it is reasonable to assume that optimal tuning for Bcl *g'* leads to a comparable range-separation parameter. We have verified this and find $\omega_g = 0.160\,a_0^{-1}$ when we optimally tune for Bcl *g'*. We also compared the spectrum of SPP–Acc calculated with ω_a to the one calculated with ω_g to clarify the influence that the range-separation parameter has on the excitation energies. This comparison is shown in Figure S9. It turns out that decreasing the range separation parameter induces a small red-shift, up to 0.07 eV for the forward-CT states. Otherwise, the spectra hardly change. We therefore conclude that the relevant physical effects that we focus on in our study are described correctly with either choice of range-separation parameter.

We would like to stress that we deliberately do not tune the range-separation parameter anew for each (sub-)system, but, e. g., calculate SPP–Acc, SPP–His, and Acc–Gln with the same value of ω. If the parameter would be tuned anew for each system, the calculations would effectively use different exchange-correlation approximations and could not be compared on the same footing. Furthermore, previous studies [4, 5] showed that

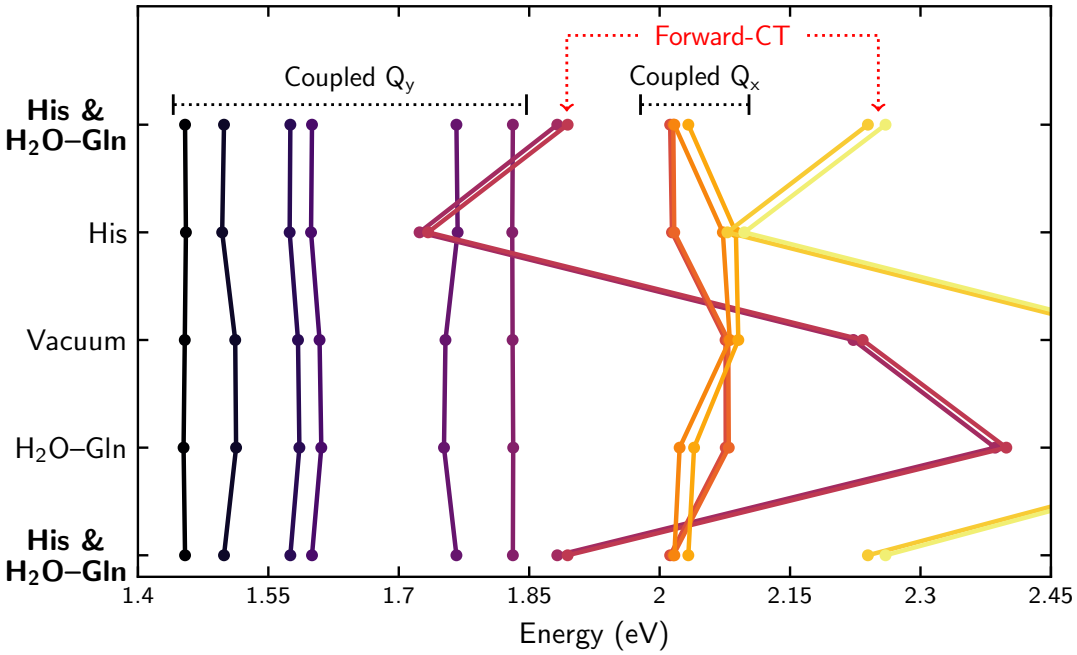

Figure S8: Influence of the coordinating molecules on the excitation energies of the SPP–Acc system, calculated with the 6–31G basis set. The configurations considered are: without any coordinating molecules ("vacuum"), with His, with H_2O–Gln, and with both His and H_2O–Gln (bold label, shown twice for ease of comparison). The latter corresponds to the spectrum shown in the main text. The order of the excitations changes, as indicated by the connecting lines.

tuning for conjugated systems of increasing size can reveal artifacts due to the semi-local functional pieces in the range-separated hybrid, leading to unrealistically low values of the range-separation parameter. Effectively, the range-separated hybrid then turns into an almost semi-local functional, with the corresponding shortcomings, e. g., regarding the description of CT excitations.

Protein Environment

In the main text, we discuss the influence of the protein environment by comparing the excitation spectrum of the SPP–Acc system embedded into a particular selection of amino acid residues, defined in Table 1 (main text), to that of the bare SPP–Acc system. We further mention that certain polar or aromatic amino acids from this selection, i. e., Trp, Thr, and Tyr, have the largest influence on the excitation spectrum. Figure S10 provides additional information on this point by comparing the excitation energies of the SPP–Acc system within three different amino acid selections – Trp; Trp, Thr, and Tyr; the full amino acid selection – to those of the SPP–Acc system alone. This graphical

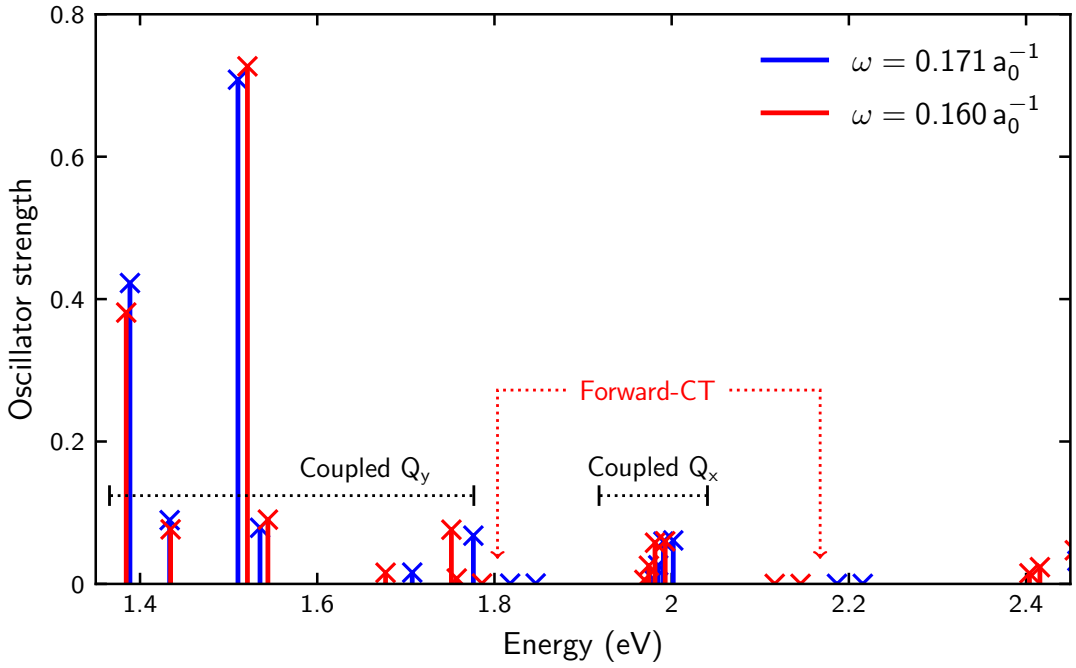

Figure S9: Excitation spectrum of SPP–Acc for different range separation parameters: $\omega = 0.171\,a_0^{-1}$ (from [1], used throughout this work) and $\omega = 0.160\,a_0^{-1}$ (from OT of a single Bcl *g'*), both calculated with the 6–31G(d,p) basis set. The character of the states is indicated as in the main text.

representation supports our conclusions from the main text, i. e., adding Trp alone red-shifts the forward-CT states by $\sim 0.14\,eV$. Adding both Thr and Tyr induces a blue-shift of similar size.

We also checked which influence the phythyl tails of the Bcl *g'* from the SPP, which coordinate the Accs, have on the excitation spectrum, cf. Figure S10. We find that they have little impact on the excitation spectrum as they only induce an overall shift $\lesssim 0.04\,eV$.

Born-Oppenheimer Molecular Dynamics

In the main text, we discuss the influence of the nuclear motion on the excitation spectrum of SPP–Acc by comparing a histogram of the forward-CT states to an ensemble-averaged excitation spectrum. The latter constitutes a transparent way of representing the huge number of excitation spectra for the different geometries from the BOMD simulation in an efficient manner. However, it does not provide insights into the nature of the underlying excitations, i. e., whether their character is similar to Q_y or Q_x transitions, and their time dynamics. A pragmatic way to shed light on this matter is to plot the time evolution of certain energy levels which represent the main features of the BOMD-based

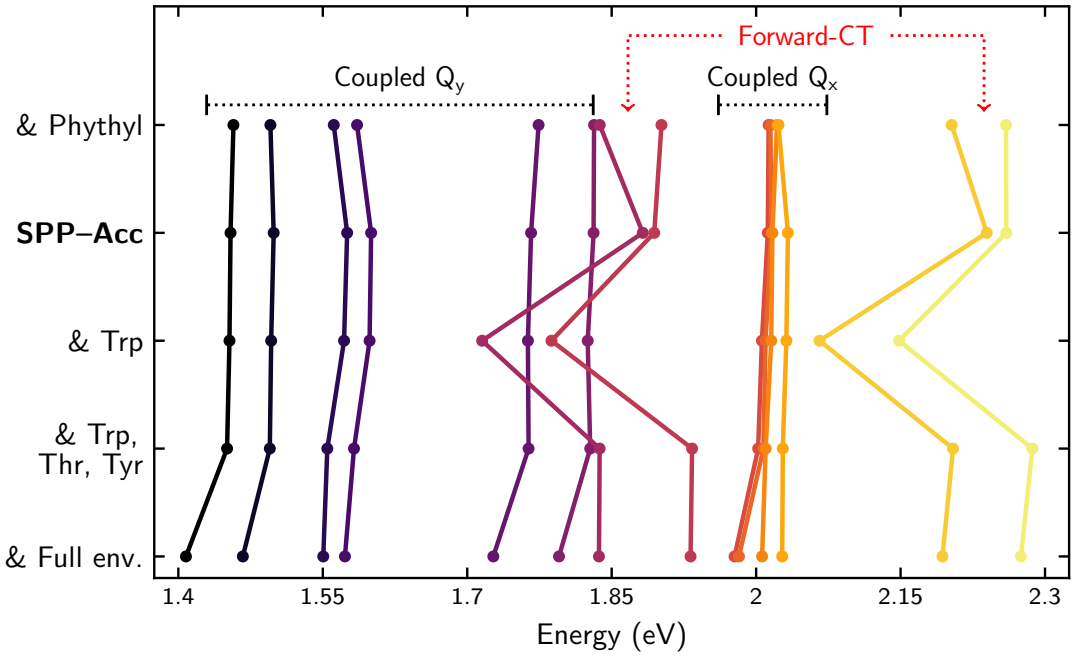

Figure S10: Influence of the environment on the excitation energies of SPP–Acc, calculated with the 6–31G basis set. Displayed are the energies of SPP–Acc alone (bold label) as well as combined with the phythyl tails of the SPP Bcl *g*'s (above) and certain amino acid selections: Trp; Trp, Thr, and Tyr; the full environment amino acid selection (cf. text). The order of the excitations changes, as indicated by the connecting lines.

excitation spectra. To that end we define three energy levels – named *main* Q_y, *mean* Q_x, and *lowest forward-CT* – whose time evolution is depicted in Figure S11.

The *main* Q_y energy level is defined as the energy of the excitation with the highest oscillator strength. This will be one of the coupled Q_y excitations. We choose this excitation for representing the typical Q_y energy, because in our experience the coupled Q_y excitations are typically dominated by a single excitation. In the case of the coupled Q_x excitations the picture is different. Normally, there is no single dominant excitation. In our experience, however, the average of the two Q_x excitations with the highest oscillator strengths represents this type of excitation well. We refer to this average energy as the *mean* Q_x energy level. On the technical side, we determine these two excitation energies by first excluding the six excitations with lowest energy (which will be the coupled Q_y's), and then searching among the remaining excitations for the two ones with the oscillator strengths. Obtaining the *lowest forward-CT* energy is straightforward as we can just extract it from the histogram data that is discussed in the main text: We select from the already-known forward-CT excitations the one with lowest energy.

From Figure S11 we can draw several conclusions which support our line of argument in the main text. The main Q_y energy level fluctuates between 1.6 and 1.8 eV, the mean

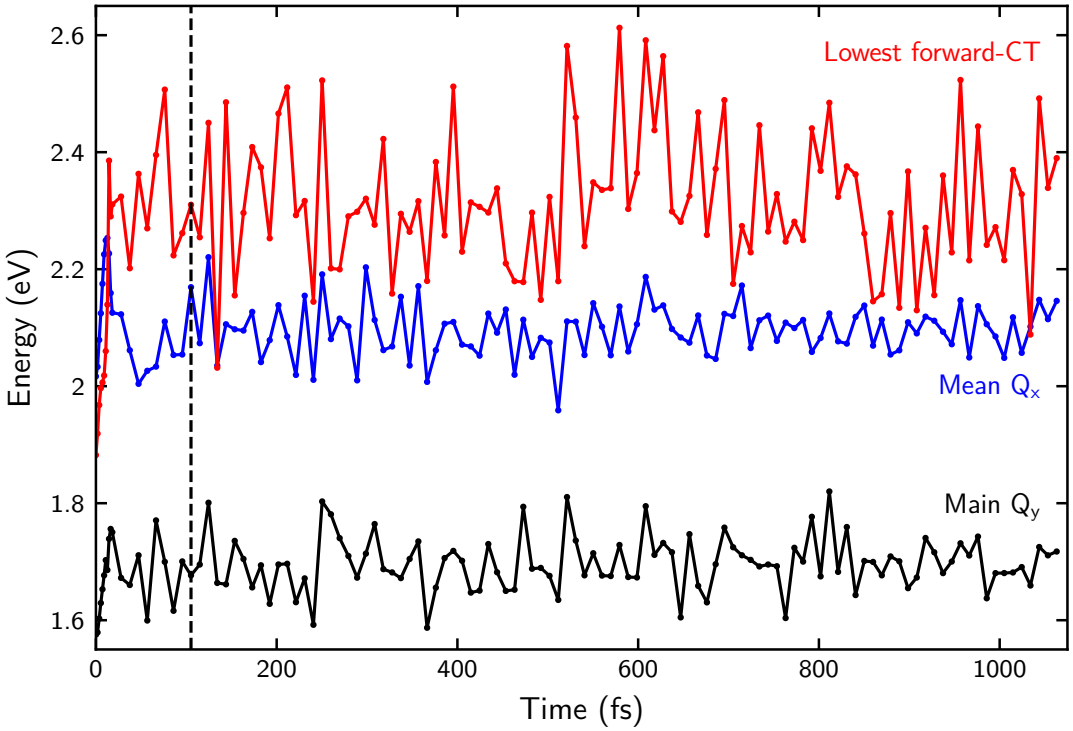

Figure S11: Time evolution of the lowest forward-CT excitation energy and energy levels representing the coupled Q_y and Q_x excitations (see text for their definitions). The dashed line (at 105.2 fs) marks the end of the equilibration phase and the beginning of the sampling for the histogram Figure 7 (main text).

Q_x between 2.0 and 2.2 eV. The lowest forward-CT excitation is somewhat higher in energy; it lies mostly between 2.1 and 2.5 eV. Notably, there are a few snapshots where the lowest forward-CT energy is close to or even below the mean Q_x. By contrast, the main Q_y and lowest forward-CT energies are separated by $\gtrsim 0.4$ eV during the whole BOMD run.

In the previous discussion we have excluded the data from the first ~ 100 fs (until the dashed line in Figure S11). During this time span, which we refer to as the "initial equilibration phase" in the main text, the pigment structures – initially in the X-ray geometry – equilibrate to the canonical ensemble mimicked by the MD simulation. The first few points in Figure S11 show this process. In the beginning, the energy levels are still close to the ones of the crystal structure, and, hence, do not represent the influence of the thermally driven nuclear motion.

Experimental Spectra

A direct comparison of our calculated spectra to the available experimental absorption spectrum of the HbRC from [6] is difficult. Our study focuses on the electronic effects in the vicinity of the special pair and our simulations neither includes the complete protein environment nor the solvent. The latter can be expected to induce a global shift of the excitation energies. Moreover, our SPP–Acc system is limited to 4 out of 58 Bcl pigments in total. Especially the OH-Chl *a* pigments, whose spectral properties differ significantly from those of Bcl *g* [7, 8] and which give rise to another absorption band peak at $\sim 1.85\,\mathrm{eV}$ in the experimental spectrum, are absent in our current simulations. However, our calculations obtain qualitative agreement with the experimental peak positions of the Q_y and Q_x bands, $\sim 1.6\,\mathrm{eV}$ and $\sim 2.2\,\mathrm{eV}$, respectively. This is in line with earlier findings showing that TDDFT with non-local exchange-correlation approximations can describe the excitations of different Bcls with reasonable accuracy [9–11].

Tables of the Excitation Spectra

For the sake of completeness and transparency the following Tables S1 to S5 list the excitation energies and oscillator strengths of the relevant excitations of all spectra depicted in the main text and the Supporting Information of this article. We chose to present the excitations in the order in which they appear in the SPP–Acc system, i. e., first the (coupled) Q_y excitations, then the forward-CT pair with lower energy, then the (coupled) Q_x excitations, and finally the second forward-CT pair (for subsystems: as far as the excitations occur).

References

[1] I. Schelter, J. M. Foerster, A. T. Gardiner, A. W. Roszak, R. J. Cogdell, G. M. Ullmann, T. B. de Queiroz, and S. Kümmel, Assessing density functional theory in real-time and real-space as a tool for studying bacteriochlorophylls and the light-harvesting complex 2, J. Chem. Phys. **151**, 134114 (2019).

[2] M. Kasha, H. R. Rawls, and M. A. El-Bayoumi, The exciton model in molecular spectroscopy, Pure Appl. Chem. **11**, 371 (1965).

[3] A. Köhler and H. Bässler, *Electronic Processes in Organic Semiconductors* (Wiley-VCH Verlag GmbH & Co. KGaA, May 2015).

[4] T. Körzdörfer, J. S. Sears, C. Sutton, and J.-L. Brédas, Long-range corrected hybrid functionals for π-conjugated systems: dependence of the range-separation parameter on conjugation length, J. Chem. Phys. **135**, 204107 (2011).

[5] T. B. de Queiroz and S. Kümmel, Charge-transfer excitations in low-gap systems under the influence of solvation and conformational disorder: exploring range-separation tuning, J. Chem. Phys. **141**, 084303 (2014).

	SPP–Acc	SPP	Acc	Bcl g' & His	Bcl g & Gln
Q_y	1.389 (0.423) 1.433 (0.090) 1.510 (0.708) 1.535 (0.079) 1.707 (0.016) 1.776 (0.068)	1.398 (0.350) 1.446 (0.023) 1.709 (0.016) 1.774 (0.077)	 1.534 (0.613) 1.554 (0.066) 	1.567 (0.265)	1.543 (0.322)
CT	1.818 (0.000) 1.847 (0.001)				
Q_x	1.980 (0.006) 1.985 (0.026) 1.991 (0.059) 2.002 (0.061)	1.992 (0.016) 1.995 (0.023) 	 2.018 (0.049) 2.020 (0.066)	2.001 (0.032)	2.019 (0.059)
CT	2.187 (0.000) 2.216 (0.000)				

Table S1: Excitation energies (in eV) and oscillator strengths (in parentheses) corresponding to Figure 4 (main text) and Figure S1. The excitations of the SPP and Accs, respectively, are arranged to indicate the correspondence to the excitations of the SPP–Acc system.

	Original structure	Symmetrized I	Symmetrized II
Q_y	1.454 (0.449) 1.499 (0.090) 1.575 (0.729) 1.600 (0.080) 1.766 (0.016) 1.831 (0.061)	1.446 (0.433) 1.496 (0.085) 1.579 (0.735) 1.603 (0.078) 1.770 (0.017) 1.834 (0.063)	1.460 (0.460) 1.502 (0.094) 1.572 (0.726) 1.598 (0.076) 1.765 (0.016) 1.830 (0.060)
CT	1.882 (0.000) 1.894 (0.001)	1.846 (0.001) 1.847 (0.001)	1.925 (0.000) 1.927 (0.001)
Q_x	2.012 (0.015) 2.016 (0.034) 2.017 (0.082) 2.033 (0.078)	2.010 (0.009) 2.012 (0.049) 2.035 (0.050) 2.035 (0.107)	2.013 (0.049) 2.013 (0.059) 2.018 (0.062) 2.018 (0.034)
CT	2.240 (0.000) 2.260 (0.000)	2.214 (0.000) 2.215 (0.000)	2.283 (0.000) 2.284 (0.000)

Table S2: Excitation energies (in eV) and oscillator strengths (in parentheses) corresponding to Figure S5.

	6–31G	$\omega = 0.171\,a_0^{-1}$ 6–31G(d,p)	6–311G(d,p)	$\omega = 0.160\,a_0^{-1}$ 6–31G(d,p)
Q_y	1.454 (0.449)	1.389 (0.423)	1.369 (0.431)	1.384 (0.381)
	1.499 (0.090)	1.433 (0.090)	1.410 (0.094)	1.435 (0.077)
	1.575 (0.729)	1.510 (0.708)	1.483 (0.706)	1.521 (0.727)
	1.600 (0.080)	1.535 (0.079)	1.509 (0.076)	1.544 (0.090)
	1.766 (0.016)	1.707 (0.016)	1.692 (0.015)	1.677 (0.016)
	1.831 (0.061)	1.776 (0.068)	1.758 (0.063)	1.751 (0.076)
CT	1.882 (0.000)	1.818 (0.000)	1.796 (0.001)	1.757 (0.008)
	1.894 (0.001)	1.847 (0.001)	1.823 (0.001)	1.786 (0.001)
Q_x	2.012 (0.015)	1.980 (0.006)	1.959 (0.003)	1.969 (0.006)
	2.016 (0.034)	1.985 (0.026)	1.965 (0.025)	1.974 (0.026)
	2.017 (0.082)	1.991 (0.059)	1.971 (0.055)	1.981 (0.058)
	2.033 (0.078)	2.002 (0.061)	1.982 (0.057)	1.993 (0.060)
CT	2.240 (0.000)	2.187 (0.000)	2.166 (0.000)	2.116 (0.000)
	2.260 (0.000)	2.216 (0.000)	2.194 (0.000)	2.146 (0.000)

Table S3: Excitation energies (in eV) and oscillator strengths (in parentheses) corresponding to Figure S7 and Figure S9.

	His & H_2O–Gln	His	H_2O–Gln	Vacuum
Q_y	1.454 (0.449)	1.455 (0.447)	1.452 (0.454)	1.454 (0.452)
	1.499 (0.090)	1.497 (0.088)	1.513 (0.102)	1.512 (0.101)
	1.575 (0.729)	1.575 (0.713)	1.586 (0.707)	1.584 (0.699)
	1.600 (0.080)	1.599 (0.079)	1.611 (0.071)	1.609 (0.070)
	1.766 (0.016)	1.768 (0.017)	1.752 (0.016)	1.754 (0.017)
	1.831 (0.061)	1.831 (0.062)	1.832 (0.074)	1.831 (0.075)
CT	1.882 (0.000)	1.724 (0.001)	2.386 (0.001)	2.223 (0.001)
	1.894 (0.001)	1.734 (0.001)	2.399 (0.001)	2.233 (0.001)
Q_x	2.012 (0.015)	2.014 (0.024)	2.023 (0.071)	2.076 (0.022)
	2.016 (0.034)	2.017 (0.032)	2.040 (0.070)	2.079 (0.046)
	2.017 (0.082)	2.073 (0.066)	2.076 (0.009)	2.081 (0.033)
	2.033 (0.078)	2.088 (0.053)	2.079 (0.033)	2.091 (0.062)
CT	2.240 (0.000)	2.078 (0.015)	2.732 (0.001)	2.570 (0.000)
	2.260 (0.000)	2.097 (0.001)	2.755 (0.003)	2.587 (0.000)

Table S4: Excitation energies (in eV) and oscillator strengths (in parentheses) corresponding to Figure S8.

	No env.	Phythyl	Trp	Trp–Thr–Tyr	Full env.
Q_y	1.454 (0.449)	1.457 (0.468)	1.453 (0.431)	1.451 (0.440)	1.408 (0.418)
	1.499 (0.090)	1.496 (0.091)	1.496 (0.095)	1.495 (0.105)	1.467 (0.083)
	1.575 (0.729)	1.561 (0.661)	1.572 (0.780)	1.555 (0.788)	1.550 (0.765)
	1.600 (0.080)	1.586 (0.071)	1.599 (0.076)	1.582 (0.063)	1.573 (0.056)
	1.766 (0.016)	1.774 (0.019)	1.716 (0.001)	1.764 (0.022)	1.727 (0.020)
	1.831 (0.061)	1.832 (0.064)	1.788 (0.001)	1.828 (0.048)	1.795 (0.042)
CT	1.882 (0.000)	1.838 (0.002)	1.763 (0.020)	1.837 (0.001)	1.837 (0.001)
	1.894 (0.001)	1.902 (0.001)	1.825 (0.054)	1.933 (0.001)	1.932 (0.001)
Q_x	2.012 (0.015)	2.013 (0.004)	2.006 (0.012)	2.002 (0.012)	1.978 (0.016)
	2.016 (0.034)	2.015 (0.054)	2.010 (0.041)	2.008 (0.072)	1.982 (0.051)
	2.017 (0.082)	2.022 (0.050)	2.016 (0.076)	2.010 (0.050)	2.006 (0.080)
	2.033 (0.078)	2.023 (0.106)	2.031 (0.073)	2.028 (0.074)	2.027 (0.076)
CT	2.240 (0.000)	2.203 (0.000)	2.066 (0.002)	2.204 (0.000)	2.193 (0.000)
	2.260 (0.000)	2.260 (0.000)	2.148 (0.000)	2.287 (0.000)	2.275 (0.000)

Table S5: Excitation energies (in eV) and oscillator strengths (in parentheses) corresponding to Figure 6 (main text) and Figure S10.

[6] A. Chauvet, J. Sarrou, S. Lin, S. P. Romberger, J. H. Golbeck, S. Savikhin, and K. E. Redding, Temporal and spectral characterization of the photosynthetic reaction center from *Heliobacterium modesticaldum*, Photosynth. Res. **116**, 1 (2013).

[7] M. Kobayashi, E. J. van de Meent, C. Erkelens, J. Amesz, I. Ikegami, and T. Watanabe, Bacteriochlorophyll *g* epimer as a possible reaction center component of heliobacteria, Biochim. Biophys. Acta **1057**, 89 (1991).

[8] E. J. van de Meent, M. Kobayashi, C. Erkelens, P. A. van Veelen, J. Amesz, and T. Watanabe, Identification of 8^1-hydroxychlorophyll *a* as a functional reaction center pigment in heliobacteria, Biochim. Biophys. Acta **1058**, 356 (1991).

[9] D. Sundholm, A density-functional-theory study of bacteriochlorophyll b, Phys. Chem. Chem. Phys. **5**, 4265 (2003).

[10] J. Linnanto and J. Korppi-Tommola, Quantum chemical simulation of excited states of chlorophylls, bacteriochlorophylls and their complexes, Phys. Chem. Chem. Phys. **8**, 663 (2006).

[11] Z.-L. Cai, M. J. Crossley, J. R. Reimers, R. Kobayashi, and R. D. Amos, Density Functional Theory for Charge Transfer: The Nature of the N-Bands of Porphyrins and Chlorophylls Revealed through CAM-B3LYP, CASPT2, and SAC-CI Calculations, J. Phys. Chem. B **110**, 15624 (2006).

Reprint of publication [B2]

Publication [B2]

M. Brütting, H. Bahmann, and S. Kümmel

Hybrid functionals with local range separation: Accurate atomization energies and reaction barrier heights

J. Chem. Phys. **156**, 104109 (2022)

DOI: 10.1063/5.0082957

Author contribution statement: M.B. and S.K. conceptualized the work and discussed the functional construction with support from H.B. M.B. implemented the functionals and did the calculations with help from H.B. M.B. prepared all the tables. M.B. and S.K. wrote the first version of the manuscript. All authors discussed the results and the final version of the manuscript.

The Journal of Chemical Physics ARTICLE scitation.org/journal/jcp

Hybrid functionals with local range separation: Accurate atomization energies and reaction barrier heights

Cite as: J. Chem. Phys. 156, 104109 (2022); doi: 10.1063/5.0082957
Submitted: 20 December 2021 • Accepted: 21 February 2022 •
Published Online: 14 March 2022

Moritz Brütting,[1] Hilke Bahmann,[2] and Stephan Kümmel[1,a)]

AFFILIATIONS

[1] Theoretical Physics IV, University of Bayreuth, 95440 Bayreuth, Germany
[2] Physical and Theoretical Chemistry, Saarland University, 66123 Saarbrücken, Germany

[a)] Author to whom correspondence should be addressed: stephan.kuemmel@uni-bayreuth.de

ABSTRACT

Range-separated hybrid approximations to the exchange–correlation density functional mix exact and semi-local exchange in a position-dependent manner. In their conventional form, the range separation is controlled by a constant parameter. Turning this constant into a density functional leads to a locally space-dependent range-separation function and thus a more powerful and flexible range-separation approach. In this work, we explore the self-consistent implementation of a local range-separated hybrid, taking into account a one-electron self-interaction correction and the behavior under uniform density scaling. We discuss different forms of the local range-separation function that depend on the electron density, its gradient, and the kinetic energy density. For test sets of atomization energies, reaction barrier heights, and total energies of atoms, we demonstrate that our best model is a clear improvement over common global range-separated hybrid functionals and can compete with density functionals that contain multiple empirical parameters. Promising results for equilibrium bond lengths, harmonic vibrational frequencies, and vertical ionization potentials further underline the potential and flexibility of our approach.

I. INTRODUCTION

Over the past two decades, range-separated hybrid (RSH) functionals[1,2] have come into widespread use within density functional theory (DFT)[3,4] and its time-dependent variant (TDDFT).[5,6] They have demonstrated their power especially in the context of calculating callenging spectroscopic properties,[7] such as excitations with charge-transfer character,[8–11] and fundamental gaps.[12–14]

At the heart of the RSH concept is the splitting of the Coulomb interaction into a long-range and a short-range component.[15,16] For reasons of computational performance in quantum chemistry programs that use Gaussian basis sets, this is most commonly done by employing the Gaussian error function erf(·),

$$\frac{1}{|\boldsymbol{r}-\boldsymbol{r}'|} = \underbrace{\frac{\mathrm{erf}\big(\omega_\sigma(\boldsymbol{r})|\boldsymbol{r}-\boldsymbol{r}'|\big)}{|\boldsymbol{r}-\boldsymbol{r}'|}}_{\text{long range}} + \underbrace{\frac{1-\mathrm{erf}\big(\omega_\sigma(\boldsymbol{r})|\boldsymbol{r}-\boldsymbol{r}'|\big)}{|\boldsymbol{r}-\boldsymbol{r}'|}}_{\text{short range}}. \quad (1)$$

The transition between long range and short range is controlled by the (space-dependent) range-separation function (RSF) $\omega_\sigma(\mathbf{r})$. To keep the physics transparent, we here deliberately do not consider generalizations of Eq. (1) that include a fraction of short-range exact exchange via a further parameter.[17,18] In the limit $\omega_\sigma \to \infty$, the splitting (1) reduces to its long-range part, and in the opposite limit, $\omega_\sigma \to 0$, it reduces to its short-range part. Formally, the RSF is a functional of the density.[19,20] However, in practical realizations, the RSF has almost always been replaced by a constant parameter $\omega_0 = \omega_\uparrow(\mathbf{r}) \equiv \omega_\downarrow(\mathbf{r})$.

Depending on the systems of interest, past work has modeled either the short-range or the long-range contribution of the interaction [cf. Eq. (1)] to the exchange energy by exact exchange.[21] A prominent example for the former is the Heyd–Scuseria–Ernzerhof (HSE) functional, which is typically employed in solid-state calculations.[22–24] In our work here, we focus on functionals in which the proper long-range asymptotics of the potential is of interest, and thus, the long-range contribution to the exchange energy is covered by exact exchange,

$$E_{\mathrm{LR-x}}^{\mathrm{EXX}} = \sum_{\sigma} \int \mathrm{d}\boldsymbol{r}\, \varepsilon_{\mathrm{LR-x}\sigma}^{\mathrm{EXX}}(\boldsymbol{r}) = -\frac{1}{2}\sum_{\sigma}\sum_{i,j} \int \mathrm{d}\boldsymbol{r} \int \mathrm{d}\boldsymbol{r}'\, \phi_{i\sigma}^{*}(\boldsymbol{r})\phi_{j\sigma}^{*}(\boldsymbol{r}') \times \frac{\mathrm{erf}\left(\omega_{\sigma}(\boldsymbol{r})|\boldsymbol{r}-\boldsymbol{r}'|\right)}{|\boldsymbol{r}-\boldsymbol{r}'|}\phi_{i\sigma}(\boldsymbol{r}')\phi_{j\sigma}(\boldsymbol{r}), \tag{2}$$

while its short-range counterpart is approximated by a short-range semi-local density functional, $E_{\mathrm{SR-x}}^{\mathrm{DFA}}$. The correlation energy that is modeled by a semi-local approximation, $E_{\mathrm{c}}^{\mathrm{DFA}}$ is independent of the choice for the RSF. In summary, the exchange–correlation (xc) energy of RSHs of the form (1) is split into three distinct parts,

$$E_{\mathrm{xc}}^{\mathrm{RSH}} = E_{\mathrm{LR-x}}^{\mathrm{EXX}} + E_{\mathrm{SR-x}}^{\mathrm{DFA}} + E_{\mathrm{c}}^{\mathrm{DFA}}. \tag{3}$$

Hence, the range-separation approach allows for a more flexible mixing of semi-local and exact exchange than, e.g., global hybrid functionals, and its form is well suited to capture the interplay between long- and short-range interactions. As a consequence, RSHs have favorable properties, such as the correct asymptotic form of the xc potential,[25,26] due to full exact exchange at long range while maintaining the compatibility of semi-local exchange and correlation at short range.

In practice, the range separation is commonly controlled by a constant parameter. Determining this parameter empirically by optimizing to a reference test set has led to some widely and effectively used functionals.[17,24,27,28] A different and very successful approach is to fix the value of the constant parameter by a non-empirical optimal-tuning procedure.[12,20,29,30] The latter is based on enforcing the IP theorem,[31–33] i.e., the identity of the ionization potential (IP) as computed from a total energy difference, and the negative of the highest occupied molecular orbital (HOMO) eigenvalue for a particular system of interest,

$$-\varepsilon_{\mathrm{HOMO}} \overset{!}{=} \mathrm{IP} \equiv E_0^{(N-1)} - E_0^{(N)}. \tag{4}$$

The optimal-tuning approach can be seen as an implicit way to account for the density dependence of the RSF. However, the fact that the density dependence is not known explicitly prevents one to develop this idea further. Likewise, taking this idea seriously would require that one considers the additional contributions to the functional derivative of the long-range exchange energy that arise from the density dependence of the RSF.[34] This cannot be done, though, as the explicit form of this density dependence remains unknown within the optimal-tuning approach. Moreover, this system-specific way of determining the range-separation parameter violates the physical concept of size consistency.[20,34,35] This hampers, e.g., the reliable prediction of atomization energies from optimally tuned RSHs. A computational disadvantage of the optimal-tuning procedure is that additional DFT calculations are required to determine the range-separation parameter. A further drawback that is conceptually inherent[36] to the optimal tuning approach can occur for systems of increasing size in which the orbitals delocalize:[37,38] In such cases, the tuning procedure tends to spuriously lead to an increasingly semilocal functional with increasing extension of the system.[39] Special measures must be taken if one wants to use optimal tuning in such situations.[14,40]

Apart from that, the usual RSH functionals with a constant range-separation parameter suffers from one-electron self-interaction errors.[41,42] This constitutes a formal deficiency as the important limiting case of one-electron systems is not described correctly, and it can have practical relevance regarding the accurate description of properties related to one-electron processes. Furthermore, experience so far suggests that one cannot choose a universal value for the range-separation parameter that would be appropriate for the description of both ground-state properties, such as atomization energies, and charge-transfer excitations or IPs.[43] This problem is shared by many functionals that combine exact and semi-local exchange, as discussed in Refs. 44 and 45, and constitutes a parameter dilemma.

Equation (1) reveals, however, that the RSH approach in itself already offers the chance to address these issues by explicitly taking into account the density dependence of the RSF, i.e., by going from the commonly used *global* to a *local* RSH functional. In doing so, one encounters two major challenges: finding an appropriate model for the RSF and developing a self-consistent implementation of local RSHs.

To the best of our knowledge, the work of Krukau *et al.*[46] constitutes the first tested and successful development of a density-dependent RSF. In their work, Krukau *et al.* proposed an expansion in terms of the spin-density $n_{\sigma}(\mathbf{r})$ and its gradient $|\nabla n_{\sigma}(\mathbf{r})|$. They achieved their best results with

$$\omega_{\sigma}(\boldsymbol{r}) = \eta\frac{|\nabla n_{\sigma}(\boldsymbol{r})|}{n_{\sigma}(\boldsymbol{r})}, \tag{5}$$

where they determined $\eta = 0.135$ empirically by optimization with respect to atomization energies. Aschebrock and Kümmel[47] further improved this RSF by taking into account the scaling behavior in the high-density limit[48,49] via an additional logarithmic term,

$$\omega_{\sigma}(\boldsymbol{r}) = \eta\frac{|\nabla n_{\sigma}(\boldsymbol{r})|}{n_{\sigma}(\boldsymbol{r})}\left(1+\ln\left(1+\delta\frac{|\nabla n_{\sigma}(\boldsymbol{r})|}{n_{\sigma}(\boldsymbol{r})}\right)\right). \tag{6}$$

Here, δ is a further parameter that was determined empirically as no constraint that would fix it could be found. More importantly yet, Aschebrock and Kümmel proposed a way of constructing a local RSH that eliminates one-electron self-interaction,[42] thus suggesting a way to resolve one of the two major drawbacks connected to a constant range-separation parameter. Recently, Maier *et al.*[50] showed that Eq. (5) can be rationalized from the expansion of the exchange energy in terms of the reduced density gradient. They, thus, obtained $\eta = \sqrt{5}/18 \simeq 0.124$ as a non-empirical estimate for the prefactor in Eq. (5).

Further important progress has recently also been made with respect to how local RSHs can be used computationally. Klawohn and Bahmann[51] reported the first self-consistent implementation of local RSHs. As compared to global RSHs, the numerical realization of RSHs with local range separation is challenging: While for RSHs with a constant range-separation parameter a fully analytical integration of the Fock integral (2) is feasible in implementations using Gaussian basis sets, the density dependence of the RSF prohibits to apply this strategy directly to local RSHs. Instead, similar to previously introduced approaches for global and local hybrids,[52–54] one integration ("over $\mathbf{r}'$") is computed analytically on each point

of a numerical grid, while the second integral ("over $\mathbf{r}$") is performed numerically on this grid. The latter becomes computationally efficient by employing several prescreening techniques.[55,56] Not having this implementation at their hands, the earlier approaches by Krukau *et al.*[46] and Aschebrock and Kümmel[47] relied on the hyper-generalized gradient approximation (GGA) to Eq. (2) instead. By that, they could approximately evaluate the long-range exact exchange energy numerically without the above-mentioned specialized integration technique. However, self-consistent local RSH calculations could not be done in these earlier works.

In this work, we take a step forward by bringing together the developments in both fields. That is, we integrate local RSHs with freedom from one-electron self-interaction as proposed by Aschebrock and Kümmel[47] into the self-consistent implementation by Klawohn and Bahmann.[51] Thereby, we are motivated by the previous study[47] in which promising results had been obtained in non-selfconsistent calculations with a local RSH functional with self-interaction correction (SIC). In particular, when optimizing the parameters η and δ in Eq. (6) to atomization energies, it turned out that a broad band of tuples (η, δ) is able to provide a description very close to the global optimum. This raised the hope that the existing degree of freedom can be used to optimize for further properties.

Our work stands in contrast to the recent work of Maier *et al.*,[50] which has put the usefulness of the local RSH approach into question. These authors have compared RSHs with a constant range-separation parameter and RSFs based upon the electron density and its gradient, similar to Eq. (5), for a set of atomization energies and reaction barriers. They concluded that local RSHs cannot provide a relevant improvement in accuracy over global RSHs. Contrary to these conclusions, our results show that adding SIC to local RSH functionals leads to a significant improvement in accuracy, and thus, using a local functional instead of a constant parameter for range separation becomes very beneficial.

The outline of our paper is as follows: In Sec. II, we briefly review the known formal constraints on the RSF. Then, we discuss a way of integrating these constraints into a model for the RSF. In Sec. III, we describe how we model the semi-local components of the xc energy by the local density approximation (LDA). Afterward, in Secs. IV–VI, we present and discuss the results from our local RSH calculations. To put our results into perspective, we compare them to semi-local, global hybrid, and conventional (i.e., global) RSH density functional approximations. In the course of this work, our focus is twofold: On the one hand, we highlight the conceptual advances that local RSH functionals can provide. On the other hand, we demonstrate that the accuracy achieved by a local model for range separation that fully takes advantage of those advances can be very high, rivaling the accuracy of functionals with up to ~ 60 empirical parameters.

II. THE RANGE-SEPARATION FUNCTION

We begin with a brief review of the known formal constraints on the density-dependent RSF in Sec. II A. These are important as guidelines and motivate the locally space-dependent RSF, which we discuss in Secs. II B and II C. We model the RSF as a functional of the spin-density $n_\sigma(\mathbf{r})$, its gradient $|\nabla n_\sigma(\mathbf{r})|$, and the non-interacting kinetic energy density,

$$\tau_\sigma(\boldsymbol{r}) = \frac{1}{2}\sum_i |\nabla \phi_{i\sigma}(\boldsymbol{r})|^2. \tag{7}$$

Here and in the following, we use Hartree atomic units.

Instead of considering the most general case of a RSF $\omega_\sigma(\mathbf{r}, \mathbf{r}')$ that depends on both electronic coordinates $\mathbf{r}$ and $\mathbf{r}'$, we focus on the special case of a locally space-dependent $\omega_\sigma(\mathbf{r})$. This corresponds to Eq. (1), which is the functional form that has been studied in previous works.[46,47,50,51] For this case, we have guidance in earlier functional development, such as local hybrid constructions.[45,57–64,93] The seeming asymmetry with respect to $\mathbf{r}$ and $\mathbf{r}'$ is not problematic, as pointed out in Ref. 46: The long-range exchange energy (2) can formally always be symmetrized with respect to the interchange of electrons $(\mathbf{r} \leftrightarrow \mathbf{r}')$.

A. Formal constraints

A first natural constraint on the RSF is the homogeneous-electron-gas limit. If the semi-local ingredients to Eq. (3) correctly describe this limit (as e.g., LDA does), it is reasonable to require[47]

$$\omega_\sigma(\boldsymbol{r}) \to 0 \tag{8}$$

in the limit of a slowly varying density. If one would enforce $\omega_\sigma(\mathbf{r}) \to \infty$ in this limit, the combination with, e.g., LDA correlation would still be formally exact, but Fock exchange is tedious to evaluate for large systems that do not have an appreciable eigenvalue gap.

Second, it is instructive to consider the gradient expansion of the exchange energy density (per volume),[4]

$$\varepsilon_{\mathrm{x}\sigma}(\boldsymbol{r}) = \varepsilon_{\mathrm{x}\sigma}^{\mathrm{LDA}}(\boldsymbol{r})\left(1 + \frac{10}{81}s_\sigma^2(\boldsymbol{r}) + \cdots\right), \tag{9}$$

where

$$\varepsilon_{\mathrm{x}\sigma}^{\mathrm{LDA}}(\boldsymbol{r}) = -\frac{3}{4\pi}k_{\mathrm{F}\sigma}(\boldsymbol{r})n_\sigma(\boldsymbol{r}) \tag{10}$$

is the LDA exchange energy density and

$$s_\sigma(\boldsymbol{r}) = \frac{|\nabla n_\sigma(\boldsymbol{r})|}{2k_{\mathrm{F}\sigma}(\boldsymbol{r})n_\sigma(\boldsymbol{r})} \tag{11}$$

is the reduced density gradient.[67] Here, $k_{\mathrm{F}\sigma} = \left(6\pi^2 n_\sigma\right)^{1/3}$ is the Fermi wave vector. Following Maier *et al.*,[50] one can obtain a non-empirical expression for the RSF by imposing the equality of Eq. (9) to the leading terms of the long-range and short-range exchange energy density. That is,

$$\varepsilon_{\mathrm{x}\sigma}(\boldsymbol{r}) \equiv \varepsilon_{\mathrm{LR-x}\sigma}^{\mathrm{EXX}}(\boldsymbol{r}) + \varepsilon_{\mathrm{SR-x}\sigma}^{\mathrm{LDA}}(\boldsymbol{r}), \tag{12}$$

with[65]

$$\varepsilon_{\mathrm{LR-x}\sigma}^{\mathrm{EXX}}(\boldsymbol{r}) = -\frac{n_\sigma(\boldsymbol{r})\omega_\sigma(\boldsymbol{r})}{\sqrt{\pi}} + \ldots \tag{13}$$

and

$$\varepsilon_{\mathrm{SR-x}\sigma}^{\mathrm{LDA}}(\boldsymbol{r}) = \varepsilon_{\mathrm{x}\sigma}^{\mathrm{LDA}}(\boldsymbol{r})\left(1 - \frac{4\sqrt{\pi}}{3}\frac{\omega_\sigma(\boldsymbol{r})}{k_{\mathrm{F}\sigma}(\boldsymbol{r})} + 2\frac{\omega_\sigma^2(\boldsymbol{r})}{k_{\mathrm{F}\sigma}^2(\boldsymbol{r})} + \cdots\right), \tag{14}$$

with the short-range LDA exchange detailed in Sec. III. As the terms linear in ω_σ in Eqs. (13) and (14) cancel each other out, one ends up with

$$\omega_\sigma(\boldsymbol{r}) = \frac{\sqrt{5}}{18}\frac{|\nabla n_\sigma(\boldsymbol{r})|}{n_\sigma(\boldsymbol{r})} \simeq 0.124\,\frac{|\nabla n_\sigma(\boldsymbol{r})|}{n_\sigma(\boldsymbol{r})} \tag{15}$$

as an expression for the RSF. Interestingly, this has the same form and a similar prefactor as the RSF proposed by Krukau *et al.*[46] In passing, we note that the derivation of Eq. (15) is specifically tied to employing LDA as the short-range exchange functional; an extension to GGAs may not be straightforward.[50]

Third, we consider the scaling behavior of the RSF under uniform density scaling to the high-density limit,[48]

$$n(\boldsymbol{r}) \to n_\lambda(\boldsymbol{r}) = \lambda^3 n(\lambda\boldsymbol{r}), \quad \text{as} \quad \lambda \to \infty. \tag{16}$$

In this limit, the exact exchange energy should prevail,[49] and hence, in the context of local RSHs, the long-range exchange contribution to Eq. (3) should dominate. This is ensured by a RSF that scales up faster than linearly under a uniform scaling of the density,[46,47]

$$\omega_\sigma([n_\lambda],\boldsymbol{r}) \gg \lambda\omega_\sigma([n],\lambda\boldsymbol{r}) \quad \text{as} \quad \lambda \to \infty. \tag{17}$$

Last but not least, the RSF should be chosen such that the condition of being one-electron self-interaction free,[42]

$$E_\mathrm{H}[n_{i\sigma}(\boldsymbol{r})] + E_\mathrm{xc}[n_{i\sigma}(\boldsymbol{r}), 0] \equiv 0, \tag{18}$$

where E_H denotes the usual Hartree energy, is upheld for one-electron ground-state densities. In our approach, we follow the logic of self-interaction corrections and ensure this condition for any one-spin-orbital density $n_{i\sigma}(\boldsymbol{r}) = |\phi_{i\sigma}(\boldsymbol{r})|^2$. Subtleties inherent to this choice that stem from $|\phi_{i\sigma}(\boldsymbol{r})|^2$ not necessarily having ground-state character have been discussed in Ref. 66, Sec. II A. Being one-electron self-interaction free is achieved when, first, a one-electron self-interaction free density functional is used for $E_\mathrm{c}^\mathrm{DFA}$ and, second, when

$$\omega_\sigma(\boldsymbol{r}) \to \infty \tag{19}$$

for one-electron densities.[47] In this limit, the exchange contribution reduces to exact exchange, which is one-electron self-interaction free by definition.

B. The model

In this work, we utilize the following mathematical structure to integrate conditions (8), (15), (17), and (19) into a model for a locally space-dependent RSF,[47]

$$\omega_\sigma(\boldsymbol{r}) = \Omega_\sigma([n_\sigma, |\nabla n_\sigma|], \boldsymbol{r})\,\Theta\big(z_\sigma(\boldsymbol{r})\zeta^2(\boldsymbol{r})\big). \tag{20}$$

Therein, Ω_σ is a functional of the spin-density and its gradient, which we approximate by

$$\Omega_\sigma(\boldsymbol{r}) = c_1\frac{|\nabla n_\sigma(\boldsymbol{r})|}{n_\sigma(\boldsymbol{r})} + c_2\frac{|\nabla n_\sigma(\boldsymbol{r})|^2}{n_\sigma^{7/3}(\boldsymbol{r})} + c_3\frac{|\nabla n_\sigma(\boldsymbol{r})|^3}{n_\sigma^{11/3}(\boldsymbol{r})}, \tag{21}$$

where the exponents of the density, 1, 7/3, and 11/3, are chosen such that c_1 to c_3 become dimensionless numbers. The whole RSF has the dimension $1/a_0$. This ansatz was motivated by Krukau *et al.*[46] in the spirit of a gradient expansion. Adding terms beyond the first one can also be motivated by the following consideration. Far from the center of a finite system where $r \to \infty$, the density falls off exponentially. In such regions, the first term goes to a constant, whereas the second term goes to infinity. Thus, the second term can introduce a more rapid approach to full exact exchange for $r \to \infty$ by ensuring $\omega_\sigma(\boldsymbol{r}) \to \infty$ in this case.

The gradient expansion (21) fulfills the homogeneous-electron-gas limit (8) and, for $c_1 \simeq 0.124$ and $c_2 = c_3 = 0$, reduces to the non-empirical form (15). Because it scales linearly under uniform density scaling to the high-density limit,[67]

$$\Omega_\sigma([n_\lambda],\boldsymbol{r}) = \lambda\Omega_\sigma([n],\lambda\boldsymbol{r}) \quad \text{as} \quad \lambda \to \infty, \tag{22}$$

it "almost" fulfills the scaling condition (17). As suggested by Aschebrock and Kümmel,[47] this deficiency can be fixed [for any RSF that scales as in Eq. (22)] by modifying Ω_σ by a logarithmic term,[47]

$$\Omega_\sigma(\boldsymbol{r}) \to \Omega_\sigma(\boldsymbol{r})\,(1 + \ln(1 + \gamma\,\Omega_\sigma(\boldsymbol{r}))), \tag{23}$$

where γ is a parameter with dimension a_0. The expression on the right-hand side of Eq. (23) scales as

$$\begin{aligned}\Omega_\sigma([n_\lambda],\boldsymbol{r}) &= \lambda\,\ln(\lambda)\Omega_\sigma([n],\lambda\boldsymbol{r}) \\ &\gg \lambda\Omega_\sigma([n],\lambda\boldsymbol{r}) \quad \text{as} \quad \lambda \to \infty\end{aligned} \tag{24}$$

but leaves the behavior of the RSF mostly unchanged otherwise.

In Eq. (20), the second contribution to ω_σ, $\Theta(\cdot)$, accounts for one-electron self-interaction errors. One-electron regions can be detected with a combination of iso-orbital indicator functions and spin functions.[69–71] We use, first, the ratio z_σ of the non-interacting kinetic energy density and its single-orbital limit, τ_σ^W (*von Weizäcker* kinetic energy density),

$$z_\sigma(\boldsymbol{r}) = \frac{\tau_\sigma^\mathrm{W}(\boldsymbol{r})}{\tau_\sigma(\boldsymbol{r})} = \frac{|\nabla n_\sigma(\boldsymbol{r})|^2}{8n_\sigma(\boldsymbol{r})\tau_\sigma(\boldsymbol{r})}, \tag{25}$$

and, second, the spin-polarization,

$$\zeta(\boldsymbol{r}) = \frac{n_\uparrow(\boldsymbol{r}) - n_\downarrow(\boldsymbol{r})}{n_\uparrow(\boldsymbol{r}) + n_\downarrow(\boldsymbol{r})}. \tag{26}$$

z_σ is bound between its homogeneous-electron-gas limit, 0, and its single-orbital limit, 1; ζ^2 obtains its maximum, 1, for $n_\uparrow = 0$ or $n_\downarrow = 0$, respectively, and vanishes for spin-unpolarized systems, where $n_\uparrow \equiv n_\downarrow$. These quantities can be used to satisfy the constraint formulated in Eq. (19) by ensuring that $\Theta\big(z_\sigma\zeta^2\big)$ exhibits a singularity in the one-spin-orbital limit, $z_\sigma\zeta^2 \to 1$. Aschebrock and Kümmel[47] obtained the best results with a pole of the form

$$\Theta(x) = \frac{1}{1-x}. \tag{27}$$

Therefore, we adopt this form here. In summary, Eqs. (20), (21), (23), and (27) together define the most general model for the RSF that we study here. It has four parameters c_1, c_2, c_3, and γ, but as we show in the following, one can restrict oneself to two parameters in practice.

C. Spin scaling

The RSH approach formally involves the mixing of two different exchange energies. Therefore, it may seem natural to apply the spin-scaling relation for exchange[72] also to the RSF. Then, any RSF $\omega_\sigma(\mathbf{r})$ should follow from a corresponding spin-unpolarized model $\omega(\mathbf{r})$ according to[46,47]

$$\omega_\sigma([n_\sigma, |\nabla n_\sigma|, \tau_\sigma], \boldsymbol{r}) = \omega([2n_\sigma, 2|\nabla n_\sigma|, 2\tau_\sigma], \boldsymbol{r}). \tag{28}$$

However, range separation can also be viewed as a way of modeling correlation. This can be rationalized by rewriting Eq. (3) as

$$E_{\mathrm{xc}}^{\mathrm{RSH}} = E_{\mathrm{x}}^{\mathrm{EXX}} + E_{\mathrm{c}}^{\mathrm{RSH}}, \tag{29}$$

where $E_{\mathrm{x}}^{\mathrm{EXX}}$ is the (full) exact exchange energy, and hence, the remaining parts,

$$E_{\mathrm{c}}^{\mathrm{RSH}} \equiv -E_{\mathrm{SR-x}}^{\mathrm{EXX}} + E_{\mathrm{SR-x}}^{\mathrm{DFA}} + E_{\mathrm{c}}^{\mathrm{DFA}}, \tag{30}$$

essentially describe correlation effects. This is not just a formal rearrangement of terms, but the above equations reflect an important piece of physics: The (semi-)local exchange functionals do not model exact exchange but effectively model the combined contributions of exact exchange and left–right (non-dynamical) correlation in an approximate and density-averaged manner. This conclusion follows from exchange–correlation hole considerations[73–75] as well as from analyzing densities.[76] In Eq. (30), the first two terms depend upon the RSF. Thus, it is evident that in the local RSH approach, the RSF must capture correlation physics, and from this perspective, it does not seem natural to enforce the spin-scaling for exchange for it. Equation (20) follows this logic; due to the dependence on the spin polarization, it deliberately deviates from Eq. (28).

As an alternative path for a RSF that follows the spin-scaling relation (28),[47] we also study the form

$$\omega_\sigma(\boldsymbol{r}) = \Omega_\sigma([n_\sigma, |\nabla n_\sigma|], \boldsymbol{r})\Theta(z_\sigma(\boldsymbol{r})). \tag{31}$$

It should be noted that this form of SIC exhibits a singularity in the single-orbital limit, $z_\sigma \to 1$, which, in general, does not coincide with the one-spin-orbital limit, $z_\sigma\zeta^2 \to 1$, in which Eq. (20) exhibits a singularity. Apart from that, we consider a third alternative also proposed by Aschebrock and Kümmel,[47] with a RSF variant with a common RSF for both spin channels,

$$\omega_\uparrow(\boldsymbol{r}) \equiv \omega_\downarrow(\boldsymbol{r}) = \Omega([n, |\nabla n|], \boldsymbol{r})\Theta\big(z(\boldsymbol{r})\zeta^2(\boldsymbol{r})\big), \tag{32}$$

which depends on $n \equiv n_\uparrow + n_\downarrow$, $|\nabla n|$, and $\tau \equiv \tau_\uparrow + \tau_\downarrow$.

We note that our perspective on Eq. (30), and, as a consequence, thus also our view on the spin dependence of the RSF, differs from the one of Maier *et al.*[50] They discussed uniform coordinate scaling with $0 \ll \lambda < \infty$ [cf. Eq. (16)] for the stretched H_2 molecule and pointed out that also in this case, the non-dynamical correlation should be non-local, whereas the first two terms in Eq. (30) become semi-local. Thus, they concluded that an interpretation of the first two terms in Eq. (30) as non-dynamical correlation "does not seem natural from the scaling perspective." They then argued further that as a consequence, one should restrict oneself to RSFs with an exchange-like spin scaling. From the perspective of Maier *et al.*,[50] Eq. (31) would therefore be a better justified approximation than Eq. (20). While indeed non-dynamical correlation, in principle, should retain its non-locality also under high-density scaling, we do not agree with the conclusion that this forces one to abandon RSFs that deviate from exchange-like spin scaling. The high-density limit is dominated by (exact) exchange, not correlation, and the non-locality of the non-dynamical correlation in this limit is hardly probed in typical, real-world electronic structure problems. Furthermore, Eqs. (20) and (31) have the same uniform coordinate scaling, but Eq. (20) correctly captures one-electron self-interaction, whereas Eq. (31) leads to $\omega_\sigma(\boldsymbol{r}) \to \infty$ (corresponding to full exact exchange) for any one-orbital system and thus also for H_2 at all bond lengths. Equation (20) is thus clearly better justified. The good results that we obtain in Sec. V based on Eq. (20) support our point of view.

III. SEMI-LOCAL EXCHANGE–CORRELATION FUNCTIONALS

In this work, we model the semi-local components of the xc energy [cf. Eq. (3)] by LDA. For the short-range exchange energy, we employ the expression derived by Gill *et al.*,[77]

$$\begin{aligned} E_{\mathrm{SR-x}}^{\mathrm{LDA}} &= \sum_\sigma \int \mathrm{d}\boldsymbol{r}\, \varepsilon_{\mathrm{SR-x}\sigma}^{\mathrm{LDA}}(\boldsymbol{r}) \\ &= \sum_\sigma \int \mathrm{d}\boldsymbol{r}\, \varepsilon_{\mathrm{x}\sigma}^{\mathrm{LDA}}(\boldsymbol{r}) F_{\mathrm{SR-x}}^{\mathrm{LDA}}\left(\frac{\omega_\sigma(\boldsymbol{r})}{k_{\mathrm{F}\sigma}(\boldsymbol{r})}\right), \end{aligned} \tag{33}$$

where $F_{\mathrm{SR-x}}^{\mathrm{LDA}}$ is the enhancement factor of short-range LDA exchange,

$$F_{\mathrm{SR-x}}^{\mathrm{LDA}}(\lambda) = 1 - \frac{2\lambda}{3}\left(2\sqrt{\pi}\mathrm{erf}(1/\lambda) - 3\lambda + \lambda^3 + \left(2\lambda - \lambda^3\right)\exp\left(-1/\lambda^2\right)\right). \tag{34}$$

The short-range exchange energy thus depends on the RSF.

On the other hand, we model $E_{\mathrm{c}}^{\mathrm{LDA}}$ in a way that is independent of the RSF: We use the parameterization of Perdew and Wang[78] for the LDA correlation energy density $\varepsilon_{\mathrm{c}}^{\mathrm{LDA}}$. In order to guard against one-electron self-interaction [cf. Eq. (18)], an appropriate form of SIC is required not only for the RSF but also for $E_{\mathrm{c}}^{\mathrm{LDA}}$. In this work, we employ two simple SIC schemes: One variant involves both the ratio z and the spin-polarization,[45,47]

$$E_{\mathrm{c-SPZ}}^{\mathrm{LDA}} = \int \mathrm{d}\boldsymbol{r}\, \left(1 - z(\boldsymbol{r})\zeta^2(\boldsymbol{r})\right)\varepsilon_{\mathrm{c}}^{\mathrm{LDA}}[n_\uparrow(\boldsymbol{r}), n_\downarrow(\boldsymbol{r})], \tag{35}$$

and leaves the correlation energy unchanged for spin-unpolarized systems. In the second scheme that we use, the SIC is controlled by $z_\uparrow$ and $z_\downarrow$,[79]

$$E_{\mathrm{c-Z}}^{\mathrm{LDA}} = \int \mathrm{d}\boldsymbol{r}\, \left(\varepsilon_{\mathrm{c}}^{\mathrm{LDA}}[n_\uparrow(\boldsymbol{r}), n_\downarrow(\boldsymbol{r})] - \sum_\sigma z_\sigma(\boldsymbol{r})\varepsilon_{\mathrm{c}}^{\mathrm{LDA}}[n_\sigma(\boldsymbol{r}), 0]\right). \tag{36}$$

Here, the correlation energy is altered to some extent also for spin-unpolarized systems. In the following, we refer to the first SIC variant [Eq. (35)] as *LDA-SPZ* (for "spin-polarization and z dependent") and the second variant [Eq. (36)] as *LDA-Z*.

IV. COMPUTATIONAL DETAILS

We have integrated our models for the space-dependent RSF and the corresponding semi-local contributions to the xc energy

into the self-consistent implementation of local RSH functionals[51] in TURBOMOLE,[80] development version 7.5. All calculations have been performed using the def2-TZVP basis set, grid size 3, and a convergence threshold of 10^{-6} for the self-consistent calculations.

In addition to the local RSH calculations, we also show results for other density functionals for comparison. These have been obtained with Q-CHEM,[81] version 5.2.2, at numerical settings comparable to those used for the TURBOMOLE calculations.

In order to assess the performance of our RSF models, we use four different test sets. As a computationally lightweight test set, we use an in-house set of 11 atomization energies of diatomic molecules that covers single, double, and triple bonds (H_2, LiH, Li_2, LiF, CO, N_2, NO, OH, O_2, HF, and F_2).[47] We refer to this set as *AE11D* in the following. Furthermore, we use a test set of 17 atomic ground-state energies (from H to Cl).[80,92,94] Finally, we use the AE6 and BH6 test sets of atomization energies and reaction barrier heights.[81,95,96] These are still small sets that are, however, designed to be representative for larger thermochemical test sets.

In addition, we also study the equilibrium bond lengths and harmonic vibrational frequencies of the molecules in the AE11D test set as well as the vertical IPs and HOMO eigenvalues of the molecules in the AE6 test set. More details on how the calculations are done and on the test sets employed can be found in the supplementary material.

V. RESULTS AND DISCUSSION

In the following, we explore for each of our test sets and for the different combinations of RSF and correlation models, which values of the yet undetermined parameters [cf. Eqs. (21) and (23)] yield reasonable results. The details of this optimization procedure [with respect to the mean absolute error (MAE)] are described in the supplementary material. For comparison of the different functionals, we use their MAEs and mean signed errors (MSEs) in the following. The MAEs provide a general impression of the overall accuracy, while the MSEs can additionally indicate biases. More detailed data, which make the performance for the individual systems of a test set transparent to the reader, are included in the supplementary material. When calculating the equilibrium bond lengths and harmonic vibrational frequencies of the molecules in the AE11D test set as well as the vertical IPs of the molecules in the AE6 test set, we use the parameters optimized for the atomization energies of the respective test sets.

The global and local RSH functionals we discuss most frequently are summarized in Table I. In the most simple functional, which we refer to as *ωLDA*, $\omega_\sigma(\mathbf{r})$ is approximated by a constant parameter ω_0. The second functional, called *K-ωLDA*, is based on a RSF of the form proposed by Krukau *et al.*,[46] which is the first-order term of the gradient expansion (21), i.e.,

$$\omega_\sigma(\mathbf{r}) = \Omega_\sigma^{\mathrm{K}}(\mathbf{r}) \equiv \eta \frac{|\nabla n_\sigma(\mathbf{r})|}{n_\sigma(\mathbf{r})}, \tag{37}$$

with parameter η. The RSF of the third functional, called *SIC-ωLDA*, combines this $\Omega_\sigma^{\mathrm{K}}$ with the logarithmic high-density correction (23) and SIC according to Eq. (20),

$$\omega_\sigma(\mathbf{r}) = \Omega_\sigma^{\mathrm{K}}(\mathbf{r}) \left(1 + \ln\left(1 + \gamma\, \Omega_\sigma^{\mathrm{K}}(\mathbf{r})\right)\right)\Theta\left(z_\sigma(\mathbf{r})\zeta^2\right), \tag{38}$$

TABLE I. Summary of the global and local RSH functionals most frequently considered in our analysis.

Name	RSF $\omega_\sigma(\mathbf{r})$	Correlation
ωLDA	$\omega_0 = const.$	LDA
K-ωLDA	$\Omega_\sigma^{\mathrm{K}}(\mathbf{r}) \equiv \eta \frac{\lvert\nabla n_\sigma(\mathbf{r})\rvert}{n_\sigma(\mathbf{r})}$	LDA
SIC-ωLDA	$\Omega_\sigma^{\mathrm{K}}\left(1 + \ln\left(1 + \gamma\, \Omega_\sigma^{\mathrm{K}}\right)\right)\Theta\left(z_\sigma\zeta^2\right)$	LDA-SPZ

with parameters η and γ. Regarding the correlation functional, ωLDA and K-ωLDA rely on the usual LDA correlation, while in the SIC-ωLDA functional, the self-interaction corrected LDA-SPZ correlation [cf. Eq. (35)] is employed. For comparison, we also consider a variant of SIC-ωLDA where the parameter γ is fixed at $\gamma \equiv 0$, i.e., it is not part of the optimization. We refer to this variant as SIC-ωLDA $(\gamma \equiv 0)$.

Our analysis is structured as follows: In Sec. V A, we begin with the computationally lightweight AE11D test set and compare several different local RSH functionals. This analysis is going to reveal that among the present approaches, the K-ωLDA and SIC-ωLDA models are the most promising ones. We then focus on these and check atomization energies for the AE6 test set, atomic ground-state energies (cf. Sec. V B), and the reaction barrier heights of BH6 (cf. Sec. V C). Afterward, we examine whether our most promising local RSH functionals can provide a reasonable description of equilibrium bond lengths, and harmonic vibrational frequencies (cf. Sec. V D) as well as vertical IPs (cf. Sec. V E), even if the functional parameters are not specifically optimized for these properties. Finally, in Sec. V F, we put our results on atomization energies and reaction barrier heights into perspective by comparing them to semi-local, global hybrid, and conventional RSH density functional approximations.

A. Atomization energies

We begin by examining atomization energies because they test a functional's ability to properly describe electronic binding, which is the most basic and important requirement on an xc approximation. Our results from the optimization of the local RSH functionals with respect to the AE11D test set are summarized in Table II. For the global RSH ωLDA, we obtain a MAE of 3.8 kcal/mol. This value can serve as a reference against which the different local RSH functionals can be compared; a reasonable model should exhibit a better performance.

In a first step, we compare the different terms of the gradient expansion (21) for the RSF. In order to keep this procedure transparent and to reveal the importance of the different terms, we do not apply our optimization procedure to the full expansion but rather consider the three terms separately in different functionals (cf. Table II). For the model involving the first-order term (corresponding to the K-ωLDA functional), the performance is slightly better than for ωLDA with a MAE of 3.6 kcal/mol. This is underlined by comparing the MSEs where we obtain −0.6 kcal/mol for K-ωLDA but only 1.8 kcal/mol for ωLDA. If instead only the second or third-order terms are employed as the RSF, the results are somewhat worse than for ωLDA. We further verified (not shown in the table) that a linear combination of the three terms does also not lead to further improvement. This outcome is in agreement with the work of

TABLE II. Atomization energies of different local RSH functionals for the AE11D test set. For comparison, also the results from LDA and ωLDA calculations with TURBOMOLE are displayed. The MAEs and MSEs are given in kcal/mol. Boldface denotes the smallest MAE found for each functional class.

Functional			Atomization energies (AE11D)		
Name	RSF $\omega_\sigma(\mathrm{r})$	Correlation	Optimal parameter	MAE	MSE
LDA	...		...	24.8	24.6
ωLDA	$\omega_0 = const.$	LDA	$\omega_0 = 0.548/a_0$	**3.8**	1.8
K-ωLDA	$\eta\lvert\nabla n_\sigma(\mathbf{r})\rvert/n_\sigma(\mathbf{r})$		$\eta = 0.124$	**3.6**	−0.6
...	$\eta\lvert\nabla n_\sigma(\mathbf{r})\rvert^2/n_\sigma^{7/3}(\mathbf{r})$	LDA	$\eta = 9.67\cdot10^{-3}$	5.2	−0.4
...	$\eta\lvert\nabla n_\sigma(\mathbf{r})\rvert^3/n_\sigma^{11/3}(\mathbf{r})$		$\eta = 4.23\cdot10^{-5}$	3.9	2.3
...	$\Omega_\sigma^{\mathrm{K}}(\mathbf{r})\,\Theta(z_\sigma)$	LDA-SPZ	$\eta = 0.176$	18.7	−4.4
...		LDA-Z	$\eta = 0.317$	20.5	−19.5
SIC-ωLDA ($\gamma \equiv 0$)	$\Omega_\sigma^{\mathrm{K}}(\mathbf{r})\,\Theta(z_\sigma\zeta^2)$	LDA-SPZ	$\eta = 0.128$	**2.1**	−0.1
...		LDA-Z	$\eta = 0.101$	15.3	−9.4
...	$\Omega^{\mathrm{K}}(\mathbf{r})\,\Theta(z\zeta^2)$	LDA-SPZ	$\eta = 0.159$	3.2	0.9
...		LDA-Z	$\eta = 0.117$	13.1	−7.7

Krukau *et al.*[46] where the best performance has also been obtained with the first-order term of the gradient expansion. Interestingly, our empirical prefactor of K-ωLDA perfectly matches the corresponding non-empirical estimate by Maier *et al.*[50] [cf. Eq. (15)]. We conclude from these results that the straightforward Krukau RSF $\eta|\nabla n_\sigma|/n_\sigma$ already has a promising form, but further ingredients are required to fully exploit the potential of the local RSH approach.

Therefore, in a second step, we correct for one-electron self-interaction. We combine the Krukau RSF with one of the three different forms of the SIC pole function: $\Theta(z_\sigma)$, $\Theta(z_\sigma\zeta^2)$, or $\Theta(z\zeta^2)$. For the correlation functional, we compare the two variants LDA-SPZ and LDA-Z. Hence, we look at a total of six somewhat different self-interaction corrected local RSH functionals. Comparing LDA-SPZ and LDA-Z, we obtain a pronounced trend, independent of the form of the SIC pole function: LDA-SPZ is clearly more accurate, with MAEs smaller by ~ 2–13 kcal/mol. Regarding the different pole functions, we find that the results obtained from $\Theta(z_\sigma\zeta^2)$ and $\Theta(z\zeta^2)$ are almost comparable, with MAEs of 2.1 and 3.2 kcal/mol, respectively. In fact, this outcome is to be expected as the mathematical structure of the two RSF models is similar and their behavior becomes essentially identical for closed-shell systems. The picture changes significantly when we compare to the pole function $\Theta(z_\sigma)$, which only reaches a MAE of 18.7 kcal/mol. All these trends are also reflected by the corresponding MSEs. The significantly different behavior of $\Theta(z_\sigma)$ can be rationalized from the absence of the spin-polarization ζ in this RSF model: While $\Theta(z_\sigma\zeta^2)$ diverges only in one-spin-orbital regions, $\Theta(z_\sigma)$ already exhibits a singularity in the single-orbital limit. As a consequence, the latter can overestimate the fraction of exact exchange in systems such as H_2. We conclude that the SIC scheme employed in the SIC-ωLDA functional is particularly effective in reducing one-electron self-interaction errors. Eventually, this can lead to a substantially improved performance as compared to the simpler K-ωLDA or ωLDA functionals.

In our discussion so far, we have not included the logarithmic high-density correction [cf. Eq. (38)]. The reason is that it cannot provide a further improvement for the AE11D test set, i.e., when including its parameter γ in the optimization, the best description is obtained with $\gamma = 0$. However, by that, one should not be misled to assume that the logarithmic correction term would not be useful in general. That this is not the case is demonstrated by our results for the AE6 test set [cf. Table III]. Here, the SIC-ωLDA functional with γ fixed at 0 yields a MAE of 3.65 kcal/mol. While this already constitutes an improvement over ωLDA and K-ωLDA, including the parameter γ in the optimization brings another relevant gain in accuracy, leading to a MAE of only 1.51 kcal/mol. We attribute this observation, i.e., that the logarithmic high-density correction is beneficial for AE6 but not for AE11D, to the presence of heavier atoms in the AE6 set. The trend observed in the MAEs is in overall agreement with that in the MSEs: Remarkably, for the SIC-ωLDA functional with γ fixed at 0, a MSE of only 1.96 kcal/mol is obtained, while including the logarithmic term in the optimization leads to a reduction to 0.21 kcal/mol.

However, this does not imply that SIC-ωLDA with $\gamma \neq 0$ would yield an unsatisfactory description of atomization energies for the AE11D test set. In fact, for the parameters $\eta = 0.114$ and $\gamma = 0.218\ a_0$ (which are optimal for AE6), we obtain a MAE of 2.4 kcal/mol for AE11D, which is close to the optimum of 2.1 kcal/mol. More general, it turns out that a broad band of tuples (η, γ) is able to provide a description very close to the global optimum, similar to the observation already described in the work of Aschebrock and Kümmel[47]

TABLE III. Atomization energies of different local RSH functionals for the AE6 test set. For comparison, also the results from LDA and ωLDA calculations with TURBOMOLE are displayed. The MAEs and MSEs are given in kcal/mol.

	Atomization energies (AE6)		
Functional	Optimal parameter(s)	MAE	MSE
LDA	...	74.93	74.93
ωLDA	$\omega_0 = 0.601/a_0$	9.70	1.85
K-ωLDA	$\eta = 0.131$	4.82	−0.68
SIC-ωLDA ($\gamma \equiv 0$)	$\eta = 0.132$	3.65	1.96
SIC-ωLDA	$\eta = 0.114$, $\gamma = 0.218\ a_0$	1.51	0.21

(cf. Fig. 3 therein). This raises the hope that the existing degree of freedom can be used to simultaneously optimize for other observables. By contrast, the ωLDA functional with its constant parameter for range-separation does not provide a similar flexibility. Hereby, for $\omega_0 = 0.601/a_0$, the optimal value for AE6, we obtain a MAE of 4.9 kcal/mol for AE11D. This indicates another strength of the local RSH approach apart from its accuracy: It promises to offer a good description of different properties or different types of systems with one and the same set of functional parameters.

B. Atomic ground-state energies

Next, we turn to the test set of atomic ground-state energies. This test set explores a different type of physics for two reasons. First, it includes a balanced mix of both small and large atoms (from H to Cl). Second, atomization energies are energy differences and, therefore, are sensitive mostly to the description of the valence and not to the core electrons, whereas the core is relevant to the total atomic energy. Thus, the atomic test set can help to clarify the importance of the logarithmic correction term. Our results are summarized in Table IV. For the global RSH ωLDA, we obtain a MAE per electron of 0.014 a.u. Accounting for the space-dependence of the RSF can improve this result substantially: For K-ωLDA and SIC-ωLDA with γ fixed at 0, we find MAEs per electron of 0.008 and 0.007 a.u., respectively. If the high-density correction is considered, i.e., γ is included in the optimization, both results are further improved to 0.004 a.u. Regarding the MSEs per electron, we also obtain a continuous improvement from ωLDA with −0.008 a.u. to SIC-ωLDA with −0.002 a.u. The finding that we also obtain an improvement when adding the logarithmic correction term to K-ωLDA is unique to the atomic test set, i.e., we neither observe this trend for AE6 nor for BH6 (cf. below). This stresses the relevance of the high-density correction for atomic ground-state energies.

The optimal parameter tuple for this test set, $\eta = 0.117$ and $\gamma = 2.72\ a_0$, differs strongly from that for atomization energies. If we employ the parameters optimal for AE6, $\eta = 0.114$ and $\gamma = 0.218\ a_0$, for our atomic test set, we indeed obtain a MAE per electron of 0.030 a.u., which constitutes a significant decline in accuracy as compared to the optimum (0.004 a.u.). Similarly, for the K-ωLDA functional, the choice $\eta = 0.131$ leads to a MAE per electron of 0.032 a.u. However, we obtain a similar trend also for our global RSH functional ωLDA where the choice $\omega_0 = 0.601/a_0$ yields a MAE per electron of 0.042 a.u. Hence, the fact that parameters that yield good results for atomization energies are less suitable for atomic ground-state calculations should not be seen as a problem specifically tied to the local RSH approach. Instead, we attribute this to the conceptual difference between atomization energies, on the one hand, and pure ground-state energies, on the other hand. In any case, the comparison to ωLDA shows that the local range-separation constitutes an improvement in both the K-ωLDA and the SIC-ωLDA form.

In passing, we point at another subtlety inherent to the optimization of the functional parameters to atomic energies: As commonly known, LDA is particularly poorly for atomic energies, whereas the behavior of exact exchange is fairly acceptable. Therefore, the optimization may tend to lead to an overestimation of the fraction of exact exchange by the RSH functionals.

TABLE IV. Atomic ground-state energies for different local RSH functionals. For comparison, also the results from LDA and ωLDA calculations with TURBOMOLE are displayed. This table lists the MAE and MSE *per electron* (both in Hartree a.u.).

	Atomic ground-state energies		
Functional	Optimal parameter(s)	MAE	MSE
LDA	⋯	0.067	0.067
ωLDA	$\omega_0 = 3.00/a_0$	0.014	−0.008
K-ωLDA	$\eta = 0.263$	0.008	−0.004
K-ωLDA $(+\gamma)$[a]	$\eta = 0.113$, $\gamma = 3.11\ a_0$	0.004	−0.003
SIC-ωLDA $(\gamma \equiv 0)$	$\eta = 0.266$	0.007	−0.003
SIC-ωLDA	$\eta = 0.117$, $\gamma = 2.72\ a_0$	0.004	−0.002

[a]This local RSH model is based upon the RSF $\omega_\sigma(\boldsymbol{r}) = \Omega_\sigma^{\mathrm{K}}\,(1 + \ln(1 + \gamma\,\Omega_\sigma^{\mathrm{K}}))$ but is otherwise the same as the K-ωLDA model.

C. Reaction barrier heights

In the following, we examine if we can exploit the existing degree of freedom in the SIC-ωLDA functional that has become apparent in the optimization for atomization energies (cf. Sec. V A) to optimize for further thermochemical properties. Therefore, we study the reaction barrier heights of the BH6 test set. Our results from the optimization for BH6 are summarized in Table V. We find that already the ωLDA functional with a constant parameter for range separation yields a good description with a MAE of 1.76 kcal/mol. Here, the K-ωLDA functional, which relies on the simple Krukau RSF, cannot provide a further improvement. However, our most promising SIC scheme, i.e., the SIC-ωLDA functional, is able to provide a better performance than ωLDA, with a MAE of only 1.53 kcal/mol. In this case, the MSEs exhibit a somewhat different trend as they increase from −0.21 kcal/mol for ωLDA to −1.19 kcal/mol for SIC-ωLDA. However, in relation to other density functionals (cf. Sec. V F), this value is still more than acceptable. The optimum of SIC-ωLDA is obtained for $\gamma = 0$. Including the logarithmic correction term, i.e., $\gamma \neq 0$, can yield results of similar quality. In particular, for the parameters $\eta = 0.114$ and $\gamma = 0.218\ a_0$, which are optimal for the AE6 set, we obtain a MAE of 1.73 kcal/mol with SIC-ωLDA. By contrast, ωLDA with $\omega_0 = 0.601/a_0$ (optimum for AE6) yields a MAE of 2.88 kcal/mol. Thus, we conclude that with one set of parameters, an equally good description of both atomization energies and reaction barrier heights is indeed possible with our local RSH SIC-ωLDA, whereas the corresponding global RSH ωLDA requires different parameters for each test set.

TABLE V. Reaction barrier heights of different local RSH functionals for the BH6 test set. For comparison, also the results from LDA and ωLDA calculations with TURBOMOLE are displayed. The MAEs and MSEs are given in kcal/mol.

	Reaction barrier heights (BH6)		
Functional	Optimal parameter	MAE	MSE
LDA	⋯	17.49	17.49
ωLDA	$\omega_0 = 0.486/a_0$	1.76	−0.21
K-ωLDA	$\eta = 0.144$	2.62	−1.85
SIC-ωLDA $(\gamma \equiv 0)$	$\eta = 0.128$	1.53	−1.19

TABLE VI. Equilibrium bond lengths and harmonic vibrational frequencies for the molecules in the AE11D test set by different local RSH functionals. For comparison, also the results from LDA and ωLDA calculations with TURBOMOLE are displayed. For each of the RSH functionals, we used the parameters that were obtained by optimizing atomization energies, cf. Table II.

Functional		Bond lengths (in Å)		Vibrational frequencies (in cm^{-1})	
Name	Parameter	MAE	MSE	MAE	MSE
LDA	⋯	0.0154	0.0068	82.3	−21.0
ωLDA	$\omega_0 = 0.548/a_0$	0.0209	−0.0117	150.9	150.9
K-ωLDA	$\eta = 0.124$	0.0192	0.0048	72.5	51.7
SIC-ωLDA ($\gamma \equiv 0$)	$\eta = 0.128$	0.0195	0.0043	71.9	57.2

D. Equilibrium bond lengths and harmonic vibrational frequencies

Bond lengths and harmonic vibrational frequencies are further observables that are of interest in typical DFT applications. Therefore, we check how well these quantities are represented by the here studied functionals. For computational reasons, cf. the supplementary material, we restrict this study to the AE11D test set. For each functional we choose the parameters that emerged as being optimal for the atomization energies of the AE11D test set, cf. Sec. V A.

The corresponding results are displayed in Table VI for equilibrium bond lengths (center), and harmonic vibrational frequencies (right). It is know that LDA, despite its rather limited accuracy for thermochemical properties, yields fairly acceptable bond lengths. We find a MAE of 0.0154 Å with LDA, and a similar accuracy for SIC-ωLDA with a MAE of 0.0195 Å. The MSE is reduced from 0.0068 Å for LDA to 0.0043 Å for SIC-ωLDA. Regarding vibrational frequencies, the relation is similar: Here, the MAE of 71.9/cm for SIC-ωLDA is somewhat better than the 82.3/cm obtained with LDA, while the trend is the opposite for the MSEs. It is worthwhile to also note that again SIC-ωLDA is consistently more accurate than ωLDA with an improvement up to a factor of ~2(for vibrational frequencies), Furthermore, the fact that this accuracy is reached using functional parameters optimized for a rather different property illustrates the flexibility and transferability of the local RSH approch.

E. Vertical ionization potentials and HOMO eigenvalues

As a final observable we briefly discuss the prediction of vertical IPs, either from ΔSCF calculations, i.e., as a ground-state energy difference of the neutral system and its cation, or from HOMO eigenvalues. This is of interest particularly in view of the widespread use that RSH functionals have found in the past for predicting a reliable density of states from the eigenvalues.[9] Table VII shows the HOMO eigenvalues calculated for the molecules in the AE6 test set, the vertical IPs from ΔSCf calculations, and the experimental vertical IPs (where available). At least two findings emerge from Table VII. On the one hand ωLDA with the atomization-energy optimal value for the range-separation parameter leads for the AE6 set to a fairly good consistency between $-\varepsilon_{HOMO}$ and the IP calculated in the ΔSCF apporach. On the other hand, however, both K-ωLDA and SIC-ωLDA predict the IP in better agreement with the experimental

TABLE VII. Vertical IPs from ΔSCF calculations and HOMO eigenvalues ε_{HOMO} for the molecules in the AE6 test set calculated by different local RSH functionals. For comparison, also the results from LDA and ωLDA calculations with TURBOMOLE as well as experimental data for vertical IPs (taken from Ref. 84) are displayed. All values are in eV. For each of the RSH functionals, we used the parameters that were obtained by optimizing atomization energies, cf. Table III.

Functional parameter(s)	Ref. —	LDA —		ωLDA $\omega_0 = 0.601/a_0$		K-ωLDA $\eta = 0.131$		SIC-ωLDA $\eta = 0.114$, $\gamma = 0.218$ a_0	
		IP	$-\varepsilon_{HOMO}$	IP	$-\varepsilon_{HOMO}$	IP	$-\varepsilon_{HOMO}$	IP	$-\varepsilon_{HOMO}$
SiH_4	12.30	12.19	8.53	13.54	13.86	12.50	11.44	12.56	11.23
SiO	(11.49)[a]	11.51	7.54	12.26	12.58	11.60	10.60	11.64	10.40
S_2	9.55	9.52	5.77	10.51	10.79	9.69	8.58	9.53	8.27
C_3H_4	10.37	10.49	6.64	10.82	11.53	10.34	9.47	10.36	9.26
$C_2H_2O_2$	10.60	10.12	6.40	11.79	12.09	10.61	9.89	10.56	9.67
C_4H_8	10.70	10.67	7.32	11.68	12.51	10.80	9.95	10.78	9.75

[a]In the case of SiO, no experimental value for the vertical IP has been available. Therefore, in this case, the adiabatic IP is given.

numbers, with respect to both the ΔSCF approach and $-\varepsilon_{\mathrm{HOMO}}$. These findings indicate that a detailed investigation of the eigenvalues obtained by a local RSH functional may be a worthwhile task for a future study. However, the quality of the results, especially in light of the fact that the functional parameters used here were not specifically optimized for the IPs, but taken from the optimization for atomization energies, cf. Sec. V A, underlines the usefulness of the local RSH approach.

F. Final discussion

The previous discussion of our numerical results has already indicated that our best local RSH functional, SIC-ωLDA, is able to provide an accurate description of different test sets of atomization energies and reaction barrier heights. In the following, we want to further illustrate this strength. Therefore, we consider the AE6 and BH6 test sets and the ωLDA, K-ωLDA, and SIC-ωLDA functionals. The functional parameters are not taken from the previous optimizations but have been re-optimized for the combined AE6-BH6 set in order to obtain the parameter values that provide the best description across both test sets. The results from this optimization are displayed at the bottom of Table VIII. For ωLDA and K-ωLDA, a similar optimization has been done by Maier *et al.*;[50] the results reported in their work are in good agreement with ours. For ωLDA, the performance differs strongly between AE6 and BH6; on average, a MAE of 6.29 kcal/mol is obtained. The performance for AE6 is strongly improved in the K-ωLDA functional, resulting in an average MAE of 4.10 kcal/mol. Both functionals are clearly outperformed by SIC-ωLDA for which we obtain an overall MAE of only 1.60 kcal/mol. This functional also offers a particularly well-balanced description of atomization energies and reaction barrier heights with MAEs of 1.53 kcal/mol for AE6 and 1.66 kcal/mol for BH6 as well as satisfying values for the MSEs with 0.24 and −1.66 kcal/mol, respectively.

To put this performance into perspective, we compare to other established xc functionals. Our aim here is not to provide a comprehensive comparison to all the xc approximations that have been suggested in the past, but we focus on some widely used and well known functional families. These are, on the one hand, the PBE and BLYP GGAs and global hybrid and RSH functionals derived from them. As paradigm examples for the empirical xc construction strategy, we include representatives of the Minnesota family of density functionals[92] (M11-L, MN15-L, M11, and MN15) in the comparison. The Minnesota functionals contain ~ 40 to 60 empirical parameters that are optimized to a broad database of chemical properties.

The results for these functionals are displayed in the upper part of Table VIII. With the exception of MN15, the performance of our SIC-ωLDA functional is superior to all conventional density functional approximations that we looked at. For AE6, the accuracy of SIC-ωLDA is also higher than that of MN15. Only for BH6, the description provided by MN15 is better than that of SIC-ωLDA. In total, MN15 is somewhat better than SIC-ωLDA with an average MAE of 1.31 kcal/mol. To put the comparison in Table VIII into perspective, we have to keep in mind that our functional is specifically optimized for AE6 and BH6, while in the development of the Minnesota functionals, considerably larger tests sets have been considered. On the other hand, the accuracy of the Minnesota

TABLE VIII. Performance of various density functionals for the AE6 and BH6 test sets. For each functional, the MAE of calculated and reference values is given for AE6 and BH6, as well as their mean value across both test sets. The results for the conventional GGA, meta-GGA, global hybrid, and most global RSH functionals have been obtained using Q-CHEM. For the global and local RSH functionals ωLDA, K-ωLDA, and SIC-ωLDA, our TURBOMOLE implementation has been used. The parameters of these functionals have been re-optimized for both AE6 and BH6 together. The MAEs and MSEs are given in kcal/mol. Boldface denotes the smallest MAE from the literature and the present work, respectively.

Functional			MAE			MSE	
Name	Parameter(s)	Type	AE6	BH6	Mean	AE6	BH6
LDA[78,a]	⋯	⋯	74.93	17.49	46.21	74.93	−17.49
PBE[85]	⋯	GGA	14.27	9.22	11.75	10.40	−9.22
PBE0[86]	⋯	Global hybrid	5.22	4.49	4.86	−1.70	−4.49
ωPBE[27]	$\omega = 0.4/a_0$[b]	Global RSH	5.34	1.42	3.38	−2.20	−1.22
BLYP[87]	⋯	GGA	6.98	7.80	7.39	−3.52	−7.80
B3LYP[73,87]	⋯	Global hybrid	4.21	4.68	4.45	−4.21	−4.68
CAM-B3LYP[17]	⋯	Global RSH	1.95	3.75	2.85	−1.83	−3.75
M11-L[88]	⋯	meta-GGA	7.53	1.26	4.40	−2.88	0.19
MN15-L[89]	⋯⋯	meta-GGA	4.00	1.45	2.73	−1.26	−0.16
M11[90]	⋯	Global RSH	3.14	1.41	2.28	−3.14	−1.40
MN15[91]	⋯	Global hybrid	**1.62**	**0.99**	**1.31**	−0.04	−0.47
ωLDA	$\omega_0 = 0.600/a_0$	Global RSH	9.71	2.87	6.29	1.92	2.82
K-ωLDA	$\eta = 0.131$	Local RSH	4.82	3.38	4.10	−0.68	−3.30
SIC-ωLDA	$\eta = 0.115$, $\gamma = 0.202\ a_0$	Local RSH	**1.53**	**1.66**	**1.60**	0.24	−1.66

[a]For LDA, we have encountered convergence issues for some systems when using Q-CHEM. Therefore, in this case, the results from TURBOMOLE are displayed here.
[b]We have taken the range-separation parameter for ωPBE from the original publication.[27]

functionals is obtained via a complex structure with many fitted parameters. By contrast, already two parameters are sufficient to achieve the favorable performance of SIC-ωLDA. One may interpret this as indicating that, in the latter case, the functional form itself has already built in a lot of the proper physics. As the AE6 and BH6 test sets are designed as to be representative for a broader set of thermochemical properties,[83] these results provide a first impression of the accuracy possible with the local RSH approach.

VI. CONCLUSIONS AND OUTLOOK

In summary, we have presented and analyzed several approaches toward a RSH functional with local range separation. Guided by formal constraints, we have constructed a RSF depending on the electron density, its gradient, and the kinetic energy density. In the subsequent numerical analysis, we have revealed the importance of the different constituents of our RSF model. Most notably, we have shown that correcting for one-electron self-interaction errors in an appropriate way can lead to a significant improvement in accuracy over the simpler models. The success of our best model is documented by the comparison to established density functionals for a small, yet representative test set of atomization energies and reaction barrier heights. If there are no special requirements in a calculation and if there is no additional information about the system or observables of interest, we recommend to use our SIC-ωLDA functional with the parameters $\eta = 0.115$ and $\gamma = 0.202$ a_0 (cf. Table VIII) for ground-state properties. Despite its simplicity, our approach is able to compete with density functionals containing up to ~ 60 empirical parameters. This outcome demonstrates the potential of the local RSH approach and is encouraging regarding its further development.

Several conclusions about the modeling of the locally space-dependent RSF can be drawn from our work. First, we recall that the favorable performance of our functionals relies upon the integration of one-electron SIC in a suitable way. Not only can this satisfy a fundamental formal constraint, our numerical results demonstrate that this is also relevant in practice and provides a noticeable improvement over the corresponding global RSH functional. In this respect, our conclusions differ from the ones of Maier *et al.*,[50] who have not considered the influence of SIC, and therefore, from our perspective, their approach does not exploit the potential of the local RSH approach to full extent. The results regarding SIC also support our perspective on the spin-scaling behavior of local RSH functionals (cf. Sec. II C). A comparison of different forms of SIC has shown that the form $\Theta(z_\sigma\zeta^2)$, which is consistent with the correlation-like treatment suggested in this work, yields by far the best results. We believe that these insights are useful guidelines for further functional development.

Furthermore, our results demonstrate that the Krukau RSF $\eta|\nabla n_\sigma|/n_\sigma$ already exhibits a promising form and performance. On the other hand, however, we have also seen, e.g., when considering the combined AE6-BH6 test set, that additional ingredients are required to provide the flexibility to accurately describe different properties. One way how one may try to achieve this is by considering higher-order terms in the gradient expansion for the RSF [cf. Eq. (21)]. However, the numerical results show that this does not enhance the performance in practice. Thus, a more sophisticated GGA-like approach might be better suited for providing further improvement. In this spirit, the generic form

$$\omega_\sigma(\boldsymbol{r}) = \eta\frac{|\nabla n_\sigma(\boldsymbol{r})|}{n_\sigma(\boldsymbol{r})}F_{\omega\sigma}^{\mathrm{GGA}}(\boldsymbol{r})\Theta(z_\sigma\zeta^2) \tag{39}$$

appears as a promising general ansatz for subsequent improvement of the RSF. Thereby, one can rely on the so-far successful ingredients, the Krukau RSF as a non-empirical form in the limit of slowly varying density and the pole function $\Theta(z_\sigma\zeta^2)$ for SIC, and combine them with a GGA-like enhancement factor $F_{\omega\sigma}^{\mathrm{GGA}}(\boldsymbol{r})$ depending on the spin-density $n_\sigma(\mathbf{r})$ and its gradient $|\nabla n_\sigma(\mathbf{r})|$. To engineer explicit forms of this enhancement factor, further formal constraints are desirable. In this context, the scaling behavior of the RSF in the high-density limit [cf. Eq. (17)] can be viewed as one such constraint. As it has been done in this work, it can be incorporated into the RSF via a logarithmic correction term [cf. Eq. (23)]. By that, promising results have been obtained. Other constraints may lead to a different form of the enhancement factor. In any case, hybrid functionals with local range separation appear as a very promising concept in DFT.

SUPPLEMENTARY MATERIAL

In the supplementary material, we provide further details on the test sets employed, the optimization procedure of the parameters of the local RSH functionals, and on how the equilibrium bond lengths and harmonic vibrational frequencies are calculated. We give more detailed insights into the analysis of our functionals by including detailed listings that make the performance for individual systems (atoms, molecules, or chemical reactions) transparent to the reader. Finally, we comment on the computational effort required for the local RSH calculations.

ACKNOWLEDGMENTS

We acknowledge helpful discussions with Sascha Klawohn about the self-consistent implementation of local range-separated hybrid functionals. S.K. and M.B. gratefully acknowledge financial support from the Elite Study Program "Biological Physics" of the Elite Network of Bavaria; from the Bavarian Polymer Institute in terms of computing resources; and from the Bavarian State Ministry of Science, Research, and the Arts for the Collaborative Research Network "Solar Technologies go Hybrid." M.B. acknowledges support from the "Studienstiftung des Deutschen Volkes." H.B. acknowledges funding from the Deutsche Forschungsgemeinschaft (DFG, German Research Foundation)—Project No. 418140043.

AUTHOR DECLARATIONS

Conflict of Interest

The authors declare no conflicts of interest.

DATA AVAILABILITY

The data that support the findings of this study are available within the article and its supplementary material. The data that support the findings of this study are available from the corresponding author upon reasonable request.

REFERENCES

[1]T. Leininger, H. Stoll, H.-J. Werner, and A. Savin, "Combining long-range configuration interaction with short-range density functionals," Chem. Phys. Lett. **275**, 151–160 (1997).

[2]H. Iikura, T. Tsuneda, T. Yanai, and K. Hirao, "A long-range correction scheme for generalized-gradient-approximation exchange functionals," J. Chem. Phys. **115**, 3540–3544 (2001).

[3]R. M. Dreizler and E. K. U. Gross, *Density Functional Theory* (Springer Berlin Heidelberg, 1990).

[4]J. P. Perdew and S. Kurth, "Density functionals for non-relativistic Coulomb systems in the new century," in *A Primer in Density Functional Theory*, edited by C. Fiolhais, F. Nogueira, and M. Marques (Springer Berlin Heidelberg, 2003), pp. 1–55.

[5]*Time-Dependent Density Functional Theory*, edited by M. Marques, C. Ullrich, F. Nogueira, A. Rubio, K. Burke, and E. Gross (Springer Berlin, 2006).

[6]M. E. Casida, "Time-dependent density functional response theory for molecules," in *Recent Advances in Density Functional Methods, Recent Advances in Computational Chemistry*, edited by D. P. Chong (World Scientific, Singapore, 1995), Vol. 1, pp. 155–192.

[7]L. Kronik and S. Kümmel, "Piecewise linearity, freedom from self-interaction, and a Coulomb asymptotic potential: Three related yet inequivalent properties of the exact density functional," Phys. Chem. Chem. Phys. **22**, 16467–16481 (2020).

[8]Y. Tawada, T. Tsuneda, S. Yanagisawa, T. Yanai, and K. Hirao, "A long-range-corrected time-dependent density functional theory," J. Chem. Phys. **120**, 8425–8433 (2004).

[9]L. Kronik, T. Stein, S. Refaely-Abramson, and R. Baer, "Excitation gaps of finite-sized systems from optimally tuned range-separated hybrid functionals," J. Chem. Theory Comput. **8**, 1515–1531 (2012).

[10]S. Kümmel, "Charge-transfer excitations: A challenge for time-dependent density functional theory that has been met," Adv. Energy Mater. **7**, 1700440 (2017).

[11]N. T. Maitra, "Charge transfer in time-dependent density functional theory," J. Phys.: Condens. Matter **29**, 423001 (2017).

[12]T. Stein, H. Eisenberg, L. Kronik, and R. Baer, "Fundamental gaps in finite systems from eigenvalues of a generalized Kohn-Sham method," Phys. Rev. Lett. **105**, 266802 (2010).

[13]S. Refaely-Abramson, R. Baer, and L. Kronik, "Fundamental and excitation gaps in molecules of relevance for organic photovoltaics from an optimally tuned range-separated hybrid functional," Phys. Rev. B **84**, 075144 (2011).

[14]D. Wing, G. Ohad, J. B. Haber, M. R. Filip, S. E. Gant, J. B. Neaton, and L. Kronik, "Band gaps of crystalline solids from Wannier-localization-based optimal tuning of a screened range-separated hybrid functional," Proc. Natl. Acad. Sci. U. S. A. **118**, e2104556118 (2021).

[15]J. Toulouse, F. Colonna, and A. Savin, "Short-range exchange and correlation energy density functionals: Beyond the local-density approximation," J. Chem. Phys. **122**, 014110 (2005).

[16]A. Savin, "Models and corrections: Range separation for electronic interaction—Lessons from density functional theory," J. Chem. Phys. **153**, 160901 (2020).

[17]T. Yanai, D. P. Tew, and N. C. Handy, "A new hybrid exchange-correlation functional using the Coulomb-attenuating method (CAM–B3LYP)," Chem. Phys. Lett. **393**, 51–57 (2004).

[18]M. J. G. Peach, T. Helgaker, P. Sałek, T. W. Keal, O. B. Lutnæs, D. J. Tozer, and N. C. Handy, "Assessment of a Coulomb-attenuated exchange–correlation energy functional," Phys. Chem. Chem. Phys. **8**, 558–562 (2006).

[19]R. Baer and D. Neuhauser, "Density functional theory with correct long-range asymptotic behaviour," Phys. Rev. Lett. **94**, 043002 (2005).

[20]E. Livshits and R. Baer, "A well-tempered density functional theory of electrons in molecules," Phys. Chem. Chem. Phys. **9**, 2932 (2007).

[21]S. Kümmel and L. Kronik, "Orbital-dependent density functionals: Theory and applications," Rev. Mod. Phys. **80**, 3–60 (2008).

[22]J. Heyd, G. E. Scuseria, and M. Ernzerhof, "Hybrid functionals based on a screened Coulomb potential," J. Chem. Phys. **118**, 8207–8215 (2003); "Erratum: Hybrid functionals based on a screened Coulomb potential [J. Chem. Phys. 118, 8207 (2003)]," **124**, 219906 (2006).

[23]J. Heyd and G. E. Scuseria, "Assessment and validation of a screened Coulomb hybrid density functional," J. Chem. Phys. **120**, 7274–7280 (2004).

[24]O. A. Vydrov, J. Heyd, A. V. Krukau, and G. E. Scuseria, "Importance of short-range versus long-range Hartree-Fock exchange for the performance of hybrid density functionals," J. Chem. Phys. **125**, 074106 (2006).

[25]M. Levy, J. P. Perdew, and V. Sahni, "Exact differential equation for the density and ionization energy of a many-particle system," Phys. Rev. A **30**, 2745–2748 (1984).

[26]D. J. Tozer, "The asymptotic exchange potential in Kohn-Sham theory," J. Chem. Phys. **112**, 3507–3515 (2000).

[27]O. A. Vydrov and G. E. Scuseria, "Assessment of a long-range corrected hybrid functional," J. Chem. Phys. **125**, 234109 (2006).

[28]J.-D. Chai and M. Head-Gordon, "Systematic optimization of long-range corrected hybrid density functionals," J. Chem. Phys. **128**, 084106 (2008).

[29]T. Stein, L. Kronik, and R. Baer, "Reliable prediction of charge transfer excitations in molecular complexes using time-dependent density functional theory," J. Am. Chem. Soc. **131**, 2818–2820 (2009).

[30]N. Kuritz, T. Stein, R. Baer, and L. Kronik, "Charge-transfer-like $\pi \rightarrow \pi^*$ excitations in time-dependent density functional theory: A conundrum and its solution," J. Chem. Theory Comput. **7**, 2408–2415 (2011).

[31]J. P. Perdew, R. G. Parr, M. Levy, and J. L. Balduz, "Density-functional theory for fractional particle number: Derivative discontinuities of the energy," Phys. Rev. Lett. **49**, 1691–1694 (1982).

[32]J. P. Perdew and M. Levy, "Physical content of the exact Kohn-Sham orbital energies: Band gaps and derivative discontinuities," Phys. Rev. Lett. **51**, 1884–1887 (1983).

[33]J. P. Perdew and M. Levy, "Comment on 'Significance of the highest occupied Kohn-Sham eigenvalue,'" Phys. Rev. B **56**, 16021–16028 (1997).

[34]A. Karolewski, L. Kronik, and S. Kümmel, "Using optimally tuned range separated hybrid functionals in ground-state calculations: Consequences and caveats," J. Chem. Phys. **138**, 204115 (2013).

[35]A. Savin, "Is size-consistency possible with density functional approximations?," Chem. Phys. **356**, 91–97 (2009).

[36]V. Vlček, H. R. Eisenberg, G. Steinle-Neumann, L. Kronik, and R. Baer, "Deviations from piecewise linearity in the solid-state limit with approximate density functionals," J. Chem. Phys. **142**, 034107 (2015).

[37]T. Körzdörfer, J. S. Sears, C. Sutton, and J.-L. Brédas, "Long-range corrected hybrid functionals for π-conjugated systems: Dependence of the range-separation parameter on conjugation length," J. Chem. Phys. **135**, 204107 (2011).

[38]A. Karolewski, A. Neubig, M. Thelakkat, and S. Kümmel, "Optical absorption in donor–acceptor polymers–alternating vs random," Phys. Chem. Chem. Phys. **15**, 20016 (2013).

[39]T. B. de Queiroz and S. Kümmel, "Charge-transfer excitations in low-gap systems under the influence of solvation and conformational disorder: Exploring range-separation tuning," J. Chem. Phys. **141**, 084303 (2014).

[40]T. B. de Queiroz and S. Kümmel, "Tuned range separated hybrid functionals for solvated low bandgap oligomers," J. Chem. Phys. **143**, 034101 (2015).

[41]J. P. Perdew, "Orbital functional for exchange and correlation: Self-interaction correction to the local density approximation," Chem. Phys. Lett. **64**, 127–130 (1979).

[42]J. P. Perdew and A. Zunger, "Self-interaction correction to density-functional approximations for many-electron systems," Phys. Rev. B **23**, 5048–5079 (1981).

[43]M. A. Rohrdanz and J. M. Herbert, "Simultaneous benchmarking of ground- and excited-state properties with long-range-corrected density functional theory," J. Chem. Phys. **129**, 034107 (2008).

[44]R. A. Mendes, R. L. A. Haiduke, and R. J. Bartlett, "The Devil's triangle of Kohn-Sham density functional theory and excited states," J. Chem. Phys. **154**, 074106 (2021).

[45]T. Schmidt, E. Kraisler, A. Makmal, L. Kronik, and S. Kümmel, "A self-interaction-free local hybrid functional: Accurate binding energies vis-à-vis accurate ionization potentials from Kohn-Sham eigenvalues," J. Chem. Phys. **140**, 18A510 (2014).

[46]A. V. Krukau, G. E. Scuseria, J. P. Perdew, and A. Savin, "Hybrid functionals with local range separation," J. Chem. Phys. **129**, 124103 (2008).

[47]T. Aschebrock and S. Kümmel, "Exploring local range separation: The role of spin scaling and one-electron self-interaction," J. Chem. Phys. **151**, 154108 (2019).
[48]M. Levy and J. P. Perdew, "Hellman-Feynman virial, and scaling requisites for the exact universal density functionals. Shape of the correlation potential and diamagnetic susceptibility for atoms," Phys. Rev. A **32**, 2010–2021 (1985).
[49]M. Levy, "Density-functional exchange correlation through coordinate scaling in adiabatic connection and correlation hole," Phys. Rev. A **43**, 4637–4646 (1991).
[50]T. M. Maier, Y. Ikabata, and H. Nakai, "Assessing locally range-separated hybrid functionals from a gradient expansion of the exchange energy density," J. Chem. Phys. **154**, 214101 (2021).
[51]S. Klawohn and H. Bahmann, "Self-consistent implementation of hybrid functionals with local range separation," J. Chem. Theory Comput. **16**, 953–963 (2020).
[52]H. Bahmann and M. Kaupp, "Efficient self-consistent implementation of local hybrid functionals," J. Chem. Theory Comput. **11**, 1540–1548 (2015).
[53]T. M. Maier, H. Bahmann, and M. Kaupp, "Efficient semi-numerical implementation of global and local hybrid functionals for time-dependent density functional theory," J. Chem. Theory Comput. **11**, 4226–4237 (2015).
[54]S. Klawohn, H. Bahmann, and M. Kaupp, "Implementation of molecular gradients for local hybrid density functionals using seminumerical integration techniques," J. Chem. Theory Comput. **12**, 4254–4262 (2016).
[55]F. Neese, F. Wennmohs, A. Hansen, and U. Becker, "Efficient, approximate and parallel Hartree-Fock and hybrid DFT calculations. A 'chain-of-spheres' algorithm for the Hartree-Fock exchange," Chem. Phys. **356**, 98–109 (2009).
[56]P. Plessow and F. Weigend, "Seminumerical calculation of the Hartree-Fock exchange matrix: Application to two-component procedures and efficient evaluation of local hybrid density functionals," J. Comput. Chem. **33**, 810–816 (2012).
[57]T. Schmidt, E. Kraisler, L. Kronik, and S. Kümmel, "One-electron self-interaction and the asymptotics of the Kohn–Sham potential: An impaired relation," Phys. Chem. Chem. Phys. **16**, 14357–14367 (2014).
[58]A. V. Arbuznikov and M. Kaupp, "Local hybrid exchange-correlation functionals based on the dimensionless density gradient," Chem. Phys. Lett. **440**, 160–168 (2007).
[59]A. V. Arbuznikov, H. Bahmann, and M. Kaupp, "Local hybrid functionals with an explicit dependence on spin polarization," J. Phys. Chem. A **113**, 11898–11906 (2009).
[60]H. Bahmann, A. Rodenberg, A. V. Arbuznikov, and M. Kaupp, "A thermochemically competitive local hybrid functional without gradient corrections," J. Chem. Phys. **126**, 011103 (2007).
[61]P. de Silva and C. Corminboeuf, "Local hybrid functionals with orbital-free mixing functions and balanced elimination of self-interaction error," J. Chem. Phys. **142**, 074112 (2015).
[62]T. M. Maier, A. V. Arbuznikov, and M. Kaupp, "Local hybrid functionals: Theory, implementation, and performance of an emerging new tool in quantum chemistry and beyond," Wiley Interdiscip. Rev.: Comput. Mol. Sci. **9**, e1378 (2019).
[63]J. P. Perdew, V. N. Staroverov, J. Tao, and G. E. Scuseria, "Density functional with full exact exchange, balanced nonlocality of correlation, and constraint satisfaction," Phys. Rev. A **78**, 052513 (2008).
[64]E. R. Johnson, "Local-hybrid functional based on the correlation length," J. Chem. Phys. **141**, 124120 (2014).
[65]Our Eq. (13), in principle, corresponds to the leading term in Eq. (29) of Maier *et al.*[50] One sees this by inserting their Eqs. (8) and (11) into their Eq. (29), with their $F_\sigma^x = 0$ for the case of LDA. However, their Eq. (29) is misprinted; thus, our Eq. (13) corresponds to Eq. (29) of Maier *et al.*[50] multiplied by a factor $\sqrt{\pi}$.
[66]D. Hofmann and S. Kümmel, "Self-interaction correction in a real-time Kohn-Sham scheme: Access to difficult excitations in time-dependent density functional theory," J. Chem. Phys. **137**, 064117 (2012).
[67]We note that Ref. 15 connected the screened interaction with a gradient coefficient of 7/81.
[68]In the notation of Eqs. (22) and (24), we suppress the dependence of Ω_σ on $|\nabla n|$ for brevity.
[69]A. D. Becke, "Local exchange-correlation approximations and first-row molecular dissociation energies," Int. J. Quantum Chem. **27**, 585–594 (1985).
[70]J. F. Dobson, "Spin-density functionals for the electron correlation energy with automatic freedom from orbital self-interaction," J. Phys.: Condens. Matter **4**, 7877–7890 (1992).
[71]S. Kümmel and J. P. Perdew, "Two avenues to self-interaction correction within Kohn—Sham theory: Unitary invariance is the shortcut," Mol. Phys. **101**, 1363–1368 (2003).
[72]G. L. Oliver and J. P. Perdew, "Spin-density gradient expansion for the kinetic energy," Phys. Rev. A **20**, 397–403 (1979).
[73]A. D. Becke, "Density-functional thermochemistry. III. The role of exact exchange," J. Chem. Phys. **98**, 5648–5652 (1993).
[74]R. Neumann, R. H. Nobes, and N. C. Handy, "Exchange functionals and potentials," Mol. Phys. **87**, 1–36 (1996).
[75]K. Burke, J. P. Perdew, and M. Ernzerhof, "Why the generalized gradient approximation works and how to go beyond it," Int. J. Quantum Chem. **61**, 287–293 (1997).
[76]D. Cremer, "Density functional theory: Coverage of dynamic and non-dynamic electron correlation effects," Mol. Phys. **99**, 1899–1940 (2001).
[77]P. M. W. Gill, R. D. Adamson, and J. A. Pople, "Coulomb-attenuated exchange energy density functionals," Mol. Phys. **88**, 1005–1009 (1996).
[78]J. P. Perdew and Y. Wang, "Accurate and simple analytic representation of the electron-gas correlation energy," Phys. Rev. B **45**, 13244–13249 (1992).
[79]A. V. Arbuznikov and M. Kaupp, "Importance of the correlation contribution for local hybrid functionals: Range separation and self-interaction corrections," J. Chem. Phys. **136**, 014111 (2012).
[80]R. Ahlrichs, M. Bär, M. Häser, H. Horn, and C. Kölmel, "Electronic structure calculations on workstation computers: The program system TURBOMOLE," Chem. Phys. Lett. **162**, 165–169 (1989).
[81]Y. Shao *et al.*, "Advances in molecular quantum chemistry contained in the Q-Chem 4 program package," Mol. Phys. **113**, 184–215 (2015).
[82]S. J. Chakravorty, S. R. Gwaltney, E. R. Davidson, F. A. Parpia, and C. F. p Fischer, "Ground-state correlation energies for atomic ions with 3 to 18 electrons," Phys. Rev. A **47**, 3649–3670 (1993).
[83]B. J. Lynch and D. G. Truhlar, "Small representative benchmarks for thermochemical calculations," J. Phys. Chem. A **107**, 8996–8999 (2003); "Small representative benchmarks for thermochemical calculations," **108**, 1460 (2004).
[84]R. D. Johnson III, "NIST computational chemistry comparison and benchmark database," NIST Standard Reference Database Number 101, 2020, release 21.
[85]J. P. Perdew, K. Burke, and M. Ernzerhof, "Generalized gradient approximation made simple," Phys. Rev. Lett. **77**, 3865–3868 (1996).
[86]C. Adamo and V. Barone, "Toward reliable density functional methods without adjustable parameters: The PBE0 model," J. Chem. Phys. **110**, 6158–6170 (1999); M. Ernzerhof and G. E. Scuseria, "Assessment of the Perdew-Burke-Ernzerhof exchange-correlation functional," *ibid.* **110**, 5029–5036 (1999).
[87]A. D. Becke, "Density-functional exchange-energy approximation with correct asymptotic behavior," Phys. Rev. A **38**, 3098–3100 (1988); C. Lee, W. Yang, and R. G. Parr, "Development of the Colle-Salvetti correlation-energy formula into a functional of the electron density," Phys. Rev. B **37**, 785–789 (1988); P. J. Stephens, F. J. Devlin, C. F. Chabalowski, and M. J. Frisch, "*Ab initio* calculation of vibrational absorption and circular dichroism spectra using density functional force fields," J. Phys. Chem. **98**, 11623–11627 (1994).
[88]R. Peverati and D. G. Truhlar, "M11-L: A local density functional that provides improved accuracy for electronic structure calculations in chemistry and physics," J. Phys. Chem. Lett. **3**, 117–124 (2012).
[89]H. S. Yu, X. He, and D. G. Truhlar, "MN15-L: A new local exchange-correlation functional for Kohn-Sham density functional theory with broad accuracy for atoms, molecules, and solids," J. Chem. Theory Comput. **12**, 1280–1293 (2016).
[90]R. Peverati and D. G. Truhlar, "Improving the accuracy of hybrid meta-GGA density functionals by range separation," J. Phys. Chem. Lett. **2**, 2810–2817 (2011).
[91]H. S. Yu, X. He, S. L. Li, and D. G. Truhlar, "MN15: A Kohn-Sham global-hybrid exchange-correlation density functional with broad accuracy for multi-reference and single-reference systems and noncovalent interactions," Chem. Sci. **7**, 5032–5051 (2016); "Correction: MN15: A Kohn-Sham global-hybrid

exchange-correlation density functional with broad accuracy for multi-reference and single-reference systems and noncovalent interactions," **7**, 6278–6279 (2016).
[92]R. Peverati and D. G. Truhlar, "Quest for a universal density functional: The accuracy of density functionals across a broad spectrum of databases in chemistry and physics," Philos. Trans. R. Soc., A **372**, 20120476 (2014).
[93]T. Schmidt and S. Kümmel, "One- and many-electron self-interaction error in local and global hybrid functionals," Phys. Rev. B **93**, 165120-1–165120-14 (2016).
[94]R. Peverati and D. G. Truhlar, "Communication: A global hybrid generalized gradient approximation to the exchange-correlation functional that satisfies the second-order density-gradient constraint and has broad applicability in chemistry," J. Chem. Phys. **135**, 191102 (2011).
[95]Y. Zhao and D. G. Truhlar, "The M06 suite of density functionals for main group thermochemistry, thermochemical kinetics, noncovalent interactions, excited states, and transition elements: Two new functionals and systematic testing of four M06-class functionals and 12 other functionals," Theor. Chem. Acc. **120**, 215–241 (2008).
[96]J. Zheng, Y. Zhao, and D. G. Truhlar, "The DBH24/08 database and its use to assess electronic structure model chemistries for chemical reaction barrier heights," J. Chem. Theory Comput. **5**, 808–821 (2009).

Supplementary Material for

Hybrid Functionals with Local Range Separation: Accurate Atomization Energies and Reaction Barrier Heights

Journal of Chemical Physics

Moritz Brütting,[1] Hilke Bahmann,[2] and Stephan Kümmel[1]

[1] Theoretical Physics IV, University of Bayreuth
[2] Physical and Theoretical Chemistry, Saarland University

In this supplementary material, we give more detailed insights into the properties of our local range-separated hybrid (RSH) functionals, and illustrate how we assess their performance and optimize the functional parameters. Furthermore, we explain how we calculate the equilibrium bond lengths and harmonic vibrational frequencies of diatomic molecules, and comment on the computational effort required for the local RSH calculations.

We use four different test sets. First, we use an in-house set [1] of 11 atomization energies of diatomic molecules (H_2, LiH, Li_2, LiF, CO, N_2, NO, OH, O_2, HF, and F_2) at experimental bond lengths from Ref. [2] (see also Table S6). The experimental reference values for the atomization energies (with zero point vibration removed) have been taken from Ref. [3]. Furthermore, we use a test set of 17 atomic ground-state energies (from H to Cl) with the reference values taken from the Minnesota database 2.0 [4–6]. Additionally, we use the AE6 and BH6 test sets of atomization energies and reaction barrier heights [7, 8]. Here, we also use the updated reference values (without vector-relativistic effects) and molecule geometries from the Minnesota database 2.0 [4, 9, 10]. Finally, we calculate the equilibrium bond lengths and harmonic vibrational frequencies (as detailed below) for the molecules in the AE11D test set. The corresponding experimental reference data is taken from Ref. [2].

For all these properties, we quantify the deviation of calculated and reference values by:

$$\Delta V \equiv V_{\mathrm{calc}} - V_{\mathrm{ref}}, \tag{S1}$$

where V_{calc} and V_{ref} refer to the calculated and reference values, respectively, for a certain system (molecule, chemical reaction, or atom). By averaging the (absolute) values of ΔV over all systems in a certain test set, we determine the mean signed error (MSE) or mean absolute error (MAE), respectively. Below we provide explicit listings of the reference values V_{ref} and the deviations ΔV for individual systems: For the AE11D test set, the atomization energies are given in Table S3. The atomization energies and barrier heights for the AE6 and BH6 test sets are provided in Tables S1, S2, and S4. Table S5 lists the atomic ground-state energies. The equilibrium bond lengths of the molecules in the AE11D test set are given in Table S6, the harmonic vibrational frequencies in Table S7. In these tables, we use the functional names introduced in the main text, cf. especially Table I therein.

Parameter Optimization

The values of the parameters in our functionals are optimized for atomization energies, reaction barrier heights, and atomic ground-state energies. Thereby, we determine the parameter tuples that minimize

the MAE for each functional and test set. For the atomic test set we consider ΔV and the MAE *per electron*. The parameters were varied in discrete steps within certain intervals of values. For clarity we give a specific example: For determining the optimal values for the SIC-ωLDA functional mentioned in Table VIII of the main text we varied η from 0.113 to 0.118 in steps of 0.001, and γ from $0.180\,\mathrm{a_0}$ to $0.220\,\mathrm{a_0}$ in steps of $0.001\,\mathrm{a_0}$, and checked which combination of the two parameters minimized the sum of the MAEs of the AE6 and the BH6 test sets. Before, coarser grids have been used to determine the approximate position of the optimum and to ensure that this parameter combination yields the global, and not only a local minimum of the combined MAEs.

Equilibrium Bond Lengths and Harmonic Vibrational Frequencies

Typically, equilibrium bond lengths and harmonic vibrational frequencies are calculated via molecular gradients, i. e., derivatives of the total energy with respect to nuclear displacements. However, as our self-consistent implementation of local RSH functionals is a very recent development, such an algorithm is not yet available. Nevertheless, for diatomic molecules bond lengths and harmonic vibrational frequencies can readily be obtained by calculating the ground-state energy $E(l)$ at different bond lengths l. In principle, the equilibrium bond length of a molecule is then directly given as that bond length l_0 which minimizes $E(l)$.

The harmonic vibrational frequency can be calculated from the (numerical) second derivative of $E(l)$:

$$\omega = \sqrt{\frac{1}{\mu}\left.\frac{\partial^2 E(l)}{\partial l^2}\right|_{l=l_0}}, \tag{S2}$$

where $\mu = m_1 m_2/(m_1 + m_2)$ is the reduced mass of the molecule with atomic masses m_1 and m_2. In practice, it is advantageous not to determine the equilibrium bond length and the harmonic vibrational frequency directly from the numerical data but to approximate $E(l)$ by a model function,

$$\mathcal{E}(l) = E_0 + \frac{k}{2}(l - l_0)^2 + \frac{a}{6}(l - l_0)^3 + \frac{b}{24}(l - l_0)^4, \tag{S3}$$

in an interval around the minimum of $E(l)$. The form of $\mathcal{E}(l)$ can be motivated by a Taylor series expansion. The parameters E_0, l_0, k, a, and b in Eq. (S3) are determined by fitting $\mathcal{E}(l)$ to $E(l)$. Then, the equilibrium bond length is given by the optimal value for l_0, and the harmonic vibrational frequency follows by inserting k into Eq. (S2).

In our work, we sample $E(l)$ in steps of $\Delta l = 0.001\,\text{Å}$ for each molecule and functional. Then, the model $\mathcal{E}(l)$ is fitted to $E(l)$ in an interval of $\pm 0.02\,\text{Å}$ around the approximate position of the minimum (estimated from the minimum of the raw numerical data for $E(l)$) using a standard non-linear least squares algorithm as implemented in the `optimize.curve_fit` function of Python's SciPy package (Python version 2.7, SciPy version 1.2.2). Due to the excellent agreement of model and data, the uncertainty of l_0 and k that results from the fitting procedure is negligible. The atomic masses that enter into Eq. (S2) are taken from Ref. [11].

Computational Effort

Our semi-numerical implementation of local RSHs in `TURBOMOLE` [12] is – at its present stage – not yet optimized for computational efficiency. Therefore, directly comparing the computational effort to that of other density functional implementations, e. g., standard (analytical) global RSH implementations, is currently not reasonable. However, comparing different RSH functionals with constant and

space-dependent range-separation functions (RSFs), respectively, within our semi-numerical RSH implementation, can provide a first impression of the additional computational effort required for the evaluation of the hybrid functionals with local range separation. Doing this comparison we find that the computation time required for SIC-ωLDA is a few 10 % higher than that for ωLDA (for the molecules in the AE6 test set, and with the same functional parameters as in Table S4) while the scaling with system size is similar for both functionals. The latter is to be expected also from formal considerations.

Table S1: Details on the assessment of the atomization energies of the AE6 test set, corresponding to Table III of the main text. For each molecule (cf. column 1) we list the reference value (column 2), and the deviation ΔV of calculated and reference values for the different functionals (column 3 to 7). Additionally, the resulting MAEs and MSEs are given for the different functionals. All values are in kcal/mol.

Functional Parameter(s)	Ref. —	LDA —	ωLDA $\omega_0 = 0.601\,/\mathrm{a_0}$	K-ωLDA $\eta = 0.131$	SIC-ωLDA ($\gamma \equiv 0$) $\eta = 0.132$	SIC-ωLDA $\eta = 0.114$, $\gamma = 0.218\,\mathrm{a_0}$
SiH_4	324.95	22.00	14.84	6.57	5.16	0.24
SiO	193.06	30.28	−6.70	−10.10	−4.67	−3.65
S_2	104.25	30.99	−16.76	−0.08	2.14	4.89
C_3H_4	705.06	95.34	3.56	0.15	3.31	0.01
$C_2H_2O_2$	633.99	118.06	−0.07	−6.30	−0.40	0.03
C_4H_8	1149.37	152.91	16.25	5.71	6.22	−0.25
MAE	—	74.93	9.70	4.82	3.65	1.51
MSE		74.93	1.85	−0.68	1.96	0.21

Table S2: Details on the assessment of the reaction barrier heights of the BH6 test set, corresponding to Table V of the main text. For each reaction (cf. column 1) we list the reference value (column 2), and the deviation ΔV of calculated and reference values for the different functionals (column 3 to 6). Additionally, the resulting MAEs and MSEs are given for the different functionals. All values are in kcal/mol. The *forward* reactions are denoted by F, the *reverse* reactions by R.

Functional Parameter		Ref. —	LDA —	ωLDA $\omega_0 = 0.486\,/\mathrm{a_0}$	K-ωLDA $\eta = 0.144$	SIC-ωLDA ($\gamma \equiv 0$) $\eta = 0.128$
$OH + CH_4 \rightarrow$	F	6.50	−22.70	0.00	−0.04	−2.27
$CH_3 + H_2O$	R	19.60	−18.48	1.51	−2.21	−3.18
$H + OH \rightarrow$	F	10.50	−12.70	−2.16	−7.06	−2.44
$O + H_2$	R	12.87	−24.49	−2.81	0.32	0.07
$H + H_2S \rightarrow$	F	3.50	−9.87	−0.94	−4.07	−0.29
$H_2 + HS$	R	16.76	−16.69	3.13	1.99	0.94
MAE		—	17.49	1.76	2.62	1.53
MSE			17.49	−0.21	−1.85	−1.19

Table S3: Details on the assessment of the atomization energies of the AE11D test set, corresponding to Table II of the main text. For each molecule (cf. column 1) we list the reference value (column 2), and the deviation ΔV of calculated and reference values for the different functionals (column 3 to 13). Additionally, the resulting MAEs and MSEs are given for the different functionals. All values are in kcal/mol.

Functional	Ref.	LDA	ωLDA	K-ωLDA	—	—	...
RSF ω_σ			$\omega_0 = const.$	$\eta\lvert\nabla n_\sigma\rvert/n_\sigma$	$\eta\lvert\nabla n_\sigma\rvert^2/n_\sigma^{7/3}$	$\eta\lvert\nabla n_\sigma\rvert^3/n_\sigma^{11/3}$	
Correlation	—	—	LDA		LDA		
Parameter			$\omega_0 = 0.548\,/\mathrm{a}_0$	$\eta = 0.124$	$\eta = 9.67 \cdot 10^{-3}$	$\eta = 4.23 \cdot 10^{-5}$	
H_2	109.5	3.3	4.2	5.4	6.1	2.9	
LiH	58.0	2.0	5.6	1.0	0.0	7.0	
Li_2	24.7	−1.4	−3.5	−6.6	−7.5	−3.6	
LiF	138.3	14.3	7.6	−7.5	−9.2	14.4	
CO	259.5	39.5	−0.2	−2.6	−4.2	−4.3	
N_2	228.3	39.0	−4.8	−5.7	−11.2	0.0	...
NO	152.5	46.3	0.9	0.9	0.0	2.4	
OH	107.1	15.1	3.4	0.9	−0.1	−0.5	
O_2	120.5	54.6	4.2	7.4	11.1	4.3	
HF	141.1	18.4	4.7	0.8	1.6	−0.4	
F_2	38.4	39.4	−2.6	−0.3	6.4	2.7	
MAE	—	24.8	3.8	3.6	5.2	3.9	...
MSE		24.6	1.8	−0.6	−0.4	2.3	

...	—	—	SIC-ωLDA ($\gamma \equiv 0$)	—	—	—
	$\Omega_\sigma^\mathrm{K}\,\Theta(z_\sigma)$		$\Omega_\sigma^\mathrm{K}\,\Theta(z_\sigma\zeta^2)$		$\Omega^\mathrm{K}\,\Theta(z\zeta^2)$	
	LDA-SPZ	LDA-Z	LDA-SPZ	LDA-Z	LDA-SPZ	LDA-Z
	$\eta = 0.176$	$\eta = 0.317$	$\eta = 0.128$	$\eta = 0.101$	$\eta = 0.159$	$\eta = 0.117$
	33.5	4.7	1.9	−33.3	8.6	−29.3
	23.2	0.5	1.1	−25.7	6.9	−21.4
	9.4	−2.9	−2.8	−17.3	2.1	−12.6
	−6.2	−9.3	−5.6	−7.7	−5.2	−6.3
	−24.7	−34.9	0.8	−0.2	−1.0	−0.1
...	−5.5	−51.9	−1.6	−26.2	0.8	−23.3
	−21.9	−46.4	2.3	−3.6	1.4	−2.6
	12.5	−0.8	−0.6	−13.5	2.0	−11.8
	−40.5	−40.8	5.1	19.5	0.4	18.7
	−0.1	−4.3	−1.0	−8.1	0.3	−7.0
	−28.6	−28.8	−0.3	12.7	−6.0	10.5
...	18.7	20.5	2.1	15.3	3.2	13.1
	−4.4	−19.5	−0.1	−9.4	0.9	−7.7

Table S4: Details on the comparison of various density functionals for the AE6 and BH6 test sets, corresponding to Table VIII of the main text. For each molecule or reaction, respectively, (cf. column 1) we list the reference value (column 2), and the deviation ΔV of calculated and reference values for different functionals (column 3 to 16). Additionally, the resulting MAEs (for AE6, BH6, and across both test sets) and MSEs (individually for AE6, and BH6) are given. All values are in kcal/mol. The *forward* reactions of BH6 are denoted by *F*, the *reverse* reactions by *R*. Details on the functionals and their parameters can be found in Table VIII of the main text.

Functional		Ref.	LDA	PBE	PBE0	ωPBE	BLYP	B3LYP	...
Parameter(s)		—	—	—	—	$\omega = 0.4\,/\mathrm{a_0}$	—	—	
SiH_4		324.95	22.00	−11.60	−9.77	−7.17	−7.26	−1.37	
SiO		193.06	30.28	2.43	−11.01	−8.60	1.48	−6.04	
S_2		104.25	30.99	10.76	2.38	−5.92	2.89	−1.24	...
C_3H_4		705.06	95.34	15.09	1.85	−0.91	−4.56	−3.52	
$C_2H_2O_2$		633.99	118.06	28.64	0.53	2.92	6.03	−4.09	
C_4H_8		1149.37	152.91	17.08	5.81	6.50	−19.68	−9.02	
MAE (AE6)		—	74.93	14.27	5.22	5.34	6.98	4.21	...
MSE (AE6)			74.93	10.40	−1.70	−2.20	−3.52	−4.21	
$OH + CH_4 \rightarrow$	*F*	6.50	−22.70	−11.34	−4.05	−0.80	−8.52	−3.83	
$CH_3 + H_2O$	*R*	19.60	−18.48	−11.92	−6.68	−2.10	−10.39	−6.85	
$H + OH \rightarrow$	*F*	10.50	−12.70	−7.40	−3.96	−0.50	−9.66	−7.07	...
$O + H_2$	*R*	12.87	−24.49	−13.32	−6.19	−4.07	−10.58	−5.87	
$H + H_2S \rightarrow$	*F*	3.50	−9.87	−4.43	−2.13	0.60	−5.54	−3.87	
$H_2 + HS$	*R*	16.76	−16.69	−6.88	−3.97	−0.45	−2.12	−0.59	
MAE (BH6)		—	17.49	9.22	4.49	1.42	7.80	4.68	...
MSE (BH6)			−17.49	−9.22	−4.49	−1.22	−7.80	−4.68	
MAE (AE6BH6)		—	46.21	11.75	4.86	3.38	7.39	4.45	...

...	CAM-B3LYP	M11-L	MN15-L	M11	MN15	ωLDA	K-ωLDA	SIC-ωLDA
	—	—	—	—	—	$\omega_0 = 0.600\,/\mathrm{a_0}$	$\eta = 0.131$	$\eta = 0.115$, $\gamma = 0.202\,\mathrm{a_0}$
	0.35	2.15	6.17	−1.77	1.18	14.82	6.57	0.50
	−5.21	−9.20	−5.51	−6.05	1.02	−6.64	−10.10	−3.75
...	−4.04	11.79	2.05	−0.61	0.39	−16.72	−0.08	4.72
	−1.07	−5.55	−4.50	−3.21	−1.89	3.64	0.15	0.11
	−0.57	−5.58	−0.21	−2.87	2.17	0.08	−6.30	−0.11
	−0.46	−10.90	−5.56	−4.30	−3.10	16.34	5.71	0.00
...	1.95	7.53	4.00	3.14	1.62	9.71	4.82	1.53
	−1.83	−2.88	−1.26	−3.14	−0.04	1.92	−0.68	0.24
	−2.82	2.49	1.36	−1.07	−0.28	4.36	−2.15	−2.91
	−5.42	−1.94	−1.53	−2.50	−2.12	4.85	−3.62	−4.22
...	−5.42	−1.15	−3.31	−2.18	−0.84	−0.13	−7.60	−2.47
	−5.53	−0.14	0.46	−1.83	−1.14	1.70	−2.05	−0.32
	−2.69	1.50	0.57	−0.84	1.16	0.18	−4.63	0.01
	−0.63	0.36	1.50	0.03	0.41	5.97	0.24	−0.06
...	3.75	1.26	1.45	1.41	0.99	2.87	3.38	1.66
	−3.75	0.19	−0.16	−1.40	−0.47	2.82	−3.30	−1.66
...	2.85	4.40	2.73	2.28	1.31	6.29	4.10	1.60

Table S5: Details on the assessment of the ground-state energies of the atomic test set, corresponding to Table IV of the main text. For each atom (cf. column 1) we list the reference value (column 2), and the deviation ΔV per electron of calculated and reference values for the different functionals (column 3 to 8). Additionally, the resulting MAEs and MSEs per electron are given for the different functionals. All values are in Hartree atomic units.

Functional Parameter(s)	Ref. —	LDA —	ωLDA $\omega_0 = 3.00\,/\mathrm{a}_0$	K-ωLDA $\eta = 0.263$	K-ωLDA (+γ) $\eta = 0.113$, $\gamma = 3.11\,\mathrm{a}_0$	...
H	−0.500	0.022	−0.022	−0.014	−0.004	
He	−2.904	0.036	−0.035	−0.021	−0.011	
Li	−7.478	0.045	−0.034	−0.019	−0.012	
Be	−14.667	0.056	−0.028	−0.013	−0.008	
B	−24.654	0.060	−0.024	−0.011	−0.007	
C	−37.845	0.063	−0.018	−0.009	−0.006	
N	−54.589	0.066	−0.013	−0.007	−0.005	
O	−75.067	0.068	−0.008	−0.005	−0.004	
F	−99.734	0.070	−0.004	−0.003	−0.002	...
Ne	−128.938	0.072	−0.001	−0.001	0.000	
Na	−162.255	0.075	0.001	0.000	0.000	
Mg	−200.053	0.078	0.003	0.002	0.001	
Al	−242.346	0.080	0.004	0.003	0.002	
Si	−289.359	0.083	0.007	0.005	0.002	
P	−341.259	0.085	0.009	0.006	0.003	
S	−398.110	0.087	0.011	0.007	0.003	
Cl	−460.148	0.088	0.012	0.008	0.004	
MAE	—	0.067	0.014	0.008	0.004	...
MSE		0.067	−0.008	−0.004	−0.003	

...	SIC-ωLDA ($\gamma \equiv 0$) $\eta = 0.266$	SIC-ωLDA $\eta = 0.117$, $\gamma = 2.72\,\mathrm{a}_0$
	0.000	0.000
	−0.021	−0.012
	−0.016	−0.011
	−0.013	−0.008
	−0.010	−0.007
	−0.008	−0.006
	−0.006	−0.004
	−0.005	−0.004
...	−0.004	−0.002
	−0.002	0.000
	0.000	0.000
	0.001	0.001
	0.003	0.002
	0.005	0.002
	0.007	0.003
	0.007	0.003
	0.008	0.004
...	0.007	0.004
	−0.003	−0.002

Table S6: Details on the assessment of the equilibrium bond lengths of the molecules in the AE11D test set, corresponding to Table VI of the main text. For each molecule (cf. column 1) we list the reference value (column 2), and the deviation ΔV of calculated and reference values for the different functionals (column 3 to 6). Additionally, the resulting MAEs and MSEs are given for the different functionals. All values are in Å.

Functional Parameter	Ref. —	LDA —	ωLDA $\omega_0 = 0.548\,/\mathrm{a}_0$	K-ωLDA $\eta = 0.124$	SIC-ωLDA ($\gamma \equiv 0$) $\eta = 0.128$
H_2	0.7414	0.0254	0.0066	0.0105	0.0098
LiH	1.5949	0.0109	−0.0115	0.0120	0.0118
Li_2	2.6730	0.0517	0.0397	0.0901	0.0914
LiF	1.5639	−0.0100	−0.0006	0.0063	0.0069
CO	1.1282	−0.0003	−0.0178	−0.0041	−0.0042
N_2	1.0977	−0.0020	−0.0227	−0.0073	−0.0075
NO	1.1508	−0.0041	−0.0270	−0.0102	−0.0113
OH	0.9697	0.0179	0.0004	0.0072	0.0059
O_2	1.2075	−0.0034	−0.0358	−0.0141	−0.0161
HF	0.9168	0.0165	0.0034	0.0058	0.0053
F_2	1.4119	−0.0276	−0.0639	−0.0433	−0.0441
MAE	—	0.0154	0.0209	0.0192	0.0195
MSE		0.0068	−0.0117	0.0048	0.0043

Table S7: Details on the assessment of the harmonic vibrational frequencies of the molecules in the AE11D test set, corresponding to Table VI of the main text. For each molecule (cf. column 1) we list the reference value (column 2), and the deviation ΔV of calculated and reference values for the different functionals (column 3 to 6). Additionally, the resulting MAEs and MSEs are given for the different functionals. All values are in 1/cm.

Functional Parameter	Ref. —	LDA —	ωLDA $\omega_0 = 0.548\,/\mathrm{a}_0$	K-ωLDA $\eta = 0.124$	SIC-ωLDA ($\gamma \equiv 0$) $\eta = 0.128$
H_2	4401.2	−213.0	73.9	−50.8	−42.4
LiH	1405.5	−24.4	72.0	−6.5	−4.8
Li_2	351.4	−20.4	9.0	−18.7	−18.5
LiF	910.6	46.4	54.4	40.3	40.2
CO	2169.8	10.1	182.8	62.2	64.6
N_2	2358.6	44.0	268.9	112.3	115.5
NO	1904.1	49.0	266.4	122.4	130.1
OH	3737.8	−153.6	106.5	−30.1	−14.3
O_2	1580.2	39.9	284.5	135.2	145.4
HF	4138.4	−156.5	70.5	−8.6	−1.1
F_2	916.9	147.4	271.2	211.0	214.2
MAE	—	82.3	150.9	72.5	71.9
MSE		−21.0	150.9	51.7	57.2

Acronyms

DFT density functional theory

GGA generalized gradient approximation

HOMO highest occupied molecular orbital

IP ionization potential

LDA local density approximation

MAE mean absolute error

MSE mean signed error

RSF range-separation function

RSH range-separated hybrid

SIC self-interaction correction

xc exchange-correlation

References

[1] T. Aschebrock and S. Kümmel, Exploring local range separation: The role of spin scaling and one-electron self-interaction, J. Chem. Phys. **151**, 154108 (2019).

[2] Russell D. Johnson III, *NIST Computational Chemistry Comparison and Benchmark Database, NIST Standard Reference Database Number 101*, Release 21, 2020, `http://cccbdb.nist.gov/`.

[3] J. Rumble, ed., *CRC Handbook of Chemistry and Physics*, 98th ed. (CRC Press, 2017).

[4] R. Peverati and D. G. Truhlar, Quest for a universal density functional: the accuracy of density functionals across a broad spectrum of databases in chemistry and physics, Philos. Trans. R. Soc. A: Math. Phys. Eng. Sci. **372**, 20120476 (2014).

[5] S. J. Chakravorty, S. R. Gwaltney, E. R. Davidson, F. A. Parpia, and C. F. Fischer, Ground-state correlation energies for atomic ions with 3 to 18 electrons, Phys. Rev. A **47**, 3649 (1993).

[6] R. Peverati and D. G. Truhlar, Communication: a global hybrid generalized gradient approximation to the exchange-correlation functional that satisfies the second-order density-gradient constraint and has broad applicability in chemistry, J. Chem. Phys. **135**, 191102 (2011).

[7] B. J. Lynch and D. G. Truhlar, Small Representative Benchmarks for Thermochemical Calculations, J. Phys. Chem. A **107**, 8996 (2003).

[8] B. J. Lynch and D. G. Truhlar, Small Representative Benchmarks for Thermochemical Calculations, J Phys Chem A **108**, 1460 (2004).

[9] Y. Zhao and D. G. Truhlar, The M06 suite of density functionals for main group thermochemistry, thermochemical kinetics, noncovalent interactions, excited states, and transition elements: two new functionals and systematic testing of four M06-class functionals and 12 other functionals, Theor Chem Acc **120**, 215 (2008).

[10] J. Zheng, Y. Zhao, and D. G. Truhlar, The DBH24/08 Database and Its Use to Assess Electronic Structure Model Chemistries for Chemical Reaction Barrier Heights, J. Chem. Theory Comput. **5**, 808 (2009).

[11] P. Linstrom, *NIST Chemistry WebBook, NIST Standard Reference Database 69*, 2022.

[12] S. Klawohn and H. Bahmann, Self-Consistent Implementation of Hybrid Functionals with Local Range Separation, J. Chem. Theory Comput. **16**, 953 (2020).

Reprint of publication [B3]

Publication [B3]

M. Brütting, J. M. Foerster, and S. Kümmel

Understanding primary charge separation in the heliobacterial reaction center

J. Phys. Chem. Lett. **14**, 3092 (2023)

DOI: 10.1021/acs.jpclett.3c00377

Author contribution statement: M.B. and S.K. conceptualized the work. M.B. prepared the structural models, did all the TDDFT and BOMD calculations, and prepared all figures and tables. J.F. supported the structure preparation and performed the titration analysis and the positioning of the interstital water molecules. All authors disucssed the results. M.B. and S.K. wrote the manuscript, and J.F. proofread it and gave comments.

THE JOURNAL OF PHYSICAL CHEMISTRY LETTERS
A JOURNAL OF THE AMERICAN CHEMICAL SOCIETY

pubs.acs.org/JPCL

Letter

Understanding Primary Charge Separation in the Heliobacterial Reaction Center

Moritz Brütting, Johannes M. Foerster, and Stephan Kümmel*

Cite This: *J. Phys. Chem. Lett.* 2023, 14, 3092−3102

Read Online

ACCESS | Metrics & More | Article Recommendations | Supporting Information

ABSTRACT: The homodimeric reaction center of heliobacteria retains features of the ancestral reaction center and can thus provide insights into the evolution of photosynthesis. Primary charge separation is expected to proceed in a two-step mechanism along either of the two reaction center branches. We reveal the first charge-separation step from first-principles calculations based on time-dependent density functional theory with an optimally tuned range-separated hybrid and *ab initio* Born−Oppenheimer molecular dynamics: the electron is most likely localized on the electron transfer cofactor 3 (EC3, OH-chlorophyll *a*), and the hole on the adjacent EC2. Including substantial parts of the surrounding protein environment into the calculations shows that a distinct structural mechanism is decisive for the relative energetic positioning of the electronic excitations: specific charged amino acids in the vicinity of EC3 lower the energy of charge-transfer excitations and thus facilitate efficient charge separation. These results are discussed considering recent experimental insights.

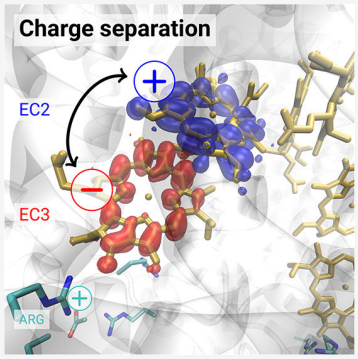

Photosynthesis is a fascinating biological process by which plants, certain bacteria, and algae are able to exploit the energy provided by the sun in an impressively efficient manner.[1−3] In the initial steps of light harvesting, incident solar radiation is absorbed and the resulting excitation energy is used to create a charge-separated state. This is achieved by the fine-tuned interplay of one or several pigment−protein complexes with mainly chlorophyll (Chl) and bacteriochlorophyll (BChl) pigments integrated into the polypeptide chains. One refers to the domain where charge separation takes place as the reaction center (RC), and the other parts are denominated as the antenna domain. While the structure of the antenna domain differs strongly among the different species, all RCs share common structural features.[4−8] Primary charge separation takes place on a cluster of six pigments which are arranged in two branches. Although both branches are composed of virtually the same pigments, charge separation typically proceeds along only one of them. An important exception is the RC of heliobacteria where the charge separation branches are enclosed by two identical, homodimeric core polypeptides.[9−12] Due to this homodimeric nature it is believed that the heliobacterial RC most closely resembles the ancestral RC and, thus, may provide insights into the evolution of photosynthesis.[13−15]

Until recently, a detailed understanding of the mechanisms underlying the light-harvesting process in heliobacteria[16−25] has been hindered by the fact that no structural information was available. This has changed with the work of Gisriel et al.[26] who have resolved the crystal structure of the RC complex of *Heliobacterium modesticaldum* by X-ray analysis. This pigment−protein complex is the only one present in the light-harvesting apparatus of heliobacteria and contains both the antenna domain and the actual RC domain. The charge separation branches consist of two close-lying BChl *g*′ forming the special pair (SPP), followed by two BChl *g* which we refer to as electron transfer cofactor 2 (EC2), and two 8^1-hydroxychlorophyll *a* pigments (referred to as EC3). The arrangement of the BChl and Chl chromophores is depicted in Figure 1a,b. From various experimental studies, the SPP^+EC3^- charge transfer (CT) state is known to be an intermediate state in charge separation,[11,27−31] before the electron is further transferred toward the terminal iron−sulfur cluster (not displayed in Figure 1). However, the details of how the SPP^+EC3^- state is formed are a matter of ongoing research; recent experimental insights have been gained especially by Orf and Redding[32] and Song et al.[33]

Here, we present a theoretical study that allows us to obtain detailed atomistic insights into the electronic dynamics that are at the core of charge separation. Since its structure has been published, the heliobacterial RC has already been the subject of theoretical studies. Kimura and co-workers[34−36] have investigated the excitonic coupling of the chromophores in the RC complex via model Hamiltonian approaches. In our previous work[37] we have calculated the CT states of a reduced system of SPP and EC2. In this work, we take a further step forward and consider the full charge separation branches of the

Received: February 9, 2023
Accepted: March 20, 2023
Published: March 23, 2023

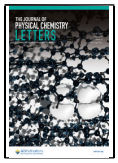

https://doi.org/10.1021/acs.jpclett.3c00377
J. Phys. Chem. Lett. 2023, 14, 3092−3102

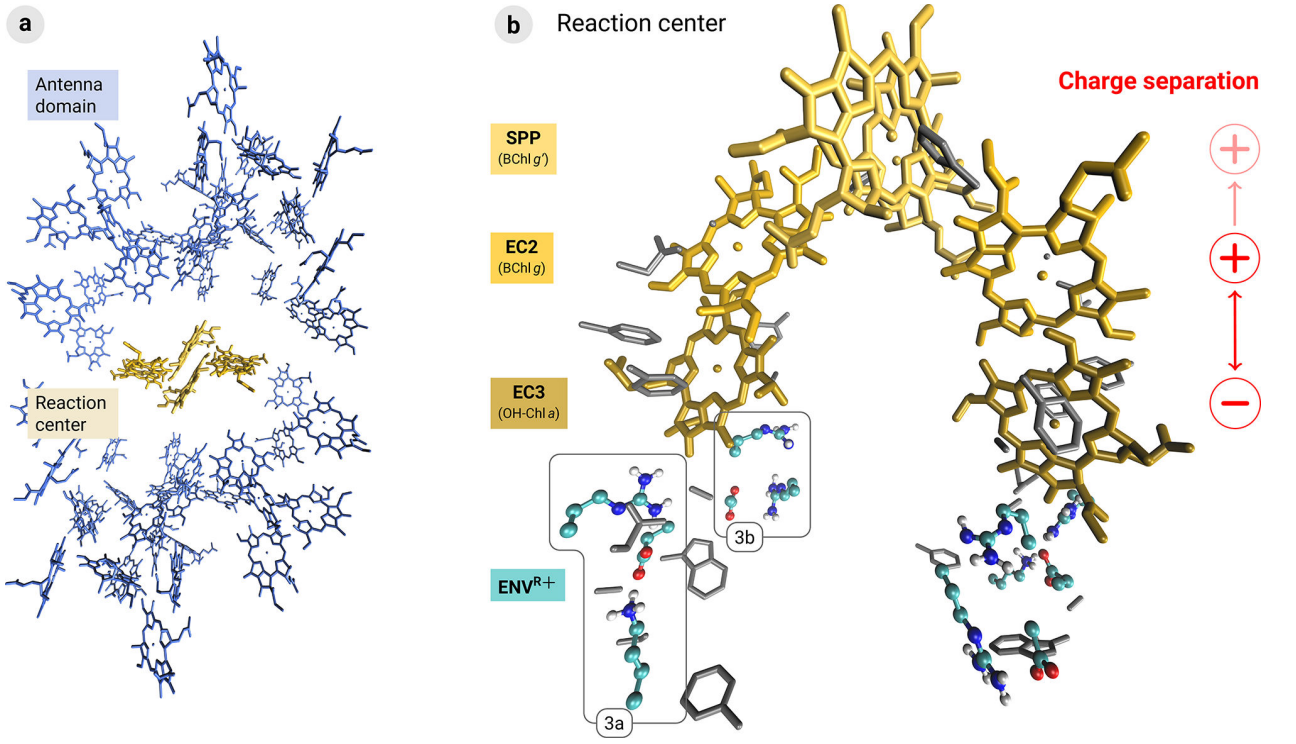

Figure 1. Overview of the structure and function of the most relevant parts of the heliobacterial RC complex. Panel a shows the location of the RC branches within the antenna domain. In panel b, the arrangement of the cofactors of charge separation (yellow) and the cluster of charge amino acids in the vicinity of EC3 (named ENV^{R+}, colored according to atom types) is depicted. In addition, the most relevant uncharged (polar or aromatic) amino acids that coordinate the chromophores or are in close contact to ENV^{R+}, are displayed (gray) (see Figure 3 for a more detailed view of ENV^{R+}). The H atoms of the relevant functional groups are shown to indicate the charge of the amino acids. Otherwise H atoms as well as phythyl tails are omitted for clarity.

heliobacterial RC in a study based on time-dependent density functional theory (TDDFT) and Born−Oppenheimer molecular dynamics (BOMD). In our calculations, $EC2^{+}EC3^{-}$ is the most likely intermediate state in primary charge separation. Furthermore, we reveal that the CT states are decisively influenced by a cluster of charged amino acids in the vicinity of EC3. This might be a clue toward an understanding of the microscopic origin of efficient charge separation.

It is an established computational protocol[38−42] to assess light-harvesting complexes in general and charge separation in RCs in particular by coupling quantum-chemical calculations with TDDFT[43] and a description of the nuclear motion via BOMD[44,45] simulations. Modern TDDFT implementations can offer the numerical efficiency to handle up to several hundreds of atoms and, hence, allow directly including all relevant chromophores and a substantial part of the surrounding protein environment into the description. At the same time, TDDFT can offer the accuracy to reliably predict different types of electronic excitations. In practice, the performance of TDDFT depends sensitively on the exchange−correlation functional employed. While semilocal and global hybrid functionals suffer from an inadequate description of excited states with CT character,[46−48] range-separated hybrid functionals, based on a mixing of semilocal and nonlocal, Fock-like exchange that is controlled by a range-separation parameter, can overcome this limitation.[49−52] In many functionals, empirically determined values are employed for the range-separation parameter, e.g., in the popular functionals CAM-B3LYP[49] and the ωB97 family of functionals.[51,53] Such functionals have been used successfully for studying light-harvesting systems.[54−58] On the other hand, the optimal tuning procedure provides for a nonempirical way of determining the parameter by enforcing formal constraints related to the IP theorem of DFT.[52,59,60] In this way, the frontier eigenvalues of the generalized Kohn−Sham system[61] are endowed with physical meaning,[62] and consequently, the description of the excited states and especially those with CT character reaches an appreciable reliability without empiricial input. In addition, this procedure has already been used successfully in some previous studies of light-harvesting systems.[63−66]

Typically, the basic input structure for the TDDFT study of a light-harvesting complex is its experimentally determined crystal structure. Calculations based on this structure can provide a first, qualitative description which suffers from several shortcomings, though. First, the experimental resolution is not high enough to display structural details such as, e.g., bond length alternation in conjugated systems with the accuracy desirable for reliable quantum-chemical calculations.[38,67,68] Moreover, static structures miss fluctuations due to temperature effects; the crystal structure can be viewed only as a superposition of multiple possible conformations of the system.[45] These limitations can be overcome by ground-state BOMD simulations. Snapshots from the resulting trajectories can be used as an input to subsequent TDDFT calculations. In this context, classical force fields may be problematic, e.g., due to the so-called "geometry mismatch problem".[42,69−72] One way to avoid such issues is to perform the BOMD simulations on the basis of DFT.[73−75] There is, however, a computational price to pay for this gain in accuracy.

https://doi.org/10.1021/acs.jpclett.3c00377
J. Phys. Chem. Lett. 2023, 14, 3092−3102

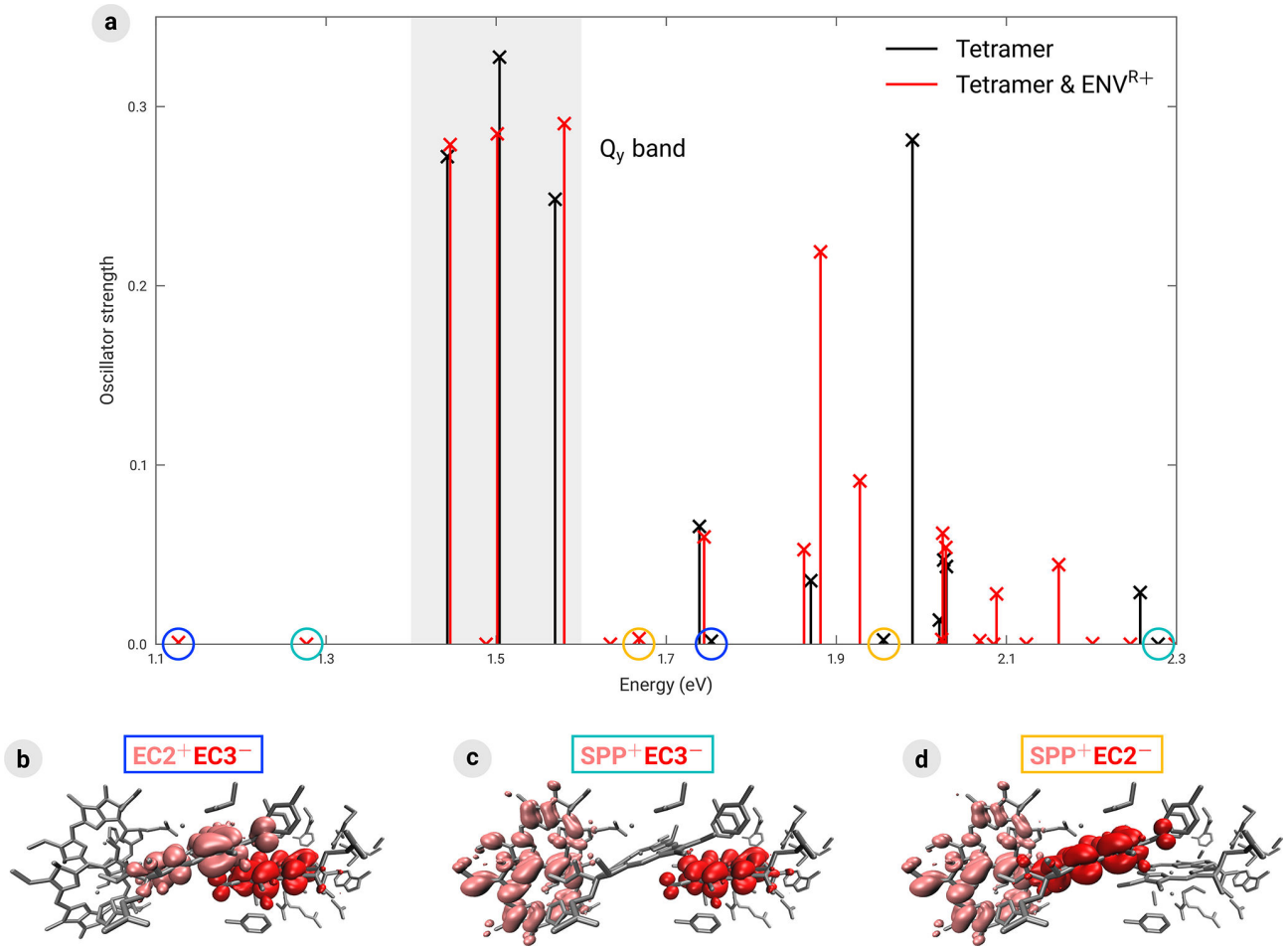

Figure 2. TDDFT excitation spectrum of the tetramer model without and with the most relevant charged amino acids (named ENV^{R+}, see Figure 1 and text). In panel a, the gray box indicates the band of the brightest BChl *g* Q_y excitations. The circles indicate the lowest CT excitations of each type (blue: EC2$^+$EC3$^-$; teal: SPP$^+$EC3$^-$; yellow: SPP$^+$EC2$^-$; cf. Table 1 for a listing of the energy values). In panels b–d, the difference densities of the lowest CT excitations with ENV^{R+} are shown (isosurfaces with an isovalue of $\pm 0.0002 a_0^{-3}$).

There are various ways of adapting these methods to larger systems by introducing further levels of approximation.[41,69,72,76−79] Quantum-chemical calculations based on model Hamiltonians efficiently cover the electronic interaction of multiple chromophores. In multiscale approaches the quantum mechanical treatment of a small subsystem (typically a few chromophores) is coupled to the semiclassical, molecular mechanics description of the remaining protein complex, where the interaction with the environment atoms is approximated by empirical force fields. By introducing a dielectric medium one can account for (additional) screening effects. MD calculations can be performed using force fields specifically reparametrized for photosynthetic pigments.[38,45] These methods can lead to further valuable insights.[42,56,65,66,68,80−87]

For our study of the heliobacterial RC we choose an approach that does not require relying on empirical input. We perform linear-response[88] TDDFT calculations using the optimally tuned range-separated hybrid ωPBE[89] and *ab initio* BOMD simulations using the PBE0 functional[90,91] with D3 dispersion correction.[92,93] In our calculations, we consider the six BChl and Chl pigments in the RC branches and the amino acids within a distance of ∼6 to 10 Å from these pigments.[94]

In the first step, we perform TDDFT calculations based on the crystal structure of the heliobacterial RC. This allows us to efficiently assess the influence and importance of different components of the structure. Our minimal model of the RC consists of both SPP chromophores, one EC2, and one EC3 chromophore (all without the phythyl tails), i.e., one full charge separation branch. We have checked that this is sufficient to reproduce the relevant excited-state properties (in terms of primary charge separation) of the whole two branches. In all calculations we additionally include a few amino acids (histidine, glutamine, serine, and phenylalanine) and waters that coordinate the BChls and Chls and are known to have a relevant influence on the excited states.[37] These molecules are displayed along with the chromophores in Figure 1a (upper part). For a detailed description of all structural units as well as additional TDDFT excitation spectra that complement our discussion, we refer to the Supporting Information.

We label the minimal model of four pigments the *tetramer* model. The excitation spectrum of this subsystem is depicted in Figure 2a. It is dominated by a band of bright excitations between ∼1.4 and 1.6 eV that arise from the coupling of the BChl Q_y transitions. Furthermore, the spectrum contains several states that correspond to CT along the RC branches:

https://doi.org/10.1021/acs.jpclett.3c00377
J. Phys. Chem. Lett. 2023, 14, 3092−3102

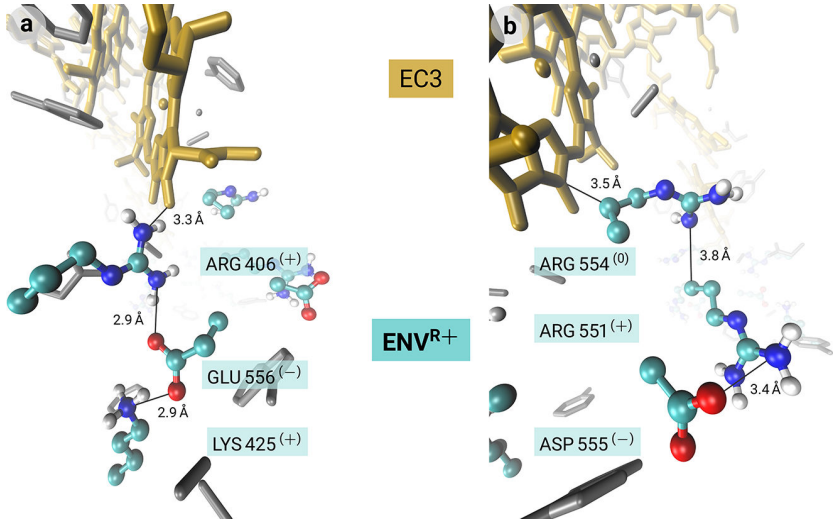

Figure 3. Enlarged view of the charged amino acids contained in ENV^{R+}. In panels a and b, different parts of ENV^{R+} are shown (cf. Figure 1 for an overview). The indicated lengths are the respective end-to-end distances between non-H atoms. The H atoms of the relevant functional groups are shown to indicate the charge of the amino acids. Otherwise H atoms as well as phythyl tails are omitted for clarity.

the lowest EC2$^+$EC3$^-$ state is obtained at 1.75 eV, the SPP$^+$EC2$^-$ state at 1.96 eV, and the SPP$^+$EC3$^-$ state at 2.28 eV, respectively. Thereby, the CT character of the excitations is determined from the difference of the respective excited-state and ground-state electron densities (referred to as *difference density*). The relation between the Q_y band and these CT states is of particular relevance in terms of possible charge separation pathways: most likely, the electronic processes on the RC will be initiated by the formation of an excited state originating from the Q_y transitions, either by excitation energy transfer from the antenna domain or by direct light absorption. Then, this valence excited state will couple to a CT state. An important prerequisite for this coupling to take place is that a CT state with a similar or a lower excitation energy than the Q_y band is available. In the tetramer spectrum, a clear candidate for such a CT state is not found. The lowest CT state, EC2$^+$EC3$^-$, is already ∼0.2 eV above the Q_y band; the differences from the SPP$^+$EC2$^-$ and SPP$^+$EC3$^-$ states are even larger (∼0.4 and 0.7 eV, respectively).

This picture, however, changes if certain amino acids in the vicinity of the pigments—especially arginine (ARG), aspartate (ASP), glutamate (GLU), and lysine (LYS)—are included. Depending on their protonation state (determined by a standard titration analysis, cf. Computational Methods), these types of amino acids may be charged, and thus, their influence on electronic excitations can become particularly strong. In this respect, it is a remarkable structural feature that ARG 406 and ARG 554 are spaced only 3 to 4 Å apart from EC3.[95] While ARG 554 is predicted to be neutral, for ARG 406 both the neutral and the positively charged state appear to be likely. Close to ARG 406 and ARG 554 there are four more charged amino acids on each branch (ARG 551, ASP 555, GLU 556, and LYS 425). We refer to this "cluster" of amino acids with ARG 406 *positive* as ENV^{R+}. The arrangement of ENV^{R+} is depicted in Figure 3a,b. Apart from LYS 425, all constituents of ENV^{R+} are less than 8 Å from EC3. Remarkably, no charged amino acids are present in a comparable distance of SPP or EC2.

The influence of the charged amino acids in the vicinity of EC3 is striking. Figure 2a shows how the excitation spectrum of the tetramer model changes when the corresponding branch of ENV^{R+} (together with some polar and aromatic amino acids, cf. Figure 1) is included in the TDDFT calculation. We see that the impact on the bright excitations, e.g., the dominant Q_y band, is small. However, the shifts in the CT excitations can be very significant; while the lowest SPP$^+$EC2$^-$ state is shifted only from 1.96 to 1.67 eV, the lowest EC2$^+$EC3$^-$ state changes from 1.75 to 1.13 eV and the lowest SPP$^+$EC3$^-$ state even from 2.28 to 1.28 eV. The analysis of the corresponding difference densities (cf. Figure 2b−d) reveals that their CT character is very pronounced; one can evaluate the integral over the difference density in the subspace associated with one type of pigment, i.e., SPP, EC2, or EC3. This yields absolute values >0.95 for the pigments active in a certain excitation (e.g., EC2 and EC3 for EC2$^+$EC3$^-$) and absolute values <0.01 for the "inactive" pigment (e.g., SPP for EC2$^+$EC3$^-$). This means that electron and hole are well localized on specific pigments. In summary, these results show that the EC2$^+$EC3$^-$ and SPP$^+$EC3$^-$ states of the system including ENV^{R+} are substantially shifted toward energies below those of the dominant Q_y excitations, and hence, downhill energy transfer from the brightest excitations to a state corresponding to CT along one of the RC branches becomes possible. If ARG 406 is assumed to be neutral, the energetic shifts of the CT excitations are strongly reduced, which shows the importance that this particular amino acid has for the RC function.

The effect that ENV^{R+} has on the CT states is considerably larger than that of all other components of the environment that we have examined (cf. Table 1 for an overview). Taking into account all other (uncharged) amino acids, i.e., except for ARG, ASP, GLU, and LYS, within a distance of 6 Å of the RC pigments shifts the CT excitations only by $\lesssim$0.1 eV. Considering the charged amino acids within a distance of 8 to 10 Å of the pigments (in addition to ENV^{R+}) can induce shifts of ∼0.1 to 0.5 eV, i.e., with somewhat larger magnitudes, yet still below those induced by ENV^{R+} (cf. the Supporting Information). However, screening effects, e.g., by interjacent parts of the protein, likely further diminish these shifts. In the case of ENV^{R+}, we do not expect significant screening due to the close contact of, e.g., ARG 406 to EC3 (distance 3.3 Å).

https://doi.org/10.1021/acs.jpclett.3c00377
J. Phys. Chem. Lett. 2023, 14, 3092−3102

Table 1. Overview of the Influence of the Most Relevant Parts of the Structure on the CT States[a]

	lowest CT excitation energies (in eV)		
structure	$EC2^+EC3^-$	SPP^+EC3^-	SPP^+EC2^-
two branches	1.72	2.19	1.91
tetramer	**1.75**	**2.28**	**1.96**
tetramer & 6A-ENV[b]	1.65	—[c]	1.97
tetramer & ENV^{R0}	1.60	2.08	1.93
tetramer & ENV^{R+}	**1.13**	**1.28**	**1.67**
tetramer & ENV^{R+} & 4A-ENV[d]	1.18	1.30	1.63
tetramer & ENV^{R+} & HOH-ENV[e]	1.19	1.34	1.67
tetramer & ENV^{R+} & PHY[f]	1.19	1.34	1.67

[a]Considered are the amino acids that are within ∼6−8 Å from the chromophores. Details on the structural units and the full excitation spectra are provided in the Supporting Information. [b]Uncharged amino acids within 6 Å from the chromophores. [c]No SPP^+EC3^- CT state is found within the computed excited states (up to 1.98 eV). [d]Polar and aromatic amino acids within 4 Å from the chromophores. [e]Interstitial water molecules in the vicinity of ENV^{R+}. [f]Relevant parts of the phythyl tails of the chromophores.

This expectation is supported by further calculations in which we assess the impact of the most relevant uncharged amino acids within 4 Å of the pigments, the phythyl tails of the pigments, and some interstitial water molecules that may be located near ENV^{R+}.[96] In all cases, the CT states in the spectrum of ENV^{R+} are shifted by less than 0.1 eV. These results indicate that the influence of ENV^{R+} on the CT states in the excitation spectrum of the RC branches is robust and the dominating effect.

Thus, we further explore the electronic dynamics of the subsystem containing the tetramer of two SPP pigments, one EC2, and one EC3 pigment as well as the ENV^{R+} environment and consider the influence of changes in the nuclear structure. Therefore, for this subsystem we perform *ab initio* BOMD simulations and generate five BOMD trajectories with lengths of ∼1.8 to 2.4 ps. To assess the impact of the BOMD dynamics on the excitation properties, we take snapshots of the structure every ∼0.1 ps along the BOMD trajectories after an initial equilibration phase of ∼0.5 ps. This yields a total number of 95 snapshots for which we calculate the respective TDDFT excitation spectra as above. To make the evaluation of this considerable number of spectra feasible, we employ an automated protocol which is described in full detail in the Supporting Information. In a nutshell, in each spectrum we treat the three lowest excitations with significant oscillator strength as the (temporary) Q_y band. We calculate its center as the average of the involved excitation energies weighted with the respective oscillator strengths. The CT excitations are again determined based on the difference densities. In the following, we summarize the most relevant findings from the TDDFT analysis. More details and additional data are provided in the Supporting Information.

The overall influence of the nuclear motion on the TDDFT excitation spectra is visualized in an ensemble-averaged spectrum that can directly be computed from the energies and oscillator strengths of the excitations.[37] We display the (total) ensemble-averaged spectrum as well as the contribution from only the Q_y band (as defined above) in Figure 4a. The total spectrum exhibits two peaks: the first one at 1.7 to 1.8 eV arises predominantly from the Q_y excitations of the BChl *g* pigments; the second one at 2.1 to 2.2 eV comes from the Q_y excitations of EC3 and the Q_x excitations of the BChl *g* pigments. Compared to the excitation spectrum of the crystal structure, the ensemble-averaged spectrum is blue-shifted by ∼0.2 eV.[37] Although the main focus of this work is to describe the CT properties of the heliobacterial RC appropriately rather than to reproduce all details of the experimental absorption spectrum,[21,27,30] one might want to compare the calculated results to the experimental data. Thereby, one must take into account that our BOMD simulation is for only a part of the reaction center complex and that choices made in the theoretical description may influence the absolute excitation energies more strongly than their relative ordering. We discuss this in greater detail in the Supporting Information.

In terms of possible charge separation pathways, the temporary energy gap between the CT excitations and the Q_y band is of particular interest. Therefore, for each spectrum we determine the lowest excitation of each type, i.e., $EC2^+EC3^-$, SPP^+EC3^-, and SPP^+EC2^-, and compute their respective energetic separation (energy gap) to the center of the Q_y band. The resulting histogram is depicted in Figure 4b. Very strikingly, most of the $EC2^+EC3^-$ counts are around or slightly below the center of the Q_y band whereas the SPP^+EC3^- and SPP^+EC2^- excitations are found mostly above this band. Especially, there is a gap of $\gtrsim$0.3 eV between the center of the Q_y band and the SPP^+EC2^- excitations, in agreement with our previous work.[37] This outcome clearly suggests that the SPP^+EC2^- states presumably do not participate in primary charge separation, while $EC2^+EC3^-$ is a likely candidate for the first charge-separated state.

This is underlined by findings from further analyzing the BOMD data: $EC2^+EC3^-$ is (almost) always the CT excitation in the spectrum with the lowest energy (in 97% of the spectra), with an energetic separation of typically ∼0.1 to 0.5 eV to the lowest SPP^+EC3^- and ∼0.2 to 0.7 eV to the lowest SPP^+EC2^- state. In 75% of the spectra the CT state closest to the Q_y band is an $EC2^+EC3^-$ excitation, whereas in 24% of the cases it is an SPP^+EC3^- state, and only in 1% it is an SPP^+EC2^- excitation.

The data also provide more detailed information on the characteristics of the "relevant" CT excitations (we here consider the excitations with an energy below 2 eV, i.e., in the same range as the Q_y band):bu while virtually all of them (except for 2%) are dark (oscillator strength below 0.01) for SPP^+EC3^- and SPP^+EC2^-, multiple $EC2^+EC3^-$ states have significant oscillator strength, with 10% of them even above 0.1. One can also examine whether the "inactive" pigments (cf. the discussion of Figure 2b−d for an explanation) contribute to the CT excitations and finds that this is not a relevant effect. Especially, only in 1% of the $EC2^+EC3^-$ and SPP^+EC3^- excitations does the integral over the difference (electron) density in the subspace associated with the "inactive" pigment yield a value smaller than −0.03. That is, the hole is (almost) always well localized on the "active" pigment.

In view of the geometric relations apparent from the crystal structure and the earlier experimental studies,[11,23,27−29,31] Gisriel et al.[26] proposed a two-step mechanism for the formation of the SPP^+EC3^- state, either with SPP^+EC2^- or $EC2^+EC3^-$ as the intermediate step. Both variants are present in different types of photosynthetic RCs.[83−87,97−102] Our results from TDDFT and BOMD calculations on the heliobacterial RC strongly favor the second mechanism with $EC2^+EC3^-$ as an intermediate step. In all our calculations—with different parts of the protein environment and for

https://doi.org/10.1021/acs.jpclett.3c00377
J. Phys. Chem. Lett. 2023, 14, 3092−3102

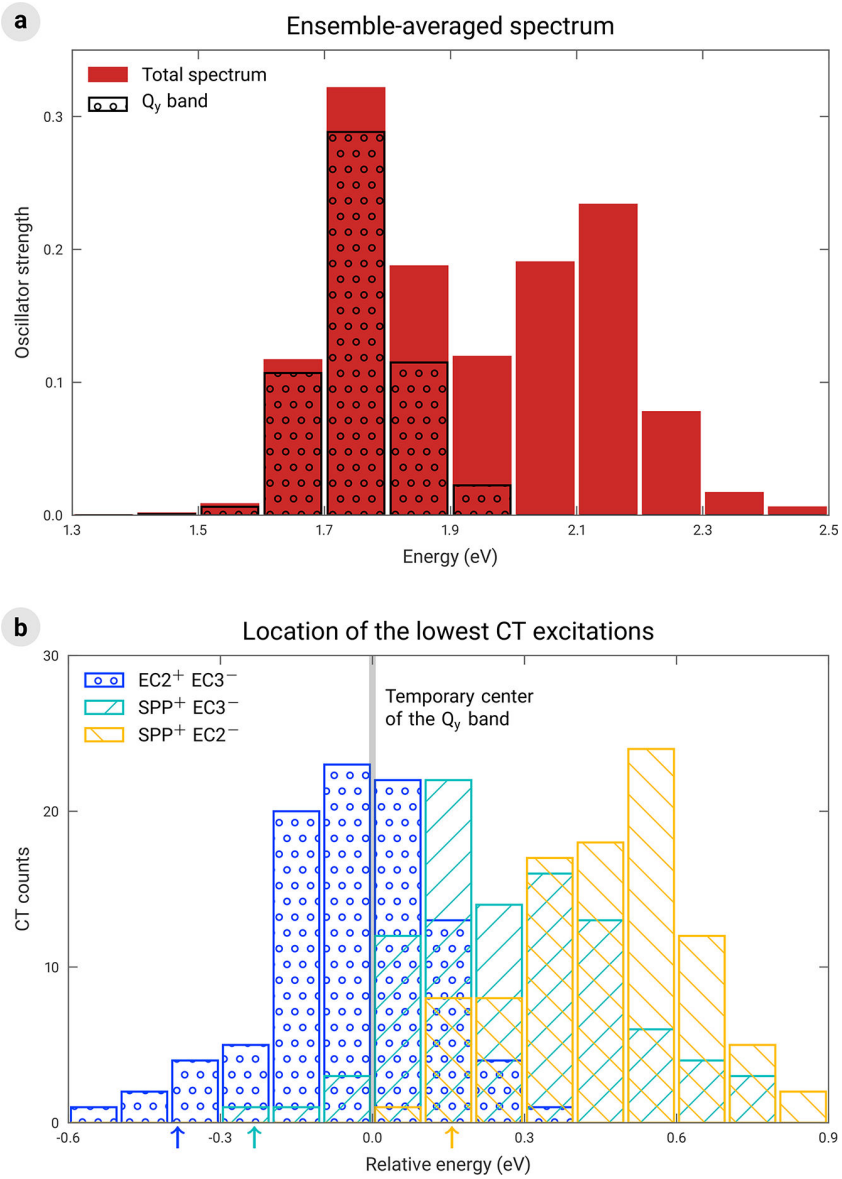

Figure 4. Overview of the results from the BOMD analysis (structure: tetramer model with ENV^{R+}). In panel a, the ensemble-averaged total spectrum and the contribution from the Q_y band are shown; panel b shows the temporary energy gap between the lowest CT excitation of each type and the center of the Q_y band. The arrows indicate the positions of the CT excitations in the corresponding crystal structure-based spectrum (cf. Figure 2a) for comparison.

different BOMD geometries—we consistently obtain an energy gap of several tenths of an eV between the $EC2^+EC3^-$ and SPP^+EC2^- excitations. Especially, downhill energy transfer from the Q_y band of the BChl pigments to $EC2^+EC3^-$, but not SPP^+EC2^-, appears possible. The detailed mechanism of primary charge separation has also been the subject of recent experimental studies by Song et al.[33] and Orf and Redding.[32] Independently and based on different methods, both groups argue that EC3 is involved in the first CT step and serves as the primary electron acceptor. In this respect, our findings are consistent with their results. Moreover, our results indicate that distinct structural features, especially a cluster of charged amino acids in the vicinity of EC3, are decisive for the energetic positioning of the CT excitations. In particular, this structural unit facilitates downhill energy transfer from the Q_y band to $EC2^+EC3^-$. We note that quite generally, the protein environment can have a substantial influence on electronic excitations,[103] and specifically, the importance that certain environment amino acids may have for charge separation is also being discussed for other photosynthetic RCs.[83,84,86,87,104]

Concerning the detailed nature of the CT intermediate, Song et al. propose that the hole in the first CT step is delocalized over both SPP and EC2. Orf and Redding also discuss this option motivated by the excitonic coupling of SPP and EC2 observed in an earlier theoretical study.[34] Indeed, depending on the exact (BOMD) geometry such a coupling can be observed in our TDDFT calculations.[37] However, we have examined our data thoroughly in view of the hypothesis that the hole is initially delocalized over both SPP and EC2 but do not find any evidence for this; neither in our calculations including different parts of the protein environment nor in an appreciable number of snapshots from the BOMD do we

https://doi.org/10.1021/acs.jpclett.3c00377
J. Phys. Chem. Lett. 2023, 14, 3092−3102

obtain a delocalization of the hole in the $EC2^{+}EC3^{-}$ or $SPP^{+}EC3^{-}$ states in the energetically relevant region. Therefore, the mechanism of primary charge separation that appears to agree best with our results is

$$RC^{*} \rightarrow EC2^{+}EC3^{-} \rightarrow SPP^{+}EC3^{-}$$

In our BOMD analysis, we find several $EC2^{+}EC3^{-}$ states with significant oscillator strength. This may facilitate the direct coupling to an antenna excited state without prior excitation-energy transfer to the RC. This is in line with the study by Song et al., who propose both variants of coupling to the first CT state, i.e., either from an excited state of the RC or the antenna domain.

In conclusion, we have presented first-principles TDDFT and BOMD calculations on the full charge-separation branches of the heliobacterial RC. We have included a considerable part of the surrounding protein environment and have extensively investigated the effect of structural changes by considering multiple BOMD snapshots in our TDDFT analysis. All results consistently indicate that the $EC2^{+}EC3^{-}$ state is the first step of charge separation. Furthermore, we have revealed that the energies of the CT states are specifically adjusted by the interaction with a small group of charged amino acids. The electrostatic interaction with this charged environment has a pronounced effect on the CT excitation energies, lowering them with respect to the non-CT bright excitations. This can enable downhill energy transfer from the Q_y band of the BChl pigments to an $EC2^{+}EC3^{-}$ state. The physical principle that a charged environment can alter the position of CT states relative to non-CT states is quite general. It may therefore be a worthwhile task for future work to check whether it is realized also in other light-harvesting structures.

COMPUTATIONAL METHODS

The crystal structure of the RC complex of *Heliobacterium modesticaldum* is obtained from the Protein Data Bank under file ID 5V8K.[26] Before this structure can be used for the TDDFT and BOMD calculations, several modifications are required which have been described in detail previously.[37,64] Very briefly, the positions of the H atoms, which cannot be resolved from the X-ray data, are energetically optimized using the CHARMM[105] force field. The phythyl tails of the chromophores are cropped from their ester linkages to the side chains of the bacteriochlorin rings and replaced by a H atom. Furthermore, the bonds of the amino acid residues to the polypeptide chains are cut between C_α and C_β and saturated by further H atoms. The protonation states of the titratable amino acids were determined on the basis of the CHARMM-optimized structure using in-house versions of the MEAD[106] and GMCT[107] programs. The ion concentration is set to 150 mM, and the dielectric constant is set to 4 for the protein and 80 for water. For further analysis, only the protonation states with the highest probability were chosen.

The TDDFT calculations of the electronic excitations employ the (full linear-response) Casida approach and are performed using Q-Chem, version 5.2.2.[108] We use the range-separated hybrid functional ωPBE with the range-separation parameter $\omega = 0.171 a_0^{-1}$. The basic idea behind choosing this particular value of ω is the one of optimal tuning.[52,60,109−120] We explain the reasoning behind our specific choice of the range-separation parameter in detail in the Supporting Information. We use the 6-31G basis set which was demonstrated to be sufficient for obtaining reliable results in terms of the relative energetic positioning of the excitations.[37] We calculate up to 25 excited states for each spectrum.

The *ab initio* BOMD calculations are performed using Turbomole, version 7.6.[121] For the DFT calculations, we use the PBE0 functional with D3 dispersion correction. We use the def2-SV(P) basis set and the resolution-of-the-identity in combination with the multipole-accelerated-resolution-of-the-identity approximation to speed up the calculations. For the MD, a Nose−Hoover thermostat with a relaxation time of 30 au is used to keep the pseudotemperature around 300 K. The step size of the propagation is 5 au. We incorporate the mechanical constraints that the remaining protein environment exerts on the motion of the chromophores and the amino acids as described in detail previously:[37] We fix the terminal C_β of the amino acids, as this is the linkage of the tails to the polypeptide chains, and the terminal O of the phythyl tails of the BChl and Chl, as the phythyl side chains are sterically hindered within the protein matrix due to their length. This strategy has already been employed in previous BOMD studies of bacterial RCs.[74,75] It is sufficient to sustain the relative arrangement within the structure and to inhibit an overall drift. With this setup, we generate 5 BOMD trajectories: two with 100 500 au, two with 92 500 au, and one with 76 500 au length. For the TDDFT analysis, we take snapshots every 4000 au beginning at 20 000 au.

ASSOCIATED CONTENT

Supporting Information

The Supporting Information is available free of charge at https://pubs.acs.org/doi/10.1021/acs.jpclett.3c00377.

Description of the different structural units; details on the TDDFT excitation spectra, and the BOMD analysis; automated protocol for the analysis of excitation spectra (PDF)

AUTHOR INFORMATION

Corresponding Author

Stephan Kümmel − *University of Bayreuth, Bayreuth 95440, Germany;* orcid.org/0000-0001-5914-6635; Email: stephan.kuemmel@uni-bayreuth.de

Authors

Moritz Brütting − *University of Bayreuth, Bayreuth 95440, Germany;* orcid.org/0000-0002-1021-0007

Johannes M. Foerster − *University of Bayreuth, Bayreuth 95440, Germany;* orcid.org/0000-0003-0442-9413

Complete contact information is available at: https://pubs.acs.org/10.1021/acs.jpclett.3c00377

Notes

The authors declare no competing financial interest.

ACKNOWLEDGMENTS

This work was supported by the Elite Study Program "Biological Physics" of the Elite Network of Bavaria. M.B. is grateful for support by the "Studienstiftung des Deutschen Volkes" and by the University of Bayreuth Graduate School. We further acknowledge support from the Bavarian State Ministry of Science, Research, and the Arts for the Collaborative Research Network "Solar Technologies go Hybrid", and from the Bavarian Polymer Institute in terms of computing resources.

https://doi.org/10.1021/acs.jpclett.3c00377
J. Phys. Chem. Lett. 2023, 14, 3092−3102

REFERENCES

(1) Blankenship, R. E. *Molecular Mechanisms of Photosynthesis*, 2nd ed.; Wiley Blackwell: Chichester, 2014.
(2) Mirkovic, T.; Ostroumov, E. E.; Anna, J. M.; van Grondelle, R.; Govindjee; Scholes, G. D. Light Absorption and Energy Transfer in the Antenna Complexes of Photosynthetic Organisms. *Chem. Rev.* **2017**, *117*, 249−293.
(3) Renger, G. *Primary Processes of Photosynthesis, Part 1: Principles and Apparatus*; Royal Society of Chemistry, 2007; pp 5−35.
(4) Chen, J.-H.; Wu, H.; Xu, C.; Liu, X.-C.; Huang, Z.; Chang, S.; Wang, W.; Han, G.; Kuang, T.; Shen, J.-R.; et al. Architecture of the photosynthetic complex from a green sulfur bacterium. *Science* **2020**, *370*, eabb6350.
(5) Cogdell, R. J.; Gall, A.; Köhler, J. The architecture and function of the light-harvesting apparatus of purple bacteria: from single molecules to *in vivo* membranes. *Q. Rev. Biophys.* **2006**, *39*, 227−324.
(6) Gisriel, C. J.; Azai, C.; Cardona, T. Recent advances in the structural diversity of reaction centers. *Photosynth. Res.* **2021**, *149*, 329−343.
(7) Gorka, M.; Baldansuren, A.; Malnati, A.; Gruszecki, E.; Golbeck, J. H.; Lakshmi, K. V. Shedding Light on Primary Donors in Photosynthetic Reaction Centers. *Front. Microbiol.* **2021**, *12*, 735666.
(8) Romero, E.; Novoderezhkin, V. I.; van Grondelle, R. Quantum design of photosynthesis for bio-inspired solar-energy conversion. *Nature* **2017**, *543*, 355−365.
(9) Amesz, J. The heliobacteria, a new group of photosynthetic bacteria. *J. Photochem. Photobiol., B* **1995**, *30*, 89−96.
(10) Heinnickel, M.; Golbeck, J. H. Heliobacterial photosynthesis. *Photosynth. Res.* **2007**, *92*, 35−53.
(11) Neerken, S.; Amesz, J. The antenna reaction center complex of heliobacteria: composition, energy conversion and electron transfer. *Biochim. Biophys. Acta* **2001**, *1507*, 278−290.
(12) Oh-oka, H. Type 1 Reaction Center of Photosynthetic Heliobacteria. *Photochem. Photobiol.* **2007**, *83*, 177−186.
(13) Orf, G. S.; Gisriel, C.; Redding, K. E. Evolution of photosynthetic reaction centers: insights from the structure of the heliobacterial reaction center. *Photosynth. Res.* **2018**, *138*, 11−37.
(14) Taylor, N.; Kassal, I. Why are photosynthetic reaction centres dimeric? *Chem. Sci.* **2019**, *10*, 9576−9585.
(15) Tcherkez, G.; Papon, N. Origin and Evolution of Photosystems: Lessons from Green Sulfur Bacteria. *ChemPhotoChem.* **2021**, *5*, 418−420.
(16) Agostini, A.; Bortolus, M.; Ferlez, B.; Walters, K.; Golbeck, J. H.; van der Est, A.; Carbonera, D. Differential sensitivity to oxygen among the bacteriochlorophylls *g* in the type-I reaction centers of *Heliobacterium modesticaldum*. *Photochem. Photobiol. Sci.* **2021**, *20*, 747−759.
(17) Johnson, W. A.; Redding, K. E. Reconstitution of the heliobacterial photochemical reaction center and cytochrome c_{553} into a proteoliposome system. *Photosynth. Res.* **2020**, *143*, 241−250.
(18) Kashey, T. S.; Luu, D. D.; Cowgill, J. C.; Baker, P. L.; Redding, K. E. Light-driven quinone reduction in heliobacterial membranes. *Photosynth. Res.* **2018**, *138*, 1−9.
(19) Kondo, T.; Itoh, S.; Matsuoka, M.; Azai, C.; Oh-oka, H. Menaquinone as the Secondary Electron Acceptor in the Type I Homodimeric Photosynthetic Reaction Center of *Heliobacterium modesticaldum*. *J. Phys. Chem. B* **2015**, *119*, 8480−8489.
(20) Kondo, T.; Matsuoka, M.; Azai, C.; Kobayashi, M.; Itoh, S.; Oh-oka, H. Light-Induced Electron Spin-Polarized (ESP) EPR Signal of the $P800^+$ $Menaquinone^-$ Radical Pair State in Oriented Membranes of *Heliobacterium modesticaldum*: Role/Location of Menaquinone in the Homodimeric Type I Reaction Center. *J. Phys. Chem. B* **2018**, *122*, 2536−2543.
(21) Kondo, T.; Mutoh, R.; Tabe, H.; Kurisu, G.; Oh-Oka, H.; Fujiyoshi, S.; Matsushita, M. Cryogenic Single-Molecule Spectroscopy of the Primary Electron Acceptor in the Photosynthetic Reaction Center. *J. Phys. Chem. Lett.* **2020**, *11*, 3980−3986.
(22) Kondo, T.; Mutoh, R.; Arai, S.; Kurisu, G.; Oh-oka, H.; Fujiyoshi, S.; Matsushita, M. Energy transfer fluctuation observed by single-molecule spectroscopy of red-shifted bacteriochlorophyll in the homodimeric photosynthetic reaction center. *J. Chem. Phys.* **2022**, *156*, 105102.
(23) Neerken, S.; Aartsma, T. J.; Amesz, J. Pathways of Energy Transformation in Antenna Reaction Center Complexes of *Heliobacillus mobilis*. *Biochemistry* **2000**, *39*, 3297−3303.
(24) Orf, G. S.; Gisriel, C. J.; Granstrom, J.; Baker, P. L.; Redding, K. E. The PshX subunit of the photochemical reaction center from Heliobacterium modesticaldum acts as a low-energy antenna. *Photosynth. Res.* **2022**, *151*, 11−30.
(25) Sarrou, I.; Khan, Z.; Cowgill, J.; Lin, S.; Brune, D.; Romberger, S.; Golbeck, J. H.; Redding, K. E. Purification of the photosynthetic reaction center from *Heliobacterium modesticaldum*. *Photosynth. Res.* **2012**, *111*, 291−302.
(26) Gisriel, C.; Sarrou, I.; Ferlez, B.; Golbeck, J. H.; Redding, K. E.; Fromme, R. Structure of a symmetric photosynthetic reaction center-photosystem. *Science* **2017**, *357*, 1021−1025.
(27) Chauvet, A.; Sarrou, J.; Lin, S.; Romberger, S. P.; Golbeck, J. H.; Savikhin, S.; Redding, K. E. Temporal and spectral characterization of the photosynthetic reaction center from *Heliobacterium modesticaldum*. *Photosynth. Res.* **2013**, *116*, 1−9.
(28) Chiou, H.-C.; Lin, S.; Blankenship, R. E. Time-Resolved Spectroscopy of Energy Transfer and Trapping upon Selective Excitation in Membranes of Heliobacillus mobilis at Low Temperature. *J. Phys. Chem. B* **1997**, *101*, 4136−4141.
(29) Ferlez, B.; Cowgill, J.; Dong, W.; Gisriel, C.; Lin, S.; Flores, M.; Walters, K.; Cetnar, D.; Redding, K. E.; Golbeck, J. H. Thermodynamics of the Electron Acceptors in *Heliobacterium modesticaldum*: An Example of an Early Homodimeric Type I Photosynthetic Reaction Center. *Biochemistry* **2016**, *55*, 2358−2370.
(30) Kojima, R.; Yamamoto, H.; Azai, C.; Uragami, C.; Hashimoto, H.; Kosumi, D.; Oh-oka, H. Energy transfer and primary charge separation upon selective femtosecond excitation at 810 nm in the reaction center complex from Heliobacterium modesticaldum. *J. Photochem. Photobiol., A* **2020**, *401*, 112758.
(31) Lin, S.; Chiou, H. C.; Kleinherenbrink, F. A.; Blankenship, R. E. Time-Resolved Spectroscopy of Energy and Electron Transfer Processes in the Photosynthetic Bacterium *Heliobacillus mobilis*. *Biophys. J.* **1994**, *66*, 437−445.
(32) Orf, G. S.; Redding, K. E. Perturbation of the primary acceptor chlorophyll site in the heliobacterial reaction center by coordinating amino acid substitution. *Biochim. Biophys. Acta, Bioenerg.* **2021**, *1862*, 148324.
(33) Song, Y.; Sechrist, R.; Nguyen, H. H.; Johnson, W.; Abramavicius, D.; Redding, K. E.; Ogilvie, J. P. Excitonic structure and charge separation in the heliobacterial reaction center probed by multispectral multidimensional spectroscopy. *Nat. Commun.* **2021**, *12*, 2801.
(34) Kimura, A.; Itoh, S. Theoretical Model of Exciton States and Ultrafast Energy Transfer in Heliobacterial Type I Homodimeric Reaction Center. *J. Phys. Chem. B* **2018**, *122*, 11852−11859.
(35) Kitoh-Nishioka, H.; Shigeta, Y.; Itoh, S.; Kimura, A. Excitonic Coupling on a Heliobacterial Symmetrical Type-I Reaction Center: Comparison with Photosystem I. *J. Phys. Chem. B* **2020**, *124*, 389−403.
(36) Kimura, A.; Kitoh-Nishioka, H.; Shigeta, Y.; Itoh, S. Comparison between the Light-Harvesting Mechanisms of Type-I Photosynthetic Reaction Centers of Heliobacteria and Photosystem I: Pigment Site Energy Distribution and Exciton State. *J. Phys. Chem. B* **2021**, *125*, 3727−3738.
(37) Brütting, M.; Foerster, J. M.; Kümmel, S. Investigating Primary Charge Separation in the Reaction Center of *Heliobacterium modesticaldum*. *J. Phys. Chem. B* **2021**, *125*, 3468−3475.
(38) Cignoni, E.; Slama, V.; Cupellini, L.; Mennucci, B. The atomistic modeling of light-harvesting complexes from the physical models to the computational protocol. *J. Chem. Phys.* **2022**, *156*, 120901.
(39) Cupellini, L.; Jurinovich, S.; Campetella, M.; Caprasecca, S.; Guido, C. A.; Kelly, S. M.; Gardiner, A. T.; Cogdell, R.; Mennucci, B.

https://doi.org/10.1021/acs.jpclett.3c00377
J. Phys. Chem. Lett. 2023, 14, 3092−3102

An Ab Initio Description of the Excitonic Properties of LH2 and Their Temperature Dependence. *J. Phys. Chem. B* **2016**, *120*, 11348−11359.
(40) Cupellini, L.; Calvani, D.; Jacquemin, D.; Mennucci, B. Charge transfer from the carotenoid can quench chlorophyll excitation in antenna complexes of plants. *Nat. Commun.* **2020**, *11*, 662.
(41) Curutchet, C.; Mennucci, B. Quantum Chemical Studies of Light Harvesting. *Chem. Rev.* **2017**, *117*, 294−343.
(42) Maity, S.; Bold, B. M.; Prajapati, J. D.; Sokolov, M.; Kubař, T.; Elstner, M.; Kleinekathöfer, U. DFTB/MM Molecular Dynamics Simulations of the FMO Light-Harvesting Complex. *J. Phys. Chem. Lett.* **2020**, *11*, 8660−8667.
(43) Marques, M., Ullrich, C., Nogueira, F., Rubio, A., Burke, K., Gross, E., Eds.; *Time-dependent Density Functional Theory*; Springer: Berlin, 2006.
(44) Marx, D.; Hutter, J. *Ab Initio Molecular Dynamics: Basic Theory and Advances Methods*; Cambridge University Press, 2009.
(45) Liguori, N.; Croce, R.; Marrink, S. J.; Thallmair, S. Molecular dynamics simulations in photosynthesis. *Photosynth. Res.* **2020**, *144*, 273−295.
(46) Dreuw, A.; Head-Gordon, M. Failure of Time-Dependent Density Functional Theory for Long-Range Charge-Transfer Excited States: The Zincbacteriochlorin-Bacteriochlorin and Bacteriochlorophyll-Spheroidene Complexes. *J. Am. Chem. Soc.* **2004**, *126*, 4007−4016.
(47) Kehrer, J.; Richter, R.; Foerster, J. M.; Schelter, I.; Kümmel, S. Self-interaction correction, electrostatic, and structural influences on time-dependent density functional theory excitations of bacteriochlorophylls from the light-harvesting complex 2. *J. Chem. Phys.* **2020**, *153*, 144114.
(48) Maitra, N. T. Charge transfer in time-dependent density functional theory. *J. Phys.: Condens. Matter* **2017**, *29*, 423001.
(49) Yanai, T.; Tew, D. P.; Handy, N. C. A new hybrid exchange-correlation functional using the Coulomb-attenuating method (CAM−B3LYP). *Chem. Phys. Lett.* **2004**, *393*, 51−57.
(50) Iikura, H.; Tsuneda, T.; Yanai, T.; Hirao, K. A long-range correction scheme for generalized-gradient-approximation exchange functionals. *J. Chem. Phys.* **2001**, *115*, 3540−3544.
(51) Chai, J.-D.; Head-Gordon, M. Systematic optimization of long-range corrected hybrid density functionals. *J. Chem. Phys.* **2008**, *128*, 084106.
(52) Stein, T.; Kronik, L.; Baer, R. Reliable Prediction of Charge Transfer Excitations in Molecular Complexes Using Time-Dependent Density Functional Theory. *J. Am. Chem. Soc.* **2009**, *131*, 2818−2820.
(53) Mardirossian, N.; Head-Gordon, M. Thirty years of density functional theory in computational chemistry: an overview and extensive assessment of 200 density functionals. *Mol. Phys.* **2017**, *115*, 2315−2372.
(54) Higashi, M.; Kosugi, T.; Hayashi, S.; Saito, S. Theoretical Study on Excited States of Bacteriochlorophyll *a* in Solutions with Density Functional Assessment. *J. Phys. Chem. B* **2014**, *118*, 10906−10918.
(55) Frankcombe, T. J. Explicit calculation of the excited electronic states of the photosystem II reaction centre. *Phys. Chem. Chem. Phys.* **2015**, *17*, 3295−3302.
(56) Cupellini, L.; Caprasecca, S.; Guido, C. A.; Müh, F.; Renger, T.; Mennucci, B. Coupling to Charge Transfer States is the Key to Modulate the Optical Bands for Efficient Light Harvesting in Purple Bacteria. *J. Phys. Chem. Lett.* **2018**, *9*, 6892−6899.
(57) Nottoli, M.; Jurinovich, S.; Cupellini, L.; Gardiner, A. T.; Cogdell, R.; Mennucci, B. The role of charge-transfer states in the spectral tuning of antenna complexes of purple bacteria. *Photosynth. Res.* **2018**, *137*, 215−226.
(58) Kavanagh, M. A.; Karlsson, J. K. G.; Colburn, J. D.; Barter, L. M. C.; Gould, I. R. A TDDFT investigation of the Photosystem II reaction center: Insights into the precursors to charge separation. *Proc. Natl. Acad. Sci. U. S. A.* **2020**, *117*, 19705−19712.
(59) Kuritz, N.; Stein, T.; Baer, R.; Kronik, L. Charge-Transfer-Like $\pi \rightarrow \pi^*$ Excitations in Time-Dependent Density Functional Theory: A Conundrum and Its Solution. *J. Chem. Theory Comput.* **2011**, *7*, 2408−2415.
(60) Livshits, E.; Baer, R. A well-tempered density functional theory of electrons in molecules. *Phys. Chem. Chem. Phys.* **2007**, *9*, 2932−2941.
(61) Seidl, A.; Görling, A.; Vogl, P.; Majewski, J. A.; Levy, M. Generalized Kohn-Sham schemes and the band-gap problem. *Phys. Rev. B* **1996**, *53*, 3764−3774.
(62) Kronik, L.; Stein, T.; Refaely-Abramson, S.; Baer, R. Excitation Gaps of Finite-Sized Systems from Optimally Tuned Range-Separated Hybrid Functionals. *J. Chem. Theory Comput.* **2012**, *8*, 1515−1531.
(63) Li, X.; Parrish, R. M.; Liu, F.; Schumacher, S. I. L. K.; Martínez, T. J. An Ab Initio Exciton Model Including Charge-Transfer Excited States. *J. Chem. Theory Comput.* **2017**, *13*, 3493−3504.
(64) Schelter, I.; Foerster, J. M.; Gardiner, A. T.; Roszak, A. W.; Cogdell, R. J.; Ullmann, G. M.; de Queiroz, T. B.; Kümmel, S. Assessing density functional theory in real-time and real-space as a tool for studying bacteriochlorophylls and the light-harvesting complex 2. *J. Chem. Phys.* **2019**, *151*, 134114.
(65) Aksu, H.; Schubert, A.; Geva, E.; Dunietz, B. D. Explaining Spectral Asymmetries and Excitonic Characters of the Core Pigment Pairs in the Bacterial Reaction Center Using a Screened Range-Separated Hybrid Functional. *J. Phys. Chem. B* **2019**, *123*, 8970−8975.
(66) Aksu, H.; Schubert, A.; Bhandari, S.; Yamada, A.; Geva, E.; Dunietz, B. D. On the Role of the Special Pair in Photosystems as a Charge Transfer Rectifier. *J. Phys. Chem. B* **2020**, *124*, 1987−1994.
(67) Dreuw, A.; Harbach, P. H. P.; Mewes, J. M.; Wormit, M. Quantum chemical excited state calculations on pigment-protein complexes require thorough geometry re-optimization of experimental crystal structures. *Theor. Chem. Acc.* **2010**, *125*, 419−426.
(68) Sirohiwal, A.; Neese, F.; Pantazis, D. A. How Can We Predict Accurate Electrochromic Shifts for Biochromophores? A Case Study on the Photosynthetic Reaction Center. *J. Chem. Theory Comput.* **2021**, *17*, 1858−1873.
(69) Renger, T.; Müh, F. Understanding photosynthetic light-harvesting: a bottom up theoretical approach. *Phys. Chem. Chem. Phys.* **2013**, *15*, 3348−3371.
(70) Jurinovich, S.; Viani, L.; Curutchet, C.; Mennucci, B. Limits and potentials of quantum chemical methods in modelling photosynthetic antennae. *Phys. Chem. Chem. Phys.* **2015**, *17*, 30783−30792.
(71) Rosnik, A. M.; Curutchet, C. Theoretical Characterization of the Spectral Density of the Water-Soluble Chlorophyll-Binding Protein from Combined Quantum Mechanics/Molecular Mechanics Molecular Dynamics Simulations. *J. Chem. Theory Comput.* **2015**, *11*, 5826−5837.
(72) Maity, S.; Kleinekathöfer, U. Recent progress in atomistic modeling of light-harvesting complexes: A mini review. *Photosynth. Res.* **2022**. DOI: 10.1007/s11120-022-00969-w
(73) Blau, S. M.; Bennett, D. I. G.; Kreisbeck, C.; Scholes, G. D.; Aspuru-Guzik, A. Local protein solvation drives direct down-conversion in phycobiliprotein PC645 via incoherent vibronic transport. *Proc. Natl. Acad. Sci. U. S. A.* **2018**, *115*, E3342−E3350.
(74) Eisenmayer, T. J.; de Groot, H. J.; van de Wetering, E.; Neugebauer, J.; Buda, F. Mechanism and Reaction Coordinate of Directional Charge Separation in Bacterial Reaction Centers. *J. Phys. Chem. Lett.* **2012**, *3*, 694−697.
(75) Eisenmayer, T. J.; Lasave, J. A.; Monti, A.; de Groot, H. J. M.; Buda, F. Proton Displacements Coupled to Primary Electron Transfer in the *Rhodobacter sphaeroides* Reaction Center. *J. Phys. Chem. B* **2013**, *117*, 11162−11168.
(76) Jang, S. J.; Mennucci, B. Delocalized excitons in natural light-harvesting complexes. *Rev. Mod. Phys.* **2018**, *90*, 035003.
(77) Mennucci, B. Polarizable continuum model. *WIREs Comput. Mol. Sci.* **2012**, *2*, 386−404.
(78) Mennucci, B.; Corni, S. Multiscale modelling of photoinduced processes in composite systems. *Nature Reviews Chemistry* **2019**, *3*, 315−330.

https://doi.org/10.1021/acs.jpclett.3c00377
J. Phys. Chem. Lett. 2023, 14, 3092−3102

(79) Salahub, D. R. Multiscale molecular modelling: from electronic structure to dynamics of nanosystems and beyond. *Phys. Chem. Chem. Phys.* **2022**, *24*, 9051−9081.
(80) Bold, B. M.; Sokolov, M.; Maity, S.; Wanko, M.; Dohmen, P. M.; Kranz, J. J.; Kleinekathöfer, U.; Höfener, S.; Elstner, M. Benchmark and performance of long-range corrected time-dependent density functional tight binding (LC-TD-DFTB) on rhodopsins and light-harvesting complexes. *Phys. Chem. Chem. Phys.* **2020**, *22*, 10500−10518.
(81) Cupellini, L.; Qian, P.; Nguyen-Phan, T. C.; Gardiner, A. T.; Cogdell, R. J. Quantum chemical elucidation of a sevenfold symmetric bacterial antenna complex. *Photosynth. Res.* **2022**. DOI: 10.1007/s11120-022-00925-8
(82) Maity, S.; Daskalakis, V.; Elstner, M.; Kleinekathöfer, U. Multiscale QM/MM molecular dynamics simulations of the trimeric major light-harvesting complex II. *Phys. Chem. Chem. Phys.* **2021**, *23*, 7407−7417.
(83) Mitsuhashi, K.; Tamura, H.; Saito, K.; Ishikita, H. Nature of Asymmetric Electron Transfer in the Symmetric Pathways of Photosystem I. *J. Phys. Chem. B* **2021**, *125*, 2879−2885.
(84) Sirohiwal, A.; Neese, F.; Pantazis, D. A. Protein Matrix Control of Reaction Center Excitation in Photosystem II. *J. Am. Chem. Soc.* **2020**, *142*, 18174−18190.
(85) Sirohiwal, A.; Pantazis, D. A. The Electronic Origin of Far-Red-Light-Driven Oxygenic Photosynthesis. *Angew. Chem., Int. Ed.* **2022**, *61*, e202200356.
(86) Tamura, H.; Saito, K.; Ishikita, H. Acquirement of water-splitting ability and alteration of the charge-separation mechanism in photosynthetic reaction centers. *Proc. Natl. Acad. Sci. U. S. A.* **2020**, *117*, 16373−16382.
(87) Tamura, H.; Saito, K.; Ishikita, H. The origin of unidirectional charge separation in photosynthetic reaction centers: nonadiabatic quantum dynamics of exciton and charge in pigment−protein complexes. *Chem. Sci.* **2021**, *12*, 8131−8140.
(88) Casida, M. E. In *Recent Advances in Density Functional Methods*; Chong, D. P., Ed.; Recent Advances in Computational Chemistry; World Scientific: Singapore, 1995; Vol. *1*; pp 155−192.
(89) Vydrov, O. A.; Scuseria, G. E. Assessment of a long-range corrected hybrid functional. *J. Chem. Phys.* **2006**, *125*, 234109.
(90) Adamo, C.; Barone, V. Toward reliable density functional methods without adjustable parameters: The PBE0 model. *J. Chem. Phys.* **1999**, *110*, 6158−6170.
(91) Ernzerhof, M.; Scuseria, G. E. Assessment of the Perdew-Burke-Ernzerhof exchange-correlation functional. *J. Chem. Phys.* **1999**, *110*, 5029−5036.
(92) Grimme, S.; Antony, J.; Ehrlich, S.; Krieg, H. A consistent and accurate ab initio parametrization of density functional dispersion correction (DFT-D) for the 94 elements H-Pu. *J. Chem. Phys.* **2010**, *132*, 154104.
(93) Grimme, S. Density functional theory with London dispersion corrections. *WIREs Comput. Mol. Sci.* **2011**, *1*, 211−228.
(94) Within in this work, all intermolecular distances refer to the respective end-to-end distances between non-H atoms.
(95) In the nomenclature that we use to refer to specific amino acid residues we follow the one from the original PDB file which is publicly available from the Protein Data Bank under file ID 5V8K.[26] All amino acids mentioned in the main text share the chain ID A.
(96) Till, M. S.; Ullmann, G. M. McVol − A program for calculating protein volumes and identifying cavities by a Monte Carlo algorithm. *J. Mol. Mod.* **2010**, *16*, 419−429.
(97) Dubas, K.; Szewczyk, S.; Białek, R.; Burdziński, G.; Jones, M. R.; Gibasiewicz, K. Antagonistic Effects of Point Mutations on Charge Recombination and a New View of Primary Charge Separation in Photosynthetic Proteins. *J. Phys. Chem. B* **2021**, *125*, 8742−8756.
(98) Müller, M. G.; Slavov, C.; Luthra, R.; Redding, K. E.; Holzwarth, A. R. Independent initiation of primary electron transfer in the two branches of the photosystem I reaction center. *Proc. Natl. Acad. Sci. U. S. A.* **2010**, *107*, 4123−4128.
(99) Niedringhaus, A.; Policht, V. R.; Sechrist, R.; Konar, A.; Laible, P. D.; Bocian, D. F.; Holten, D.; Kirmaier, C.; Ogilvie, J. P. Primary processes in the bacterial reaction center probed by two-dimensional electronic spectroscopy. *Proc. Natl. Acad. Sci. U. S. A.* **2018**, *115*, 3563−3568.
(100) Romero, E.; van Stokkum, I. H. M.; Novoderezhkin, V. I.; Dekker, J. P.; van Grondelle, R. Two Different Charge Separation Pathways in Photosystem II. *Biochemistry* **2010**, *49*, 4300−4307.
(101) Yoneda, Y.; Arsenault, E. A.; Yang, S.-J.; Orcutt, K.; Iwai, M.; Fleming, G. R. The initial charge separation step in oxygenic photosynthesis. *Nat. Commun.* **2022**, *13*, 2275.
(102) Zinth, W.; Wachtveitl, J. The First Picoseconds in Bacterial Photosynthesis? − Ultrafast Electron Transfer for the Efficient Conversion of Light Energy. *ChemPhysChem* **2005**, *6*, 871−880.
(103) Fresch, E.; Meneghin, E.; Agostini, A.; Paulsen, H.; Carbonera, D.; Collini, E. How the Protein Environment Can Tune the Energy, the Coupling, and the Ultrafast Dynamics of Interacting Chlorophylls: The Example of the Water-Soluble Chlorophyll Protein. *J. Phys. Chem. Lett.* **2020**, *11*, 1059−1067.
(104) Kanda, T.; Ishikita, H. Energetics of the Electron Transfer Pathways in the Homodimeric Photosynthetic Reaction Center. *Biochemistry* **2022**, *61*, 2621−2627.
(105) Brooks, B. R.; Bruccoleri, R. E.; Olafson, B. D.; States, D. J.; Swaminathan, S.; Karplus, M. CHARMM: A program for macromolecular energy, minimization, and dynamics calculations. *J. Comput. Chem.* **1983**, *4*, 187−217.
(106) Bashford, D. In *Scientific Computing in Object-Oriented Parallel Environments: Proceedings of the First International Conference, ISCOPE 97*; Marina del Rey, California, USA, December 8−11, 1997; Ishikawa, Y., Oldehoeft, R. R., Reynders, J. V. W., Tholburn, M., Eds.; Springer: Berlin, 1997; pp 233−240.
(107) Ullmann, R. T.; Ullmann, G. M. GMCT: A Monte Carlo simulation package for macromolecular receptors. *J. Comput. Chem.* **2012**, *33*, 887−900.
(108) Shao, Y.; Gan, Z.; Epifanovsky, E.; Gilbert, A. T.; Wormit, M.; Kussmann, J.; Lange, A. W.; Behn, A.; Deng, J.; Feng, X.; et al. Advances in molecular quantum chemistry contained in the Q-Chem 4 program package. *Mol. Phys.* **2015**, *113*, 184−215.
(109) Kümmel, S. Charge-Transfer Excitations: A Challenge for Time-Dependent Density Functional Theory That Has Been Met. *Adv. Energy Mater.* **2017**, *7*, 1700440.
(110) Karolewski, A.; Kronik, L.; Kümmel, S. Using optimally tuned range separated hybrid functionals in ground-state calculations: Consequences and caveats. *J. Chem. Phys.* **2013**, *138*, 204115.
(111) Körzdörfer, T.; Sears, J. S.; Sutton, C.; Brédas, J.-L. Long-range corrected hybrid functionals for π-conjugated systems: Dependence of the range-separation parameter on conjugation length. *J. Chem. Phys.* **2011**, *135*, 204107.
(112) de Queiroz, T. B.; Kümmel, S. Charge-transfer excitations in low-gap systems under the influence of solvation and conformational disorder: Exploring range-separation tuning. *J. Chem. Phys.* **2014**, *141*, 084303.
(113) Refaely-Abramson, S.; Sharifzadeh, S.; Jain, M.; Baer, R.; Neaton, J. B.; Kronik, L. Gap renormalization of molecular crystals from density-functional theory. *Phys. Rev. B* **2013**, *88*, 081204.
(114) Refaely-Abramson, S.; Jain, M.; Sharifzadeh, S.; Neaton, J. B.; Kronik, L. Solid-state optical absorption from optimally tuned time-dependent range-separated hybrid density functional theory. *Phys. Rev. B* **2015**, *92*, 081204.
(115) de Queiroz, T. B.; Kümmel, S. Tuned range separated hybrid functionals for solvated low bandgap oligomers. *J. Chem. Phys.* **2015**, *143*, 034101.
(116) Bhandari, S.; Cheung, M.; Geva, E.; Kronik, L.; Dunietz, B. D. Fundamental Gaps of Condensed-Phase Organic Semiconductors from Single-Molecule Calculations using Polarization-Consistent Optimally Tuned Screened Range-Separated Hybrid Functionals. *J. Chem. Theory Comput.* **2018**, *14*, 6287−6294.
(117) Kronik, L.; Kümmel, S. Dielectric Screening Meets Optimally Tuned Density Functionals. *Adv. Mater.* **2018**, *30*, 1706560.

https://doi.org/10.1021/acs.jpclett.3c00377
J. Phys. Chem. Lett. 2023, 14, 3092−3102

(118) Aschebrock, T.; Kümmel, S. Exploring local range separation: The role of spin scaling and one-electron self-interaction. *J. Chem. Phys.* **2019**, *151*, 154108.
(119) Maier, T. M.; Ikabata, Y.; Nakai, H. Assessing locally range-separated hybrid functionals from a gradient expansion of the exchange energy density. *J. Chem. Phys.* **2021**, *154*, 214101.
(120) Brütting, M.; Bahmann, H.; Kümmel, S. Hybrid functionals with local range separation: Accurate atomization energies and reaction barrier heights. *J. Chem. Phys.* **2022**, *156*, 104109.
(121) Balasubramani, S. G.; Chen, G. P.; Coriani, S.; Diedenhofen, M.; Frank, M. S.; Franzke, Y. J.; Furche, F.; Grotjahn, R.; Harding, M. E.; Hättig, C.; et al. TURBOMOLE: Modular program suite for ab initio quantum-chemical and condensed-matter simulations. *J. Chem. Phys.* **2020**, *152*, 184107.

https://doi.org/10.1021/acs.jpclett.3c00377
J. Phys. Chem. Lett. 2023, 14, 3092−3102

Supporting Information for

Understanding Primary Charge Separation in the Heliobacterial Reaction Center

The Journal of Physical Chemistry Letters

Moritz Brütting, Johannes M. Foerster, and Stephan Kümmel*

University of Bayreuth, Bayreuth 95440, Germany

* Corresponding author, email: stephan.kuemmel@uni-bayreuth.de

Contents

S1 Structural Information

In the following, we give additional information on the different structural units that we discuss in the main text. We provide listings of the constituents (amino acids and water molecules) of the different structural units. To facilitate the orientation of the reader in the rather detailed data, all different structural units and the related details tables are summarized in Table S1. The details listings are provided in Table S2 to S4 and S6 to S9. Except for Table S8 where we provide the cartesian coordinates explicitly, we give the residue names, sequence numbers, and chain IDs of the amino acids and water molecules. Thereby, we follow the nomenclature from the original PDB file which is publicly available from the Protein Data Bank under file ID 5V8K.[1] Thus, it is transparent to the reader how the relevant information on the coordinates of the residues considered can be obtained from PDB file 5V8K. Note that each residue appears twice in the full reaction center (RC) complex – once in each half of the homodimer. In the case of ARG,

Table S1: Overview over the different structural units and which tables provide the corresponding details listings (amino acid residues and water molecules) or TDDFT excitation data (cf. Section S2 below).

Structural unit	Description	Details listing	TDDFT data
Two branches	Both SPP, EC2, and EC3 chromophores; corresponding coordinating amino acids.	S2	S11
Tetramer	Both SPP, one EC2, and one EC3 chromophore; corresponding coordinating amino acids.	S2	S12
PHY	Relevant parts of the phythyl tails of the chromophores included (up to C_{10} for SPP, up to C_5 for EC2 and EC3).		S18
ENV^{R+}	Cluster of charged amino acids near EC3 (with ARG 406 positive); polar and aromatic amino acids within 4 Å.	S6	S15
ENV^{R0}	Same as ENV^{R+}, but with ARG 406 neutral.	S6	S14
ENV^{K+}	Charged amino acids within 10 Å to the chromophores (except for those included in ENV^{R+}, with LYS 562 positive); polar and aromatic amino acids within 4 Å.	S7	S19
ENV^{K0}	Same as ENV^{K+}, but with LYS 562 neutral.	S7	S20
6A-ENV	Uncharged amino acids within 6 Å to the chromophores.	S3, S4	S5, S13
4A-ENV	Polar and aromatic amino acids within 4 Å to the chromophores.	S3	S16
HOH-ENV	Interstitial water molecules and close-lying amino acids in the vicinity of ENV^{R+}.	S8, S9	S17

Table S2: Amino acids and water molecules (HOH) that coordinate the chromophores.

Residue name	Chain ID	Residue sequence number
PHE	A	399
PHE	A	450
GLN	A	458
HIS	A	537
PHE	A	542
SER	A	545
HOH	A	1193
HOH	A	1276

Table S3: Amino acids that are contained in 4A-ENV.

Residue name	Chain ID	Residue sequence number
TYR	A	341
PHE	A	454
PHE	A	475
TYR	A	510
PHE	A	511
THR	A	518
PHE	A	538
TRP	A	540
PHE	A	544
PHE	A	548
TYR	A	550
SER	A	553
PHE	A	591
THR	A	598

ASP, GLU, and LYS, the charges according to the protonation states that emerge from the titration analysis are included in the listings. The other types of amino acids are all uncharged.

In our time-dependent density functional theory (TDDFT) calculations we consider the full two charge transfer (CT) branches of the heliobacterial RC and a reduced tetramer model where only one branch, i. e., both special pair (SPP), one electron transfer cofactor 2 (EC2), and one EC3 pigments are considered. In both cases we include the amino acids and water molecules that coordinate the chromophores (cf. Table S2). In most calculations, we do not consider the phythyl tails but crop them before the C_1 atom from the main part of the bacteriochlorophyll (BChl) and chlorophyll (Chl) chromophores. To assess the impact of the phythyl tails on the TDDFT results, we perform some calculations where the phythyl tails are included up to C_{10} for SPP and up to C_5 for EC2 and EC3. In the case of SPP, we consider a larger part of the phythyl tail as this one coordinates the neighboring EC2 pigment. We refer to structures where these relevant parts of the phythyl tails are included by the acronym PHY.

Table S4: Amino acids that are contained in 6A-ENV in addition to the ones from Table S3.

Residue name	Chain ID	Residue sequence number
MET	A	330
ALA	A	333
PHE	A	334
ILE	A	337
THR	A	345
THR	A	348
VAL	A	402
GLN	A	448
LEU	A	451
LEU	A	457
ALA	A	461
PHE	A	465
TYR	A	510
ILE	A	514
ILE	A	515
GLN	A	517
MET	A	521
LEU	A	533
LEU	A	534
ALA	A	541
PHE	A	544
ALA	A	558
LEU	A	561
TYR	A	577
ALA	A	580
MET	A	597
CYS	A	601
MET	A	602
ALA	A	604
LEU	A	605

We take into account the influence of the protein environment that surrounds the chromophores by explicitly including the closest amino acids and water molecules in several structural units. We consider the charged amino acids – ARG, ASP, GLU, and LYS – within a distance of 10 Å to the chromophores and the uncharged amino acids within 6 Å to the chromophores. The latter is referred to as 6A-ENV and its constituents are listed in Table S3 and S4.[2] As a subunit of the 6A-ENV, we take the polar and aromatic amino acids – ASN, CYS, GLN, PHE, SER, THR, TRP, and TYR – within 4 Å (referred to as 4A-ENV, cf. Table S3). Our choice to focus on these types of amino acids can be rationalized by analyzing the influence that the individual types of uncharged amino acids have on the CT states. We show this influence for two different reduced systems consisting of four chromophores each (SPP and EC2 or EC2 and EC3, respectively) in Table S5. This shows that only PHE, SER, THR, TRP, and TYR can

Table S5: Shifts in the CT states induced by the different types of uncharged amino acids. We consider two different reduced systems consisting of four chromophores: SPP and EC2 or EC2 and EC3, respectively, with the coordinating amino acids and water molecules ("coordination", cf. Table S2) and compare them to systems that additionally contain all (uncharged) amino acids of one type that are within 6 Å of the chromophores (cf. Table S3 and S4). As an example, in the line denoted by "+ CYS" we consider the respective chromophores, their coordination, and the CYS residues within 6 Å of the chromophores. For each system, we provide the excitation energies for the lowest two CT states (CT1 and CT2: $SPP^{+}EC2^{-}$; CT3 and CT4: $EC2^{+}EC3^{-}$) and the average shift with respect to the system containing only the chromophores with coordination (first data line). All values are in eV. Boldface denotes shifts larger than 0.05 eV.

	SPP–EC2			EC2–EC3		
Environment	CT1	CT2	Shift	CT3	CT4	Shift
Coordination	1.9221	1.9284		1.7222	1.7374	
+ ALA	1.9184	1.9244	−0.0039	1.7327	1.7478	0.0105
+ CYS	1.9247	1.9307	0.0025			
+ GLN	1.9246	1.9309	0.0025	1.7170	1.7321	−0.0053
+ ILE	1.9295	1.9358	0.0074	1.7209	1.7360	−0.0014
+ LEU	1.9391	1.9453	0.0170	1.7261	1.7395	0.0030
+ MET	1.9539	1.9611	0.0323	1.7192	1.7343	−0.0061
+ PHE	1.9289	1.9361	0.0073	1.7856	1.8021	**0.0641**
+ SER				1.6295	1.6707	**−0.0797**
+ THR	1.9810	1.9839	**0.0572**	1.7059	1.7193	−0.0172
+ TRP	1.7774	1.7823	**−0.1454**	1.7325	1.7469	0.0099
+ TYR	1.9957	2.0078	**0.0765**	1.6866	1.7549	−0.0091
+ VAL				1.7233	1.7383	0.0010

Table S6: Amino acids that are contained in ENV^{R+} (with ARG 406 positive) and ENV^{R0} (with ARG 406 neutral). The horizontal bar separates ARG, ASP, GLU, and LYS from the polar and aromatic amino acids within 4 Å to them.

Residue name	Chain ID	Residue sequence number	Charge
ARG	A	406	Positive / neutral
LYS	A	425	Positive
ARG	A	551	Positive
ARG	A	554	Neutral
ASP	A	555	Negative
GLU	A	556	Negative
SER	A	414	
TRP	A	416	
THR	A	417	
PHE	A	430	
GLN	A	448	
SER	A	553	

Table S7: Amino acids that are contained in ENV^{K+} (with LYS 562 positive) and ENV^{K0} (with LYS 562 neutral). The horizontal bar separates ARG, ASP, GLU, and LYS from the polar and aromatic amino acids within 4 Å to them.

Residue name	Chain ID	Residue sequence number	Charge
LYS	A	269	Positive
ASP	A	447	Negative
ASP	A	468	Negative
LYS	A	562	Positive / neutral
ARG	A	579	Positive
GLU	A	585	Negative
LYS	A	587	Positive
ASN	A	263	
SER	A	442	
SER	A	444	
TYR	A	450	
TRP	A	464	
SER	A	503	
TYR	A	513	
GLN	A	517	
GLN	A	549	
GLN	A	566	
ASN	A	578	
SER	A	582	

Table S8: Cartesian coordinates (in Å) of the interstitial water molecules (separated by horizontal bars) contained in HOH-ENV.

Atom	x	y	z
O	138.371	66.772	−0.551
H	138.038	67.565	−0.039
H	138.958	66.379	0.147
O	141.035	68.282	−0.439
H	141.818	68.090	0.096
H	140.757	69.145	−0.104
O	136.245	68.702	−14.364
H	135.508	68.057	−14.339
H	135.796	69.495	−14.669
O	140.136	68.346	−14.377
H	140.768	68.253	−15.093
H	140.713	68.299	−13.592

Table S9: Amino acids that are contained in HOH-ENV in addition to the water molecules listed in Table S8.

Residue name	Chain ID	Residue sequence number
MET	A	330
VAL	A	402
LEU	A	451
MET	A	546
GLN	A	549
LEU	A	581

have an appreciable influence (shifts larger than 0.05 eV) on the CT states ($SPP^{+}EC2^{-}$ or $EC2^{+}EC3^{-}$, respectively). The shifts induced by CYS and GLN are much smaller and the influence of ASN is not assessed as it is not present in the vicinity of the pigments. Nevertheless, these three types of amino acids are generally considered as being "polar" (like SER or THR) and are, therefore, considered in the 4A-ENV as well.

The charged amino acids are divided into two structural units: In the first unit, referred to as ENV^{R+} or ENV^{R0}, respectively, depending on the protonation state of ARG 406, we include the charged amino acids within 8 Å of the chromophores. In addition, we further include LYS 425 as it is in close interaction with GLU 556 (cf. Figure 3 in the main text). Along with these charged amino acids, we also consider the polar and aromatic amino acids that are within 4 Å to them. All amino acids of this structural unit are summarized in Table S6. In the second unit of charged amino acids, referred to as ENV^{K+} or ENV^{K0}, respectively, depending on the protonation state of LYS 562, we include the charged amino acids within 10 Å to the chromophores that are not included in ENV^{R+}. In addition, we further include LYS 269 and GLU 585 as these are in close interaction with ASP 468 and ARG 579, respectively. Along with these charged amino acids, we also consider the polar and aromatic amino acids that are within 4 Å of them. All amino acids of this structural unit are summarized in Table S7. The amino acids in Table S2 and S6 are included in Figure 1 and 3 in the main text.

Despite the dense arrangement of the protein matrix, there are some small cavities in the crystal structure that might be filled with additional interstitial water molecules *in vivo*. We here consider four water molecules that might be located in the vicinity of ENV^{R+}. Their coordinates are provided in Table S8. Along with these water molecules, we consider a few amino acids that are forming the cavities (together with the amino acids already included in ENV^{R+}). These are listed in Table S9. The water molecules are determined with the program McVol.[3] Therefore, a probe sphere with a radius of 1.3 Å is used to discover possible cavities for water placement. Surface collisions for the placement are rejected. Only reasonable water positions are chosen for further analysis. These water molecules are then again minimized with CHARMM and the CHARMM force field while the whole protein backbone is kept fixed. Hydrogen atoms in the vicinity of the placed water molecules are kept flexible to allow possible hydrogen bond formation.

S2 Details on the TDDFT Excitation Spectra

In the following, we provide additional information on the TDDFT spectra that are shown in Figure 2 and summarized in Table 1 in the main text. We begin by discussing a technical aspect visible in the spectrum of the tetramer model with ENV^{R+} (cf. Figure 2). In this spectrum, we obtain a few excited states that correspond to CT between one of the chromophores and the charged amino acids. These states are referred to as "spurious" states (cf. below) and are listed in Table S10. The other excited states in this spectrum are listed in Table S15 below. The "spurious" states are very sensitive to the computational setup. For example, they are not emerging in the spectra based on the Born-Oppenheimer molecular dynamics (BOMD) trajectories (at least not in the energy range up to $\sim 2.5 \ldots 3\,\mathrm{eV}$ which is covered by our calculations). Moreover, they are sensitive to the structural units chosen. Especially, including the polar and aromatic amino acids in the vicinity of the charged amino acids (that *are* included in ENV^{R+} and ENV^{K+}) reduces the number of these states substantially. Therefore, we consider them as being "spurious", i. e., not being related to the real physics of the system, and do not further include them in our analysis.

To make the results of our TDDFT calculations transparent to the reader, we show the numerical data of all excitation spectra which are referred to in Figure 2 and Table 1 in the main text in Table S12 to S20. All these spectra are based on the crystal structure geometry and correspond to the structural units introduced in Section S1. To facilitate the orientation of the reader, the correspondence between the structural units and the TDDFT data tables is indicated in Table S1. For the sake of clarity, we limit the tables to the physical states, i. e., exclude the "spurious" CT states.

Whenever computationally feasible we calculated the spectra with 25 excited states. For larger systems this was not always possible as the associated computational effort can be prohibitive. However, we calculated at least 10 excited states (in the case of the tetramer with the 6A-ENV, cf. Table S13). For each excited state, we display the excitation energy and the oscillator strength which are directly output by the linear-response TDDFT calculations. Additionally, we provide the integrals over the difference density (difference of the electron densities of the respective excited and ground states, cf. below) in the subspace associated with one type of pigment (SPP, EC2, and EC3) if their absolute values are at least 0.01. It should be noted that in the tables some excitations show an electron or hole transfer character of very "low magnitude" (integral values below 0.1). This can arise from the coupling with an energetically close CT state and therefore does not indicate that these excitations really exhibit CT character. Hence, these excitations are not considered in Table 1 in the main text.

Table S10: "Spurious" CT states in the excitation spectrum of the tetramer with ENV^{R+}.

Energy	1.4881	2.0850	2.2014	2.3416	2.3770
Oscillator strength	0.0000	0.0000	0.0004	0.0000	0.0000

Table S11: Excited states of the full two branches. For each state, the excitation energy (in eV), the oscillator strength, and the integrals over the difference (electron) density in the subspaces associated with the different types of pigments are given. For clarity, the difference density integrals are omitted if their absolute value is smaller than 0.01. As in this table both branches are considered, we distinguish herein for EC2 and EC3 between the different branches (1 and 2) by the labels EC2-1, EC2-2, EC3-1, and EC3-2.

		Difference density integral				
Energy	Oscillator strength	SPP	EC2-1	EC2-2	EC3-1	EC3-2
1.4582	0.4855					
1.4954	0.1430					
1.5494	0.6192					
1.5778	0.1148					
1.7217	0.0020			−0.97		0.97
1.7386	0.0017		−0.97		0.97	
1.7739	0.0206					
1.8337	0.0634					
1.9123	0.0003	−0.99	0.57	0.41		
1.9137	0.0015	−0.98	0.41	0.57		
1.9900	0.1966					
1.9956	0.3698					
2.0138	0.0079					
2.0161	0.0402					
2.0289	0.0359					
2.0307	0.0502					
2.1890	0.0000	−1.00				0.99
2.2036	0.0000	−1.00			0.99	
2.2579	0.0339					
2.2610	0.0267					
2.2700	0.0000	−0.99		0.99		
2.2765	0.0000	−0.99	0.99			
2.4650	0.0019					
2.4818	0.0044					
2.5204	0.0015	−0.17		−0.80		0.97

Furthermore, we comment on the differences in the excitation spectra of the full two branches and the tetramer model (cf. Table S11 and S12): Both structural units contain a different number of chromophores (6 vs. 4). This is reflected by the structure of the associated excitation spectra: Regarding the CT excitations we obtain each type of excitation (i. e., $EC2^+EC3^-$, SPP^+EC3^-, and SPP^+EC2^-) twice in the calculation based on the full two branches – once for each RC branch. These excitations always emerge as pairs, with an energetic separation of $\lesssim 0.01\,\mathrm{eV}$. For the tetramer model we inherently obtain only one excitation of each pair. However this has only a small effect on the respective excitation energies (shifts by less than 0.1 eV) and, thus, the tetramer model covers the relevant information on the CT states. Also the number of bright (Q_y and Q_x) excitations is reduced for the tetramer model as compared to

Table S12: Excited states of the tetramer model. The structure of the table is the same as in Table S11.

		Difference density integral		
Energy	Oscillator strength	SPP	EC2	EC3
1.4426	0.2720			
1.5040	0.3276			
1.5693	0.2483			
1.7390	0.0657			
1.7531	0.0017		−0.97	0.97
1.8700	0.0354			
1.9555	0.0024	−0.98	0.98	
1.9895	0.2813			
2.0212	0.0135			
2.0263	0.0470			
2.0295	0.0434			
2.2573	0.0289			
2.2783	0.0000	−1.00		0.99
2.3668	0.0000	−0.99	0.99	
2.3836	0.0004			
2.5314	0.0276			
2.5470	0.0018		−0.95	0.95
2.5538	0.0290			
2.6088	0.0437			
2.6412	0.0035	−0.84	−0.14	0.99
2.6424	0.0212	−0.01		
2.6465	0.0249	−0.15	−0.83	0.98
2.6662	0.3350			
2.6834	0.0280			
2.7261	0.0001			

Table S13: Excited states of the tetramer model with the 6A-ENV. The structure of the table is the same as in Table S11.

		Difference density integral		
Energy	Oscillator strength	SPP	EC2	EC3
1.4048	0.3832			
1.4672	0.2227			
1.5362	0.2838			
1.6548	0.0023		−0.97	0.97
1.7134	0.0372			
1.8099	0.0354			
1.9506	0.3229			
1.9716	0.0205	−0.43	0.43	
1.9751	0.0175	−0.55	0.55	
1.9834	0.0444			

Table S14: Excited states of the tetramer model with ENV^{R0}. The structure of the table is the same as in Table S11.

Energy	Oscillator strength	Difference density integral SPP	EC2	EC3
1.4460	0.2831			
1.5031	0.3265			
1.5672	0.2326		−0.07	0.07
1.6018	0.0217		−0.90	0.90
1.7431	0.0604			
1.8687	0.0374			
1.9329	0.0041	−0.98	0.98	
1.9469	0.3107			
2.0220	0.0090			
2.0263	0.0566			
2.0294	0.0553			
2.0791	0.0000	−1.00		0.99

Table S15: Excited states of the tetramer model with ENV^{R+}. The structure of the table is the same as in Table S11.

Energy	Oscillator strength	Difference density integral SPP	EC2	EC3
1.1264	0.0010		−0.98	0.98
1.2770	0.0000	−0.99		0.99
1.4460	0.2787			
1.5013	0.2848	−0.03	0.03	
1.5801	0.2905			
1.6343	0.0000	−1.00		1.00
1.6681	0.0031	−0.96	0.96	
1.7445	0.0599			
1.8620	0.0528	−0.01		
1.8814	0.2189		−0.36	0.36
1.9277	0.0911		−0.61	0.61
2.0240	0.0027			
2.0251	0.0619	−0.03	0.03	
2.0288	0.0540			0.01
2.0688	0.0020	−0.95	0.95	
2.0884	0.0281		−0.94	0.94
2.1234	0.0000	−0.99		0.99
2.1615	0.0444		−0.04	0.04
2.2457	0.0000	−1.00		1.00
2.2985	0.0000	−1.00		0.99

Table S16: Excited states of the tetramer model with ENV^{R+} and the 4A-ENV. The structure of the table is the same as in Table S11.

		Difference density integral		
Energy	Oscillator strength	SPP	EC2	EC3
1.1775	0.0009		−0.98	0.98
1.2998	0.0000	−0.99		0.99
1.4455	0.3158			
1.4869	0.2139	−0.04	0.04	
1.5549	0.2691			
1.6282	0.0055	−0.95	0.94	
1.6394	0.0000	−1.00		1.00
1.7522	0.0305			
1.8245	0.0497	−0.02	0.02	
1.8855	0.3264		−0.07	0.07
1.9739	0.0129		−0.89	0.89
1.9930	0.0033	−0.87	0.87	
2.0154	0.0101	−0.02	0.02	
2.0179	0.0388	−0.07	0.07	
2.0214	0.0806	−0.01	0.01	
2.1553	0.0002	−0.99		0.99
2.1609	0.0443		−0.69	0.70
2.1836	0.0315		−0.30	0.30

Table S17: Excited states of the tetramer model with ENV^{R+} and HOH-ENV. The structure of the table is the same as in Table S11.

		Difference density integral		
Energy	Oscillator strength	SPP	EC2	EC3
1.1855	0.0013		−0.98	0.98
1.3434	0.0000	−0.99		0.99
1.4453	0.2744			
1.5017	0.2907	−0.03	0.03	
1.5802	0.2889			
1.6676	0.0031	−0.96	0.96	
1.7013	0.0000	−0.99		0.99
1.7435	0.0600			
1.8639	0.0448	−0.01	0.01	
1.9041	0.2870		−0.12	0.12
1.9767	0.0245		−0.85	0.85
2.0243	0.0033			
2.0256	0.0625	−0.03	0.03	
2.0292	0.0545			
2.0694	0.0020	−0.95	0.94	
2.1265	0.0233		−0.95	0.95
2.1894	0.0000	−0.99		0.99

Table S18: Excited states of the tetramer model with PHY and ENV^{R+}. The structure of the table is the same as in Table S11.

Energy	Oscillator strength	Difference density integral SPP	EC2	EC3
1.1907	0.0010		−0.97	0.98
1.3444	0.0000	−0.99		0.99
1.4481	0.2939			
1.4975	0.3038	−0.03	0.03	
1.5650	0.2555			
1.6693	0.0024	−0.96	0.95	
1.7008	0.0000	−1.00		1.00
1.7496	0.0575			
1.8583	0.0552	−0.01	0.01	
1.8865	0.2958		−0.10	0.10
1.9606	0.0174	−0.01	−0.86	0.87
2.0136	0.0569	−0.01		
2.0243	0.0437	−0.02	0.02	
2.0252	0.0269	−0.01	0.01	
2.0677	0.0017	−0.95	0.94	
2.1395	0.0449		−0.63	0.64
2.1635	0.0259		−0.35	0.35
2.1904	0.0000	−1.00		0.99

Table S19: Excited states of the tetramer model with ENV^{R+} and ENV^{K+}. The structure of the table is the same as in Table S11.

Energy	Oscillator strength	Difference density integral SPP	EC2	EC3
0.7957	0.0000	−0.98		0.99
0.8662	0.0008		−0.97	0.98
1.1520	0.0000	−1.00		0.99
1.4493	0.2673	−0.51	0.50	
1.4633	0.1338	−0.30	0.30	
1.5253	0.2016	−0.18	0.18	
1.5961	0.2652		−0.03	0.03
1.6428	0.0215	−0.20	−0.76	0.96
1.6483	0.0051	−0.79	−0.19	0.98
1.7600	0.0000	−0.99		0.99
1.7638	0.0596			

Table S20: Excited states of the tetramer model with ENV^{R+} and ENV^{K0}. The structure of the table is the same as in Table S11.

		Difference density integral		
Energy	Oscillator strength	SPP	EC2	EC3
1.0352	0.0008	−0.01	−0.97	0.98
1.1157	0.0000	−0.99		0.99
1.4458	0.2899			
1.4746	0.0000	−1.00		1.00
1.5014	0.2992	−0.07	0.07	
1.5821	0.2700			
1.6113	0.0183	−0.92	0.91	
1.7458	0.0659			
1.8127	0.0303		−0.94	0.94
1.8688	0.0462	−0.02	0.02	
1.9319	0.2837		−0.04	0.04
1.9597	0.0001	−1.00		0.99
1.9907	0.0150		−0.96	0.96

the full two branches. Due to the absence of one EC2 and one EC3 pigment in the tetramer model, both the number of Q_y and Q_x excitations is reduced by 2. However this does not change the energetic position of the Q_y and Q_x excitations on a relevant scale. Especially, the energetic range of the dominant band of BChl Q_y excitations between $\sim 1.4 \ldots 1.6\,\mathrm{eV}$ remains largely unchanged (although the number of states is reduced from 4 to 3). Therefore, we conclude that the tetramer of four pigments is sufficient to reproduce the relevant excited state properties in terms of CT pathways of the whole two branches.

We have also analyzed the character of the excitations in the energy range of the Q_y band in both the tetramer model and the two-branch model with respect to the question of whether the SPP is involved. The transition densities reveal that excitations 1, 4, and 6 (counted from the top in Table S12) of the tetramer model are of Q_y character involving only the SPP, excitations 2 and 3 are of Q_y character involving SPP and EC2, and excitation 8 is of Q_y character involving only EC3. Performing the same analysis for the full two-branch model shows that excitations 1, 3, 7, and 8 (counted from the top in Table S11) involve only the SPP, excitations 2 and 4 involve both SPP and EC2, and excitations 11 and 12 involve only EC3. The different ordering and structure in the two models is due to the effects that have been discussed in detail above.

Finally, when comparing the calculated excitation spectra to experimental ones,[4–6] a number of factors have to be taken into account. For example, the simulations on which Figure 4 of the main paper is based are for the tetramer model with ENV^{R+}. This model captures the relative ordering of the excitations reliably, but the absolute values of the excitation energies are expected to differ to some extent from the ones that one would obtain for the full reaction center. This trend is visible, e. g., when one compares the excitation energies in Table S12 to the ones that one obtains with an extended

environment, cf. Table S13: With the extended environment, the excitation energies are slightly lower, e. g., by 0.04 eV for the first excitation. Further factors that influence the absolute position of the excitation energies are the exchange-correlation functional and the size of the basis set, with a larger basis set typically leading to lower excitation energies (see, e.g., Figure S7 of Ref. 7). Finally, one should keep in mind that in our study only the parts of the RC complex are considered that are relevant for the CT process, i. e., the SPP, EC2, and EC3 pigments as well as parts of the protein environment. By contrast, the experimental absorption spectra arise from the full RC complex, i. e., especially also the contributions from the chromophores in the antenna domain are included.

S3 Details on the BOMD Analysis

We here provide additional histograms that complement the discussion of the results from the BOMD analysis in the main text. Figure S1 shows the difference between the energy of the lowest SPP^+EC3^- excitation (SPP^+EC2^-, respectively) and the energy of the lowest $EC2^+EC3^-$ CT state for different snapshots of the BOMD runs. This reveals that only in 3 out of 95 spectra, there are CT states (always of the type SPP^+EC3^-) that are energetically below the lowest $EC2^+EC3^-$ state. In these few cases, the SPP^+EC3^- excitations are at similar energies as the Q_y band, i. e., direct coupling may be possible in principle. However, typically the lowest SPP^+EC3^- state is found $\sim 0.1 \ldots 0.5\,\text{eV}$ above the lowest $EC2^+EC3^-$ state; the lowest SPP^+EC2^- state is found $\sim 0.2 \ldots 0.7\,\text{eV}$ above the lowest $EC2^+EC3^-$ state. In Figure S2, the temporary energetic difference to the center of the Q_y band is shown for those CT excitations that are closest in energy to the center of the Q_y band (for different snapshots of the BOMD runs). We see that in 71 out of 95 spectra, it is a CT state of type $EC2^+EC3^-$, in 23 spectra it is a SPP^+EC3^- state, and only in 1 spectrum it is a SPP^+EC2^- state.

As mentioned in the main text, we have also further analyzed the characteristics of the "relevant" CT excitations (where we consider the excitations with an energy below 2 eV, which is in the same range as the Q_y band, as "relevant"). Figure S3 shows the distribution of the oscillator strengths for $EC2^+EC3^-$ and SPP^+EC3^-. In the case

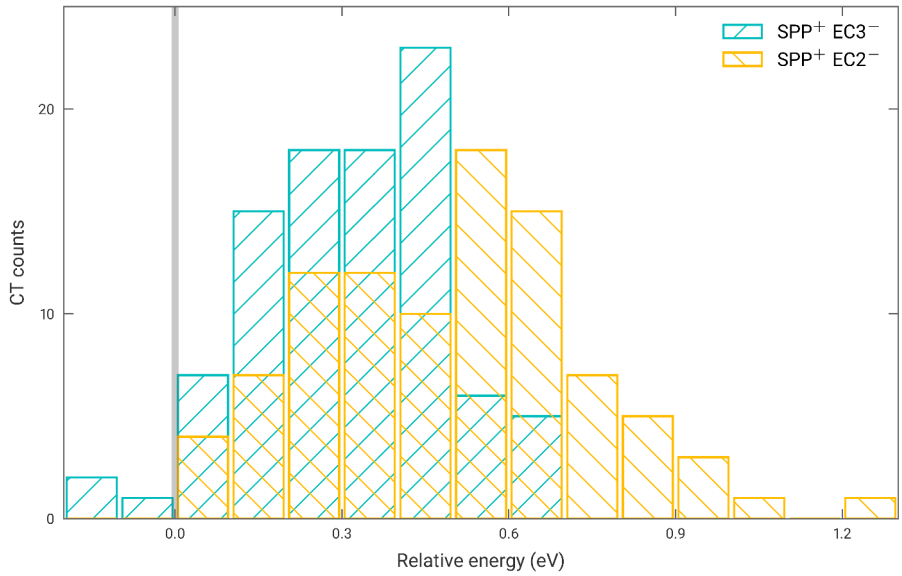

Figure S1: Histogram of the difference between the energy of the lowest SPP^+EC3^- excitation (teal bars; yellow bars: SPP^+EC2^-, respectively) and the energy of the lowest $EC2^+EC3^-$ excitation for different snapshots of the BOMD runs. CT states on the left (right) hand side of the gray bar are energetically below (above) the respective $EC2^+EC3^-$ states.

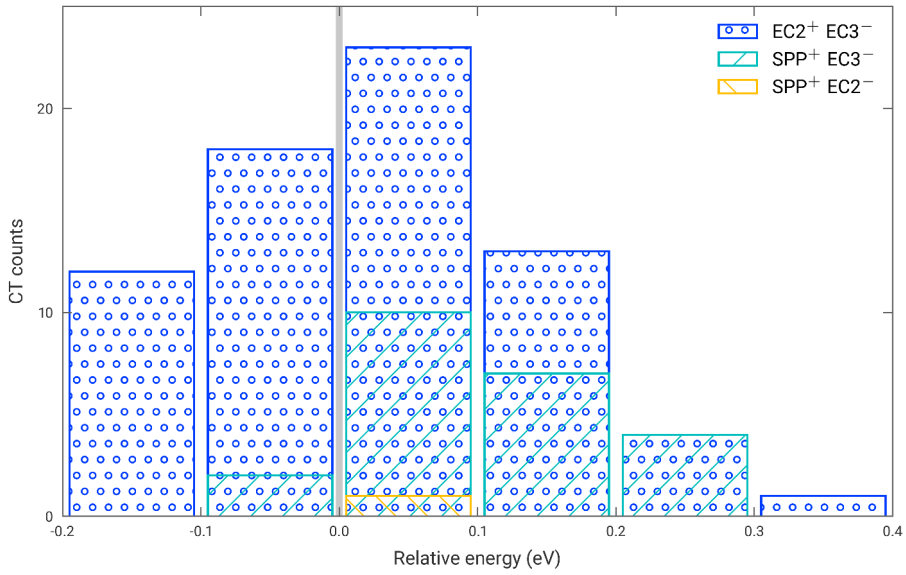

Figure S2: Histogram of the CT states closest in energy to the temporary center of the Q_y band. The energy axis denotes the energetic difference between the CT excitations and the center of the Q_y band. The latter is denoted by the gray bar as a guide for the eye).

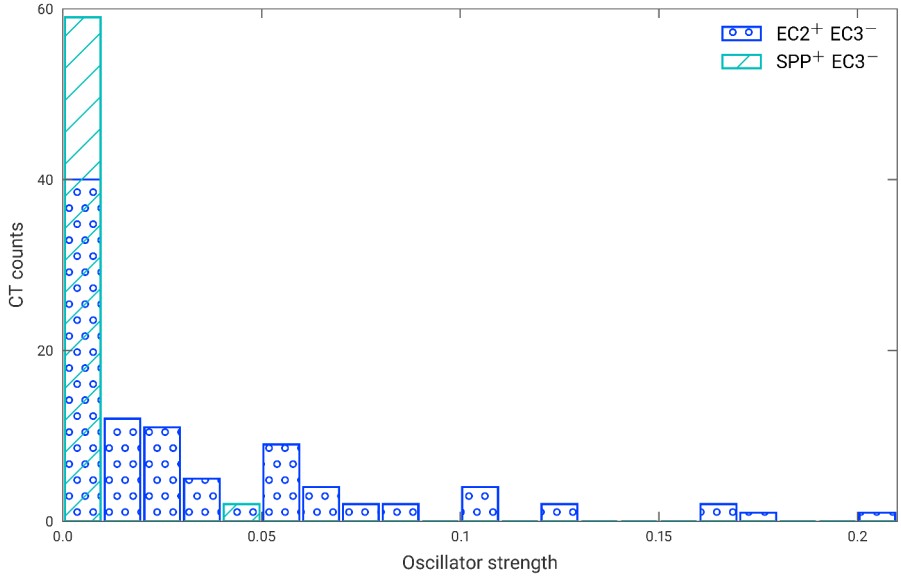

Figure S3: Histogram of the oscillator strengths of the $EC2^+EC3^-$ and SPP^+EC3^- excitations with an excitation energy below 2 eV.

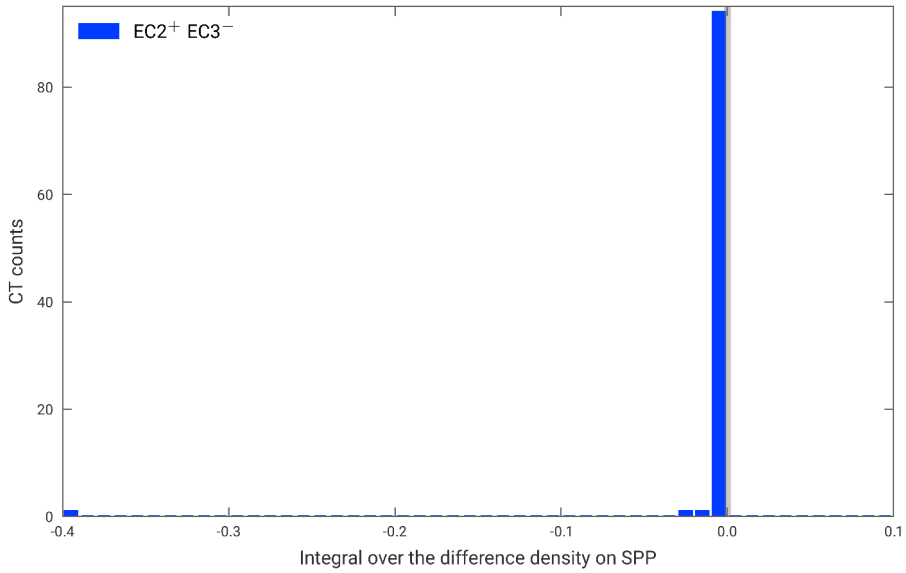

Figure S4: Histogram of the integral over the difference (electron) density in the subspace associated with SPP for the EC2$^+$EC3$^-$ excitations with an energy below 2 eV. For the CT states on the left (right) hand side of the gray bar, the hole (electron) is delocalized over SPP.

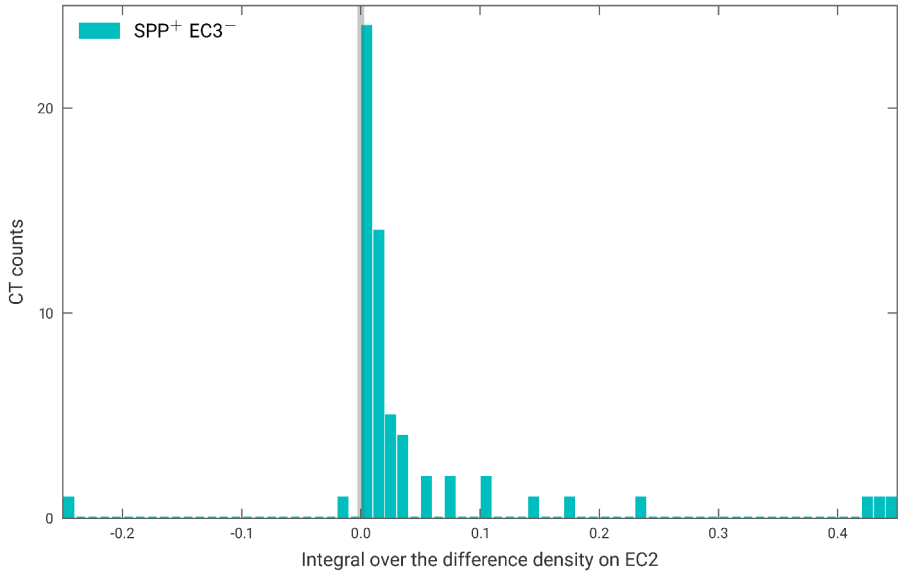

Figure S5: Histogram of the integral over the difference (electron) density in the subspace associated with EC2 for the SPP$^+$EC3$^-$ excitations with an energy below 2 eV. For the CT states on the left (right) hand side of the gray bar, the hole (electron) is delocalized over EC2.

of SPP^+EC2^- (not displayed), all excitations in this energy range have an oscillator strength below 0.01. While in the case of SPP^+EC3^- only 2 of 61 excitations exhibit an oscillator strength above 0.01, the picture is much more diverse in the case of $EC2^+EC3^-$. For 10 of 97 excitations we even find an oscillator strength above 0.1, a value which is comparable to the brightest excitations of Q_y character.

We also address the issue of whether the hole in the intermediate CT step is delocalized over both SPP and EC2. This questions has been raised by Song *et al.*[8] To this end, we examine for the $EC2^+EC3^-$ and SPP^+EC3^- states (with an energy below 2 eV) whether the "inactive" pigment, i. e., SPP or EC2, respectively, contribute to the CT ($EC2^+EC3^-$ or SPP^+EC3^-) excitations by calculating the integral over the difference density in the subspace associated with the respective "inactive" pigment. The resulting histograms are shown in Figure S4 and S5. In both figures, we find the majority of the counts very close to zero, indicating that the "inactive" pigment typically does not contribute to the CT. In the case of SPP^+EC3^-, we find a few states where the *electron* is partially delocalized over both EC2 and EC3. However, regarding the delocalization of the hole over SPP and EC2, we find only 2 of 158 states (combining Figure S4 and S5) where this is a relevant effect. (These are the two counts for integral values smaller than -0.03.)

Finally, we comment on one aspect in which the outcome of our work differs from similar theoretical studies on other RCs:[9,10] Further downhill energy transfer from $EC2^+EC3^-$ to the next CT step, SPP^+EC3^-, is not apparent from our data. There are two possible explanations for this observation: Including further parts of the protein environment may invert the relatively small energy gap between $EC2^+EC3^-$ and SPP^+EC3^-. Alternatively, the transition to the first CT step, $EC2^+EC3^-$, may induce a rearrangement of the structure such that the energy of SPP^+EC3^- is lowered compared to $EC2^+EC3^-$. In our BOMD analysis, we also obtain SPP^+EC3^- as the lowest CT state for some geometries (see above). This issue can be further addressed in a future study.

S4 Automated Protocol for the Analysis of Excitation Spectra

To make the evaluation of a large number of TDDFT excitation spectra – as required for the evaluation of the BOMD – feasible, we employ an automated protocol. Thereby, we analyze each spectrum in two steps.

First, we determine the SPP^+EC2^-, $EC2^+EC3^-$, and SPP^+EC3^- CT states. To this end, we calculate the electron density for each excited state (within Q-Chem[11]) and subtract the respective ground-state density. This yields the so-called *difference density* discretized on a cubic grid. Then, we divide the volume which contains the difference density into subspaces associated with one type of RC pigment, i. e., SPP, EC2, or EC3. Therefore, we assign each point of the difference-density grid to the RC pigment which contains the atom (considering all atoms, including hydrogen) that is closest to the given grid point. Afterwards, we calculate the integrals over the difference density in these (three) subspaces. This yields values between 0 (no CT) and ± 1 (maximum CT, transfer of a "full" electron) for each subspace. Excitations where more than a fraction of 0.4 of an electron is transferred from one pigment (subspace) to another are considered as CT excitations. Their character is determined from the two pigments (subspaces) where the largest fraction of electron transfer is detected. From our experience, the threshold 0.4 is well-suited to capture also excitations with partial CT character that emerge when a CT excitation and a valence excitation, e. g., from the Q_y band, are close in energy and couple. However, we note that typical CT excitations exhibit a very pronounced CT character with a fraction of ≥ 0.9. On the other hand, typical excitations without CT character have only very small fractions of electron transfer (far below 0.4).

In the second step, we characterize the bright excitations. The most relevant feature for us is the Q_y band which arises from the Q_y excitations of the BChl chromophores. In the tetramer model, we have three BChl chromophores and, therefore, also (mostly) three low-energy, bright Q_y excitations (around $\sim 1.5\,\mathrm{eV}$ in the crystal structure-based spectrum). From our experience, the following procedure is a pragmatic but quite reliable way to determine this Q_y band in an automated manner: From the non-CT excitations, we select those excitations with an oscillator strength above 0.02. Thereof, the three excitations with the lowest excitation energy are referred to as the Q_y band. The (additional) filtering with regard to the oscillator strength is required as a few dark excitations emerge in the spectra that do not have CT character. From our experience, the value 0.02 of the threshold is appropriate to distinguish Q_y (and Q_x) excitations (above) from CT and other dark excitations (below).

S5 Choice of the Range-Separation Parameter

For the purposes of computing spectroscopic observables of a single molecule or one well-defined molecular donor-acceptor system with TDDFT, range-separated hybrid functionals with a range-separation parameter chosen by optimal tuning typically yield very reliable results, especially for charge-transfer excitations.[12,13] The typical tuning procedure[14] is to adjust the range-separation parameter such that the highest-occupied molecular orbital eigenvalue becomes as close as possible to the first ionization potential, and the lowest unoccupied molecular eigenvalue effectively becomes as close as possible to the electron affinity, where the reference values for ionization potential and electron affinity are calculated self-consistently from total energy differences. This procedure adjusts the range-separation parameter to a value that is system specific. While the tuning procedure endows the frontier orbital energies with physical meaning,[15] it also leads to a serious drawback because it violates size-consistency.[16,17] The intrinsic limitation of optimal tuning also has to be kept in mind when one wants to compare spectroscopic observables for different systems to one another. In particular it has been demonstrated that a serious problem arises when one uses the optimal tuning procedure for (conjugated) molecular systems of increasing size:[18,19] With increasing system size, the optimally tuned range-separation parameter falls to artificially low values. Consequently, the tuned functional is dominated by semilocal exchange, and thus the reliability of the prediction of charge-transfer excitations deteriorates dramatically.

These problems require one to carefully consider the choice of the range-separation parameter in a study such as ours, in which a reliable comparison of systems of different size is mandatory. For the reasons explained in the preceding paragraph, re-tuning the functional for each of the different (sub-)systems is not suggested. Instead, the range-separation parameter should be optimally tuned such that the physics of the dominating chromophore is properly described. In our system, this is BChl. In earlier work, optimal tuning has been done for BChl *a*, leading to a range-separation parameter of $0.171\,\mathrm{a_0}^{-1}$,[20] and for BChl *g'*, leading to a range-separation parameter of $0.160\,\mathrm{a_0}^{-1}$.[7] It has further been shown that the differences one obtains in the photoabsorption spectrum of SPP and EC2 with these two values are small.[7] This confirms that some value of ω within the above mentioned range leads to reasonable results, and we chose $0.171\,\mathrm{a_0}^{-1}$ for consistency with earlier publications.

One may also wonder about including dielectric screening into the tuning procedure. The question of when and how to combine optimal tuning with screening models has found a lot of interest, see, e. g., Refs. 19, 21–27. The decisive idea of our work is to include the most relevant parts of the protein environment explicitly into the calculation. Therefore, the direct screening effects that result from the closer protein environment are accounted for. What our study does not capture is the indirect effect that might result when the protein would be included in the optimal tuning procedure, and thus may influence the range-separation parameter. However, for the reasons discussed in the preceding paragraph, re-tuning for different system sizes, i. e., amino acid selections in this case, is not advisable, and we therefore work with a fixed value of the range-separation

parameter. Future work may address this problem on a more advanced level by using a functional with local range separation, i. e., with a range-separation parameter that is itself a functional of the density.[28,29] First results with a recently developed functional of this type are promising.[30]

Author contribution statement

M. B. and S. K. conceptualized the work. M. B. prepared the structural models, did all the TDDFT and BOMD calculations, and prepared all figures and tables. J. F. supported the structure preparation and performed the titration analysis and the positioning of the interstital water molecules. All authors disucssed the results. M. B. and S. K. wrote the manuscript, and J. F. proofread it and gave comments.

References

(1) Gisriel, C.; Sarrou, I.; Ferlez, B.; Golbeck, J. H.; Redding, K. E.; Fromme, R. Structure of a symmetric photosynthetic reaction center-photosystem. *Science* **2017**, *357*, 1021–1025.

(2) Within in this work, all intermolecular distances refer to the respective end-to-end distances between non-hydrogen atoms.

(3) Till, M. S.; Ullmann, G. M. McVol – A program for calculating protein volumes and identifying cavities by a Monte Carlo algorithm. *J. Mol. Mod.* **2010**, *16*, 419–429.

(4) Chauvet, A.; Sarrou, J.; Lin, S.; Romberger, S. P.; Golbeck, J. H.; Savikhin, S.; Redding, K. E. Temporal and spectral characterization of the photosynthetic reaction center from *Heliobacterium modesticaldum*. *Photosynth. Res.* **2013**, *116*, 1–9.

(5) Kondo, T.; Mutoh, R.; Tabe, H.; Kurisu, G.; Oh-Oka, H.; Fujiyoshi, S.; Matsushita, M. Cryogenic Single-Molecule Spectroscopy of the Primary Electron Acceptor in the Photosynthetic Reaction Center. *J. Phys. Chem. Lett.* **2020**, *11*, 3980–3986.

(6) Kojima, R.; Yamamoto, H.; Azai, C.; Uragami, C.; Hashimoto, H.; Kosumi, D.; Oh-oka, H. Energy transfer and primary charge separation upon selective femtosecond excitation at 810 nm in the reaction center complex from Heliobacterium modesticaldum. *J. Photochem. Photobiol., A* **2020**, *401*, 112758-1–112758-7.

(7) Brütting, M.; Foerster, J. M.; Kümmel, S. Investigating Primary Charge Separation in the Reaction Center of *Heliobacterium modesticaldum*. *J. Phys. Chem. B* **2021**, *125*, 3468–3475.

(8) Song, Y.; Sechrist, R.; Nguyen, H. H.; Johnson, W.; Abramavicius, D.; Redding, K. E.; Ogilvie, J. P. Excitonic structure and charge separation in the heliobacterial reaction center probed by multispectral multidimensional spectroscopy. *Nat. Commun.* **2021**, *12*, 2801-1–2801-8.

(9) Tamura, H.; Saito, K.; Ishikita, H. Acquirement of water-splitting ability and alteration of the charge-separation mechanism in photosynthetic reaction centers. *Proc. Natl. Acad. Sci. U. S. A.* **2020**, *117*, 16373–16382.

(10) Mitsuhashi, K.; Tamura, H.; Saito, K.; Ishikita, H. Nature of Asymmetric Electron Transfer in the Symmetric Pathways of Photosystem I. *J. Phys. Chem. B* **2021**, *125*, 2879–2885.

(11) Shao, Y.; Gan, Z.; Epifanovsky, E.; Gilbert, A. T.; Wormit, M.; Kussmann, J.; Lange, A. W.; Behn, A.; Deng, J.; Feng, X., et al. Advances in molecular quantum chemistry contained in the Q-Chem 4 program package. *Mol. Phys.* **2015**, *113*, 184–215.

(12) Stein, T.; Kronik, L.; Baer, R. Reliable Prediction of Charge Transfer Excitations in Molecular Complexes Using Time-Dependent Density Functional Theory. *J. Am. Chem. Soc.* **2009**, *131*, 2818–2820.

(13) Kümmel, S. Charge-Transfer Excitations: A Challenge for Time-Dependent Density Functional Theory That Has Been Met. *Adv. Energy Mater.* **2017**, *7*, 1700440-1–1700440-6.

(14) Kuritz, N.; Stein, T.; Baer, R.; Kronik, L. Charge-Transfer-Like $\pi \rightarrow \pi^*$ Excitations in Time-Dependent Density Functional Theory: A Conundrum and Its Solution. *J. Chem. Theory Comput.* **2011**, *7*, 2408–2415.

(15) Kronik, L.; Stein, T.; Refaely-Abramson, S.; Baer, R. Excitation Gaps of Finite-Sized Systems from Optimally Tuned Range-Separated Hybrid Functionals. *J. Chem. Theory Comput.* **2012**, *8*, 1515–1531.

(16) Livshits, E.; Baer, R. A well-tempered density functional theory of electrons in molecules. *Phys. Chem. Chem. Phys.* **2007**, *9*, 2932–2941.

(17) Karolewski, A.; Kronik, L.; Kümmel, S. Using optimally tuned range separated hybrid functionals in ground-state calculations: Consequences and caveats. *J. Chem. Phys.* **2013**, *138*, 204115-1–204115-11.

(18) Körzdörfer, T.; Sears, J. S.; Sutton, C.; Brédas, J.-L. Long-range corrected hybrid functionals for π-conjugated systems: Dependence of the range-separation parameter on conjugation length. *J. Chem. Phys.* **2011**, *135*, 204107-1–204107-6.

(19) De Queiroz, T. B.; Kümmel, S. Charge-transfer excitations in low-gap systems under the influence of solvation and conformational disorder: Exploring range-separation tuning. *J. Chem. Phys.* **2014**, *141*, 084303-1–084303-10.

(20) Schelter, I.; Foerster, J. M.; Gardiner, A. T.; Roszak, A. W.; Cogdell, R. J.; Ullmann, G. M.; de Queiroz, T. B.; Kümmel, S. Assessing density functional theory in real-time and real-space as a tool for studying bacteriochlorophylls and the light-harvesting complex 2. *J. Chem. Phys.* **2019**, *151*, 134114-1–134114-12.

(21) Refaely-Abramson, S.; Sharifzadeh, S.; Jain, M.; Baer, R.; Neaton, J. B.; Kronik, L. Gap renormalization of molecular crystals from density-functional theory. *Phys. Rev. B* **2013**, *88*, 081204(R)-1–081204(R)-6.

(22) Refaely-Abramson, S.; Jain, M.; Sharifzadeh, S.; Neaton, J. B.; Kronik, L. Solid-state optical absorption from optimally tuned time-dependent range-separated hybrid density functional theory. *Phys. Rev. B* **2015**, *92*, 081204(R)-1–081204(R)-6.

(23) De Queiroz, T. B.; Kümmel, S. Tuned range separated hybrid functionals for solvated low bandgap oligomers. *J. Chem. Phys.* **2015**, *143*, 034101-1–034101-10.

(24) Bhandari, S.; Cheung, M.; Geva, E.; Kronik, L.; Dunietz, B. D. Fundamental Gaps of Condensed-Phase Organic Semiconductors from Single-Molecule Calculations using Polarization-Consistent Optimally Tuned Screened Range-Separated Hybrid Functionals. *J. Chem. Theory Comput.* **2018**, *14*, 6287–6294.

(25) Kronik, L.; Kümmel, S. Dielectric Screening Meets Optimally Tuned Density Functionals. *Adv. Mater.* **2018**, *30*, 1706560-1–1706560-14.

(26) Aksu, H.; Schubert, A.; Geva, E.; Dunietz, B. D. Explaining Spectral Asymmetries and Excitonic Characters of the Core Pigment Pairs in the Bacterial Reaction Center Using a Screened Range-Separated Hybrid Functional. *J. Phys. Chem. B* **2019**, *123*, 8970–8975.

(27) Aksu, H.; Schubert, A.; Bhandari, S.; Yamada, A.; Geva, E.; Dunietz, B. D. On the Role of the Special Pair in Photosystems as a Charge Transfer Rectifier. *J. Phys. Chem. B* **2020**, *124*, 1987–1994.

(28) Aschebrock, T.; Kümmel, S. Exploring local range separation: The role of spin scaling and one-electron self-interaction. *J. Chem. Phys.* **2019**, *151*, 154108-1 –154108-11.

(29) Maier, T. M.; Ikabata, Y.; Nakai, H. Assessing locally range-separated hybrid functionals from a gradient expansion of the exchange energy density. *J. Chem. Phys.* **2021**, *154*, 214101-1–214101-16.

(30) Brütting, M.; Bahmann, H.; Kümmel, S. Hybrid functionals with local range separation: Accurate atomization energies and reaction barrier heights. *J. Chem. Phys.* **2022**, *156*, 104109-1–104109-14.

Reprint of publication [B4]

Publication [B4]

M. Brütting, H. Bahmann, and S. Kümmel

Predicting fundamental gaps accurately from density functional theory with non-empirical local range separation

J. Chem. Phys. **160**, 181101 (2024) *Rapid Communication*

DOI: 10.1063/5.0204379

Author contribution statement: M.B. and S.K. conceptualized the work and discussed the functional construction. H.B. participated in the discussions about functional construction. M.B. implemented the functional, did the calculations, and prepared the figures in discussion with S.K. M.B. and S.K. wrote the manuscript, with comments and proofreading from H.B.

The Journal of Chemical Physics COMMUNICATION pubs.aip.org/aip/jcp

Predicting fundamental gaps accurately from density functional theory with non-empirical local range separation

Cite as: J. Chem. Phys. 160, 181101 (2024); doi: 10.1063/5.0204379
Submitted: 21 February 2024 • Accepted: 22 April 2024 •
Published Online: 8 May 2024

Moritz Brütting,[1] Hilke Bahmann,[2] and Stephan Kümmel[1,a)]

AFFILIATIONS

[1] Theoretical Physics IV, University of Bayreuth, 95440 Bayreuth, Germany
[2] Physical and Theoretical Chemistry, University of Wuppertal, 42097 Wuppertal, Germany

[a)] Author to whom correspondence should be addressed: stephan.kuemmel@uni-bayreuth.de

ABSTRACT

We present an exchange–correlation approximation in which the Coulomb interaction is split into long- and short-range components and the range separation is determined by a non-empirical density functional. The functional respects important constraints, such as the homogeneous and slowly varying density limits, leads to the correct long-range potential, and eliminates one-electron self-interaction. Our approach is designed for spectroscopic purposes and closely approximates the piecewise linearity of the energy as a function of the particle number. The functional's accuracy for predicting the fundamental gap in generalized Kohn–Sham theory is demonstrated for a large number of systems, including organic semiconductors with a notoriously difficult electronic structure.

I. INTRODUCTION

Density functional theory (DFT)[1–3] is a central pillar of electronic structure theory as it typically offers useful accuracy at a moderate computational cost. The first and traditional purpose for which DFT is employed is the prediction of the ground-state energy and structural properties that follow from it. However, DFT is also used for the second purpose of calculating spectroscopic properties. One of the most important spectroscopic observables is the fundamental gap, defined by the difference between the first ionization potential (IP) and the first electron affinity (EA),

$$\Delta_g = \mathrm{IP} - \mathrm{EA}. \tag{1}$$

The gap determines the character of a material, e.g., as a metal or semiconductor, and in today's research, predicting Δ_g reliably and efficiently[4] is of particular relevance because of the quest for energy-converting materials: Δ_g is a decisive factor for determining whether a material is suitable for, e.g., a solar cell or a photo-catalyst.[5,6]

The predictive power of a DFT calculation hinges on the accuracy of the employed exchange–correlation (xc) approximation. For DFT's first purpose, i.e., predicting the ground-state energy, years of development have equipped the community with an impressive selection of xc approximations, which allow one to target the level of accuracy and computational cost that is required for the task at hand, e.g., see Refs. 1, 2, 7, and 8 for reviews. In fact, for predicting the ground-state energy, by now DFT can rival wavefunction-based methods.[9]

For the second purpose, i.e., predicting spectroscopic observables and especially Δ_g, the situation is more complex. This is to a certain extent a natural consequence of the very nature of DFT: it focuses on the density, and orbitals were originally introduced just as auxiliary objects for evaluating the kinetic energy. Thus, it is no surprise that the single particle gap between the lowest unoccupied (L) and highest occupied (H) orbital,

$$\Delta_\varepsilon = \varepsilon_\mathrm{L} - \varepsilon_\mathrm{H} \tag{2}$$

in Kohn–Sham theory does not correspond to Δ_g even for the exact xc functional.[10–13] In a quasi-particle picture, the physical processes corresponding to IP and EA, i.e., inserting or removing an electron, can be considered as creating a quasi-electron or quasi-hole, respectively. These quasi-particles contain the response effects of the

correlated many-electron system to the presence of the extra electron or hole. In many-body perturbation theory, the GW approach[14–16] provides for a natural way of calculating the quasi-particle energies.

By going from Kohn–Sham to generalized Kohn–Sham theory, it is possible to establish the equality $\Delta_g = \Delta_\varepsilon$ within DFT.[17] While one can define more than one non-interacting reference systems in generalized Kohn–Sham theory, generalized Kohn–Sham is not a heuristic construct[18] and the gap is a well-defined observable.[19,20] Thus, being able to predict the many-body observable Δ_g reliably in an inexpensive single particle-like calculation is extremely attractive. However, constructing xc approximations that fulfill this promise in practice is a challenge because several of DFT's most demanding aspects have to be addressed for reliable gap prediction: one-electron self-interaction must be corrected to avoid erroneous offsets of the occupied eigenvalues,[21] a non-zero derivative discontinuity is required in the Kohn–Sham scheme to correctly lift up the unoccupied eigenvalues,[11–13,22] the xc potential must have the proper asymptotics,[23,24] the energy should be a straight line as a function of particle number between integers,[10,25,26] and correspondingly, the highest occupied eigenvalue should not depend on its occupation number.[27–29]

II. RANGE SEPARATION

A decisive step forward in the reliability of DFT predicted gaps was reached based on range separation, i.e., by splitting the Coulomb interaction into a long- and a short-range component.[30–32] In practice, this is often done in the form

$$\frac{1}{|\mathbf{r}-\mathbf{r}'|} = \underbrace{\frac{\mathrm{erf}\big(\omega|\mathbf{r}-\mathbf{r}'|\big)}{|\mathbf{r}-\mathbf{r}'|}}_{\text{long range}} + \underbrace{\frac{1-\mathrm{erf}\big(\omega|\mathbf{r}-\mathbf{r}'|\big)}{|\mathbf{r}-\mathbf{r}'|}}_{\text{short range}}, \tag{3}$$

where the range-separation parameter, ω, plays a decisive role. In recent years, range-separated hybrid (RSH) functionals have mostly been developed along two lines.

In one line of development, successful functionals have been constructed empirically by determining a value for ω by fitting to reference data.[8,33–38] Many different forms have been devised, e.g., using exact exchange in either short- or long-range or both, and possibly combining Eq. (3) with further concepts, such as the one of local hybrids.[39–42] In this class of functionals, there are two recently developed ones that are particularly interesting in the present context because they lead to promising results for both binding effects and spectroscopic properties. The DM21[43] functional reaches remarkable accuracy; however, it is hard to deduce insight into xc effects from the underlying trained neural network. The ωLH22t[44–46] functional is of a different nature. Its form is guided by functional development concepts, with nine parameters that are fitted empirically, and it is accurate for many ground- and excited-state observables. As it is one of the most accurate functionals with an exceptionally wide range of application, we return to ωLH22t below for comparison.

A second, alternative way of using Eq. (3) is the concept of determining ω by optimal tuning (OT).[47–49] Here, we refer to OT that uses exact exchange in the long range with just one parameter ω that is determined non-empirically: It exploits the IP theorem[10,28] and adjusts ω such that the frontier eigenvalues become as close as possible to IP and EA as calculated from total energy differences between the neutral, the cation, and the anion systems. The OT approach is specifically designed to yield a functional for spectroscopy. It has been extremely successful and, thus inspired RSHs have been further developed, e.g., to incorporate the effects of screening.[50–53] OT allows avoiding the empirical fitting of parameters. This is desirable as the final form of empirical approaches depends on the details of the fitting procedure,[54] and developing non-empirical functionals is part of the quest for deeper understanding and universality in DFT.[3,55,56]

The widespread use of OT underlines the strong need for functionals that predict spectroscopic properties reliably. However, OT also has non-negligible drawbacks. First, the tuning is computationally involved, requiring many calculations also for charged systems. Second, tuning violates size consistency,[47,57,58] and the system-specific determination of ω can have further surprising consequences.[59] Third, the applicability of OT is limited by intrinsic questions of consistency. Tuning can fail, e.g., for donor–acceptor systems of largely different chemical nature. More importantly, yet, for systems with delocalized electrons, the tuning procedure spuriously yields ever smaller values of ω for systems of increasing size.[60,61] Thus, the functional becomes increasingly semilocal, and consequently, the well-known problems of semilocal functionals, such as too low fundamental gaps,[62] reappear. Ultimately, these failures have their origin in the fact that OT is system-specific, and thus, ω is turned into a density functional, but one that is only very implicitly defined. One can mitigate the problems by judiciously tuning only for a subsystem.[63–66] However, this works reliably only up to a certain system size, and the originally high predictive power of OT might eventually be compromised.

III. A CONSTRAINT-GUIDED EXCHANGE–CORRELATION FUNCTIONAL WITH LOCAL RANGE SEPARATION

These problems can be overcome by going from global to local range separation, i.e., one continues to use Eq. (3), yet makes ω an explicit density functional $\omega([n],\mathbf{r})$. In the following, we thus solve the problems that arise with the only implicitly defined density functional of OT, as the explicit dependence on the density naturally leads to different forms of $\omega([n],\mathbf{r})$ for different systems. At the same time, we avoid empiricism by designing $\omega([n],\mathbf{r})$ such that it fulfills the important fundamental constraints of the homogeneous electron gas, of the slowly varying density limit, and of being free from one-electron self-interaction.

Previous studies using local range separation[67–71] focused on finding functionals for traditional ground-state properties and relied on empirically fitted parameters. Our aim here is different, as our focus is on constructing a functional that will allow reliably predicting the fundamental gap Δ_g from first principles. Therefore in our functional construction, we deliberately focus on those properties of the xc functional that are relevant for gap prediction, and not on atomization energies.

Making use of Eq. (3), one can write the xc energy in the form

$$E_{\mathrm{xc}}^{\mathrm{lRSH}} = E_{\mathrm{x}}^{\mathrm{LR,ex}} + E_{\mathrm{x}}^{\mathrm{SR,sl}} + E_{\mathrm{c}}^{\mathrm{sl}}. \tag{4}$$

Here, $E_x^{LR,ex}$ denotes exact long-range exchange, i.e., the Fock-integral evaluated with the first term on the right-hand side of Eq. (3). This choice by construction guarantees the correct long-range asymptotics of the potential. Here, $E_x^{SR,sl}$ and E_c^{sl} are semilocal functionals, taking into account short-range exchange and correlation, respectively. The key idea for the non-empirical construction is to use Eq. (4) in combination with the range-separation functional

$$\omega_\sigma(\mathbf{r}) = C_{GE}\frac{|\nabla n_\sigma(\mathbf{r})|}{n_\sigma(\mathbf{r})}\frac{1}{1-\frac{1}{2}\left(z_\sigma(\mathbf{r})\zeta^2(\mathbf{r})+z_\sigma(\mathbf{r})\right)}. \tag{5}$$

Here, $n_\sigma(\mathbf{r})$ is the spin-density, $|\nabla n_\sigma(\mathbf{r})|$ is its gradient, and $\tau_\sigma(\mathbf{r}) = \frac{1}{2}\sum_i |\nabla\phi_{i\sigma}(\mathbf{r})|^2$ is the non-interacting kinetic energy density (in Hartree atomic units). The functions $z_\sigma(\mathbf{r})$ and $\zeta^2(\mathbf{r})$ refer to the ratio of τ_σ and its single orbital (von Weizsäcker) limit, i.e., $z_\sigma = |\nabla n_\sigma|^2/(8n_\sigma\tau_\sigma)$, and the spin-polarization, $\zeta = (n_\uparrow - n_\downarrow)/(n_\uparrow + n_\downarrow)$. $C_{GE} = \sqrt{5}/18 \simeq 0.124226$ is a non-empirical coefficient (see below). We base the ω-dependent short-range exchange $E_x^{sl,SR}$ on the local density approximation (LDA) in the analytical form given in Ref. 72. The correlation

$$E_c^{sl} = \int \mathrm{d}\mathbf{r}\left(\varepsilon_c^{LDA}[n_\uparrow(\mathbf{r}), n_\downarrow(\mathbf{r})] - \sum_\sigma z_\sigma(\mathbf{r})\varepsilon_c^{LDA}[n_\sigma(\mathbf{r}), 0]\right) \tag{6}$$

is based on LDA with a self-interaction correction (SIC), where ε_c^{LDA} is the correlation energy density in the parametrization by Perdew and Wang.[73]

This functional is motivated by the following considerations. First, it respects the homogeneous-electron-gas limit: $\omega_\sigma(\mathbf{r})$ vanishes in this limit[71] and the correlation energy of Eq. (6) reduces to LDA. Second, we incorporate the slowly varying limit (gradient expansion to second order) of the exchange energy density,[74] $\varepsilon_{x\sigma} = C_0 n_\sigma^{4/3}\left(1 + C_2(|\nabla n_\sigma|/n_\sigma^{4/3})^2 + \cdots\right)$, with $C_0 = -3(6\pi^2)^{1/3}/4\pi$ and $C_2 = 10/(81\cdot 4(6\pi^2)^{2/3})$. This is ensured as our $\omega_\sigma(\mathbf{r})$ has

$$\omega_\sigma^{GE}(\mathbf{r}) = C_{GE}\frac{|\nabla n_\sigma(\mathbf{r})|}{n_\sigma(\mathbf{r})} \tag{7}$$

as the leading term of is gradient expansion, and the choice $C_{GE} = \sqrt{5}/18$ yields the proper gradient expansion coefficient.[70,71]

Third, it corrects for one-electron self-interaction. Here, a delicate balance is required. If one corrects straightforwardly for one-electron self-interaction as done in Hartree–Fock or Perdew–Zunger SIC, one typically overcorrects. A manifestation of overcorrection is that the energy as a function of particle number, $E(N)$, is concave. On the other hand, if one does not correct enough, then the functional retains too much of its semilocal character, which manifests in a convex $E(N)$. However, a straight-line $E(N)$ is important for obtaining physically meaningful eigenvalues,[26,75,76] and the straight-line condition provides a guide rail in functional construction in addition to the exact constraints. We can reach the proper balance with local range separation by using iso-orbital indicators and spin functions[77–84] as done in Eq. (5) with the last multiplicative term on the right-hand side. This term tends to infinity when the denominator vanishes, making the functional go to full exact exchange in this case.[68,71] How this limit is reached is controlled by z_σ and ζ. Here, z_σ distinguishes between the homogeneous-electron-gas limit ($z_\sigma \to 0$) and the *one-orbital* limit ($z_\sigma \to 1$). On the other hand, $z_\sigma\zeta^2$ is bound between its value in closed-shell systems or the homogeneous electron gas ($z_\sigma\zeta^2 \to 0$) and its value in *one-electron* regions ($z_\sigma\zeta^2 \to 1$). The linear combination of z_σ and $z_\sigma\zeta^2$ ensures that one-electron systems are fully self-interaction corrected, while other systems are subjected to a more moderate correction, with the spatial profile of the density being taken into account via the n_σ, ∇n_σ, and τ_σ contributions. The interplay between the homogeneous electron gas limit on the one hand and, on the other hand, ensuring a vanishing interaction for one-electron system while also guaranteeing

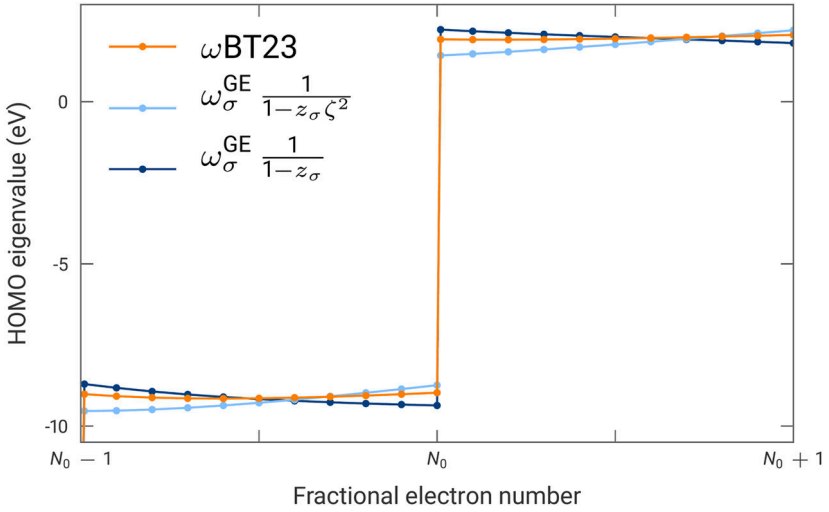

FIG. 1. Highest occupied eigenvalue of benzene as a function of the fractional electron number (N_0 electrons: neutral system) calculated with the functional of Eqs. (4)–(6), labeled ωBT23. See the main text for a discussion of the other two curves.

a general correction, is also the guiding principle in the correlation functional of Eq. (6).[85,114]

IV. RESULTS

Figure 1 shows the fractional charge behavior that our functional reaches for the paradigm case of the benzene molecule. It shows the dependence of ε_H on the particle number. This dependence directly reflects the curvature in $E(N)$.[26–28,76,86] For our functional (labeled ωBT23, where the acronym "BT" refers to "Bayreuth," the university city of the first author), the eigenvalue is independent of the particle number in an excellent approximation both below and above the integer. As a reference and to illustrate the above-mentioned balance, we also show the curves that would be obtained when one would only use either $1 - z_\sigma\zeta^2$ or $1 - z_\sigma$ in the denominator of the last term in Eq. (5). One would clearly obtain a positive or negative curvature in $E(N)$, respectively. That the linear combination of the two terms tends to balance their individual trends is an observation that we made for all systems for which we made this analysis.

These and all the following calculations involving local range separation were performed with a development version of TURBOMOLE,[87] into which we implemented our functional. The self-consistent evaluation relies on the developments of Klawohn and Bahmann.[69] See the supplementary material for more details.

Having explained and verified the guiding principles of our functional construction, we proceed to use it for the prediction of fundamental gaps of a set of molecules.[88] We chose this set because it is ideally suited for several reasons: First, the molecules are practically relevant as they are typical for the type of systems that are used in organic electronics. Second, they cover a considerable range of sizes and chemical compositions. Third and most importantly, reliable reference data are available for this set: On the one hand, highly accurate results have been obtained in wavefunction-based calculations,[88] and on the other hand, several different versions of DFT[89] and diligently conducted GW calculations[90] have been reported for these systems. Figure 2 shows the fundamental gap calculated as the difference between the generalized Kohn–Sham frontier eigenvalues of our functional plotted against the wavefunction reference. One sees that there are a few systems for which the difference is as large as a few 0.1 eV, but overall, the results are close to the diagonal dashed line that indicates perfect agreement. The mean absolute error (MAE) across the set is 0.20 eV for ωBT23. This finding is put into perspective when one compares it to the accuracy reached with other methods. On the one hand, for the same set of molecules, OT with an individual adjustment of the range-separation parameter for each molecule leads to an MAE of

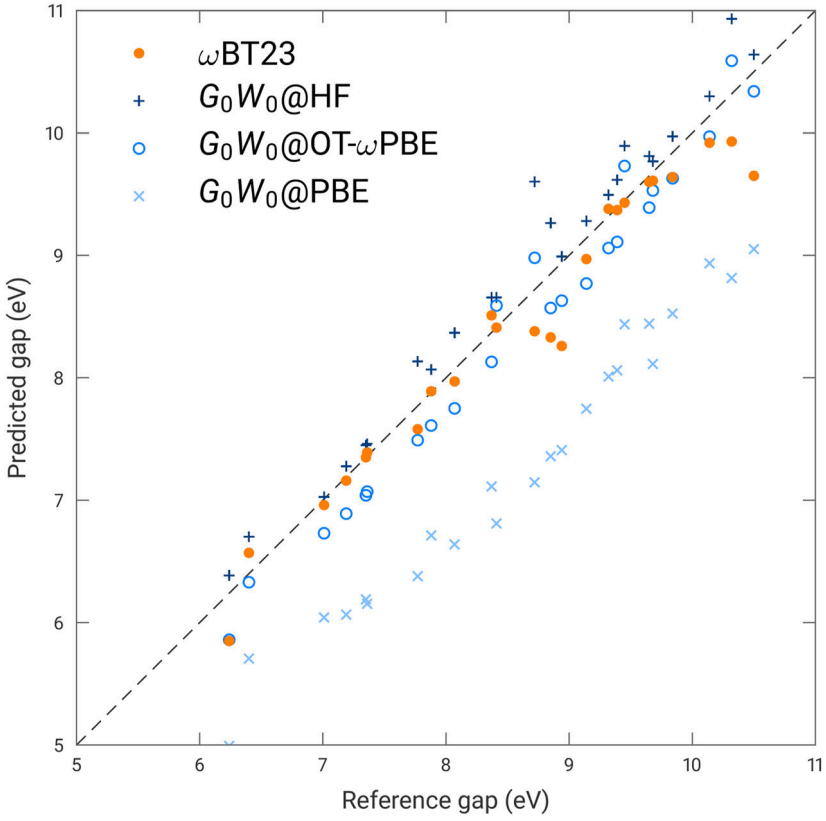

FIG. 2. Fundamental gaps of organic molecules calculated as the difference of the frontier eigenvalues of the ωBT23 density functional plotted against the reference gaps calculated from CCSD(T)[88] (cf. the supplementary material for raw data). Three variants of G_0W_0,[89,90] namely, using PBE, Hartree–Fock, and OT-ωPBE as a starting point, respectively, are also shown. Ideal agreement is indicated by the dashed line.

0.38 eV.[89] On the other hand, Fig. 2 shows the gaps that are obtained with different variants of G_0W_0: with a Perdew–Burke–Ernzerhof (PBE) calculation as the starting point, one finds a serious underestimation, whereas with Hartree–Fock (HF) as the starting point, one finds a slight overestimation. Putting G_0W_0 on top of OT-ωPBE, which has been identified[90] as one of the best possible GW approaches for this benchmark set, leads to an MAE of 0.26 eV.[89] Thus, gap prediction based on non-empirical generalized Kohn–Sham DFT with ωBT23 can clearly compete with both non-empirical OT and G_0W_0 with a diligently chosen starting point. While reaching this accuracy in the GW approach requires one to perform a DFT calculation with a range-separated hybrid first and then in addition the computationally expensive G_0W_0 calculation, our locally RSH functional yields the same accuracy from the DFT calculation alone. The fact that DFT can rival GW in accuracy has recently also been demonstrated for the ωLH22t functional, for which an MAE of 0.23 eV has been reported in Ref. 45 for the gaps of this set. In the supplementary material, we report further comparisons to ωLH22t.

The accuracy of our functional is also confirmed when looking at the eigenvalues of the organic semiconductor molecules NTCDA (i.e., 1,4,5,8-naphthalene-tetracarboxylic dianhydride) and PTCDA (i.e., 3,4,9,10-perylene-tetracarboxylic acid dianhydride), which have been studied in detail both experimentally and theoretically, e.g., in Refs. 91–93. They constitute a formidable challenge to conventional DFT because of their mixture of delocalized and localized orbitals[94] and are also tricky for non-empirical optimal tuning[95] because a judiciously chosen fraction of short-range exact exchange is needed for a correct description.[96] For NTCDA, the first IP is 9.67 eV experimentally and 9.62 eV with ωBT23, and for PTCDA, the values are 8.20 and 8.16 eV, respectively. With a consistently chosen starting point, G_0W_0 yields 9.65 and 8.13 eV for the first IP.[45,97] For the second IP, G_0W_0 yields 10.34 and 9.76 eV, respectively, whereas the numbers are 10.39 and 10.00 eV, respectively, with ωBT23. Thus, even for these particularly difficult systems, the ωBT23 results are in a similar trust range as the G_0W_0 results.

Finally, we check whether the non-empirical local range separation can remedy the issues that one encounters with optimal tuning for conjugated systems of increasing size. Figure 3 shows the fundamental gaps calculated with ωBT23 and OT-ωPBE[60] for the paradigm case of oligoacenes of increasing size, plotted as a function of the accurate wavefunction-based reference gaps.[98,99] While the absolute accuracy achieved with optimal tuning is quite good for the smaller systems, the trend that the errors increase noticeably with the system size is clearly visible in the deviation from the diagonal dashed line. However, in particular larger-size systems with lower gaps are of technological interest. Therefore, it is reassuring to

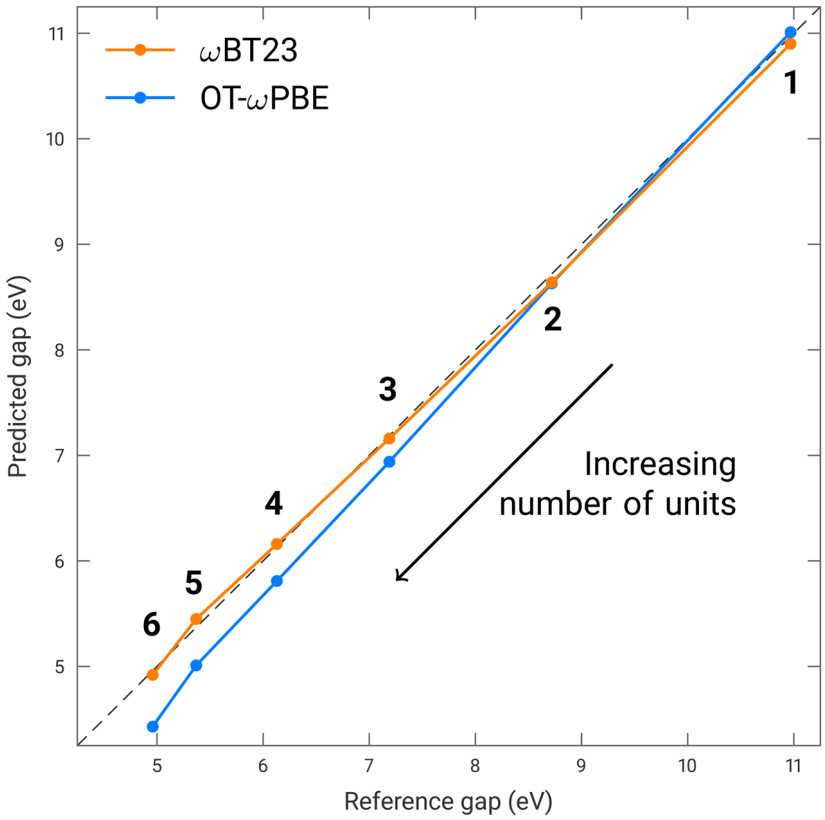

FIG. 3. Size dependence of the fundamental gap for the series of oligoacenes (from benzene to hexacene, i.e., one to six molecular units) calculated with the ωBT23 functional and OT-ωPBE[60] and plotted with respect to the reference gaps calculated from CCSD(T)[98,99] (cf. the supplementary material for raw data).

see that with our local range separation the accuracy is consistently high (deviations below 0.1 eV) for all system sizes, with an MAE of 0.06 eV.

V. CONCLUSION AND OUTLOOK

On summarizing our findings, we conclude that the successful concept of RSHs becomes particularly powerful when the range separation is governed by a density functional. We have developed such an explicit functional from first principles for the purposes of predicting the fundamental gap without adjustable parameters. Our construction is guided by the constraints of yielding the proper long-range asymptotic potential, respecting the homogeneous electron gas limit, fulfilling the second-order gradient expansion, and eliminating one-electron self-interaction. This leads to a functional for which the energy as a function of the particle number approximates a straight line, which can be interpreted as a sign for the reduction of many-electron self-interaction.[100,101]

In view of this success, one should nevertheless be aware that ωBT23 is not a panacea. We report some atomization energies and barrier heights in the supplementary material. For ground-state energetics, other functionals, e.g., the ones from Refs. 44 and 71, are considerably more accurate. Furthermore, calculations with a constant range-separation parameter run efficiently in many codes. Therefore, we do not expect ωBT23 to generally replace OT or well-calibrated general-purpose functionals. However, ωBT23's specific non-empirical design for spectroscopic purposes makes it ideal for applications where other methods, such as OT or GW, reach their limits, i.e., its intended application is similar to the one of OT functionals.

In this context, having the density functional $\omega([n],\mathbf{r})$ instead of a (tuned) parameter has several advantages. First, it makes the functional universal. Thus eliminating the need for the system specific determination of parameters not only simplifies computational procedures but also avoids the size-consistency problem of OT. Second, whereas OT may fail for, e.g., donor–acceptor systems that require largely different values of the range-separation parameter for donor and acceptor, respectively, the functional $\omega([n],\mathbf{r})$ can adjust individually to the separate components. Third, possible problems that OT faces for systems of increasing size are avoided. As a final outlook, we note that local range separation is promising not only from the perspective of DFT but also from the one of time-dependent DFT (TDDFT). Based on general arguments[102] and the experience from optimally tuned RSHs[24,48,76,103–105] and range-separated local hybrids,[44,45] one expects that functionals that yield frontier eigenvalues that reflect ionization potential and electron affinity, respectively, will also be accurate in TDDFT for charge-transfer excitations. Implementing the equations of TDDFT for RSHs with local range separation is beyond the scope of the present work. However, the concept of developing RSHs with an explicit density dependence, an example of which we have given in this paper, is also promising from this perspective.

SUPPLEMENTARY MATERIAL

The supplementary material, which includes Refs. 106–113, contains computational details, the data underlying Figs. 2 and 3, further comparison of ωBT23 and ωLH22t, and information about atomization energies and barrier heights with ωBT23.

ACKNOWLEDGMENTS

S.K. acknowledges the financial support from the Deutsche Forschungsgemeinschaft (DFG, German Research Foundation) Project No. 457582427 and from the Bavarian State Ministry of Science, Research, and the Arts for the Collaborative Research Network "Solar Technologies go Hybrid." M.B. and S.K. acknowledge the support from the Elite Study Program "Biological Physics" of the Elite Network of Bavaria. M.B. further acknowledges the support by the "Studienstiftung des Deutschen Volkes" and by the University of Bayreuth Graduate School. H.B. acknowledges funding from the DFG, Project No. 418140043.

AUTHOR DECLARATIONS

Conflict of Interest

The authors have no conflicts to disclose.

Author Contributions

M.B. and S.K. conceptualized the work and discussed the functional construction. H.B. participated in the discussions about functional construction. M.B. implemented the functional, did the calculations, and prepared the figures in discussion with S.K. M.B. and S.K. wrote the manuscript, with comments and proofreading from H.B.

Moritz Brütting: Conceptualization (equal); Formal analysis (equal); Investigation (equal); Software (lead); Validation (lead); Visualization (lead); Writing – original draft (equal); Writing – review & editing (equal). **Hilke Bahmann**: Investigation (supporting); Software (supporting); Writing – review & editing (equal). **Stephan Kümmel**: Conceptualization (equal); Formal analysis (equal); Funding acquisition (lead); Investigation (equal); Project administration (lead); Supervision (lead); Writing – original draft (equal); Writing – review & editing (equal).

DATA AVAILABILITY

The data that support the findings of this study are available within the article and its supplementary material.

REFERENCES

[1] K. Burke, "Perspective on density functional theory," J. Chem. Phys. **136**, 150901 (2012).
[2] A. M. Teale *et al.*, "DFT exchange: Sharing perspectives on the workhorse of quantum chemistry and materials science," Phys. Chem. Chem. Phys. **24**, 28700–28781 (2022).
[3] A. D. Becke, "Density-functional theory vs density-functional fits," J. Chem. Phys. **156**, 214101 (2022).
[4] P. Borlido, J. Schmidt, A. W. Huran, F. Tran, M. A. L. Marques, and S. Botti, "Exchange-correlation functionals for band gaps of solids: Benchmark, reparametrization and machine learning," npj Comput. Mater. **6**, 96 (2020).

[5]J.-L. Brédas, J. E. Norton, J. Cornil, and V. Coropceanu, "Molecular understanding of organic solar cells: The challenges," Acc. Chem. Res. **42**, 1691–1699 (2009).
[6]X. Yang and D. Wang, "Photocatalysis: From fundamental principles to materials and applications," ACS Appl. Energy Mater. **1**, 6657–6693 (2018).
[7]S. Kümmel and L. Kronik, "Orbital-dependent density functionals: Theory and applications," Rev. Mod. Phys. **80**, 3–60 (2008).
[8]N. Mardirossian and M. Head-Gordon, "Thirty years of density functional theory in computational chemistry: An overview and extensive assessment of 200 density functionals," Mol. Phys. **115**, 2315–2372 (2017).
[9]J. Erhard, P. Bleiziffer, and A. Görling, "Power series approximation for the correlation kernel leading to Kohn–Sham methods combining accuracy, computational efficiency, and general applicability," Phys. Rev. Lett. **117**, 143002 (2016).
[10]J. P. Perdew, R. G. Parr, M. Levy, and J. L. Balduz, "Density-functional theory for fractional particle number: Derivative discontinuities of the energy," Phys. Rev. Lett. **49**, 1691–1694 (1982).
[11]L. J. Sham and M. Schlüter, "Density-functional theory of the energy gap," Phys. Rev. Lett. **51**, 1888–1891 (1983).
[12]J. P. Perdew and M. Levy, "Physical content of the exact Kohn-Sham orbital energies: Band gaps and derivative discontinuities," Phys. Rev. Lett. **51**, 1884–1887 (1983).
[13]R. W. Godby, M. Schlüter, and L. J. Sham, "Accurate exchange-correlation potential for silicon and its discontinuity on addition of an electron," Phys. Rev. Lett. **56**, 2415–2418 (1986).
[14]G. Onida, L. Reining, and A. Rubio, "Electronic excitations: Density-functional versus many-body Green's-function approaches," Rev. Mod. Phys. **74**, 601–659 (2002).
[15]L. Reining, "The GW approximation: Content, successes and limitations," Wiley Interdiscip. Rev.: Comput. Mol. Sci. **8**, e1344 (2017).
[16]D. Golze, M. Dvorak, and P. Rinke, "The *GW* compendium: A practical guide to theoretical photoemission spectroscopy," Front. Chem. **7**, 377 (2019).
[17]A. Seidl, A. Görling, P. Vogl, J. A. Majewski, and M. Levy, "Generalized Kohn-Sham schemes and the band-gap problem," Phys. Rev. B **53**, 3764–3774 (1996).
[18]R. Garrick, A. Natan, T. Gould, and L. Kronik, "Exact generalized Kohn-Sham theory for hybrid functionals," Phys. Rev. X **10**, 021040 (2020).
[19]L. Kronik, T. Stein, S. Refaely-Abramson, and R. Baer, "Excitation gaps of finite-sized systems from optimally tuned range-separated hybrid functionals," J. Chem. Theory Comput. **8**, 1515–1531 (2012).
[20]J. P. Perdew, W. Yang, K. Burke, Z. Yang, E. K. U. Gross, M. Scheffler, G. E. Scuseria, T. M. Henderson, I. Y. Zhang, A. Ruzsinszky, H. Peng, J. Sun, E. Trushin, and A. Görling, "Understanding band gaps of solids in generalized Kohn–Sham theory," Proc. Natl. Acad. Sci. U. S. A. **114**, 2801–2806 (2017).
[21]J. P. Perdew and A. Zunger, "Self-interaction correction to density-functional approximations for many-electron systems," Phys. Rev. B **23**, 5048–5079 (1981).
[22]M. J. Allen and D. J. Tozer, "Eigenvalues, integer discontinuities and NMR shielding constants in Kohn–Sham theory," Mol. Phys. **100**, 433–439 (2002).
[23]C.-O. Almbladh and U. von Barth, "Exact results for the charge and spin densities, exchange-correlation potentials, and density-functional eigenvalues," Phys. Rev. B **31**, 3231–3244 (1985).
[24]L. Kronik and S. Kümmel, "Piecewise linearity, freedom from self-interaction, and a Coulomb asymptotic potential: Three related yet inequivalent properties of the exact density functional," Phys. Chem. Chem. Phys. **22**, 16467–16481 (2020).
[25]W. Yang, Y. Zhang, and P. W. Ayers, "Degenerate ground states and a fractional number of electrons in density and reduced density matrix functional theory," Phys. Rev. Lett. **84**, 5172–5175 (2000).
[26]P. Mori-Sánchez, A. J. Cohen, and W. Yang, "Localization and delocalization errors in density functional theory and implications for band-gap prediction," Phys. Rev. Lett. **100**, 146401 (2008).
[27]J. F. Janak, "Proof that $\partial E\ \partial n_i = \varepsilon$ in density-functional theory," Phys. Rev. B **18**, 7165–7168 (1978).
[28]J. P. Perdew and M. Levy, "Comment on 'Significance of the highest occupied Kohn-Sham eigenvalue,'" Phys. Rev. B **56**, 16021–16028 (1997).
[29]I. Dabo, A. Ferretti, N. Poilvert, Y. Li, N. Marzari, and M. Cococcioni, "Koopmans' condition for density-functional theory," Phys. Rev. B **82**, 115121 (2010).
[30]T. Leininger, H. Stoll, H.-J. Werner, and A. Savin, "Combining long-range configuration interaction with short-range density functionals," Chem. Phys. Lett. **275**, 151–160 (1997).
[31]H. Iikura, T. Tsuneda, T. Yanai, and K. Hirao, "A long-range correction scheme for generalized-gradient-approximation exchange functionals," J. Chem. Phys. **115**, 3540–3544 (2001).
[32]A. Savin, "Models and corrections: Range separation for electronic interaction—Lessons from density functional theory," J. Chem. Phys. **153**, 160901 (2020).
[33]J. Heyd, G. E. Scuseria, and M. Ernzerhof, "Hybrid functionals based on a screened Coulomb potential," J. Chem. Phys. **118**, 8207–8215 (2003).
[34]T. Yanai, D. P. Tew, and N. C. Handy, "A new hybrid exchange–correlation functional using the Coulomb-attenuating method (CAM-B3LYP)," Chem. Phys. Lett. **393**, 51–57 (2004).
[35]J. Heyd and G. E. Scuseria, "Assessment and validation of a screened Coulomb hybrid density functional," J. Chem. Phys. **120**, 7274–7280 (2004).
[36]O. A. Vydrov and G. E. Scuseria, "Assessment of a long-range corrected hybrid functional," J. Chem. Phys. **125**, 234109 (2006).
[37]J.-D. Chai and M. Head-Gordon, "Systematic optimization of long-range corrected hybrid density functionals," J. Chem. Phys. **128**, 084106 (2008).
[38]M. A. Rohrdanz, K. M. Martins, and J. M. Herbert, "A long-range-corrected density functional that performs well for both ground-state properties and time-dependent density functional theory excitation energies, including charge-transfer excited states," J. Chem. Phys. **130**, 054112 (2009).
[39]J. Jaramillo, G. E. Scuseria, and M. Ernzerhof, "Local hybrid functionals," J. Chem. Phys. **118**, 1068–1073 (2003).
[40]H. Bahmann, A. Rodenberg, A. V. Arbuznikov, and M. Kaupp, "A thermochemically competitive local hybrid functional without gradient corrections," J. Chem. Phys. **126**, 011103 (2007).
[41]J. P. Perdew, V. N. Staroverov, J. Tao, and G. E. Scuseria, "Density functional with full exact exchange, balanced nonlocality of correlation, and constraint satisfaction," Phys. Rev. A **78**, 052513 (2008).
[42]T. M. Maier, A. V. Arbuznikov, and M. Kaupp, "Local hybrid functionals: Theory, implementation, and performance of an emerging new tool in quantum chemistry and beyond," Wiley Interdiscip. Rev.: Comput. Mol. Sci. **9**, e1378 (2019).
[43]J. Kirkpatrick, B. McMorrow, D. H. P. Turban, A. L. Gaunt, J. S. Spencer, A. G. D. G. Matthews, A. Obika, L. Thiry, M. Fortunato, D. Pfau, L. R. Castellanos, S. Petersen, A. W. R. Nelson, P. Kohli, P. Mori-Sánchez, D. Hassabis, and A. J. Cohen, "Pushing the frontiers of density functionals by solving the fractional electron problem," Science **374**, 1385–1389 (2021).
[44]S. Fürst, M. Haasler, R. Grotjahn, and M. Kaupp, "Full implementation, optimization, and evaluation of a range-separated local hybrid functional with wide accuracy for ground and excited states," J. Chem. Theory Comput. **19**, 488 (2023).
[45]S. Fürst and M. Kaupp, "Accurate ionization potentials, electron affinities, and band gaps from the ωLH22t range-separated local hybrid functional: No tuning required," J. Chem. Theory Comput. **19**, 3146–3158 (2023).
[46]S. Fürst, M. Kaupp, and A. Wodyński, "Range-separated local hybrid functionals with small fractional-charge and fractional-spin errors: Escaping the zero-sum game of DFT functionals," J. Chem. Theory Comput. **19**, 8639 (2023).
[47]E. Livshits and R. Baer, "A well-tempered density functional theory of electrons in molecules," Phys. Chem. Chem. Phys. **9**, 2932–2941 (2007).
[48]T. Stein, L. Kronik, and R. Baer, "Reliable prediction of charge transfer excitations in molecular complexes using time-dependent density functional theory," J. Am. Chem. Soc. **131**, 2818–2820 (2009).
[49]T. Stein, H. Eisenberg, L. Kronik, and R. Baer, "Fundamental gaps in finite systems from eigenvalues of a generalized Kohn-Sham method," Phys. Rev. Lett. **105**, 266802 (2010).
[50]S. Refaely-Abramson, S. Sharifzadeh, M. Jain, R. Baer, J. B. Neaton, and L. Kronik, "Gap renormalization of molecular crystals from density-functional theory," Phys. Rev. B **88**, 081204(R) (2013).
[51]H. Phillips, Z. Zheng, E. Geva, and B. D. Dunietz, "Orbital gap predictions for rational design of organic photovoltaic materials," Org. Electron. **15**, 1509 (2014).

[52]J. Zhan, M. Govoni, and G. Galli, "Nonempirical range-separated hybrid functional with spatially dependent screened exchange," J. Chem. Theory Comput. **19**, 5851–5862 (2023).
[53]J. Yang, S. Falletta, and A. Pasquarello, "Range-separated hybrid functionals for accurate prediction of band gaps of extended systems," npj Comput. Mater. **9**, 108 (2023).
[54]S. Vuckovic, T. Gould, B. Chang, and S. Dale, "Transferable diversity: A data-driven approach to chemical representation," chemRxiv:2023-5075x-v2 (2023).
[55]S. Schwalbe, K. Trepte, and S. Lehtola, "How good are recent density functionals for ground and excited states of one-electron systems?," J. Chem. Phys. **157**, 174113 (2022).
[56]R. Pederson and K. Burke, "The difference between molecules and materials: Reassessing the role of exact conditions in density functional theory," J. Chem. Phys. **159**, 214113 (2023).
[57]A. Savin, "Is size-consistency possible with density functional approximations?," Chem. Phys. **356**, 91–97 (2009).
[58]A. Karolewski, L. Kronik, and S. Kümmel, "Using optimally tuned range separated hybrid functionals in ground-state calculations: Consequences and caveats," J. Chem. Phys. **138**, 204115 (2013).
[59]M. Friede, S. Ehlert, S. Grimme, and J.-M. Mewes, "Do optimally tuned range-separated hybrid functionals require a reparametrization of the dispersion correction? It depends," J. Chem. Theory Comput. **19**, 8097–8107 (2023).
[60]T. Körzdörfer, J. S. Sears, C. Sutton, and J.-L. Brédas, "Long-range corrected hybrid functionals for π-conjugated systems: Dependence of the range-separation parameter on conjugation length," J. Chem. Phys. **135**, 204107 (2011).
[61]T. B. de Queiroz and S. Kümmel, "Charge-transfer excitations in low-gap systems under the influence of solvation and conformational disorder: Exploring range-separation tuning," J. Chem. Phys. **141**, 084303 (2014).
[62]R. Godby and I. White, "Density-relaxation part of the self-energy," Phys. Rev. Lett. **80**, 3161 (1998).
[63]C. Halsey-Moore, P. Jena, and J. T. McLeskey, "Tuning range-separated DFT functionals for modeling the peak absorption of MEH-PPV polymer in various solvents," Comput. Theor. Chem. **1162**, 112506 (2019).
[64]H. Aksu, A. Schubert, S. Bhandari, A. Yamada, E. Geva, and B. D. Dunietz, "On the role of the special pair in photosystems as a charge transfer rectifier," J. Phys. Chem. B **124**, 1987–1994 (2020).
[65]T. B. de Queiroz, E. R. de Figueroa, M. D. Coutinho-Neto, C. D. Maciel, E. Tapavicza, Z. Hashemi, and L. Leppert, "First principles theoretical spectroscopy of methylene blue: Between limitations of time-dependent density functional theory approximations and its realistic description in the solvent," J. Chem. Phys. **154**, 044106 (2021).
[66]M. Brütting, J. M. Foerster, and S. Kümmel, "Understanding primary charge separation in the heliobacterial reaction center," J. Phys. Chem. Lett. **14**, 3092–3102 (2023).
[67]A. V. Krukau, G. E. Scuseria, J. P. Perdew, and A. Savin, "Hybrid functionals with local range separation," J. Chem. Phys. **129**, 124103 (2008).
[68]T. Aschebrock and S. Kümmel, "Exploring local range separation: The role of spin scaling and one-electron self-interaction," J. Chem. Phys. **151**, 154108 (2019).
[69]S. Klawohn and H. Bahmann, "Self-consistent implementation of hybrid functionals with local range separation," J. Chem. Theory Comput. **16**, 953–963 (2020).
[70]T. M. Maier, Y. Ikabata, and H. Nakai, "Assessing locally range-separated hybrid functionals from a gradient expansion of the exchange energy density," J. Chem. Phys. **154**, 214101 (2021).
[71]M. Brütting, H. Bahmann, and S. Kümmel, "Hybrid functionals with local range separation: Accurate atomization energies and reaction barrier heights," J. Chem. Phys. **156**, 104109 (2022).
[72]P. M. W. Gill, R. D. Adamson, and J. A. Pople, "Coulomb-attenuated exchange energy density functionals," Mol. Phys. **88**, 1005–1009 (1996).
[73]J. P. Perdew and Y. Wang, "Accurate and simple analytic representation of the electron-gas correlation energy," Phys. Rev. B **45**, 13244–13249 (1992).
[74]J. P. Perdew and S. Kurth, "Density functionals for non-relativistic Coulomb systems in the new century," in *A Primer in Density Functional Theory*, edited by C. Fiolhais, F. Nogueira, and M. Marques (Springer, Berlin, Heidelberg, 2003), pp. 1–55.
[75]A. J. Cohen, P. Mori-Sánchez, and W. Yang, "Fractional charge perspective on the band gap in density-functional theory," Phys. Rev. B **77**, 115123 (2008).
[76]T. Stein, J. Autschbach, N. Govind, L. Kronik, and R. Baer, "Curvature and frontier orbital energies in density functional theory," J. Phys. Chem. Lett. **3**, 3740–3744 (2012).
[77]A. D. Becke, "A new inhomogeneity parameter in density-functional theory," J. Chem. Phys. **109**, 2092–2098 (1998).
[78]J. Toulouse, A. Savin, and C. Adamo, "Validation and assessment of an accurate approach to the correlation problem in density functional theory: The Kriger–Chen–Iafrate–Savin model," J. Chem. Phys. **117**, 10465–10473 (2002).
[79]J. P. Perdew, S. Kurth, A. Zupan, and P. Blaha, "Accurate density functional with correct formal properties: A step beyond the generalized gradient approximation," Phys. Rev. Lett. **82**, 2544–2547 (1999).
[80]J. P. Perdew, J. Tao, V. N. Staroverov, and G. E. Scuseria, "Meta-generalized gradient approximation: Explanation of a realistic nonempirical density functional," J. Chem. Phys. **120**, 6898–6911 (2004).
[81]A. D. Becke, "Density-functional thermochemistry. IV. A new dynamical correlation functional and implications for exact-exchange mixing," J. Chem. Phys. **104**, 1040–1046 (1996).
[82]A. D. Becke, "Local exchange-correlation approximations and first-row molecular dissociation energies," Int. J. Quantum Chem. **27**, 585–594 (1985).
[83]J. F. Dobson, "Spin-density functionals for the electron correlation energy with automatic freedom from orbital self-interaction," J. Phys.: Condens. Matter **4**, 7877–7890 (1992).
[84]S. Kümmel and J. P. Perdew, "Two avenues to self-interaction correction within Kohn–Sham theory: Unitary invariance is the shortcut," Mol. Phys. **101**, 1363–1368 (2003).
[85]One obtains very similar results with the correlation functional used in Ref. 71, but Eq. (6) has slight advantages for the gaps of smaller molecules. The form of this correlation correction is inspired by Ref. 114, but there it was used only for the short-range contribution, whereas here it is used for the full range.
[86]V. Vlček, H. R. Eisenberg, G. Steinle-Neumann, L. Kronik, and R. Baer, "Deviations from piecewise linearity in the solid-state limit with approximate density functionals," J. Chem. Phys. **142**, 034107 (2015).
[87]Y. J. Franzke *et al.*, "TURBOMOLE: Today and tomorrow," J. Chem. Theory Comput. **19**, 6859–6890 (2023).
[88]R. M. Richard, M. S. Marshall, O. Dolgounitcheva, J. V. Ortiz, J.-L. Brédas, N. Marom, and C. D. Sherrill, "Accurate ionization potentials and electron affinities of acceptor molecules I. Reference data at the CCSD(T) complete basis set limit," J. Chem. Theory Comput. **12**, 595–604 (2016).
[89]L. Gallandi, N. Marom, P. Rinke, and T. Körzdörfer, "Accurate ionization potentials and electron affinities of acceptor molecules II: Non-empirically tuned long-range corrected hybrid functionals," J. Chem. Theory Comput. **12**, 605–614 (2016).
[90]J. W. Knight, X. Wang, L. Gallandi, O. Dolgounitcheva, X. Ren, J. V. Ortiz, P. Rinke, T. Körzdörfer, and N. Marom, "Accurate ionization potentials and electron affinities of acceptor molecules III: A benchmark of *GW* methods," J. Chem. Theory Comput. **12**, 615–626 (2016).
[91]N. Dori, M. Menon, L. Kilian, M. Sokolowski, L. Kronik, and E. Umbach, "Valence electronic structure of gas-phase 3,4,9,10-perylene tetracarboxylic acid dianhydride: Experiment and theory," Phys. Rev. B **73**, 195208 (2006).
[92]P. Puschnig, S. Berkebile, A. J. Fleming, G. Koller, K. Emtsev, T. Seyller, J. D. Riley, C. Ambrosch-Draxl, F. P. Netzer, and M. G. Ramsey, "Reconstruction of molecular orbital densities from photoemission data," Science **326**, 702–706 (2009).
[93]M. Dauth, T. Körzdörfer, S. Kümmel, J. Ziroff, M. Wiessner, A. Schöll, F. Reinert, M. Arita, and K. Shimada, "Orbital density reconstruction for molecules," Phys. Rev. Lett. **107**, 193002 (2011).
[94]T. Körzdörfer, S. Kümmel, N. Marom, and L. Kronik, "When to trust photoelectron spectra from Kohn-Sham eigenvalues: The case of organic semiconductors," Phys. Rev. B **79**, 201205(R) (2009).
[95]T. Körzdörfer, R. M. Parrish, N. Marom, J. S. Sears, C. D. Sherrill, and J.-L. Brédas, "Assessment of the performance of tuned range-separated hybrid density functionals in predicting accurate quasiparticle spectra," Phys. Rev. B **86**, 205110 (2012).

[96]S. Refaely-Abramson, S. Sharifzadeh, N. Govind, J. Autschbach, J. B. Neaton, R. Baer, and L. Kronik, "Quasiparticle spectra from a nonempirical optimally tuned range-separated hybrid density functional," Phys. Rev. Lett. **109**, 226405 (2012).
[97]T. Körzdörfer and N. Marom, "Strategy for finding a reliable starting point for G_0W_0 demonstrated for molecules," Phys. Rev. B **86**, 041110 (2012).
[98]M. S. Deleuze, L. Claes, E. S. Kryachko, and J.-P. François, "Benchmark theoretical study of the ionization threshold of benzene and oligoacenes," J. Chem. Phys. **119**, 3106–3119 (2003).
[99]B. Hajgató, M. S. Deleuze, D. J. Tozer, and F. De Proft, "A benchmark theoretical study of the electron affinities of benzene and linear acenes," J. Chem. Phys. **129**, 084308 (2008).
[100]P. Mori-Sánchez, A. J. Cohen, and W. Yang, "Many-electron self-interaction error in approximate density functionals," J. Chem. Phys. **125**, 201102 (2006).
[101]A. Ruzsinszky, J. P. Perdew, G. I. Csonka, O. A. Vydrov, and G. E. Scuseria, "Spurious fractional charge on dissociated atoms: Pervasive and resilient self-interaction error of common density functionals," J. Chem. Phys. **125**, 194112 (2006).
[102]D. Tozer, "Relationship between long-range charge-transfer excitation energy error and integer discontinuity in Kohn–Sham theory," J. Chem. Phys. **119**, 12697–12699 (2003).
[103]N. T. Maitra, "Charge transfer in time-dependent density functional theory," J. Phys.: Condens. Matter **29**, 423001 (2017).
[104]T. Stein, L. Kronik, and R. Baer, "Prediction of charge-transfer excitations in coumarin-based dyes using a range-separated functional tuned from first principles," J. Chem. Phys. **131**, 244119 (2009).
[105]N. Kuritz, T. Stein, R. Baer, and L. Kronik, "Charge-transfer-like $\pi \rightarrow \pi^*$ excitations in time-dependent density functional theory: A conundrum and its solution," J. Chem. Theory Comput. **7**, 2408–2415 (2011).
[106]E. Caldeweyher, S. Ehlert, A. Hansen, H. Neugebauer, S. Spicher, C. Bannwarth, and S. Grimme, "A generally applicable atomic-charge dependent London dispersion correction," J. Chem. Phys. **150**, 154122 (2019).
[107]A. D. Becke, "Density-functional exchange-energy approximation with correct asymptotic behavior," Phys. Rev. A **38**, 3098–3100 (1988).
[108]C. Lee, W. Yang, and R. G. Parr, "Development of the Colle-Salvetti correlation-energy formula into a functional of the electron density," Phys. Rev. B **37**, 785–789 (1988).
[109]A. D. Becke, "Density-functional thermochemistry. III. The role of exact exchange," J. Chem. Phys. **98**, 5648–5652 (1993).
[110]B. J. Lynch and D. G. Truhlar, "Small representative benchmarks for thermochemical calculations," J. Phys. Chem. A **107**, 8996–8999 (2003).
[111]T. Schmidt, E. Kraisler, A. Makmal, L. Kronik, and S. Kümmel, "A self-interaction-free local hybrid functional: Accurate binding energies vis-à-vis accurate ionization potentials from Kohn-Sham eigenvalues," J. Chem. Phys. **140**, 18A510 (2014).
[112]R. Peverati and D. G. Truhlar, "Quest for a universal density functional: The accuracy of density functionals across a broad spectrum of databases in chemistry and physics," Philos. Trans. R. Soc., A **372**, 20120476 (2014).
[113]R. D. Johnson III, NIST computational chemistry comparison and benchmark database, NIST standard reference database number 101, release 21, 2020.
[114]A. V. Arbuznikov and M. Kaupp, "Importance of the correlation contribution for local hybrid functionals: Range separation and self-interaction corrections," J. Chem. Phys. **136**, 014111 (2012).

Supplemental Material for

Predicting fundamental gaps accurately from density functional theory with non-empirical local range separation

The Journal of Chemical Physics Communications

Moritz Brütting,[1] Hilke Bahmann,[2] and Stephan Kümmel[1,*]

[1] Theoretical Physics IV, University of Bayreuth, 95440 Bayreuth, Germany
[2] Physical and Theoretical Chemistry, University of Wuppertal, 42097 Wuppertal, Germany
[*] Corresponding author: stephan.kuemmel@uni-bayreuth.de

S1 Computational details

All calculations with the ωBT23 and ωLH22t functionals have been done using a development version of Turbomole [1] (module `ridft`). Our implementation of ωBT23 relies on the developments of Klawohn and Bahmann [2], for ωLH22t we use the implementation by Kaupp and coworkers [3]. Unless noted otherwise, we have used the cc-pVTZ basis set, grid size 3, a convergence threshold of 10^{-7}, and the resolution-of-the-identity approximation. These are standard settings that are well-established for ground-state density functional theory (DFT) calculations of eigenvalue gaps of organic molecules. The structures of the molecules were determined with a DFT-based structure optimization that we have performed using the commercial version of Turbomole 7.6. Following the choice made for the geometry optimizations underlying the benchmark CCSD(T) calculations we have employed the B3LYP [4–6] functional, D4 dispersion correction [7], cc-pVTZ basis set, resolution-of-the-identity approximation, and standard settings otherwise.

S2 Detailed data about molecular gaps

In the first part of this section we report the numbers for the fundamental gaps for the set of organic acceptor molecules compiled by Körzdörfer and coworkers [8] and the series of oligoacenes (benzene to hexacene) underlying Fig. 2 and 3 in the main text. The data for the organic acceptor molecules is shown in Tab. S1, the data for the oligoacenes in Tab. S2. In both cases, the ωBT23 and ωLH22t results for the HOMO–LUMO eigenvalue gap, $\Delta_\varepsilon = \varepsilon_{\mathrm{LUMO}} - \varepsilon_{\mathrm{HOMO}}$, have been obtained using Turbomole as described in section S1; the other DFT and GW results stem from the literature [8, 9, 11]. We compare these results to the respective reference values from CCSD(T) calculations [10, 12, 13]. For each method and molecule, we provide the predicted value for the gap (Δ_ε) as well as the error with respect to the CCSD(T) data, and for each method the mean absolute and

Table S1: Fundamental gaps (from frontier eigenvalues) for the set of organic acceptor molecules compiled by Körzdörfer and coworkers [8] (corresponding to Fig. 2 in the main text). The results from our ωBT23 functional, several GW methods [8, 9], and ωLH22t are compared to CCSD(T) calculations [10]. The molecule names follow Fig. 1 of Ref. [8]. All values are in eV.

	CCSD(T)	ωBT23		G_0W_0@OT-ωPBE		G_0W_0@PBE		G_0W_0@HF		ωLH22t	
	Reference	Δ_ε	Error	Δ_ε	Error	Δ_ε	Error	Δ_ε	Error	Δ_ε	Error
Anthracene	7.19	7.16	−0.03	6.89	−0.30	6.07	−1.13	7.28	0.09	7.33	0.14
Acridine	7.35	7.35	0.00	7.04	−0.31	6.19	−1.16	7.45	0.10	7.49	0.14
Phenazine	7.36	7.39	0.03	7.07	−0.29	6.15	−1.21	7.46	0.10	7.49	0.13
Azulene	7.01	6.96	−0.05	6.73	−0.28	6.04	−0.97	7.03	0.02	7.12	0.11
Benzoquinone	8.72	8.38	−0.34	8.98	0.26	7.15	−1.57	9.60	0.88	8.50	−0.22
Naphthalenedione	8.41	8.41	0.00	8.59	0.18	6.81	−1.60	8.66	0.25	8.48	0.07
Dichlone	8.07	7.97	−0.10	7.75	−0.32	6.64	−1.43	8.37	0.30	8.09	0.02
F4-benzoquinone	8.85	8.33	−0.52	8.57	−0.28	7.36	−1.49	9.26	0.41	8.32	−0.53
Cl4-benzoquinone	7.77	7.58	−0.19	7.49	−0.28	6.38	−1.39	8.13	0.36	7.69	−0.08
Nitrobenzene	9.65	9.60	−0.05	9.39	−0.26	8.44	−1.21	9.81	0.16	9.56	−0.09
F4-pDCNB	9.14	8.97	−0.17	8.77	−0.37	7.75	−1.39	9.28	0.14	9.02	−0.12
Dinitrobenzonitrile	9.39	9.37	−0.02	9.11	−0.28	8.06	−1.33	9.62	0.23	9.35	−0.04
Nitrobenzonitrile	9.32	9.38	0.06	9.06	−0.26	8.01	−1.31	9.49	0.17	9.36	0.04
Benzonitrile	10.14	9.92	−0.22	9.97	−0.17	8.94	−1.21	10.30	0.16	10.06	−0.08
Fumaronitrile	10.50	9.65	−0.85	10.34	−0.16	9.05	−1.45	10.64	0.14	9.74	−0.76
mDCNB	9.84	9.64	−0.20	9.63	−0.21	8.52	−1.32	9.97	0.13	9.78	−0.06
TCNE	8.94	8.26	−0.68	8.63	−0.31	7.41	−1.53	8.99	0.05	8.35	−0.59
TCNQ	6.24	5.85	−0.39	5.86	−0.38	4.99	−1.25	6.39	0.15	6.01	−0.23
Maleic anhydride	10.32	9.93	−0.39	10.59	0.27	8.82	−1.50	10.93	0.61	9.81	−0.51
Phthalic anhydride	9.68	9.61	−0.07	9.53	−0.15	8.11	−1.57	9.77	0.09	9.68	0.00
Phthalimide	9.45	9.43	−0.02	9.73	0.28	8.44	−1.01	9.89	0.44	9.53	0.08
Cl4-isobenzofurandione	8.37	8.51	0.14	8.13	−0.24	7.11	−1.26	8.66	0.29	8.62	0.25
NDCA	7.88	7.89	0.01	7.61	−0.27	6.71	−1.17	8.07	0.19	8.01	0.13
Boron-dipyrromethene	6.40	6.57	0.17	6.33	−0.07	5.71	−0.69	6.70	0.30	6.70	0.30
MAE			0.20		0.26		1.30		0.24		0.20
MSE			−0.16		−0.17		−1.30		0.24		−0.08

Table S2: Fundamental gaps (from frontier eigenvalues) for the series of oligoacenes (corresponding to Fig. 3 in the main text). The results from our ωBT23 functional, OT-ωPBE [11], and ωLH22t are compared to CCSD(T) calculations [12, 13]. All values are in eV.

	CCSD(T)	ωBT23		OT-ωPBE		ωLH22t	
	Reference	Δ_ε	Error	Δ_ε	Error	Δ_ε	Error
Benzene	10.97	10.90	−0.07	11.01	0.04	11.07	0.10
Naphthalene	8.72	8.64	−0.08	8.63	−0.09	8.82	0.10
Anthracene	7.19	7.16	−0.03	6.94	−0.25	7.33	0.14
Tetracene	6.13	6.16	0.03	5.81	−0.32	6.31	0.18
Pentacene	5.37	5.45	0.08	5.01	−0.36	5.58	0.21
Hexacene	4.96	4.92	−0.04	4.43	−0.53	5.03	0.07
MAE			0.06		0.26		0.13
MSE			−0.02		−0.25		0.13

mean signed errors (MAE and MSE). We note that the results from the literature have been obtained with numerical settings that are comparable to ours, especially using the same basis set. In our calculations we have used molecular geometries that we optimized ourselves (according to the protocol above). This ensures that all the results obtained with ωBT23 for the different sets of molecules are consistent. From our experience, the results obtained from these geometries are comparable to the literature results. This can be seen, e. g., by comparing the results obtained with standard functionals with those reported in the literature. For completeness, we further note that OT-ωPBE refers to the ωPBE functional with values of ω from optimal tuning. Thereby, as a tuning condition the error in the IP theorem, $\delta_{\mathrm{IP}} = |\varepsilon_{\mathrm{HOMO}} + E_0(N-1) - E_0(N)|$, has been used [8, 11]. Comparing ωBT23 and ωLH22t, the performance is rather similar for these sets of molecules: for the organic acceptor molecules a MAE of 0.20 eV is obtained with both functionals, for the oligoacenes MAEs of 0.06 eV (ωBT23) and 0.13 eV (ωLH22t) are obtained. The values for ωLH22t are slightly different from the ones reported in Ref. [14] due to the slightly different molecular geometries. The other findings of Tab. S1 and S2 are discussed in the main text.

In addition to the data that is discussed in the main text, we list in Tab. S3 a comparison of the fundamental gaps obtained with ωBT23 and ωLH22t for a set of diatomic molecules. It comprises different types of atoms as well as single, double, and triple bonds. We are not aware of high-quality reference data for all of these molecules, therefore we base the comparison on the IP theorem. For each molecule and functional we report the fundamental gap from a ΔSCF calculation ($\Delta_{\mathrm{g}} = E(N_0) - E(N_0 - 1) - (E(N_0 + 1) - E(N_0))$), the frontier eigenvalue gap from the generalized Kohn-Sham calculation (Δ_ε), and the difference between the two numbers. As discussed in the main text this comparison is relevant as in a judiciously constructed generalized Kohn-Sham scheme Δ_{g} and Δ_ε can become identical. In this respect the performance of both functionals is

Table S3: Fundamental gaps of diatomic molecules. Displayed are the gap from a ΔSCF calculation (Δ_g), the frontier eigenvalue gap (Δ_ε), and their difference. All values are in eV. The calculations have been performed using an aug-cc-pVTZ basis set and a convergence threshold of 10^{-8}. The molecular geometries were taken from the NIST database [15] (Li_2 and LiH) and the Minnesota database 2.0 [16] (otherwise).

	ωBT23			ωLH22t		
	Δ_g	Δ_ε	Difference	Δ_g	Δ_ε	Difference
Cl_2	10.68	9.60	−1.08	10.76	9.79	−0.97
CO	14.99	14.79	−0.19	15.53	14.78	−0.75
F_2	15.80	14.74	−1.07	15.73	13.05	−2.68
H_2	17.04	16.61	−0.43	17.26	17.20	−0.06
HF	16.17	15.91	−0.26	16.68	15.47	−1.22
Li_2	4.43	4.42	−0.01	4.89	5.10	0.21
LiH	7.23	7.46	0.23	7.60	7.88	0.28
N_2	18.06	16.85	−1.20	18.10	16.52	−1.58
NO	10.39	9.36	−1.03	10.38	8.38	−1.99
O_2	13.52	12.54	−0.98	13.01	10.78	−2.24
OH	11.29	12.07	0.78	11.45	9.64	−1.80
PH	9.63	9.13	−0.50	9.11	8.27	−0.84
S_2	8.41	7.59	−0.82	8.18	7.47	−0.71
SH	8.06	7.90	−0.16	8.13	7.12	−1.01
SiO	11.19	10.76	−0.44	11.48	10.93	−0.56
MAE			0.61			1.13
MSE			−0.48			−1.06

somewhat mixed. ωLH22t yields a MAE of 1.13 eV. This is a great improvement over many existing functionals where one would obtain a MAE of a few eV (e. g., 2.88 eV for CAM-B3LYP). ωBT23 can further improve upon ωLH22t, yielding a MAE of 0.61 eV. The data shows that this improvement arises in part from an improved description of some of the systems containing hydrogen (HF, PH, SH), which might suggest a relation to the correction of one-electron self-interaction. On the other hand, none of the functionals is very accurate for some of the systems involving double or triple bonds (N_2, NO, O_2). This might suggest a relation to the description of static correlation. In conclusion, this data indicates that ωBT23 tends to be more reliable for the spectroscopic properties, but further steps of development are required for both functionals to improve the description of smaller systems.

S3 Atomization energies and barrier heights

We here report the results that one finds with ωBT23 for the AE6 and BH6 test sets. The atomization energies are displayed in the upper part of Table S4, the barrier heights in the lower part. Additionally, we show the resulting MAE and MSE for both test

Table S4: Atomization energies of the AE6 test set (upper part) and reaction barrier heights of the BH6 test set (lower part) [17] calculated with our ωBT23 functional. The calculated values are compared to the reference values from the Minnesota database 2.0 [16]. All values are in kcal/mol.

			ωBT23	
		Reference	Value	Error
SiH_4		324.95	288.64	−36.31
SiO		193.06	148.72	−44.34
S_2		104.25	87.43	−16.82
C_3H_4		705.06	620.33	−84.73
$C_2H_2O_2$		633.99	533.70	−100.29
C_4H_8		1149.37	1027.26	−122.11
MAE (AE6)				67.43
MSE (AE6)				−67.43
$OH + CH_4 \rightarrow$	F	6.50	12.01	5.51
$CH_3 + H_2O$	R	19.60	22.60	3.00
$H + OH \rightarrow$	F	10.50	7.52	−2.98
$O + H_2$	R	12.87	21.24	8.37
$H + H_2S \rightarrow$	F	3.50	3.08	−0.42
$H_2 + HS$	R	16.76	19.98	3.22
MAE (BH6)				3.92
MSE (BH6)				2.78
MAE (AE6BH6)				35.68

sets as well as an equally weighted average of the MAEs of AE6 and BH6. While the barrier heights turn out to be fairly acceptable, the results for atomization energies are not at all impressive. This shows that ωBT23, which was designed for spectroscopic purposes, is not very reliable for binding properties. Such a "conflict" between reliable atomization energies on the one hand, and reliable eigenvalues on the other hand, is found for many functional classes as discussed in Ref. [18], e. g., optimally tuned range-separated hybrids [19]. Resolving this conflict is the task of ongoing research.

References

[1] Y. J. Franzke et al., J. Chem. Theory Comput. **19**, 6859 (2023).

[2] S. Klawohn and H. Bahmann, J. Chem. Theory Comput. **16**, 953 (2020).

[3] S. Fürst, M. Haasler, R. Grotjahn, and M. Kaupp, J. Chem. Theory Comput. **19**, 488 (2023).

[4] A. D. Becke, J. Chem. Phys. **98**, 5648 (1993).

[5] A. D. Becke, Phys. Rev. A **38**, 3098 (1988).

[6] C. Lee, W. Yang, and R. G. Parr, Phys. Rev. B **37**, 785 (1988).

[7] E. Caldeweyher, S. Ehlert, A. Hansen, H. Neugebauer, S. Spicher, C. Bannwarth, and S. Grimme, J. Chem. Phys. **150**, 154122 (2019).

[8] L. Gallandi, N. Marom, P. Rinke, and T. Körzdörfer, J. Chem. Theory Comput. **12**, 605 (2016).

[9] J. W. Knight, X. Wang, L. Gallandi, O. Dolgounitcheva, X. Ren, J. V. Ortiz, P. Rinke, T. Körzdörfer, and N. Marom, J. Chem. Theory Comput. **12**, 615 (2016).

[10] R. M. Richard, M. S. Marshall, O. Dolgounitcheva, J. V. Ortiz, J.-L. Brédas, N. Marom, and C. D. Sherrill, J. Chem. Theory Comput. **12**, 595 (2016).

[11] T. Körzdörfer, J. S. Sears, C. Sutton, and J.-L. Brédas, J. Chem. Phys. **135**, 204107 (2011).

[12] M. S. Deleuze, L. Claes, E. S. Kryachko, and J.-P. François, J. Chem. Phys. **119**, 3106 (2003).

[13] B. Hajgató, M. S. Deleuze, D. J. Tozer, and F. De Proft, J. Chem. Phys. **129**, 084308 (2008).

[14] S. Fürst and M. Kaupp, J. Chem. Theory Comput. **19**, 3146 (2023).

[15] Russell D. Johnson III, Release 21, 2020, `http://cccbdb.nist.gov/`.

[16] R. Peverati and D. G. Truhlar, Philos. Trans. R. Soc. A: Math. Phys. Eng. Sci. **372**, 20120476 (2014).

[17] B. J. Lynch and D. G. Truhlar, J. Phys. Chem. A **107**, 8996 (2003).

[18] T. Schmidt, E. Kraisler, A. Makmal, L. Kronik, and S. Kümmel, J. Chem. Phys. **140**, 18A510 (2014).

[19] A. Karolewski, L. Kronik, and S. Kümmel, J. Chem. Phys. **138**, 204115 (2013).

Reprint of publication [B5]

Publication [B5]

M. Brütting, H. Bahmann, and S. Kümmel

Combining local range separation and local hybrids: A step in the quest for obtaining good energies and eigenvalues from one functional

J. Phys. Chem. A **128**, 5212 (2024)

DOI: 10.1021/acs.jpca.4c02787

Author contribution statement: M.B. and S.K. conceptualized the work with support from H.B. M.B. wrote the required routines in Turbomole with help from H.B. M.B. did all the calculations, and prepared all the figures and tables. S.K. wrote the first version of the manuscript with support from M.B. All authors discussed the results and the final version of the manuscript.

Note: On finalizing the manuscript of the dissertation, we realized that the definition of $t^2(\mathbf{r})$ in Pub. [B5], between Eqs. (12) and (13) therein, is misprinted. Eq. (5.38) in the dissertation is the correct form, in agreement with the definition of $t^2(\mathbf{r})$ common in the literature [see, e. g., Schmidt *et al.*, J. Chem. Phys. **140**, 18A510 (2014)].

THE JOURNAL OF PHYSICAL CHEMISTRY A
A JOURNAL OF THE AMERICAN CHEMICAL SOCIETY

pubs.acs.org/JPCA Article

Combining Local Range Separation and Local Hybrids: A Step in the Quest for Obtaining Good Energies and Eigenvalues from One Functional

Published as part of The Journal of Physical Chemistry A virtual special issue "Gustavo Scuseria Festschrift".

Moritz Brütting, Hilke Bahmann, and Stephan Kümmel*

Cite This: *J. Phys. Chem. A* 2024, 128, 5212−5223 Read Online

ACCESS | Metrics & More | Article Recommendations | Supporting Information

ABSTRACT: Some of the most successful exchange−correlation approximations in density functional theory are "hybrids", i.e., they rely on combining semilocal density functionals with exact nonlocal Fock exchange. In recent years, two classes of hybrid functionals have emerged as particularly promising: range-separated hybrids on the one hand, and local hybrids on the other hand. These functionals offer the hope to overcome a long-standing "observable dilemma", i.e., the fact that density functionals typically yield either a good description of binding energies, as obtained, e.g., in global and local hybrids, or physically interpretable eigenvalues, as obtained, e.g., in optimally tuned range-separated hybrids. Obtaining both of these characteristics from one and the same functional with the same set of parameters has been a long-standing challenge. We here discuss combining the concepts of local range separation and local hybrids as part of a constraint-guided quest for functionals that overcome the observable dilemma.

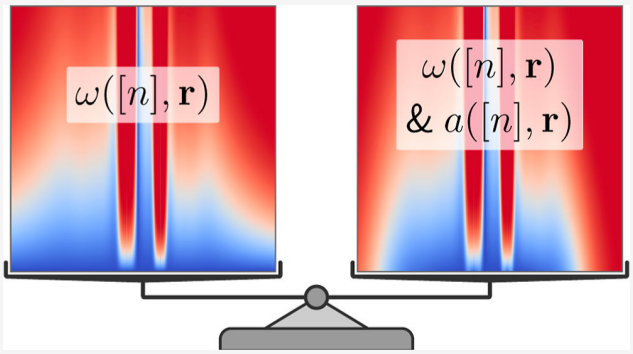

1. INTRODUCTION: HYBRID FUNCTIONALS AND THE OBSERVABLE DILEMMA

Since the idea of hybrid functionals was first proposed,[1] combining semilocal density functional approximations with nonlocal exact Fock exchange has become an extremely successful concept in density functional theory (DFT). Hybrid functionals can be motivated and understood[1,2] in terms of the coupling constant integration,[3,4] which writes the exchange correlation (xc) energy E_{xc} as an integral over the coupling constant λ

$$E_{xc} = \int_0^1 E_{xc,\lambda}\, d\lambda \tag{1}$$

where

$$E_{xc,\lambda} = \langle \psi_\lambda | V_{ee} | \psi_\lambda \rangle - E_H \tag{2}$$

with $|\psi_\lambda\rangle$ being the ground state that minimizes the expectation value of the Hamiltonian $H_\lambda = T + V_\lambda + \lambda V_{ee}$. Here, $V_{ee} = (1/2) \sum_{\substack{i,j=1 \\ i\neq j}}^{N} e^2/|\mathbf{r}_i - \mathbf{r}_j|$ denotes the Coulomb interaction in the N-electron system, E_H is the Hartree energy, and for every value $0 \le \lambda \le 1$ the potential V_λ is chosen such that the ground-state density n_λ that corresponds to $|\psi_\lambda\rangle$ is equal to the ground-state density of the Hamiltonian at full coupling strength $\lambda = 1$. The coupling constant integration leads from the noninteracting Kohn−Sham system ($\lambda = 0$) to the true fully interacting system ($\lambda = 1$) under the assumption that there is an adiabatic connection between the two.

Global hybrids use a constant fraction $0 < a < 1$ of exact exchange in combination with a fraction $1 - a$ of semilocal exchange, and full semilocal correlation. As exchange is related to the $\lambda = 0$ end of the coupling constant integration range,[1] the exchange mixing with a constant a shifts the curve of $E_{xc,\lambda}$ (as a function of λ) by a global constant. Thus, the integral of eq 1 can be brought closer to the exact value of E_{xc}. Apart from the global shift, however, the shape of the $E_{xc,\lambda}$-curve that appears in the coupling-constant integrand stays as determined by the semilocal functional components.[5] Thus, while global hybrid functionals lead to a considerably more accurate description of electronic binding than generalized gradient approximations, as measured by, e.g., atomization energies, other observables are much less improved.

Received: April 29, 2024
Revised: June 3, 2024
Accepted: June 7, 2024
Published: June 21, 2024

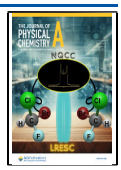

https://doi.org/10.1021/acs.jpca.4c02787
J. Phys. Chem. A 2024, 128, 5212−5223

Particular attention is often paid to the eigenvalues that an xc approximation yields. Here, a careful distinction has to be made. The coupling-constant integration is usually discussed in the context of Kohn−Sham theory. On the other hand, practical calculations with hybrid functionals usually invoke generalized Kohn−Sham theory.[6] While for a given orbital-dependent xc approximation total energies and occupied eigenvalues are typically very similar in Kohn−Sham and generalized Kohn−Sham for systematic reasons,[7,8] the unoccupied eigenvalues in most cases differ substantially: in generalized Kohn−Sham theory, they are usually upshifted in energy with respect to their Kohn−Sham counterparts. The magnitude of this upshift is related to Δ_{xc}, the derivative discontinuity of Kohn−Sham theory.[9]

The highest occupied eigenvalue ε_H has a rigorous meaning in terms of the IP theorem: it corresponds exactly to the negative of the first ionization potential (IP) in both Kohn−Sham[10] and generalized Kohn−Sham theory[11] (for the exact xc functional). Therefore, a hallmark test by which one can check in a nonempirical way whether a given xc approximation yields eigenvalues that one can call "reliable" is the IP theorem, i.e., the fact that the exact functional fulfills the relation

$$\varepsilon_H = E_N - E_{N-1} \tag{3}$$

where E_N denotes the ground-state energy of the N-electron system. Equation 3 therefore, plays a prominent role in the present work.

However, one should furthermore note that also the other eigenvalues are endowed with physical meaning, though only approximately. This has repeatedly been pointed out in the literature. For example, the occupied eigenvalues reflect relaxed IPs,[12] and it has been argued that Kohn−Sham unoccupied−occupied eigenvalue differences can approximate electronic excitation energies.[13,14] In the generalized Kohn−Sham framework, one can choose the noninteracting reference system such that the lowest unoccupied eigenvalue ϵ_L is a good approximation to the electron affinity,[15] and the optimally tuned range-separated hybrids that are discussed below take advantage of this property. For the same reason, generalized Kohn−Sham theory is also attractive in the context of condensed matter physics. For crystalline solids, the eigenvalues form the band structure, and in generalized Kohn−Sham theory, the eigenvalue gap can directly reflect the fundamental gap. This can allow for the efficient prediction of fundamental gaps,[16] which is attractive for computational material design. Finally, the eigenvalues enter the Casida linear-response equations of time-dependent DFT.[17,18] When an xc approximation yields eigenvalues that approximate (the negative of) the IP and the electron affinity, a reliable description of even difficult excitations, e.g., ones of charge-transfer character, can readily be obtained.[19−21] Furthermore, the combination of accurate bond energies and, at the same time, a reliable description of energy levels is needed in simulations in which both electron bonds and charge-transfer processes must be represented accurately. Such situations typically occur, e.g., in energy converting materials, such as light-harvesting complexes or photocatalysts, and are therefore of significant practical interest.

For all of these reasons, it is desirable to have xc approximations that yield accurate binding energies and physically interpretable eigenvalues at the same time. Some progress can be made with correction schemes such as DFT + U,[22] Koopmans-compliant functionals,[23] and the localized orbital scaling correction.[24] Our focus here, however, is on exploring in how far the goal of obtaining reliable atomization energies and reliable eigenvalues can be reached within one usual xc functional, i.e., one that does not rely on additional correction steps. This has been considered a "consistency condition"[25,26] in DFT, and we here focus on whether it can be reached with functionals of the hybrid type.

Global hybrid functionals can hardly reach this aim, as one can see from analyzing their potential. In Kohn−Sham theory, the exact xc potential of a finite system is dominated by x and decays like $-e^2/r$ for large distances from the system's center. In a global hybrid, the constant mixing fraction a directly transfers to the potential and leads to a decay of $-ae^2/r$. For hybrid functionals that are designed to yield good atomization energies, such as B3LYP[27] and PBE0,[28] a takes values of about 0.2 to 0.25.[29] Consequently, the mid- and long-range potential is not binding strongly enough, and ε_H is therefore not negative enough to yield a reasonable approximation to the first IP. The same problem affects all other eigenvalues. While this argument is based on the local Kohn−Sham potential, a similar argument can be made in the context of generalized Kohn−Sham theory.

On the other hand, it has been shown that eigenvalues that are physically interpretable, e.g., as reflecting the fundamental gap, can be achieved from a global hybrid with much larger values of $a \approx 0.75$.[30,31] At such large fractions of exact exchange, however, the usual global hybrid functionals yield a poor description of binding energies. Thus, on the level of global hybrid functionals the observable dilemma leads to a parameter dilemma.[32]

It has been noted early[5,33,34] that the coupling constant integration suggests that the mixing of exact exchange and semilocal exchange should not be determined by a constant a, but by a density functional $a[n]$. Realizing this density dependence might be a way of how to get out of the observable dilemma because by making the mixing coefficient a density functional $a[n]$, one can go beyond just shifting the $E_{xc,\lambda}$ curve by a constant and instead modify the shape of the curve itself.[32,35] This led to the concept of local hybrid functionals, which can be written in the form

$$E_{xc}^{lh}[n] = \int [a(\mathbf{r})\epsilon_x^{ex}[n](\mathbf{r}) + (1 - a(\mathbf{r}))\epsilon_x^{sl}[n](\mathbf{r})]d^3r + E_c^{sl}[n] \tag{4}$$

where we omitted spin indices for clarity of notation. Here, ϵ_x^{ex} and ϵ_x^{sl} define the exact and the semilocal exchange energy density, respectively. The crucial aspect of the local hybrid form is that $a(\mathbf{r})$ is a density functional.

An explicit form for a local hybrid functional was pioneered by Scuseria and co-workers,[36] and local hybrids were further explored by different groups.[32,35,37−41] A local hybrid can fulfill constraints that the global hybrid cannot match, such as taking into account full exact exchange and being one-electron self-interaction free, approximating the high-density limit well and reducing to semilocal exchange in the electron gas limit. Curing many-electron self-interaction is challenging also within the local hybrid form,[42] but many observables can be very well described with local hybrids.[43] The nonuniqueness of the exchange-energy density is a conceptual challenge in the local hybrid form, but calibration functions have been developed to

https://doi.org/10.1021/acs.jpca.4c02787
J. Phys. Chem. A 2024, 128, 5212−5223

reduce this problem.[44] Another challenge lies in the computational realization, which is less straightforward for local than for global hybrids. The seminumerical integration techniques that have been developed in refs 45−47 are a decisive step forward, though, and can bring calculations with local hybrid functionals to a similar level of efficiency as with global hybrids. However, while a lot of progress has thus been made based on the local hybrid form, eq 4 does not ensure that the proper $-e^2/r$ asymptotics of the potential is achieved.[48] Therefore, also the local hybrid form does not resolve the observable dilemma conclusively, which is reflected, e.g., in the fact that typical local hybrids offer only limited improvement in problems of long-range charge transfer.[42,43,49]

A different way of combining exact and semilocal exchange components is realized in range-separated hybrids. They rely on splitting the Coulomb interaction into long- and short-range components, often in the form

$$\frac{1}{|\mathbf{r}-\mathbf{r}'|} = \frac{\mathrm{erf}(\omega|\mathbf{r}-\mathbf{r}'|)}{|\mathbf{r}-\mathbf{r}'|} + \frac{1-\mathrm{erf}(\omega|\mathbf{r}-\mathbf{r}'|)}{|\mathbf{r}-\mathbf{r}'|} \quad (5)$$

Range separation has been pioneered by Savin and coworkers[50,51] and different xc approximations have been derived from this idea. Heyd, Scuseria, and Ernzerhof[52,53] used exact exchange in the short-range and semilocal exchange in the long-range to derive an xc approximation that is very successfully used in particular in solid-state physics for band gap prediction. Many other functionals chose to use exact exchange in the long-range and semilocal exchange in the short-range, or combinations thereof.[54−59] When 100% of exact exchange are used in the long-range, the correct long-range asymptotic potential for finite systems is guaranteed.

A particularly successful way of choosing the range-separation parameter ω nonempirically is optimal tuning.[20] Its central idea is to endow the eigenvalues as good as possible with physical meaning by enforcing the IP theorem, i.e., by choosing ω such that ε_H becomes as close as possible to the IP calculated from total energy differences (see the reviews[15,60,61] for details). As a consequence, optimally tuned functionals allow one to predict fundamental gaps from their eigenvalues and have been demonstrated to reliably predict charge-transfer excitations. Optimal tuning is the paradigm example for xc functional development that focuses on spectroscopic purposes instead of ground-state energetics.

Unfortunately, there is also a parameter dilemma in range-separated hybrids[20] because for almost all systems, the values of ω that yield physically interpretable eigenvalues do not yield good atomization energies and vice versa. This is exemplified by the functional of ref 56, where good energetics require much larger values of ω (e.g., $\omega \approx 0.5a_0^{-1}$[62]) than the ones that one typically finds by optimal tuning (e.g., $\omega \lesssim 0.2a_0^{-1}$[63]). Here, a_0 denotes the atomic unit of length (bohr). A further example for the manifestation of the parameter dilemma in range-separated hybrids is seen in the computation of the linear and nonlinear polarizabilities of conjugated oligomers: the values of the range-separation parameter that result from optimal tuning do not necessarily lead to a reliable prediction of the polarizabilities.[64−66] Furthermore, it has been found that in complex systems, results can depend decisively on the chosen tuning strategy.[67]

Very early, it has been suggested to combine the different hybrid functional concepts,[68] and recently, functionals have been developed that combine the concepts of local hybrids and range separation.[69,70] This is promising because such functionals benefit from the functional flexibility of local exchange mixing via $a[n](\mathbf{r})$, cf. eq 4, while guaranteeing the correct potential asymptotics via ω and eq 5. For the ωLH22t functional of ref 70, which belongs to this functional class, very good accuracy has been demonstrated for many observables, including atomization energies. At the same time, it has been shown that it is accurate for the fundamental gaps of organic semiconductor molecules.[71] However, as discussed in Section 3 below, the consistency between the IPs calculated from total energy differences ("ΔSCF") and $-\varepsilon_H$, and also how closely $-\varepsilon_H$ matches the experimental vertical IP, does not yet generally reach the accuracy that optimally tuned functionals achieve. So, while ωLH22t is, to the best of our knowledge, the functional that presently does best in reducing the observable dilemma, it does not fully eliminate it.

Another approach for combining exact and semilocal exchange components with a spatial dependence governed by a density functional is local range separation, which was pioneered by Krukau, Scuseria, Perdew, and Savin.[72] Recently, this type of xc approximation has found renewed interest[73−76] for at least two reasons. On the one hand, it has become possible to evaluate such functionals self-consistently.[74] On the other hand, it has been demonstrated that locally range-separated hybrids can fulfill important constraints and reach remarkable accuracy for atomization energies and barrier heights.[76] The constraint-guided approach has led to the nonempirical locally range-separated hybrid ωBT23 that avoids any parameter adjustment and is very accurate in predicting the fundamental gap of molecular systems and remedies shortcomings of optimal tuning.[77] However, also local range separation so far did not resolve the observable dilemma: the functional ωBT23 is not accurate for atomization energies, and the functional of ref 76 is accurate for atomization energies and it yields values for $-\varepsilon_H$ that are much closer to vertical IPs than the eigenvalues of semilocal functionals—however, the latter do not reach the accuracy of optimal tuning or of ωBT23.

In this paper, we therefore explore whether the combination of the concepts of the local hybrid and local range separation can further reduce the observable dilemma. In Section 2 we compare two functional forms: the previously developed locally range-separated hybrid from refs 73 and 76, and a new locally range-separated local hybrid that fulfills the same constraints, yet via different functional ingredients. For each of the functionals, we determine the underlying parameters in two different ways: once by an empirical fit to atomization energies and barrier heights, and once in a nonempirical way by minimizing the deviation from the IP theorem, cf. eq 3. In Section 3 we discuss the resulting observables and also compare to other xc approximations, with a particular focus on the observable dilemma. We analyze our results in terms of the local fraction of exchange in Section 4, and we close with conclusions and a summary in Section 5.

2. METHODS: COMBINING LOCAL RANGE SEPARATION AND LOCAL HYBRID EXCHANGE

The functionals that we study make use of exact (ex) and semilocal (sl) exchange by combining the concepts of the local hybrid and the locally range-separated hybrid. They can be written in the general form

https://doi.org/10.1021/acs.jpca.4c02787
J. Phys. Chem. A 2024, 128, 5212−5223

$$E_{xc} = E_x^{lr,ex} + \sum_{\sigma=\uparrow,\downarrow} \int [a(\mathbf{r})\epsilon_{x,\sigma}^{sr,ex} + (1 - a(\mathbf{r}))\epsilon_{x,\sigma}^{sr,sl}] d^3r + E_c^{sl} \quad (6)$$

The long-range (lr) and short-range (sr) superscripts refer to the usual range-separation splitting of eq 5. For E_c^{sl}, we combine the LDA correlation energy density $\epsilon_c^{LDA}[n_\uparrow, n_\downarrow]$ in the parametrization of ref 78 with an iso-orbital indicator-based one-electron self-interaction correction[32,77,79]

$$E_c^{sl} = \int (1 - z\zeta^2)\epsilon_c^{LDA}\, d^3r \quad (7)$$

Here

$$z = \frac{\tau^W}{\tau} = \frac{\hbar^2}{8m}\frac{|\nabla n|^2}{n\tau} \quad (8)$$

$\zeta = (n_\uparrow - n_\downarrow)/n$ and τ denotes the (generalized) Kohn−Sham kinetic energy density. For $\epsilon_{x,\sigma}^{sr,LDA}$, we use the short-range LDA energy density as parametrized in ref 80. The long-range exact exchange is given by $E_x^{lr,ex} = \sum_{\sigma=\uparrow,\downarrow} \int \epsilon_{x,\sigma}^{x,lr}\, d^3r$ with

$$\epsilon_{x,\sigma}^{x,lr} = -\frac{e^2}{2}\sum_{i,j=1}^{N_\sigma} \int \varphi_{i,\sigma}^*(\mathbf{r})\varphi_{i,\sigma}(\mathbf{r}')\varphi_{j,\sigma}^*(\mathbf{r}')\varphi_{j,\sigma}(\mathbf{r}) \frac{\mathrm{erf}(\omega_\sigma(\mathbf{r})|\mathbf{r} - \mathbf{r}'|)}{|\mathbf{r} - \mathbf{r}'|} d^3r' \quad (9)$$

and $\epsilon_{x,\sigma}^{sr,ex}$ is its 1 − erf counterpart.

Within this general form, one of the functionals that we study is the one from refs 73 and 76 (called SICω-LDA in ref 76, but in the following denoted ωBT21 for brevity), which is defined by

$$a(\mathbf{r}) = 0 \quad (10)$$

and

$$\omega_\sigma(\mathbf{r}) = c_G\frac{|\nabla n_\sigma|}{n_\sigma}\left(1 + \ln\left(c_{HDL}a_0c_G\frac{|\nabla n_\sigma|}{n_\sigma}\right)\right)\frac{1}{1 - z_\sigma\zeta^2} \quad (11)$$

where $z_\sigma = \frac{\hbar^2}{8m}\frac{|\nabla n_\sigma|^2}{n_\sigma\tau_\sigma}$ denotes the equivalent of eq 8 within the spin channel σ.

A second, new functional form that we study (denoted ωBT21a in the following) is defined by

$$a(\mathbf{r}) = 1 - \frac{1}{1 + c_{HDL}^a t^2} \quad (12)$$

where $t^2 = (\pi/3)^{1/3}\frac{a_0}{[4((1+\zeta)^{2/3} + (1-\zeta)^{2/3})]^2}\frac{|\nabla n|^2}{n^{7/3}}$ and

$$\omega_\sigma(\mathbf{r}) = c_G^a\frac{|\nabla n_\sigma|}{n_\sigma}\frac{1}{1 - z_\sigma\zeta^2} \quad (13)$$

The functional $a(\mathbf{r})$ implicitly carries a spin dependence via the spin-dependence of the reduced gradient t.

Both of these functionals fulfill important exact constraints. First, they reduce to LDA in the homogeneous electron gas limit, as both $\omega_\sigma(\mathbf{r})$ and $a(\mathbf{r})$ go to zero in this limit. Second, in the limit $z_\sigma = 1$ and $\zeta = 1$, $\omega_\sigma(\mathbf{r})$ tends to infinity. For $\omega_\sigma(\mathbf{r}) \to \infty$, full exact exchange is used in spin channel σ. Thus, for one electron systems that are characterized by full spin polarization and just one orbital, this condition together with eq 7 guarantees being one-electron self-interaction free.

Another formal constraint is the second-order gradient expansion for exchange. The choice $\omega_\sigma \propto |\nabla n_\sigma|/n_\sigma$ corresponds to the functional form that is suggested by the gradient expansion.[75,76] Here, we treat the prefactor (c_G or c_G^a, respectively) as a free parameter. We note, however, that the optimizations that we describe below yield values that are of similar magnitude as the nonempirical value $\sqrt{5}/18 \approx 0.124 \ldots a_0^{-1}$ that the gradient expansion suggests.

Finally, both functionals contain elements that have been devised in view of the high-density limit as defined via uniform coordinate scaling, $n(\mathbf{r}) \to n_\lambda(\mathbf{r}) = \lambda^3 n(\lambda\mathbf{r})$ with $\lambda \to \infty$. Krukau, Scuseria, Perdew, and Savin pointed out[72] that locally range-separated hybrids can fulfill the condition

$$\lim_{\lambda\to\infty} E_{xc}[n_\lambda]/E_x^x[n_\lambda] = 1 \quad (14)$$

whereas a constant range-separation parameter does not. They further discussed that the (in their case spin-independent) choice $\omega(\mathbf{r}) = |\nabla n|/n$ scales like $\lambda\omega(\lambda\mathbf{r})$. Fulfilling eq 14 fully would require that $\omega(\mathbf{r})$ scales up faster than $\lambda\omega(\lambda\mathbf{r})$. Thus, the $\omega(\mathbf{r})$ of Krukau is close to the proper behavior. In eq 11, these considerations have been taken one step further. By adding the ln(···)-term, the range-separation parameter has been made to scale up faster while else changing very little. Adding this term adds another parameter c_{HDL} that is left undetermined by the constraints and, therefore, has to be fixed in other ways, as discussed below. In line with the reasoning that motivated the ln-term, its influence on binding energies is relatively small.[76] Therefore, the construction of ωBT21a takes a different approach at the high-density limit. The local hybrid term of eq 12 exploits that t^2 scales like λ. Thus, in the high-density limit $a(\mathbf{r}) \to 1$ and the functional goes to full exact exchange independent of the specific value of ω that is used in the range separation.

So in summary, ωBT21 is a pure locally range separated hybrid, while ωBT21a is a locally range-separated local hybrid. These functionals on the one hand differ in how they approach the high density limit. On the other hand, the second, potentially yet more important, difference is that while ωBT21 uses exact exchange only in the long-range, ωBT21a allows exact exchange in both long- and short-range. It is in particular this latter difference, which we are interested in the context of the observable dilemma.

For each of the two functionals, we determined two sets of values for the free parameters c_{HDL}, c_G, and c_{HDL}^a, c_G^a, respectively. On the one hand, we chose them empirically such that the combined errors for a small test set of six atomization energies (AE6) and six reaction barrier heights (BH6)[81] were minimized. We consider these the "energy optimal" versions of the functionals and in the following refer to these versions by ωBT21 and ωBT21a, respectively.

On the other hand, in a second, alternative approach, we chose the parameters nonempirically such that the difference between the IP as calculated from a ΔSCF procedure and $-\varepsilon_H$ is minimized. This way of choosing the parameters guarantees that the functionals fulfill the internal consistency condition of the IP theorem, cf. eq 3. This choice should also guarantee that

https://doi.org/10.1021/acs.jpca.4c02787
J. Phys. Chem. A 2024, 128, 5212−5223

the total energy as a function of the electron number will approximate a straight line.[82] We consider these second functionals the "IP optimal" versions and denote them by ωBT21-IP and ωBT21a-IP, respectively. For simplicity, we here do the minimization for the molecules in the AE6 test set, but as discussed in the Supporting Information, the test on the IP theorem consistency can easily be extended to other systems. The details of how the optimizations were done numerically are given in the Supporting Information, Section S1. Table 1 lists the parameters for the different versions of the functionals. The parameters listed for ωBT21 are identical to the ones determined in ref 76.

Table 1. Functional Parameters as Obtained from the Minimizations Described in the Main Text

parameter	ωBT21	ωBT21-IP
c_G	0.115	0.220
c_{HDL}	0.202	0.225
parameter	ωBT21a	ωBT21a-IP
c_G^a	0.120	0.190
c_{HDL}^a	0.068	1.379

3. RESULTS

Before looking at detailed results, some trends can already be discussed by just looking at Table 1, i.e., at the parameters that result from the different optimizations. We start by looking at ωBT21, i.e., the upper half of the table, because having only the local range separation and no local hybrid component simplifies the analysis. Comparing ωBT21 to ωBT21-IP shows that having the functional to obey (on average across the test set) the IP theorem requires a more than 90% increase in c_G. There is a plausible explanation for this observation: a larger value of c_G leads to a value of ω that is larger on average. As a consequence, when starting to go outward from a finite system's center, the amount of exact exchange increases earlier. This will make the potential more attractive in the region of space in which ε_H is mostly determined and that apparently is required to lower ε_H enough to make it agree with the IP. Similarly, c_{HDL} increases by 11%. The change in c_{HDL} thus also goes into the direction of increasing ω. However, as c_{HDL} mostly (only) affects the high-density regions, which are close to the atomic cores, whereas ε_H is determined by much more distant regions, the value of c_{HDL} changes rather little when the optimization is shifted from the energies to the IP theorem. Comparing the parameters that are obtained for ωBT21 and ωBT21-IP thus clearly shows the cause of the observable dilemma: having the eigenvalue reflect the IP requires on average larger amounts of (long-range) exact exchange than needed for a good description of atomization energies and barrier heights. Qualitatively, the situation seems to be similar to the one discussed for the global hybrids in Section 1.

This finding suggests that the more general ansatz of also allowing for exact exchange in the short-range in the form of the local hybrid term may alleviate the parameter dilemma because the presence of short-range exchange may lead to an overall more attractive potential and thus more strongly bound eigenvalues without requiring larger (on average) values of ω. In other words, having both long- and short-range exact exchange in the functional may be beneficial for solving the parameter dilemma because the burden of having to fulfill the IP theorem is not only on the range-separation parameter ω alone.

Comparing the parameter values that Table 1 shows for ωBT21a to the ones of ωBT21 reveals that in terms of atomization energies and barrier heights, the local hybrid term does not seem to add much to the functional: the range-separation prefactor is similar in both functionals, and the high-density limit parameter that is obtained for ωBT21a in the empirical energy-driven optimization is quite small. According to eq 12, this indicates that also $a(\mathbf{r})$ is overall small. This shows that the local range separation alone already captures the decisive physics of the AE6 and BH6 optimization, and little is to be gained here from adding the local hybrid term. Comparing the nonempirical variants that are optimized for the IP theorem, i.e., the values in the second column of Table 1 for ωBT21-IP and ωBT21a-IP, shows larger differences: the range-separation factor c_G^a = 0.190 of ωBT21a-IP is smaller than the 0.220 one of ωBT21-IP, which is the right direction for having better energetics. Furthermore, by going from ωBT21a to ωBT21a-IP, the value of c_G^a increases by only about 50%, which is less than the 90% increase that was seen without the local hybrid component.

We, therefore, now look at the first set of detailed results, as presented in Table 2. It shows the atomization energies of the AE6 set and the barrier heights obtained for the BH6 set, computed with nine different xc approximations. The upper half of the table from left to right shows the atomization energies as obtained with Hartree−Fock (HF) theory, the PBE-GGA,[83] and the combination of the two in the PBE0-hybrid.[28] We show these numbers as a reminder of what accuracy is reached on the pure exchange and purely semilocal scale, respectively, and which accuracy can be expected from a nonfitted global hybrid that combines these components. The next column shows the results obtained with the MN15 global hybrid functional[84,85] as an example for which accuracy can be reached with a global hybrid in a very empirical multiparameter fit. The rightmost column finally shows the numbers for ωLH22t[70] as an example for one of the most recent advanced functionals that combines global range separation with the local hybrid concept. The lower half of the table presents the results for our functionals: from left to right it shows the results that we found for ωBT21 and ωBT21a with the energy optimal parameters, and then the results for the respective IP theorem-optimized versions of these two functionals.

A somewhat mixed picture emerges from these results. On the very positive side, it shows that the energy-optimized functionals with local range separation reach an accuracy that is comparable to the one that is reached by MN15 and ωLH22t, despite the fact that only two free parameters have been adjusted, i.e., with noticeably fewer parameters than in the other functionals. Table 3 (detailed data in the Supporting Information) confirms this general picture for a larger database. One can interpret this as a sign that the functional form contains elements that are in itself appropriate and therefore do not require many parameters.

On the other hand, it is somewhat surprising to see that ωBT21 is more accurate than ωBT21a. One might argue that in terms of conceptual "hybrid complexity", the two variants of ωBT21a are the most advanced functionals in the table because both their (long-range) range-separation ω and their (short-range) multiplicative hybrid factor a have a spatial dependence. However, adding the local hybrid component, at least in the form that we used here, does not seem to add new

https://doi.org/10.1021/acs.jpca.4c02787
J. Phys. Chem. A 2024, 128, 5212−5223

Table 2. Atomization Energies of the AE6 Test Set and Reaction Barrier Heights of the BH6 Test Set[a]

		ref.	HF	PBE	PBE0	MN15	ωLH22t
SiH_4		324.95	−70.73	−12.68	−11.06	1.25	−2.71
SiO		193.06	−86.01	0.63	−13.14	−1.27	−5.68
S_2		104.25	−55.27	8.43	0.18	−1.85	−0.33
C_3H_4		705.06	−181.48	15.99	2.45	−1.92	−0.34
$C_2H_2O_2$		633.99	−213.33	29.39	0.84	1.23	0.66
C_4H_8		1149.37	−279.84	18.79	7.23	−2.28	4.48
MAE (AE6)			147.78	14.32	5.82	1.63	2.37
MSE (AE6)			−147.78	10.09	−2.25	−0.81	−0.65
$OH + CH_4 \rightarrow CH_3 + H_2O$	*F*	6.50	20.00	−11.70	−4.41	−0.60	−1.81
	R	19.60	8.21	−12.21	−6.85	−2.17	−4.41
$H + OH \rightarrow O + H_2$	*F*	10.50	6.49	−7.50	−3.98	−0.98	−1.43
	R	12.87	20.21	−13.44	−6.32	−1.19	−0.68
$H + H_2S \rightarrow H_2 + HS$	*F*	3.50	8.22	−4.78	−2.49	0.54	0.16
	R	16.76	10.78	−6.83	−3.90	0.05	1.35
MAE (BH6)			12.32	9.41	4.66	0.92	1.64
MSE (BH6)			12.32	−9.41	−4.66	−0.72	−1.14
MAE (AE6BH6)			80.05	11.86	5.24	1.28	2.00

			local range separation			
		ref.	ωBT21	ωBT21a	ωBT21-IP	ωBT21a-IP
SiH_4		324.95	−0.82	3.28	37.48	51.04
SiO		193.06	−5.85	−5.80	−31.80	−23.70
S_2		104.25	2.66	1.81	−18.05	−15.52
C_3H_4		705.06	0.20	1.37	−11.35	16.63
$C_2H_2O_2$		633.99	−0.08	0.15	−58.39	−33.83
C_4H_8		1149.37	1.00	4.30	6.30	49.87
MAE (AE6)			1.77	2.78	27.23	31.76
MSE (AE6)			−0.48	0.85	−12.64	7.42
$OH + CH_4 \rightarrow CH_3 + H_2O$	*F*	6.50	−3.31	−2.12	10.88	11.84
	R	19.60	−4.54	−4.02	3.48	3.70
$H + OH \rightarrow O + H_2$	*F*	10.50	−2.67	−2.50	−7.00	−5.26
	R	12.87	−0.58	0.52	15.44	15.82
$H + H_2S \rightarrow H_2 + HS$	*F*	3.50	−0.35	−0.43	−2.47	−2.13
	R	16.76	−0.03	1.76	15.36	17.11
MAE (BH6)			1.91	1.89	9.11	9.31
MSE (BH6)			−1.91	−1.13	5.95	6.85
MAE (AE6BH6)			1.84	2.34	18.17	20.54

[a]The numbers (in kcal/mol) correspond to the difference of the calculated values to the reference values from the Minnesota database 2.0. MAE and MSE refer to the mean absolute error and the mean signed error. See the main text for discussion and further details.

Table 3. Errors in the Atomization Energies of the MGAE109 Test Set[a]

functional	MAE	MSE
HF	146.70	−146.70
PBE	14.53	12.64
PBE0	5.01	−0.64
MN15	2.90	−0.01
ωLH22t	2.57	0.03
ωBT21	2.74	−0.46
ωBT21a	4.06	0.47
ωBT21-IP	28.96	−18.01
ωBT21a-IP	31.15	1.41

[a]All numbers are in kcal/mol. The detailed data are given in Table S1 in the Supporting Information.

flexibility that would increase the accuracy for the tested energetics.

Therefore, we next turn to Table 4, which shows how well the IP theorem is fulfilled for the same set of functionals. Plain HF, which was by far worst in the AE6 and BH6 test, fares much better for the IP theorem than PBE, PBE0, and MN15. This is the paradigm example of the observable dilemma. Only the functionals with range separation fulfill the IP theorem better than HF. This underlines the importance of range separation. The functional ωBT21-IP fulfills the IP theorem very consistently with a very small error. It is noteworthy that although its parameters have only been optimized for the average of the test set, ωBT21-IP reaches an accuracy that can compete with optimally tuned range-separated hybrids, where the parameters need to be adjusted anew for each system individually. Table 5 confirms these trends for a larger database of molecules. This finding is in line with the findings of ref 77, which showed that local range separation even in a completely nonempirical form can reach higher accuracy than optimal tuning.

However, we again note that somewhat surprisingly, addition of the local hybrid term does not increase the accuracy over the level that already has been reached with local range separation alone: also for the IP theorem, ωBT21-IP is somewhat more accurate than ωBT21-IPa, and the only improvement that we obtain from adding the local hybrid

https://doi.org/10.1021/acs.jpca.4c02787
J. Phys. Chem. A 2024, 128, 5212−5223

Table 4. Deviation from the IP Theorem for the Molecules in the AE6 Test Set[a]

		HF			PBE			PBE0	
SiH_4	11.97	13.24	1.27	12.15	8.53	−3.62	12.45	9.88	−2.57
SiO	10.40	11.90	1.51	11.30	7.47	−3.83	11.41	8.83	−2.58
S_2	9.53	10.39	0.86	9.48	5.83	−3.64	9.72	7.13	−2.58
C_3H_4	8.97	10.47	1.50	10.24	6.52	−3.72	10.24	7.74	−2.50
$C_2H_2O_2$	10.63	12.01	1.37	9.96	6.32	−3.63	10.41	7.91	−2.49
C_4H_8	10.37	11.83	1.46	10.55	7.22	−3.32	11.03	8.56	−2.46
MAE			1.33			3.63			2.53
MSE			1.33			−3.63			−2.53
								local range separation	
		MN15			ωLH22t			ωBT21	
SiH_4	12.68	10.61	−2.07	12.78	12.52	−0.26	12.55	11.24	−1.31
SiO	11.52	9.53	−2.00	11.57	11.09	−0.47	11.66	10.45	−1.21
S_2	9.70	7.68	−2.02	9.73	9.22	−0.51	9.57	8.36	−1.20
C_3H_4	10.33	8.46	−1.87	10.37	9.95	−0.41	10.36	9.29	−1.07
$C_2H_2O_2$	10.71	8.82	−1.89	10.73	10.30	−0.43	10.59	9.73	−0.86
C_4H_8	10.87	9.28	−1.59	10.82	10.64	−0.19	10.78	9.76	−1.01
MAE			1.91			0.38			1.11
MSE			−1.91			−0.38			−1.11
					local range separation				
		ωBT21a			ωBT21-IP			ωBT21a-IP	
SiH_4	12.61	11.34	−1.27	13.19	12.82	−0.37	13.41	13.08	−0.34
SiO	11.67	10.50	−1.17	11.79	11.70	−0.08	11.92	11.92	0.00
S_2	9.56	8.41	−1.16	9.91	9.65	−0.26	10.03	9.80	−0.23
C_3H_4	10.37	9.34	−1.03	10.36	10.49	0.14	10.50	10.65	0.15
$C_2H_2O_2$	10.61	9.78	−0.83	11.18	11.28	0.10	11.50	11.65	0.15
C_4H_8	10.79	9.81	−0.98	11.05	11.05	0.00	12.12	11.24	−0.88
MAE			1.07			0.16			0.29
MSE			−1.07			−0.08			−0.19

[a]For each functional and molecule, the first column shows the IP as calculated from a total energy difference ($E_{N-1} - E_N$, i.e., "ΔSCF calculation"), the second column the negative of the HOMO eigenvalue, and the third column their difference. All values are in eV.

Table 5. Deviation from the IP Theorem Evaluated as in Table 4 for a Larger Set of Molecules[a]

functional	MAE	MSE
HF	1.72	1.38
PBE	4.47	−4.47
PBE0	3.04	−3.04
MN15	2.37	−2.37
ωLH22t	0.74	−0.74
ωBT21	1.38	−1.38
ωBT21a	1.33	−1.33
ωBT21-IP	0.36	−0.03
ωBT21a-IP	0.43	0.04

[a]All numbers are in eV. The detailed data are given in Table S2 in the Supporting Information.

component is that ωBT21a does slightly better for the IP theorem than ωBT21. Furthermore, we see and have to accept the unpleasant result that the combination of local range separation and local hybrid in the form that we presently explored does not help to reduce the parameter dilemma beyond the level that is reached with local range separation alone: local range separation allows one to build functionals that are very accurate for energetics, and it allows one to build functionals that fulfill the IP theorem very closely, but we do not reach very high accuracy for both with the same set of parameters. However, one should also note that the concept of combining exact exchange with (semi)local functional components in a spatially dependent way, either via local range separation (ωBT21) or via global range separation combined with a local hybrid (ωLH22t) does considerably reduce the observable dilemma when one compares to global hybrids: Tables 4 and 5 show that compared to the global hybrids, the deviation from the IP theorem can be reduced by a factor of ca. two to three.[86] However, the additional flexibility that our local hybrid term in principle adds to the locally range-separated functional does not translate to a higher accuracy in practice. This finding calls for an explanation.

4. DISCUSSION: ANALYZING THE LOCAL FRACTION OF EXCHANGE

In order to understand why adding the local hybrid term does not lead to qualitatively different results despite the resulting greater flexibility in the spatially resolved combination of exact exchange and semilocal functional components, we investigate the local fraction of exact exchange. In the locally range-separated local hybrid form, the Coulomb interaction is separated according to

$$\frac{1}{|\mathbf{r}-\mathbf{r}'|} = \frac{\mathrm{erf}(\omega_\sigma(\mathbf{r})|\mathbf{r}-\mathbf{r}'|)}{|\mathbf{r}-\mathbf{r}'|} + a(\mathbf{r})\frac{1-\mathrm{erf}(\omega_\sigma(\mathbf{r})|\mathbf{r}-\mathbf{r}'|)}{|\mathbf{r}-\mathbf{r}'|} + [1-a(\mathbf{r})]\frac{1-\mathrm{erf}(\omega_\sigma(\mathbf{r})|\mathbf{r}-\mathbf{r}'|)}{|\mathbf{r}-\mathbf{r}'|} \quad (15)$$

The last term on the right-hand side is taken into account via the (semi)local functional components, whereas the first two

https://doi.org/10.1021/acs.jpca.4c02787
J. Phys. Chem. A 2024, 128, 5212−5223

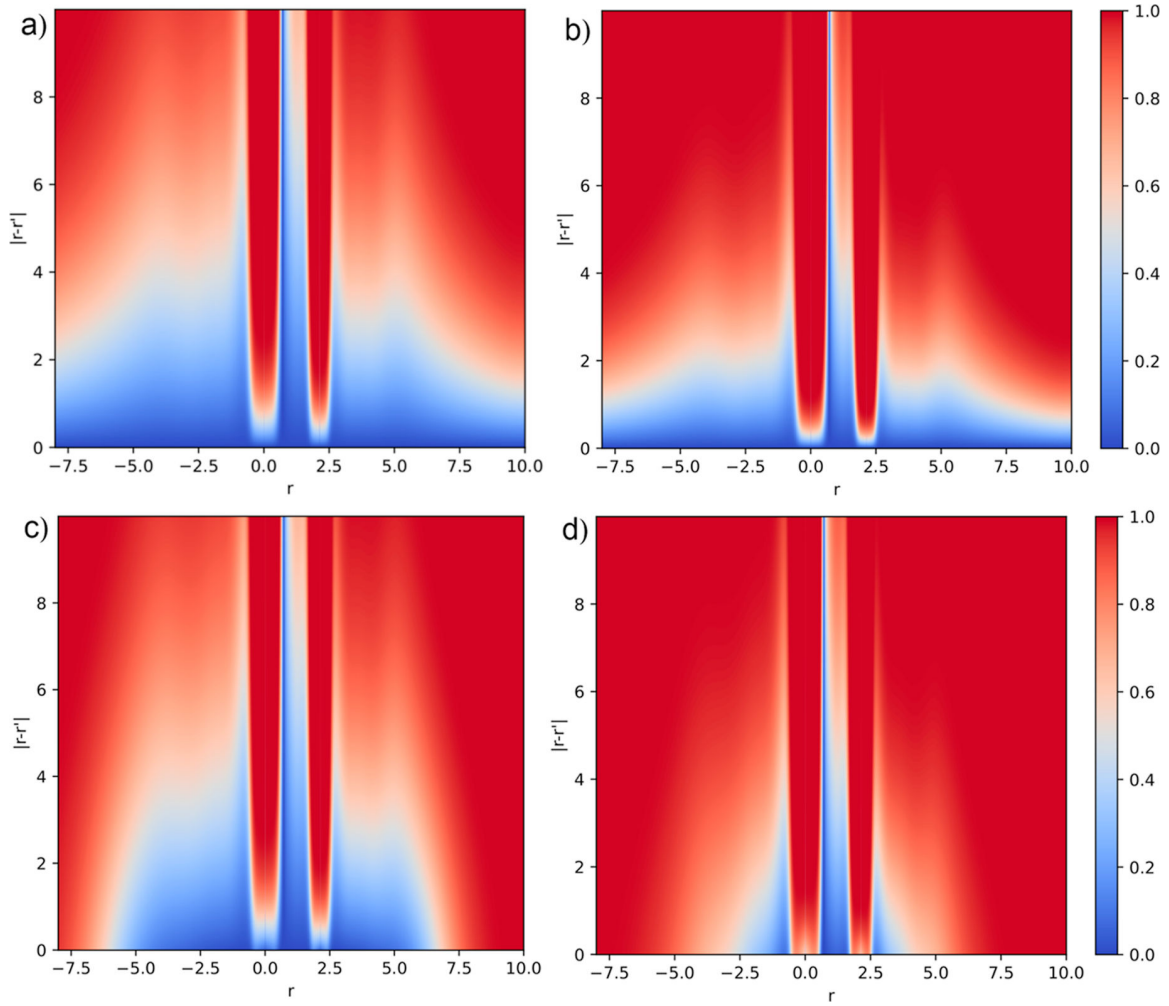

Figure 1. Plots of the fraction of exact exchange, cf. eq 16, for (a) ωBT21, (b) ωBT21-IP, (c) ωBT21a, and (d) ωBT21a-IP, for the CO molecule, color-coded as a function of the distance from the center of the coordinate system r along the bonding axis (C atom at 0.000, O atom at 2.132), and the relative distance $|\mathbf{r} - \mathbf{r}'|$ (in a_0). See the main text for discussion. There is no difference between the two spin channels for the CO molecule.

terms are represented using exact exchange. Therefore, it is natural to define

$$f_\sigma^{\mathrm{EXX}}(\mathbf{r},|\mathbf{r}-\mathbf{r}'|) := \mathrm{erf}(\omega_\sigma(\mathbf{r})|\mathbf{r}-\mathbf{r}'|) + a(\mathbf{r})[1 - \mathrm{erf}(\omega_\sigma(\mathbf{r})|\mathbf{r}-\mathbf{r}'|)] \quad (16)$$

as the spatially resolved local fraction of exact exchange for our functionals. Figure 1 shows this fraction for the CO molecule for all four variants of our functionals: the upper two panels depict the fraction of exact exchange for ωBT21 and ωBT21-IP, i.e., without the local hybrid component, and the lower two panels depict it for the functionals ωBT21a and ωBT21a-IP, i.e., with the local hybrid component. There is no difference between the two spin channels for CO; therefore, it is sufficient to look at just one of them.

The distance r from the center of the coordinate system along the bond axis serves as the x-axis, and the relative distance $|\mathbf{r} - \mathbf{r}'|$ as the y-axis. First comparing panels (a), i.e., the locally range-separated hybrid without short-range exact exchange evaluated with the energy-optimized parameters, to panel (b), i.e., the same functional form but evaluated with the IP-optimized parameters, visually demonstrates that the main difference is that the IP-optimized functional goes more rapidly toward full exact exchange (full red color) with increasing values of $|\mathbf{r} - \mathbf{r}'|$. Within the core regions, which are visible as the red vertical lines around the nuclear positions at $r = 0$ and $r = 2.132$ a_0, both functional variants are dominated by exact exchange except for very small values of $|\mathbf{r} - \mathbf{r}'|$. Comparing panels (a) and (c) shows that adding the local hybrid component changes the spatial distribution of exact exchange noticeably: with the local hybrid [panel (c)], full exact exchange is reached for values of r larger than ca. 6 a_0 independent of the value of $|\mathbf{r} - \mathbf{r}'|$. The IP theorem-optimized version of the locally range-separated local hybrid [panel (d)] uses exact exchange in most regions, with semilocal contributions only in those regions of space that are relatively close to the nuclei yet outside of the nuclear cores.

The figure thus shows that adding the local hybrid term does change the spatial distribution of the exact exchange noticeably, as one might expect, and its minor influence on the results therefore appears yet more as a puzzle. The explanation for its little influence emerges from Figure 2. It shows the density weighted fraction of exact exchange, i.e., $n(\mathbf{r})$ $f_\sigma^{\mathrm{EXX}}(\mathbf{r},|\mathbf{r} - \mathbf{r}'|)$ in the same ordering and fashion as used in Figure 1. Comparing panels (a) and (c) shows that density weighted, there is hardly any difference between the

https://doi.org/10.1021/acs.jpca.4c02787
J. Phys. Chem. A 2024, 128, 5212−5223

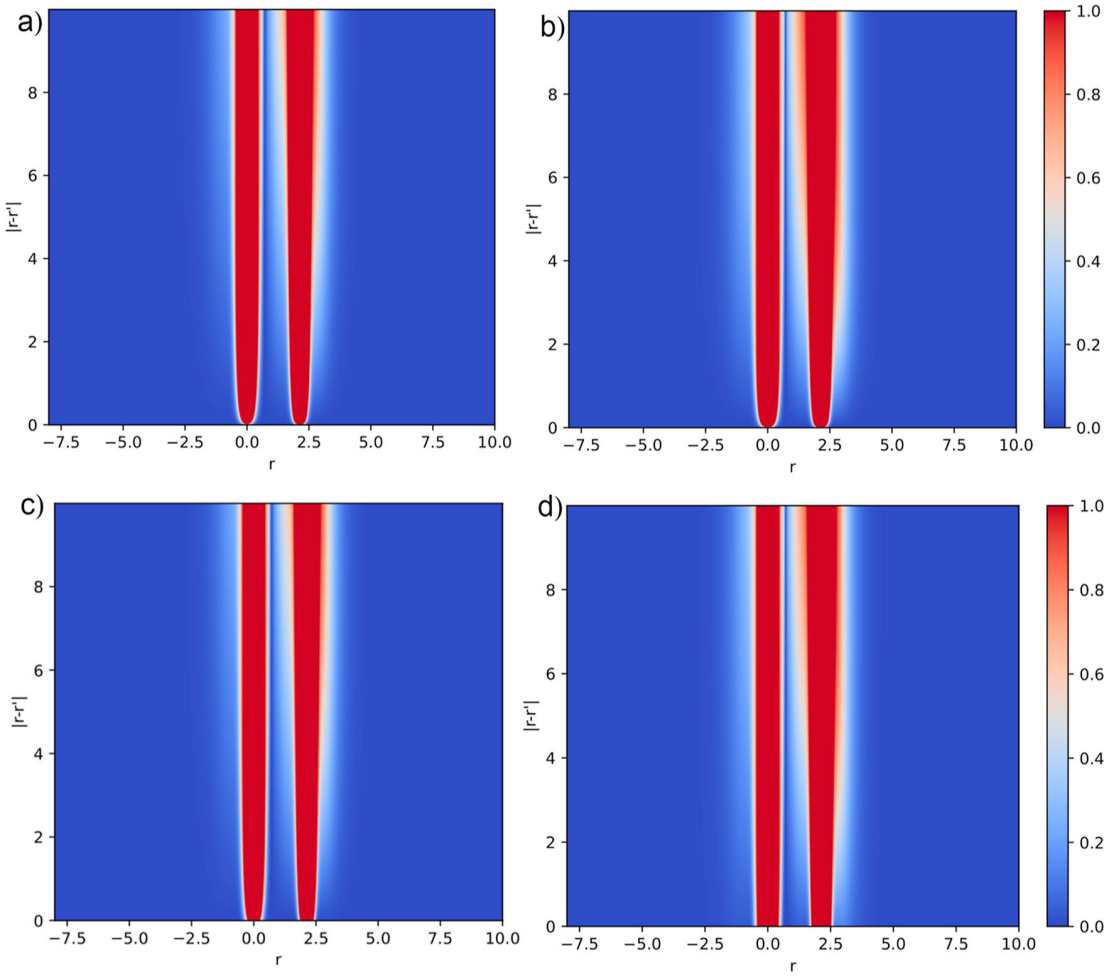

Figure 2. Plots of the density-weighted fraction of exact exchange for (a) ωBT21, (b) ωBT21-IP, (c) ωBT21a, and (d) ωBT21a-IP, for the CO molecule, color-coded as a function of the distance from the center of the coordinate system r along the bonding axis (C atom at 0.000, O atom at 2.132), and the relative distance $|\mathbf{r} - \mathbf{r}'|$ (in a_0). See main text for discussion. We note that $n(\mathbf{r})f_\sigma^{\mathrm{EXX}}(\mathbf{r},|\mathbf{r} - \mathbf{r}'|)$ takes values larger than 1 in the core regions. Since we are interested not in the core regions, but in those regions that are relevant for electron bonds and the IP, the plot displays all values larger than 1 in the same color.

distributions. For ωBT21a, we observe larger fractions of exact exchange close to the nuclei for both the energy optimized- [panel (c)] and the IP-optimized (panel (d)) variant. This difference, however, will hardly affect the observables that we looked at such as atomization energies and the IP. The differences that are seen between the energy-optimized functionals and their IP-optimized counterparts, e.g., by comparing panels (a) and (b) of Figure 2, are also less pronounced than the differences seen in Figure 1a,b, but yet clearly visible, with a broader region of exact exchange seen in the IP-optimized functionals.

5. SUMMARY AND CONCLUSIONS

We discussed different types of hybrid functionals from the perspective of two different properties that are often required from xc approximations in DFT: on the one hand, one would like reliable energetics as measured, e.g., by atomization energies, and on the other hand, one would like the highest occupied eigenvalue to reflect the IP. The large majority of conventional explicit xc approximations can yield one of these properties but not the other. Hybrid functionals that make use of range separation in the Coulomb interaction can reduce this dilemma.

We here studied the combination of local, density-dependent range separation with locally resolved short-range exchange in the local hybrid form. Our functional design was guided by the aim to fulfill important exact constraints. For both a locally range-separated hybrid ansatz and for a locally range-separated local hybrid ansatz, we determined the two free parameters that we could not fix via constraints in two different ways: in a first, conventional empirical approach, we fitted them to atomization energies and barrier heights. In a second, less conventional and nonempirical approach that does not require external reference data, we determined the parameters such that the deviation from the IP theorem is minimized, i.e., we ensured an internal consistency condition.

Our functionals allow one to reach high accuracy for atomization energies and barrier heights, and they also allow one to eliminate the deviation from the IP theorem to a very high degree—but different parameters are needed for the different tasks. Somewhat surprisingly, we found that adding the local hybrid component to the local range separation did not have a profound influence on the observables that we studied. Analyzing the spatially resolved local fraction of exact exchange shed light on these observations: in our functional construction, the local hybrid component as expected has a

https://doi.org/10.1021/acs.jpca.4c02787
J. Phys. Chem. A 2024, 128, 5212−5223

noticeable influence on the spatial distribution of the mixing of exact exchange and semilocal components. However, the differences between the locally range-separated hybrid and the locally range-separated local hybrid are large only in regions of space where the density is low, or close to the nuclei. None of these regions are very important for the observables that we studied here.

The good results that we found on the one hand for our own locally range-separated functional ωBT21, but on the other hand, also for the local hybrid with global range separation functional ωLH22t, indicate that different forms of "locally resolved" hybrids can be successful. In comparison to simpler functional forms, such as GGAs or global hybrids, both allow us to considerably reduce the observable dilemma. A conclusion that we draw for our own functional forms is that invoking the high-density limit as the guiding constraint for the local hybrid component is not ideal, and it seems advisible to have the local hybrid component guided by other constraints. Improving the accuracy for energetics further may also require to go beyond the local density approximation for the short-range components, and combining the concepts of range-separation with recently developed new approaches that improve band gaps and electrical response properties[79,87] appears as an attractive option. Such steps then may necessitate to also involve a calibration function. Future work will follow these lines and might also profit from the insights that we recently gained with the ωBT23 functional[77] about approximating the straight line condition nonempirically. Furthermore, it will be interesting to check whether these approaches improve the description of hallmark tests, such as the prediction of the polarizabilities of conjugated systems,[64,65] and other tests, such as the ones reported in the Supporting Information.[88−91] The present results in any case underline the promise that local exchange mixing holds for building improved functionals that aim to overcome the observable dilemma.

■ ASSOCIATED CONTENT

Supporting Information

The Supporting Information is available free of charge at https://pubs.acs.org/doi/10.1021/acs.jpca.4c02787.[88−91]

Description of the numerical optimization of the functional parameters; information about numerical settings used; tables with the detailed data that underlies the summarizing tables in the main article; and author contribution statement (PDF)

■ AUTHOR INFORMATION

Corresponding Author

Stephan Kümmel − *Theoretical Physics IV, University of Bayreuth, 95440 Bayreuth, Germany;* orcid.org/0000-0001-5914-6635; Phone: +49 (0)921 553220; Email: stephan.kuemmel@uni-bayreuth.de; Fax: +49 (0) 921 553223

Authors

Moritz Brütting − *Theoretical Physics IV, University of Bayreuth, 95440 Bayreuth, Germany;* orcid.org/0000-0002-1021-0007

Hilke Bahmann − *Physical and Theoretical Chemistry, University of Wuppertal, 42097 Wuppertal, Germany*

Complete contact information is available at: https://pubs.acs.org/10.1021/acs.jpca.4c02787

Notes

The authors declare no competing financial interest.

■ ACKNOWLEDGMENTS

S.K. acknowledges financial support from the Deutsche Forschungsgemeinschaft (DFG, German Research Foundation) project 457582427 and from the Bavarian State Ministry of Science, Research, and the Arts for the Collaborative Research Network "Solar Technologies go Hybrid". M.B. and S.K. acknowledge support from the Elite Study Program "Biological Physics" of the Elite Network of Bavaria. M.B. further acknowledges support by the "Studienstiftung des Deutschen Volkes". H.B. acknowledges funding from the DFG, project 418140043.

■ REFERENCES

(1) Becke, A. D. Density-functional thermochemistry. III. The role of exact exchange. *J. Chem. Phys.* **1993**, *98*, 5648−5652.

(2) Becke, A. D. A new mixing of Hartree−Fock and local density-functional theories. *J. Chem. Phys.* **1993**, *98*, 1372−1377.

(3) Harris, J.; Jones, R. O. The surface energy of a bounded electron gas. *J. Phys. F: Met. Phys.* **1974**, *4*, 1170−1186.

(4) Perdew, J. P.; Kurth, S. Density functionals for non-relativistic coulomb systems in the new century. *A Primer in Density Functional Theory*; Springer, Berlin, Heidelberg, 2003; pp 1−55.

(5) Ernzerhof, M.; Perdew, J. P.; Burke, K. Coupling-constant dependence of atomization energies. *Int. J. Quantum Chem.* **1997**, *64*, 285−295.

(6) Seidl, A.; Görling, A.; Vogl, P.; Majewski, J. A.; Levy, M. Generalized Kohn-Sham schemes and the band-gap problem. *Phys. Rev. B* **1996**, *53*, 3764−3774.

(7) Kümmel, S.; Perdew, J. P. Optimized effective potential made simple: orbital functionals, orbital shifts, and the exact Kohn-Sham exchange potential. *Phys. Rev. B* **2003**, *68*, 035103.

(8) Kümmel, S.; Kronik, L. Orbital-dependent density functionals: theory and applications. *Rev. Mod. Phys.* **2008**, *80*, 3−60.

(9) Perdew, J. P.; Parr, R. G.; Levy, M.; Balduz, J. L. Density-functional theory for fractional particle number: derivative discontinuities of the energy. *Phys. Rev. Lett.* **1982**, *49*, 1691−1694.

(10) Almbladh, C.-O.; von Barth, U. Exact results for the charge and spin densities, exchange-correlation potentials, and density-functional eigenvalues. *Phys. Rev. B* **1985**, *31*, 3231−3244.

(11) Baer, R.; Livshits, E.; Salzner, U. Tuned range-separated hybrids in density functional theory. *Annu. Rev. Phys. Chem.* **2010**, *61*, 85−109.

(12) Chong, D. P.; Gritsenko, O. V.; Baerends, E. J. Interpretation of the Kohn−Sham orbital energies as approximate vertical ionization potentials. *J. Chem. Phys.* **2002**, *116*, 1760−1772.

(13) Filippi, C.; Umrigar, C. J.; Gonze, X. Excitation energies from density functional perturbation theory. *J. Chem. Phys.* **1997**, *107*, 9994−10002.

(14) Baerends, E. J.; Gritsenko, O. V.; van Meer, R. The Kohn−Sham gap, the fundamental gap and the optical gap: the physical meaning of occupied and virtual Kohn−Sham orbital energies. *Phys. Chem. Chem. Phys.* **2013**, *15*, 16408.

(15) Kronik, L.; Stein, T.; Refaely-Abramson, S.; Baer, R. Excitation gaps of finite-sized systems from optimally tuned range-separated hybrid functionals. *J. Chem. Theory Comput.* **2012**, *8*, 1515−1531.

(16) Lebeda, T.; Aschebrock, T.; Sun, J.; Leppert, L.; Kümmel, S. Right band gaps for the right reason at low computational cost with a meta-GGA. *Phys. Rev. Mater.* **2023**, *7*, 093803.

(17) Casida, M. E. *Recent Developments and Applications in Density-Functional Theory*; Elsevier: Amsterdam, 1996; pp 391−439.

(18) *Time-Dependent Density Functional Theory*; Marques, M., Ullrich, C., Nogueira, F., Rubio, A., Burke, K., Gross, E., Eds.; Springer: Berlin, 2006.
(19) Tozer, D. Relationship between long-range charge-transfer excitation energy error and integer discontinuity in Kohn−Sham theory. *J. Chem. Phys.* **2003**, *119*, 12697−12699.
(20) Stein, T.; Kronik, L.; Baer, R. Reliable prediction of charge transfer excitations in molecular complexes using time-dependent density functional theory. *J. Am. Chem. Soc.* **2009**, *131*, 2818−2820.
(21) Kümmel, S. Charge-transfer excitations: a challenge for time-dependent density functional theory that has been met. *Adv. Energy Mater.* **2017**, *7*, 1700440.
(22) Kulik, H. J.; Cococcioni, M.; Scherlis, D. A.; Marzari, N. Density functional theory in transition-metal chemistry: a self-consistent Hubbard *U* approach. *Phys. Rev. Lett.* **2006**, *97*, 103001.
(23) Borghi, G.; Park, C.-H.; Nguyen, N. L.; Ferretti, A.; Marzari, N. Variational minimization of orbital-density-dependent functionals. *Phys. Rev. B* **2015**, *91*, 155112.
(24) Su, N. Q.; Mahler, A.; Yang, W. Preserving symmetry and degeneracy in the localized orbital scaling correction approach. *J. Phys. Chem. Lett.* **2020**, *11*, 1528−1535.
(25) Verma, P.; Bartlett, R. J. Increasing the applicability of density functional theory. III. Do consistent Kohn-Sham density functional methods exist? *J. Chem. Phys.* **2012**, *137*, 13410.
(26) Verma, P.; Bartlett, R. J. Increasing the applicability of density functional theory. IV. Consequences of ionization-potential improved exchange-correlation potentials. *J. Chem. Phys.* **2014**, *140*, 18A534.
(27) Stephens, P. J.; Devlin, F. J.; Chabalowski, C. F.; Frisch, M. J. Ab initio calculation of vibrational absorption and circular dichroism spectra using density functional force fields. *J. Phys. Chem.* **1994**, *98*, 11623−11627.
(28) Adamo, C.; Barone, V. Toward reliable density functional methods without adjustable parameters: the PBE0 model. *J. Chem. Phys.* **1999**, *110*, 6158−6170.
(29) Perdew, J. P.; Ernzerhof, M.; Burke, K. Rationale for mixing exact exchange with density functional approximations. *J. Chem. Phys.* **1996**, *105*, 9982−9985.
(30) Sai, N.; Barbara, P. F.; Leung, K. Hole localization in molecular crystals from hybrid density functional theory. *Phys. Rev. Lett.* **2011**, *106*, 226403.
(31) Imamura, Y.; Kobayashi, R.; Nakai, H. Linearity condition for orbital energies in density functional theory (II): application to global hybrid functionals. *Chem. Phys. Lett.* **2011**, *513*, 130−135.
(32) Schmidt, T.; Kraisler, E.; Makmal, A.; Kronik, L.; Kümmel, S. A self-interaction-free local hybrid functional: accurate binding energies vis-à-vis accurate ionization potentials from Kohn-Sham eigenvalues. *J. Chem. Phys.* **2014**, *140*, 18A510.
(33) Burke, K.; Ernzerhof, M.; Perdew, J. P. The adiabatic connection method: a non-empirical hybrid. *Chem. Phys. Lett.* **1997**, *265*, 115−120.
(34) Cruz, F. G.; Lam, K.-C.; Burke, K. Exchange-correlation energy density from virial theorem. *J. Phys. Chem. A* **1998**, *102*, 4911−4917.
(35) Arbuznikov, A. V.; Kaupp, M.; Bahmann, H. From local hybrid functionals to "localized local hybrid" potentials: formalism and thermochemical tests. *J. Chem. Phys.* **2006**, *124*, 204102.
(36) Jaramillo, J.; Scuseria, G. E.; Ernzerhof, M. Local hybrid functionals. *J. Chem. Phys.* **2003**, *118*, 1068−1073.
(37) Mori-Sánchez, P.; Cohen, A. J.; Yang, W. Self-interaction-free exchange-correlation functional for thermochemistry and kinetics. *J. Chem. Phys.* **2006**, *124*, 091102.
(38) Perdew, J. P.; Staroverov, V. N.; Tao, J.; Scuseria, G. E. Density functional with full exact exchange, balanced nonlocality of correlation, and constraint satisfaction. *Phys. Rev. A* **2008**, *78*, 052513.
(39) Arbuznikov, A. V.; Kaupp, M. Local hybrid exchange-correlation functionals based on the dimensionless density gradient. *Chem. Phys. Lett.* **2007**, *440*, 160−168.
(40) Bahmann, H.; Rodenberg, A.; Arbuznikov, A. V.; Kaupp, M. A thermochemically competitive local hybrid functional without gradient corrections. *J. Chem. Phys.* **2007**, *126*, 011103.
(41) Johnson, E. R. Local-hybrid functional based on the correlation length. *J. Chem. Phys.* **2014**, *141*, 124120.
(42) Schmidt, T.; Kümmel, S. One- and many-electron self-interaction error in local and global hybrid functionals. *Phys. Rev. B* **2016**, *93*, 165120.
(43) Haasler, M.; Maier, T. M.; Grotjahn, R.; Gückel, S.; Arbuznikov, A. V.; Kaupp, M. A local hybrid functional with wide applicability and good balance between (de)localization and left−right correlation. *J. Chem. Theory Comput.* **2020**, *16*, 5645−5657.
(44) Arbuznikov, A. V.; Kaupp, M. Towards improved local hybrid functionals by calibration of exchange-energy densities. *J. Chem. Phys.* **2014**, *141*, 204101.
(45) Bahmann, H.; Kaupp, M. Efficient self-consistent implementation of local hybrid functionals. *J. Chem. Theory Comput.* **2015**, *11*, 1540−1548.
(46) Maier, T. M.; Bahmann, H.; Kaupp, M. Efficient seminumerical implementation of global and local hybrid functionals for time-dependent density functional theory. *J. Chem. Theory Comput.* **2015**, *11*, 4226−4237.
(47) Klawohn, S.; Bahmann, H.; Kaupp, M. Implementation of molecular gradients for local hybrid density functionals using seminumerical integration techniques. *J. Chem. Theory Comput.* **2016**, *12*, 4254−4262.
(48) Schmidt, T.; Kraisler, E.; Kronik, L.; Kümmel, S. One-electron self-interaction and the asymptotics of the Kohn−Sham potential: an impaired relation. *Phys. Chem. Chem. Phys.* **2014**, *16*, 14357−14367.
(49) Maier, T. M.; Bahmann, H.; Arbuznikov, A. V.; Kaupp, M. Validation of local hybrid functionals for TDDFT calculations of electronic excitation energies. *J. Chem. Phys.* **2016**, *144*, 074106.
(50) Leininger, T.; Stoll, H.; Werner, H.-J.; Savin, A. Combining long-range configuration interaction with short-range density functionals. *Chem. Phys. Lett.* **1997**, *275*, 151−160.
(51) Savin, A. Models and corrections: range separation for electronic interaction—lessons from density functional theory. *J. Chem. Phys.* **2020**, *153*, 160901.
(52) Heyd, J.; Scuseria, G. E.; Ernzerhof, M. Hybrid functionals based on a screened Coulomb potential. *J. Chem. Phys.* **2003**, *118*, 8207−8215.
(53) Heyd, J.; Scuseria, G. E.; Ernzerhof, M. Erratum: "Hybrid functionals based on a screened Coulomb potential" [J. Chem. Phys. 118, 8207 (2003)]. *J. Chem. Phys.* **2006**, *124*, 219906.
(54) Iikura, H.; Tsuneda, T.; Yanai, T.; Hirao, K. A long-range correction scheme for generalized-gradient-approximation exchange functionals. *J. Chem. Phys.* **2001**, *115*, 3540−3544.
(55) Yanai, T.; Tew, D. P.; Handy, N. C. A new hybrid exchange-correlation functional using the Coulomb-attenuating method (CAM−B3LYP). *Chem. Phys. Lett.* **2004**, *393*, 51−57.
(56) Baer, R.; Neuhauser, D. Density functional theory with correct long-range asymptotic behavior. *Phys. Rev. Lett.* **2005**, *94*, 043002.
(57) Gerber, I. C.; Ángyán, J. G. Hybrid functional with separated range. *Chem. Phys. Lett.* **2005**, *415*, 100−105.
(58) Chai, J.-D.; Head-Gordon, M. Systematic optimization of long-range corrected hybrid density functionals. *J. Chem. Phys.* **2008**, *128*, 084106.
(59) Cohen, A. J.; Mori-Sánchez, P.; Yang, W. Development of exchange-correlation functionals with minimal many-electron self-interaction error. *J. Chem. Phys.* **2007**, *126*, 191109.
(60) Autschbach, J.; Srebro, M. Delocalization error and functional tuning in Kohn-Sham calculations of molecular properties. *Acc. Chem. Res.* **2014**, *47*, 2592−2602.
(61) Kronik, L.; Kümmel, S. Dielectric screening meets optimally tuned density functionals. *Adv. Mater.* **2018**, *30*, 1706560.
(62) Livshits, E.; Baer, R. A well-tempered density functional theory of electrons in molecules. *Phys. Chem. Chem. Phys.* **2007**, *9*, 2932.
(63) Karolewski, A.; Stein, T.; Baer, R.; Kümmel, S. Communication: tailoring the optical gap in light-harvesting molecules. *J. Chem. Phys.* **2011**, *134*, 151101.
(64) Nénon, S.; Champagne, B.; Spassova, M. I. Assessing long-range corrected functionals with physically-adjusted range-separated

https://doi.org/10.1021/acs.jpca.4c02787
J. Phys. Chem. A 2024, 128, 5212−5223

parameters for calculating the polarizability and the second hyperpolarizability of polydiacetylene and polybutatriene chains. *Phys. Chem. Chem. Phys.* **2014**, *16*, 7083−7088.
(65) Oviedo, M. B.; Ilawe, N. V.; Wong, B. M. Polarizabilities of π-conjugated chains revisited: improved results from broken-symmetry range-separated DFT and new CCSD(T) benchmarks. *J. Chem. Theory Comput.* **2016**, *12*, 3593−3602.
(66) Xu, L.; Kumar, A.; Wong, B. M. Linear polarizabilities and second hyperpolarizabilities of streptocyanines: results from broken-symmetry DFT and new CCSD(T) benchmarks. *J. Comput. Chem.* **2018**, *39*, 2350−2359.
(67) Zobel, J. P.; Kruse, A.; Baig, O.; Lochbrunner, S.; Bokarev, S. I.; Kühn, O.; González, L.; Bokareva, O. S. Can range-separated functionals be optimally tuned to predict spectra and excited state dynamics in photoactive iron complexes? *Chem. Sci.* **2023**, *14*, 1491−1502.
(68) Henderson, T. M.; Janesko, B. G.; Scuseria, G. E. Range separation and local hybridization in density functional theory. *J. Phys. Chem. A* **2008**, *112*, 12530−12542.
(69) Kirkpatrick, J.; McMorrow, B.; Turban, D. H. P.; Gaunt, A. L.; Spencer, J. S.; Matthews, A. G. D. G.; Obika, A.; Thiry, L.; Fortunato, M.; Pfau, D.; et al. Pushing the frontiers of density functionals by solving the fractional electron problem. *Science* **2021**, *374*, 1385−1389.
(70) Fürst, S.; Haasler, M.; Grotjahn, R.; Kaupp, M. Full implementation, optimization, and evaluation of a range-separated local hybrid functional with wide accuracy for ground and excited states. *J. Chem. Theory Comput.* **2023**, *19*, 488−502.
(71) Fürst, S.; Kaupp, M. Accurate ionization potentials, electron affinities, and band gaps from the ωLH22t range-separated local hybrid functional: no tuning required. *J. Chem. Theory Comput.* **2023**, *19*, 3146−3158.
(72) Krukau, A. V.; Scuseria, G. E.; Perdew, J. P.; Savin, A. Hybrid functionals with local range separation. *J. Chem. Phys.* **2008**, *129*, 124103.
(73) Aschebrock, T.; Kümmel, S. Exploring local range separation: the role of spin scaling and one-electron self-interaction. *J. Chem. Phys.* **2019**, *151*, 154108.
(74) Klawohn, S.; Bahmann, H. Self-consistent implementation of hybrid functionals with local range separation. *J. Chem. Theory Comput.* **2020**, *16*, 953−963.
(75) Maier, T. M.; Ikabata, Y.; Nakai, H. Assessing locally range-separated hybrid functionals from a gradient expansion of the exchange energy density. *J. Chem. Phys.* **2021**, *154*, 214101.
(76) Brütting, M.; Bahmann, H.; Kümmel, S. Hybrid functionals with local range separation: accurate atomization energies and reaction barrier heights. *J. Chem. Phys.* **2022**, *156*, 104109.
(77) Brütting, M.; Bahmann, H.; Kümmel, S. Predicting fundamental gaps accurately from density functional theory with non-empirical local range separation. *J. Chem. Phys.* **2024**, *160*, 181101.
(78) Perdew, J. P.; Wang, Y. Accurate and simple analytic representation of the electron-gas correlation energy. *Phys. Rev. B* **1992**, *45*, 13244−13249.
(79) Lebeda, T.; Aschebrock, T.; Kümmel, S. First steps towards achieving both ultranonlocality and a reliable description of electronic binding in a meta-generalized gradient approximation. *Phys. Rev. Res.* **2022**, *4*, 023061.
(80) Gill, P. M. W.; Adamson, R. D.; Pople, J. A. Coulomb-attenuated exchange energy density functionals. *Mol. Phys.* **1996**, *88*, 1005−1009.
(81) Lynch, B. J.; Truhlar, D. G. Small representative benchmarks for thermochemical calculations. *J. Phys. Chem. A* **2003**, *107*, 8996−8999.
(82) Mori-Sánchez, P.; Cohen, A. J.; Yang, W. Localization and delocalization errors in density functional theory and implications for band-gap prediction. *Phys. Rev. Lett.* **2008**, *100*, 146401.
(83) Perdew, J. P.; Burke, K.; Ernzerhof, M. Generalized gradient approximation made simple. *Phys. Rev. Lett.* **1996**, *77*, 3865−3868.
(84) Yu, H. S.; He, X.; Li, S. L.; Truhlar, D. G. MN15: a Kohn-Sham global-hybrid exchange-correlation density functional with broad accuracy for multi-reference and single-reference systems and noncovalent interactions. *Chem. Sci.* **2016**, *7*, 5032−5051.
(85) Yu, H. S.; He, X.; Li, S. L.; Truhlar, D. G. Correction: MN15: a Kohn-Sham global-hybrid exchange-correlation density functional with broad accuracy for multi-reference and single-reference systems and noncovalent interactions. *Chem. Sci.* **2016**, *7*, 6278−6279.
(86) We note in passing that we did some tests also for other xc functionals, but we did not include all the data in the article as this would have seriously limited the transparency of our analysis. We note, though, that our results also confirm the observation that any form of range separation, e.g., also the one used in ωB97,[58] helps to reduce the parameter dilemma.
(87) Aschebrock, T.; Lebeda, T.; Brütting, M.; Richter, R.; Schelter, I.; Kümmel, S. Exact exchange-like electric response from a meta-generalized gradient approximation: a semilocal realization of ultranonlocality. *J. Chem. Phys.* **2023**, *159*, 234107.
(88) Franzke, Y. J.; Holzer, C.; Andersen, J. H.; Begušić, T.; Bruder, F.; Coriani, S.; Della Sala, F.; Fabiano, E.; Fedotov, D. A.; Fürst, S.; et al. TURBOMOLE: today and tomorrow. *J. Chem. Theory Comput.* **2023**, *19*, 6859−6890.
(89) Peverati, R.; Truhlar, D. G. Communication: a global hybrid generalized gradient approximation to the exchange-correlation functional that satisfies the second-order density-gradient constraint and has broad applicability in chemistry. *J. Chem. Phys.* **2011**, *135*, 191102.
(90) Peverati, R.; Truhlar, D. G. Quest for a universal density functional: the accuracy of density functionals across a broad spectrum of databases in chemistry and physics. *Philos. Trans. R. Soc., A* **2014**, *372*, 20120476.
(91) Russell, D. J., III NIST computational chemistry comparison and benchmark database *NIST Standard Reference Database Number 101*, 2022. https://cccbdb.nist.gov/expgeom1x.asp.

https://doi.org/10.1021/acs.jpca.4c02787
J. Phys. Chem. A 2024, 128, 5212−5223

Supporting Information for

Combining Local Range Separation and Local Hybrids: A Step in the Quest for Obtaining Good Energies and Eigenvalues from One Functional

The Journal of Physical Chemistry A

Moritz Brütting,[1] Hilke Bahmann,[2] and Stephan Kümmel[1,*]

[1] Theoretical Physics IV, University of Bayreuth, 95440 Bayreuth, Germany
[2] Physical and Theoretical Chemistry, University of Wuppertal, 42097 Wuppertal, Germany
[*] Corresponding author: stephan.kuemmel@uni-bayreuth.de

Contents

S1 Computational details

All calculations have been done using a development version of Turbomole.[1] For the functionals with local range separation we rely on the implementation of Klawohn and Bahmann[2] which we have extended to allow for the space-dependent admixture of exact exchange at short range. Into this framework we have implemented the ωBT21a functional. The ωBT21 functional has been implemented and optimized for AE6BH6 in a previous work.[3] The optimal parameters of the other functional variants are determined similar to the protocol described in that work: In the case of ωBT21a, the parameters are also chosen such that they minimize the equally weighted mean absolute error (MAE) of the AE6 and BH6 test sets. The parameters of ωBT21-IP and ωBT21a-IP are fixed by a condition related to the IP theorem: we minimize the mean absolute deviation between the ionization potential from a Δ SCF calculation and the negative of the HOMO eigenvalue for the molecules in the AE6 test set. On a technical level, we proceed similar as in our previous work: We vary the parameters in steps of 0.001 within a suitable interval around the approximate position of the optimum which has been determined before by using coarser grids. In passing we note that, as in previous works,[3,4] we observe for all functional variants that there is a band of parameter tuples that provide a performance close to the respective optimum.

As in Ref. 3, a def2-TZVP basis set and a convergence threshold of 10^{-6} have been used to perform the Turbomole calculations for the minimization procedure. For the calculations of AE6BH6 and MGAE109 displayed in this manuscript a cc-pVTZ basis set and a convergence threshold of 10^{-7} have been used. The numbers displayed for the IP theorem have been obtained with an aug-cc-pVTZ basis set and a convergence threshold of 10^{-8}. Grid size 3 and the resolution-of-the-identity approximation have been used in all calculations.

The molecular geometries and reference values of the AE6, BH6, and MGAE109 test sets have been taken from the Minnesota database 2.0.[5–7] The geometries of the molecules for which we assess the IP theorem have been taken from the Minnesota database 2.0 as well, where available. Only the geometries of Li_2, LiH, and LiF have been take from the NIST database.[3,8]

S2 Additional data

In the following, we provide the detailed data underlying Table 3 and 5 in the main text. In Table S1 we provide details on the evaluation of the MGAE109 test set and in Table S2 we provide details on the assessment of the IP theorem for a larger set of molecules. Note that both tables extend over several pages and that the tables are divided in several parts where the values for different functionals are displayed.

Table S1: Atomization energies of the MGAE109 test set. The numbers (in kcal/mol) correspond to the difference of the calculated values to the reference values from the Minnesota database 2.0.

	Ref.	HF	PBE	PBE0	MN15
CH	84.23	−27.73	0.05	−1.64	−2.83
CH_2 (1A1)	181.46	−55.18	−3.17	−5.68	−3.79
CH_3	307.88	−65.27	2.01	0.35	−2.25
CH_4	420.43	−92.44	−0.05	−2.55	−2.86
NH	83.10	−32.42	4.49	1.36	−2.40
NH_2	182.59	−66.00	4.46	−0.81	−1.63
NH_3	298.02	−98.47	1.99	−4.64	−2.04
OH	107.22	−39.57	1.13	−2.75	−1.12
H_2O	232.98	−78.62	−1.55	−8.20	−3.41
HF	141.63	−45.74	−1.90	−6.56	−2.09
SiH_2 (3B1)	131.48	−32.29	4.54	4.10	11.38
SiH_2 (1A1)	152.22	−42.74	−4.95	−5.66	1.34
SiH_3	228.01	−49.35	−6.43	−5.47	2.47
SiH_4	324.95	−70.73	−12.68	−11.06	1.25
PH_2	153.20	−45.73	0.37	−1.12	1.32
PH_3	242.27	−71.54	−4.34	−6.21	−0.37
H_2S	183.91	−55.71	−3.02	−5.19	−0.19
HCl	107.50	−31.15	−1.80	−3.22	−0.74
C_2H_2	405.53	−112.71	9.21	−1.51	−2.12
C_2H_4	563.69	−135.94	8.02	−0.02	−2.83
C_2H_6	712.98	−162.00	4.36	−0.72	−4.16
CN	181.36	−91.80	15.98	−3.00	−6.11
HCN	313.43	−115.10	12.72	−2.73	−1.98
CO	259.74	−86.00	9.35	−4.46	−0.78
HCO	279.43	−97.73	15.60	0.66	−1.21
H_2CO	374.67	−118.02	11.12	−2.71	−1.07
CH_3OH	513.54	−145.12	5.40	−4.73	−1.75
N2	228.48	−114.12	14.68	−3.74	−2.63
NH_2NH_2	438.60	−172.39	12.20	−2.44	1.03
NO	152.75	−99.98	19.43	0.26	0.41
O_2	120.83	−87.75	23.12	3.58	0.27
H_2O_2	269.03	−134.63	11.93	−6.61	0.60
F_2	39.03	−3.35	15.11	−3.20	0.83
CO_2	390.16	−144.00	26.67	1.47	2.42
Si_2	76.38	−47.85	3.13	−3.29	−2.74
P_2	117.59	−81.62	2.16	−8.00	−4.68
S_2	104.25	−55.27	8.43	0.18	−1.85
Cl_2	59.75	−42.36	4.24	−1.82	−0.84
SiO	193.06	−86.01	0.63	−13.14	−1.27
SC	171.76	−76.50	6.12	−5.45	−1.65
SO	126.48	−74.78	10.72	−3.23	−3.05
ClO	65.45	−61.53	13.14	−0.73	−1.07

Continued on next page.

Continued from previous page.

ClF	62.79	−56.54	7.73	−3.57	0.64
Si_2H_6	535.89	−121.97	−17.67	−15.37	2.23
CH_3Cl	396.44	−100.57	3.00	−1.63	−2.19
CH_3SH	474.49	−125.14	2.72	−2.48	−0.75
HOCl	166.24	−88.99	7.28	−4.99	−0.37
SO_2	260.63	−163.05	7.45	−19.21	−12.41
$AlCl_3$	312.64	−71.85	−9.46	−10.69	5.02
AlF_3	430.95	−118.45	−9.68	−25.13	−2.41
BCl_3	325.45	−82.64	8.53	2.07	7.68
BF_3	470.96	−108.57	13.42	−2.87	11.40
C_2Cl_4	469.82	−183.86	27.36	6.79	6.09
C_2F_4	591.06	−215.37	42.52	7.16	16.58
C_3H_4 (pro)	705.06	−181.48	15.99	2.45	−1.92
C_4H_4O	994.33	−284.93	37.75	11.33	5.36
C_4H_4S	963.65	−270.23	31.22	10.28	1.33
C_4H_5N	1071.93	−307.27	38.93	14.12	4.43
C_4H_6 (tra)	1012.37	−251.28	22.53	5.48	−3.38
C_4H_6 (yne)	1004.13	−250.99	21.95	5.63	−2.40
C_5H_5N	1238.14	−347.33	47.33	17.25	2.72
CCH	265.31	−80.47	11.58	1.01	−0.96
CCl_4	316.19	−140.01	13.92	−0.82	0.45
CF_3CN	641.17	−239.62	42.73	4.99	10.22
CF_4	477.93	−162.77	28.94	3.29	13.60
CH_2OH	410.08	−121.29	10.71	−0.14	0.34
CH_3CN	616.02	−182.92	19.53	1.47	−1.59
CH_3NH_2	582.31	−166.74	7.50	−2.09	−1.85
CH_3NO_2	601.82	−261.18	39.94	3.20	1.18
$CHCl_3$	345.79	−124.40	10.97	−0.08	−0.10
CHF_3	458.73	−145.58	21.93	1.32	9.16
ClF_3	127.31	−99.93	30.60	−4.53	−3.58
H_2	109.49	−25.74	−4.71	−5.00	−1.23
CH_2CH	446.09	−108.68	11.75	3.40	−2.00
$HCOOCH_3$	785.90	−239.18	25.95	0.46	3.38
HCOOH	501.53	−170.76	20.88	−1.37	2.21
NF_3	205.67	−167.32	39.96	4.35	9.86
PF_3	365.01	−135.89	3.85	−15.74	1.17
SH	87.00	−26.72	0.32	−0.92	1.22
$SiCl_4$	388.73	−109.78	−8.25	−11.71	4.21
SiF_4	576.30	−155.92	−12.80	−29.95	0.18
C_2H_5	603.93	−135.79	8.20	3.29	−2.59
C_4H_6 (bic)	987.56	−259.58	24.52	10.29	1.53
C_4H_6 (cyc)	1001.97	−256.31	22.58	7.52	−2.13
HCOCOH	633.99	−213.33	29.39	0.84	1.23
CH_3CHO	677.44	−187.49	17.21	0.45	−1.39
C_2H_4O	651.11	−191.67	18.71	2.68	2.44
C_2H_5O	699.05	−181.60	14.50	1.75	−2.04
CH_3OCH_3	798.46	−213.06	11.73	−1.87	0.02

Continued on next page.

Continued from previous page.

CH_3CH_2OH	810.77	−215.04	10.10	−2.73	−2.59
C_3H_4 (all)	703.47	−181.57	20.58	5.65	0.02
C_3H_4 (cyc)	683.01	−186.40	18.76	5.50	0.06
CH_3COOH	803.68	−240.57	24.65	0.21	1.06
CH_3COCH_3	978.46	−257.49	22.02	2.73	−1.76
C_3H_6	853.68	−208.68	15.06	5.84	−0.34
CH_3CHCH_2	860.88	−206.37	13.14	2.30	−3.66
C_3H_8	1007.14	−232.29	8.60	0.93	−5.09
$C_2H_5OCH_3$	1095.62	−283.01	16.30	0.07	−0.89
C_4H_{10} (iso)	1303.40	−304.44	11.42	1.21	−6.68
C_4H_{10} (anti)	1301.68	−303.02	12.40	2.17	−6.41
C_4H_8 (cyc)	1149.37	−279.84	18.79	7.23	−2.28
C_4H_8 (iso)	1158.97	−277.92	17.06	3.57	−4.94
C_5H_8	1284.73	−326.32	31.45	14.77	2.60
C_6H_6	1368.10	−344.14	42.04	17.40	−0.63
CH_3CO	581.99	−166.65	21.64	3.78	−1.25
CH_3CHCH_3	901.02	−206.71	13.77	5.76	−3.10
C_4H_9	1199.70	−279.16	17.55	6.58	−4.89
CH_2CO	532.73	−162.44	25.77	5.17	3.17
MAE		146.70	14.53	5.01	2.90
MSE		−146.70	12.64	−0.64	−0.01

		Local range separation			
	ωLH22t	ωBT21	ωBT21a	ωBT21-IP	ωBT21a-IP
CH	−2.04	−0.52	1.40	8.15	14.11
CH_2 (1A1)	−3.91	−1.75	1.41	12.85	24.04
CH_3	−0.77	0.97	3.19	19.96	32.16
CH_4	−0.43	0.75	4.24	25.09	42.28
NH	−0.21	−1.17	1.32	6.53	13.63
NH_2	−1.10	−2.29	1.81	9.52	22.74
NH_3	−1.45	−2.62	2.22	11.29	29.21
OH	−1.64	−1.78	−0.17	−0.98	5.21
H_2O	−4.02	−3.33	−1.14	−3.37	7.08
HF	−3.09	−2.58	−2.19	−6.95	−2.55
SiH_2 (3B1)	9.09	13.21	15.69	32.97	41.09
SiH_2 (1A1)	−1.16	3.43	5.91	22.68	30.64
SiH_3	−2.10	2.31	4.91	29.78	38.22
SiH_4	−2.71	−0.82	3.28	37.48	51.04
PH_2	0.80	6.98	9.29	23.88	31.74
PH_3	−1.68	5.52	8.77	28.55	40.35
H_2S	−2.99	2.38	3.96	11.00	18.11
HCl	−2.10	0.40	0.91	2.18	5.41
C_2H_2	−1.65	−1.40	−0.85	−13.32	3.20
C_2H_4	−0.10	0.43	2.87	7.15	29.73
C_2H_6	−0.12	0.41	4.63	25.96	54.43
CN	−7.90	−7.48	−6.03	−37.36	−26.71

Continued on next page.

Continued from previous page.

HCN	−2.01	−3.06	−0.47	−22.93	−6.37
CO	−2.12	−0.92	−0.31	−30.80	−21.85
HCO	−0.32	0.46	0.81	−25.61	−15.38
H_2CO	−1.02	−0.26	1.31	−17.28	−2.15
CH_3OH	−1.11	−1.39	1.62	0.05	21.47
N2	−2.29	−4.47	0.33	−30.51	−14.30
NH_2NH_2	0.76	−2.60	4.31	1.68	30.35
NO	0.44	0.46	2.87	−32.23	−23.20
O_2	2.33	4.44	4.20	−34.55	−33.16
H_2O_2	−1.68	−0.35	1.66	−25.27	−13.67
F_2	−1.28	0.72	−0.60	−35.45	−38.35
CO_2	0.49	1.06	0.34	−59.85	−45.69
Si_2	−6.24	−0.71	−1.00	−10.26	−7.40
P_2	−3.74	8.60	9.33	−4.63	3.14
S_2	−0.33	2.66	1.81	−18.05	−15.52
Cl_2	−0.98	1.21	0.11	−16.34	−15.98
SiO	−5.68	−5.85	−5.80	−31.80	−23.70
SC	−5.41	0.93	0.98	−21.58	−16.13
SO	−2.33	−2.88	−3.58	−33.87	−30.66
ClO	−1.17	−0.69	−1.12	−28.59	−26.02
ClF	−0.99	−0.75	−2.18	−27.39	−27.06
Si_2H_6	−4.10	−1.38	4.15	50.81	72.02
CH_3Cl	−0.25	0.26	1.88	5.01	19.56
CH_3SH	−0.41	3.08	5.66	14.05	32.56
HOCl	−1.77	−0.81	−0.44	−22.59	−16.27
SO_2	−14.80	−13.96	−14.80	−75.66	−66.43
$AlCl_3$	−2.78	−8.82	−10.78	−30.09	−23.51
AlF_3	−7.66	−21.18	−23.95	−62.44	−47.50
BCl_3	1.01	−0.53	−4.47	−39.63	−33.55
BF_3	4.18	−3.98	−8.93	−61.34	−47.47
C_2Cl_4	2.09	1.42	−4.98	−80.61	−70.05
C_2F_4	7.70	2.27	−5.56	−108.50	−93.46
C_3H_4 (pro)	−0.34	0.20	1.37	−11.35	16.63
C_4H_4O	6.36	3.56	1.81	−59.23	−23.48
C_4H_4S	3.51	4.00	2.20	−47.46	−13.70
C_4H_5N	7.12	3.00	3.52	−46.91	−3.14
C_4H_6 (tra)	0.35	−0.04	1.79	−12.12	27.47
C_4H_6 (yne)	0.31	1.02	2.82	−10.12	29.31
C_5H_5N	6.24	2.36	2.48	−62.90	−12.45
CCH	−3.73	−1.63	−2.69	−21.91	−11.14
CCl_4	−1.44	−2.42	−7.27	−63.71	−58.91
CF_3CN	5.17	−1.76	−5.76	−106.77	−83.85
CF_4	7.38	1.42	−4.86	−87.28	−76.17
CH_2OH	0.40	0.53	2.11	−6.13	10.38
CH_3CN	−0.26	−1.35	1.89	−20.51	7.74
CH_3NH_2	0.00	−1.77	3.80	13.38	42.30
CH_3NO_2	1.65	2.17	4.63	−58.82	−31.66

Continued on next page.

Continued from previous page.

$CHCl_3$	−0.42	−0.74	−3.34	−39.29	−30.88
CHF_3	5.68	0.61	−3.07	−59.39	−46.56
ClF_3	−2.92	−5.39	−10.51	−85.56	−85.60
H_2	−0.79	0.40	2.95	21.56	26.39
CH_2CH	−0.78	0.94	2.00	0.26	17.68
$HCOOCH_3$	3.40	0.29	1.52	−42.20	−11.00
HCOOH	1.24	0.31	0.93	−42.73	−22.75
NF_3	6.67	4.91	3.32	−71.54	−65.67
PF_3	−1.43	−9.30	−12.70	−66.02	−52.81
SH	−0.33	2.98	3.88	7.94	11.65
$SiCl_4$	−3.29	−10.39	−13.79	−48.96	−41.53
SiF_4	−9.29	−25.91	−30.65	−88.24	−68.84
C_2H_5	0.01	1.37	4.30	20.68	44.38
C_4H_6 (bic)	6.89	2.18	3.23	−15.25	21.66
C_4H_6 (cyc)	2.76	0.70	2.16	−13.90	23.42
HCOCOH	0.66	−0.08	0.15	−58.39	−33.83
CH_3CHO	0.30	0.52	2.62	−16.36	10.35
C_2H_4O	4.21	1.38	3.23	−17.86	7.12
C_2H_5O	0.86	−1.82	1.17	−1.76	27.42
CH_3OCH_3	1.54	−0.54	3.05	1.17	33.67
CH_3CH_2OH	−0.35	−1.89	1.68	−0.14	32.78
C_3H_4 (all)	1.45	3.24	4.33	−10.04	17.67
C_3H_4 (cyc)	2.74	1.80	2.63	−13.26	13.03
CH_3COOH	1.52	−0.41	0.73	−43.00	−11.38
CH_3COCH_3	1.41	0.39	2.98	−16.42	21.87
C_3H_6	4.81	2.36	5.01	7.22	40.32
CH_3CHCH_2	0.34	0.44	3.43	7.26	41.17
C_3H_8	0.39	−0.38	4.42	25.67	65.49
$C_2H_5OCH_3$	2.21	−1.01	3.13	1.01	44.98
C_4H_{10} (iso)	−0.01	−2.84	2.41	22.99	74.21
C_4H_{10} (anti)	0.48	−1.58	3.80	24.89	76.06
C_4H_8 (cyc)	4.48	1.00	4.30	6.30	49.87
C_4H_8 (iso)	0.22	−0.87	2.60	5.71	51.01
C_5H_8	10.11	4.95	6.61	−10.94	37.89
C_6H_6	4.46	2.85	1.36	−52.54	−2.02
CH_3CO	1.22	1.42	2.48	−23.54	−1.47
CH_3CHCH_3	0.60	1.37	4.88	20.49	55.69
C_4H_9	−0.03	−0.37	3.63	18.16	64.84
CH_2CO	2.42	4.05	4.11	−33.86	−13.25
MAE	2.57	2.74	4.06	28.96	31.15
MSE	0.03	−0.46	0.47	−18.01	1.41

Table S2: Assessment of the IP theorem for a set of molecules. For each functional and molecule, the first column shows the ionization potential from a ΔSCF calculation, the second column the negative of the HOMO eigenvalue, and the third column their difference. All values are in eV.

	HF			PBE			PBE0		
$C_2H_2O_2$	10.63	12.01	1.37	9.96	6.32	−3.63	10.41	7.91	−2.49
C_2H_2	9.78	11.18	1.40	11.41	7.19	−4.21	11.27	8.43	−2.84
C_2H_4	12.89	10.27	−2.62	10.66	6.77	−3.89	10.48	7.89	−2.60
C_2H_6	11.92	13.24	1.32	11.88	8.14	−3.74	12.21	9.60	−2.61
C_3H_4	8.97	10.47	1.50	10.24	6.52	−3.72	10.24	7.74	−2.50
C_4H_8	10.37	11.83	1.46	10.55	7.22	−3.32	11.03	8.56	−2.46
CH_2OH	7.80	9.25	1.45	8.09	3.87	−4.22	8.25	5.35	−2.90
CH_3CH_2OH	9.48	12.04	2.56	10.20	6.21	−3.99	10.47	7.87	−2.60
CH_3CN	11.62	12.59	0.97	12.13	8.12	−4.01	12.18	9.48	−2.70
CH_3NH_2	8.36	10.64	2.28	9.52	5.41	−4.12	9.55	6.89	−2.66
CH_3OCH_3	8.85	11.56	2.70	9.76	5.88	−3.88	9.90	7.47	−2.43
CH_4	13.32	14.83	1.52	14.12	9.45	−4.67	14.17	10.99	−3.18
Cl_2	11.15	12.15	1.00	11.23	7.36	−3.87	11.50	8.78	−2.72
CO_2	18.41	14.83	−3.58	13.67	9.08	−4.59	13.75	10.72	−3.03
CO	13.08	15.10	2.03	13.86	9.05	−4.82	14.01	10.75	−3.26
F_2	16.05	18.07	2.02	15.30	9.39	−5.91	15.79	11.76	−4.03
H_2O	10.99	13.89	2.90	12.80	7.25	−5.55	12.61	9.09	−3.53
H_2	15.33	16.17	0.84	16.22	10.37	−5.85	16.24	11.99	−4.25
HCN	12.39	13.52	1.13	13.95	9.03	−4.91	13.92	10.41	−3.52
HCOOH	10.00	12.93	2.93	11.31	6.95	−4.36	11.35	8.62	−2.73
HF	14.35	17.71	3.36	16.33	9.66	−6.68	16.11	11.85	−4.26
Li_2	4.35	4.95	0.60	5.26	3.23	−2.03	5.20	3.80	−1.41
LiF	10.00	12.96	2.95	12.29	6.13	−6.15	11.96	7.95	−4.01
LiH	7.00	8.21	1.21	8.05	4.36	−3.69	8.00	5.44	−2.56
N_2	15.65	16.73	1.08	15.40	10.27	−5.12	15.75	12.21	−3.54
NH_2	11.80	12.62	0.83	12.91	7.23	−5.69	12.85	8.78	−4.07
NH_3	9.37	11.67	2.30	10.94	6.16	−4.78	10.81	7.72	−3.09
NO	10.20	11.67	1.47	9.91	4.53	−5.38	10.21	6.45	−3.76
O_2	13.32	15.15	1.83	12.51	6.77	−5.74	12.93	8.98	−3.96
OH	11.38	13.98	2.59	13.30	7.38	−5.91	13.10	9.24	−3.86
PH_2	9.33	10.26	0.93	9.98	6.05	−3.92	10.01	7.26	−2.76
PH_3	9.39	10.53	1.13	10.44	6.67	−3.77	10.44	7.83	−2.61
PH	9.66	10.51	0.86	10.25	6.19	−4.06	10.29	7.42	−2.87
S_2	9.53	10.39	0.86	9.48	5.83	−3.64	9.72	7.13	−2.58
SH	9.18	10.37	1.19	10.40	6.23	−4.17	10.37	7.49	−2.88
SiH_4	11.97	13.24	1.27	12.15	8.53	−3.62	12.45	9.88	−2.57
SiO	10.40	11.90	1.51	11.30	7.47	−3.83	11.41	8.83	−2.58
MAE			1.72			4.47			3.04
MSE			1.38			−4.47			−3.04

Continued on next page.

Continued from previous page.

	MN15			ωLH22t			Local range separation ωBT21		
$C_2H_2O_2$	10.71	8.82	−1.89	10.73	10.30	−0.43	10.59	9.73	−0.86
C_2H_2	11.33	9.17	−2.16	11.34	10.67	−0.67	11.39	10.04	−1.35
C_2H_4	10.55	8.61	−1.94	10.54	10.06	−0.48	10.60	9.51	−1.10
C_2H_6	12.38	10.34	−2.04	12.45	12.10	−0.35	12.26	11.04	−1.22
C_3H_4	10.33	8.46	−1.87	10.37	9.95	−0.41	10.36	9.29	−1.07
C_4H_8	10.87	9.28	−1.59	10.82	10.64	−0.19	10.78	9.76	−1.01
CH_2OH	8.13	5.89	−2.24	8.11	7.47	−0.64	8.15	7.09	−1.06
CH_3CH_2OH	10.69	8.79	−1.89	10.68	10.34	−0.34	10.60	9.75	−0.85
CH_3CN	12.26	10.24	−2.02	12.35	11.78	−0.57	12.32	11.18	−1.14
CH_3NH_2	9.73	7.77	−1.97	9.68	9.28	−0.40	9.73	8.63	−1.10
CH_3OCH_3	10.09	8.36	−1.73	10.07	9.86	−0.21	10.02	9.34	−0.69
CH_4	14.37	11.75	−2.62	14.28	13.55	−0.72	14.36	12.44	−1.91
Cl_2	11.74	9.63	−2.11	11.67	11.08	−0.60	11.63	10.36	−1.27
CO_2	13.88	11.57	−2.31	13.93	13.09	−0.84	13.93	12.75	−1.19
CO	14.11	11.64	−2.47	14.29	13.47	−0.82	14.13	12.49	−1.64
F_2	16.09	12.89	−3.21	16.08	14.55	−1.53	15.92	14.35	−1.57
H_2O	12.78	10.11	−2.68	12.74	11.64	−1.10	12.78	11.23	−1.55
H_2	16.66	12.82	−3.85	16.32	15.36	−0.95	16.46	13.80	−2.66
HCN	13.88	11.18	−2.70	14.07	12.73	−1.35	14.11	12.19	−1.92
HCOOH	11.54	9.57	−1.97	11.52	11.06	−0.46	11.52	10.60	−0.92
HF	16.29	12.91	−3.37	16.28	14.55	−1.73	16.25	14.35	−1.90
Li_2	5.50	3.95	−1.55	5.15	5.24	0.09	5.12	4.41	−0.71
LiF	12.04	8.92	−3.12	12.10	10.56	−1.55	12.04	10.27	−1.77
LiH	8.13	6.07	−2.06	8.02	7.98	−0.04	8.11	6.80	−1.31
N_2	15.97	13.17	−2.80	16.08	14.90	−1.18	16.00	14.08	−1.92
NH_2	12.58	9.66	−2.93	12.63	11.30	−1.33	12.72	10.80	−1.91
NH_3	10.95	8.63	−2.33	10.91	10.17	−0.74	10.95	9.55	−1.40
NO	10.09	7.17	−2.92	10.22	8.91	−1.31	10.06	8.41	−1.65
O_2	12.86	9.77	−3.09	13.00	11.50	−1.51	12.78	11.12	−1.67
OH	13.32	10.32	−3.00	13.19	11.89	−1.30	13.11	11.60	−1.51
PH_2	9.95	7.60	−2.34	9.85	9.24	−0.61	9.88	8.55	−1.34
PH_3	10.53	8.51	−2.02	10.51	10.06	−0.45	10.56	9.23	−1.33
PH	10.23	7.80	−2.43	10.14	9.44	−0.70	10.16	8.80	−1.36
S_2	9.70	7.68	−2.02	9.73	9.22	−0.51	9.57	8.36	−1.20
SH	10.48	8.25	−2.23	10.45	9.75	−0.70	10.55	9.15	−1.41
SiH_4	12.68	10.61	−2.07	12.78	12.52	−0.26	12.55	11.24	−1.31
SiO	11.52	9.53	−2.00	11.57	11.09	−0.47	11.66	10.45	−1.21
MAE			2.37			0.74			1.38
MSE			−2.37			−0.74			−1.38

	Local range separation ωBT21a			ωBT21-IP			ωBT21a-IP		
$C_2H_2O_2$	10.61	9.78	−0.83	11.18	11.28	0.10	11.50	11.65	0.15
C_2H_2	11.39	10.09	−1.30	11.25	11.24	−0.01	11.39	11.39	0.00

Continued on next page.

Continued from previous page.

C_2H_4	10.60	9.55	−1.05	10.42	10.60	0.17	10.55	10.71	0.16
C_2H_6	12.31	11.13	−1.18	12.86	12.63	−0.23	13.11	12.91	−0.20
C_3H_4	10.37	9.34	−1.03	10.36	10.49	0.14	10.50	10.65	0.15
C_4H_8	10.79	9.81	−0.98	11.05	11.05	0.00	12.12	11.24	−0.88
CH_2OH	8.11	7.10	−1.00	8.38	8.57	0.19	8.47	8.73	0.26
CH_3CH_2OH	10.64	9.83	−0.81	10.91	11.45	0.54	11.11	11.80	0.69
CH_3CN	12.32	11.23	−1.09	12.31	12.49	0.18	12.46	12.71	0.24
CH_3NH_2	9.76	8.71	−1.05	9.85	10.22	0.37	10.03	10.50	0.47
CH_3OCH_3	10.05	9.41	−0.64	10.26	10.99	0.73	10.45	11.34	0.89
CH_4	14.40	12.54	−1.85	14.64	14.11	−0.53	14.85	14.40	−0.45
Cl_2	11.64	10.42	−1.22	12.01	11.76	−0.25	12.22	12.00	−0.22
CO_2	13.94	12.79	−1.14	13.98	14.29	0.31	14.23	14.70	0.47
CO	14.21	12.60	−1.62	14.65	14.39	−0.26	14.99	14.79	−0.20
F_2	15.95	14.43	−1.52	16.61	16.78	0.18	17.11	17.50	0.39
H_2O	12.80	11.31	−1.49	12.62	13.15	0.53	12.83	13.56	0.73
H_2	16.57	13.96	−2.61	17.38	15.82	−1.56	17.59	16.16	−1.42
HCN	14.17	12.23	−1.94	14.30	13.50	−0.80	14.54	13.69	−0.84
HCOOH	11.52	10.65	−0.87	11.48	12.25	0.77	11.69	12.64	0.95
HF	16.26	14.44	−1.82	16.01	16.64	0.63	16.28	17.23	0.95
Li_2	5.15	4.44	−0.71	5.47	5.03	−0.44	5.53	5.05	−0.49
LiF	12.02	10.33	−1.69	11.58	12.12	0.54	11.84	12.64	0.80
LiH	8.17	6.88	−1.29	8.71	8.14	−0.57	8.88	8.34	−0.54
N_2	16.04	14.16	−1.88	16.58	16.05	−0.52	16.89	16.49	−0.40
NH_2	12.64	10.92	−1.72	12.68	12.51	−0.16	12.69	12.85	0.16
NH_3	10.98	9.63	−1.35	10.94	11.22	0.27	11.14	11.52	0.38
NO	10.02	8.43	−1.59	10.45	10.38	−0.07	10.74	10.77	0.03
O_2	12.74	11.14	−1.60	13.35	13.41	0.06	13.69	13.89	0.19
OH	13.18	11.70	−1.48	13.08	13.59	0.51	13.43	14.06	0.63
PH_2	9.86	8.59	−1.27	9.96	9.68	−0.28	9.95	9.74	−0.21
PH_3	10.59	9.30	−1.29	10.70	10.45	−0.24	10.88	10.62	−0.26
PH	10.14	8.84	−1.30	10.22	9.88	−0.35	10.21	9.94	−0.26
S_2	9.56	8.41	−1.16	9.91	9.65	−0.26	10.03	9.80	−0.23
SH	10.58	9.21	−1.37	10.69	10.45	−0.23	10.88	10.61	−0.27
SiH_4	12.61	11.34	−1.27	13.19	12.82	−0.37	13.41	13.08	−0.34
SiO	11.67	10.50	−1.17	11.79	11.70	−0.08	11.92	11.92	0.00
MAE			1.33			0.36			0.43
MSE			−1.33			−0.03			0.04

Author contribution statement

M. B. and S. K. conceptualized the work with support from H. B. M. B. wrote the required routines in Turbomole with help from H. B. M. B. did all the calculations, and prepared all the figures and tables. S. K. wrote the first version of the manuscript with support from M. B. All authors discussed the results and the final version of the manuscript.

References

(1) Franzke, Y. J.; Holzer, C.; Andersen, J. H.; Begušić, T.; Bruder, F.; Coriani, S.; Sala, F. D.; Fabiano, E.; Fedotov, D. A.; Fürst, S., et al. TURBOMOLE: Today and Tomorrow. *J. Chem. Theory Comput.* **2023**, *19*, 6859–6890.

(2) Klawohn, S.; Bahmann, H. Self-Consistent Implementation of Hybrid Functionals with Local Range Separation. *J. Chem. Theory Comput.* **2020**, *16*, 953–963.

(3) Brütting, M.; Bahmann, H.; Kümmel, S. Hybrid functionals with local range separation: Accurate atomization energies and reaction barrier heights. *J. Chem. Phys.* **2022**, *156*, 104109.

(4) Aschebrock, T.; Kümmel, S. Exploring local range separation: The role of spin scaling and one-electron self-interaction. *J. Chem. Phys.* **2019**, *151*, 154108.

(5) Lynch, B. J.; Truhlar, D. G. Small Representative Benchmarks for Thermochemical Calculations. *J. Phys. Chem. A* **2003**, *107*, 8996–8999.

(6) Peverati, R.; Truhlar, D. G. Communication: A global hybrid generalized gradient approximation to the exchange-correlation functional that satisfies the second-order density-gradient constraint and has broad applicability in chemistry. *J. Chem. Phys.* **2011**, *135*, 191102.

(7) Peverati, R.; Truhlar, D. G. Quest for a universal density functional: the accuracy of density functionals across a broad spectrum of databases in chemistry and physics. *Philos. Trans. R. Soc. A: Math. Phys. Eng. Sci.* **2014**, *372*, 20120476.

(8) Russell D. Johnson III NIST Computational Chemistry Comparison and Benchmark Database, NIST Standard Reference Database Number 101, last visited on 05/31/2024, 2022.

Postface

Danksagungen

Zunächst möchte ich mich bei Hilke Bahmann und Johannes M. Foerster bedanken, die mit ihrer fachlichen Expertise eine sehr wertvolle Hilfe in Teilbereichen dieses Projekts aber auch darüber hinaus waren. Auch die Zusammenarbeit bei der Erstellung der Publikationen verlief jedes Mal sehr angenehm und reibungslos.

Ich möchte Kieron Burke dafür danken, dass er mir im Rahmen eines Forschungsaufenthalts an der University of California, Irvine, den ich während meiner Promotion absolvierte, eine neue Sichtweise auf einige Aspekte der Dichtefunktionaltheorie aufgezeigt hat.

Ich möchte mich auch bei Markus, Bettina, Christina und Monika Birkelbach für ihre unschätzbare Hilfe bei Problemen verschiedener Art bedanken.

Bedanken möchte ich auch bei allen Mitgliedern der Arbeitsgruppe TPIV für die freundschaftliche Atmosphäre und Hilfsbereitschaft. Besonderer Dank geht an dieser Stelle an Tom, Timo und Sophie für wertvolle Diskussionen zu Lichtsammelkomplexen bzw. zur Entwicklung von Dichtefunktionalen und für Korrekturhinweise zu diesem Manuskript.

Mein ganz besonderer Dank gilt Stephan Kümmel. Die Zusammenarbeit insgesamt und die Betreuung dieses Projekts im Besonderen empfand und empfinde ich als außerordentlich positiv. Die zahlreichen Gespräche waren nicht nur in fachlicher Hinsicht, sondern auch weit darüber hinaus extrem hilfreich und bereichernd. Auch für die große Freiheit und Eigenständigkeit, die ich in meiner gesamten Arbeit habe, bin ich sehr dankbar.

Besonders danken möchte ich auch Nancy, Felix, Tom und Bianca, die mich durch Studium und Promotion begleitet haben. Tom verdient besonderen Dank auch dafür, dass er es seit mittlerweile fast sieben Jahren während Bachelorarbeit, Masterarbeit und Promotion mit mir zusammen im Büro ausgehalten hat.

Abschließend möchte ich mich ganz besonders bei meiner Familie bedanken, die mich immer uneingeschränkt auf meinem Weg unterstützt hat.

Während meiner Promotion wurde ich durch ein Promotionsstipendium der Studienstiftung des Deutschen Volkes und im Rahmen des Elitestudienprogramms Biological Physics im Elitenetzwerk Bayern gefördert.

Eidesstattliche Versicherung

Hiermit versichere ich an Eides statt, dass ich die vorliegende Arbeit selbstständig verfasst und keine anderen als die von mir angegebenen Quellen und Hilfsmittel verwendet habe.

Weiterhin erkläre ich, dass ich die Hilfe von gewerblichen Promotionsberatern bzw. -vermittlern oder ähnlichen Dienstleistern weder bisher in Anspruch genommen habe, noch künftig in Anspruch nehmen werde.

Zusätzlich erkläre ich hiermit, dass ich keinerlei frühere Promotionsversuche unternommen habe.

Bayreuth, den 23. Mai 2025

Moritz Brütting